



Università degli Studi di Ferrara

DOTTORATO DI RICERCA IN "SCIENZE DELL'INGEGNERIA"

CICLO XXVIII

COORDINATORE Prof. Trillo Stefano

Investigation on welding and corrosion properties of
the UNS S32304 & UNS S32570 duplex stainless steels
and development of Nickel-Tungsten Carbide hardfacing by
Plasma Transferred Arc (PTA) process

Settore Scientifico Disciplinare ING-IND/21

Dottorando

Dott. Tahaei Ali

(firma)

Tutore

Prof. Garagnani Gian Luca

(firma)

Anni 2013/2015

In the name of Almighty

To my endlessly loving parents

Preface

This dissertation is the result of three years full time PhD research study at the Engineering Department (ENDIF) of the University of Ferrara in Italy from January 2013 to December 2015 under supervision of Professor Gian Luca Garagnani as a main supervisor and Dr Ing. Mattia Merlin and Professor Felipe Arturo Reytez Valdez as co-supervisors. The project was performed in collaboration with Corporacion Mexicana de Investigacion en Materiales (COMIMSA) and Centro de Investigacion en Materiales Avanzados (Cimav) both in Mexico for this reason I stayed in Mexico for a period of six months.

During the PhD period, I was involved with the following: heat treatment of duplex stainless steels for observation of intermetallic phases, laser and friction stir welding of stainless steels, hardfacing methods specially with plasma transferred arc process, heat treatment and mechanical properties of the aluminum alloys, shape memory alloys (development of nickel-titanium alloys for producing one way and training for two ways shape memory effects), metallography and characterization of different types of steel, materials selection for different applications, addition of different types of nanoparticles to the commercial powders for hardfacing and welding of stainless steels with plasma transferred arc process. I was also involved in co-supervision of nine bachelor and master degree thesis in matters relating to aluminium alloys, shape memory alloy (nickel-titanium), copper alloys, cutting by Electro Discharge Machine (EDM), dual phase, trip and tool steels.

Moreover, for characterization of materials, I dealt with different kinds of sample preparations and metallography, using optical microscope and relevant image analyser softwares for acquiring the images, hardness test, stereomicroscope, scanning electron microscope, EDS analysis, laser welding equipped with robot, Gas tungsten arc welding, plasma transferred arc equipment, Differential Thermal Analysis (DTA), nanoindentation, X-ray diffraction, wear test (pin-on-disk) and 3D optical profilometer. Also, during that period I worked as teaching and research assistant on different courses and industrial projects.

The main activities of my thesis consist of two main parts, in first part I worked on the development of Gas tungsten arc welding and corrosion resistance quality of duplex (UNS S32304) and super duplex (UNS S32570) stainless steel by addition of nickel powder, nitrogen gas, post weld heat treatment using combination of methods. The aim of this part was to observe which method is appropriate to reach optimum welding and corrosion properties. In the second part I studied surface quality improvement of the tool steel by using nickel base powders reinforced by tungsten carbide in both micro and nano size.

These two main parts are divided into six chapters, in the first chapter I explained back ground theory and literature review about properties of duplex stainless steels and recent research done to improve the welding quality of duplex stainless steels. This part is an introduction to two chapters which follow. In chapter two, I explained details regarding experimental procedure and obtained results for the welding quality improvement of both duplex and super duplex stainless steel after addition of alloying elements and post weld heat treatment.

Chapter three, focuses on the experimental tests and procedure of pitting corrosion resistance of the duplex stainless steel (UNS S32304), I have explained all details regarding electrochemical tests and I have calculated pitting corrosion resistance number in different conditions for different phases to find a relation between this value and obtained pitting potential.

Part two of the thesis which relates to hardfacing by plasma transferred arc welding consists of three chapters. In chapter four I have explained some basic principles relating to hardfacing in particular, PTA process and material and powder characterization. I have also, briefly explained the specification and procedure of using different equipments for material and surface characterization. In chapter five, I focused on development of the mathematical model to find the optimum process parameters to reach appropriate hardface layer on the surface of tool steel. In chapter six, I used the optimum hardfacing process parameters and I added tungsten carbide nanoparticles in different percentage to the existing industrial nickel base woka powder. Different characterizations were performed on the samples to find optimum percentage of nanoparticles.

In addition, with obtained results I have prepared the following papers for International conferences and journals.

A. Tahaei, A. F.Miranda Perez, M. Merlin, F.A Reyes Valdez, G.L.Garagnani ,**Effect of addition of nickel alloy and post weld heat treatment on the properties of duplex stainless steels**, 5th International Congress in Welding, Industrial Engineering & Manufacturing (WIEM), 4-6 Nov. 2015, Saltillo, Mexico.

B. A.Tahaei, F.Garcia Vzque, M.Merlin, A.Arizmendi, F.Reyes Valdez G.L.Garagnani, **Metallurgical characterization of a weld bead coating applied by PTA process on the D2 tool steel**, 5th International Congress in Welding, Industrial Engineering & Manufacturing (WIEM), 4-6 Nov. 2015, Saltillo, Mexico.

C. A. Tahaei, A. F.Miranda Perez, M. Merlin, F.A Reyes Valdez, G.L.Garagnani, **Effect of nickel powder addition and post weld heat treatment on the metallurgical and mechanical properties of welded UNS S 32304 duplex stainless steel**. Submitted to International Journal Soldagem & Inspecao.

D. A.Tahaei, F.Garcia, M.Merlin, A.Arizmendi, F.Reyes Valdez G.L.Garagnani, **Metallurgical characterization of a weld bead coating applied by PTA process on the D2 tool steel**. Submitted to International Journal Soldagem & Inspecao.

E. Ali Tahaei, Paul Horley, Mattia Merlin, David Torres-Torres, Gian Luca Garagnania, Rolando Praga, Felipe J. Garcia Vazquez, Ana Arizmendi-Morquecho, **Optimization and characterization of Ni-WC composite weld matrix deposited by plasma-transferred arc process**, submitted to the Journal of Alloys and Compounds.

F. A. Tahaei, A.F. Miranda Perez, G.Y. Perez Medina, M. Merlin, F.A. Reyes Valdes, G.L. Garagnani, **Effect of Nickel, Nitrogen and Heat Treatment on Properties of the Welded UNS S32304 Duplex Stainless Steel**, in the final step for submission

G. A. Tahaei, F. Zanotto, V.Grassi, M.Merlin, G.L. Garagnani, F. Zucchi, **Pitting corrosion resistance of welded UNS S32304 duplex stainless steels after addition of nickel and nitrogen followed by PWHT**, in the final step for submission

Ali Tahaei
March 2016
Ferrara- Italy

Acknowledgements

There are a large number of people who directly and indirectly have contributed to this research project. It was a great opportunity for me to have support from many high skilled professors, researchers, colleagues and friends during this study without whom it would not have been possible to carry out the thesis.

I would like to express my deepest gratitude to the following people and institutions, who helped me during my past study and through the course of this PhD thesis.

This PhD project is financially supported by the Engineering Department of the University of Ferrara (ENDIF), IUSS 1391 in Italy, COMIMSA and Cimav in Mexico by the Mexican National Council of Science and Technology (CONACYT).

First of all thanks to my parents for their love, support and constant encouragements. during the entire period of study I hope they are satisfied with this work because it was them who made it all possible. Special thanks to my great supervisor Prof. Gian Luca Garagnani for offering this PhD project to me and his constant support, patience and excellent guidance in different steps of the doctoral study. Many thanks to Dr. Ing Mattia Merlin my second supervisor for everyday support and guidance during all parts of the thesis. Many thanks also to Prof. Felipe Arturo Reyez Valdez for offering a collaborating project about duplex stainless steel with Comimsa and Dr Ana Arizmendi Morquecho for her support, guidance and offering the research project of hardfacing by Plasma Transferred arc welding and special support to perform experiments in Cimav. In addition I wish to say thank you to the following persons.

Dr Chiara Soffritti for her guidance in using scanning electron microscopy and optical profilometer, Professor Vincenzo Gabrielli for his constant support during experimental analysis.

Dr Argelia Miranda Perez and Dr Gladys Perez Medina from Comimsa for their support in part of the welding of duplex and superduplex stainless steel. Dr Felipe Garcia Vazquez from Comimsa for his support in hardfacing project. Dr Rolando Praga from comimsa and Dr Paul Horley from Cimav for their support in part of mathematical modelling and design of experiment.

Prof. Fabrizio Zucchi, Prof. Cecilia Monticelli, Prof. Alessandro Frignani, Dr Federica Zanotto, Dr. Andrea Balbo and Dr Vincenzo Grassi from Corrosion and Metallurgical research center "Aldo Dacco" for their continue support and sharing their valuable experience and useful advice and introducing corrosion science to me.

Prof. Bertolasi and Mr Gabriele Bertocchi for their patience and support for X-ray diffraction analysis of different materials. Eng. Franco Bosi and Mr Roberto Mazza from the workshop of Engineering department for their experimental support. Prof. Alison Milne for English editing and useful suggestions for the thesis.

My kind officemates (N.026 piano verde) Marco Bortoloni, Annalisa Fortini, Dr. Agnese Mattarelli, Dr. Fabio Minghini, Elettra Fabbri and Hilal Bahlevan.

Special thanks to my supervisors during bachelor and master degree, Prof. Abbas Honarbaksh (University of Semnan), Prof. Mir Mostafa Hosseinioun (I.A Univesity Science and reseach branch-Tehran), Prof. Ali Asghar Akbari Mousavi (University of Tehran), Prof. Hongbiao Dong and Prof. Helen Atkinson (University of Leicester, UK). Eng. Ghasemi, Eng. Cheraghzadeh and Eng. Dorpoush from Mavadkaran Engineering company for their kind support.

Abstract

Duplex stainless steels show high mechanical strength, corrosion resistance and toughness with respect to ferritic, austenitic and martensitic stainless steels. These favourable properties are largely conferred by the peculiar microstructure of the material, which contains roughly equal percentage of ferrite (δ) and austenite (γ). Austenite is responsible for toughness and corrosion resistance and ferrite provides high strength; thanks to this combination, duplex stainless steel has many advantages over monophase stainless steels. This makes them better able to withstand harsher conditions, and therefore they are more applicable in different sectors such as the food, petrochemical, oil and gas, marine and power industries. As it is clear, welding is the main method for fabrication of steel structures, which cause to change the base metal properties on that zone. In fusion zone, due to melting, the balance between ferrite and austenite is destroyed and the risk of precipitation of intermetallic phases increase. Different welding methods can be applied to duplex stainless steels for the production of several equipments and structures. Nevertheless, fusion welding processes, due to intrinsic properties, cause to destroy the equal percentage of ferrite and austenite phases in the fusion zone, which is responsible for their good engineering properties. In this study I tried to use different methods to solve these problems especially for the duplex UNS S32304 and superduplex UNS S32570. Due to that, effect of addition of nickel powder, nitrogen gas, post weld heat treatment (PWHT) and combination of these methods were applied. After that, the joints were characterized by optical microscopy (OM) and the evolution of the phase percentages in the different zones was studied by means of the image analysis technique. Tensile and microhardness tests were carried out on the joints in order to evaluate the improvement of the mechanical properties. In addition electrochemical tests were applied on the samples to observe the corrosion resistance of the joints after modifications. The results showed that both the addition of nickel powder and nitrogen gas during the welding process cause to improve the welding characteristics but the effect of applying PWHT is better than addition of alloying elements especially in restoring the phase percentages close to the base metal.

In another part of the thesis, a nickel-base powder mixed with tungsten carbide particles was applied by Plasma Transferred Arc welding (PTA) on the surface of the D2 cold work tool steel in order to improve the surface quality and to extend its life time during industrial applications. To obtain appropriate combination of hardfacing parameters and to run minimum number of tests, the Design of Experiment (DoE) method was applied. Current, travel speed and preheat were considered as variable parameters. These parameters are important to reach a final layer with an appropriate bead geometry, accompanied with good metallurgical properties. All samples were prepared for metallurgical investigations and effects of process parameters on the weld bead geometry were considered. For each run of experiment, weld bead geometry parameters including dilution, penetration and reinforcement were measured. Microstructures and the distribution of tungsten carbide particles after welding were analysed by Optical Microscopy (OM) and Scanning Electron Microscopy (SEM) equipped with EDS microprobe. In addition, microhardness tests were performed to evaluate the mechanical properties of the weld bead layers. Finally, among all the experiments, the best sample with appropriate bead geometry and microstructure was selected. In the last part, I tried to study the effect of addition of tungsten carbide nanoparticles on the mechanical and metallurgical behavior of the existing nickel powder. For these samples, in addition to the above tests mentioned, wear test and surface profilometry analysis was performed for comparison and selecting optimum percentage of the addition of nanoparticles. Details of each experiments and methods are explained in the abstract of each chapter separately.

Keywords: Duplex stainless steel, Welding, Corrosion, Nickel powder, Hardfacing, tungsten carbide nanoparticles, plasma transferred arc (PTA) process

Sommario

Gli acciai inossidabili duplex presentano proprietà meccaniche, resistenza alla corrosione e tenacità superiori rispetto agli acciai inossidabili ferritici, austenitici e martensitici. L'ottimo bilanciamento delle loro proprietà è dovuto alla particolare microstruttura che è costituita da percentuali pressoché uguali di ferrite (δ) e di austenite (γ). L'austenite è responsabile della resistenza a corrosione e della tenacità, la ferrite fornisce l'elevata resistenza meccanica; grazie a questa combinazione di proprietà l'acciaio inossidabile duplex offre molti vantaggi rispetto agli acciai inossidabili monofasici. Gli acciai duplex possono sopportare condizioni di esercizio più gravose e possono essere utilizzati in svariati settori industriali come l'alimentare, il petrolchimico, l'oil & gas, la trasmissione di potenza ed in ambiente marino.

La saldatura è il principale metodo per la fabbricazione delle strutture in acciaio inossidabile e molteplici sono i processi che possono essere utilizzati a tale scopo. Tuttavia, la saldatura determina inevitabilmente un cambiamento delle proprietà del materiale base nella zona interessata dall'alterazione microstrutturale. Nella zona di saldatura si può assistere alla perdita del giusto bilanciamento delle due principali fasi, nonché si può verificare la precipitazione di fasi intermetalliche complesse.

I processi di saldatura applicabili agli acciai inossidabili duplex possono essere molteplici; in questo lavoro sono stati studiati gli effetti prodotti da alcune varianti del tradizionale processo TIG sulla saldatura dell'acciaio duplex UNS S32304 e dell'acciaio superduplex UNS S32570.

In particolare, sono stati considerati gli effetti dell'aggiunta di polveri di nichel, dell'utilizzo di azoto come gas di processo e dell'esecuzione di uno specifico trattamento termico a valle della realizzazione dei giunti saldati.

È stata successivamente effettuata una caratterizzazione microstrutturale al microscopio ottico metallografico (MO) e sono state utilizzate tecniche di analisi di immagine al fine di studiare l'evoluzione delle percentuali di fase nelle diverse zone dei giunti. Prove di trazione e prove di microdurezza hanno consentito di valutare i miglioramenti ottenuti sulle proprietà meccaniche. Inoltre, su campioni ricavati dai giunti stessi sono state eseguite prove elettrochimiche per studiare la resistenza a corrosione al variare delle condizioni di processo e del trattamento termico.

I risultati ottenuti mostrano che, sia l'aggiunta delle polveri di nichel, sia l'utilizzo dell'azoto come gas di processo determinano un incremento delle proprietà meccaniche e microstrutturali dei giunti. Risulta tuttavia che il processo che consente il miglior incremento prestazionale è l'esecuzione del trattamento termico post saldatura, in quanto tende a ripristinare le percentuali delle fasi ferritica e austenitica a livelli confrontabili con quelli del metallo base.

Nella seconda parte della tesi sono state studiate le proprietà di un riporto a base di polveri di nichel e particelle di carburo di tungsteno applicato mediante processo PTA (Plasma Transferred Arc) sulla superficie dell'acciaio da utensili D2, adatto per lavorazioni a freddo. Con un riporto superficiale di tale tipologia è possibile incrementare sia la qualità dell'acciaio sia aumentare la sua vita in esercizio in molte applicazioni industriali.

Per ottenere una appropriata combinazione dei parametri di processo e per eseguire il numero minimo di prove, è stato utilizzato la metodologia DoE (Design of Experiment). Come parametri variabili sono stati considerati la corrente, la velocità di avanzamento e il preriscaldamento. Questi parametri sono importanti per ottenere un riporto finale con una appropriata geometria del cordone di saldatura e con buone proprietà metallurgiche.

Tutti i campioni sono stati preparati per le necessarie caratterizzazioni metallografiche ed è stato considerato l'effetto dei parametri di processo sulla geometria del cordone di saldatura.

Nel corso di ciascun esperimento sono stati misurati i parametri della geometria del cordone tra cui la diluizione, la penetrazione e il rinforzo.

Le microstrutture e la distribuzione delle particelle di carburo di tungsteno sono stati analizzati sia al microscopio ottico metallografico (OM) sia al microscopio elettronico a scansione (SEM) dotato di microsonda EDS. Inoltre, sono state eseguite prove di microdurezza per valutare le proprietà meccaniche dei riporti realizzati. Infine, fra tutti gli esperimenti, è stato selezionato il campione con l'appropriata geometria del cordone e l'adeguata microstruttura.

Nell'ultima parte della tesi si è cercato di valutare l'effetto dell'aggiunta di nanoparticelle di carburo di tungsteno sul comportamento meccanico e metallurgico dell'esistente polvere di nichel.

Per questi campioni, in aggiunta a quelli sopra menzionati, sono stati eseguiti test di usura ed analisi mediante profilometro sulla superficie, al fine di confrontare e selezionare l'ottima percentuale di aggiunta di nanoparticelle.

I dettagli degli esperimenti e dei metodi sono descritti negli abstracts relativi a ciascun capitolo.

Parole chiave: Acciaio inossidabile duplex, saldatura, corrosione, polvere di nichel, riporto, nanoparticelle di carburo di tungsteno, processo PTA (Plasma Transferred Arc)

Abbreviations

Ar: Argon

ASTM: American Society for Testing and Materials

B.M: Base Metal

D2: Type of Tool steel

DOE: Design of Experiment

DSS: Duplex stainless steel

EDS: Energy Dispersive Spectroscopy

F.Z: Fusion Zone

GBA: Grain Boundary Austenite

GTAW: Gas Tungsten Arc Welding

HAZ: Heat Affected Zone

HRC: Hardness Rockwell C

HV: Vickers Hardness

IGA: Intergranular Austenite

N₂: Nitrogen

Ni: Nickel

NiCrBSi: Nickel-Chrome-Boron-Silicon

NP: Nano-particles

O₂: Oxygen

OM: Optical Microscopy

PAW: Plasma Arc Welding

PTA: Plasma Transferred Arc process

PWHT: Post Weld Heat Treatment

RT: Room Temperature

SCE: Saturated Calomel Electrode

SDSS: Superduplex Stainless steel

SEM : Scanning Electron Microscopy

TEM: Transmission Electron Microscopy

TIG: Tungsten Inert Gas

VC: Vanadium Carbide

WD: Widmanstätten Austenite

WC: Tungsten Carbide

Table of contents

Preface	iii
Acknowledgements	vii
Abstract	ix
Sommario	xi
Abbreviations	xiii
Table of contents	xv
Chapter 1: Literature review of duplex stainless steels: welding and corrosion properties	1
Abstract	3
1.1. Brief history of stainless steel	5
1.2. Different types of stainless steels	5
1.3. Effect of Alloying elements on properties of duplex stainless steels	11
1.4. Some problems of using stainless steels	16
1.5. The most used types of duplex stainless steels	17
1.6. Phase Diagrams	18
1.6.1. Fe-Cr-Ni phase diagram	18
1.6.2. Phase diagrams for prediction of ferrite phase	22
1.7. Intermetallic phases in Duplex stainless steel	24
1.7.1. Sigma (σ) phase	28
1.7.2. Secondary austenite	34
1.7.3. Chi (χ) phase	37
1.7.4. Nitrides	39
1.7.5. Carbides	42
1.7.6. Alpha prime (α' - 475 embrittlement)	43
1.8. Solution Annealing Treatment and cooling rate	44
1.9. Etching solutes for duplex stainless steel	45
1.10. Determination of phase percentages	46
1.11. Welding parameters for stainless steels	47
1.11.1. Welding Metallurgy of Duplex stainless steels	50
1.11.2. Microstructure of heat affected zone	54
1.11.3. Post weld heat treatment	55
1.11.4. Effect of nitrogen on steel	56
1.12. Element partitioning	57

1.12.1.	Partitioning of elements in duplex stainless steels	60
1.13.	Fundamental of corrosion resistance for stainless steels	61
1.13.1.	Different types of corrosion (Pitting, Crevice, SCC)	62
1.13.2.	Effects of alloying elements and ferrite percentage.....	65
1.13.3.	Surface conditions and post cleaning process	66
1.13.4.	Pitting Resistance Equivalent Number (PREN) parameter	67
1.13.5.	Standards for evaluation of corrosion properties and acceptance criteria	69
1.14.	literature review for welding and corrosion of duplex stainless steels	69
Chapter 2:	Effect of addition of nickel, nitrogen and PWHT on welding properties of the duplex stainless steel.....	81
	Abstract	83
2.1.	Materials and experimental procedure.....	85
2.1.1.	Materials and welding procedures	85
2.1.2.	Methods of materials investigations	88
2.2.	Results and discussions	89
2.2.1.	Base and weld metal structure	89
2.2.2.	Microstructure evolution	91
2.2.3.	Determination of phase percentage	98
2.2.4.	X-Ray diffraction analysis.....	100
2.2.5.	Microhardness profile.....	104
2.2.6.	Tensile test.....	106
2.2.7.	Fracture surface analysis	110
2.3.	Welding characteristics of super duplex stainless steels	115
2.3.1.	Materials and welding procedure for super duplex	115
2.3.2.	Results and discussions	117
2.4.	Conclusions	133
Chapter 3:	Pitting corrosion resistance of welded duplex stainless steels after addition of alloying elements and PWHT.....	135
	Abstract	137
3.1.	Experimental procedure.....	139
3.1.1.	Material and heat treatment	139
3.1.2.	Microstructure analysis.....	140
3.1.3.	Sample preparation for the electrochemical test.....	140
3.1.4.	Electrochemical test.....	141
3.2.	Results and discussions	142
3.2.1.	Microstructure evolution	142

3.2.2.	EDS analysis and distribution of alloying elements	147
3.2.3.	Precipitation of secondary phases.....	153
3.2.4.	Partitioning of elements after welding and heat treatment	157
3.2.5.	Pitting potential and its relation to PREN value	161
3.2.6.	Formation and morphology of the Pits	167
3.3.	Conclusions	172
Chapter 4:	Literature review of hardfacing by PTA process and methods for surface evaluations	173
Abstract	175
4.1.	Hardfacing.....	177
4.2.	Plasma transferred arc (PTA) process	178
4.2.1.	Gases for PTA	180
4.2.2.	Characteristics of PTA process.....	180
4.2.3.	Comparison between PTAW and PAW and GTAW process.....	181
4.3.	Materials.....	182
4.3.1.	Tools steel.....	182
4.3.2.	Cold work tool steel (D-type).....	183
4.3.3.	Powder NiCrBSi-WC	184
4.3.4.	Tungsten carbide particles	185
4.4.	Design of Experiment- Response surface methodology (RSM).....	187
4.4.1.	Mathematical modeling and effect of process parameters.....	188
4.5.	Wear of the materials.....	190
4.5.1.	Wear mechanisms.....	190
4.5.2.	Wear test (Pin on disk) by tribometer.....	191
4.6.	Equipment for surface evaluation.....	194
4.6.1.	Optical and Scanning Electron Microscopy	194
4.6.2.	X-ray diffraction analysis	197
4.6.3.	Nanoindentation and microhardness.....	199
4.6.4.	Surface topography analysis by optical profilometer	201
4.6.5.	Wear surface analysis by 3D optical profilometer	203
4.7.	Literature review of the previous works.....	203
Chapter 5:	Process optimization, weld bead geometry and microstructural evolution of nickel base powder (Ni-WC) deposited by PTA process on tool steel	211
Abstract	213
5.1.	Materials and Experimental procedure.....	215

5.1.1.	Base metal	215
5.1.2.	Powder NiCrBSi-WC	216
5.1.3.	PTA Welding for this experiment.....	217
5.2.	Design of Experiment- Response surface methodology.....	218
5.3.	Characterization of the samples.....	220
5.4.	Results and discussions	221
5.4.1.	Characterization of deposited layers.....	221
5.4.2.	Microstructure evolutions.....	222
5.4.3.	Distribution of Tungsten carbide.....	227
5.4.4.	Weld bead geometry	228
5.4.5.	Microhardness profiles	229
5.4.6.	SEM and EDS analysis of WC and matrix.....	232
5.5.	Effect of process parameters on bead geometry (Simple prediction).....	235
5.5.1.	Mathematical modeling and effect of process parameters.....	236
5.6.	Optimization of the obtained data	239
5.7.	Characterization of optimized sample	240
5.7.1.	Hardness profile.....	240
5.7.2.	Microstructure evolution and EDS analysis	240
5.7.3.	Surface profilometry.....	242
5.7.4.	X-ray diffraction analysis	244
5.7.5.	Element distribution and effect of pre heat temperature.....	244
5.7.6.	Nanoindentation.....	247
5.8.	Conclusions	248
Chapter 6:	Influence of addition of WC nano-particles on the hardfacing properties of the nickel-based coating deposited by PTA process.....	251
	Abstract	253
6.1.	Materials and experimental procedure.....	255
6.1.1.	Base Material.....	255
6.1.2.	Powder filler materials.....	256
6.1.3.	Plasma Transferred Arc (PTA) process.....	258
6.1.4.	Microstructural characterization.....	259
6.1.5.	Microhardness and nanoindentation	259
6.2.	Results and discussions	260
6.2.1.	Weld bead geometry measurement.....	260
6.2.2.	Microstructure evolution by optical microscopy	261
6.2.3.	Microstructure evolution by SEM and EDS analysis	264

6.2.4.	X-Ray diffraction analysis.....	267
6.2.5.	Decomposition of tungsten carbide in the matrix.....	270
6.2.6.	Microhardness and nanoindentation.....	271
6.2.7.	Wear test results.....	276
6.2.8.	SEM analysis of the surface after wear test.....	282
6.2.9.	Wear surface analysis by 3D optical profilometer.....	286
6.2.10.	Wear rate measurement by profilometer.....	291
6.3.	Conclusions.....	298
References	301

Chapter 1: Literature review of duplex stainless steels: welding and corrosion properties

Abstract

This chapter consists of a brief description of metallurgical behavior, welding characterization and corrosion resistance properties of duplex and super duplex stainless steel and a literature review of previous research work relating to the use of novel methods to improve welding and corrosion properties of welded duplex and super duplex stainless steels. A brief history of different types of stainless steels, and their relevant properties is discussed. Then the effects of different alloying elements on properties of stainless steels and phase diagrams for prediction of the phases are explained.

Due to the importance of intermetallic phases in duplex stainless steel, a brief explanation of Sigma phase formation, chi, carbide and nitrides is given. Different etching solutes used by many authors to reveal the microstructure and intermetallic phases are summarised. Then, different welding procedure considerations are explained. Due to the unique corrosion properties of duplex stainless steel, some principles of corrosion have been explained and different types of definitions relevant to the electrochemical tests are explained. Following this, a literature review regarding the effect of addition of alloying elements such as nitrogen and nickel followed by applying post weld heat treatment is discussed.

Key words. Duplex stainless steels, phase diagrams, welding metallurgy, corrosion, PREN.

1.1. Brief history of stainless steel

In 1821 Berthier started to investigate the possibility of creating stainless steel by adding chromium to normal steel. Then in 1897, Goldenschmidt developed this method. Between 1904 and 1909, experiments continued by addition of 13% and 17% chromium to the carbon steel. In 1913, Brearly produced the first commercial casting ingot of stainless steels. Finally, in 1916 US army tried to produce steel with 9-16% chromium with less than 0,7% carbon [1]. The first commercially wrought duplex stainless steel was produced in Sweden in 1930 and it was used for the paper industry. At the same time first casting duplex steel was produced in Finland and France. During World War II, addition of alloying elements continued to improve the quality of the alloy, and it was used for construction of heat exchanger where stress corrosion cracking resistance was required. After 1960, with improved refining techniques using electric furnaces, it was possible to produce alloys with low amounts of carbon contents and reduce the level of impurities to reach higher quality stainless steels products [2]. In the 1970s, more advances were made for producing different types of higher quality stainless steels, and make them more applicable in a wide range of industries such as pressure vessels, tanks, pipelines and etc.

1.2. Different types of stainless steels

Stainless steels can be categorized as corrosion and heat resisted steels both at high and low temperatures containing high alloying elements (minimum 10.5% Cr) mainly based on Fe-Cr, Fe-Cr-C and Fe-Cr-Ni systems. Based on different applications and requirements (corrosion resistance, toughness, strength), there are many different types of stainless steels which can be used in different industries from commercial products to marine and high technology industries. The commercial stainless steels can be categorized in five different main families which include austenitic, ferritic, martensitic, duplex and precipitation hardened. Each family has specific properties and application based on atomic structure, magnetic properties, strength and corrosion resistance. Table. 1-1 indicates some general comparison of different properties of austenitic and ferritic stainless steels.

Table. 1-1. Comparing some properties of different stainless steels

Properties	Austenitic	Ferritic	Martensitic
Toughness	Very high	Moderate	Low
Ductility	Very high	Moderate	Low
Weldability	Good	Limited	Hard
Thermal expansion	High	Moderate	
Stress corrosion cracking resistance	Low	Very high	
Magnetic properties	Non-magnetic	Ferro magnetic	Ferro magnetic

Generally, there are more applications of austenitic steels with respect to other types because of appropriate properties and relatively ease of fabrication. The main characteristic of stainless steels is corrosion resistance. This property can be increased by adding specific alloying elements which could have a beneficial effect on toughness.

For instance niobium and titanium cause an increase in intergranular corrosion resistance which can mix with carbon to form carbide. Nitrogen improves the strength and sulphur increase machinability due to formation of manganese sulphides. Besides nickel there are other elements that tend to make the structure austenitic. These elements are called austenite formers (nickel, nitrogen, carbon, manganese and copper). Alloying elements which tend to make the structure ferritic are called ferrite formers (iron, chromium, molybdenum, silicon).

Ferritic stainless steels

These types of stainless steels are not heat treatable and contain 11-17% chromium which is sufficient to completely stabilize the ferrite phase. Carbon is limited to keep high toughness and ductility and to prevent austenite formation. Ferritic stainless steels are magnetic, resistant to atmosphere corrosion and have moderate combination of strength and toughness. The main applications are magnetic valves, razor blades and car body trim. The microstructure of ferritic stainless steels mainly consists of ferrite in which fine carbides are distributed [3,4]. Delta ferrite is a chromium content phase which can be converted to hard and brittle intermetallic phase in temperatures between 700 and 950 °C. Heating above 1050 °C followed by quenching can mean an elimination of this phase.

Martensitic stainless steels

They are heat treatable alloys with medium carbon content, 12-18.5% chromium and 2-4% nickel. These types of stainless steel are high corrosion, temperature and creep resistance. The main applications of this alloy can be categorized as knives, hooks and tweezers in medical applications in addition to some parts of airplanes. Based on different heat treatments the microstructure can be diverse from pure martensite to fine tempered martensite. Alloys based on dimension and semi-finished products need different time and temperatures of heat treatment.

Austenitic stainless steels

These types such as ferritic stainless steels are not heat treatable but rapid cooling causes the formation of softer microstructure. These are considered as the main types of stainless steels and other types can be produced by modifications. They mainly contain 0.03-0.05% carbon, 17-24% chromium, 8-25% nickel, 2-4% molybdenum, in addition existing niobium and titanium causes carbide formation.

These alloys have high ductility, high corrosion resistance, very good forming properties and easy to work and machining. Some main applications of these alloys can be categorized as screw, implants, pipes and vessels in chemical and food industries in addition to kitchen utensils. The microstructure of this alloy, mainly consists of austenite grains. Heating of this alloy to 600-700°C cause to formation of complex carbides within austenite grains, which this leads to precipitation of chromium in austenite solid solution which enhance the susceptibility to intergranular corrosion or oxidation [1]. Generally austenitic stainless steels are very good for application in corrosive environment, the main problem of that occurs when it used under stress corrosion situation especially in halide environment. To concur this problem, first extra molybdenum and nickel added to the alloy and the problem mainly was solved. Due to existing different types of stainless steels, there is summary diagram shown in Fig. 1-1. This figure indicates that with considering the austenitic steel 304 as a main alloy, by addition and decreasing of different alloying elements what will happen and what kinds of stainless steel can be formed.

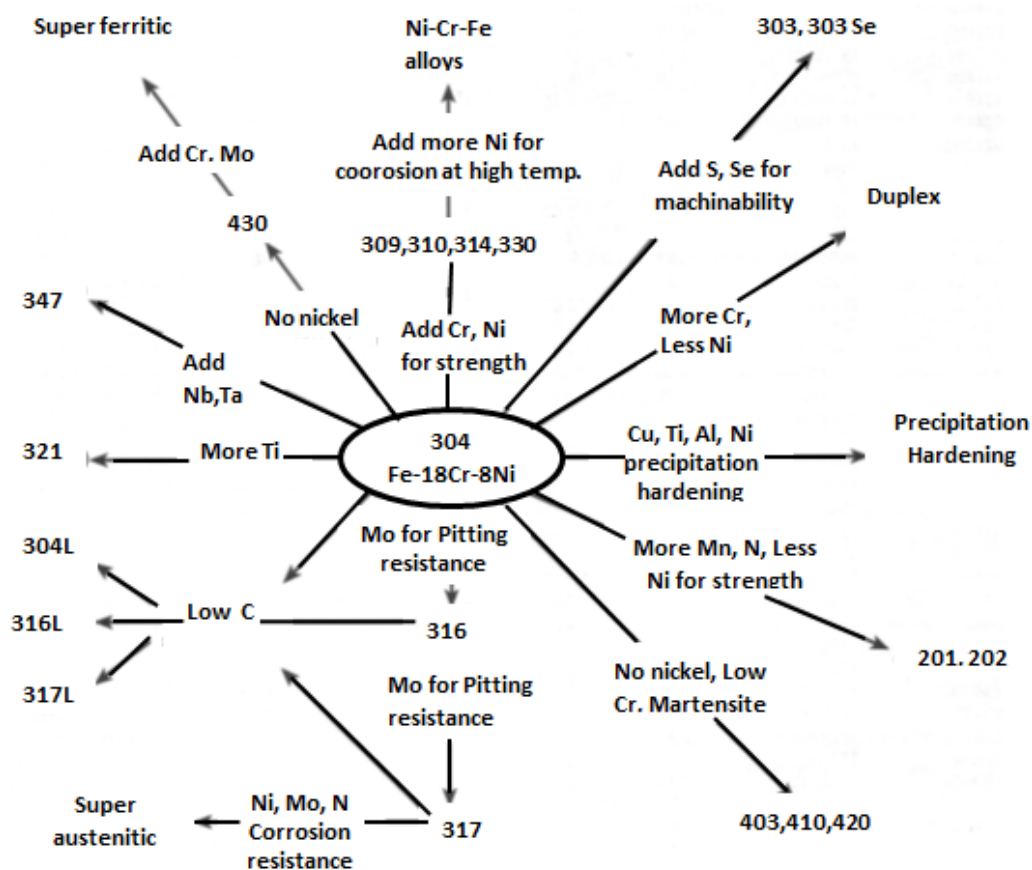


Fig. 1-1. Effect of alloying elements on formation of different types of stainless steels [5]

Duplex stainless steels

As brief history of duplex stainless steel it can be said that, the first commercially wrought duplex stainless steel produced in Sweden in 1930 and it was used for paper industry. It was mainly produced for substitution of austenitic stainless steels with higher strength. Parallely casting duplex steel was produced in Finland and France. Also, it is interesting to say that in 1936 invention of duplex stainless steels occurred due to mistake of one workman in French steel making company by accidently addition of more amount of chromium in austenitic duplex stainless steel [6]. The first generation had around 60-65% ferrite in solution annealed conditions. Another important advantages of duplex stainless steels is higher intergranular corrosion resistance [7]. The reason could be due to chromium depletion around chromium carbide and chromium nitride. Because of high diffusion rate in ferrite, chromium depletion was less occur. Higher bulk chromium contribute to a less sensitive material. The range of carbon content is between 0.08-0.1% and nitrogen deliberately added. In 1950s, it was found that microstructure of ferritic and austenitic showed appropriate properties in condition of stress corrosion cracking. For developing the characteristics of duplex steel, tried to reduce the carbon content to around 0.03%.

It was reported by addition of nickel and nitrogen the amount of austenite phase increase and susceptibility of intergranular corrosion decrease. In 1970s, 22% Cr duplex steel developed in Germany with higher corrosion resistance compare to austenitic stainless steels. For filler metal of this alloy, higher nickel content should be considered. This type is mainly used in different industries. In 1980, the development occurred to reach super duplex stainless steel with 25% Cr, 7% Ni and 0.2-0.3% N₂ for application in harsh situation. In this grade due to high amount of alloying elements, there is risk of precipitation of intermetallic phases. After 1990 decade, duplex stainless steels become more applicable instead of austenitic stainless steels. These types of stainless steel, not only have lower cost but also indicate higher metallurgical properties and weldability. Duplex stainless steels is appropriate solution when high corrosion resistance is desired.

General properties of duplex stainless steels

Duplex stainless steels are one important and relatively new type of stainless steels which consists specific chemical composition with high amount of chromium, less nickel and addition of little nitrogen and molybdenum compare to austenitic stainless steels, this cause to reach microstructure include roughly equal amount of austenite and ferrite phases. Higher amount of chromium, nitrogen and molybdenum cause to reach better crevice and pitting corrosion resistance and finer grains in duplex stainless steel compare to other types of stainless steels. These alloys have finer grain size compare to other types of stainless steels.

Consequently, duplex steels showed higher strength compare to austenitic stainless steels and better corrosion resistance in comparison with ferritic stainless steels. Also it shows high resistance to stress corrosion cracking and chloride ions attack [4].

Duplex stainless steels based on chemical compositions can be categorized as low alloy (lean), medium alloy (normal), high alloy (super) and hyper duplex. These alloys contain both ferrite and austenite in microstructure, they contain 24-28% chromium, 4-6 % nickel and 2-3 % molybdenium. This alloy is fatigue resistance in corrosive media and it has good stress corrosion cracking resistance. This type of stainless steel contain both ferritic and austenitic microstructure with roughly equal percentage. Early production of this steel was considered as austenitic stainless steels. But later, with considering special microstructure and very high corrosion resistance it was considered as a separate group. The application of these alloys is increasing due to existing high strength and corrosion resistance.

Because it includes more amount of ferrite compare with austenitic steels, in addition to lower thermal expansion and higher thermal conductivity. Also, they show high resistance to pitting and stress corrosion cracking, which makes them suitable for marine, pipes and oil & gas, (petro)chemical, offshore and biomedical and pharmacology, biofuel and pressure vessel industries. This kind of steels have higher strength compare to austenitic steel and higher toughness compare to the ferritic steel.

With considering the advantages of this type of steels, duplex stainless steels are prone to precipitate some unwanted intermetallic phases, which limit its application for temperature mainly less than 300 °C. Also, due to difficulties to produce final shape for application, it is more expensive than other type of stainless steels. Also, the strength of this alloy is two times more than austenitic steels and it indicates low ductile, brittle transition temperature around -40 °C, which is another limitation and cannot be used for cryogenic applications. Generally mechanical properties of duplex stainless steel are very good at temperature between -50 to 300 °C. More than 300 °C, different reaction happen inside of the material and it causes to formation of unwanted brittle intermetallic precipitates which have negative effect on the corrosion resistance and mechanical properties of the steel. Less than -50 °C , there is risk of ductile to brittle transformation temperature. This issue should be consider for designing and application of duplex stainless steels [8]. This type of steel have fully ferritic microstructure just after solidification. Then solid state transformation of ferrite to austenite occur. Also, it was reported that austenitic stainless steels with primary ferritic microstructure are less susceptible to solidification cracking. The beneficial effect of the ferritic mode is often increase to the greater solubility of impurities such as phosphor and Sulphur of ferrite. Less solidification shrinkage and thermal expansion contribute to reduce risk of crack formation. Transformation in solid state below solidus line gives increase grain boundary area and reduce the risk of low melting liquid wetting the ferrite-ferrite grain boundaries.

This phase transformation have crack arresting effect by making the pass irregular. Vareststraint test showed that duplex steels are less susceptible to solidification cracking compare to austenitic steels which first solidify as austenite, but if solidification of austenitic steel occur in ferrite steel shows higher resistance to solidification cracking.

Low alloy (Lean) duplex stainless steels

Emergence of lean duplex stainless steels is very important development of duplex stainless steels. Due to increasing the cost of nickel and molybdenum, is highly demanded to replace this type with 316L austenitic steel which has more strength and lower weight. The diffusional transformation of ferrite to ferrite and austenite consists partitioning of the elements between two phases. At high cooling rate, elements such as Cr, Ni and Mo are equal in both phases but interstitial elements such as carbon and nitrogen mainly concentrated in austenite. The equilibrium partitioning factor for nitrogen is increasing with temperature. As austenite form at high temperature, high amount of nitrogen can precipitate. This type mainly designed to replace with AISI304 and 316 stainless steels, where mainly higher stress corrosion cracking resistance is required. The main steel type of this group consists of UNS S32304 are UNS S32101.

Medium alloy (Normal) duplex stainless steels

This type consists of 22% chromium, 5% nickel and 3% molybdenum. The famous grade of this type is UNS S32250 and UNS S32404. For this type duplex steels with 0.14 % nitrogen, mainly consists of 0.4 % nitrogen in austenite, the partitioning ratio of nitrogen is around 10. The corrosion resistance of this type is between AISI 316 and 6% molybdenum and nitrogen grade.

Superduplex stainless steels

Super duplex steels include some types of duplex steel with more value of important alloying elements (Cr, Ni and N₂). Application of super duplex stainless steels are mainly in oil and gas industry, offshore, platforms, heat exchangers, firefighting systems, vessels and sea water piping. Superduplex steels, because of existing high amount of chromium and molybdenum, makes it extremely resistant to uniform corrosion by organic and inorganic acids. Also, it has very good corrosion resistance to localized corrosion up to 70 °C. Addition of copper and tungsten improve the resistance to mineral acids. Nitrogen act like the same role in duplex steel and cause to improve the corrosion resistance and keep the amount of ferrite and austenite constant. Also, the pitting resistance equivalent number (PREN) which is obtained by the formula of %Cr + 3.3 %Mo + 16 %N is more than 40 which is really good value for corrosion resistance and mainly because of this high value it is called super duplex.

Also, corrosion resistance of the materials depends on microstructure, proportion of ferrite-austenite, presence of intermetallic phases and element partitioning. Optimum corrosion resistance for duplex steels obtained in equal percentage of ferrite-austenite without presence of sigma, chi, carbide and nitride phases. The good properties of the duplex and super duplex steels are because of fine grain size of ferritic austenitic microstructure.

Also, existing elements such as Cr, Mo, N and Ni are important. simultaneous increase of Cr (29%) ,decrease of Mo (2% instead of 3.5-4%) and increase of nitrogen (up to 0.4%) is a good way to develop superduplex grades with higher structural stability. Chromium+ molybdenum contents below 21% are limited by the risk of martensite formation in the austenitic phase during cold deformation. Chromium + molybdenum contents over 35 % are limited by the stability of the ferritic phase (precipitation of intermetallic). Earlier grades containing 0.1–0.2% nitrogen have now been replaced by higher-nitrogen versions. The addition of nitrogen is obviously limited by the nitrogen solubility limits. The main type of this group are UNS S32570.

Hyperduplex stainless steels

Recently by adding more amount of alloying elements such as nitrogen till 0.5%, new grade of duplex stainless steels was developed for severe marine conditions. The PREN value for this alloy is higher than 45. It contains very high Cr+Mo+W with significant nitrogen additions (0.4%). One example is the UNS 32707 grade (SAF 2707) with 27%Cr and 5%Mo and the second the UNS 39274 DP3W grade (25Cr, 3.3Mo, 2.1W). Higher amount of Cr, Mo and Nitrogen make this type of steel appropriate for high strength and high corrosion resistance applications. Also, Alloys such as aluminum, titanium, copper and molybdenum can be considered for increasing precipitation reaction and cause to harden the alloy. Austenitic precipitation hardened alloy can form Ni_3Al and Ni_3Ti phases (gamma prime) and can be compare with nickel base superalloys.

1.3. Effect of Alloying elements on properties of duplex stainless steels

Chromium (Cr)

Chrome is the most alloying element for stainless steels which exist minimum 10.5% to form the passive layer on the surface for increasing corrosion resistance. With addition of chromium, an oxide of stoichiometry $(Fe,Cr)_2O_3$ form on the surface. This amount reach to 20-30% in duplex stainless steels which can increase the ferrite content and it can be worked in high aggressive environments. More than this amount there is the risk of precipitation of intermetallic phase which mainly has negative effect on ductility and corrosion resistance.

Also, chrome is useful to achieve uniform corrosion and decrease the pit propagation. Chromium increase the pitting potential, the critical pitting and crevice temperatures (CPT,CCT) and improve the passive film stability in acidic environment. This element is carbide former ($M_{23}C_6$ and M_7C_3), also it can combine with nitrogen to form nitride (Cr_2N). In addition it was reported that, Chromium play a key role to formation of intermetallic compounds. Chromium which has substitutional behavior can act as solid solution strengthen of alloy. High chromium ferritic grades must be treated carefully. High chromium content increase the risk of precipitation of intermetallic phases.

Nickel (Ni)

Nickel is critical element in stainless steels, the important role of nickel is to stabilize and expand austenite phase and can change the structure from BCC to FCC. Also, nickel is not carbide former and it can delay the formation of intermetallic phase, but in this case is not as strong as nitrogen. This element is added between 4-6% in duplex steels which is less than necessary amount for austenitic steels. Also, the main function of nickel is to control the balance of ferrite and austenite phases by optimizing the chromium and molybdenum content, in addition to controlling the element partitioning. It has good effect for formation of duplex stainless steels. Also This is important for both corrosion resistance and good mechanical properties especially toughness. But it was reported that [9] addition of nickel cause to increase the stress corrosion cracking resistance especially in aggressive environments. But more addition of nickel increase the risk of formation of unwanted alpha prime phase. Also, addition of nickel to ferritic steel can decrease the DBTT. In case of adding less nickel, more ferrite form and it causes to decrease the ductility. The filler metal for duplex stainless steels should contain 7-10 % nickel. Formation of duplex stainless steel and austenitic steels based on different amount of nickel. Increasing nickel cause to more dilution in austenite phase with regards to nitrogen which in turn decrease the pitting corrosion resistance number (PREN) of austenite. In case of high sensitivity to precipitation of chromium nitride, nickel has positive effect. Fig. 1-2 indicates changes in microstructure of different types of stainless steels with addition of nickel.

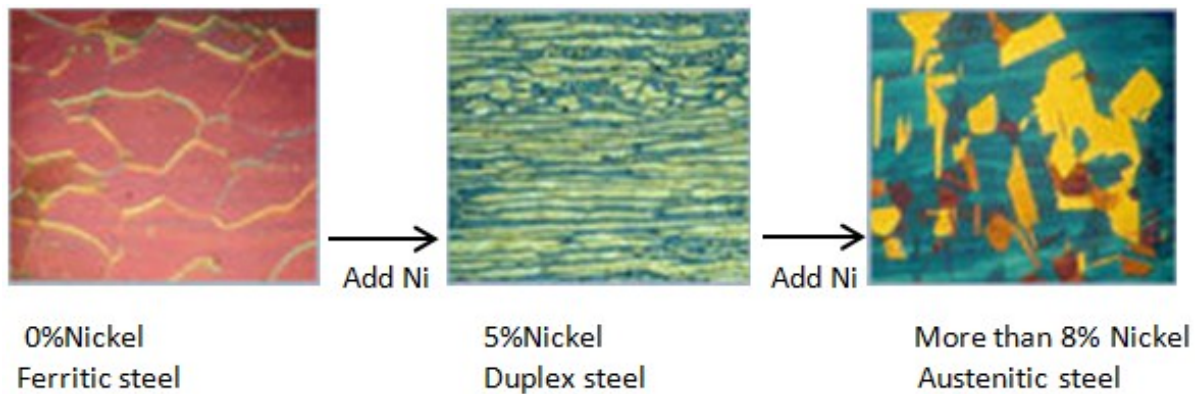


Fig. 1-2. Changing the microstructure with addition of nickel [7]

Molybdenum (Mo)

This element with amount of 3-6% can be added to stainless steels to support chromium to improve specially pitting and crevice corrosion resistance specially in chloride environment and sea water. For austenitic steels, this element can improve high temperature strength. Also, it is ferrite former element, and in case of existing more than 4% in duplex steels and 7% in austenitic steel can increase probability of the formation of intermetallic phase especially sigma and alpha prime phases which are detrimental in microstructure and corrosion properties. Also Mo stabilize the passive film of the surface directly or through enrichment beneath the film. From pitting resistance equivalent number, the coefficient of 3.3 is considered for the formula [10].

Nitrogen (N₂)

Nitrogen like carbon acts as interstitial elements and mainly exist as a impurity in stainless steel and deliberately added to the duplex stainless steels and it works as solid solution strengthening. Addition of 0.15% nitrogen in austenitic steel can improve its strength. This element is well known austenite stabilizer. Based on size of this element, it is interstitial element and can replace with some nickel, which can act as solid solution strengthener. It plays role to improve weldability of duplex steels accompanied with increasing the pitting and crevice corrosion resistance. But the solubility of this element in stainless steel and specially in ferrite phase is limited, which addition of manganese increase the solubility of nitrogen. nitrogen is austenite stabilizer element, it cause to increase pitting and crevice corrosion resistance, austenite content and strength of the alloy. Also it was reported that nitrogen cause to delay the formation of intermetallic phases but increase the risk of precipitation of chromium nitride specially in ferrite phase [11]. Also, Nitrogen cause to formation of ferrite to austenite at elevated temperature. In this way it causes to save the balance between percentage of ferrite and austenite after rapid thermal cycle in heat affected zone. High amount of nitrogen causes to decrease the influence of cooling rate on microstructure consequently the sensitivity to welding become less.

Also, in ferritic and duplex stainless steel, in case of increasing the solubility, there is risk of precipitation of chromium nitride in ferrite phase and ferrite austenite grain boundaries. Ogawa et al. [12] showed that the increase in amount of nitrogen improve the pitting resistance of the weld metal and HAZ by more formation of austenite during cooling and avoiding formation of large ferrite with amount of chromium carbide precipitates. Carbon and nitrogen are strong austenite stabilizer and their level must be controlled precisely to keep the phase balance. Nitrogen pick up from atmosphere can produce a departure from the desired microstructure if shielding is not enough. Also, during welding of duplex steels there is a risk of nitrogen loss, which can be substitute with adding external nitrogen during welding.

This element with low cost, added to alloys with high percentage of chrome and molybdenum can decrease the partitioning of these elements between ferrite and austenite which stop the formation of intermetallic phase especially sigma phase. Consequently the ductility and corrosion resistance increase. It promotes the start of austenite precipitation at higher temperature during cooling of the weld. In duplex stainless steels, the amount of nickel, is adjusted to achieve desirable microstructure in sense of phase balance. Also nitrogen-containing steels are susceptible to dynamic strain aging at high temperatures. This phenomena is due to interaction between diffusion solute atoms and moving dislocations during plastic deformation at temperature [11].

Addition of nitrogen more than 0.1-0.2% is limited by the value of solubility. Nitrogen can control the microstructure of HAZ especially by increasing the value from 0.1 to 0.2%. Reduction of carbon contents to very low levels, helps to avoid problems related to ferrite-ferrite carbide precipitation. Also nitrogen cause to increase the phase ratio of ferrite austenite to around 40-50%. High carbon contents have negative effect on quality of heat affected zone, due to increasing the ferrite-ferrite grain boundaries accompanied with risk of SCC [2]. Also, nitrogen increase the pitting resistance equivalent number of austenite phase dramatically by increasing the nitrogen content of the phase and chromium and molybdenum content through the partitioning coefficient. The limitation of this element is 0.15% for molybdenum free duplex steel and 0.3% in 25chromium-molybdenum and 0.4% for 25Cr-molybdenum-manganese steel.

Silicon (Si)

This element in range of 0.3-0.6% mainly added as a deoxidizer during melting of stainless steels. But in case of adding between 1 to 3 % and 4 to 5% could improve the oxide scaling and corrosion resistance specially at high temperatures respectively. In stainless steels with adding more than 1% acts as a ferrite former. Also, it can form intermetallic silicon chromite (Cr_3Si) and iron silicide which are negative intermetallic brittle phases. Silicon, improve the fluidity of melt which is useful during welding of stainless steels (especially austenitic stainless steel).

In addition, during solidification silicon causes to segregation and formation of low melting point eutectoid phases [13]. In addition, silicon, can segregate during solidification in formation of low melting eutectic with combination with nickel. Existing sum of percentage of chromium and molybdenum less than 21% are limited because there is risk of formation of martensite in austenite phase during deformation. Also, when this value become more than 35%, there is limitation of ferrite stability and precipitation of intermetallic phases [2]. Also silicon stabilize the passive film. Silicon up to 2% solubility cause to increase structure stability and solubility of nitrogen.

Copper (Cu)

Copper has been suggested to improve the corrosion resistance of duplex steels. Also combination of copper and nitrogen enhance the corrosion resistance. But it mainly suggested for increasing the resistance in non-oxidizing solutions[14]. Copper, mainly reduce the dissolution rate of Cr but it would not influence the passivation of the stainless steel. Passivation potential is taken to be the center of the passivation range. Copper in case of existing Mo, has detrimental effect on pitting corrosion resistance but the rate of pitting resistance reduction is very small [15,16]. Also, copper particles may precipitate in the ferrite grains after heat treatment between 300-550 °C temperature. A hardening effect can be obtained. There is limitation of 2.5% in chemical composition, because more than this amount cause to reduce hot ductility [17,18]. Also addition of copper, is useful for increasing the resistance of DSS in non oxidizing solutions. The amount of that is limited to around 2.5%, because more than this amount cause to reduce the hot ductility.

Manganese (Mn)

It is an element which mainly exist in all types of steels which can combine with sulphur and make MnS to eliminate negative effect of sulphur in steels. It exists between 1-2% in austenitic and less than 1% in ferritic steels. Also, it considered as austenite former element specially for low temperature applications to prevent formation of martensite, and degree of production depends on amount of nickel. But generally, it has detrimental effect on corrosion properties of stainless steels due to formation of $(\text{FeMn})\text{Cr}_2\text{S}_4$ at high concentration. This phase can act as initiation point for pitting. Also it can be added to some type of steels to increase solubility of nitrogen in austenite phase. In addition, it has little effect on solid solution strengthening. Mn rich sulphides act as initiation points for pitting , also it can destabilize the passive film [19]. Also, Manganese is used extensively in many high-nitrogen stainless steels to increase nitrogen solubility.

Sulphur (S)

Existing high level of Sulphur in ferrite which is mainly two times more than austenite cause to deteriorate pitting corrosion resistance. Also, if there is not enough percentages of Chromium, Titanium and Cerium, it tends to initiate the pit. In optimum percentage it has positive effect on machinability.

Tungsten (W)

Addition of W cause to stabilize the sigma phase specially at high temperature. Tungsten containing stainless steels grades needs higher solution temperature for solution anneal treatment. After long term isothermal treatment the amount of sigma phase is reduced when comparing to Mo containing grade with equivalent Mo+W addition where part of the Mo is replaced by W additions. This seems to result from slower diffusion of large W atoms. Niobium, titanium, tungsten and vanadium can be added to stainless steels to improve stabilization of carbon to prevent intergranular corrosion. Also they tend to form fine MC type carbide which resist dissolution during welding and heat treatment and provide high temperature strength. Also, they prevent formation of $M_{23}C_6$ type carbide which has negative effect in intergranular corrosion resistance. In addition, these elements are consider as ferrite former.

1.4. Some problems of using stainless steels

In addition to many advantages of using stainless steel in different industries, there are some common problems during using this kind of material, some problems related to all types and some of them belongs to specific types of steels. Generally they can be cathegorized as following [20]:

1. Hydrogen embrittlement

Duplex stainless steels are susceptible to hydrogen embrittlement due to existing ferrite phase as a part of microstructure. Ferrite has higher rate of diffusivity of hydrogen compare to austenite, consequently it more tends to initiate and propaget the crack. Also, hydrogen in duplex steels promotes transgranular fracture of the ferrite phase, which induced microcrack in austenite phase [21,22]. Some effects of hydrogen embrittlement can be listed as: Hydrogen induced localized plasticity, Decrease the stacking fault energy, Formation of ϵ martensite with hydrogen, Accumulation of hydrogen at the interface of matrix and precipitates, The transport of hydrogen to precipitate tips and interactions between hydrogen and dislocations

2. Sensitization

It mainly occurs due to decreasing the amount of chromium close to grain boundaries which that area become more prone to corrosion [23]. Also precipitation of $M_{23}C_6$ cause to intergranular attack

some factors which have effect on sensitization can be categorized as chemical composition, grain size effect and deformation induced microstructure

3. Metal dusting

It is a high temperature (between 400 and 900 °C) corrosion process in which metal are saturated with carbon and disintegrate into metal particles.

4. Pitting corrosion

It is a common problem in stainless steels and one of main reason of that is existing impurities and inclusions. Also, deformation inside of the material and interface between austenite and deformation-induced martensite it is a preferential site for pitting. In addition, changing in the microstructure and residual stress due to deformation have an effect on pitting corrosion. [24,25]

5. Microbiologically induced corrosion

It is a new type of known attack and absorb much attention for research. It consists attachment of bacteria to the surface of material with attendant alternation of the composition of the material. It can be appear in form of pitting or selective dissolution of ferrite/austenite in duplex steels. In case of application of duplex steel in sea water, the susceptibility of localized corrosion increase due to shift of the corrosion potential to the noble direction induced by biofilms [26,27].

6. High temperature oxidation

7. Stress corrosion cracking

8. Sticking and surface roughening, this mainly occur during rolling and forming

9. Fatigue, creep and strain aging

1.5. The most used types of duplex stainless steels

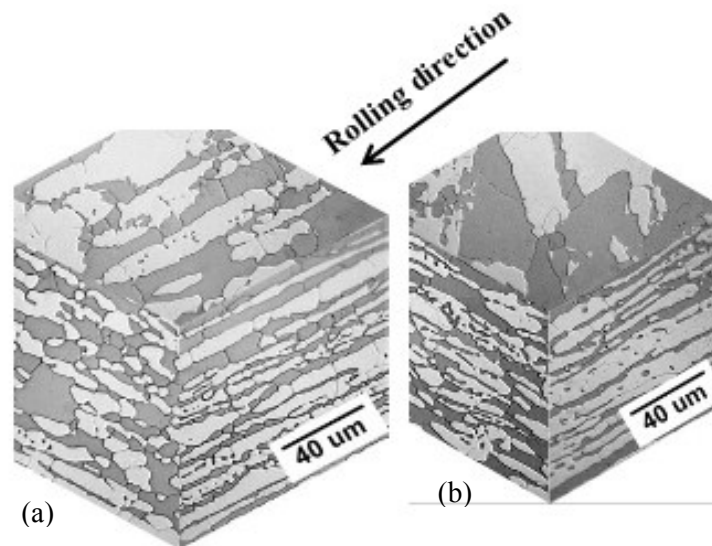
Table. 1-2 indicates list of some highly used duplex stainless steels. The early stage types of duplex steels did not have nitrogen as an alloying element. It is widely used duplex stainless steels in different industries, which contains 23 % chromium and 4 % nickel. This alloy has two times higher strength than normal austenitic steels. Also it shows better crevice and pitting corrosion resistance with appropriate weldability. The main problem for that was losing the corrosion resistance after welding process, which ,mainly can be solved by post weld heat treatment. The second generation was invented by adding 0.15 to 0.25% nitrogen which reduce chrome partitioning between ferrite and austenite phases. Consequently, corrosion resistance increase after welding. Table. 1-3 indicates the chemical analysis and mechanical properties of some high applicable types of duplex stainless steels. Fig. 1-3 depicts three dimensional microstructure of duplex and super duplex stainless steel, with considering the rolling direction.

Table. 1-2 Nominal chemical composition (wt%) of some grades of duplex and superduplex stainless steel

UNS No.	Cr	Ni	Mo	C	Mn	P	S	Si	N	Cu	Fe
S32101	21-23	1-2	<0.5	0.03	5	0.04	0.03	1	0.1-0.2	<0.6	Bal.
S32304	21-24	3-5.5	<0.6	0.03	2.5	0.04	0.03	1	<0.2	<0.6	Bal.
S32205	4.5-6.5	4-6.5	2-3.5	0.03	2	0.03	0.02	1	<0.2	-	Bal.
S32570	24-26	6-8	3-5	0.03	1.2	0.03	0.02	0.8	0.2-0.3	-	Bal.

Table. 1-3. Mechanical properties of some grades of duplex stainless steels

Alloy	UNS No.	U.T.S Mpa(Ksi)	Y.S Mpa(Ksi)	Elongation (%)
2304	S32304	600(87)	400(58)	25
2205	S31803	620(90)	450(65)	25
2507	S32750	795(116)	550(80)	25

**Fig. 1-3.** Three dimensional microstructure of duplex (a) UNS S32304 and superduplex (b) UNS S32570 stainless steel [28]

1.6. Phase Diagrams

1.6.1. Fe-Cr-Ni phase diagram

For prediction of different phases which exist in the stainless steels microstructure, phase diagram in forms of two and three dimension can be used. For stainless steels mainly binary Fe-C and ternary Fe-Cr-C and Fe-Cr-Ni have many applications; as it is clear in stainless steel there are many elements, but due to high amount these elements just phase diagrams of these elements are considered. In addition these diagram are drawn in equilibrium form, and for welding conditions which it is non equilibrium reaction which cause to limited applications.

Consequently for exact phase detection during welding using advanced software such as ThermoCalc is suggested. Fig. 1-4 indicates three dimensional diagram of Fe-Cr and Ni. In addition in this figure the cross section of 2D diagram at constant 70% Fe is specified.

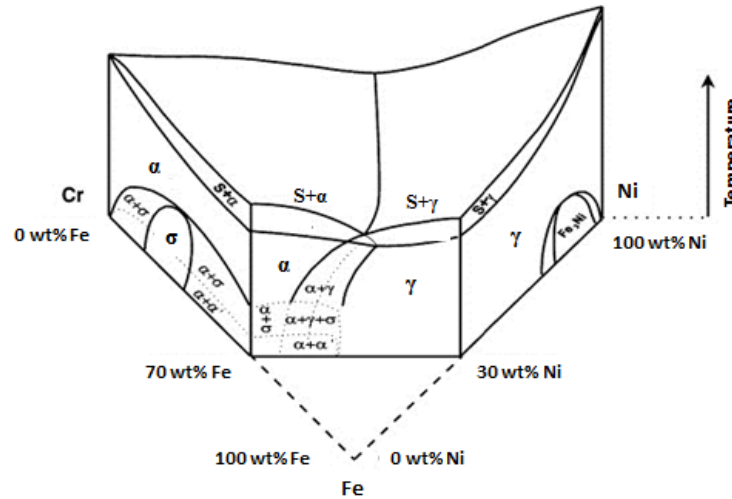


Fig. 1-4. Ternary Fe-Cr-Ni phase diagram [29]

Based on important role of chromium in stainless steel, binary phase diagram of Fe-Cr is important to explain. In Fe-Cr part of diagram, there is Gamma loop in less than 12.7% Cr at temperature range of 912-1394 °C, above this value the microstructure become completely ferrite at high temperature. Between 470 and 820 °C at 40 to 50% chromium there is risk of 475°C embrittlement phenomena which cause to formation of chromium rich particles in alpha matrix. This phase called alpha prime and mainly form at temperature of 400 and 540°C which has negative effect on mechanical properties of stainless steels especially for those with more than 14% chromium.

At low temperature equilibrium phase diagram, there is possibility of formation of sigma phase with tetragonal structure, it mainly form in alloys with chromium more than 20%. It is hard and brittle phase which mainly form at temperature range of 600-800 °C. Fig. 1-5 shows the binary phase diagram of Fe-Cr. It is well known that in Fe-Cr alloys there is a miscibility gap, where the ferrite phase may decompose into an iron-rich BCC phase (α) and a chromium-enriched BCC phase (α') either by nucleation and growth of α' precipitates or by spinodal decomposition [30].

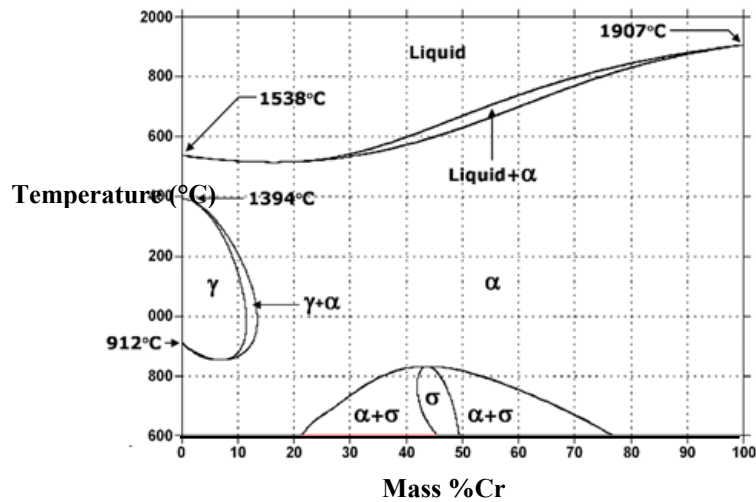


Fig. 1-5. Phase diagram of Fe-Cr [1]

Addition of nickel to Fe-Cr system cause to increase the area of austenite phase. Also, it permits the austenite phase become stable at lower temperatures. With considering constant Fe section (mainly 60 - 70%) in ternary diagram of Fe-Ni-Cr, the following diagram is achieved. Fig. 1-6 shows the 2D binary phase diagram of the Cr-Ni. The small triangle, between solidus and liquidus consists ferrite, austenite and liquid phases. It separate alloys which solidify as austenite and ferrite in left and right respectively. In solid state, the ferrite is stable at high temperature in chrome content more than 20%, with decreasing the temperature, the ferrite transform partially to austenite. For the alloys which solidifies in left part of the diagram, solidified as austenite and remain in this phase upon cooling to ambient temperature.

Alloys which solidify as ferrite at composition of more than 20% Cr, cool in two phases of ferrite and austenite which cause to formation of ferrite to austenite. At composition further to the right of the triangle, ferrite become more stable [1]. Duplex stainless steels mainly solidifies as ferrite due to existing more amount of ferrite stabilizer elements compare with austenite stabilizer elements, and based on partial solid state transformation convert to austenite.

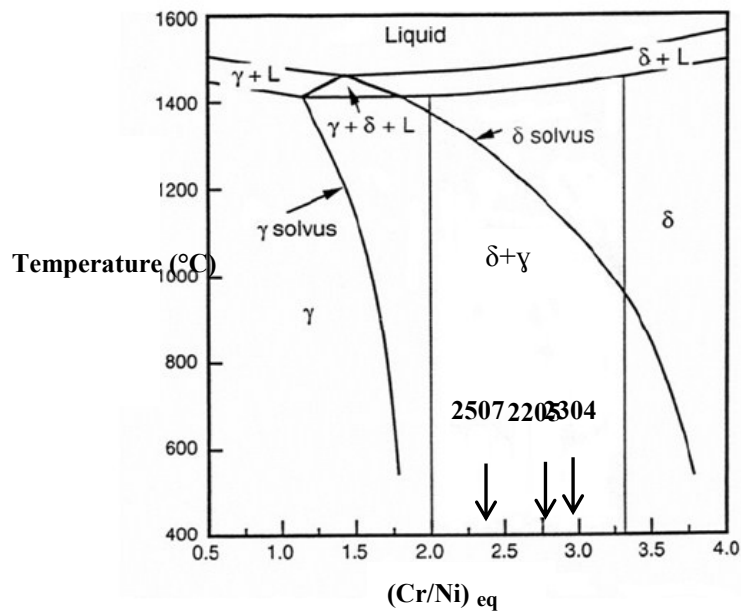


Fig. 1-6. Pseudo binary section of Fe-Cr-Ni system at 70% Fe [31]

Mainly the microstructure of duplex steels depends on fabrication process such as cold working, welding and heat treatment. Consequently understanding and prediction of the changes, have large effect on final microstructure especially after welding and heat treatment. Most problems of welding in duplex steels is due to reduction of austenite phase in fusion zone and heat affected zone in addition to high risk of precipitation of intermetallic phases. Mainly the microstructure above 1300 °C became completely ferrite and grain growth occur.

During cooling, austenite is form at grain boundaries of ferrite mainly in form of widmanstatten. Consequently the microstructure is more diverse compare to as received material and tend to reach less amount of austenite. As a result, mechanical properties, phase balance and corrosion resistance deteriorate. Generally in steels contain nitrogen, chromium and molybdenum there is more tendency to precipitation of nitride in ferrite phase. The higher ferrite content of microstructure and precipitation reduce the toughness and corrosion resistance. This problem could be decrease by using appropriate filler metal or shielding gas. Generally, for lower peak temperature, the amount of austenite decrease. Also at peak temperature a two phase microstructure maintain, grain growth tends to be minimum and microstructure is quiet close to the base metal [32]. In duplex stainless steels ferrite decompose spinodally at around 350-525 °C, consequently the working temperature of this kind of steels is limited to maximum 250 to 300 °C.

1.6.2. Phase diagrams for prediction of ferrite phase

To explain the importance of these diagrams It could be say that, a minimum ferrite content is necessary to avoid hot cracking especially in austenitic and duplex stainless steel welds. This value can control the microstructural evolution, corrosion resistance and toughness at low temperature during application. So much research focused to calculate the effect of different alloying elements on the content of ferrite in the microstructure. It is possible to modify the chemical composition of the weld. To find ferrite value, accurate method is necessary to estimate ferrite content based on chemical composition of the weld [33]. In the following some well known diagrams for this estimation explained.

Schaeffler Diagram

Anton Schaeffler, based on past information which was proposed by other researcher Maurer et al. and Newell et al. prepared one useful diagram based on considering the effect of different alloying elements on phase percentage. In his investigation, he considered a map of microstructure distribution after welding, based on different alloying elements. This diagram can be used for prediction of the stainless steel weld metal microstructure with considering the effect of chemical analysis. These elements categorized based on being austenite and ferrite stabilizer.

The horizontal axes consists of ferrite former elements in term of chromium equivalent and the vertical axes includes austenite former elements in terms of nickel equivalent. He proposed based on this information it is possible to predict the microstructure of weld in specific points of the diagram. During the years, this diagram improve by considering the exact effect of alloying elements. During the years many changes in the effect of alloying elements on formula happed. Recently, the following formula is accepted as a reference.

$$\begin{aligned} Cr_{eq} &= \%Cr + 1.5 \%Mo + 1.5\%Si + 0.5\%Nb + 5 \%V + 1.5\%Ti \\ Nieq &= \%Ni + 30\% C + 0.5\%Mn + 0.3 \%Cu + (\%N - 0.045)*X \\ X &= 30 \text{ for } N = 0.0-0.2 \% \\ X &= 22 \text{ for } N = 0.21-0.25 \% \\ X &= 20 \text{ for } N = 0.25-0.35\% \end{aligned}$$

This diagram is an important tool for predicting the constitution of austenitic Cr-Ni steel welds with carbon content up to 0.12%. However, it cannot be used for prediction of the composition and volume of the carbide. For a carbon content lower than 0.12%, due to consumption of carbon by the carbide formation process. Fig. 1-7 indicates the Schaeffler diagram which has many applications for prediction of microstructure of the stainless steels.

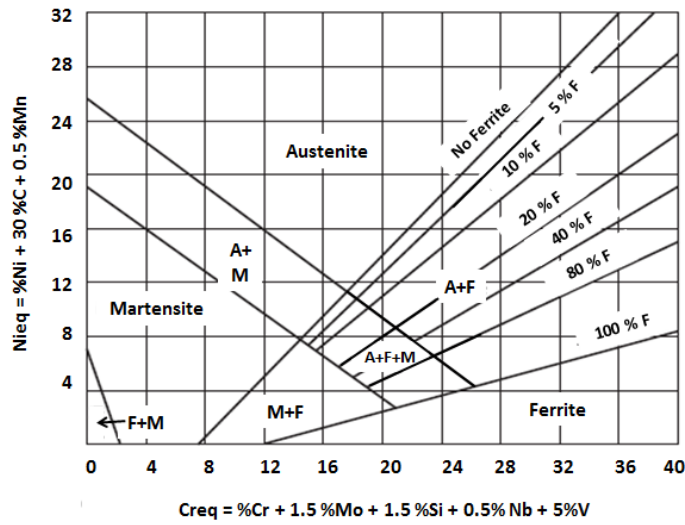


Fig. 1-7. Schaeffler diagram [4]

Delong Diagram

In 1956 and couple of years after Schaeffler, Delong et al. decided to improve the diagram especially for austenitic series 300 alloy instead of all types of stainless steels. This diagram is drawn in larger scale. Also, they considered the large effect of nitrogen as strong austenite stabilizer in nickel equivalent formula. They keep the formula of chromium equivalent the same as Schaeffler. With further development in 1973, they decided to add ferrite number scale on the original diagram. The use of ferrite number units is easier compare to measure volume fraction percentage in weld metal. This value is based on magnetic measurements due to ferromagnetic properties of the delta ferrite. For ferrite number the value less than 10 is roughly equal to volume fraction of ferrite. This diagram mainly is independent to the heat input and welding process [34]. Fig. 1-8, shows the Delong diagram for prediction of ferrite number.

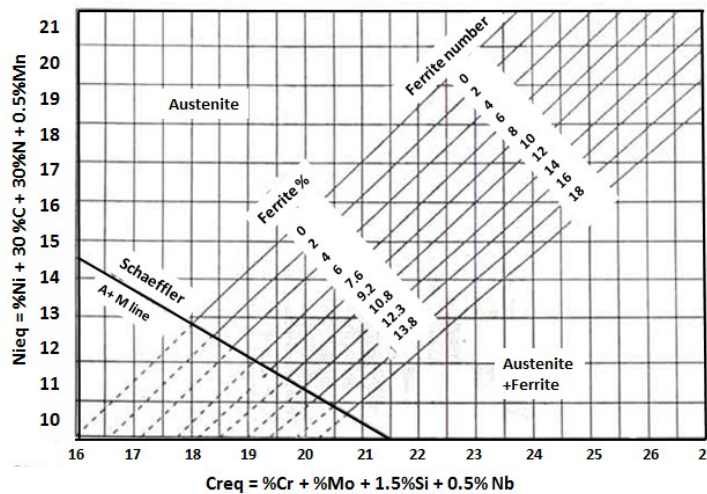


Fig. 1-8. Delong diagram [4]

WRC diagram

In 1988, Welding research council (WRC) started a project by leading of Siewert et al. to develop Schaeffler diagram. Their diagram developed based on around 1000 weld test which were performed and analysed in different universities and research centers all over the world. Also, they found that effect of manganese can be removed from nickel equivalent. Also, due to more application of duplex stainless steels, much research was performed to find the role of copper in nickel equivalent formula and to improve accuracy of ferrite number prediction. This diagram finally developed in 1992 and is the most reliable diagram for prediction of ferrite number in austenitic and duplex stainless steels. Also, due to effect of titanium to formation of the carbide finding the exact role of this alloying element is new line of research to improve the existing diagram [35]. Fig. 1-9, shows the WRC diagram.

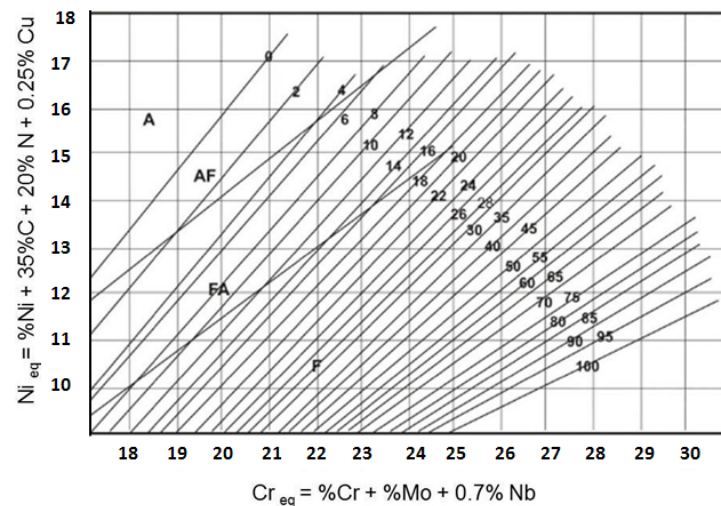


Fig. 1-9. WRC diagram 1992 [4]

Since cooling rate is not in equilibrium condition in GTAW process, Schaeffler and WRC phase diagram do not work properly and accurately and mainly it would be suggested to use pseudobinary phase diagram.

1.7. Intermetallic phases in Duplex stainless steel

Based on information of binary phase diagrams, at low temperatures mainly austenite forms at the expense of ferrite. Lower limit in temperature is accompanied with formation of unwanted intermetallic phases which have detrimental effect on mechanical and specially corrosion behavior of the alloys. Amongst σ , χ , π and R phases which mainly form, sigma phase is considered as an important and critical phase during solidification. Cr, Mo and W are the most alloying elements

which tend to form sigma phase. Fig. 1-10, indicates schematic phase diagram for prediction of intermetallic phases with considering the cooling rate and alloying elements.

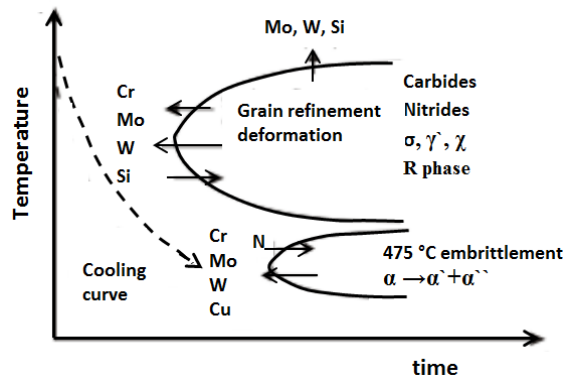


Fig. 1-10. Schematic diagram for precipitation of different phases which occur in duplex stainless steel

The diagram indicates that the effect of different alloying elements on the precipitation of unwanted intermetallic phases. For example, more alloying content of Cr, Mo and Si cause to extend the stability range of precipitation and move the curve to shorter time. The most important phase during welding and producing that steels are σ , χ , chromium nitride and secondary austenite which form in higher temperatures. Generally in duplex stainless steels, the susceptibility to intermetallic phase formation is due to chemical composition of ferrite, richer in sigma forming elements (Cr, Mo, Si), and poor in austenite stabilizer elements (C, N, Ni). Fig. 1-11 shows the SEM image of sigma and Chi phases in the microstructure of duplex stainless steel. In Table. 1-4 the chemical composition of some intermetallic phases are specified. The characteristics and temperature range of secondary intermetallic phases in duplex stainless steels can be categorized as shown in Table. 1-5.

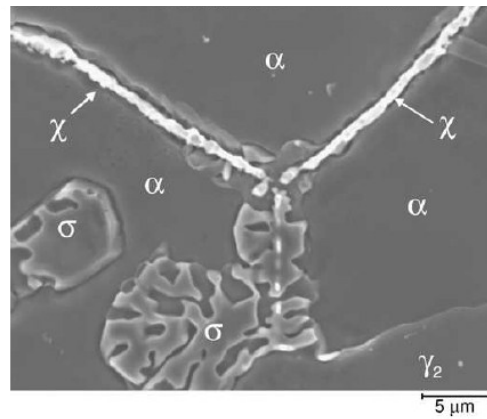


Fig. 1-11. SEM image formation of sigma and chi phase in Duplex steel [29]

Table. 1-4. Chemical composition of different intermetallic phases [36]

Element	Cr	Ni	Mo	Mn	Si
δ	26.61	5.59	5.11	0.69	0.36
γ	24.41	8.03	3.63	0.95	0.34
σ	26.7-28.2	1.4 - 4.7	7.5 - 8.2	0.77	0.5
χ	24	3.6	13	-	-

Table. 1-5. Characterization of intermetallic phases in duplex steels [16,20,37,38]

Type of precipitates	Nominal chemical formula	Lattice Type	Temperature range of formation (°C)	Place of formation Form
σ	Fe ₃₆ -Cr ₁₂ -Mo ₁₀ Fe ₃ CrMo Fe 35-55 Cr 25-40 Mo 11-25	BCT	650-950	Grain boundary α-γ Inside of α relatively gray brown particles
Chromium nitride (ε)	Cr ₂ N	Hexagonal	700-900	α-γ interface
α prime 475 embrittlement			300-525	
Chromium nitride	CrN	Cubic	Below 1000	
χ	Fe ₃₆ Cr ₁₂ Mo ₁₀ Fe ₃₆ Cr ₁₂ Mo ₃ Ti ₇ Fe ₃₅₋₅₀ Cr ₂₀₋₃₅ Mo ₂₀₋₂₂ Fe-Cr-Ni-Mo	BCC	700-900	α-α and α-γ grain boundary (Light particles)
R	Fe-Cr-Mo Fe ₃₀₋₄₀ Cr ₂₀₋₃₅ Mo ₂₀₋₂₂	Hexagonal Rhomboidal	550-800	
π	Fe ₇ Mo ₁₃ N ₄	Cubic	550-600	
τ	-	Orthorhombic	550-650	
η	Fe ₂ Mo-Fe ₂ Ti-Ti ₂ Mo Fe ₅₀ Cr ₅ Si ₅		650-950	After long time
Carbide	M ₇ C ₃		550-650	
Carbide	M ₂₃ C ₆	FCC	450-800	α-γ interface inside of α
Chromium carbide	Cr ₂₃ C ₆	HCP	600-900	Depleted surrounding matrix of chrome
Secondary austenite	γ ₂		800-950	Dark islands in ferrite wrapped with σ phase Cr-Mo depleted

Some features of the phases can be specified as following: δ phase strip and block style microstructure, γ is feathery characteristic and white, σ phase is relatively gray brown particles, γ_2 is dark islands in ferrite wrapped with σ phase chromium molybdenum depleted, χ is light particles which precipitates mainly at grain boundaries. Fig. 1-12, indicates the schematic position and microstructure of different intermetallic phases which mainly are form during heat treatment of stainless steels. Also, the stability of intermetallic phases are different in various temperatures. The schematic phase stability in duplex stainless steels is shown in Fig. 1-13.

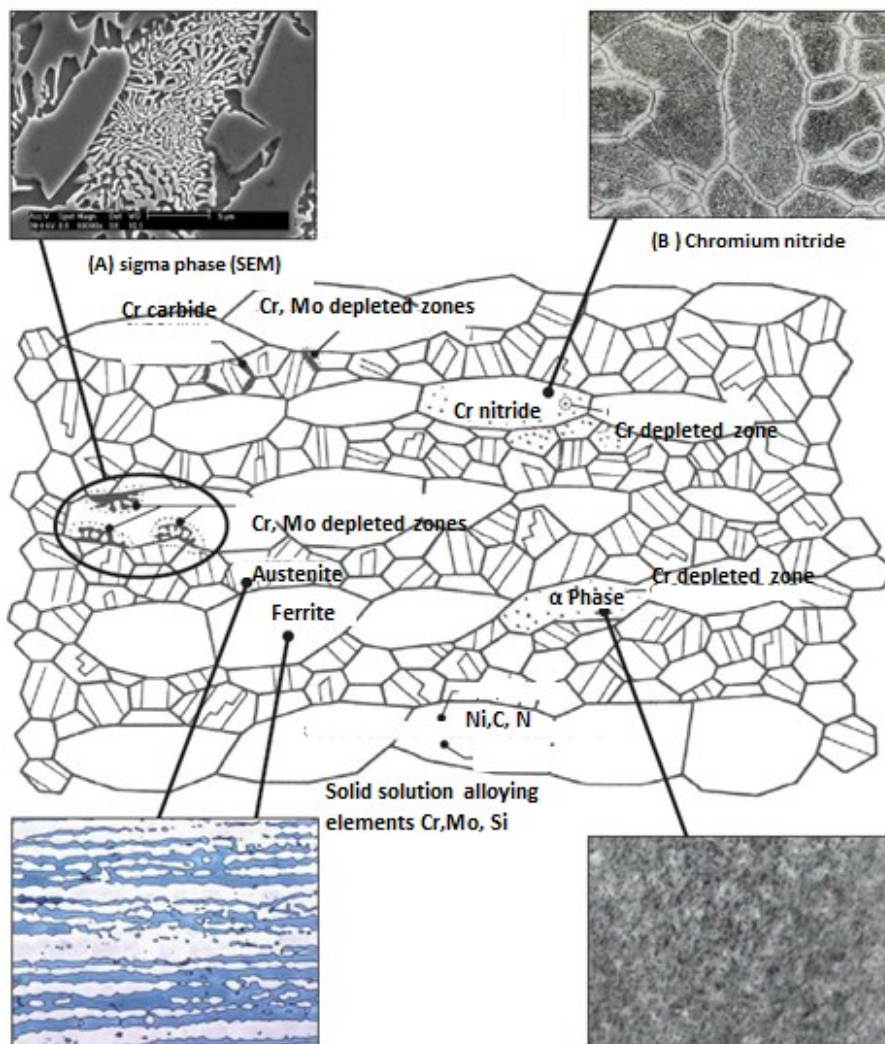


Fig. 1-12. Schematic image and microstructure of duplex steel and precipitated phases [39]

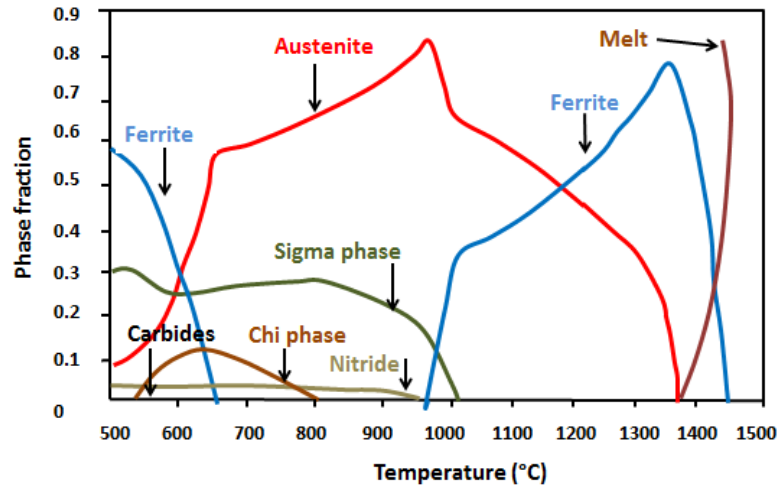


Fig. 1-13. The stability of different phases in duplex stainless steel

1.7.1. Sigma (σ) phase

Sigma phase is a non-magnetic, intermetallic, brittle and thermodynamically stable phase which form in Cr rich side of Fe-Cr-Ni ternary phase diagram. Also, it consists of Fe, Cr and Mo elements in closed packed tetragonal crystal structure with 32 atoms per unit cell, also It has tetragonal structure with $a=8.80\text{\AA}$, $c=4.56\text{\AA}$ [40]. Chevenard, firstly called this phase as “B constituent”, then Jette and Foote named it as sigma phase [41]. Existing this phase mainly cause to increases the hardness and decreases the toughness, as well as the elongation of the steel [42], in addition with increasing the amount of this phase the fracture type change from transgranular to intergranular [43,44]. Generally exposing the duplex steels at high temperature cause to partial decomposition of ferrite to austenite and sigma phase, which have negative effect on corrosion resistance and ductility of these steels. The sigma phase, mainly form between 600 and 950 °C and it accelerated between about 700 and 900 °C. The ferrite former elements such as Cr and Mo can promote the formation of σ phase.

Cooling rate is another effective parameter for precipitation of this phase, which has to be controlled (less than 0.35 °C/s). The mechanism of precipitation is a eutectic transformation of ferrite to austenite. Generally the nucleation of σ occurs in ferrite-ferrite and ferrite-austenite grain boundaries, then growth inside of ferrite grains. The heterogeneous nucleation of this phase mainly depends on interface energy and chemical driving force [45]. By many authors [45,46]. The Kurdjumov-Sachs (K-S) is considered as main orientation relationship to bring coherent and low energy ferrite-austenite interface which has an effect on formation of sigma phase. Mainly, ferrite formers such as chrome, molybdenum and silicon increase the formation of σ phase.

Compare to other elements, molybdenum is more effective in formation of σ phase, especially in higher temperature. Also, nitrogen and nickel can accelerate the formation of this phase, although they cause to reduce total amount of this phase compare to ferrite former elements.

The amount of this phase even in 1% decrease considerably the impact properties of the alloy and increasing the amount more than 10% completely deteriorate the toughness of the alloy. The mechanism of precipitation is a eutectic transformation of ferrite to austenite and σ phase. Generally the nucleation of σ occurs in ferrite-ferrite and ferrite-austenite grain boundaries, then growth inside of ferrite grains. During continuing the precipitation, the ferrite stabilizers elements such as Cr and Mo moves to the σ phase and cause to transformation of ferrite to secondary austenite. It should be mention that, the decrease of Cr is not considerable, but Mo decrease visibly and it diffuse into inside of the ferrite. Consequently, Mo is critical element for controlling the σ phase.

The morphology of the precipitated σ phase depends on the temperature. At the lower temperature (below 800°C), a coral like structure form. At beginning of formation of this phase the rate of nuclei is high and mainly depends on diffusion distance which is low at lower temperature. In higher temperature, because of more diffusion rate the sigma phase become coarser and dense, also behavior of precipitation change. Generally, this phase has characteristic gold color in optical microscopy.

For superduplex stainless steels, precipitation level increase, especially at 850 °C, because sigma phase can form just after 1min, and ferrite can transform completely after 1hour aging. Between 800 to 900°C is the range of susceptibility σ phase formation. The high susceptibility of duplex steels to σ phase formation, is attributed to chemical composition of ferrite. Ferrite is full of ferrite former elements (Cr, Mo, Si), that enrich the ferrite. With increasing the annealing temperature, the sigma phase grow through the ferrite till convert all ferrite to sigma. This phase is brittle and has negative effect on strength, toughness and corrosion resistance. The σ phase mainly form through diffusion, substitution or redistribution of alloying elements between, ferrite and austenite phases in duplex steels. This phase mainly forms at interface of austenite-ferrite phases or inside of ferrite, then growth inside of ferrite, consequently cause to reduce the amount of ferrite. The brittle σ phase is associated with plastic deformation, it cause to stop the movement of dislocations in different phases. It cause to stress concentration close to that phase, consequently cracks occurs in the fusion zone [47]. Fig. 1-14 shows schematic formation of sigma phase in grain boundary between ferrite and austenite phases accompanied with diffusion of alloying elements between phases.

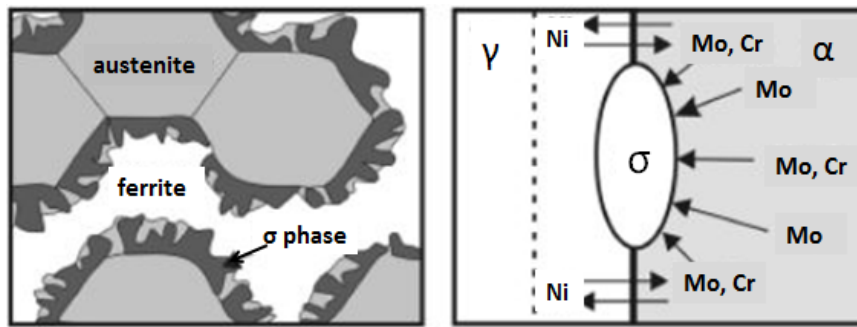


Fig. 1-14. Schematic formation and precipitation of sigma phase [48]

Fig. 1-15, indicates the precipitation mechanism of sigma phase in duplex stainless steels. At the beginning there is lamellar microstructure of ferrite and austenite side to side. With heating the lamellar cellular structure ($\sigma+\gamma_2$) are formed in ferrite/austenite grain boundaries. With continuing heating this structure grows till completely occupying the ferrite phase. Sigma phase usually forms after long holding times at temperatures between 650 and 950 °C and after cooling from high temperatures during welding. The weld thermal cycle has a decisive influence on phase precipitation [1]. Also, Fig. 1-16 indicates schematic formation of Sigma phase after decomposition of ferrite.

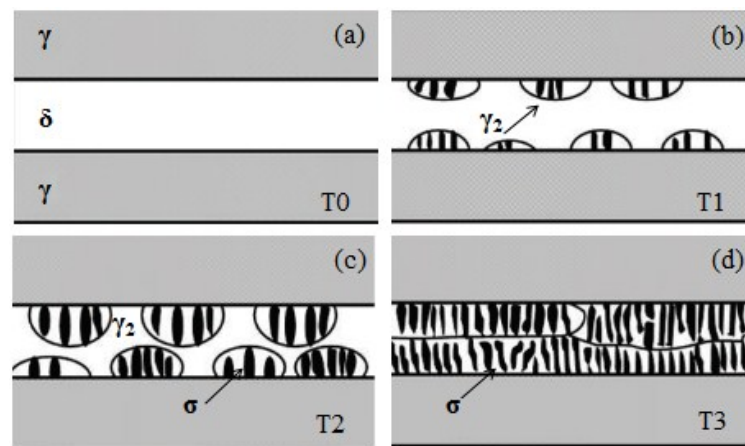


Fig. 1-15. Schematic mechanism for formation of sigma phase $T_3>T_2>T_1>T_0$ [49]

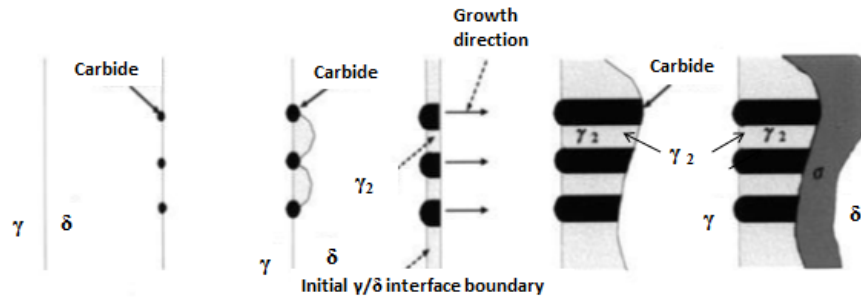


Fig. 1-16. Formation of sigma phase after decomposition of carbide [28]

As specified above, Cr, Mo and Si are the main elements which increase the susceptibility of sigma phase precipitation. Ramirez-Londono et al. based on ferrite former elements proposed sigma phase equivalent parameter to measure tendency to sigma phase precipitation [28].

$$\sigma_{eq} = X_{Cr(\delta)} + 4.5X_{Mo(\delta)} + 1.5 X_{Si(\delta)} \quad [50]$$

Where, $X_{Cr(\delta)}$, $X_{Mo(\delta)}$ and $X_{Si(\delta)}$ are the amounts of Cr, Mo and Si in the ferritic matrix.

In addition small amount of chromium carbide in form of $M_{23}C_6$ ($0.1\mu m$) can form with sigma phase especially in interface of phases. Also, this carbide particles can be surrounded by sigma phase. In addition, existing $M_{23}C_6$ carbide can be act as a site for sigma phase nucleation [51]. Michalska et al.[52], investigated on precipitation of sigma and chi phase in duplex stainless steel. They performed annealing at $750\text{ }^{\circ}C$ on the sample, they observed nucleation and precipitation of secondary phases. They observed sigma phase mainly in ferrite-austenite grain boundaries which mainly grows into the ferrite matrix. Also, they observed large and irregular sigma phase particles. In addition, they found sigma phase in form of coagulant which mainly precipitated in grain boundaries. They used electrochemical etching with 20% NaOH solution as a particular reagent which make them to observe the intermetallic phases accompanied with ferrite austenite grain boundaries. The main nucleation sites for sigma and chi phases are grain boundaries, incoherent twin boundaries and dislocations, precipitation of these phases cause to reduction of creep, ductility, toughness and corrosion resistance [53]. Fig. 1-17 shows the EBSD analysis of the duplex stainless steel which Ferrite, Austenite and Sigma phases are clear and recognizable with different colors.

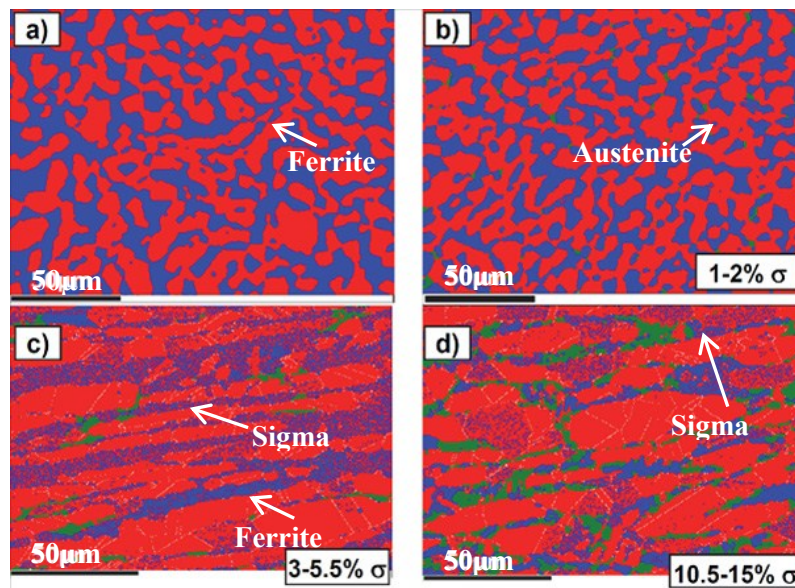


Fig. 1-17. EBSD analysis of duplex stainless steel after different annealing treatment [54]

It was reported that, just with existing 1% sigma in the microstructure, the mechanical properties of the steel deteriorated. Also, impact properties of UNS S32250 reach to less than 27J in case of existing 3-5% sigma in the microstructure [55]. Generally, The sigma phase with high content of Cr and Mo can be found in the 2205 DSS welded. The σ phase of 2205 SAW joints is formed mainly through substitution, diffusion, or redistribution of alloying elements between ferrite and austenite phases. The γ phase initially formed at the interface of the ferrite and austenite phases or within the ferrite, and then the sigma phase grows in the ferrite, so the content of ferrite is gradually reduced as result of γ phase growth [56].

Deng et al.[57] found sigma phase in UNS S32250 duplex stainless steel with chemical composition as following: 57.64Fe- 30.14 Cr- 4.2 Ni- 8.02 Mo. During formation of this phase, chromium and molybdenum diffuse from ferrite to the sigma phase which cause to localized depletion of these elements in around area of the sigma phase. These area due to lower amount of chromium and molybdenum and higher amount of nickel become unstable and cause to formation of secondary phases. Fig. 1-18 indicates detail shape of sigma and chi phases obtained from TEM. It is clear that, the position of formation of chi phase is on the boundary of sigma phase.

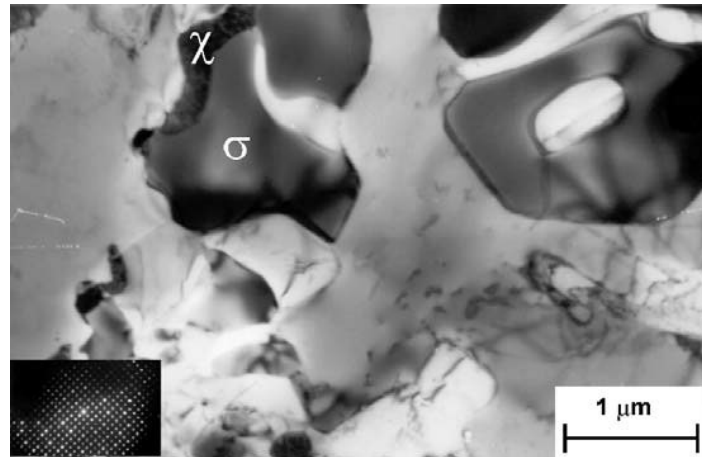


Fig. 1-18. TEM observation of sigma and chi phase [52]

In one reference σ phase is reported as following composition: 57.64Fe –30.14Cr– 4.20Ni–8.02Mo [58,59]. Chromium and molybdenum diffused from the ferrite matrix and in that area around depletion occur. These areas contain lower concentration of chromium and molybdenum and due to having higher amount of nickel they became unstable and transformed into secondary austenite (γ_2) [58,60]. Calliari et al.[36], investigated about precipitation of different phases in duplex and superduplex stainless steel, the result summarized in Table. 1-6 and Table. 1-7.

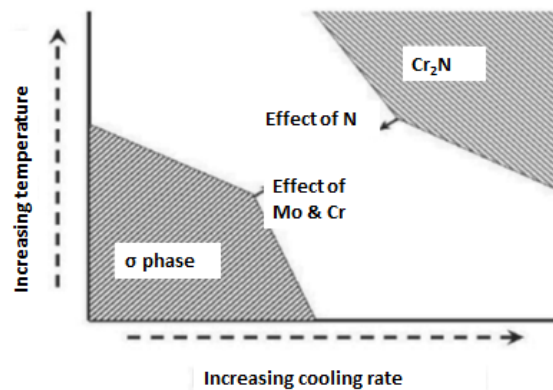
Table. 1-6. Precipitation of different phases in duplex steel [52,61,62]

Temp.(°C)	Time.(min)	Description
750 [52]	120	precipitation of χ phase
780 [61,62]	30 - 40	χ phase detectable in high magnification
850	10	χ phase detectable
	20	σ phase detectable
	30	σ and χ phase detectable, χ phase at grain boundary of α/α and α/γ
900 [61]		The first precipitated phase is χ in the grain boundaries By increasing the time σ phase form in the grain boundaries in coarse form growing to the ferrite. By increasing the time grows to large particles, moving to the boundaries into the ferrite, embedded by small chi particles.

Table. 1-7. Precipitation of different phases in superduplex steel [63]

Temp. (°C)	Time (min)	Description
800		No precipitation
850	15	χ phase appear
	20	χ phase more appear in grain boundary, no σ phase Small size of precipitation which is difficult to measure
900	5	χ phase at grain boundaries with isolated σ phase particles Small dark precipitation of Cr_2N at grain boundaries
	40	σ , χ and Cr_2N phase detected χ phase always at grain boundaries
920	120	Eutectoid dissolution of delta ferrite in secondary austenite, lacy form morphology of intermetallic
950	3	χ phase
	5	σ phase, with increasing the time σ phase increase
	30	χ phase decrease, σ phase start to form which is coarser and grow faster
	80	Transfer χ phase to σ phase
980	120	Changing morphology of sigma from lacy form to block shape, nucleation at interface and growth into the ferrite
1000	5	No σ and χ phase at grain boundary, about 0.5% inside grains
	15	σ phase max value, χ phase min value

In Fig. 1-19, schematic effect of alloying elements, temperature and cooling rate on formation of sigma and chromium nitride phase is shown. At the beginning of the formation of sigma phase, there is not so much effect on increase the hardness. [17,64]

**Fig. 1-19.** Effect of alloying elements and cooling rate on intermetallic phases [65]

1.7.2. Secondary austenite

Secondary austenite is another undesired phase like chromium nitrides, which occurs in ferrite grains. This phase has spherical or sharp edge like martensite characteristic which mainly form around existing austenite phase. It mainly form at the interface of γ/δ in temperature between 700 and 950°C as a result of the eutectoid transformation $\delta \rightarrow \sigma + \gamma_2$ and $\delta \rightarrow \text{M}_{23}\text{C}_6 + \gamma_2$. At temperature above 650 °C, there is diffusive transformation and the widmanstatten structure form [65,66].

The presence of the secondary phases in duplex steel, because of their chemical composition, morphology and distribution cause the loss of chemical stability between ferrite and austenite consequently a local decrease of corrosion resistance occur.

Moreover, the γ_2 phase is hard and brittle, which can reduce the strength, ductility, and plasticity of the welded joint [67]. Secondary austenite is in form of spherical or sharp edge, and it has martensitic characteristics. It forms at the interface of δ - γ and δ - δ boundaries during transformation of δ to carbide plus secondary austenite or δ to sigma plus secondary austenite at elevated temperatures because of high diffusion in boundaries. In addition it can nucleate in the particles of Cr_2N inside of ferrite grains. Also, this phase can form during reheating by growth of primary austenite islands. Secondary austenite contain lower nitrogen amount compare to primary austenite which form at high temperature and it causes to poor corrosion resistance [1,68]. Fig. 1-20, indicates secondary austenites which formed inside of the ferrite phase.

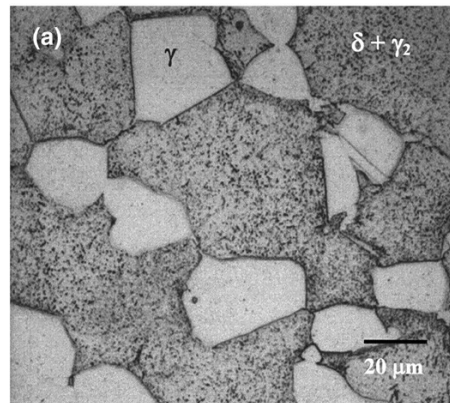


Fig. 1-20. Secondary austenite (black dots) which form inside of δ ferrite after aging [69]

There are two ways to recognize the secondary austenite from primary austenite. First is that secondary austenite is richer in nickel, chromium and molybdenum and secondly mainly it appeared in form of widmanstatten, due to that this phase is harder than primary austenite phase [66]. Secondary austenite appeared both on the boundaries and growing into the grains. It appears in two forms of A and B types which are in form of small γ_2 and large γ_2 Widmanstatten type needles respectively. The volume fraction of γ_2 strongly depended on the welding conditions (heat input), as well as annealing temperature and time. Also, A type mainly form in shorter time compare to B type. Fig. 1-21, indicates both types of secondary austenite in the microstructure.

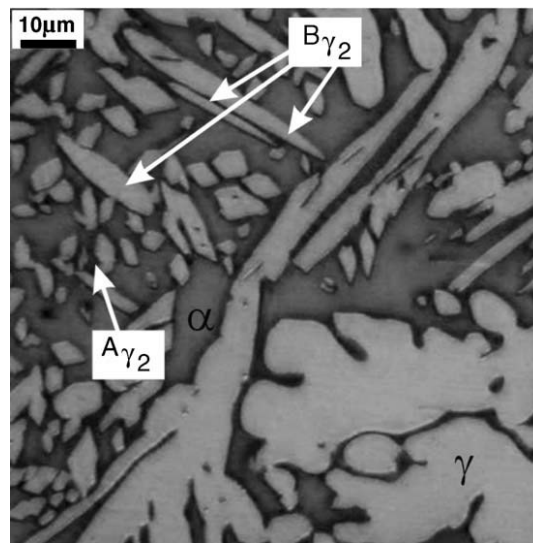


Fig. 1-21. Different types of secondary austenite [66]

The metallographic differences between primary and secondary austenite can be detected by using different types of etchant solutes which could be due to higher amount of Cr, Mo and N in secondary austenite. The differences between both types of austenite allows the observation of ferrite austenite interfaces which secondary austenite form. Generally the thickness of secondary austenite is not uniform along the boundaries [28]. This non uniformity could be due to variation of ferrite austenite interface and energy of interface, the diffusion path for the austenite forming elements. Fig. 1-22 and Fig. 1-23 indicate the SEM and optical microscopy image of secondary austenite in duplex stainless steel respectively.

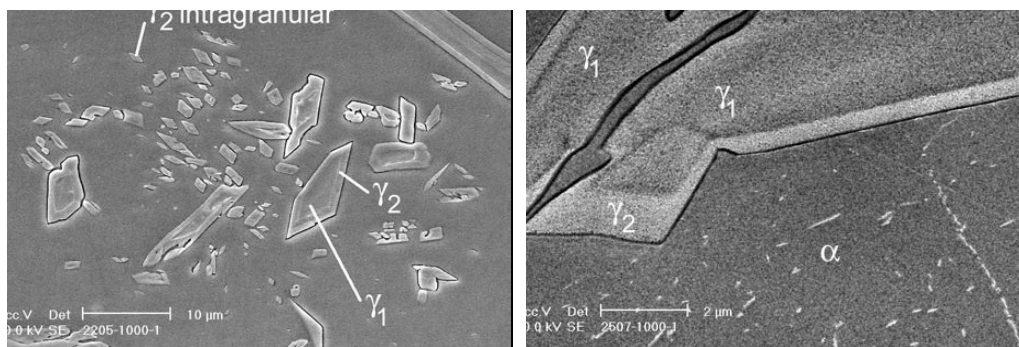


Fig. 1-22. Different thickness of secondary austenite which form from primary austenite in 2205 steel [28]

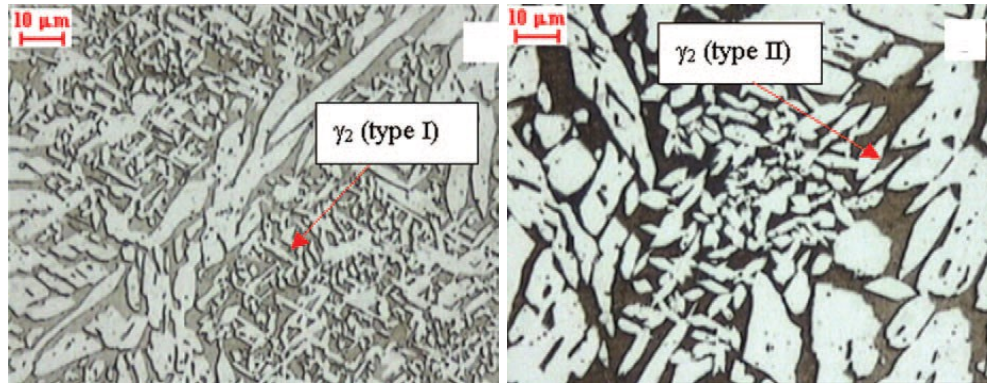


Fig. 1-23. Micrographs of the FZ: Widmanstätten-type secondary austenite (Types I and II).[65]

These phase, mainly are appears in forms of small white needle and island type [70] within the ferrite as well as along the ferrite/austenite interfaces. Nilsson et al. [71], indicated that secondary austenite increased the susceptibility of pitting attack in weld metal in terms of low concentrations of chromium, molybdenum and nitrogen. Non-eutectoid γ_2 , unlike the eutectoid γ_2 , does not affect the corrosion behavior significantly. Chemical composition of eutectoid γ_2 precipitation and its deleterious effect on localized corrosion resistance of SDSSs, was investigated by many researchers, they found degraded corrosion resistance of the microstructures is mainly related to the formation of nitrides [72–75]. Ramirez et al [76], performed detailed investigation about formation secondary austenite and chromium nitride in different types of duplex stainless steels.

1.7.3. Chi (χ) phase

As previously explained, after sigma phase, the main intermetallic phase which appears in duplex stainless steels is Chi phase. This phase was reported at first time in α -Mn type cubic structure in Cr-Ni-Mo steels by Andrew et al.[77] and Kasper et al.[78] with chemical composition of $\text{Fe}_{36}\text{Cr}_{12}\text{Mo}_{10}$, then Hughes and Llewelyn reported that this phase with similar chemical composition [77,79]. This phase mainly form in ferrite-ferrite and ferrite austenite grain boundaries and it appears in light form. Compare to sigma phase which mainly form in Fe-Cr systems, Chi phase appears in Fe-Cr-Mo and Fe-Cr-Ni-Ti systems. The chi phase is metastable phase and mainly form in ferrite-ferrite grain boundaries before precipitation of σ phase, also it has BCC crystal structure with $a=8.92 \text{ \AA}$ and this phase exist in wide range of stoichiometry [40]. In comparison with Sigma, carbon can dissolve in this phase. Because of this properties, in the past, it was considered as carbide M_{18}C type due to its ability to dissolve carbon. Also, it was reported that, this phase is richer in Cr and Mo compare to Sigma phase [79]. Precipitation of this intermetallic phase mainly accompanied with segregation of elements in the matrix, consequently ductility and corrosion resistance decrease.

These segregations are well known as the preferential nucleation sites for the heterogeneous precipitations Sigma and Chi phases. The small precipitates nucleated at austenite–ferrite interfaces in the aged specimen were considered to be the χ phase, while σ had a larger size [52]. Chi phase is much more unstable compare with σ phase and probably would transform to σ phase after increasing the aging times. As mentioned before, the χ phase with bcc structure forms in the earlier stage in the bcc ferrite of DSS due to preferential cube on cube orientation relationship. The chi phase can occur in austenitic, ferritic and duplex steels which has detrimental effect in mechanical properties. The temperature of precipitation of this phase and its amount is less than sigma. In addition, χ phase started to be disappear when it surrounded by sigma and secondary austenite phase [69,79]. Fig. 1-24 indicates schematic formation and disappearance of χ phase in duplex steels with addition of aging time.

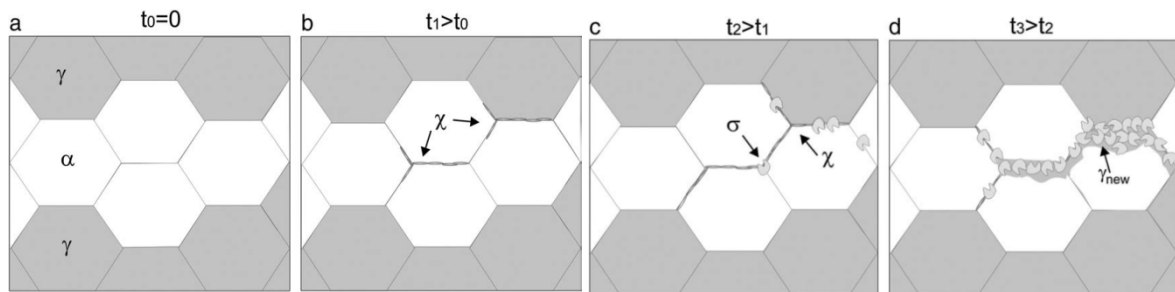


Fig. 1-24. Schematic formation of χ , σ and γ_2 phases [79]

There is not any specific condition for precipitation of χ phase, different researchers worked on this issue and they found different conditions. Calliari et al. [62] found the precipitation of χ phase at 780°C for 30 min, Michalaska et al [52] reported formation of this phase at 750°C after 2 hours aging. Fig. 1-25 indicates SEM images of σ and χ phase in the microstructure of duplex stainless steels.

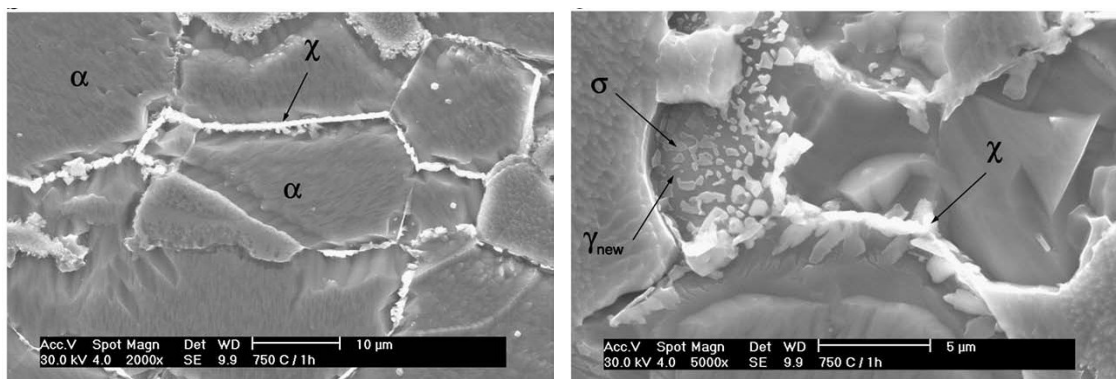


Fig. 1-25. Formation of χ phase in duplex steel, aged at 750 °C for 2hours [79]

Based on the research of Nilsson et al. [71], the Chi phase is metastable which act as a precursor of sigma phase especially at temperature around 900 °C.

1.7.4. Nitrides

The duplex stainless steels, intentionally consists of up to 0.3% nitrogen as alloying element. In solution anneal conditions, nitrogen remain constant in austenite due to high amount of solubility. Chromium nitride is a secondary phase which mainly forms during welding of duplex stainless steels in case of existing high nitrogen. High cooling rate and coarse ferrite grain cause to precipitation of this phase in ferrite austenite boundaries growth into the ferrite. Chromium nitride is a common secondary phase during the welding of high-N alloyed duplex stainless steels. The coarser ferrite grains and the fast cooling rate during the welding result in the precipitation of chromium nitride at the boundaries between ferrite and austenite grains and within ferrite grains. The existence of chromium nitride destroys the mechanical properties and corrosion resistance of duplex stainless steels [80–82].

In case of ferritic microstructure, after cooling from more than 1100 °C the ferrite become super saturated in nitrogen because of competition between chromium nitride and austenite precipitation [28]. Nitrides, can be formed as Cr_2N or CrN . Cr_2N is formed during fast cooling to form a high solution temperature because of high super saturation of nitrogen in ferrite. Also, if the formation of austenite and Cr_2N decrease, the CrN can be formed in HAZ at temperature below 1100°C. Generally, addition of nitrogen is useful for reformation of austenite till the upper limit and it should be optimized [83]. Cr_2N precipitates can be observe on polished surface without etching. Results obtained by different investigators on the effect of Cr_2N on mechanical and corrosion properties are in general agreements and mainly detrimental effects on ductility and corrosion resistance were reported [28,84,85]. Fig. 1-26 indicates schematic formation of chromium nitride and secondary austenite on ferrite-austenite grain boundaries.

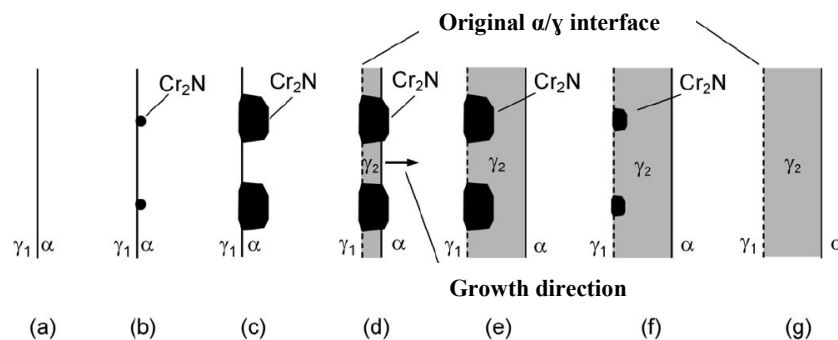


Fig. 1-26. Formation of Chromium nitride and secondary austenite in interface of ferrite/austenite [28]

Dobranszky et al. [81] Showed that the amount of Cr_2N phase at the beginning is very small, but after 24 hours aging these spots become larger. During aging process, chromium nitride can be formed and grow. In addition in this nitrides, small amount of vanadium detected which help to formation of nitrides. Fig. 1-27, shows the TEM images of chromium nitride which form in different positions of the microstructure.

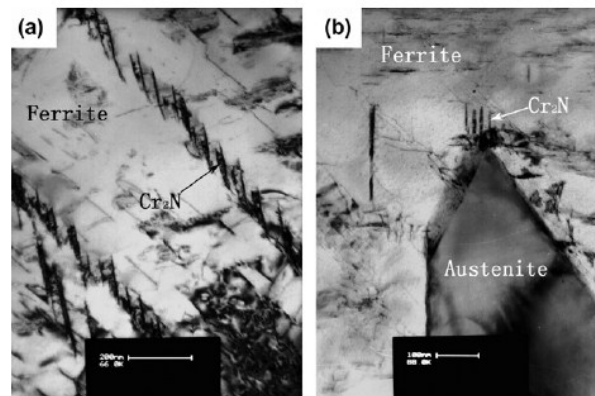


Fig. 1-27. TEM image of Cr_2N (a) Intergranular nitride (b) precipitate at interface of ferrite-austenite [86]

Yang et al. [56] investigated on effect of cooling rate on microstructure of HAZ in duplex stainless steel. They observed two types of chromium nitrides which can be categorized as tetragonal-like Cr_2N and platelet-like CrN . Fig. 1-28 indicates different types of chromium nitrides in the ferrite matrix.

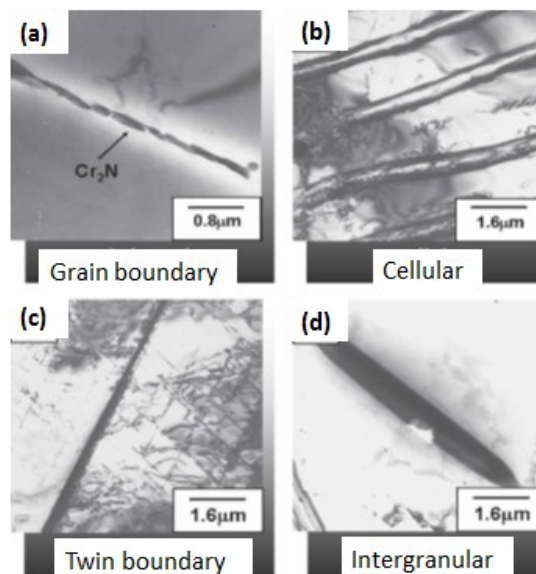


Fig. 1-28. TEM micrographs of different types of Cr_2N (a) grain boundary (b) cellular, (c) twin boundary, and (d) intragranular Cr_2N [87]

Also, as the austenite phase formed from diffusion on cooling below 1300 °C, it was reported that, by very low heat input the amount of ferrite in the microstructure increase and risk of precipitation of Cr₂N enhanced. Also at low temperature mainly the amount of ferrite and Cr₂N cause to decrease the toughness. It was reported that Cr₂N mainly occurs due to welding thermal cycles and can be act as nucleation site for pitting corrosion [88]. Also, this precipitation mainly occur due to welding thermal cycle. To detect this phase in the microstructure electrochemical etching in oxalic acid is suggested [89].

As the solubility of nitrogen in ferrite is limited especially at low temperature, nitrogen has not sufficient time to partitioning into the austenite (allotriomorph and widmanstatten). Consequently chromium nitride in form of intergranular precipitated). Reaheating the sample cause to liberation of nitride and accelerate nucleation of secondary austenite.

Chromium nitride (Cr₂N) precipitates have a high concentration of Cr and N and sometimes contain Fe, Ni and Mo, the formation of these Cr₂N within the ferritized microstructure is aided by this rapid cooling from the temperature above 1100 °C during welding, which creates a supersaturated solid solution due to low solubility of nitrogen in this phase. This results in the fact that ferrite became prime sites for pit nucleation [70,90]. Ramirez et al.[28] observed that, during heat treatment of duplex steel in temperature of more than 1100 °C, there is possibility of precipitation of Cr₂N within ferrite grains and intergranular nitrides in interface of ferrite and austenite which facilitate the precipitation of secondary austenite in ferrite/nitride interface. Migiakis et al. [91], observed nitride within ferrite grains of HAZ which associated with local formation of secondary austenite around them.

low cooling rate from solution treated temperature may cause to the precipitation of secondary phase such as sigma and Cr₂N [92]. Chen et al. [53] investigated on the effect of cooling rate from solution-treated temperature on the precipitation of different phases in duplex stainless steels. Their research had shown that a cooling rate higher than 15 °C/min could prevent the precipitation of sigma phase after the solution treatment.

Palmar et al.[93] observed precipitation of dark chromium nitrides in welded duplex steel. They found this phase precipitated due to super saturation of nitrogen in ferrite during rapid cooling between 900 and 700 °C. Chromium nitride cause to depletion of chromium inside of ferrite grains and it causes to decrease corrosion resistance. Also they found with increasing distance from the fusion zone this precipitates decrease.

1.7.5. Carbides

Also, existing carbon in range of 0.06-0.1% cause to nucleation of $M_{23}C_6$ carbide in size of about 0.1 μ m in ferrite/austenite interface. This precipitate can constitute with σ phase nucleation. The precipitation of this intermetallic occur during cooling the cast and after solidification in range of 850 to 550°C. Also, this phase mainly form in ferrite phase compare to austenite, mainly because of closer chemical composition to ferrite and more rate of diffusion in that phase. Phases with more amount of ferrite stabilizers, cause to depletion of ferrite. It should be mention that, after slow cooling rate of duplex steel from 1000°C, austenite phase grows to the delta ferrite. Also, $M_{23}C_6$ carbide is preferential site for nucleation of sigma phase. In addition this phase initially precipitated at grain boundaries of ferrite-austenite, and it can be trapped in the secondary austenite region. The formation of carbide phase can be related to less solubility of carbon in the matrix.

Also, the growth of carbide particles toward ferrite phase is due to existing more amount of chromium in this phase which let better diffusion compare to austenite phase. Migration of interface into ferrite phase is accompanied with growth of $M_{23}C_6$ carbide and secondary austenite. After completion of lamellar precipitation, the sigma phase form at the tip of lamellar precipitates because of second eutectic decomposition [63].

The sigma phase mainly nucleate at ferrite austenite interface and grows toward the ferrite grains as a result of eutectic reaction. Also, this phase may be appear directly in ferrite phase on the preferential sites such as carbides. With higher cooling rate the risk of precipitation of this phase decrease and the amount of delta ferrite increase. The fine and rounded sigma phase is more appropriate than the phase with sharp edge. The investigation of the effect of amount of σ phase on the impact properties of the UNS S32250 and UNS S32570 showed that with increasing the amount of σ phase the impact properties decrease considerably.

M_7C_3 carbides may form in a duplex steel in a temperature range 950-1050 °C and $M_{23}C_6$ at temperature lower than 950 °C, it mainly precipitate at a austenite phase region compare with δ/γ interface boundaries. This can be explained in terms of the migration of initial δ/γ interface boundaries into the δ phase region as the interface carbides preferentially have grown into the ferrite [94]. Intermetallic sigma phase, in temperature range of 600-1100 °C. Also, $Cr_{23}C_6$ precipitation is occur in duplex steel weld and base metal which have negative effect on the mechanical properties of the steel. It mainly precipitates on high energy regions such as grain boundaries [45,95]. Precipitation of this phase increase by decreasing the solubility of carbon and nitrogen in austenite [94].

1.7.6. Alpha prime (α' - 475 embrittlement)

The duplex steels are really susceptible to formation of chromium (α') brittle phase when they remain at temperature mainly between 400-500 °C. This stable phase in duplex steels mainly forms in ferrite phase and precipitation of that cause to hardening and decreasing the toughness at room temperature. This precipitation occurs by spinodal decomposition, a mechanism by which the ferrite phase decomposes into Cr-rich phase (α') and Fe-rich phases. Because this reaction occurs more rapidly at 475 °C, this process is also known as 475 °C embrittlement. The precipitation of this phase can occur in temperature of around 300 °C when it exposed in several hours (more than thousands) or exposing at 600 °C for few minutes, depending on the different steel chemical composition. Lippold et al. [96], showed that very small time of exposure at this temperature had great negative effect on impact strength of the duplex steel, but this effect is less in superduplex steel because of existing more nitrogen and less ferrite number.

In addition to existing more amount of chromium in superduplex stainless steels, which cause to more formation of α' , higher austenite formation can occur[97]. Tavares et al.[98] investigated on embrittlement of duplex stainless steels in different time, they observed that at beginning stage, hardness and toughness increase, then decrease significantly. Also, they observed many pits in the ferrite phase which causes to decrease the corrosion resistance. Fig. 1-29 indicates the SEM images of duplex stainless steel aged at 475 °C for 500hr.

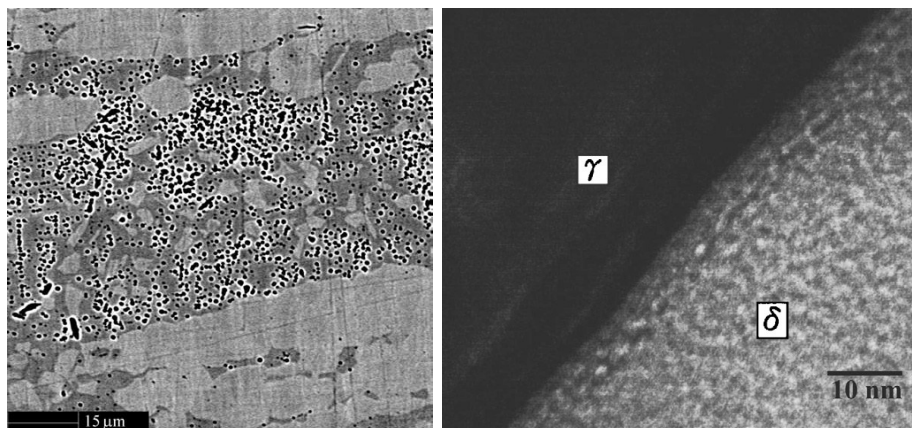


Fig. 1-29. Microstructure of duplex stainless steel aged at 475 °C (a) SEM [98] (b) TEM [97]

1.8. Solution Annealing Treatment and cooling rate

In the annealed condition, most wrought duplex stainless steels contain about 40-50% austenite in a ferrite matrix. When these materials solidify, first δ ferrite form and depending upon the composition, a varying amount of austenite is expected to form as the last material solidifies. Additional austenite forms by a solid-phase transformation during subsequent annealing. Accordingly, an annealed product is expected to contain more austenite than as-cast or as-welded material. A sufficient amount of austenite must be maintained to provide satisfactory corrosion resistance and mechanical properties. This amount of austenite may vary with the service application and with alloy composition and thermal history. Additional phases found in duplex stainless steels can include σ , χ , R, α' , carbides and nitrides. Generally, the ferrite stabilizing elements increase the formation of sigma phase. The annealing temperature has an effect on formation of sigma phase in two ways, first high annealing temperature which cause to increase the grain size and reduces the tendency to formation of sigma phase. Also, at higher temperature, delta ferrite can be present, which facilitate the formation of sigma phase during aging. The main treatment for duplex steels are heating the sample to reach the temperature of single ferrite phase, followed by water quenching which cause to supersaturate the ferrite phase at room temperature. After that, material can be cold rolled till 70-90 % followed by aging at temperature range of ferrite plus austenite (1000 °C). In this case, fine austenite in the matrix can be formed. The best performance of wrought duplex steel is obtained in solution treated condition. Annealing and hot working of these alloys mainly perform in temperature below ferrite solvents, where ferrite and austenite exists in equal percentage. Constitution tie line cannot be drawn with high accuracy in binary diagram, based on that the alloys hot worked at temperature near ferrite solvus followed by quenching, expected to reach ferrite phase with low amount of austenite. With lowering the temperature, austenite become more efficient phase. Fig. 1-30 indicates the schematic diagram for solution annealing of the duplex stainless steels.

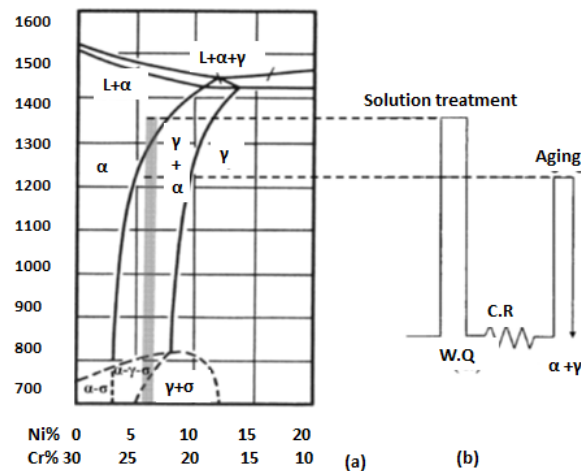


Fig. 1-30. (a) Part of Fe-Cr-Ni phase diagram
(b) Solution treatment in duplex steel [99]

Martins et al [63], investigated the effect of different aging temperatures (920 °C and 980 °C) for 2 hours on the microstructure of the stainless steel. Cooling rate is an important factor which should be considered after welding and heat treatment of duplex stainless steels. Critical cooling rate for 2205 suggested 0.35 °C/s and 0.1-0.15 °C/s to avoid sigma and chi phase precipitation, respectively. Another, cooling rate suggested by Calliari et al [61] at 0.02-0.4 °C/s in argon for 2205 steel and 0.8-0.9 °C/s for 2507 steel [36,55].

1.9. Etching solutes for duplex stainless steel

Due to difficulties of revealing the microstructure in duplex stainless steels, Different etching solutes were tried by many authors to find appropriate result. To reveal the microstructure of this alloy different chemical reagents and electrochemical etching solutions were suggested

Table. 1-8, indicates some useful reagents which were used by different researchers to reveal the microstructure of base and welded duplex stainless steels. Caliari et al. [36], investigated in depth on different etching methods for detection of intermetallic phases for 2205 and 2507 duplex steels.

Table. 1-8. Recommended reagents for the microstructure of duplex stainless steels [44,52,92,100–104]

Reagent	Chemical composition	Reference
Beraha for base	80 ml H ₂ O, 20 ml HCl, 0.3 gr K ₂ S ₂ O ₅	[101,104]
Beraha for weld	50 ml H ₂ O, 50 ml HCl, 1 gr K ₂ S ₂ O ₅ , 10 gr NH ₄ F.HF	[103]
	85 ml H ₂ O, 15 ml HCl, 1 g Potasiu metabisulphit	[105]
	80 ml H ₂ O, 40 ml hydrochloric acid, 5 g ammonium bifluoride, 1-2 g potassium metabisulfite	
Murakami 1	Aqueous solution of 10 % K ₃ Fe(CN) ₆ and 10 % KOH	[106]
Murakami 2	30 g K ₃ Fe(CN) ₆ , 30 g KOH, 60 ml H ₂ O	[103]
Villela	5 ml HCl, 1 g picric acid, 100 ml methanol or ethanol (95 %) 1 min	[106]
Marble	4 g CuSO ₄ , 20 ml HCl, 20 ml H ₂ O	[52]
Grosbeck	4 g KMnO ₄ , 4 g NaOH, 100 ml H ₂ O 1-10min, 30-60 °C	[52,107]
Glysergia	5 ml HNO ₃ , 10 ml glycerol, 15 ml HCl 1-3 min	[101,108]
Two steps	20 g Ammonium bifluoride, 0.5 g Sodium metabisulfite, 100ml H ₂ O Immersion 40-50 °C for 30-45 s 20 ml Hydrochloric acid, 1 g Sodium metabisulphite, 100 ml H ₂ O Immersion 30°C for 30-45 s	[109]
Electrochemical	10 % Oxalic acid, voltage 20V, current 5 A, time 100 s 10% Oxalic acid , 7 V, 30 s	[58,86,110,111] [92]
Electrochemical	20% or 40 % NaOH solution for color etching 1-10V, 5-60s	[56,102,112,113]
Electrochemical	10% or 30 % KOH solution 2-5V, 5-60s	[92,114,115]
Electrochemical	10 ml HNO ₃ , 20 ml glycerol 30 ml HCl to see the sigma phase	[86]
Electrochemical	10 g Pb(CH ₃ COO) ₂ , 10% H ₂ C ₂ O ₄ , 100 ml H ₂ O 6V, 30-40s	[52]
Electrochemical	10N KOH solution 2.5 V	[115]
Electrochemical	40gr KOH- 50MK H ₂ O	
Electrochemical	20 or 40 % KOH electrolyte at 2-3 V etching potential for 10-20 s	[70,116,117]
Electrochemical	2.5 V DC for 10 s in oxalic acid and 1.5 V DC for 10 s in 10 M KOH	[58]
Electrochemical	KOH solution (100 ml H ₂ O+15 g of potassium hydroxide),3 V for 12 s	[118]
Electrochemical	10 ml HCl,90 ml ethanol 1.5V	

1.10. Determination of phase percentages

The percentage of each phase can be determined by the grid point counting method. This method is based on ASTM E562 [119] which phase analysis can be categorized and measured by using area or volume fraction by manual point count. Mainly this method included the use of a grid containing 100 points at $\times 200$ magnification. In addition, with using ASTM E1245 standard [120], the inclusions and secondary phases can be measured by automatic image analyzing. The phase analysis measurement can be done with measuring the length, area, volume fraction, number of detected picture points and confidence interval.

Mainly for duplex stainless steels, measuring the percentage of phases are critical, there are different ways to measure the phases. First is using image analysis techniques where an image is homogeneously etched. The obtained image can be analysed with software to count the percentage of each phase. In this way large number of areas can be analysed quickly. But this technique mainly is not accurately usable for weld zone, because of inhomogeneity in that area. Another method is based on point count as specified in ASTM E562 standard [119]. In this method, magnification should be considered to be sufficient. Detail of this method will explain in the next chapter.

1.11. Welding parameters for stainless steels

Welding process

Generally, all fusion welding processes with considering appropriate process specifications can be applied for duplex steels. Lower arc energy welding processes such as laser beam and plasma impose lower amount of austenite due to high cooling rate and higher arc energy such as GTAW, GMAW, SMAW and FCAW increase the precipitation of austenite due to low cooling rate [121,122]. Among them GTAW provides higher efficiency in the weld joint and make it suitable especially for root pass which is critical especially in pipe welding application. For the filling passes, MMAW and GMAW process can be applied. The electrode diameter for MMAW and GMAW are mainly between 2.5-5mm and 0.8-1.6mm respectively. Also Ar, He, CO₂ or mixture of them can be selected as shielding gas [1].

Selection of filler materials

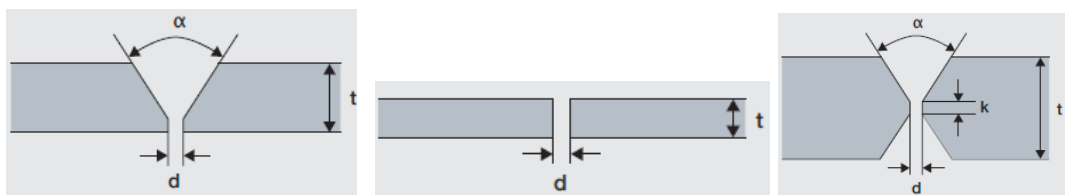
There are two types of filler materials for welding of duplex stainless steels. The first is matching composition type which has an application for manufacturing of the parts which needs post weld heat treatment. Another type is using overalloy consumables which has an application in pipework and vessels which can be installed in as welded conditions. Filler metals which mainly used for welding of duplex steels contain more amount of alloying elements especially nickel which cause to enhance formation of austenite in completed zone. Also, for welding of duplex stainless steels specific types of filler metal should be selected to reach the weld properties close to the base metal. One important and high applicable filler metal is AWS ER 2209 which contain 22% chromium and 9% nickel. It has many applications for 2205 and 2304 grade of duplex steels which contain 5% Ni. Generally AWS ER2209 and ER2594 filler metals are recommended for welding of duplex and superduplex stainless steels respectively [123]. Table. 1-9, indicates the chemical composition of filler metals which have many applications for welding of various types of duplex stainless steels

Table. 1-9. Nominal chemical composition (wt%) of some duplex stainless steel filler metals [124]

Filler metal	AWS No.	Cr	Ni	Mo	C	Mn	S, P	Si	N	Cu	Fe
E 2209	A5.4	21-23.5	8-10.5	2.5-3.5	0.04	0.5-2	0.03	1	0.08-0.2	0.75	Bal.
ER 2209	A5.9	21-23.5	7.5-9.5	2.5-3.5	0.03	0.5-2	0.03	0.9	0.08-0.2	0.7	Bal.
ER 2553	A5.4	24-27	4.5-6.5	2.9-3.9	0.04	1.5	0.03	1	0.1-0.25	1.5-2.5	Bal.
ER 2594	A5.4	24-27	8-10.5	3.5-4.5	0.04	0.5-2	0.03	1	0.2-0.3	0.75	Bal.

Joint design

Type of joint should be designed based on thickness of the materials and the welding process. It could be considered based on thickness of the material, generally less than 3mm plates do not need specific joint design considerations. More than that thickness mainly different kinds of grooves should be applied on the edge of the samples to obtain optimum welding condition. Groove welds can be prepared by machining and plasma arc cutting. To reach better consistency in fit-ups and ensure balanced heat input, the joint machining is recommended. The joint design for duplex steels are quite the same as austenitic steels, just it would be recommended to use a little wider gap, thinner root face and larger groove angle. Fig. 1-31 shows some principle joint design which are used for welding of duplex stainless steels.

**Fig. 1-31.** Some conventional joint design for welding [124]

Precleaning, preheating and interpass temperature

Before welding process, the joint should be cleaned to remove any oxides, oils, dirt and contaminations. Also, preheating with high temperature mainly should be avoided, but just after precleaning high preheating for removing the moisture is recommended. In this case it is recommended to use infrared heater or electrical resistance strip heater, because using flame spary causes to produce combustion products and porosity. In addition, interpass temperature due to importance on time of transformation. High temperature interpass cause to increase the cooling rate which is really important parameter on phase balance determination of final microstructure, in addition to formation of intermetallic phases. For critical applications, precise contact thermocouple should be used to measure the interpass temperature. Generally, for duplex and superduplex interpass temperature between 100 and 150 °C is recommended [7,125].

Prevention of nitrogen loss during welding

One major problem of welding of stainless steels is evaporation of nitrogen gas during fusion welding. Nitrogen loss from the weld occurs due to difference in nitrogen partial pressure. To solve this problem, additional nitrogen gas can be applied through direct purging or mixed with shielding gas. Also, it causes to reduce the oxygen in root gas and improve corrosion properties in that area. Low oxygen content in the gas purge means low nitrogen content. Consequently, the root has more amount of nitrogen. Also, mixing the nitrogen with argon as a shielding gas is another solution to keep up the nitrogen of the weld. Based on result from PREN, nitrogen play important role in corrosion properties of duplex stainless steels. Evaporation of existing nitrogen during welding causes to decrease the corrosion resistance due to high ferrite content and precipitation of chromium nitride. The amount of loss can be replaced by using filler material with more amount of nitrogen [7]. The austenite formation increase with adding the nitrogen in shielding gas, it has more effect than addition through filler metal. Also, the backing gas of (90-100%) N₂+ (0-10%) H₂ is recommended to save corrosion resistance [1].

Heat input control

Heat input is critical parameter to perform sound weld in duplex stainless steel. When all the weld zone remain at high temperature, more time is necessary to pass the temperature range which there is risk of precipitation of detrimental intermetallic phases. It would be more critical for the root passes in welding of the pipes. Mainly the phase balance of duplex steels controlled by the composition of the weld and by the cooling rate achieved by the combination of heat input, interpass temperature and joint geometry. In case of thicker base material, better cooling rate can be achieved. This is due to changing the heat transfer from the heat affected zone from 2D to 3D. Based on previous studies, mainly thickness more than 7-12 mm is considered as a case for 3D cooling. In the welding procedure of duplex stainless steels, heat input as a critical parameter should be specified [1,125]. This value for lean and standard duplex stainless steels is recommended between 0.5-2 kJ/mm and for super duplex between 0.4 to 1.5 kJ/mm [1].

Cold pass techniques

Mainly subsequent pass has an effect on corrosion behavior of primary pass. It was suggested that heat input of subsequent phase became 65 to 85% of the first pass which cause to minimize the heat damage and optimize the corrosion behavior. This is called cold pass technique in comparison with normal subsequent pass with the same heat input. Also, it was reported that this cold pass avoid the reheating of the previous passes and the formation of intermetallic phases [13,126].

Post weld cleaning

After welding, spatters, arc strikes, grinding marks, iron contaminations, grease and oils should be removed. It should be added, due to spreading of contaminations, using mechanical methods are not recommended. The post cleaning is as important as fabrication process. The surface condition of stainless steels are critical and product should not have contamination especially for pharmaceutical, food and nuclear plants. Stainless steels mainly form chromium oxide on the surface to reach high corrosion resistance. During thermal cycle of welding, heat tint oxide form which causes to decrease the corrosion resistance. Therefore this heat tint should be removed by means of different methods such as grinding, blasting and pickling. [123].

Welding procedure qualification

Welds of duplex steels such as other type of ferrous materials should be qualified by different standards such as ASME or ASTM. This standards also, specified general thickness range for qualification. These steels are sensitive to cooling rate, it should be controlled and optimize to reach appropriate phase balance and avoid precipitation of intermetallic phases. As cooling rate mainly controlled by heat input, interpass temperature and thickness, consequently special attention should be considered for these parameters. Also, many welding procedures for different types of ferrous materials, which are based on simple mechanical properties are not enough for duplex stainless steels. Other additional tests such as corrosion, toughness, microhardness and fatigue tests are required [1,13]. The most popular tests are specified in ASTM A923, ASTM E562 for phase percentage determination and ASTM G48 standard for the corrosion properties.

1.11.1. Welding Metallurgy of Duplex stainless steels

Duplex stainless steels, solidify as ferrite, then solid state transformation of ferrite to austenite in a range of temperature occur. Depending on composition, the ferrite phase is stable over range of elevated temperature before it falls less than temperature of ferrite solvus. Because of relatively rapid transformation, this process is not equilibrium, consequently more ferrite remains untransformed. There is no specific difference between, solidification of duplex steels and carbon steels, but the main difference is in carbon steel all of the austenite change to ferrite, bainite and martensite except a little amount of ferrite remain, but in duplex steels large amount of austenite remain in the microstructure [127].

In duplex stainless steels, generally austenite phase formed from ferrite in different forms

- Allotrimorphs at the prior ferrite grain boundaries
- Widmanstatten side-plate growing into the grains from allotrimorphs
- Intergranular precipitation

Argon shielding gas has an effect on nitrogen loss during welding which can be avoided by selecting appropriate heat input and inter-pass temperature. More ferrite phase present in argon shielded weld metal. Consequently the solubility of nitrogen in ferrite decrease with decreasing the temperature.

Also, the grains are finer in argon shield, the austenitic phase within the grains could be either intergranular precipitates or Widmanstatten austenite transverse to the long axis direction. Widmanstatten austenite, nucleates directly from prior alpha ferrite boundaries which have been covered by allotriomorphic austenite perturbation.

Solidification of duplex stainless steels weld metals starts with epitaxial growth of ferrite grains from the fusion boundaries. Columnar ferrite grain boundaries are decorated by the austenite allotriomorph when the weld cools from ferrite to ferrite plus austenite phases. With further cooling Widmenstatten austenite side plate and intragranular austenite plates can be observed. Two main mechanism of massive and paraequilibrium transformation are suggested to be rate controlling process during transformation [128].

Generally, in duplex stainless steel weldments, HAZ and weld metal consist more ferrite content, large grain size and higher intermetallic phase precipitation in addition to have more N, O and H elements. Consequently, these factors cause to reduce the toughness, ductility and corrosion resistance of duplex steel welded joints [52,56,99]. Also, the weld thermal cycle has negative effect on the toughness properties of duplex stainless steels. Slow cooling rate promote a high austenite fraction, but it causes to reach large grains and precipitation of more brittle intermetallic phases such as sigma and chi [64,129].

Generaly, phases which mainly exist in the microstructure of the welded duplex stainless steels can be specified as following: Ferrite (δ) phase is in strip and block style microstructure, austenite (γ) is white with feathery characteristic, sigma (σ) phase is relatively gray brown particles, secondary austenite (γ_2) is dark islands in ferrite wrapped with σ phase chromium molybdenum depleted and chi (χ) is light particles which mainly precipitates at grain boundaries.

Weld solidification cracking

Solidification cracking is strongly dependent on chemical composition and mainly defined based on Cr_{eq} and Ni_{eq} . Due to solidification of duplex stainless steels in ferrite phase, mainly this kind of steel is more susceptible to solidification cracking because existing more amount of ferrite-ferrite grain boundaries which are easily become wet by liquid film compare with ferrite-austenite grain boundaries. Consequently the duplex stainless steels are much more resistance to solidification cracking compare with austenitic steels. Also, it should be mentioned that, duplex steels have low impurities of grain boundaries [1].

Cold cracking (Hydrogen embrittlement)

Due to high resistance of duplex stainless steel to hydrogen induced cracking, but still there is possibility of occurring this kind of crack. It could be because of existing high content of hydrogen and lower control of the microstructure. As for this kind of cracking, existing hydrogen, stress and susceptible microstructure is required, low hydrogen welding practice is recommended. Consequently despite of useful addition of hydrogen gas for welding of austenitic steel, it is not recommended for duplex steel. To ensure, higher resistance to cold cracking of duplex steel, the control of ferrite number of fusion zone is important. With sufficient austenite in the microstructure, there are network of austenite in both grain boundaries and inside of ferrite grains cause to decrease the diffusion rate. Encapsulation of the ferrite, cause to limit diffusion of hydrogen in the microstructure.

Microstructure of the weld

Microstructure of the weld zone of the welded duplex stainless steel is really complicated due to much changes compare to the clear base metal microstructure. Fig. 1-32 shows schematic diagram for cooling and formation of different zones of welded duplex stainless steel. Duplex steels, mainly solidify in completely ferrite phase and there is no austenite during solidification and it forms with further cooling till room temperature. Ferrite grows in epitaxial form from the fusion boundaries and dendritic growth is oriented in relation to the thermal gradients. Consequently, coarse columnar ferritic structure influences the final duplex structure. Ferrite grain size and growth orientation are important factors for the morphology and microstructure [130,131]. Fig. 1-33 indicates, the microstructure of the fusion zone of welded duplex stainless steels and formation of different intermetallic phases.

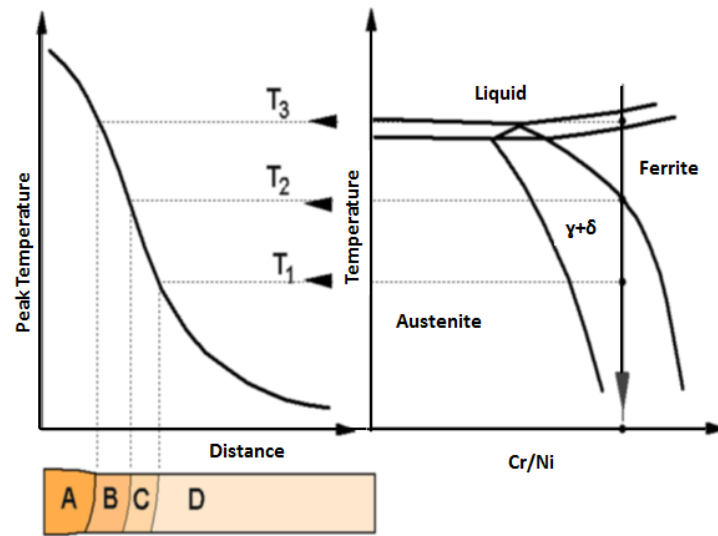


Fig. 1-32. Schematic diagram for the weld constitution of a duplex stainless steels. A – FZ, B – high temperature HAZ, C – low temperature HAZ and D – BM [32]

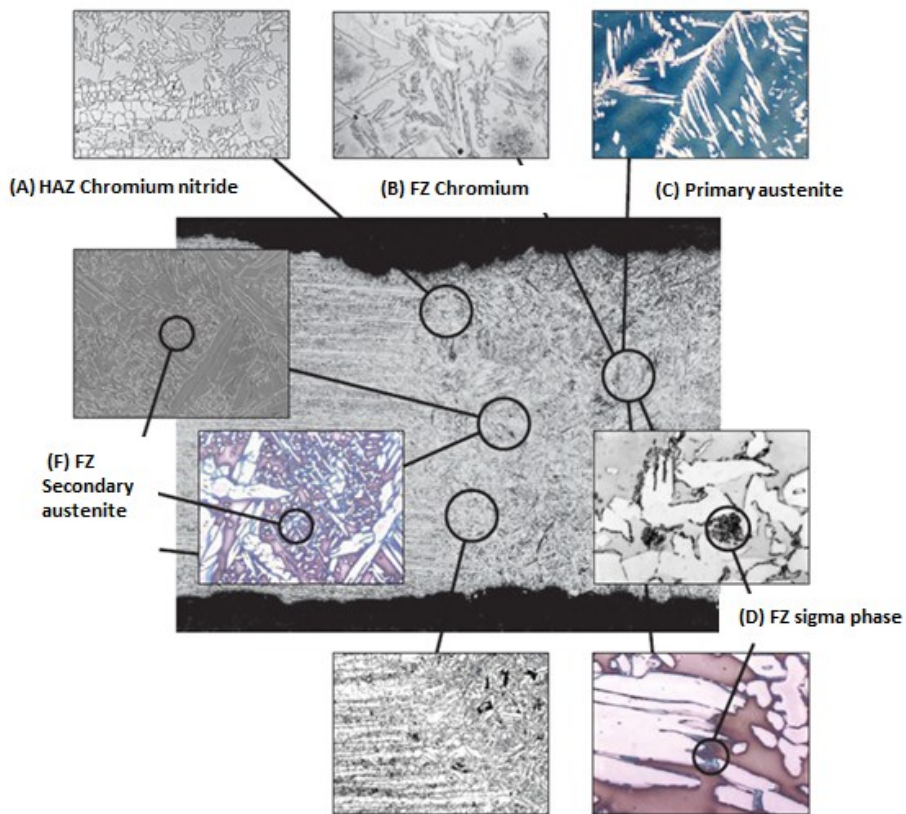


Fig. 1-33. Microstructure of welded duplex steel in different zones [39]

1.11.2. Microstructure of heat affected zone

Heat affected zone (HAZ) is the most critical part of the welded duplex stainless steels. HAZ in welded duplex steel can be divided to overheat zone close to fusion zone which temperature normally do not reach to 1300 °C, in this zone due to recrystallization, grain growth occur. This is mainly occur in ferrite grains compare to austenite due to slow dissolution rate and advancing deeply into the partially annealing zone [45]. In that area despite of welding zone, hot cracking is not occur but mainly loss of corrosion resistance due to changing the chemical composition accompanied with poor impact properties was reported in comparison with normal materials [132]. In that area, when microstructure subjected to heat treatment, one new type of austenite which called secondary austenite is form, this phase mainly consists of lower amount of alloying elements such as chromium, molybdenum and nitrogen. In addition in that zone, precipitation of nitride inside of ferrite grains and ferrite austenite grain boundaries was reported. Fig. 1-34 depicts schematic solidification procedure in duplex stainless steel. The intergranular secondary austenite formation in HAZ of the duplex stainless steel and its relation with chromium nitride was reported in detail by Ramirez et al. [28], they found liberation of nitrogen by dissolution of nitride in temperature of 1000-1200 °C, which facilitate the nucleation of secondary austenite.

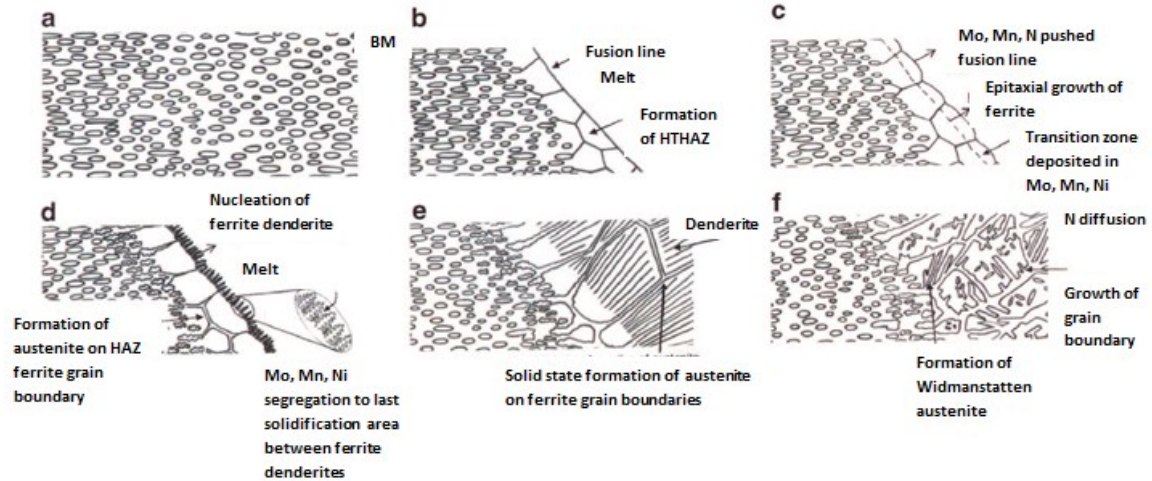


Fig. 1-34. Schematic solidification procedure in duplex stainless steel [133]

The epitaxial solidification is fully ferritic and planar, holding in solution annealing temperature cause to push all alloying elements in front of the solidification line. This could explain the decrease manganese, molybdenum and nickel in depleted fusion zone, whereas the lowest concentration of elements can be seen. By increasing the undercooling, the planar growth continues as cellular and with more growth, the planar solid-liquid interface become unstable [133].

1.11.3. Post weld heat treatment

Post weld heat treatment (PWHT) for duplex stainless steel weld for stress relieving is not recommended, because there is possibility of precipitation of intermetallic phases which cause to loss the corrosion resistance and toughness. But, for reaching the equal amount of ferrite and austenite and improve the microstructural, corrosion and mechanical properties, it is necessary to apply appropriate treatments such as changing the chemical composition, welding parameters, shielding gas and post weld heat treatment [86,109,111,134].

Normally, PWHT at solution anneal temperature followed by water quenching is suggested to reach the equal amount of ferrite and austenite in welded zone. Many research was done in this issue, Badji et al [135] applied post weld heat treatment in range of 800 to 1150°C to investigate the microstructure evolution of duplex stainless steel, they found PWHT less than 1100°C cause to precipitation of intermetallic phases. Young et al [59] found that PWHT at 1050 °C for 15 min, cause to increase the impact toughness of welded part. Another authors [136] works on the effect of different methods of PWHT by induction and furnace heating. Zhang et al. [86] investigated on the effect of short time post weld heat treatment on pitting corrosion behavior of UNS S32205 stainless steel welded part. By PWHT at high temperature, the amount of sigma phase in HAZ and fusion zone decrease. This could be due to solving much σ phase into γ phase. This change of σ phase cause to reduction of micro hardness in HAZ and fusion line. During the PWHT, Mo and Cr elements moves to δ phase. It causes to precipitation of σ phase from the interface of δ/γ . Another reason could be because of existing unstable γ_2 phase. In that zone, near the γ_2 phase, is rich of Cr and Mo and is depleted from the Ni. This cause to increase the amount of σ phase with continuous distribution characteristic and γ phase swallowed [137]. Zhang et al.[86], Indicates that, increasing the PWHT temperature cause to increase the amount of grain boundary allotriomorphs austenite and widmanstatten austenite in the weld metal and heat affected zone. They found that PWHT less than 1100 °C cause to precipitation of intermetallic phase. Also, they observed many intergranular austenite grains reveals grain growth to assume roughly spheroidal shape. The second phase, segregation of elements and diffusion of welded joint are responsible for the microhardness of the weld. Luo et al. [137] found that PWHT cause to move the σ phase from the HAZ to center of the weld. Also the amount of γ phase decrease in the weld center. They reported existing of some secondary phases in the weld center. In addition all γ phase, δ phase, secondary austenite phases exist in both PWHT and without PWHT samples. After PWHT the intensity of γ phase increase. Based on kinetics and thermodynamics of nucleation, the nucleation of σ phase is mainly depends on temperature and the grain size of the δ ferrite. Since there is high temperature gradients and high cooling rate in fusion zone, the diffusion rate of sigma (σ) phase promote element increase.

At weld center zone, the balance welding condition cause to uniform formation of element and phase distribution. The amount and segregation of Ni, Fe and Cr increase surrounding the σ phase region. The segregation of elements cause to promote the precipitation of δ and γ phase. Generally, diffusion, displacement and redistribution of alloying elements in different phases cause to formation of secondary phase and its transformation [137]. Fig. 1-35 indicates schematic figure for formation of second phase in the weld zone.

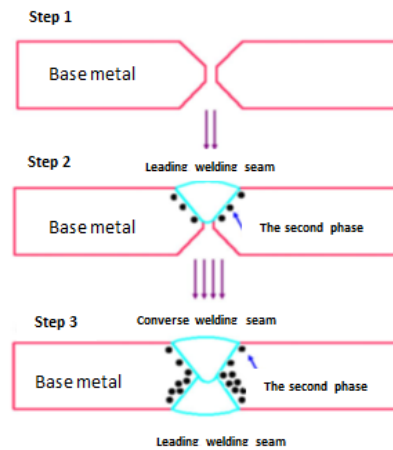


Fig. 1-35. Schematic diagram for formation of the second phases in a fusion zone affected by the converse weld seam [67]

1.11.4. Effect of nitrogen on steel

In one category if the percentage of nitrogen in austenitic steel is more than 0.4% and in martensitic steel is more than 0.08% it is considered as nitrogen alloy steel. This element is deliberately added to duplex stainless steel. There is a try to replace nitrogen with nickel especially for austenitic and duplex steel to improve high temperature mechanical properties accompanied with high corrosion and oxidation resistance. Nitrogen in solid solution is an appropriate element to improve strength without specific effect on ductility and toughness. Also the solubility of nitrogen in austenitic steel based on chemical composition is less than 0.9% [56]. More than solubility limit, causes to precipitation of Cr_2N and gas porosity in the weld zone which has negative effect on toughness and ductility. Addition of nitrogen causes to stabilize the austenite and can be work hardened to high level without risk of formation of strain induced martensite. Also, Nitrogen can reduce the stacking fault energy of stainless steels especially at low temperatures [11,138,139] which causes to improve strength, impact and fracture toughness depending on slip mode, deformation twinning and martensitic transformation. Solid solution hardening mainly depends on the atomic size misfit of the solute atoms with austenite crystal lattice. It has large effect on YS between different interstitial alloying elements.

The effect of nitrogen on grain boundary hardening can be explained with planar dislocation structures observed in stainless steel and by decreasing the effect of nitrogen on SFE. High nitrogen alloys indicated ductile brittle transition at low temperature, and mainly brittle like fracture occurs along (111) planes.

Also, by addition of nitrogen, grain boundary hardening increase therefore with increasing the nitrogen content of the steel, strong affinity between chromium, molybdenum and nitrogen atoms occurs [11,140]. Nitrogen is potent interstitial solid solution strengthener and has greater solid-solubility than carbon, it is a strong austenite stabilizer thereby reduce the required amount of nickel for stabilization; nitrogen reduce the tendency to form ferrite which causes to improves pitting corrosion resistance. By increasing the Cr, Mo and N of stainless steels, it is possible to increase crevice corrosion resistance. It accelerate the partial transformation from ferrite to austenite during cooling and it can assist to homogenize distribution of chromium between two phases [134]. Also nitrogen causes to postpone the initiation and suppress the crack growth by fast formation of passive layer on the surface [11]. In addition, it was reported that by increasing the amount of nitrogen, precipitation of chromium nitride occur and gas porosity formation take place, consequently ductility and toughness decrease. Also, nitrogen cause to decrease stacking fault energy (SFE) of austenitic stainless steels, especially at low temperature [11,138]. Overallly, main effects of addition of nitrogen can be categorized as increasing austenite content, reduce formation of chromium nitride, making austenite more corrosion resistant, reduce partitioning of solid solution alloying elements and changing the mode of solidification, delay the formation of brittle intermetallic phase, reduce the segregation of chromium between two phases, decreasing the Cr_{eq}/Ni_{eq} ratio and increases the transformation temperature of the α -phase to γ phase. Also fast cooling cause to oversaturation of nitride in ferrite phase. It should be mention during welding, almost all austenite transformed to ferrite. In this situation, the value of nitrogen is equal to nitrogen in base material [141].

1.12.Element partitioning

The phase diagram of duplex stainless steels, indicates that chemical composition of ferrite and austenite are different consequently element partitioning between phases are diverse. Normally the main partitioning occur for nitrogen, compare to other alloying elements. This is due to its low dimension and limited solubility in ferrite phase. It is accepted that, W, Mo, Si and Cr are rich in ferrite and N, Ni, Cu and Mn are rich in austenite phase. In high elements alloys, because of high annealing temperature, the partitioning coefficient tend to be in unit value. Fig. 1-36 illustrates the partitioning coefficient of elements in different temperatures.

As it is clear, ferrite stabilizer elements such as Cr, Mo and Si with increasing the temperature partitioning ratio decrease and reached to one, but for austenite stabilizer elements, with increasing the temperature partitioning ratio increase and reached to one.

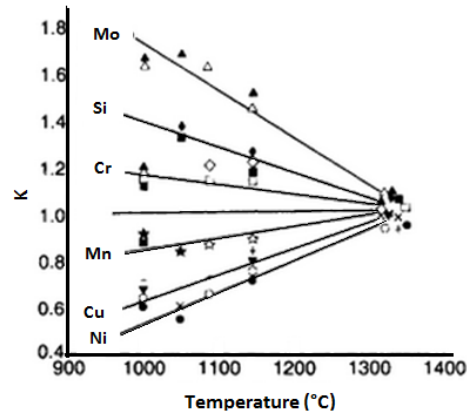


Fig. 1-36. Temperature dependence of partitioning elements [17]

For the nitrogen, the partitioning based on different alloys are different and it mainly depends on chemical composition. Specifically, Cr and Mn cause to increase the solubility of nitrogen, due to high content of these elements, but mainly it depends on the temperature. During solution annealing, the solubility of nitrogen in ferrite increase, but due to lower volume fraction of austenite, the concentration of nitrogen in austenite increase significantly, as a result the partitioning coefficient of this element increase. Nitrogen mainly concentrated in grain boundaries between ferrite and austenite close to the austenite. During cooling, volume fraction of austenite increase and ferrite become rich in nitrogen, and excess nitrogen diffuse to the austenite. The maximum solubility of nitrogen in ferrite was reported between 0.03-0.05%. Nitrogen play an important role in pitting corrosion resistance and it causes to partitioning of Cr and Mo in both phases, as a result pitting resistance increase. All discussed above have influence on the effect of solution heat treatment on microstructure and formation of secondary austenite. After solution annealing, primary austenite dissolved and during cooling formation of secondary austenite occur which contain lower amount of Cr, N and Mo with lower pitting resistance. With heat treatment at low temperature, substitutional elements can be partitioned and cause to formation of intermetallic phases. In some cases double heat treatment which consist of heat treatment above solubility of sigma phase formation and lower temperature to balance the phases was suggested. Cortie et al.[142] investigated in detail accompanied with statistical modelling on the effect of temperature and addition of nitrogen in element partitioning of the duplex stainless steels. Also, they found nitrogen as a strong element in partitioning of chromium and molybdenum.

Fig. 1-37 depicts the comparison between nitrogen content in ferrite and austenite for different duplex stainless steels.

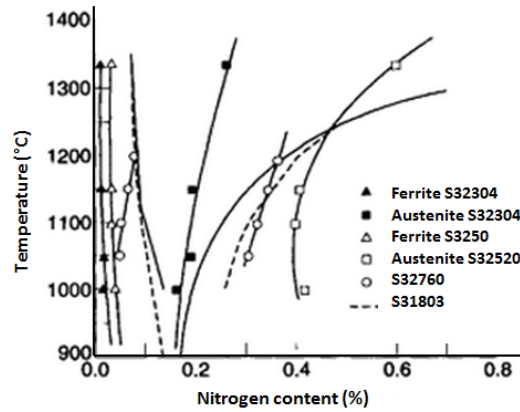


Fig. 1-37. Nitrogen content of ferrite and austenite for different alloys [17]

Based on important relation between of pitting corrosion resistance and alloying elements which specified in PREN formula which will be explain chapter three and expected differences value of PREN in ferrite and austenite, chemical analysis of all the joints were performed by SEM:EDS. The mass fraction of key elements chromium, molybdenum, nickel and manganese in both austenite and ferrite were measured, based on limited solubility of nitrogen in ferrite phase for all the samples nitrogen percentage in ferrite phase approximately was considered equal to 0.05 wt%. Based on investigation of Atamert et al. [128], the solubility of nitrogen in austenite is seven to eight times more than ferrite. The average value of minimum five analysis was considered as an average value for each element in different phases. Each value normalize with respect to the chemical composition using following equations [75,85,143].

$$C_{El}^{\gamma} = \frac{C_{El}^{total}}{V^{\gamma}(1 - P_{El}^{\gamma}) + P_{El}^{\gamma}}$$

$$C_{El}^{\alpha} = \frac{C_{El}^{total} P_{El}^{\gamma}}{V^{\gamma}(1 - P_{El}^{\gamma}) + P_{El}^{\gamma}}$$

Where

C_{El}^{tot} is the total content of the element (EL) obtained from chemical analysis

V^{γ} is volume fraction of austenite

P_{El}^{γ} is the partitioning ratio of the element calculated from experimental data and given by the ratio between the mass fraction of the element in ferrite and austenite.

Partitioning ratio is an important parameter which should be considered for pitting corrosion resistance. This value is calculated based on ratio of element in ferrite divided to element in austenite.

1.12.1. Partitioning of elements in duplex stainless steels

Atamert et al. [128], reported that amount of nitrogen in austenite phase is seven to eight times more than ferrite when annealing occurs at 1100 °C, this result confirmed by Zhang et al. [86]. Also, Cervo et al. [85] incorporated this estimation in their experiment, they calculated the amount of nitrogen by linear interpretation. With considering fast diffusivity of nitrogen at high temperature, after PWHT, the nitrogen content in the weld zone evaluated with approximation. Weight fraction of nitrogen between ferrite and austenite is critical to measure PREN value. Liljas et al. [144], reported that, with high cooling rate interstitial elements such as carbon and nitrogen are concentrated in austenite. For one estimation the partitioning of nitrogen in austenite is considered as 0.1. Fig. 1-38 indicates, typical element partitioning for different elements.

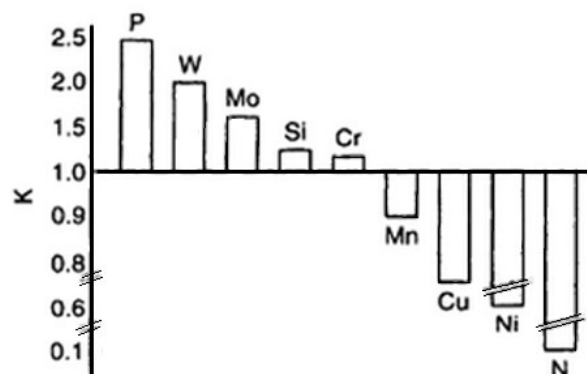


Fig. 1-38. Typical partitioning coefficients, K, for different alloying elements [17]

Due to importance of partitioning of the alloying elements in corrosion resistance, EDS analysis was performed for each condition. Tae Kim et al. [134], investigated on the effect of solution annealing followed by adding nitrogen gas into the weld pool, they observed higher pitting corrosion resistance compare to untreated weld. They found it is due to dissolution of chromium nitride phase in the ferrite matrix. Tan et al. [10], performed the EDS analysis on different phases to observe element distribution for the samples which annealed in different temperatures. Due to insensitivity of EDS to nitrogen an approximate calculation was employed to determine nitrogen concentration in each phase. As explained before, the saturation value of nitrogen in ferrite phase was considered 0.05% and the rest of nitrogen is considered in austenite phase [10,92]. It is clear that alloying elements such as Cr and Mo enrich in ferrite while N and Ni concentrated in austenite.

By increasing the annealing temperature chromium and molybdenum content decrease and nickel increase in ferrite. Cervo et al.[85], calculated partitioning ratio of molybdenum, chromium and nickel in fusion zone of welded duplex stainless steels. The value of P_{E1}^Y for Mo, Cr and Ni in the as welded condition are close to one. It means after welding due to high cooling rate, there is no time for partitioning of the elements between ferrite and austenite phases.

1.13. Fundamental of corrosion resistance for stainless steels

Mainly the corrosion resistance of stainless steels is due to formation of passive layer on the surface in oxidize environment. During corrosion of stainless steel the passive layer should be broken locally. The adherence of the film to the surface is relatively high and it can protect the surface properly. But in case of electrochemical reactions on the surface, the passive layer is broken, consequently permanent local damage occur on the surface. Some factors such as chemical environment, PH, surface condition, working temperature and method of production have an effect on corrosion properties. The electrochemical process involves an anode and cathode which connected by electrolyte. The metal as an anode corroded, but in cathode reduction reaction of hydrogen and oxygen occur. For preventing the corrosion this reaction should be stopped. Duplex stainless steels which contain both ferrite and austenite phases, show higher corrosion resistance especially for intergranular corrosion. It is mainly due to presence of ferrite phase. Because presence of ferrite grains cause to minimize the formation of continuous networks of chromium carbide. Because carbides precipitate around the ferrite grains and cause to depletion of chromium. Also, movement of grain boundaries can contribute formation of continuous path of depleted chromium area.

Passivity of stainless steels

The nature of passive film which form on the surface of stainless steels is a long term research issue due to its complexity. Due to that, Pourbaix diagram cannot exactly predict its nature in acid media on the basis of thermodynamically stable oxide layer. Working on different types of Fe-Cr alloys showed that the surface film which form after exposure to 1M H₂SO₄ in the passive range become rich in chromium in case of base metal with more than 12% chromium [145], recently these oxides can be recognized by X-ray photoelectron spectroscopy (XPS). Stainless steels show passivity behaviour just for specific range of potential. At low potentials, the passive film cannot form, consequently corrosion occurred. In high potential conditions, the passive film is oxidized and stainless steels become sensitive to local passive film breakdown which is very detrimental.

1.13.1. Different types of corrosion (Pitting, Crevice, SCC)

This term mainly is defined to explain attack that proceeds in a uniform manner over the surface. Due to that the area of corrosion the thickness decrease. The rate of general corrosion can either be measured by electrochemical techniques, resistance measurement or by weight loss tests. Different main types of corrosion which occur in stainless steels can be categorized as pitting, crevice and stress corrosion cracking. In the following a brief description of these types are explained.

Pitting corrosion

Pitting corrosion of metals is an important electrochemical corrosion process, which is a local break in the passive layer of the stainless steel. During the pit growth in Fe-based metals, the chloride solution inside the occluded pit become acidified due to the hydrolysis reaction [146]. Inside the pit, the bare surface of metal without the passive film is exposed to the acidified chloride solution, and then general corrosion of the matrix takes place. Thus the pitting propagation or growth rate is governed by the uniform dissolution rate of the matrix. In another word pitting is a form of localized corrosive attack that produces pits on the surface and grows to deep pit. It is destructive and harmful form of corrosion which has strong effect on performance of engineering structures. This type of corrosion mainly caused by chloride ions or sulphide environment and mainly nucleate above a critical or pitting potential. Fig. 1-39 indicates schematic mechanism of formation of pit on the metal surface after breaking the protective oxide layer. Pitting potential mainly defines as a least positive potential at which pits can be grown, the potential at which the metal salt of the aggressive ions in solution is in equilibrium with the metal oxide [147]. Pitting potential represent by E_{pit} which gives an indication of pitting resistance. Higher pitting potential means better corrosion resistance. At the site of pitting, where the metal is unprotected, corrosion occur if the pit does not re-passivate. The rate of dissolution of metal enable to maintain at sufficiently aggressive media to prevent re-passivation. This dissolution cause to increase the metal ion and electrons and the rate of dissolution which cause to increase differences between the electrical potential of pitting zone and other part of the material [148]. Pitting mainly occurs in the ferrite or ferrite-austenite boundaries, where the weldment has the lowest corrosion resistance. In samples with high content of ferrite, more chromium nitride precipitate and pitting occurs around this phase. Fig. 1-40 shows schematic forms of different types of pitting which mainly form on the surface. As it is clear, the pits which are mainly form and growth under the surface are really dangerous.

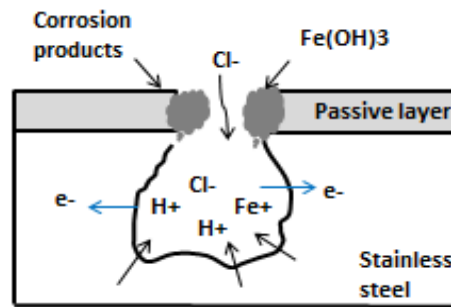


Fig. 1-39. Schematic mechanism of pitting corrosion

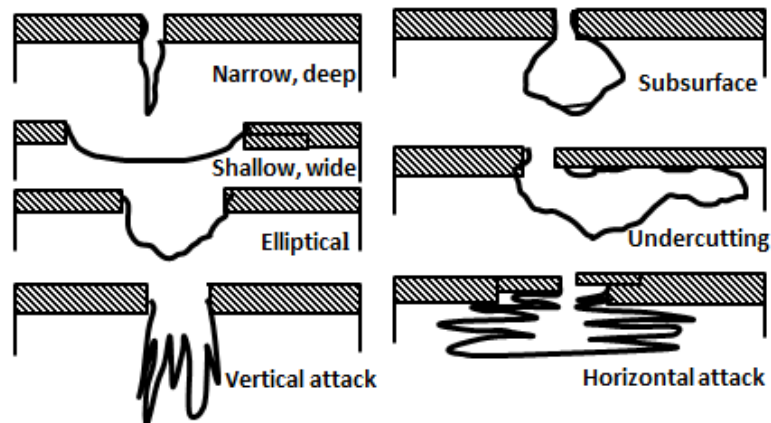


Fig. 1-40. Different shape of pitting on the surface

Based on different standards to observe the pits there is some criteria for acceptance or rejection of the components [5]. When pitting initiation occur, it continues to grow by self-sustaining mechanism. There are many factors which have effect on controlling and growth of the pits. In addition to formation of pits on surfaces containing defects such as inclusions and heterogeneity, in perfect surfaces without any defects it occur as a result of certain interactions between different ions which exist in the environment and passive surface.

Mainly breakthrough of the passive layer occur as a competitive adsorption between chloride ions and oxygen. Also, pits would tend to be randomly dispersed on a uniform metal surface. In thermodynamic point of view, pitting potential is considered as a potential, in which chloride ion is in equilibrium with oxygen. Because of that, so much effort was performed for better understanding of pitting formation on the surface. Pits normally tend to form at the specific sites and mainly initiate at some chemical or physical heterogeneity on the surface such as inclusions, second phase particles, solute-segregated grain boundaries, flaws, mechanical damage, or dislocations.

The propagation of pits is involve the dissolution of metal and maintenance of high degree of acidity at the bottom of the pit by hydrolysis of the dissolved metal ions. The anodic metal dissolution reaction at the bottom of pit is balanced with cathodic reaction on the adjacent surface. The metal chloride formed is hydrolyzed by water to the hydroxide and free acid. The pitting corrosion is normally associated with local breakdown of the protective passive layer and susceptibility to this kind of damage can be evaluated by means of critical pitting temperature and electrochemical measurement. Also, pitting is initiated when the potential reach to critical value (E_p), this value depends on chemical composition, temperature and environment. The value mainly evaluated by potentiodynamic anodic polarization test. In this test, pitting corrosion observed as an irreversible increase in current density. The higher the value of pitting potential, the higher corrosion resistance [149].

Generally, pitting initiate when the pitting potential reaches a critical value, this depends on chemical composition of the alloy and environment. This can be measured by potentiodynamic anodic polarization which one set of pitting observed as an irreversible increase in current density. The pitting potential indicates the necessary potential to initiate stable pits. If the medium potential of stainless steel become more than pitting potential, pitting does not start. Pitting can be one of the most dangerous form of corrosion due to its difficulty to detect and anticipate, it happens very fast and penetrate to metal without causing it to high weight loss. It occurs mainly in direction of gravity. It is difficult to measure. Rate of corrosion is higher than uniform corrosion due to large cathode, anode ratio. Fig. 1-41 indicates the pitting potential curve with specific points and the effects of addition of alloying elements to change the corrosion parameters. Diagram shows, E_{corr} with respect to the anodic polarization curve and current density (i) represent the corrosion rate.

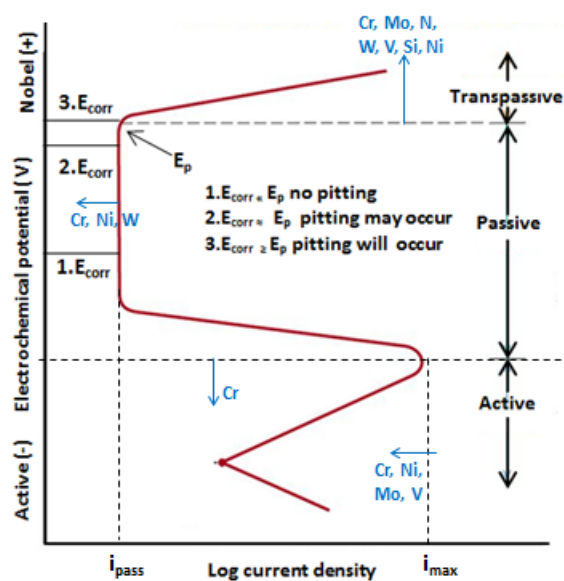


Fig. 1-41. Schematic representation of a polarization curve for determination of pitting corrosion risk

Crevice corrosion

Crevice corrosion mainly happens in crevices and confined spaces between two metals or metal-nonmetal contacts. It mainly occur due to design of component such as flanges and connections. As an oxygen content is limited inside of a tight crevice, the passive layer become weak and just as with pitting dissolved metal ions in the crevice lower the PH and allow chloride ions to migrate into the crevice. Consequently passive layer breaks down and the aggressive environment facilitate the corrosion attack. This type of corrosion cause to larger and shallower attack compare to the pitting. To avoid crevice corrosion, following options should be considered:

selecting a highly alloyed stainless steel, decreasing the content of chloride, increasing the PH, decrease the content of oxygen and other oxidizing species from the environment, improve the component design to avoid tight crevice and formation of deposits and hiring appropriate fabrication practices that produce clean surface and ensure that weld oxide area removed. In crevice corrosion testing the tendency for corrosion is dependent on experimental parameters.

Stress corrosion cracking (SCC)

This type of corrosion is a general term which describe stressed alloy failure which occur by crack propagation in corrosive media. The appearance of this failure is brittle fracture. But it can be occur even in high ductile material. For this type of corrosion, applying tensile stress is required which can be consist of residual stress. The cracks initiate and propagate in direction perpendicular to the applied stress. In microscopic point of view, cracks that run across the grains called transgranular. Also for the fracture in this mode, the microvoid coalescence mechanism is proposed. The main advantages of duplex stainless steels compare to conventional stainless steels is higher resistance to stress corrosion cracking especially in chloride environments. As an example in austenitic stainless steel, SCC occurs at 0.1% chloride in 60 °C , but superduplex stainless steel can resist under stress corrosion cracking till 250 °C in solution of 3% sodium chloride. Susceptibility of duplex stainless steels mainly depends on PH, concentration and temperature of the solution [150].

1.13.2. Effects of alloying elements and ferrite percentage

The high pitting resistance of duplex steels mainly relates to synergy effect of Cr and Mo Sugimoto1992, Boucherit [151,152]. Also it was suggested that Mo is much more effective than Cr (three times more) to improve pitting corrosion resistance. Nitrogen and molybdenum show synergic effect. Also it is suggested that the optimum amount of molybdenum in stainless steels is 3.5 %, because more than this amount, molybdenum would precipitate and it acts as initiation site for pitting corrosion and decrease the corrosion resistance.

The influence of Mn is not clear specifically, sometime reported as beneficial by Siow et al. [153], but Henthorne et al. 1970 was found that, Mn cause to formation of $(\text{Fe-Mn})\text{Cr}_2\text{S}_4$ which has negative effects on pitting corrosion resistance and encourage pitting initiation. Copper mainly known as an element which cause to decrease dissolution of chromium but it would not strong influence on the passivation of steel. However, it was reported that copper in presence of Mo has negative effect on pitting corrosion [154].

Also, it was reported that lower amount of pitting corrosion resistance of UNS S32304 steel depends on higher amount of carbon and silicon due to formation of carbide and dispersion of inclusions along grain boundaries. But mainly silicon does not have specific effect on pitting corrosion resistance.

In addition, it was reported that percentages of ferrite has an effect on corrosion resistance. It was recommended that, duplex stainless steel should contain minimum 40% to reach maximum pitting potential. The weight percentage of ferrite stabilizer elements such Cr, Mo and Si mainly are more than austenite stabilizers such as Ni, Mn, C and N but there is a doubt if this amount can produce optimum ferrite content or not. Distribution of alloying elements in stainless steels are not homogeneous. In homogeneous metals contains secondary phases because of segregation process. These phases act as an initiation site for pitting corrosion. Siow et al. [155] showed that, pits mainly initiates at ferrite austenite grain boundaries or its border to secondary phases subsequently enter to austenite phase. Phase boundaries are more reactive and thermodynamically unstable compare to grains due to higher concentration of sulphur at interface or high density of sulfides along the interface. The austenite dissolved at potential values more than passivation potential, while the ferritic phase dissolved at lower rate [156].

1.13.3. Surface conditions and post cleaning process

Surface condition is an important parameter for performance of corrosion. Surface defects and existing irregularities on the surface such as pores, cracks, spatter, incomplete penetration, metallic and non-metallic inclusions can act as a potential site for corrosion. Consequently, cleanliness of the surface is important for retaining protective passive film. Existing the scratches, coarse grinding and metal contamination have negative effect on pitting corrosion resistance. Also, the pitting resistance can be locally impaired by scratches, coarse grinding, ripples and some metallic contaminates. Also, weld oxides as heat tint or weld discoloration, can increase the susceptibility to localized corrosion attack. The backing gas reduces the amount of heat tint and discoloration on the surface, consequently the oxide can be removed by pickling [157].

For high alloyed grades, pickling treatment is difficult. In case of using clean surface and high quality backing gas the necessary time for pickling decrease. This could be performed by chemical and mechanical methods. Mechanically cleaning can be categorized as grinding, shot blasting and polishing to remove contamination from the surface. It should be remember that, just stainless steel tools should be used for cleaning, because iron brushing cause to local corrosion. Chemical cleaning include pickling and passivation. Pickling can be performed by immersion the whole part inside of bath or pickling agent spraying. The time of pickling mainly depends on surface roughness, chemical composition of the alloy, pickling temperature and quality of the weld [158]. Generally applying mechanical cleaning process followed by pickling cause to further increase to corrosion resistance [126].

The post cleaning of the weld oxide from the surface is important to achieve appropriate corrosion properties. If post weld cleaning is not an option, using purging gas is recommended. Normally Argon gas as a purging is recommended, but for duplex steels addition of nitrogen is recommended. [125,157,159]. In case of existing hydrogen, the effect of this gas should be considered, because it can react with residual oxygen and form water vapor and risk of hydrogen embrittlement increase [160,161]. Some researches showed that this effect could be minimize in case of applying suitable welding procedure. A shiny weld and yellow HAZ are sign of sufficient root protection for appropriate corrosion resistance.

1.13.4. Pitting Resistance Equivalent Number (PREN) parameter

In stainless steels pitting resistance directly depends on chemical composition and much work was performed to find a formula which can consider the effect of existing alloying elements. Pitting resistance equivalent number is the famous formula which can be defined for evaluation of corrosion resistance. PREN value is theoretical way for comparing the pitting corrosion resistance of various type of stainless steels based on chemical composition. This value is suitable for comparing the pitting corrosion resistance of different grade of stainless steels and it cannot be used for prediction of corrosion.

Generally, partitioning of elements and microstructure are critical parameters, in corrosion resistance of duplex stainless steels. The pitting resistance equivalent number (PREN) which mainly specified based on percentage of chromium, molybdenum and nitrogen, some authors suggested tungsten can be considered with coefficient equal to half of molybdenum[162]. It is an important factor for categorizing the pitting resistance of different grades of duplex stainless steels [163,164].

The addition of nitrogen can change the partitioning coefficients for chromium and molybdenum between ferrite and austenite. Consequently nitrogen increase the PREN value of austenite in duplex steel compare to ferrite. For this reason Bernhardsson et al.[18] considered the coefficient of nitrogen in PREN formula roughly two times more compare to conventional formula (from 16 to 30). Normally, the following formulas are considered for different types of stainless steel.

$$\begin{array}{ll} \text{PREN} = \%Cr + 3.3\% (\text{Mo}+0.5\%W) + (16 \text{ or } 30)\%N & \text{For Duplex} \\ \text{PREN} = \%Cr + 3.3\% \text{Mo} + 16\%N & \text{For Austenitic} \\ \text{PREN} = \%Cr + 3.3\% \text{Mo} & \text{For Ferritic} \end{array}$$

Another PREN formula for duplex stainless steels was proposed by Jonsson et al.[165], which is $\%C+3.3\%Mo+22\%N-\%Mn$, also they investigated on the effect of PREN value and Critical pitting temperature (CPT) for different types of stainless steels, they found with increasing the PREN value, CPT increase. Also, they observed measurement of PREN for each phase is more reliable compare to overall PREN. Jonsson et al.[165] investigated on the corrosion resistance properties of lean duplex stainless steel, they found most of the pits in the ferrite phase due to lower PREN value. Also, they found that even with 2 or 3 unit more value of PREN, still ferrite compare to austenite, shows weaker corrosion properties. Fig. 1-42 indicates pits in the ferrite phase after corrosion test.

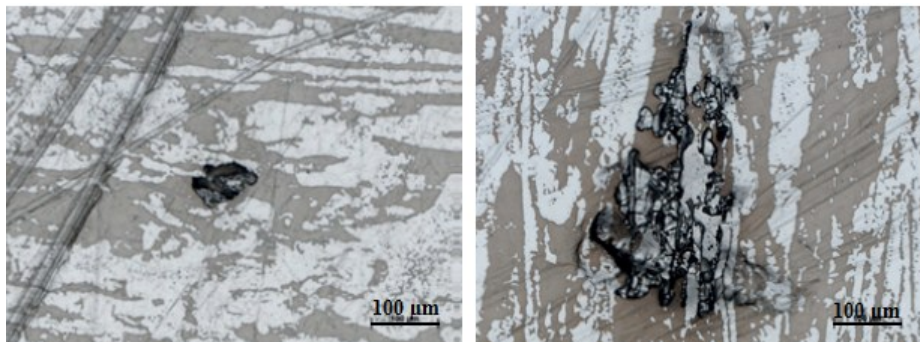


Fig. 1-42. Initialization of pits in ferrite matrix [165]

In addition to strong effect of chromium, molybdenum and nitrogen in corrosion resistance of the duplex stainless steels, many requirements should be considered to find the relationship between austenite, ferrite and pitting resistance. This could be amount of beneficial elements such as copper, harmful elements such as sulphur and phosphorous and interaction between elements such as molybdenum and nitrogen [117].

1.13.5. Standards for evaluation of corrosion properties and acceptance criteria

Common tests to find pitting resistance of stainless steels are described in ASTM G48 (A) standard. It consists of immersion the samples in 6% solution of ferric chloride for 72h at room or 50 °C. In this method the evaluation of corrosion is based on weight loss and appearance of pits on the surface. The standard ASTM G48 is another method (E) which can be used to find critical pitting temperature. For this evaluation, sample immersed in 6% FeCl₃+ 1-5% HCl for 24 h at fixed temperature. The test will continue till appearance of pit on the surface or when weight loss reach more than 5 mg in this case experiment should be repeated with increasing the temperature 5 °C in each step and the test continued for another 24 hours. The minimum temperature which pits occur called, critical pitting temperature. This test can be perform for evaluation of welded part of stainless steel to be sure about integrity of the weld.

Another important standard is ASTM A 923, for determination of intermetallic phases in duplex stainless steel, specified CPT for base metal is 25 °C and 22 °C for welded part. The acceptance criteria is weight loss which should be less than 10mg/dm²/day for example 1g/m² during 24 hours experiment.

For the superduplex alloy this temperature is specified around 50 °C and for welded part decrease to 40 °C. The Norsok standard M-601, M-630 which has many applications in oil and gas industries, specified 4 g/m² weight loss as an acceptance criteria. Another applicable standard to determine CPT is ASTM G150 and ISO 17864. Specific design should be considered for this test. The CPT is minimum temperature which pitting occurs on the surface under specific conditions. A visual inspection by microscope should be performed to observe appearance of pitting. Minimum three sample test is required to reach appropriate statistics. In this method mainly, surface is tested. These standard, mainly designed for as welded specimens with small reinforcement [161].

1.14. literature review for welding and corrosion of duplex stainless steels

As explained before, duplex stainless steels, which present roughly equal percentages of ferrite and austenite in the microstructure, are able to guarantee higher mechanical strength, corrosion resistance and toughness properties compared to ferritic, austenitic and martensitic stainless steels [72,121,135,137,166]. This good behavior is mainly achieved because of its peculiar microstructure which contains roughly equal percentages of ferrite (δ) and austenite (γ). In this microstructure austenite is responsible for high toughness and corrosion resistance, and ferrite meets the requirement for high strength [72,80,106,135,137]. These types of stainless steels, because of their peculiar properties, indicate some advantages with respect to single phase stainless steels [137,167,168] and make them more applicable in different industries and harsh conditions.

Clearly, welding is the main method for fabrication of steel structures, and this causes a change in the base metal properties on that zone [135,169]. In fusion zone, due to melting, the balance between ferrite and austenite is destroyed and risk of precipitation of intermetallic phases increases [132]. Different welding methods can be applied to duplex stainless steels for the production of several equipments and mechanical structures. Nevertheless, fusion welding processes due to intrinsic properties has a detrimental effect on the equal percentage of ferrite and austenite phases in the fusion zone [170,171].

Many authors have studied different solutions to restore the equal percentages of ferrite and austenite phases and to avoid the precipitation of the detrimental intermetallic compounds such as Sigma (σ), Chi (χ) and nitride phases after welding processes. Zhang et al. [114], Yang et al. [172] and Lippold et al. [1], suggested limiting the heat input during welding of the duplex and super duplex stainless steels in the range of 0.5-2.0 kJ/mm. Magudeeswaran et al. [173] worked on process optimization of stainless steel welds to reach appropriate weld bead quality. This range of heat input cause to avoid formation and precipitation of intermetallic phases [88,174–176]. Some other methods are suggested to improve the microstructure and mechanical properties of the duplex welded joints. They can be categorized such as adding nickel, nitrogen gas and using appropriate post weld heat treatment (PWHT). Adding nickel to the weld pool is an important solution due to its properties as an austenite stabilizer element which allows an increase in the percentages of austenite in the microstructure. Pilhagen et al. [177], worked on the effect of addition of nickel in form of powder and using filler metal with higher amount of nickel on fracture toughness of lean duplex stainless steel. They observed appropriate ferrite content and a significant increase in toughness of the weld after addition of nickel. They suggested using filler metal which contains more than 8% for obtaining a weld with similar toughness and corrosion resistance as the base metal [12].

Muthupandi et al. [170] and Migiakis et al. [91], investigated the effect of addition of nickel on the microstructure and mechanical properties of the welded duplex and super duplex stainless steels. They observed improvement in phases balance and toughness properties in the joints. Azuma et al. [178] investigated on the effect of addition of nickel on corrosion properties of stainless steels, they observed more improvement due to modification. Miyaji et al. [179] added 4- 18% nickel power to Cr-Mo steel and they observed increase in toughness properties. Tavera et al. [180] worked on the effect of addition of nickel via filler metal on corrosion fatigue properties of the welded duplex stainless steel. Generally, they observed optimum properties with addition of 4.9% nickel.

Wang et al.[181] investigated microstructure and property of a type of nickel-free DSS and found that a dual phase structure with approximately 50% austenite could be attained after completely replacing nickel by manganese and nitrogen and the steel had high yield strength and good corrosion resistance. Another solution is adding nitrogen gas mixed with argon as a shielding or adding via external lance into the weld pool. This nitrogen could be replaced instead of evaporated value from the base metal during fusion welding due to less solubility in weld pool. and austenite. Some characteristics of stainless steels which contains nitrogen can be specified as following [141,182]

- High strength, ductility and fracture toughness
- High strain hardening potential
- Resisitance to martensitic formation
- Low magnetic permeability
- High corrosion resistance

It was reported that addition of nitrogen has minimum effect on weld hardness and it mainly cause to improve the toughness properties of the joints [167]. Also, the amount of nitrogen should be optimum, because more amount of nitrogen cause to unstability of the welding arc and spattering in addition can increase the risk of formation of unwanted chromium nitride phase.

Tseng et al. [183], investigated the effect of addition of nitrogen on the mechanical behavior of welded duplex steel, they found that with increasing the nitrogen content, yield and tensile strength increase. Bhatt et al.[184], studied on the effect of addition of nitrogen to the shielding gas, they found after welding just by argon gas mainly chromium and molybdenum partitioned in ferrite and nickel in austenite, but with adding nitrogen in shielding gas, these elements distributed homogenously between phases. Muthupandi et al.[170], observed appropriate microstructure and phase balance after addition of nitrogen in welded joints without any specific change in hardness value. Also nitrogen can be added via backing gas mixed with hydrogen to prevent formation of intermetallic phases.

Generally with addition of nitrogen in shielding gas, the amount of nitrogen in fusion zone increase and the solubility of nitrogen in a molten metal is proportional to the square of partial pressure in the gas phase[185], it was reported that nitrogen absorption in weld metal is more than equilibrium solubility which specified by Sievert law [26]. The reason could be due to presence of monoatomic nitrogen. Also nitrogen cause to accelerate partial transformation from ferrite to austenite during cooling.

The high temperature during welding increase dissociation of molecular to monoatomic nitrogen with considering the free energy change. Both nitrogen and nickel elements cause to increase the transformation temperature of ferrite to austenite during solidification [184]. It was reported that use of nitrogen in shielding gas cause to cause to uniform distribution of chromium and nickel in the ferrite and austenite phase and in higher amount of austenite in the weld [184].

Bauer et al.[186] reported that mixture of Ar and N₂ was an optimal choice for laser beam welding, and nitrogen was an effective element to increase reformation of austenite phase in microstructure.

Lai et al.[187] performed comprehensive study on the effect of addition of different percentage of nitrogen mixed with argon on microstructure and corrosion properties of the welded duplex stainless steel and they observed improvement in phase percentage and corrosion properties.

Post weld heat treatment (PWHT) is another suggested solution, which can be performed on the duplex steel welded joints to restore the equal percentages of the phases, accompanied with decreasing the segregation of alloying elements. Also, appropriate PWHT with controlling the time, temperature and cooling rate causes to improve the corrosion resistance. Generally high annealing temperature followed by water quenching causes to decrease the risk of formation of intermetallic phases, nitrides and carbides [86,172].

Badji et al.[135], investigated on the effect of annealing temperature on the phase percentages after welding. They found, with increasing the annealing temperature, the amount of intermetallic phases decrease and roughly equal percentages of ferrite and austenite can be obtained. Also, they proposed, 1100 °C as an optimum annealing temperature. Generally, heat treatment of duplex stainless steels at temperature between 400 and 1000 °C is not recommended due to formation of intermetallic phases, but in more than 1050 °C microstructure improvement was observed [122].

Young et al. [59], have shown that PWHT at 1050 °C for 15 min causes to increase the austenite content of the microstructure accompanied with enhancing the impact properties. Garzon et al.[132], worked on the effect of heat treatment on the microstructure of welded UNS S32304 duplex stainless steel.

Mohammed Asif et al.[105] investigated on the effect of different temperatures of PWHT on welded duplex stainless steel and they found 1080 °C cause to reach optimum condition in case of maximum hardness finer grain size and restoring equal percentage of ferrite. Also, they found the nickel is an important element to reach the phase balance between ferrite and austenite.

Above all, in welding of duplex steels, much attention should be considered to avoid precipitation of detrimental phases such as sigma (σ), chi (χ) and chromium nitride (Cr₂N). In addition to many separate investigations on the effect of alloying elements and heat treatment of the welded duplex steels, based on knowledge of the authors still there is lack of information about effect of applying combination of post weld heat treatment after addition of nickel element to investigate the changes of the microstructure, phase percentages and mechanical properties.

Matsunaga et al.[130], found that addition of nitrogen during TIG welding of duplex steel, cause to decrease chromium nitride in weldment. With increasing nitrogen content, transformation of ferrite to austenite occur at high temperature, consequently nitrogen can diffuse faster and there is more time for diffusion from ferrite to austenite. As a result, lower content of nitrogen cause to less possibility of nitride precipitation.

Kim et al.[188] investigated on the effect of addition of nitrogen and precipitation of sigma phase on mechanical properties of superduplex stainless steels and they found higher tensile strength and elongation after addition of nitrogen. Jebaraj et al.[122] Investigated on the effect of heat treatment after welding on microstructure and toughness properties of the welded SAF 2205 duplex stainless steel. They observed high increase in toughness due to microstructure changes and decrease in hardness due to formation of intermetallic phases. Hosseini et al.[189] applied different heat input for welding of superduplex stainless steel and they monitored the effect of nitrogen loss in welding passes. Finally they recommended addition of nitrogen as a shielding gas.

Many works have been performed to improve the corrosion resistance of the duplex stainless steels welded joints. The quality of the weld zone can be modified by using high alloy filler metal, adding nickel as powder, nitrogen gas or applying appropriate heat treatment after welding [12,127,171,190,191].

Superduplex stainless steels which mainly consists of equal percentages ($50 \pm 5\%$) of both ferrite and austenite phases, can be considered as a particular category of duplex stainless steels (SDSS) with higher physical, mechanical and corrosion properties. The main differences between these two categories is the value of pitting resistance equivalent number ($PREN = [\%Cr + 3.3 \times \%Mo + 16-30\%N]$) which this parameter for superduplex due to higher amount of alloying elements is more than 40 compare to conventional duplex steel which is around 32 to 36 [192]. This could be due to high mass fraction of chromium (25-27%), molybdenum (3-4.5%) and intermediate mass fraction of nitrogen (0.25-0.28%). It was reported that nitrogen reduced the activity of chromium and molybdenum, thus it cause to decrease the driving force for precipitation of the sigma phase. Also, increasing the nitrogen content should make possible a further increase of chromium and molybdenum. The best properties of welded superduplex stainless steel achieved when the phase percentage of ferrite and austenite are roughly the same (50%), in addition to detrimental phases such as sigma (σ), chi (χ), nitrides and carbides which have negative effects on corrosion resistance and toughness are in minimum level [13]. Du et al.[193] investigated on the effect of addition of different percentages of nitrogen on microstructure and mechanical properties of the welded superduplex (SAF 2507) stainless steels. They obtained 3% N₂ cause to reach optimum result. Such as what explained for the duplex stainless steel, heat input play an important role to achieve appropriate weld quality for super duplex stainless steels.

By increasing the heat input, the weld metal stay longer in high temperature ranges and more ferrite is transformed to austenite. Consequently heat input between 0.5 to 1 kJ/mm is suggested for the welding of duplex stainless steels. Also this value cause to keep the intermetallic phases in minimum level.

Devendranath et al.[194] investigated on the effect of heat input on welding properties of super duplex stainless steel, they found GTAW as a useful method for this kind of steel. Sadeghian et al.[195] investigated on the microstructural properties of the dissimilar welded joint of superduplex stainless steel to HSLA steel with different heat input. They found with increasing the heat input, ferrite content decrease. The microstructure of weld zone in their investigation is shown in Fig. 1-43.

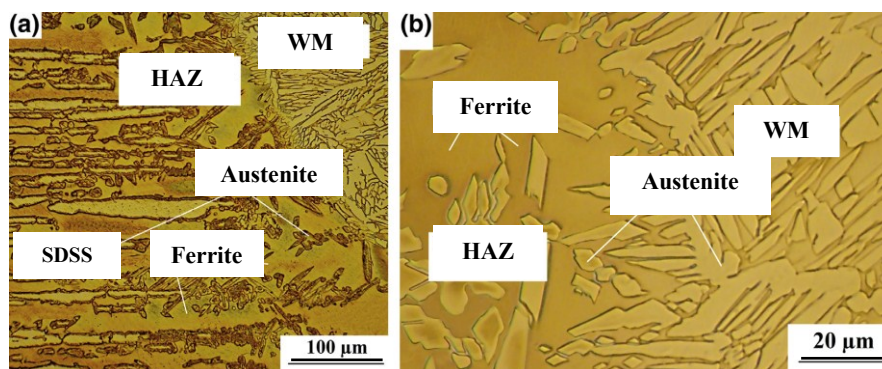


Fig. 1-43. Microstructure of weld zone in different magnification [195]

Existing both good characteristics of high mechanical properties accompanied with appropriate stress corrosion cracking resistant in chloride solutions make superduplex stainless steel as highly recommended option for harsh and aggressive conditions in different industries [47]. Tehovnik et al.[196] investigated on the effect of heat treatment on microstructure evolution of the superduplex stainless steel and they observed maximum precipitation of sigma phase at annealing temperature of 850-900 °C. Hwang et al.[115] investigated on the effect of different heat treatments on the phase ratio and microstructure of superduplex stainless steels. They found with increasing the temperature of solution annealing, ferrite content and grain size of both ferrite and austenite increase and number of grains decrease, consequently risk of precipitation of intermetallic phases decrease. Siow et al. [153], investigated on the pitting corrosion resistance of different types of duplex and super duplex stainless steels. They observed that, pits were initiated at the ferrite-austenite interface and subsequently growth into the ferrite phase.

The pitting corrosion is directly related to chemical composition and it can be calculated based on pitting corrosion equivalent number (PREN), this parameter is accepted for determination of pitting corrosion resistance of duplex stainless steels and it can be calculated according to the following formula:

$$PREN = \%Cr + 3.3\%Mo + (16-30)\%N \text{ [64,86,92,117,134]}$$

Recently some authors considered effects of manganese in the PREN formula which has a negative effect in the formula [115,143,165,197,198]. For increasing the PREN value, each effective alloying element (Cr, Mo and N) can be added, but based on high coefficient of nitrogen, this element is more potential to increase the PREN value and consequently pitting corrosion resistance [109]. Based on different investigations [199], coefficient of 16 or 30 was proposed for nitrogen, due to its strong effect on pitting corrosion resistance of the stainless steels. Generally accepted that, the higher the value of pitting potential, the higher corrosion resistance [149].

The value of PREN for different types duplex stainless steels mainly reported between 26-36. For duplex stainless steels, the PREN value should be measured separately for each phase, because mainly weaker phase can determine the corrosion resistance of the alloy [85,86]. Based on different amount of elements in ferrite and austenite phases, the corrosion resistance would be varied and weaker phase can govern the corrosion resistance of the whole sample [7,117]. The different pitting potential of ferrite and austenite phases in duplex steel was confirmed by many authors [200,201]. They observed the first site of pitting in ferrite-austenite grain boundaries, followed by ferrite grains and growth into the austenite phase. They rarely observed initiation of pitting in austenite phase. Gooch et al. [145] performed comprehensive study on corrosion resistance behaviour of different kinds of stainless steels.

Jeon et al. [202], investigated to verify the propagation mechanism of pitting in duplex stainless steels, to observe differences between corrosion resistance of different phases. Cerro et al. [85] and Merello et al. [203] tried to find statistical model for relation between PREN value and pitting corrosion resistance based on logarithmic equations. Also, they tried to find optimum solution treatment after welding to reach best pitting corrosion resistance. An important feature of the polarization behavior is the existence of different pitting potential for both ferrite and austenite, to reach optimum corrosion resistance, this value for each phase should be close to each other [143,204]. Tan et al. [89], worked on the effect of PWHT on pitting corrosion resistance of welded UNS S32304 duplex steel, they observed improvement of corrosion properties after annealing treatment especially at temperature of 1080 °C.

Gholami et al. [108] investigated on the effect of different annealing temperature on pitting corrosion resistance of duplex stainless steel and they found 1050 °C as an optimum temperature. Also they performed statistical analysis on formation of metastable pits and its conversion to stable pits. They found with increasing the annealing temperature risk of formation of chromium nitride phase increase and as a result pitting corrosion resistance decrease.

Hoffmeister et al. [205] found that increasing the amount of nitrogen in fusion zone up to 0.28% cause to increase the pitting potential. They found high cooling time cause to more austenite transformation and less precipitation of chromium nitride and pitting. Guo et al.[206] investigated on the effect of cooling rate on microstructure evolution and pitting corrosion resistance of duplex stainless steel, they found that with decreasing the cooling rate, the pitting resistance equivalent number of ferrite phase increase. Cervo et al.[207] found that, with increasing the PWHT temperature, the value of PREN increase. Chen et al.[208], worked on the effect of different cooling rates on corrosion properties of UNS S32304 duplex steel. Hwang et al. [115], investigated on the effect of different heat treatment on the phase ratio, element partitioning and corrosion resistance of the duplex stainless steels.

They found by increasing the annealing temperature Cr, Mo and W tend to decrease in ferrite phase and increase in austenite whereas Ni and N show opposite trend. It is due to increasing the solution treatment ferrite phase increase and concentration of ferrite stabilizer elements decrease and due to lower amount of austenite the concentration of these elements increase. Also, they found that with increasing the annealing temperature, the precipitation of intermetallic phase decrease. In addition with increasing the ferrite content, the probability of formation of intermetallic phases through eutectic reaction decrease. With growth of ferrite phase, the area of grain and interface boundaries where act as an appropriate site of intermetallic phase precipitation decrease, consequently precipitation of intermetallic phase decrease. Bhattacharya et al.[209], compared the corrosion resistance of different types of duplex stainless steels, they observed alloys with less amount of molybdenum indicated higher corrosion resistance. In addition, it was reported [210] that chemical composition of the filler metal and microstructure have strong effect on pitting corrosion resistance, but preheat, heat input and number of passes are not critical for the corrosion resistance. Based on the investigation of Luo et al.[204], an important feature of the polarization behavior was found as the existence of different pitting potential for both ferrite and austenite. In less than 450 mV_{SCE} the sample is passive, but more than this value pitting first occur in austenite phase and ferrite remain in safe side. By reaching the potential to 1050 mV_{SCE}, both ferrite and austenite phases become under pitting corrosion. Also, they found that pitting potential for the austenite phase before and after solution treatment are the same, consequently the pitting corrosion resistance of this steel mainly depends on pitting resistance of the ferrite phase [204].

Other researchers [200,201] confirmed the different pitting potential of ferrite and austenite phases in duplex steel. Also, they observed the first site of pitting in ferrite austenite grain boundaries, followed by ferrite and growth to the austenite. The initiation of pitting in austenite phase rarely was observed. They found with increasing the cooling rate, pitting corrosion resistance decrease. Also, they observed all the pits in ferrite phase. They justified their results based on formation of chromium nitride and inclusion in the matrix.

Ebrahimi et al. [211], investigated on correlation between critical pitting resistance and degree of sensitization for duplex steel based on different heat treatments. They found, linear relation between these two values, also they observed that with increasing the time and temperature of heat treatment, amount of precipitations increase.

Azuma et al.[178] investigated on the effect of addition of nickel on corrosion properties of stainless steels, they observed superior corrosion properties due to decreasing depassivation PH and dissolution rate in the solution. Potgieter et al.[212] investigated on the effect of addition of different nickel percentage on the corrosion behavior of duplex stainless steel, they observed improvement of pitting corrosion resistance with increasing the amount of nickel. Also, they found the effect of nickel on microstructure modification and refinement accompanied with types of films which form in different environment.

Tavara et al.[180] worked on the effect of addition of nickel via filler metal on corrosion fatigue properties of the welded duplex stainless steel. Generally, they observed optimum properties with addition of 4.9% nickel. As explain before addition of nitrogen is another solution to improve corrosion resistance of the welded duplex steel. Bhatt et al. [184], added 5 and 10% N₂ in the shielding gas of welded duplex stainless steel, they found modification in microstructure and improvement in pitting corrosion resistance of the weld compare to the non-added nitrogen weld. Nitrogen, in addition to increase the corrosion resistance, in duplex stainless steels with high amount of Cr and Mo, cause to delay the formation of intermetallic phases because it cause to decrease due the activity of the chromium. The intermetallic phases mainly form at temperature between 600 to 1000 °C due to slow cooling rate which has negative effect on corrosion resistance properties. Also, in that range of temperature there is risk of formation of carbide, nitride and secondary austenite phase which the former contain less amount of Cr, Mo and N compare to primary austenite. Lothongkum et al. [213] performed in depth study about effect of nitrogen on corrosion properties of the duplex stainless steels in NaCl solution, they observed corrosion resistance with increasing the nitrogen increase, also they found that effect of nitrogen on austenite phase is more than ferrite. Garcia Renteria et al.[214] worked on the effect of addition of oxygen and nitrogen in shielding gas of the welding process to observe the changes in corrosion properties. They found better corrosion properties in case of addition of nitrogen.

Muthupandi et al.[109] investigated on the effect of addition of different percentage of nitrogen as shielding gas on corrosion properties of welded duplex stainless steels, they observed higher pitting corrosion resistance in case of addition of more amount of nitrogen.

Petersson et al. [215], added nitrogen in shielding gas to compare the corrosion resistance of the joints with conventional argon gas, they observed nitrogen cause to stabilize the austenite phase and higher corrosion resistance. Lai et al.[187] investigated on the effect of addition of nitrogen on corrosion properties of the welded 2205 duplex stainless steel.

Garfias et al.[117], investigated on relationship between percentage of ferrite phase and susceptibility of pitting corrosion in duplex steel, they found that with increasing ferrite phase, pitting corrosion resistance decrease. Hwang et al.[115] and Tan et al.[10], investigated on the effect of ferrite phase fraction on pitting corrosion properties, they found ferrite phase between 49-51% is optimum percentage to reach appropriate pitting corrosion behavior.

Young-HA et al. [216], found the best pitting corrosion properties in the sample with 57% ferrite. Previous research [86] indicated that, for evaluation of pitting resistance of duplex steel, the pitting resistance of weaker phase play an important role and it should be considered as reference for corrosion resistance.

Many authors [10,115,117,216,217] performed a research to find optimum percentages of ferrite in the microstructure to reach appropriate pitting corrosion resistance, mainly they proposed ferrite content between 45-55% showed optimum results. Moura et al. [88], investigated on microstructure and corrosion properties of 2205 alloy under different heat treatment and deformation, they observed lower corrosion resistance in case of existing sigma and Cr_2N in the matrix. Sun et al. [217], investigated on importance of the phase balance in corrosion resistance of duplex steel, they found in case of 45-50% ferrite, minimum pitting rate can be obtained. Fig. 1-44, shows the relationship between ferrite content and pitting rate.

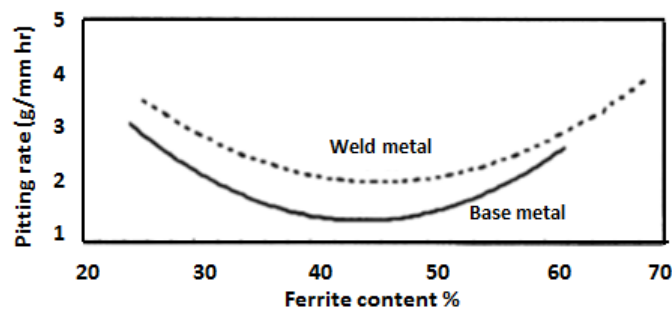


Fig. 1-44. Importance of effect of phase balance in corrosion resistance of duplex steel [217]

Bhattacharya et al. [168], compared the corrosion resistance of different types of duplex stainless steel in sulfide containing caustic environment, they obtained better corrosion resistance of UNS S32304 compare to UNS S32250 due to existing less amount of molybdenum which has detrimental effect in slightly oxidizing caustic environment. Also, they found that, magnetite and awaruite ($FeNi_3$) helped to form a more stable passive film in UNS S32304 which cause to decrease corrosion rates. Petersson et al.[215], investigated on corrosion resistance of different types of stainless steels and compared the results with as welded samples, they found that in case of weld sample, the CPT decrease between 20-40 °C, also they obtained pickling of the weld and removing the oxide cause to keep the CPT close to the base material.

Moreover, in another part of their research they added nitrogen in a shielding gas to compare the corrosion resistance of the joints with conventional argon gas, they observed nitrogen cause to stabilize the austenite phase and increase the corrosion resistance. Due to stabilizing the austenite phase with existing nitrogen this sample indicated better corrosion resistance. Tan et al. [92], worked on corrosion properties of multiple pass welded UNS S32304 stainless steel, they found that first pass is the most detrimental pass which cause to deteriorate the microstructure and decrease the corrosion resistance of the weld. They observed by increasing the number of passes. It means subsequent passes have beneficial effect on corrosion properties of the joint. The reason could be justify due to increasing the passes, ferrite content decrease and critical pitting temperature increase, consequently corrosion resistance increase. Fig. 1-45 indicates formation of pit in base metal and HAZ of the welded sample UNS S32304. Olaseinde et al.[218] worked on corrosion resistance properties of different types of duplex stainless steel in acidic and chloride solutions. They found alloy with higher amount of alloying elements shows higher corrosion resistance.

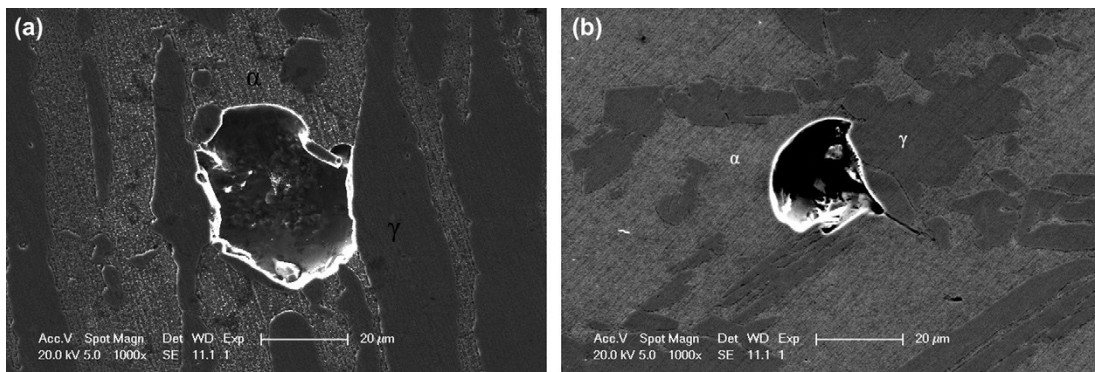


Fig. 1-45. Pit morphology of the sample in (a) base metal and (b) HAZ [92]

Jiang et al. [219], investigated on the effect of different Cr_{eq}/Ni_{eq} on microstructure and corrosion properties of the plasma welded UNS S32304 duplex stainless steels. They found that, the microstructure is more balance with austenite phase after thermal cycle in case of lower Cr_{eq}/Ni_{eq} . Also, they observed with higher value of the ratio the corrosion resistance decrease. Fig. 1-46 depicts SEM images of pit in the microstructure and pit morphology after corrosion test. Previous investigation by Deng et al.[163] indicated that, the CPT for 2205 duplex steel in chloride solution is equal to 60 °C. Also, mainly addition of alloying elements such as molybdenum has positive effect to increase the CPT of duplex steel [151,221,222]. It was suggested that alloying elements such as copper due to its reaction with nitrogen have positive effect on pitting corrosion resistance of duplex stainless steel.

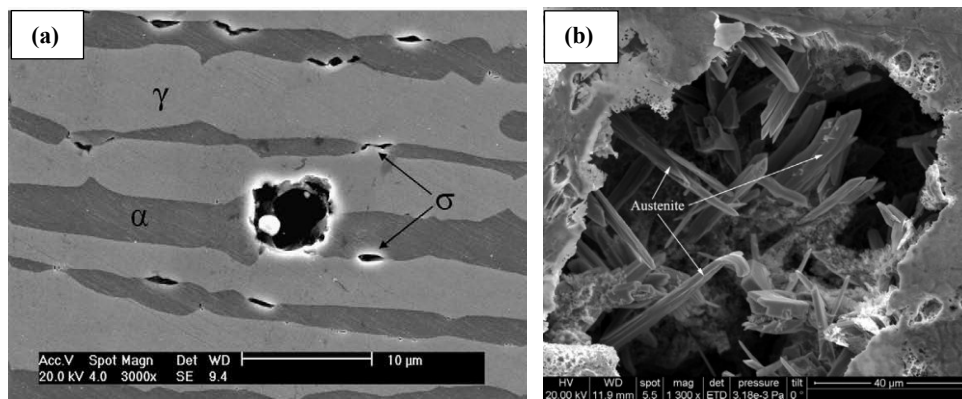


Fig. 1-46. SEM image of pit morphology after corrosion test [219,220]

The effect of sulphur and phosphorus are negative in pitting corrosion resistance, the former element mainly exists in ferrite and the latter is rich in the austenite [117]. Weber et al. [143] by using quantitative trilinear model found that, the level of the partitioning of molybdenum, chromium, nickel and nitrogen is affected by mass fraction of nickel and nitrogen accompanied with annealing temperature. Also, they found that to make high nitrogen duplex alloys to avoid precipitation of intermetallic phases, the mass fraction of molybdenum and chromium should be increased and decreased respectively. Atamerts et al. [128] worked in depth on understanding of the partitioning ratio of alloying elements between ferrite and austenite and effect of individual alloying elements on both phases balance and driving force of ferrite to ferrite and austenite transformation by means of thermodynamic model. Asif et al. [105], worked on the effect of PWHT on corrosion properties of the welded duplex stainless steels. They found with increasing the PWHT temperature, in ferrite phase percentage of chromium and molybdenum decrease and nickel increase; but in austenite phase amount of chrome and molybdenum slightly increase and nickel enhanced significantly, which could lead to phase balance distribution. Pettersson [223] has proposed a new PREN formula with different coefficients for elements. In addition, Perren et al. [75] have found that, using the composition of the bulk material for measurement of PREN value is not accurate, and this value should be measured for each phase separately by using new micro electrochemical method. They showed that the pitting resistance of duplex stainless steels should be specified by using the PREN of the weaker phase, which can either be ferrite or austenite [75]. Similar view is held by Merello et al. [224]. Bernhardsson [18] had found with increasing the temperature, the PREN of the ferrite and austenite phase in duplex steels decreases and increases respectively. Also, it is proposed that with increasing the annealing temperature, the PREN value of the phases become close to each other and the pitting behaviour will be the optimal [20].

Chapter 2: Effect of addition of nickel, nitrogen and PWHT on welding properties of the duplex stainless steel

Abstract

In the previous chapter I considered the various problems related to the welding of the duplex stainless steels. In this chapter, I will discuss how different methods were applied to optimize the welding properties of duplex and super duplex stainless steels. Consequently, the effects of these different methods, such as addition of nickel, nitrogen and the application of a post weld heat treatment (PWHT) on restoring the microstructure and mechanical properties of the welded UNS S32304 and UNS S32570 were investigated. Nickel, in the form of powder, was poured inside the joint gap before manual Gas Tungsten Arc Welding (GTAW) process. Addition of nitrogen was performed by mixing it with argon as shielding gas. The solution heat treatment was settled at 1100 °C for 10 min and was applied to all welded samples and samples with addition of alloying elements. The microstructure of the joints was characterized by optical microscopy (OM) and the evolution of phase percentages was studied by image analysis. Tensile and microhardness tests were carried out on the joints in order to evaluate the mechanical properties. Fracture surface analysis by scanning electron microscopy (SEM) showed detailed type of fracture after tensile test. X-ray diffraction (XRD) analysis was performed on the joints to identify the nature of the existing phases accompanied with phase measurement. The results showed that generally the effect of PWHT is more significant than the addition of nickel powder and nitrogen gas after welding. Also, it was found that applying PWHT on the nickel addition sample caused an improvement in the microstructure and restored the phase balance, while the sample treated with addition of nitrogen gas followed by PWHT indicated superior mechanical properties.

In this chapter the results of part of my research activity regarding an appropriate method for improving the microstructure and mechanical properties of the welded UNS S32304 lean duplex and UNS S32570 superduplex stainless steel are reported. This research involved the application of post weld heat treatment, addition of nickel powder, addition of nitrogen gas and the application of PWHT followed by addition of elements; these applications were performed on both duplex and superduplex welded joints. After characterization of the joints by means of optical microscopy, scanning electron microscopy, microhardness, tensile tests, fracture surface analysis and X-ray diffraction, the results were compared and optimum method for the final application was proposed.

Keywords: Duplex stainless steel, GTAW, Nickel powder, Nitrogen gas, PWHT, Microstructure, Phase percentage

2.1. Materials and experimental procedure

2.1.1. Materials and welding procedures

In this investigation, duplex stainless steel UNS S32304 sheet with dimension of $50 \times 50 \times 3$ mm was welded by manual gas tungsten arc welding (GTAW) process and using ER2209 filler metal (AWS A5.9). Table. 2-1 indicates the chemical compositions of the base and filler materials, which were used in this study. As we can see, filler metal has a higher amount of nickel compared to the base metal in order to guarantee the amount of austenite in the microstructure after solidification.

Table. 2-1. Chemical compositions (wt%) of the base and filler materials

Material	C	Cr	Ni	Mo	Mn	Si	Cu	N	Fe
UNS S32304	0.02	23.47	5.05	0.36	1.37	0.48	0.31	-	Bal.
ER2209	0.01	22.8	8.5	3.1	1.6	0.4	0.16	0.16	Bal.

The joint gap of the plates to be welded, was cleaned by alcohol to remove all dust and contamination. The welding was performed perpendicular to the rolling direction of the plates. The welding parameters were selected according to Table. 2-2. The schematic joint design is shown in Fig. 2-1. In addition, Fig. 2-2 indicates schematic design of using mixture of argon and nitrogen as shielding gas for welding. Fig. 2-3 indicates the appearance image of welded sample.

Table. 2-2. Welding parameters

Current (A)	Voltage (V)	Travel speed (mm/min)	Filler material (AWS A5.9)	Heat input (kJ/mm)	Shielding gas	Gas flow (l/min)
80	12-15	50-70	ER 2209	1.14	Ar 99.99%	12

Different welding conditions for metallurgical and mechanical investigations were considered. The first condition was the base metal welded solely by filler material, while the second one included the addition of nickel powder in the joint gap before welding, the third condition involved the addition of nitrogen gas accompanied with existing argon as a shielding gas.

Due to stabilization of austenite between 1000 to 1200 °C, for all above mentioned conditions post weld heat treatment at 1100 °C for 10 min followed by water quenching was performed. Fig. 2-4 indicates the furnace which was used for PWHT process. This temperature was selected because it is higher than the solubilization temperature of all deleterious intermetallic phases. As specified by Hwang et al.[115] up to 1050 °C there is still the possibility of formation of intermetallic phases. In addition he reported that, by applying this temperature on the joints, high corrosion resistance and high toughness is achievable [86,135].

Moreover, the analysis of the base metal in the as-received and after heat-treatment condition was considered as reference. Table. 2-3, indicates the nomenclature of the samples which was used in this study.

Table. 2-3. Nomenclature of the samples and welding conditions

Sample name	Conditions
BM	Base metal
BMP	Base metal after heat treatment
F	Filler metal, Argon gas
FP	PWHT on sample F
FNi	Filler metal, Argon gas- addition of nickel powder
FNiP	PWHT on sample FNi
FN2	Filler metal, Argon gas mixed with nitrogen
FN2P	PWHT on sample FN2

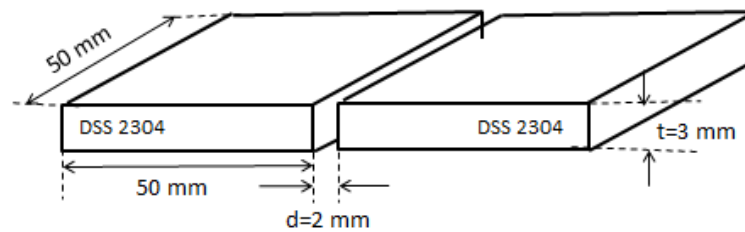


Fig. 2-1. Schematic joint design for the welding process

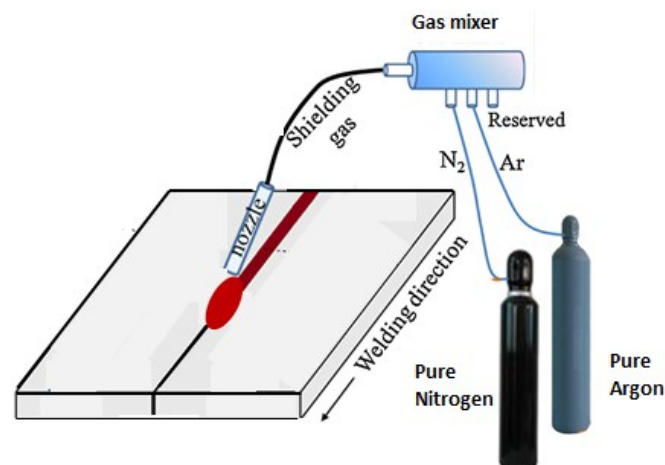


Fig. 2-2. Schematic form of using mixture of argon and nitrogen as shielding gas

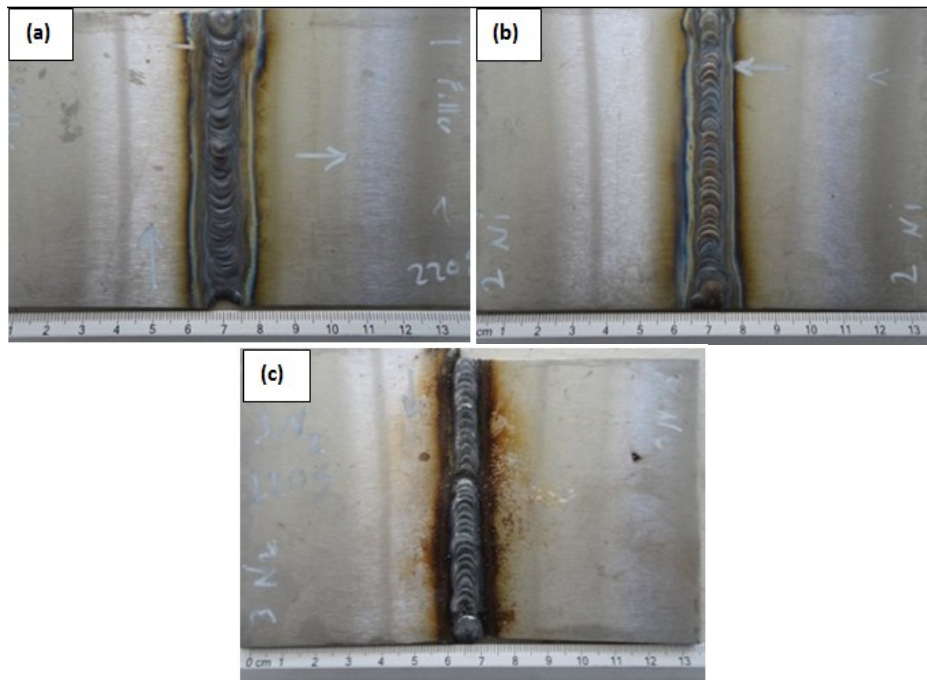


Fig. 2-3. The weld face of the samples using (a) F (b) FNi (c) FN2

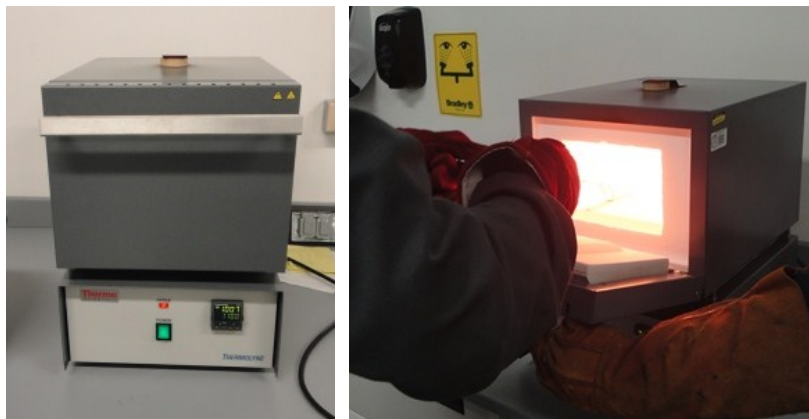


Fig. 2-4. Furnace which was used for PWHT process

2.1.2. Methods of materials investigations

Metallography analysis

Metallography investigations were performed based on ASTM E3 [225] standard. After cutting the cross section of the joints and mounting, standard sample metallography procedure consisted of grinding with series of water cooled SiC emery papers from 400 to 1200 grit size followed by polishing with 6 and 3 μm alumina. The Beraha reagent (50ml H_2O , 50ml HCl , 1g $\text{K}_2\text{S}_2\text{O}_5$, 10g $\text{NH}_4\text{F.HF}$) [103], was used for etching and revealing the microstructure of all the samples. The *Leica MEF4M* optical microscope was used for metallography investigations. The percentages of the phases were calculated by *Image proplus* software.

Hardness test

For the evaluation of mechanical properties, the vickers microhardness of the samples was measured through the base metal, heat affected zone and fusion zone. *The Future Tech microhardness* machine with applying one kg load for 15 second time was used for hardness measurement.

Tensile tests and fracture surface analysis

To investigate the tensile properties of the samples, according to standard ASTM E8M tensile subsize test samples were prepared and the test was performed by *Tinius Olsen 60* machine. Fig. 2-5 indicates the schematic tensile subsize sample based on standard. After tensile test the fracture surface of the samples were analyzed by stereomicroscope (*Leica MZ6*) and scanning electron microscope (*Zeis EVO EMA 15*). Before surface examination all the samples were cleaned ultrasonically in acetone solution for about 5 minutes to remove the dust and pollutions from the fracture surfaces.

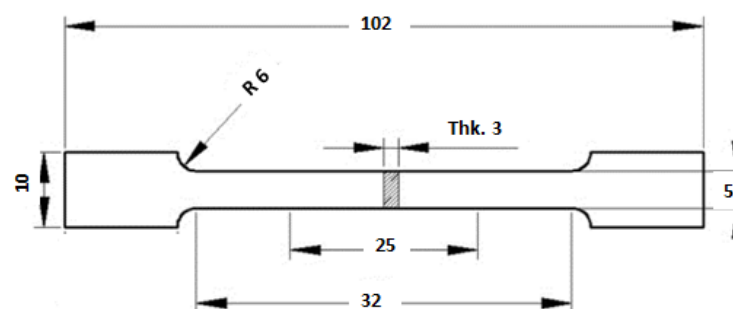


Fig. 2-5. Schematic dimension of tensile subsize sample

X-ray diffraction

To identify the nature of the observed phases in this study, X-ray diffraction analysis was performed on all the welded samples, as received base metal. The Bruker *AXS D-8 XRD* equipment was used with using CuK_α radiation ($\lambda = 0.154\text{nm}$) at 40 kV and 20 mA. The XRD spectra of the specimen was recorded in 2θ range between 10 - 110° with angular step of 0.01° and counting time 2 s. The evaluation of the peaks for detection of existing phases was performed by *DiffraC Plus evaluation* software.

2.2. Results and discussions

2.2.1. Base and weld metal structure

After cutting and preparing the samples, macrosection of the joints were evaluated to observe if there were any defects in the joints or not. Also, the size of the fusion zone and heat affected zone of each joint was measured through weld cross section. Based on the obtained results, the medium width of the welds for all the samples were between 4 to 5.7 mm, which could be due to the same value of heat input applied to all the samples. Fig. 2-6 indicates the optical microscopy images of the as received base metal (UNS S32304) which consists of roughly equal percentage of ferrite and austenite phases. Fig. 2-7 and Fig. 2-8 indicate one cross section example of the sample and one cross section as an example for measurement of different zones respectively.

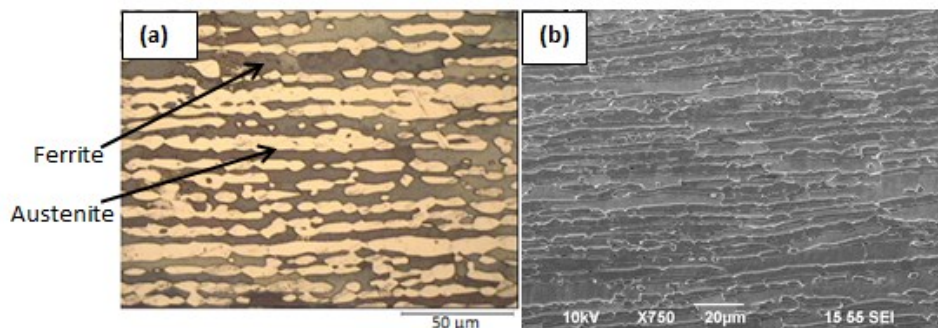


Fig. 2-6. The microstructure of the base metal UNS S32304 (a) optical microscopy (b) SEM

After cross sectioning, sample preparation and observation of the welded joints by visual inspection, no evidence of any macrocracks, slags and porosities were observed this could be due to selection of appropriate filler metal and welding parameters and high quality of the weld. Lippold et al. [226], found that wetting of the boundaries with liquid films occurred more frequently between austenite-austenite and ferrite-ferrite grain boundaries compared to ferrite-austenite boundaries due to its lower interfacial energy. Consequently, the risk of formation of solidification crack in duplex steels is less than in austenitic and ferritic steel. Table. 2-4 depicts the medium size of HAZ from both sides and fusion zone for all the samples.

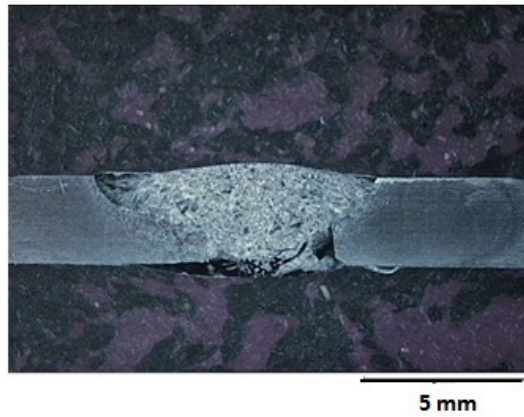


Fig. 2-7. Macrograph cross section of one welded sample

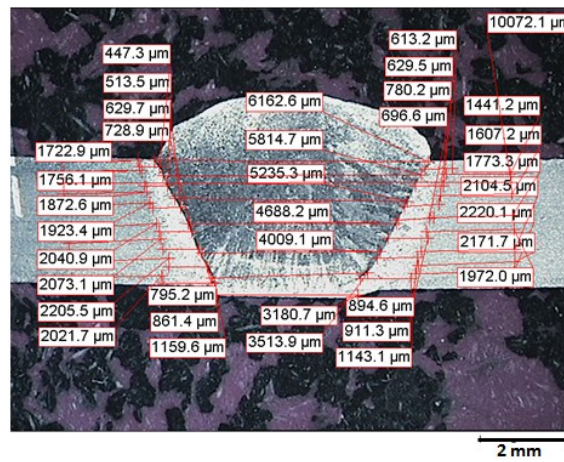


Fig. 2-8. Sample image for measurement of HAZ and fusion zone

Table. 2-4. Size of HAZ and fusion zone for all the samples

Sample Name	HAZ		HAZ total (mm)	Fusion zone (mm)
	Left (mm)	Right (mm)		
F	0.95	0.59	1.54	5.78
FP	1.12	1.03	2.16	5.04
FNi	0.91	0.73	1.64	5.78
FNiP	0.86	0.91	1.77	4.05
FN2	0.73	0.8	1.54	4.65
FN2P	0.42	0.43	0.86	5.00

2.2.2. Microstructure evolution

The microstructures of different zones in samples F and FP is shown in Fig. 2-9. Fig. 2-9(a) and (b) presents the transition zone before and after PWHT. The heat affected zone (HAZ), which is interface of the weld and base metal, is not melted but just simply affected by the heating process of welding. Interpretation of the microstructure of the HAZ is complicated and it depends on the microstructure of the base metal, peak temperature, the amount of time at peak temperature, heating and cooling rate [227].

Generally, the austenite phase in DSS weld metal is formed from ferrite in three different modes: allotriomorphs at the ferrite grain boundaries, widmanstatten side-plates which expand from grain boundaries to inside of grains and intergranular precipitates [12,127]. The microstructure of HAZ in sample F (Fig. 2-9(c)) mainly consists of large ferrite grains with intergranular austenite (IG), grain boundary austenite (GB) and widmanstatten side plate austenite (WS) which mainly nucleated in grain boundaries. Also, small secondary austenite was formed and distributed inside of the ferrite matrix. During the welding, the temperature of heat affected zone near to the fusion line reached to roughly 1450 °C and became fully ferritic on heating.

During rapid cooling, reformation of austenite phase was not sufficient to restore the duplex microstructure base metal properties. Only grain boundary allotriomorph and widmanstatten austenite form in this zone and most of the microstructure remains in ferrite phase. After applying PWHT (Fig. 2-9(d)), the morphology of the austenite changed becoming mostly intergranular/ spheroidal in shape, accompanied by an increase in the percentages of austenite. Fusion zone of sample F (Fig. 2-9(e)) consists of large elongated and columnar austenite distributed in the ferrite matrix. After PWHT (Fig. 2-9(f)), grain refining and precipitation of austenite inside of the ferrite matrix occurs and the shape of austenite changes and becomes smoother and more globular.

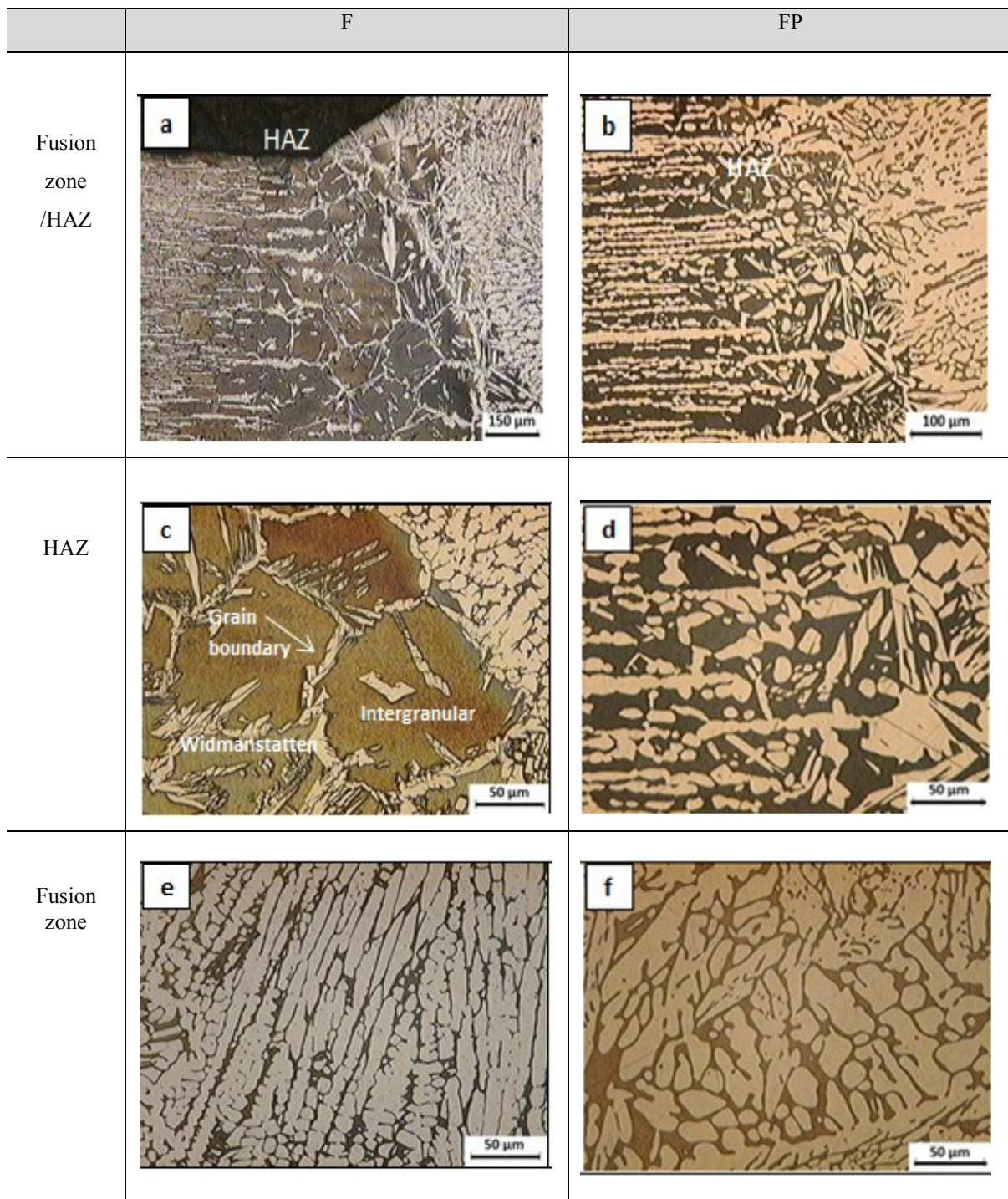


Fig. 2-9. Microstructure of the different weld zones of sample F and FP

Fig. 2-10. shows the microstructure of the FNi and FNiP samples. In Fig. 2-10(a) and (b) the microstructure of the interface between the fusion zone and HAZ before and after PWHT are shown. HAZ of the sample FNi (Fig. 2-10(c)) mainly consists of separated intergranular austenite lathes which are distributed in the ferrite matrix. After PWHT (Fig. 2-10(d)) the amount of austenite increases and becomes more uniform distributed with curve shape boundaries.

Fusion zone of the sample FNi (Fig. 2-10(e)) consists of higher amounts of coarse widmanstätten austenite, distributed in the ferrite matrix. Microstructure of fusion zone, after PWHT (Fig. 2-10(f)) becomes finer and smoother, with elongated intergranular austenite which are uniformly distributed in the ferrite matrix. This microstructure concords with the results of Zhang et al. [86] and Tan et al.[89]. By applying nickel powder in the weld joints we can observe coarser austenite grains and finer ferrite accompanied by lower amount of ferrite percentages. This could be due to presence of high concentration of nickel as an austenite stabilizer element.

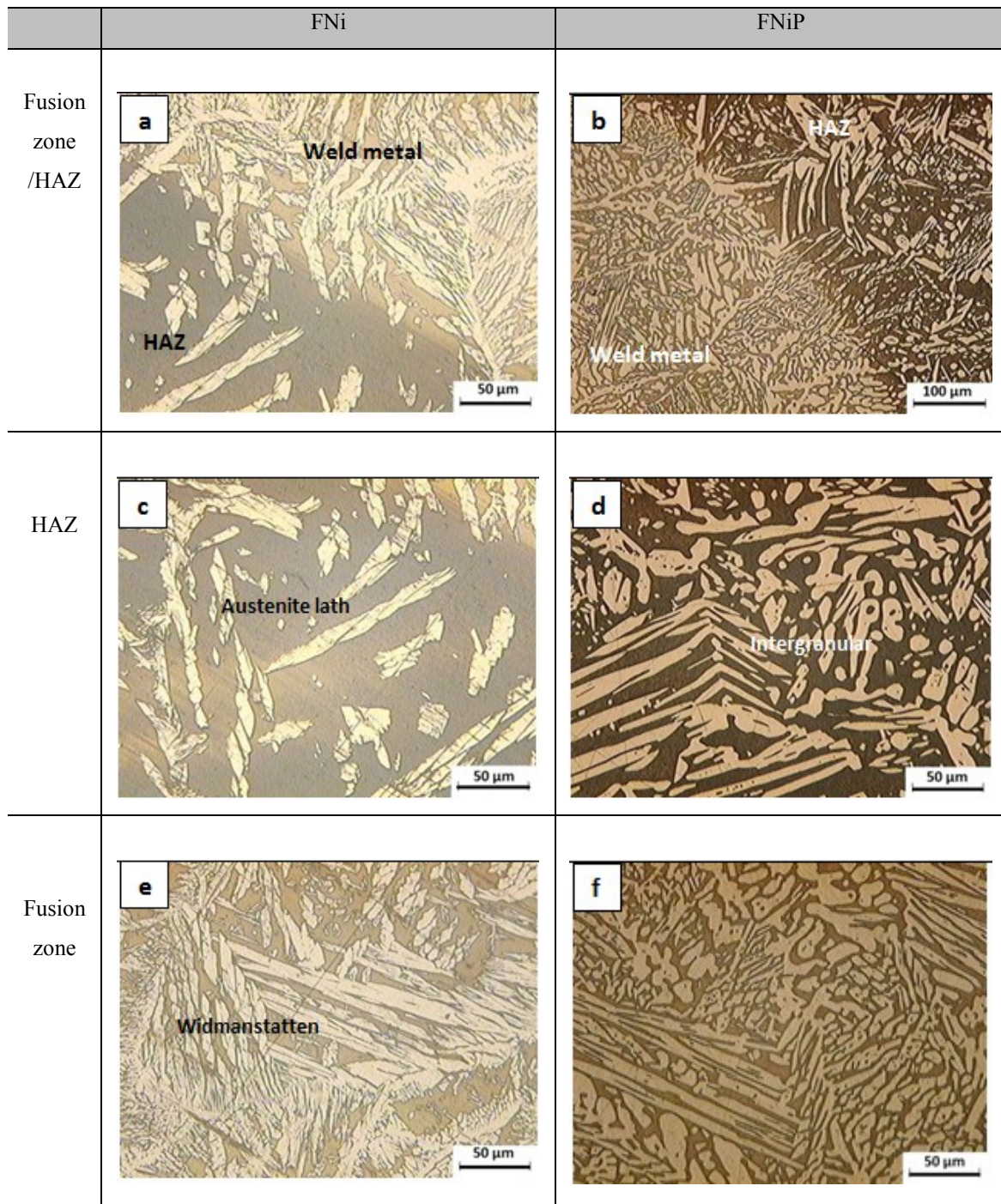


Fig. 2-10. Microstructure of the different weld zones of sample FNi and FNiP

Fig. 2-11 shows, the microstructure of the sample with the addition of nitrogen and relevant PWHT. Fig. 2-11(a) and Fig. 2-11(b) indicate the microstructure of all three zones of base metal, fusion zone and HAZ for sample FN2 and FN2P respectively. Fig. 2-11(c), depicts the microstructure of the heat affected zone of sample FN2, which is similar to the sample F. The microstructure includes grain boundary austenite, intergranular austenite and Widmanstätten austenite, the amount of Widmanstätten austenite is however more than sample F.

Following PWHT (Fig. 2-11(d)), microstructure of HAZ mainly consists of intergranular austenite which are grows significantly, taking on a spheroidal shape which is uniformly distributed in the matrix, this microstructure confirms with the results of Zhang et al. [86]. It has been reported that nitrogen in the gas mixture can diffuse into the alloy at high temperature and promote the regeneration of γ phase during cooling [228]. Also, austenite did not show any preferred growth direction, but the growth rate was significant. Fig. 2-11(e) shows the microstructure of the fusion zone for sample FN2 which is similar to the microstructure of sample FNi and includes large austenite lathes. After PWHT, the microstructure consists of coarse austenite lathes with smoother boundaries with the matrix (Fig. 2-11(f)). It was noted that [229], γ phase became stable in temperature between 900-1100 °C. The results of PWHT indicated that, the percentages of ferrite-austenite can be restore in welding zone. Moreover, the presence of lath and blocky austenite in the matrix causes an increase in crack growth resistance accompanied by reduced the anisotropy. The beneficial effect of nickel and nitrogen have been reported many times [12,230]. An increase of these elements causes a decrease of Cr_{eq}/Ni_{eq} ratio which causes an increase in ferritizing temperature and inhibits transformation of austenite to ferrite at high temperature during heating and promote ferrite to austenite transformation during cooling.

Due to existing differences in austenite at various temperatures, intergranular austenite forms at lower temperatures and may have slightly lower nitrogen content when compared to the allotriomorph grain boundary and widmanstätten which form at higher temperatures. Consequently, weld metal with addition of nitrogen shows higher corrosion resistance which could be due to promotion of higher amounts of allotriomorph and widmanstätten austenite with higher nitrogen content.

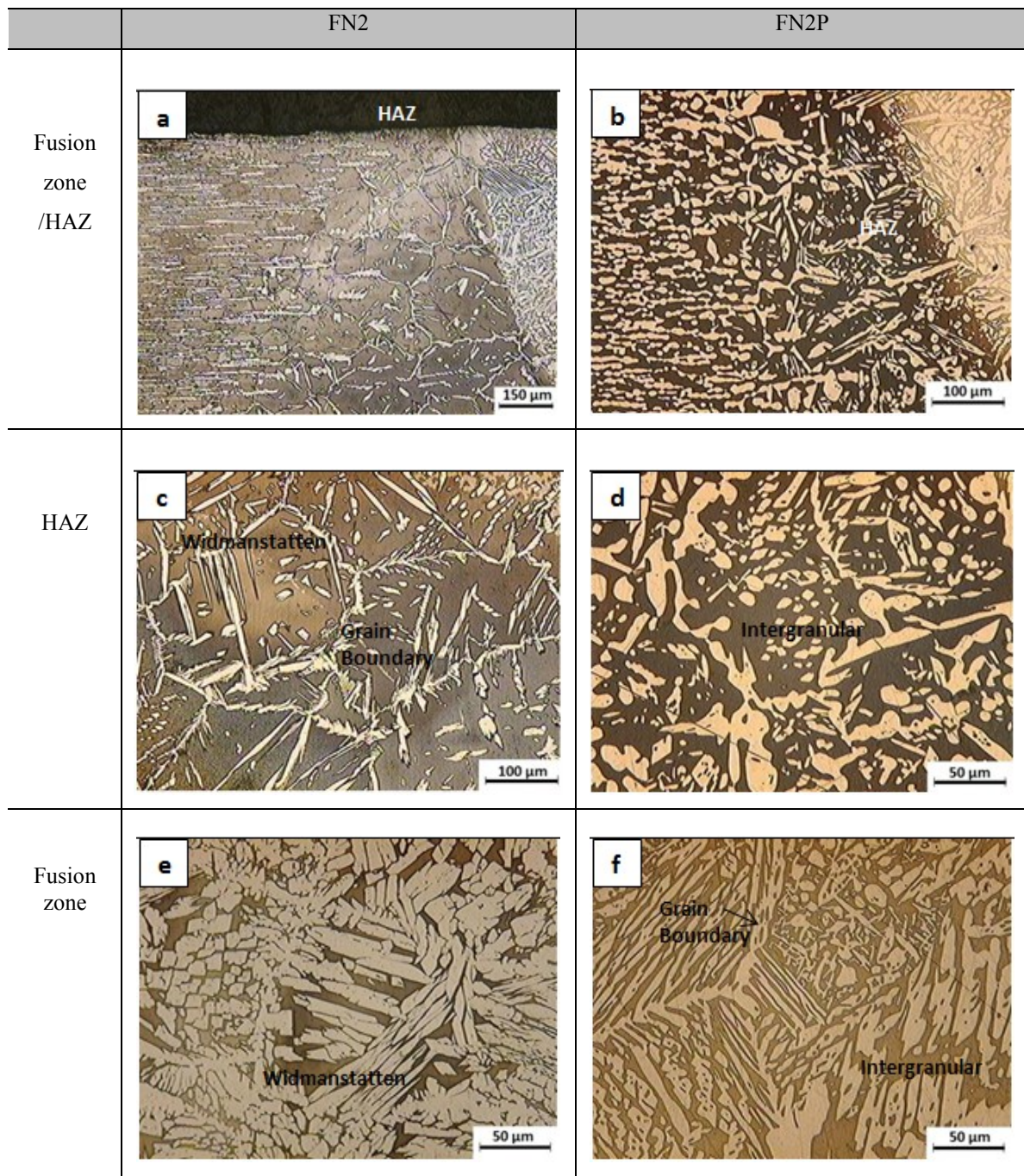


Fig. 2-11. Microstructure of different weld zones of samples FN2 and FN2P

The results of PWHT indicate that, the amount of austenite increase and the weld microstructure consisting of roughly equal percentages of ferrite and austenite. The solution heat treatment causes a change the microstructure reaching equilibrium phase percentage and restoring the phases close to as received material. This shows an increase in austenite content in solution treated weld metal, compared to as welded condition. It occurs due to growth of all three types of austenite.

As the growth of austenite did not show specific preferential direction, most of the particles solidified as spheroidal shape [190]. There is no specific difference between, solidification of duplex stainless steels and carbon steels, just in carbon steel all of the austenite change to ferrite, bainite and martensite except for a small amount of a austenite retained in ferrite matrix at room temperature. In duplex steels, however large amount of austenite remain in the matrix [127]. Due to relatively rapid transformation, this process is not equilibrium, consequently more ferrite remains untransformed [190]. In addition, the values of the phases are dependant on temperature and cooling rate [4]. In addition, based on investigation of Yang et al. [56], we can note that in welded sample firstly there is formation of grain boundaries become coarser and this is followed by the formation of wedmanstatten austenite and intergranular austenite of welded samples: first grain boundary austenite form, then by increasing the cooling time the grain boundaries become coarser, and finally there is the formation of widmanstatten austenite and intergranular austenite. Yuan et al.[231], specified that changes in microstructure in duplex steels is due to formation of an imbalance of ferrite and austenite compared with the base metal. They found multidirectional grain growth containing cellular and columnar dendrites with presence of secondary phases mainly cause a locking up of the grain boundaries. They also reported that the increasing N_2 content in the Ar- N_2 mixture changes the morphology of the welds from an acicular to a globular form of the γ -phase [127].

Differences in percentages of ferrite and austenite phases in different welds can be explained by ternary Fe-Cr-Ni diagram. A vertical section of the ternary system at constant 60 wt.% of iron “pseudo-binary” section is shown in Fig. 2-12. Diagram indicates that, solidification mainly starts from delta ferrite, and till end of the solidification stage it remains the same. During cooling in solid state, at temperature lower than ferrite solution, partial transformation of ferrite to austenite occurs. The amount of austenite, depends mainly on cooling rate. In addition the sequence of ferrite to austenite formation in cooling rates appear first as grain boundary allotriomorphs followed by widmanstatten side plate and intergranular precipitates. [109]. In higher heat input and consequently lower cooling rate, more amount of austenite remain in the microstructure.

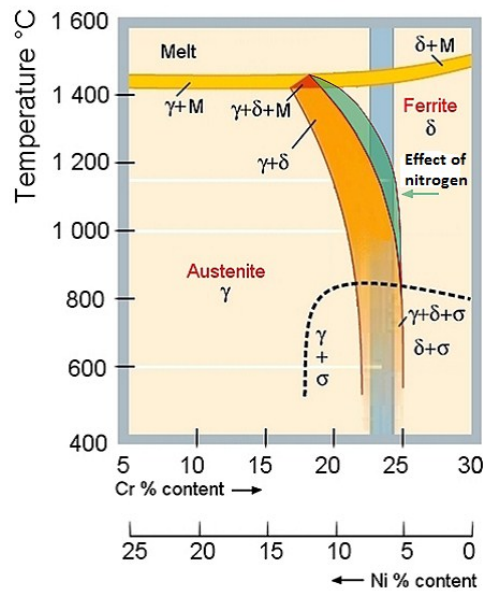


Fig. 2-12. Binary phase diagram for Ni-Cr at Fe 70% for duplex stainless steel [118]

Generally formation of grain boundary and side plate austenite during solidification requires reduced driving force and can occur at higher temperatures with low undercooling. However, the formation of intergranular acicular austenite require greater undercooling and occurs at lower temperatures. Grain boundary austenite and widmanstatten side plate form at the onset of high temperature, while intergranular austenite particles require greater driving force and precipitate later at lower temperatures [170]. At low cooling rate thin and discontinuous side plate austenite along with grain boundary and intergranular austenite is formed. With regard to the addition of nitrogen from base material during welding process. In addition this produces a higher percentage austenite in the weld and there is less risk for nitride precipitation in ferrite grains [232]. In addition, nitrogen plays two main roles in duplex stainless steel, first is to improve the pitting corrosion resistance by increasing the value of the pitting resistance equivalent number ($PREN = \% Cr + 3.3\% (Mo + 0.5\% W) + 16(30)\% N$). the second role is accelerating formation of austenite in the weld zone.

With regards to the application of post weld heat treatment it can be specified that, many intergranular austenite grains reveal significant growth and mainly become in spheroidal in shape. Moreover, austenite grains do not show preferred growth direction. Luo et al.[137], proposed a model for transferring the secondary phases from HAZ to weld zone after PWHT, which cause to relatively more hardness in that area. As shown in Fig. 2-13, after PWHT the detrimental intermetallic phases diffuse from HAZ to the fusion zone due to segregation of secondary phase elements. It should be mention that the obtained microstructure results after PWHT for all the samples, show a much higher proportion of intergranular austenite with respect to grain boundary and widmanstatten austenite, this is in agreement with the results of Muthupandi et al. [170].

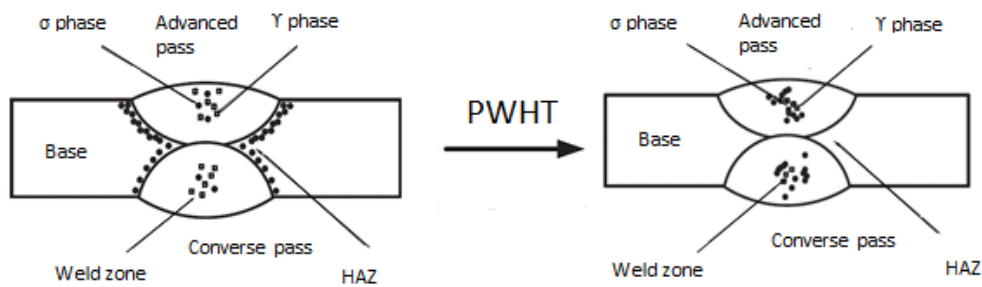


Fig. 2-13. Changing the microstructure after applying PWHT [137]

2.2.3. Determination of phase percentage

Generally the balance between percentages of ferrite and austenite phases can be achieved by controlling the chemical composition of the base metal and selecting an appropriate filler metal. The filler metal should contain higher amount of austenite stabilizer elements such as nickel and nitrogen compared to base metal [233]. The measurement of both ferrite and austenite phases in different zones was performed based on metallography investigations by using the *Image proplus* software. For each image surface area fraction which is approximately equal to the volume fraction of each phase was calculated in accordance with ASTM E1245 standard. Some images of phase determinations by software in different zones are shown in Fig. 2-14.

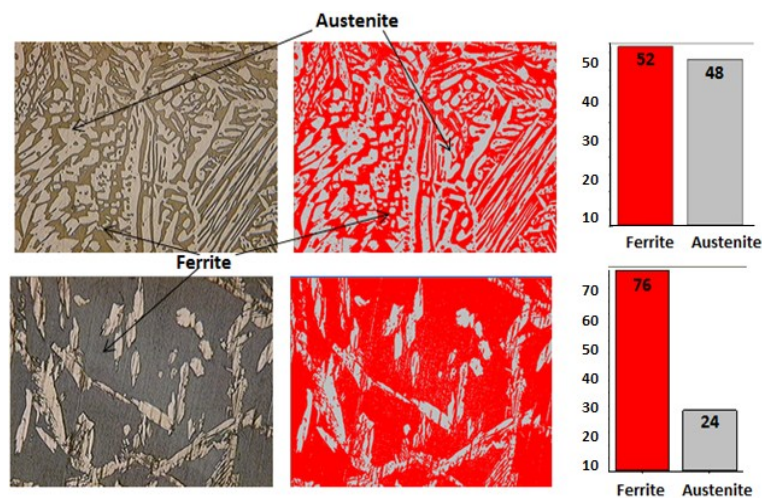


Fig. 2-14. Example of phase percentage determination in software

For each zone, five images were measured and medium value is considered as percentages of each phase in that area. Table. 2-5, indicates the results of ferrite and austenite phase percentages in fusion zone and HAZ of all the samples. Fig. 2-15, depicts the results of phase percentages by means of a histogram for easier comparison. In all conditions of welding, in the HAZ the percentages of ferrite is higher than austenite but this value in the fusion zone is diverse, in agreement with the results of Mourad et al. [121]. Generally, weld metal of duplex stainless steels have ferrite contents in the range of about 30-70 % depends on chemical composition. The value of austenite in heat affected zone of all the samples were measured in the range between 22 and 33 % which is in agreement with the results of Sieurin et al.[83].

Moreover, in the fusion zone the concentration of ferrite is less than that of austenite, probably due to the higher amount of austenite stabilizer elements such as nickel in filler metal, externally added powder and addition of nitrogen gas.

The main changes in the microstructure occur after PWHT, both phases reach to roughly equal amounts. The percentages of both phases remains constant at room temperature because of rapid cooling after PWHT. The value of austenite after PWHT increases to around 40.4 % , 48.2 and 15 % in HAZ of the samples F, FNi and FN2 respectively. It means PWHT has significant effect on improvement of the microstructure to restore the equal amount of phases. In addition, based on the results of the base metal before and after PWHT, it is clear that after PWHT the percentages of austenite phase increase and both phases become roughly the same (48 %Ferrite-52 %Austenite). For most industrial applications and piping inspection procedures austenite contents lower than 25-30% are unacceptable [190,234,235]. The results of this study, show that austenite contents of fusion zone for all the samples are acceptable for industrial applications. Moreover, according to Hagen et al [236] the optimum percentage of austenite for reaching an appropriate combination of corrosion resistance and mechanical properties should be in the range 40-60 %.

Table. 2-5. Value of phase percentage in different samples

sample	Austenite%	Ferrite%	Standard dev.
BM	42.7	57.3	2.5
BMP	48.2	51.8	3.3

sample	HAZ		Standard dev.	Fusion zone		Standard dev.
	Austenite%	Ferrite%		Austenite%	Ferrite.%	
F	24.2	75.8	2	78.4	21.6	2.3
FP	40,6	59.4	5.4	64,7	35.3	9.4
FNi	21.7	78.3	1.8	68.8	31.2	5
FNiP	41,9	58.1	1.8	54,4	45.6	1.9
FN2	34.5	65.5	5.9	67.9	32.1	4
FN2P	40.9	59.1	3.2	53.7	46.3	4

Samples F and FNi show the maximum differences between ferrite and austenite phases in both HAZ and fusion zone; samples FNiP and FN2P show the best result for reaching equal percentage of ferrite and austenite phases. This means that the effect of PWHT in phase changes is more efficient than adding alloying elements. This result is in agreement with Liu et al. [167] which states that with the application of post weld heat treatment there is a possibility of precipitation of secondary austenite phase.

Following PWHT the volume fraction of austenite generally increases and microstructure shows more balanced amounts of ferrite and austenite. It has been reported that the amount of delta-Ferrite in joints is a function of the thermal history experienced during welding. The higher the cooling rate, the higher delta-ferrite content in the joints [171].

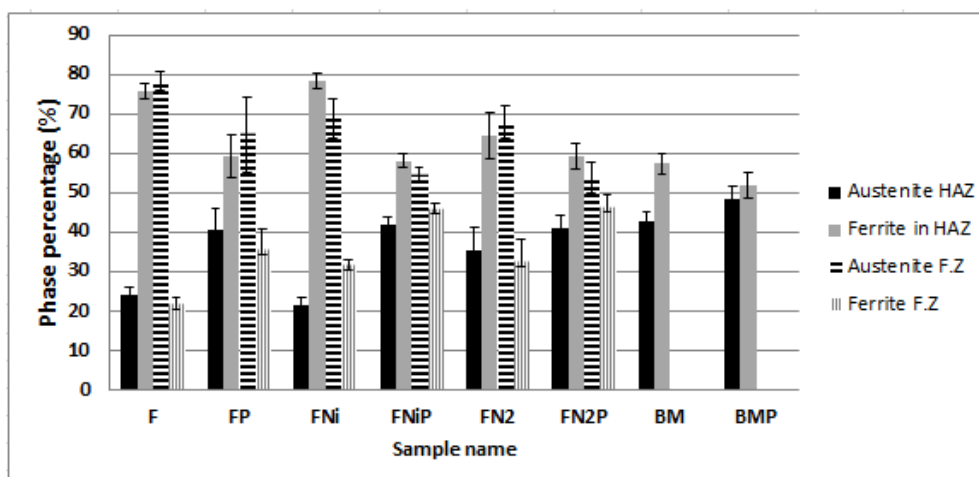


Fig. 2-15. Diagram for comparison of ferrite austenite percentage in weld and HAZ

2.2.4. X-Ray diffraction analysis

XRD analysis was performed on all the samples of as received material BM, BMP, F, FP, FNi, FNiP, FN2 and FN2P. Based on obtained data from XRD spectrums as specified in Fig. 2-16 for the samples before and after PWHT and Fig. 2-17 for all the samples, the position of peaks indicate the identification of phases. The phases are mainly ferrite and austenite with different lattice parameters which are shown on top of each peak. Comparing the result of base metal and welded samples no evidence of unwanted intermetallic phases such as σ , χ and nitride was observed (we cannot rule out the presence of phases below 5% which is minimum limit for phase detection by XRD) [237]. It is known that [238] the σ -phase possess a very strong line at lattice spacing of 1.952 Å, which corresponds to 46.5° in the spectra. These phases were also undetected by microscopic investigation and this confirms the result of XRD. As shown in Fig. 2-17, the base metal and sample welded by filler metal and nickel powder, the major peak intensity of ferrite with respect to austenite, but for the sample with addition of nitrogen, the major peak of austenite showed more intensity. During welding, the transformation of austenite to ferrite occurs completely [93] and it causes the formation of ferritic microstructure after solidification. By cooling from high temperature, ferrite partially converts to austenite but main phase remain ferrite, till room temperature.

Peak width by which we mean crystal size and inside strain was approximately the same for most of the peaks. Since duplex steels contain crystalline ferrite and phases, a specific X-ray diffraction pattern can be obtained when the sample irradiated by X-ray. Quantitative measurements of the relative volume fraction of each phase can be obtained from X-ray diffraction because total integrated intensity of all diffraction peak for each phase is proportional to the volume fraction of that phase.

If the crystalline phase or grains of each phase are randomly oriented, the integrated intensity from any single diffraction peak (hkl) crystalline plane is also proportional to the volume fraction of that phase. In addition, it can be observed that in sample F, FP and FNi, FNiP after PWHT the intensity of the peaks remains constant while in sample with addition of nitrogen after PWHT, peak intensity decreases, this could be due to strong effect and dissolution of nitrogen which has an effect on crystallinity.

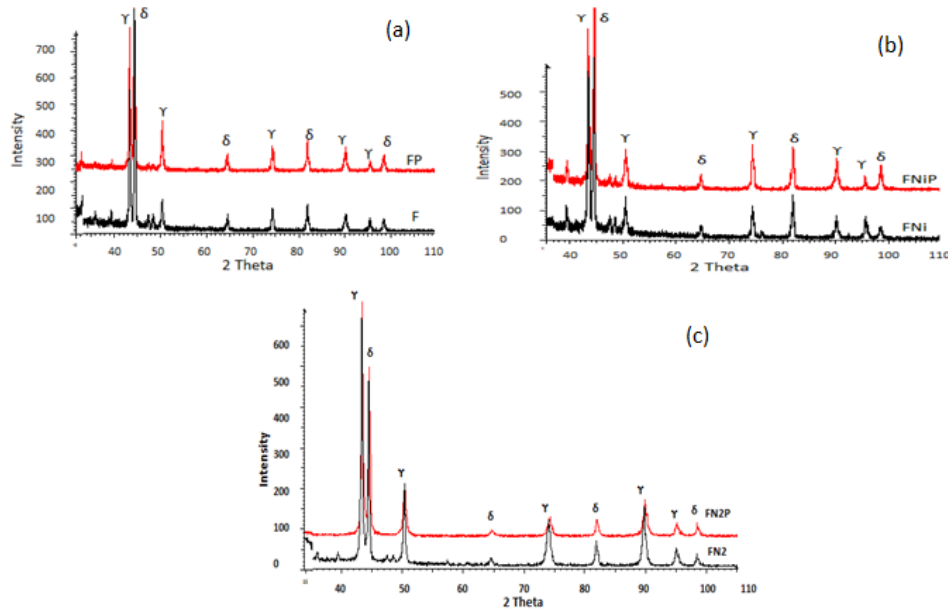


Fig. 2-16. XRD spectrum of the samples before and after PWHT (a) F, FP (b) FNi, FNiP (c) FN2, FN2P

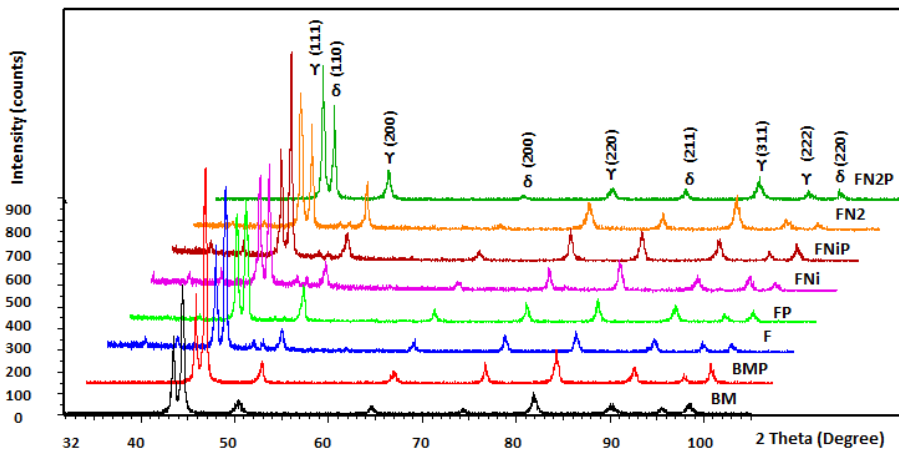


Fig. 2-17. XRD spectrum of all the samples

Quantitative analysis were performed on each separate peak obtained from XRD analysis to measure relevant intensity. Full width half maximum (FWHM) and the value of 2θ . To measure these parameters the peaks were fitted with one Gaussian peak profile function. Additional analysis is done on diffraction patterns to estimate phases percentages in the matrix and calculate the lattice parameters for both austenite and ferrite phases from the peaks of diffraction pattern.

For calculation of the lattice parameter of each phase as a function of time, the d -spacing is calculated from the relevant 2θ value for each diffraction pattern by using the well know Bragg's equation (1). Then the d -spacing was converted to the lattice parameter by using the following formula (2)

$$\lambda = 2d \sin \theta \quad (1)$$

$$a = d \sqrt{h^2 + k^2 + l^2} \quad (2)$$

In these equations,

λ is the wavelength of X-ray (0.1033 nm)

d is interplanar spacing (nm)

a is lattice parameter (nm)

h, k, l are Miller indices for each peak

The lattice parameter of each phase is the average value which calculated each single peak in the specific diffraction pattern. As is clear, the lattice parameters and value of 2θ are inversely proportional, consequently the resulting ferrite and austenite lattice parameters change in opposite direction of 2θ value. The percentage of phases quantitatively determined by measuring the sum of peak intensities for each phase calculates the ratio between these value and the sum of the peak intensities for each phase. Considering that both ferrite and austenite phases are exist at room temperature, the intensity fractions were normalized based on measurement of intensity fractions. This was considered because of existing differences between the phase balance measured from metallography (Aus.42.7%-Fer.57.3%) and diffraction intensity fraction (Aus.54%-Fer.46%) of the base metal [93].

The measurement of intensity fraction in each diffraction pattern are normalized with the quantitative metallography measurements using the equation (3) and (4):

$$\delta = C_{\delta} (\delta_{\text{XRD}}) \quad (3)$$

$$\gamma = 1 - \delta \quad (4)$$

Where

δ is the normalized volume fraction of ferrite,

C_{δ} is the normalized constant and it is equal to ($\delta_{\text{Met}}/\delta_{\text{XRD}}$)

δ_{XRD} is the fraction of δ measured in XRD pattern

δ_{Met} is the volume fraction of δ measured using quantitative metallography

Due to intrinsic properties of the X-ray diffraction which cover all the three zones of fusion zone, HAZ and base metal, the results of phase percentage cannot be compared simply with specific metallurgy measurement. By considering simply the percentages of each zone in the area covered by XRD, the value of ferrite and austenite based on metallurgy results was calculated and compared with obtained results from XRD. It should be mentioned that results of metallurgy was measured based on medium value of some random images in each area, but XRD covered all the area at the same time. It should be mentioned that, to find the exact value of phases in different zones, the relevant area percentage for each zone was measured. Fig. 2-18 and Table. 2-6 indicate the one example of area measurement and area fraction of all the samples respectively.

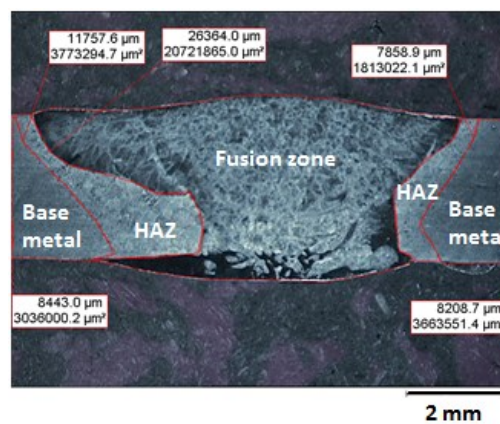


Fig. 2-18. Sample images for measurement of zone percentages

Table. 2-6. Percentage area of different zones which covered by XRD

Area	Base%	HAZ%	Weld%
F	25.5	18.9	55.6
FP	37.6	12.3	50.1
FNi	20.3	16.9	62.8
FNiP	44.9	8.9	46.2
FN2	29.6	10.9	59.5
FN2P	33.9	14.1	52

The differences between value of XRD and metallurgy were calculated between around 4 to 12 % (except for sample F where a difference of 18% was observed). This means there is appropriate agreement between the results of phase measurement by doing XRD test and metallurgy results. Consequently, it is possible to calculate percentage of phases by XRD, as an alternative to the time consuming metallurgy procedure. Table. 2-7, shows the obtained data from XRD spectrum for determination of the phases and different results with metallurgy investigation.

Table. 2-7. Phase percentage measurement based on metallography and XRD

Sample	XRD Peak intensity Aus. - Fer.	XRD FWHM Aus. - Fer.	Metallography Area of XRD Aus. - Fer.	Difference XRD & Metallography(%)
F	43 - 57	42 - 58	60.6-39.4	18.2
FP	53 - 47	52 - 48	56.4-43.6	4.1
FNi	52 - 48	51 - 49	57.2-42.8	5.7
FNiP	42 - 58	40 - 60	51.1-48.9	12.2
FN2	60 - 40	55 - 45	58.8-41.2	3.4
FN2P	70 - 30	75 - 25	50.8-49.2	13.5
BM		54 - 46	42.7-57.3	20

2.2.5. Microhardness profile

Routine microhardness profile was performed on the base metal, HAZ and fusion zone of each sample. The hardness of base metal was measured in the range of 240-250 HV₁. The results of hardness measurement for all the samples are specified in Fig. 2-19, Fig. 2-20 and Fig. 2-21. In the sample which was welded by filler metal alone (Fig. 2-19), the value of microhardness is quite uniform (240-260HV₁), also with applying the PWHT no specific changes in the value of microhardness was detected which is in agreement with the result of Udayakumar et al.[239] and Mourad et al. [121]. Also in this figure the micrograph of hardness profile is specified which shows the roughly similarity of the hardness value through different phase.

This could be due to i) the close chemical composition of base metal and filler metal and ii) the absence of precipitation of any intermetallic phases in the microstructure. In sample FNi, microhardness values in the weld metal are higher than in the base metal (260-270 HV₁ compared with 240-250 HV₁), this can be justified by considering the higher amount of rough Widmanstätten austenite in the microstructure.

It could also be due to strain induced heating and cooling cycles which caused by compression of the weld region during solidification. The microhardness profile of the sample with addition of nickel powder followed by PWHT is shown in Fig. 2-20.

Sample FNiP shows a little decrease in hardness of the fusion zone (220-240 HV₁) compared to the sample FNi. These results are in agreement with the microstructural analysis, which confirm the formation of austenite with finer, smoother and globular morphology after PWHT; moreover, an additional effect could be due to stress relieving in the weld zone [170].

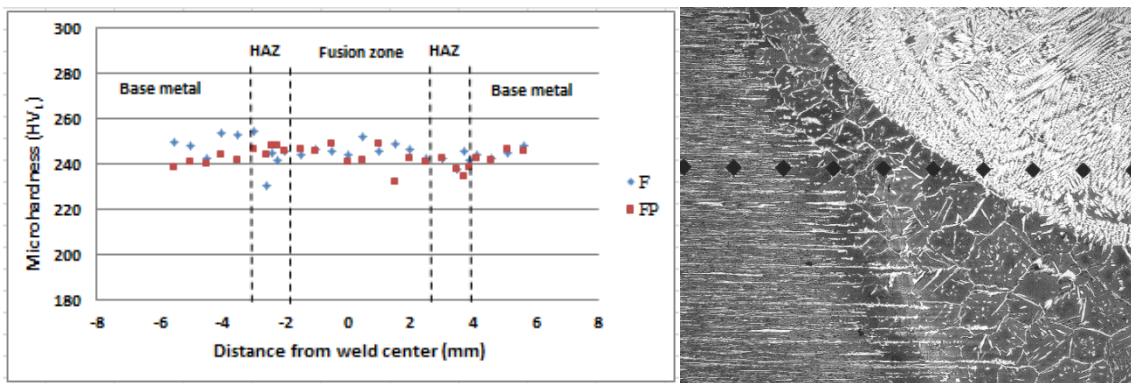


Fig. 2-19. Microhardness profile of the samples F,FP and microscopic image of indentations

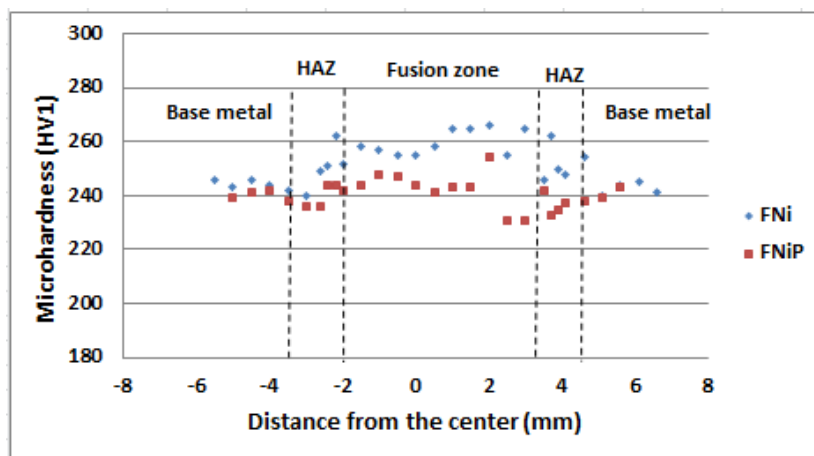


Fig. 2-20. Microhardness profile of the samples FNi and FNiP

According to Fig. 2-21 which shows the microhardness profile of the sample with nitrogen before and after PWHT, the value of hardness did not change significantly in different zones. Just for both conditions of before and after PWHT, the hardness in fusion zone was marginally more than HAZ and base metal. Tseng et al.[183] specified that, interstitial elements such as carbon and nitrogen cause an important effect on strengthening compared to substitutional elements such as chromium, nickel and molybdenum.

Nitrogen as austenite stabilizer element, tends to dissolve in austenite phase and overall cause an increase the hardness. This could be due to small precipitation of chromium nitride in the weld zone because nitrogen mainly dissolved in austenite phase due to low cooling rate. This phase cannot be recognized easily by optical microscopy and SEM, thin foil TEM investigation is required. This results agree with the investigation of Salazar et al. [228], Tavares et al. [47] and Keskitalo et al.[232].

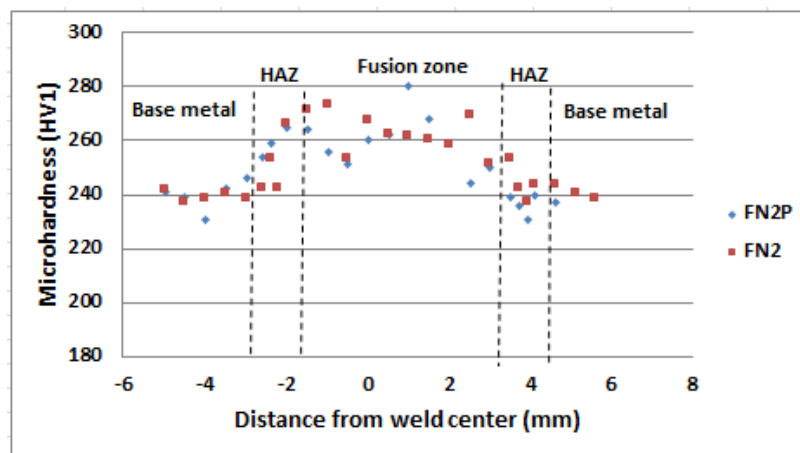


Fig. 2-21. Microhardness profile of the samples FN2 and FN2P

Due to reduced size of phases in vicinity to each other, measuring the exact value of hardness for ferrite and austenite with conventional methods is not easy and mainly value of the hardness represent for both phases [17,170] but applying 25 g load, the hardness of ferrite and austenite was measured based on medium value of five measurements. The results showed that ferrite is slightly harder than austenite (319 and 300 HV for ferrite and austenite respectively). In literature the hardness value of 315 HV for ferrite and 297 HV for austenite has been reported [121]. But Jebaraj et al.[122] measured the ferrite and austenite microhardness for multipass welded UNS S32304 duplex stainless steel, they observed higher hardness for austenite due to formation of secondary austenite phase which contains more amount of molybdenum and chromium content. Based on the obtained results, there is not specific differences between hardness of the different weld zones. Differences between percentage of ferrite and austenite phases do not have much effect on the hardness value which is in agreement with the results of Muthupandi et al.[170] and Mourad et al.[121]. Finally, It should be mentioned that, all obtained hardness results were less than maximum acceptable value of 350 HV which is maximum allowable value for industrial applications [240].

2.2.6. Tensile test

Tensile tests were performed in order to evaluate the static mechanical properties of the joints with considering the effect of nickel addition, nitrogen gas and PWHT. Subsize tensile sample were machined from the weld joints according to ASTM E8 [241].

Fig. 2-22 and Fig. 2-23, indicate the schematic location of the tensile test and prepared test specimen respectively.

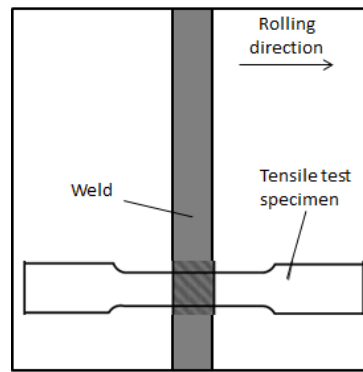


Fig. 2-22. Schematic representation of location of tensile test

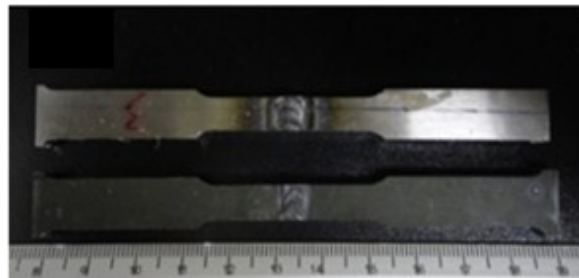


Fig. 2-23. Prepared tensile test sample

In Table. 2-8 the results of tensile tests for all the samples are collected. Sample FP shows a decrease in UTS of about 10 % in comparison with sample FP, FNiP also it shows slight drop (about 2 %) in the value of UTS with respect to FNi. After PWHT microstructural softening occurs to release the internal stresses and reduction of dislocation density. Consequently, tensile strength decreases, despite this reduction however the value of strength is more than the minimum acceptable value for the base metal.

The lowest ductility of sample F can be attributed to the widmanstätten morphology of the austenite and presence of secondary austenite in the HAZ and weld metal [91].

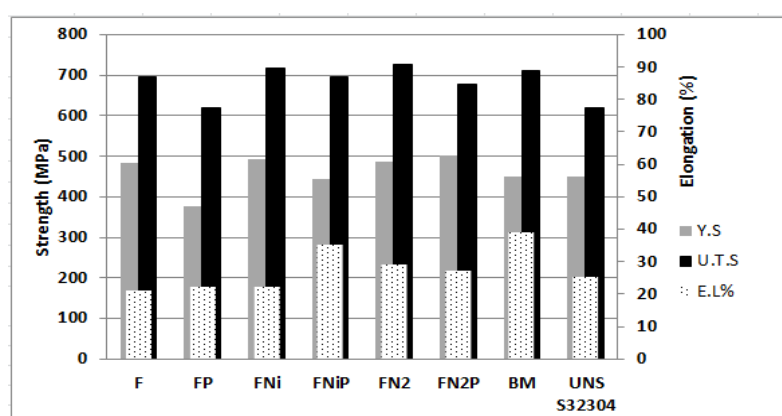
Fig. 2-24 indicates the bar chart results of tensile tests for easier comparison. By considering the result of microstructure analysis, phase determination and tensile tests, it can be said that, the effect of PWHT is mainly related to the improvement of microstructure in restoring equal percentages of the ferrite and austenite without significant changes in mechanical properties. For the sample F and FP the value of elongation was lower than minimum standard value.

For the sample FNiP, significant increase in elongation was observed, it is confirm the result of hardness tests, which showed decrease trend compares to the untreated sample. Based on different standards mainly two terms should be defined for evaluation of the tensile test results for offshore applications. First one is (Y.S/UTS) [240], this is an extremely important criteria, the greater the ratio, the smaller uniform plastic deformation before fracture. Then joint efficiency this can be defined based on UTS_{weld}/UTS_{base} ratio and a 95 % represents an acceptable result, this was obtained for all samples except FP.

Table. 2-8. Results of the tensile tests

Sample	Yield strength Y.S (MPa)	Tensile Strength U.T.S (MPa)	Elongation (%)	Y.S/U.T.S	Joint efficiency % (UTS_{weld}/UTS_{base})	Location of fracture
F	483	695	21	0.69	97	FZ ¹
FP	376	619	22	0.6	86	FZ
FNi	494	717	22	0.68	100	BM ²
FNiP	443	697	35	0.63	98	BM
FN2	486	728	29	0.66	100	BM
FN2P	503	679	27	0.74	95	HAZ ³
BM	451	712	39	0.63	-	BM

¹Fusion zone ²Base metal ³ Heat affected zone

**Fig. 2-24.** Results of tensile strength

It should be mentioned that, nickel is an effective element for solid solution strengthening; consequently it has high effect on increasing the yield and tensile strength compare with other elements [190]. The macro section of the tensile test samples after fracture are shown in Fig. 2-25. The side view macrographs of the fractured samples obtained by means of stereomicroscopy are reported in Fig. 2-26 Sample F and FP were broken in the fusion zone, while samples FNi and FNiP were broken in base metal. Macroscopically, the fracture is ductile with visible necking area in all samples. As is clear, sample F and FP were broken in the fusion zone, but samples FNi and FNiP were broken in base metal. This means that in most cases addition of nickel cause an improvement in tensile properties of the weld zone.

Most of the samples indicated ductile fracture with visible necking area in all samples. Both samples of FN2 and FN2P were fractured out of fusion zone with tensile strength of more than base metal. The maximum yield strength was obtained for the sample FN2P which shows appropriate mechanical properties of the joints after addition of nitrogen followed by PWHT.

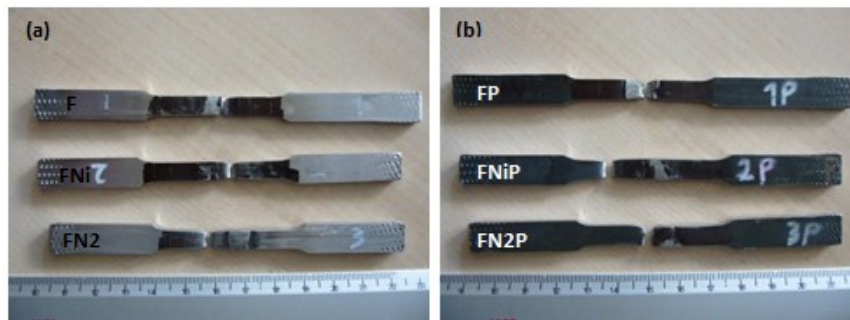


Fig. 2-25. Images of the tensile test samples (a) before and (b) after PWHT

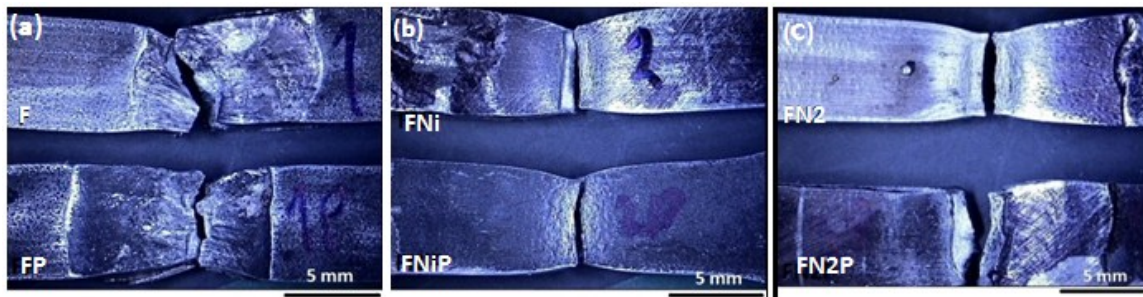


Fig. 2-26. Streammacrograph of the fracture surface of the samples (a) F, FP (b) FNi, FNiP (c) FN2, FN2P

Nitrogen has both positive and negative effects on the mechanical properties of welded duplex stainless steels. It has an effect on austenite to ferrite ratio, which can modify the microstructure and it causes the formation of nitride. It also has strengthening effect on both ferrite and austenite phases. Due to austenite stabilizing properties of this element, it tends to dissolve in the austenite phase. Consequently effect of interstitial solution strengthening by nitrogen is more evident in austenite compared to ferrite [183].

Generally, the yield strength of stainless steels increases with increased nitrogen content. This could be due to two mechanisms 1) Interaction between nitrogen as an interstitial element and dislocation motion and 2) Drag interaction between dislocations and nitrogen, with nitrogen carried along the dislocation as it moves in the lattice [242]. The low ductility of the samples, could be due to widmanstatten morphology of the austenite, presence of secondary austenite and precipitation of nitride phase [91].

Based on investigation of Pickering et al. [243], with increasing nitrogen content, the stacking fault energy of a stainless steel decreases. As a result, with addition of nitrogen the separation between two partial dislocations will be wider, consequently the dislocations to be confined to their slip plane and to form pile-ups. This causes increased rate of work hardening, tensile strength and uniform elongation.

2.2.7. Fracture surface analysis

To observe the fracture surface of the samples, stereomicroscopy and SEM investigation were performed. Fig. 2-27, depicts the top view macrograph of all fractured surfaces which were taken by stereomicroscope. The fracture surface of samples F and FP due to brake in fusion zone and HAZ, indicate very rough and unflat surfaces; while samples FNi and FNiP showed smooth fracture surfaces in base material where necking can be observed close to fracture area. These images also confirm ductile fracture nature of the samples [239]. The fracture surface analysis indicates that samples with lower elongation correspond to fully crack propagation in fusion zone or heat affected zones, while the higher elongation values are detected in samples which was broken in base metal.

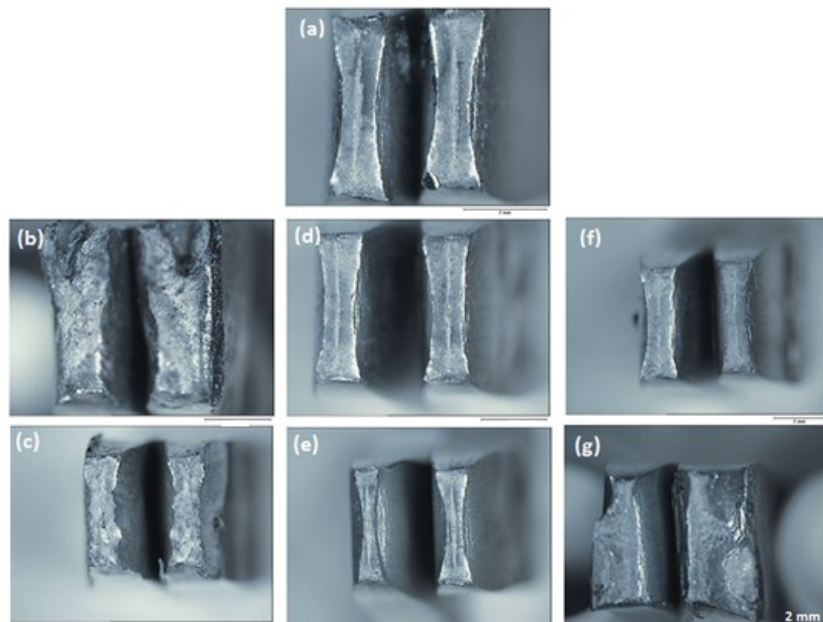


Fig. 2-27. Macrograph of fracture surfaces (a)BM (b)F (c)FP (d)FNi (e)FNiP (f)FN2 (g)FN2P

Fig. 2-28 to Fig. 2-34, indicate the fracture surface of all the tensile samples which obtained by means of scanning electron microscope (SEM). Overall, images show numerous dimple like pattern with different sizes which indicating a plastic deformation at the fracture surfaces. This indicates that major fracturing mechanism was ductile due to observation of many voids in specific orientation. When overload is the main cause of fracture, failure occurs by a process which known as micro coalescence voids (MCV).

The microvoids nucleate in the region of localized strain discontinuity, which mainly associated with second phase particles [244]. Fig. 2-28 indicates the fracture surface of the base metal, which contains lots of equiaxed deep and uniform dimples accompanied with microvoids; this means specimen fails in transgranular ductile manner under the action of tensile loading [245]. No indication of cluster and inclusions were observed which means high cleanliness of the base metal and weld zone.

In Fig. 2-29 which corresponds to the sample welded by using simply filler metal and broken from the weld metal, dimple size is larger than base metal and it can be said that, semi ductile fracture occurred Sample F, based on relatively smaller dimples in the fracture surface indicates higher ductile fracture, in sample FP however, the dimples became larger with heterogeneous size elongated in direction of tension. In addition ductile fracture mainly occurs around the pores.

Dimple shape is largely governed by stress inside the material which causes formation and coalescence of microvoids. Based on microstructure and plasticity of materials, dimples can be of deep conical shape or quite shallow and this may involve the joining of microvoids by shear along slip bands [246].

In sample FNi (Fig. 2-31) dimple size was smaller and less deep compared to sample F, which is in agreement with the obtained low results of elongation. The low ductility of these specimens should be attributed to Widmanstatten microstructure, presence of secondary austenite and precipitation of nitrides in heat affected zone. In sample FNiP (Fig. 2-32) after PWHT, dimple size was mostly reduced but some dimples increased significantly in size; this indicates in that area nucleation of the voids is more effective with respect to energy consumption than growth of microvoids and subsequent coalescence during crack propagation [247]. Generally, the nucleation sites and distribution of microvoids have an effect on the fracture surfaces appearance. Fig. 2-33 indicate the fracture surface of sample FN2 where dimple size is smaller than sample FNi and a higher percentage of separated voids is visible. Fracture surface of sample FN2P depicted in Fig. 2-34 broken in HAZ shows relatively larger dimples compared to sample FN2 and some voids are visible between the dimples; this is characteristic of ductile fracture. By comparing the fracture surfaces of the samples after PWHT, it can be concluded that the dimples mostly became deeper and wider as a result from of longer fracture path before final fracture.

Some authors [248,249], observe that crack initiation tends to occur in austenite phase, while propagation frequently occurs via transgranular cleavage of the ferrite phase. Cleavage facets belong to the ferrite phase and ductile failure occurs in the austenite phase. Micrographs of fracture surfaces with SEM shows crack propagation through base metal followed by weld metal of austenite and ferrite grains parallel to the surfaces. Sometimes this propagates transversely with sharper deformation of the austenite phase. Graziano et al. [250], observed the straight fracture profile, in case of crack propagate in fusion zone, which follows the dendrite grains.

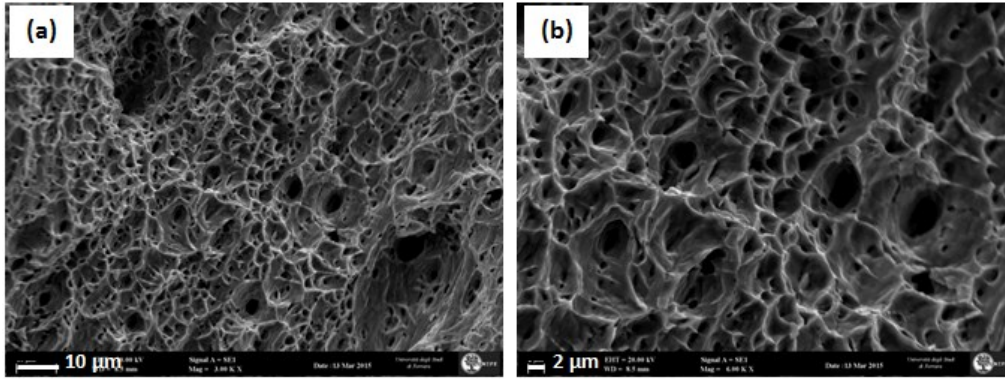


Fig. 2-28. Fracture surface of the base metal (BM)

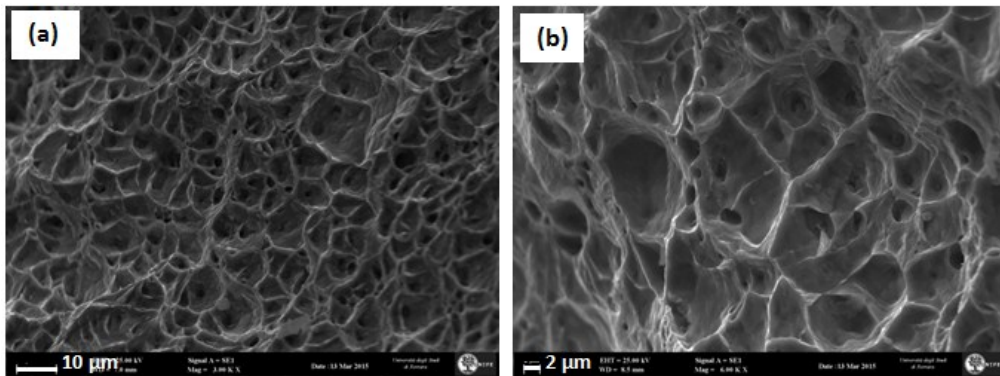


Fig. 2-29. Fracture surface of the sample F

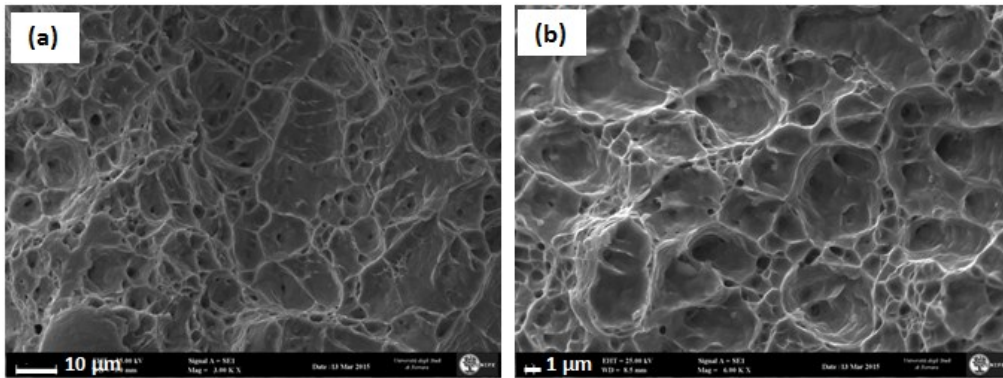


Fig. 2-30. Fracture surface of the sample FP

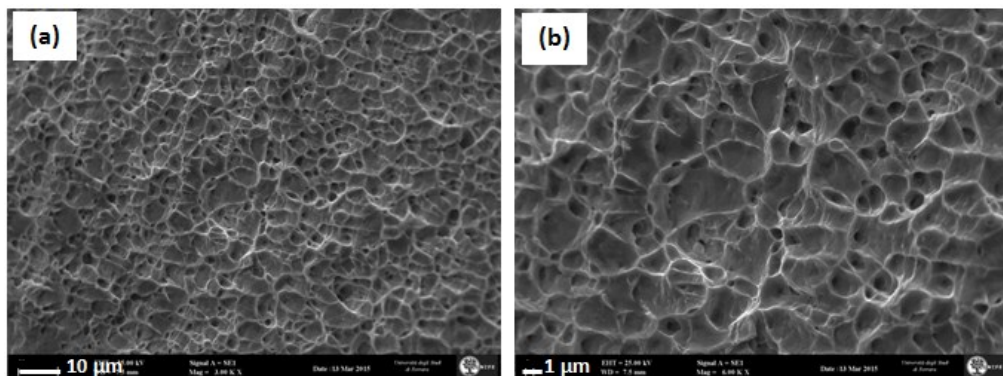


Fig. 2-31. Fracture surface of the sample FNi

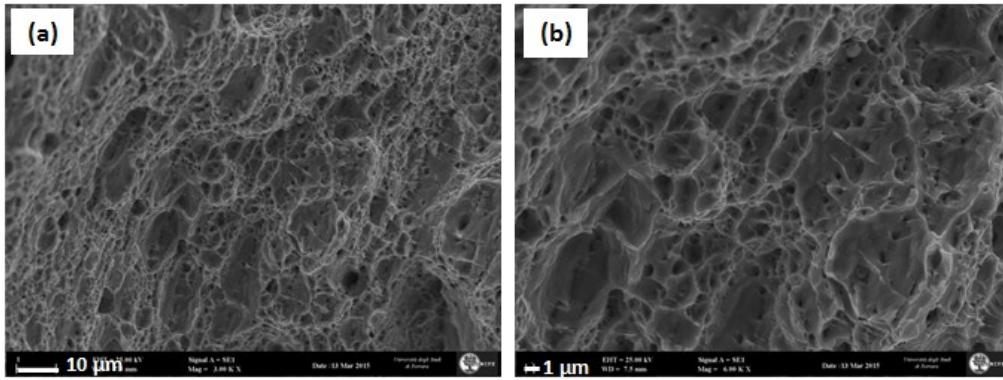


Fig. 2-32. Fracture surface of the sample FNiP

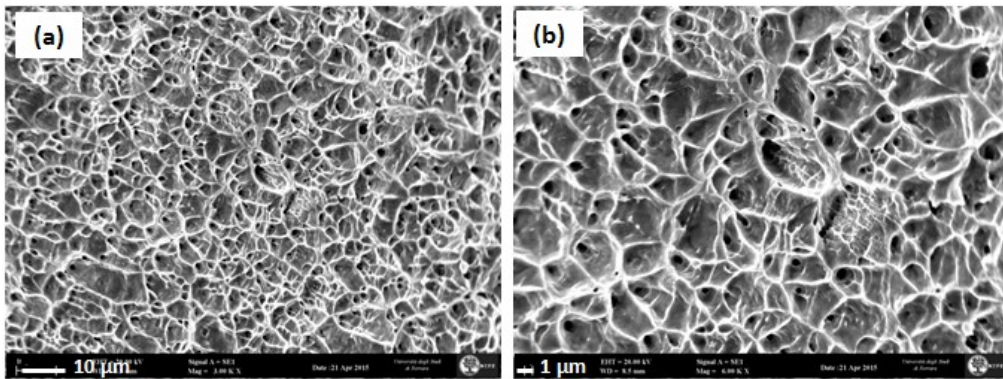


Fig. 2-33. Fracture surface of the sample FN2

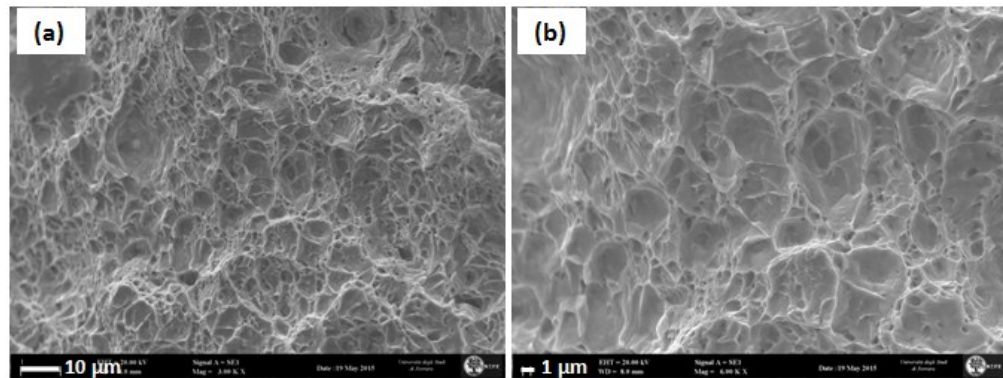


Fig. 2-34. Fracture surface of the sample FN2P

The non-uniform distribution of isolated microvoids early in the loading causes various dimples of different sizes to appear. Another reason for change in the fracture surface of all samples could be existing inhomogeneous plastic deformation due to changes in the microstructure of the fusion zone and HAZ. As can be seen from the images, the dimples are elongated through stress direction. In the center of dimples, pores and voids are visible, which act as a reduction of bearing capacity and cause failure of the specimen. No specific relation between crack initiation and existing voids was observed. It should be mentioned that the start point of failure is mainly governed by nucleation and growth of the voids. Coalescence and growth of the voids causes an increase of plastic deformation which leads to decreased capacity of the material to sustain the applied load up to failure.

EDS analysis was performed on the fracture surface of each sample (Table. 2-9) the results indicate there is not so much differences in chemical composition of the fractured surfaces, especially for the samples which were broken in base metal. Based on obtained data and calculation of R value (Cr_{eq}/Ni_{eq} for fracture surfaces), it can be said that fracture mainly occur in ferrite phase. Also, Jiang et al.[251] investigated on the effect of Cr_{eq}/Ni_{eq} ratio on the mechanical properties of the welded UNS S32304 duplex stainless steel. They found that it is an important parameter for microstructure of the weld joint. Lower ratio value, causes the formation of more austenite phase and phase balance.

Table. 2-9. Results of EDS analysis in fracture surface of the samples (wt%)

Element	Cr	Mn	Ni	Si	Mo	Fe	Cr_{eq}	Ni_{eq}	R (Cr_{eq}/Ni_{eq})
BM	23.60	1.61	5.18	0.66	0.53	Bal.	24.46	5.98	4.09
F	24.55	1.51	4.79	0.69	1.29	Bal.	26.18	5.54	4.72
FP	22.44	1.47	4.39	0.63	-	Bal.	23.38	5.11	4.57
FNi	24.1	1.47	4.39	0.63	-	Bal.	25.04	5.11	4.9
FNiP	23.98	1.47	4.43	0.61	0.53	Bal.	24.89	5.16	4.82
FN2	24.42	1.5	4.3	0.58	0.45	Bal.	25.74	4.3	5.98
FN2P	25.25	1.69	3.82	0.46	0.37	Bal.	26.31	3.82	6.88

For formation of the cracks in duplex stainless steels, the following model in Fig. 2-35 is proposed by Zou et al. [252]. They specify that, interphase boundaries between austenite and ferrite is relatively weak, consequently mainly cracks initiated and grew between ferrite and different types of austenite interfaces. When the material includes interface boundaries which are weaker than matrix, most of the voids form in the fracture of the weld metal, this is determined by the nucleation of the voids. Also, Bhattacharya et al. [168], showed that in duplex steel, it is mostly austenite that is under tension and ferrite is under compression, consequently they found crack initiation starts in austenite phase.

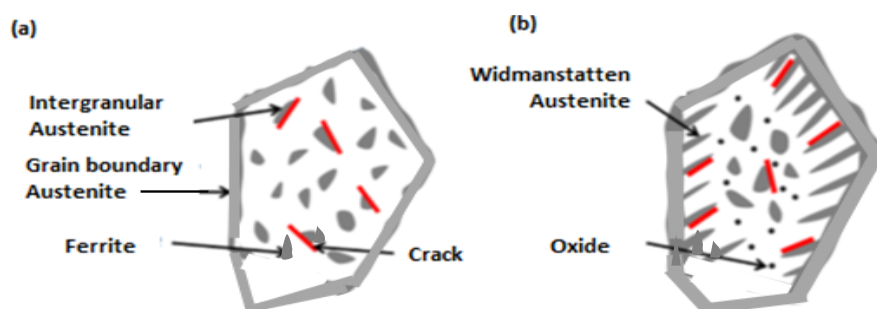


Fig. 2-35. Crack occurrence model in duplex steel [252]

2.3. Welding characteristics of super duplex stainless steels

2.3.1. Materials and welding procedure for super duplex

In addition to what has been said about the welding of duplex stainless steel (UNS S32304) samples, in this part of the study the same welding conditions are applied to improve welding quality of the superduplex stainless steel (UNS S32570) with 2mm thickness. For this material -duplex steel, ER2209 was considered as filler material. The chemical composition of the sheet plates and filler metal is listed in Table. 2-10.

Table. 2-10. Chemical composition of base metal and filler metal (wt%)

	C	Cr	Ni	Mo	Mn	Si	Cu	N	Fe
UNS S32570	<0.03	24-26	6-8	3.5-4.5	<1.2	<0.8	<0.5	0.24-0.32	Bal.
UNS S32570B.M	0.018	25.08	6.88	3.82	0.84	0.26	0.17	0.294	Bal.
ER 2209 Filler	0.01	22.8	8-9	3.1	1.6	-	-	-	Bal.

The welding conditions for the sample UNS S32570 were considered in exactly the same way as sample UNS S32304. The welding conditions and name of the samples is listed in Table. 2-11. Due to the importance of heat input for welding superduplex stainless steels, many tests were performed to find optimum welding parameters. Table. 2-12, depicts the welding parameters which were applied for all conditions. Fig. 2-36 shows the schematic figure of the joint before welding. To observe the shape of weld surface, Fig. 2-37 indicates two images of the plates after welding.

Table. 2-11. Name of the sample and welding conditions

UNS S32570	Welding conditions
SF	Filler metal ER2209
SFP	Filler metal , PWHT
SFNi	Filler, adding Nickel powder
SFNiP	Filler, adding Nickel powder, PWHT
SFN2	Filler, using mix Argon and Nitrogen gas
SFN2P	Filler, using mix Argon and Nitrogen gas, PWHT

Table. 2-12. Welding parameters for the sample UNS S32750

Sample	Current (A)	Voltage (V)	Travel speed (mm/min)	Filler metal	Heat input (kJ/mm)	Shielding gas	Shielding gas (L/min)
UNS S32570	50	12-15	50-70	ER 2209	0.7	Ar 99.99%	10-12

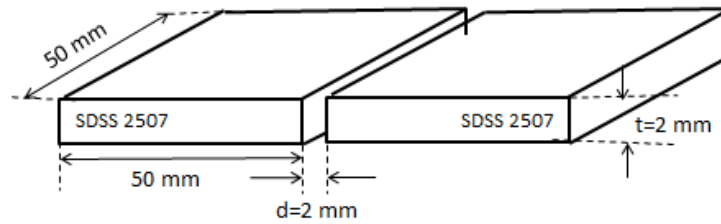


Fig. 2-36. Schematic figure of joint design for welding of superduplex

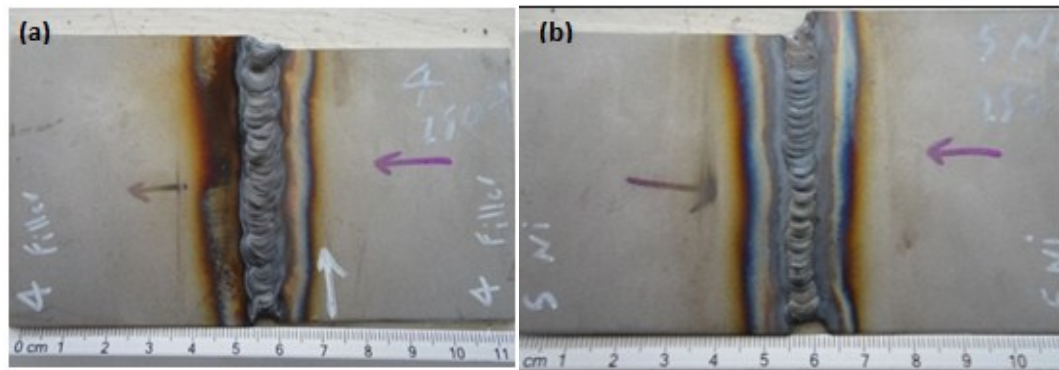


Fig. 2-37. Macro image of welded samples in different conditions (a) filler metal (b) addition of nickel

Sample preparation

Cross section of each weld joint was cut and prepared by means of normal metallurgy procedure (emery paper 400 to 1200 grit followed by 3 micron alumina polishing). The macrograph cross section of one weld profile and microstructure of the base metal is shown in Fig. 2-38. For etching of the base metal, normal Beraha solution and for weld zone samples solution of 50ml H₂O- 50ml HCl- 1gr K₂S₂O₅ and 10gr NH₄F.HF was used. This indicates the microstructure of the base metal which consists of roughly equal percentage of ferrite and austenite.

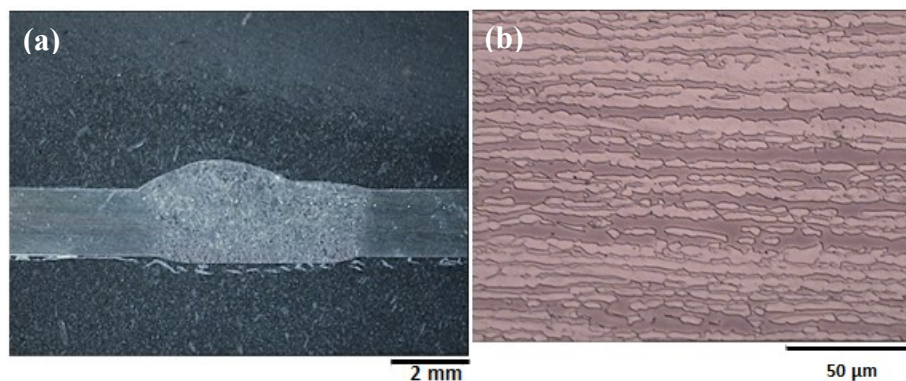


Fig. 2-38. (a) Cross section of welded joint and (b) microstructure of the base metal

Electrolytic etching

Due to high percentage of alloying elements in superduplex stainless steels, in addition to using chemical reagent, electrochemical etching was performed with power supply equipment model PS 305D using 40% NaOH electrolyte in 20 V for 15 s. In this method the cathode was a stainless steel rod and the sample is considered as anode. Fig. 2-39 indicates the set up for electrochemical etching.

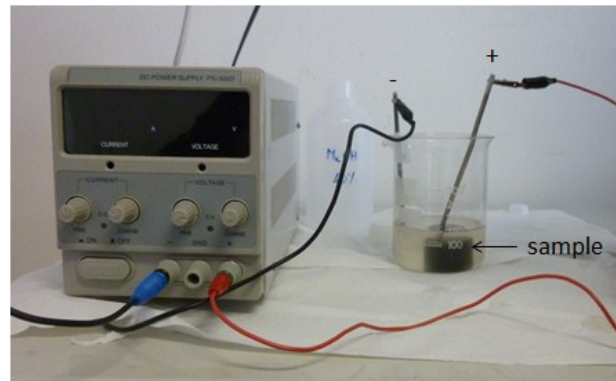


Fig. 2-39. Set up for electrochemical etching

2.3.2. Results and discussions

2.3.2.1. Microstructure evolution

For all the samples, microstructure investigation by means of optical microscope was performed. Fig. 2-40 shows the microstructure of the sample SF and SFP. In this sample in HAZ the microstructure is largely widmanstatten austenite with rough dendrite arm. After applying PWHT, the austenite lath became smoother and globular in shape. The amount of austenite decreased in this zone. In fusion zone of sample SF, again mostly widmanstatten austenite is visible but the percentage of austenite is slightly higher compared to HAZ. In fusion zone precipitation of secondary austenite was observed. This observation is in agreement with the results of Sadeghian et al.[195]. After PWHT, the microstructure of fusion zone austenite became more intergranular with round and circular shape with smooth grain boundaries.

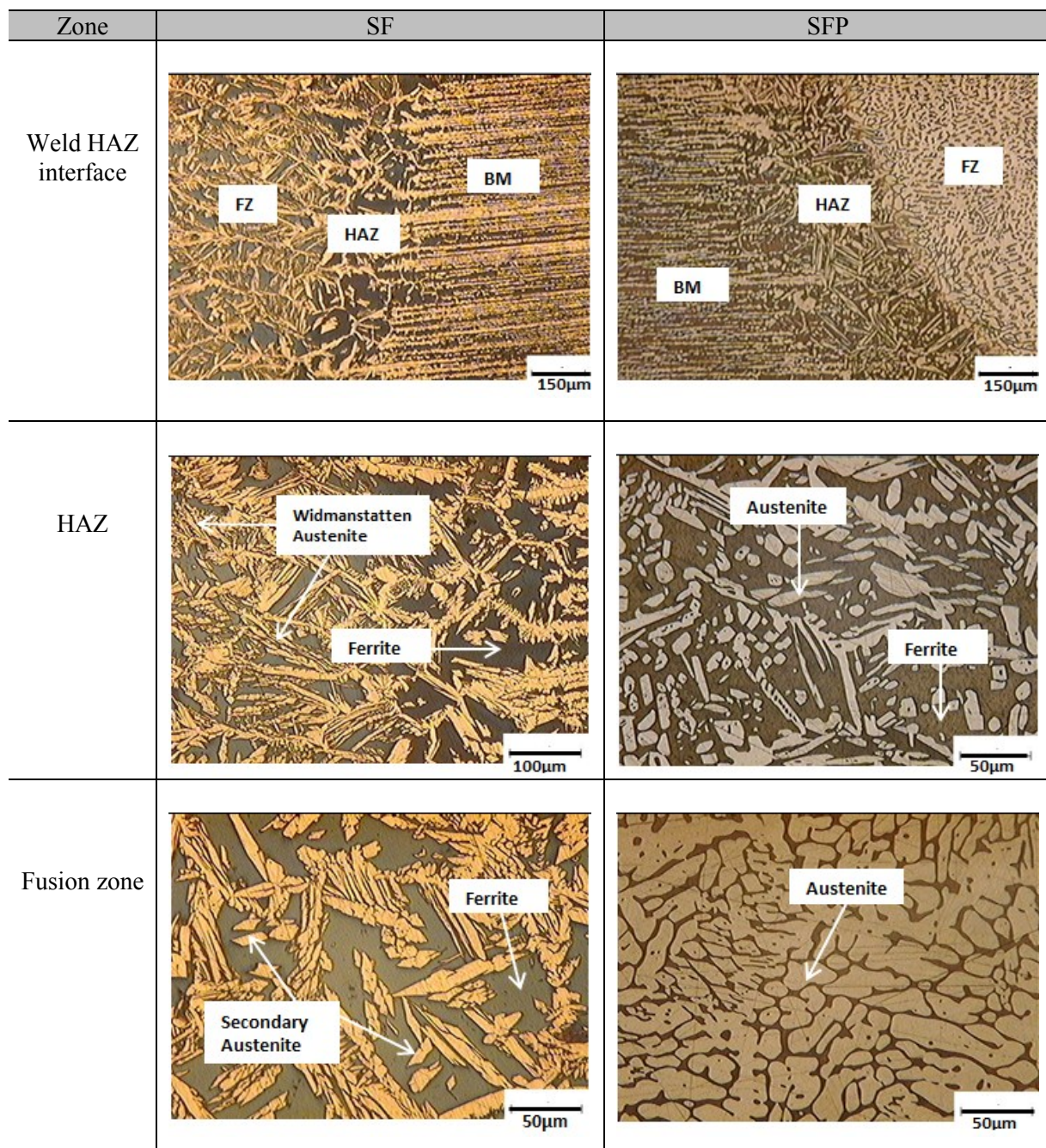


Fig. 2-40. Microstructure of weld zone in sample SF and SFP

For the sample welded with addition of nickel (SFNi) which is shown in Fig. 2-41 the microstructure of HAZ consists of mainly widmanstatten austenite and a small percentage of grain boundary austenite. After PWHT, this microstructure mostly converted to intergranular austenite. In the fusion zone, the microstructure mainly consists of intergranular and widmanstatten austenite, after PWHT few changes occurred, those mostly related to the increase in size of austenite lath. Also in this sample, precipitation of secondary austenite is visible.

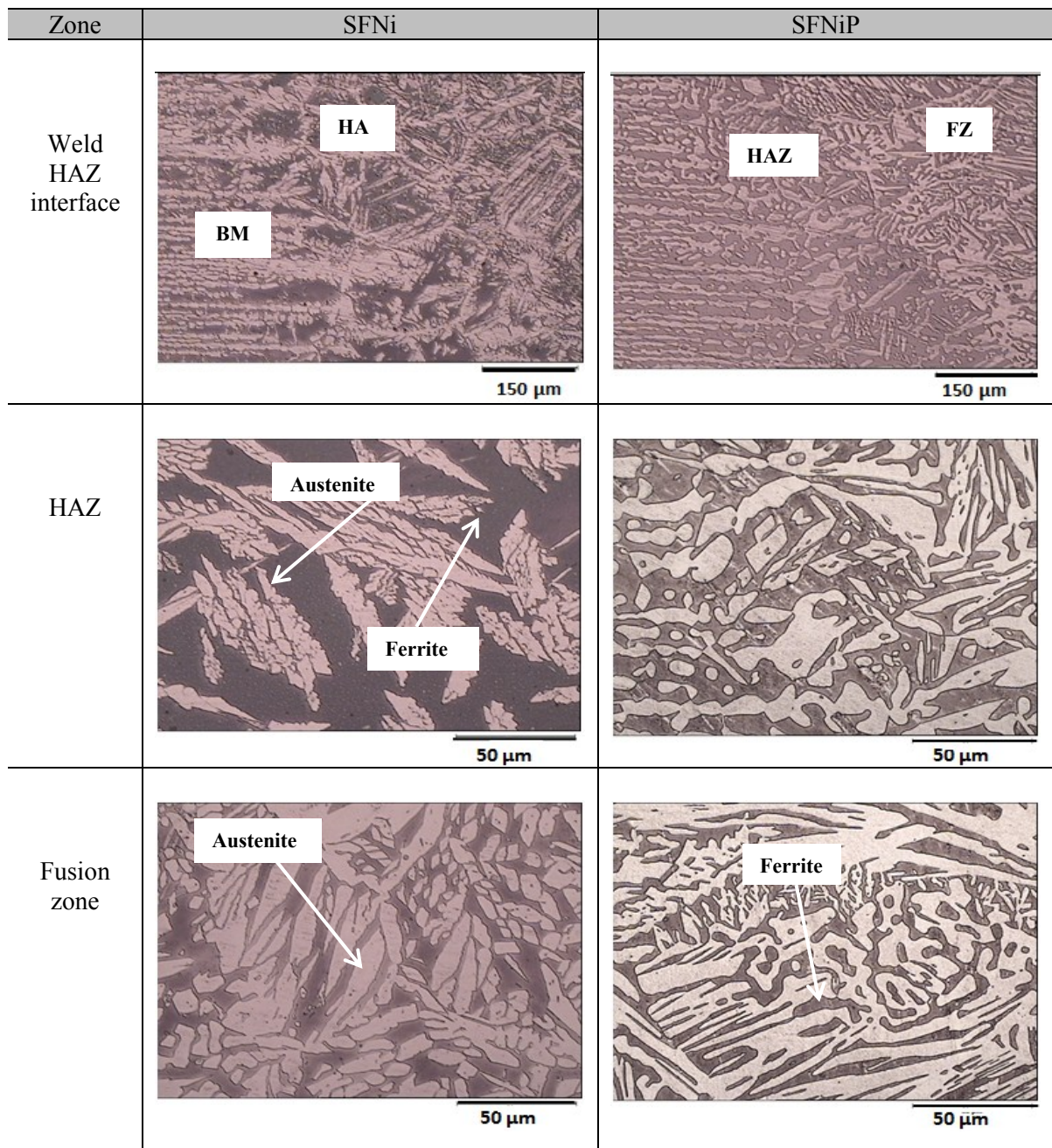


Fig. 2-41. Microstructure of weld zone in sample SFNi and SFNiP etched by reagent

Fig. 2-42 depicts the microstructure of the sample after addition of nitrogen gas. As we can clearly see, the microstructure of HAZ consists of intergranular austenite islands which are distributed in ferrite matrix. After PWHT, the microstructure mostly remains unchanged while the size of austenite lathes and globularity increase which is due to solution annealing at high temperature. In fusion zone of this sample, due to the presence of so much nitrogen as a strong austenite stabilizer, the microstructure includes complete austenite and only a few small ferrite islands remain in the microstructure. After PWHT, no specific changes in microstructure are observed.

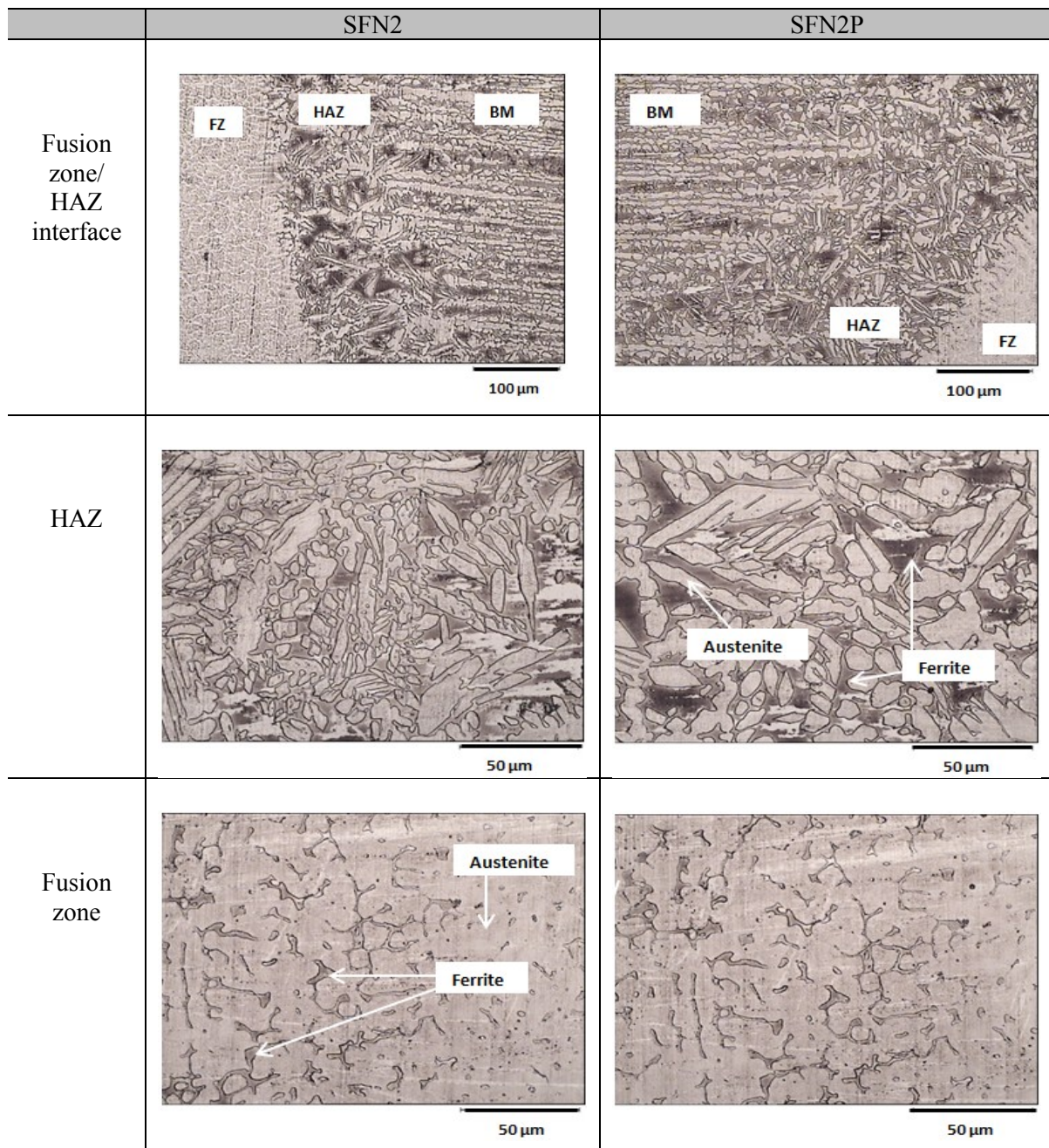


Fig. 2-42. Microstructure of weld zone in sample SFN2 and SFN2P etched by reagent

Due to the high percentage of alloying elements such as nickel and nitrogen inside the microstructure, etching by chemical reagent was not successful. For better observation, electrochemical etching was performed on these samples. The microstructure of HAZ and fusion zone after electrochemical etching is shown for samples SFNi and SFN2 are shown in Fig. 2-43 and Fig. 2-44 respectively.

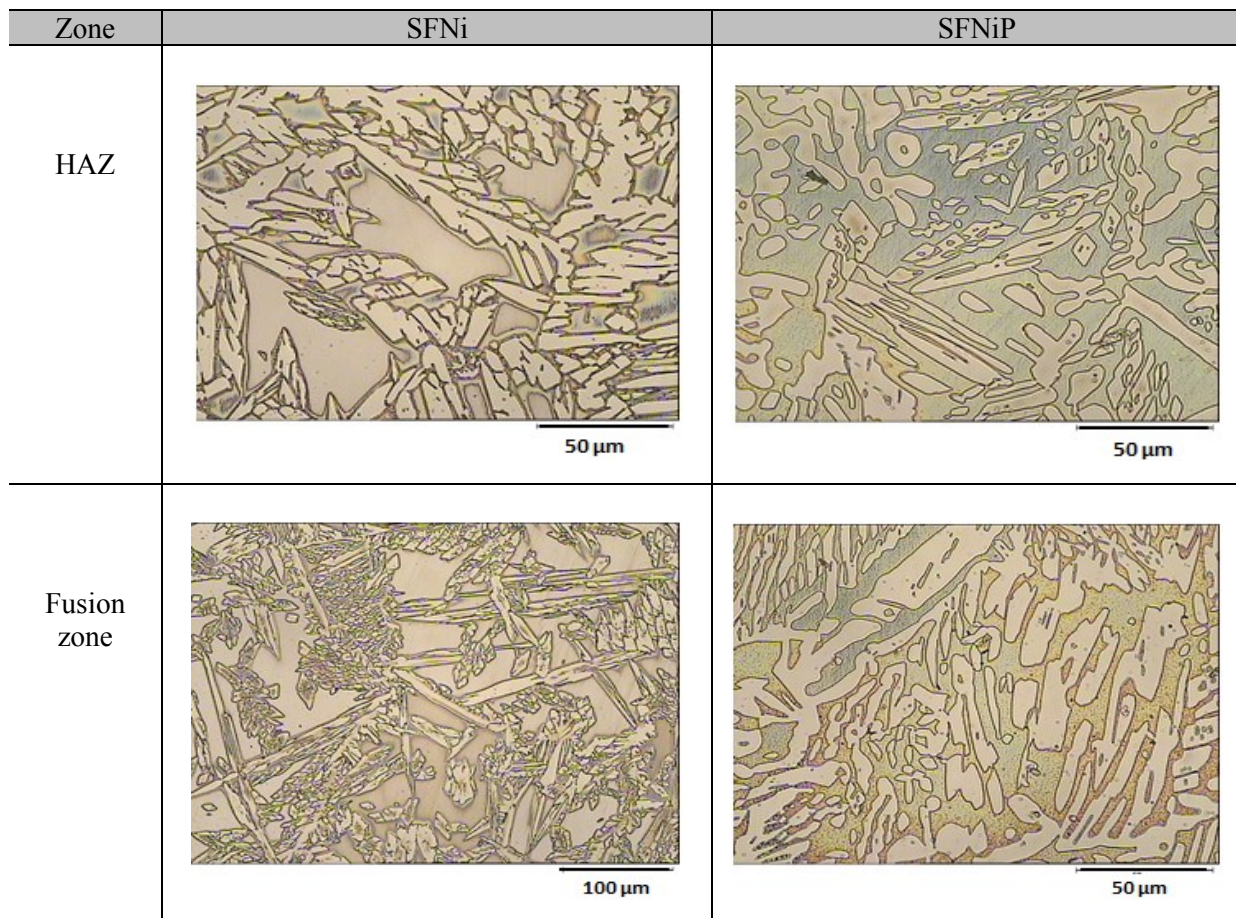


Fig. 2-43. Microstructure of weld zone in sample SFNi and SFNiP etched by electrolytic etching

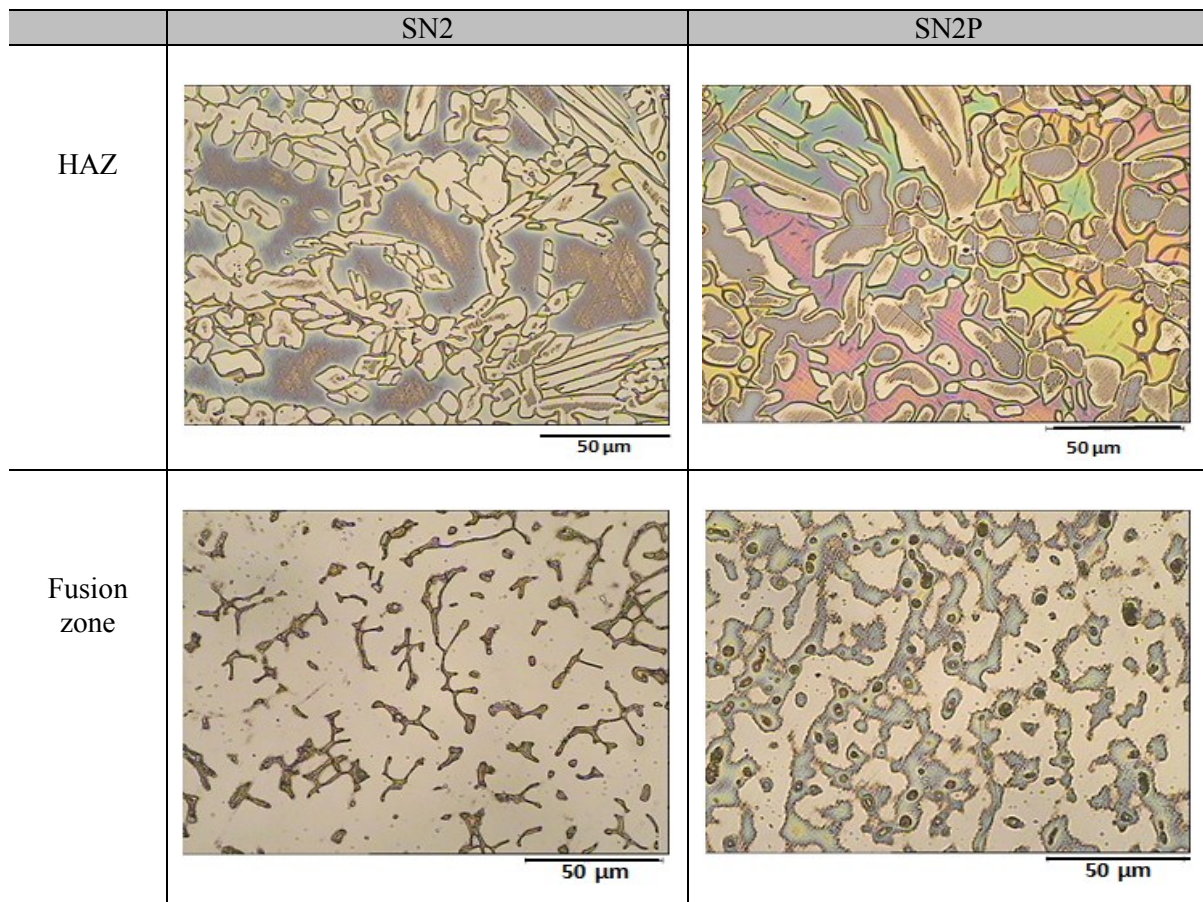


Fig. 2-44. Microstructure of weld zone in sample SFN2 and SFN2P etched by electrolytic etching

2.3.2.2. Phase measurement based on standard ASTM E562

For phase percentage measurement of the sample UNS S32570, instead of using image analyzer software, the standard ASTM E562 [119] which is based on manual count points measurement was used. For the measurement, as a guideline, magnification should be based on the initial determination of the sample areas to be tested. Micrographs with magnifications of X400 or more are preferable. The number of points per sample area should be considered. In this method 25 grid points were considered on the transparent paper. The paper was put on the metallographic images and the number of points are inside the ferrite phase counted. If the point appeared on the grain boundary, it was considered as a half point.

$$\% \alpha = \frac{P_{\alpha} + \frac{P_{\alpha/\gamma}}{2}}{P_T}$$

Where

P_{α} is number of points inside of ferrite phase

$P_{\alpha/\gamma}$ is number of points in border of ferrite and austenite

P_T is total numbers

For each zone minimum five images was considered and finally medium of percentages was considered as ferrite percentage of the zone.

For considering the standard deviation for the measurements and confidence interval

$$95\% \text{ CI} = \frac{t \times S}{\sqrt{n}}$$

Where

n is the number of images which measured

t is obtained from one table in standard which for $n = 5$ is equal to 2.776

S is standard deviation and can be obtained from following formula

$$S = \left[\frac{1}{n-1} \sum_{i=1}^n [P_p(i) - P_p]^2 \right]^{1/2}$$

$$P_p = \frac{1}{n} \sum_{i=1}^n P_p(i)$$

The acceptable ferrite to austenite ratio and location should be taken into consideration in area measurements. However, the main standards have not provided any specific direction. It is recommended though that location should be evaluated and ferrite content should be evaluated in procedure qualification record Table. 2-13 indicates the phase measurement, obtained by manual point measurement.

Table. 2-13. Phase percentage of the phases obtained by manual measurement

Sample	Austenite	Ferrite
SF	64.9	35.1
SFP	64	36
SFNi	55.2	44.8
SFNiP	59.2	40.8
SFN2	68.8	31.2
SFN2P	58.4	41.6

2.3.2.3. Microhardness profiles

Typical vickers microhardness tests profile were performed through a line consisting of base metal heat affected zone and fusion zone. The hardness of base metal for all the samples was in the range of 280-300 HV. The results of hardness measurements are reported in Fig. 2-45, Fig. 2-46 and Fig. 2-47. For all the samples, decrease in hardness value in fusion zone was observed and it reach to the value between 260-280HV. The reason for drop of the microhardness in fusion zone could be due to using filler material with relatively less amount of alloying elements compare to base metal.

Likewise applying PWHT did not show any specific effects on changing the microhardness and this remained at approximately the same value through the microhardness line profile.

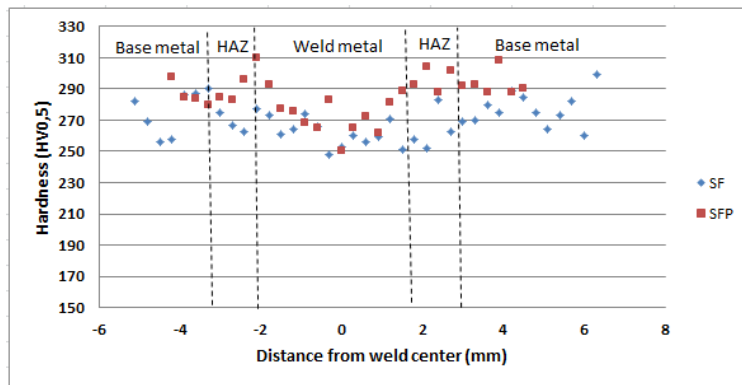


Fig. 2-45. Micro-hardness profile of sample SF and SFP

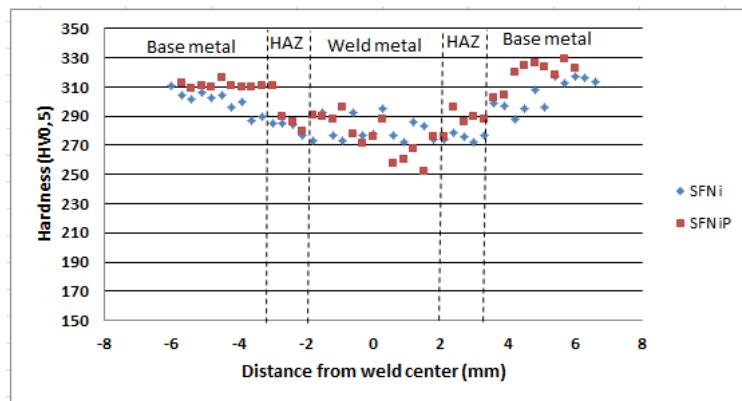


Fig. 2-46. Micro-hardness profile of sample SFNi and SFNiP

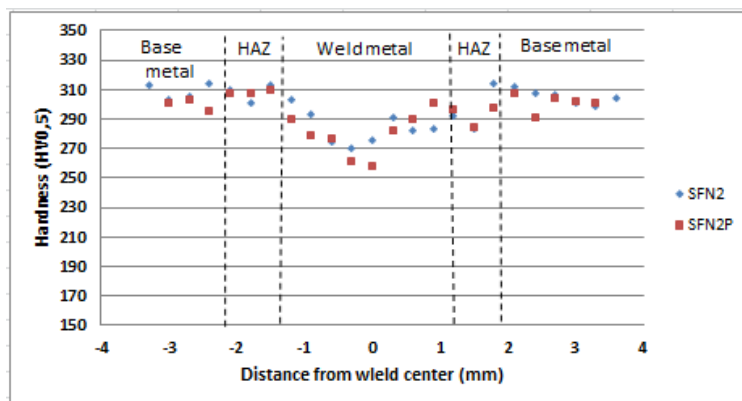


Fig. 2-47. Micro hardness profile of sample SFN2 and SFN2P

2.3.2.4. X-ray diffraction analysis

The same situation which was described in relation to the welded duplex stainless steel UNS S32304, was applied for XRD analysis of the welded superduplex UNS S32750 welded samples accompanied with base metal before and after heat treatment (see Fig. 2-48). Clearly no evidence of any intermetallic phases was observed or when observed show values of less than 5% which is lower than minimum detectable amount by XRD analysis. This was confirmed by the obtained results from metallography analysis. This means the quality of all the joints were appropriate and the welding parameters were selected appropriately. Just as for the sample with addition nickel powder after PWHT (SFNiP) one peak of nickel was detected which could be due to high amount of this element added as powder in the microstructure.

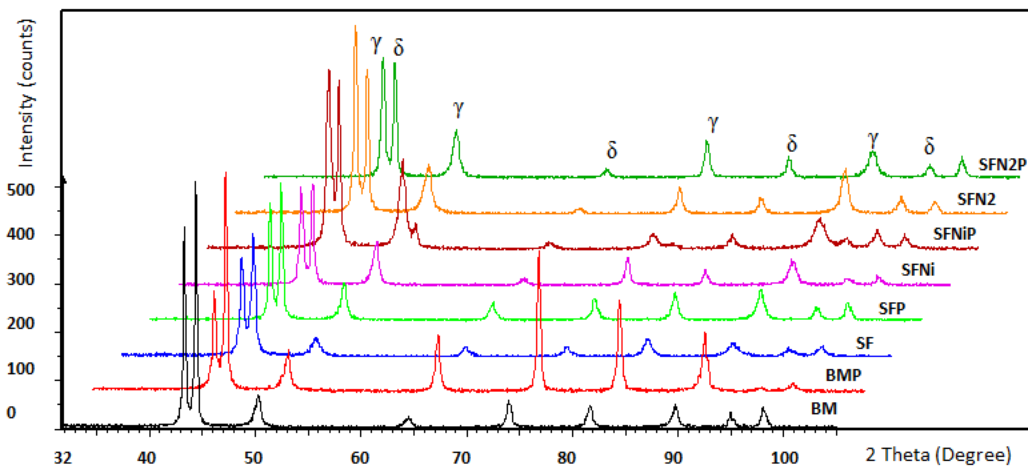


Fig. 2-48. XRD spectrums for all the samples

Based on obtained peaks from all welded samples, the phase percentage for each sample was calculated. Table. 2-14 indicates the result of phase percentage.

Table. 2-14. Phase percentage obtained from XRD result

Sample	Austenite	Ferrite
SF	45	55
SFP	54	46
SFNi	60	40
SFNiP	62	38
SFN2	64	36
SFN2P	60	40

2.3.2.5. Tensile test

The aim of tensile test is to evaluate the strength and plasticity of the joints and examine the influence of welding defects on weld quality. Normally the tensile strength of duplex stainless steel is roughly two times more than conventional austenitic stainless steels. This is due to the presence of some strengthening mechanisms such as substitutional and interstitial solid solution, presence of two phases and especially ferrite to increase the strength of the material.

Based on the size of the samples, the tensile test in sub-size dimension according to ASTM E8 was selected, the condition of preparation of the tensile test samples are equal to the sample UNS S32304 as previously explained. Table. 2-15 indicates the result of tensile test parameters (yield, tensile strength, elongation and location of fracture for all the samples). As is clear from the results, it can be concluded that, for samples SF and SFP the results of yield and tensile strength after welding is less than base metal but the value is more than what is specified in standard. For the samples with addition of nickel and nitrogen gas fracture occurred in HAZ, this could be due to existing alloying elements in the microstructure. In all cases after applying PWHT the value of the yield strength for the samples SF, SFNi and SFN2 decreased by 12, 10 and 8 % respectively. For sample SFP and SFN2P the value of elongation also increased.

Generally for all the samples, in addition to fracture in different zones, all the results produce more than minimum nominal value. Fig. 2-49 indicates the histogram for comparison of tensile test results for all the samples. With respect to the effect of nitrogen it could be the case that it causes a linear increase in yield strength and tensile strength of austenitic steel due to solid solution strengthening based on atomic size misfit of the solute atom with austenite crystal lattice. It has been reported that, amongst all interstitial elements nitrogen has more effect on yield strength [11,182].

Table. 2-15. Results of tensile test properties

Sample	Yield strength (MPa)	Tensile Strength (MPa)	Elongation (%)	YS/UTS	UTS _{weld} /UTS _{base}	Location of fracture
SF	619	888	24	0.69	0.95	F.Z
SFP	543	870	30	0.62	0.93	B.M
SFNi	570	927	26	0.62	0.98	HAZ
SFNiP	510	824	14	0.62	0.88	F.Z
SFN2	596	892	21	0.66	0.95	HAZ
SFN2P	548	844	28	0.64	0.89	B.M
S32570	744	938	28	0.79	-	-
	Min 550	Min 795	Min 15	0.69		

FZ: fusion zone, BM: base metal, HAZ: heat affected zone

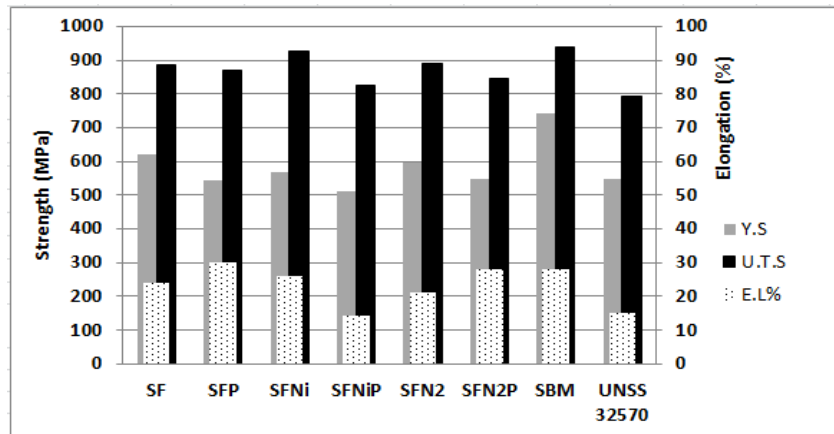


Fig. 2-49. Comparison between tensile test result of different samples

Considering the results, the phase balance between ferrite and austenite does not have so much effect on yield and tensile strength of the joints compared to base metal, while it affects ductility and corrosion resistance in a significant way. Fig. 2-50 and Fig. 2-51 depict the macro images of the samples after fracture and detail side view of fractured surfaces obtained from stereomicroscope respectively.



Fig. 2-50. Macro images of complete broken samples (a) SF, SFP (b) SFNi, SFNiP (c) SFN2, SFN2P

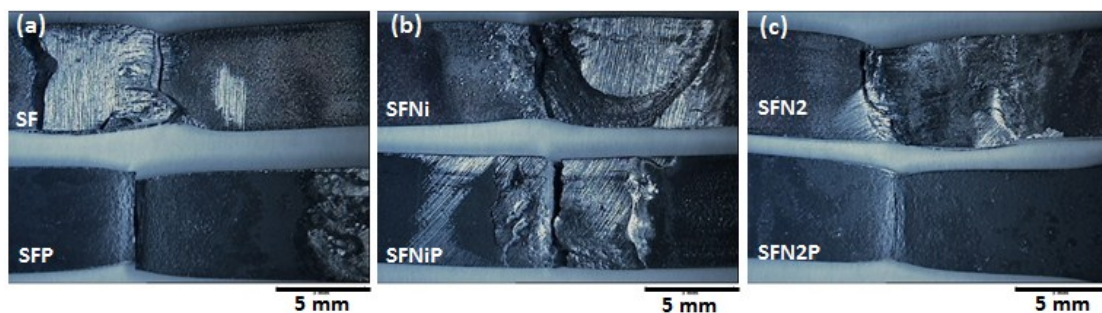


Fig. 2-51. Stereomicrograph side view of broken samples (a) SF, SFP (b) SFNi, SFNiP (c) SFN2, SFN2P

2.3.2.6. Fracture surface analysis

After tensile test and side view images of the samples, the fracture surface analysis from top view was performed first by stereomicroscope and scanning electron microscope (SEM). The images obtained from two methods of stereomicroscope and SEM are shown in Fig. 2-52 and Fig. 2-53 Sample SF which was broken in fusion zone indicates the rough fracture surface, but in this sample, after heat treatment which was broken in base metal, the surface is not so rough and necking is completely visible.

This situation occurs for sample FN2P which was broken in base metal. Fracture surface of sample FN2, which was broken from HAZ, also indicates very rough and inhomogeneous surface without any specific visible necking. This could be due to different microstructure in this zone. Also in sample SFNi, fractured in HAZ, a similar situation is present and the surface is completely rough and inhomogeneous. After applying PWHT on this sample, fracture occurred in fusion zone with a complete unsmooth surface.

Table. 2-16 indicates the EDS analysis of all fracture surfaces, as is clear in samples which are broken in base metal. For the sample SFNiP broken in fusion zone, due to addition of nickel in the joint high value, nickel is recognizable, but sample SFNi which was broken in HAZ indicates chemical composition close to the base metal. In addition, sample SFN2 which was broken in fusion zone shows little difference in chemical composition. Although this sample contains a higher percentage of nitrogen the obtained result of nitrogen from EDS analysis is not reliable and we cannot specify the exact composition for this sample. In addition, Cr_{eq} and Ni_{eq} for all the fracture surfaces were calculated. Based on consideration of pseudo binary diagram all samples were broken in ferrite phases except sample SFNiP which contained higher amounts of Ni and here fracture occurred in austenite phase.

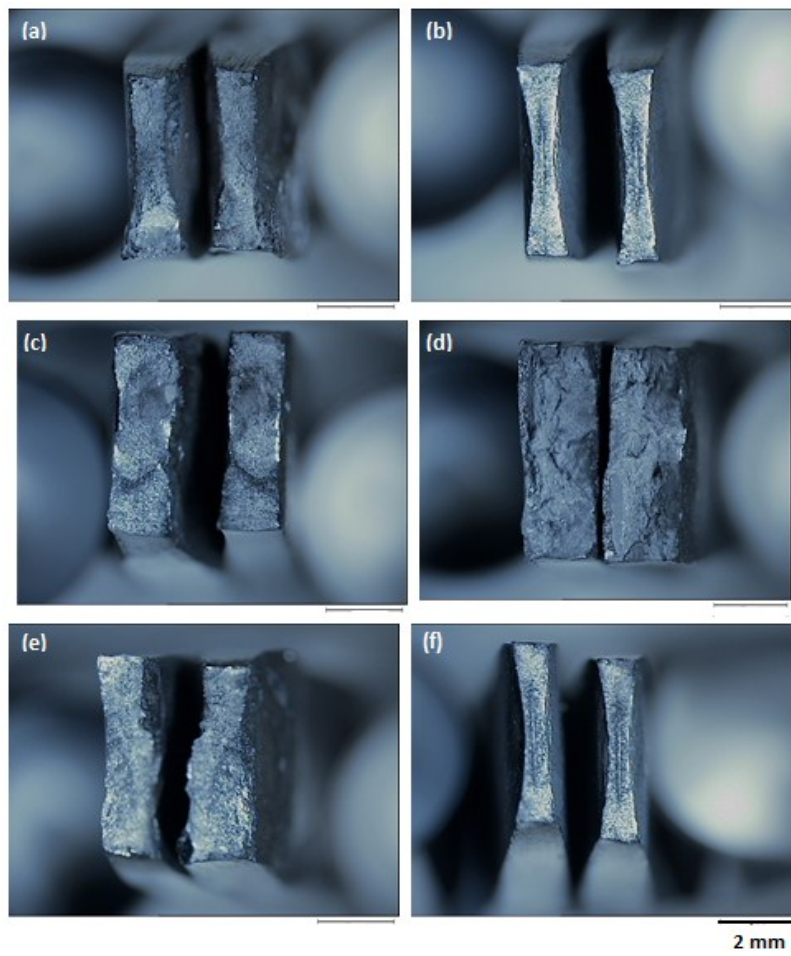


Fig. 2-52. Images of fracture surfaces (a) SF (b) SFP (c) SFNi (d) SFNiP (e) SFN2 (f) SFN2P

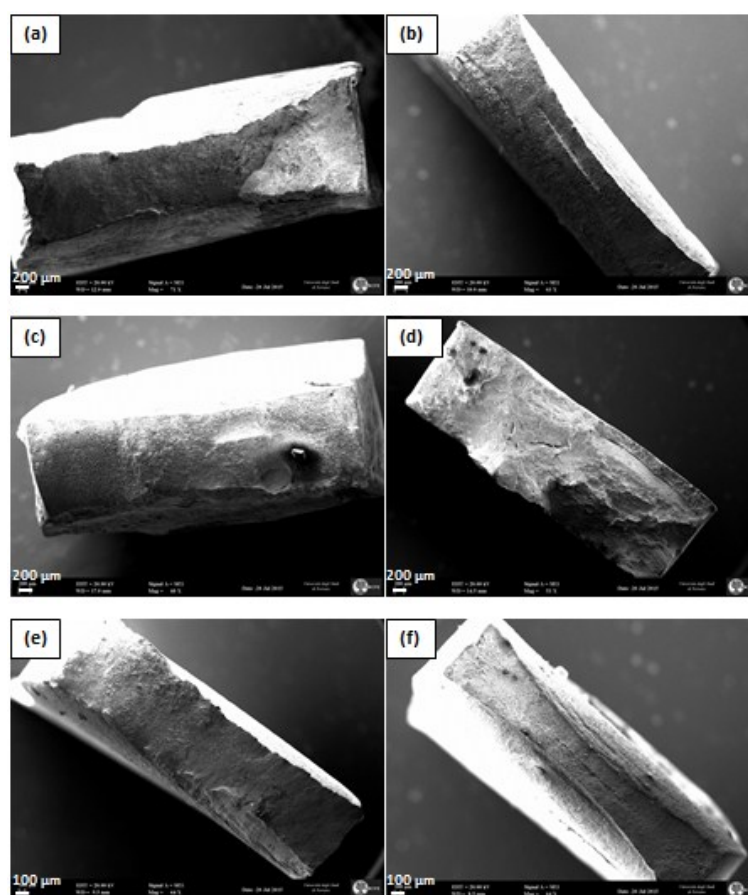


Fig. 2-53. SEM images of the fractured samples (a) SF (b) SFP (C) SFNi (d) SFNiP (e)SFN2 (f)SFN2P

Table. 2-16. Result of EDS analysis (wt%) on the fracture surfaces

Sample	Cr	Ni	Mo	Mn	Si	Fe	Cr _{eq}	Ni _{eq}	Cr _{eq} /Ni _{eq}	Location of fracture
SF	26.56	6.7	3.2	1.75	0.45	Bal.	30.43	7.57	4.02	FZ
SFP	26.8	6.31	4.8	1	0.36	Bal.	32.14	6.81	5.9	BM
SFNi	36.38	5.25	3.35	1.17	0.28	Bal.	40.15	5.83	6.88	HAZ
SFNiP	27.27	12.24	3.68	1.83	0.65	Bal.	31.92	13.15	2.35	FZ
SFN2	26.5	6.38	4.92	1.1	0.36	Bal.	31.96	6.93	4.6	HAZ
SFN2P	28.94	5.74	3.34	1.51	-	Bal.	32.28	6.49	4.97	BM

FZ: fusion zone, BM: base metal, HAZ: heat affected zone

Finally for in depth investigation of the fracture surfaces, SEM analysis with high magnification was performed. The results are shown from Fig. 2-54 to Fig. 2-59. As is clear for all the samples, dimples of different sizes are visible which means the majority of fractures are ductile, and plastic deformation occurred before fracture. When overload is the main cause of fracture, failure occurs by a process which is known as micro coalescence voids (MCV). The microvoids nucleate in the region of localized strain discontinuity, which are mainly associated with second phase particles. For sample SFP due to the effect of heat treatment the size of dimples increase and at the end of the holes, small voids are visible. The formation of this morphology could be due to fine austenite grain and smooth austenite/ferrite grain boundary [166].

The shape of dimples is mostly determined by stress inside of the materials which causes formation and coalescence of the microvoids. Based on microstructure and plasticity of the materials, dimples can be of deep conical shape or quite shallow and may involve the joining of microvoids by shear along slip bands. For the sample SFNi, due to fracture in HAZ, dimples are shallow and fracture surface became less ductile. For sample SFNiP, due to fracture in fusion zone, voids become interconnected and no proof of ductility was observed. This is in agreement with the result of elongation which is minimum compared to other samples. For sample SFN2 and SFN2P where fracture occurred in HAZ and base metal, no specific difference was detected. Also after heat treatment an increase in dimple size is visible, this could be due to high value of elongation.

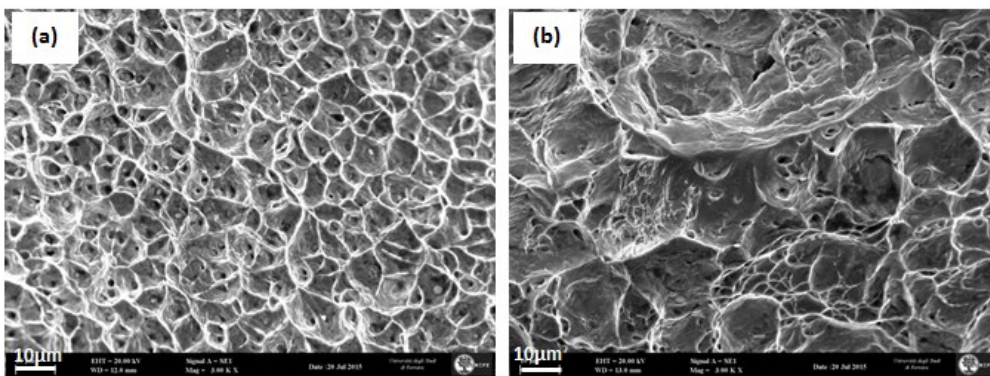


Fig. 2-54. Fracture surface of sample SF

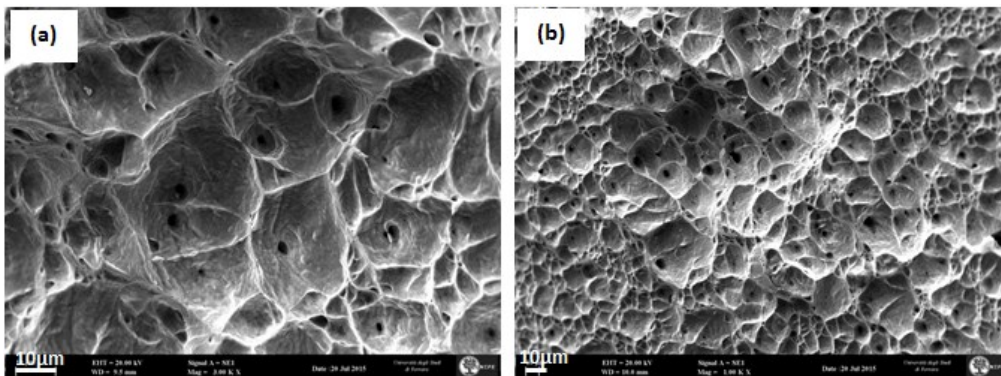


Fig. 2-55. Fracture surface of sample SFP

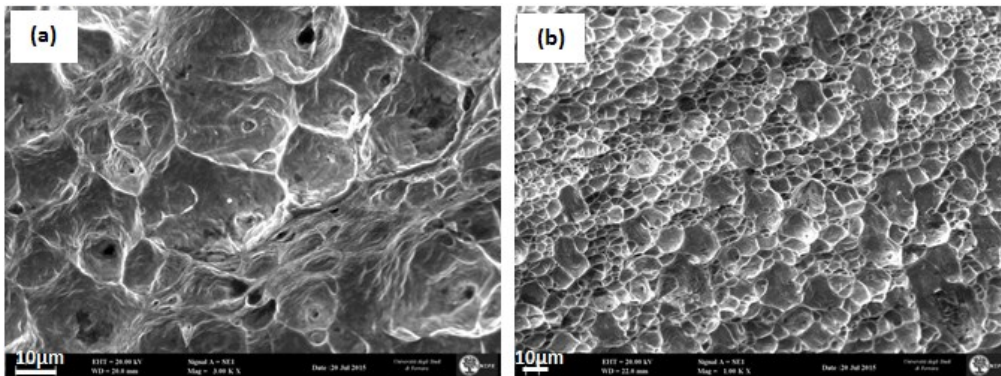


Fig. 2-56. Fracture surface of sample SFNi

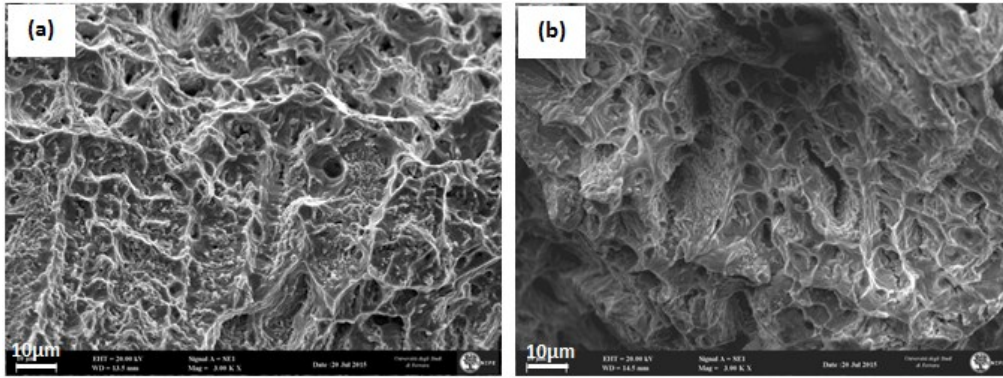


Fig. 2-57. Fracture surface of sample SFNiP

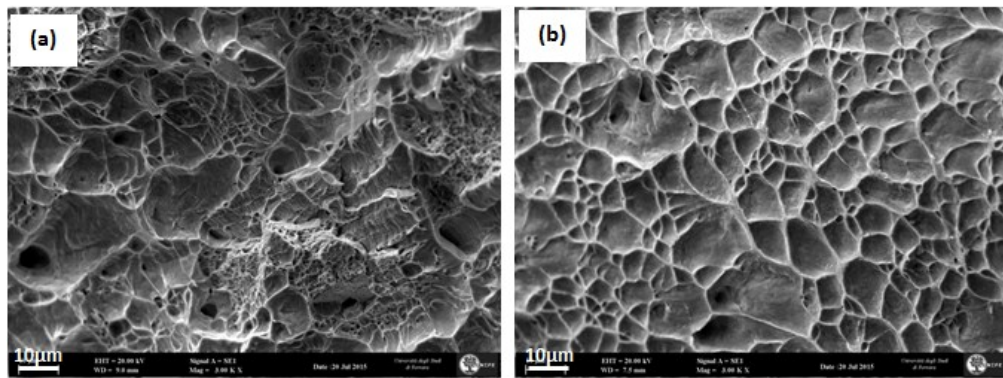


Fig. 2-58. Fracture surface of sample SFN2

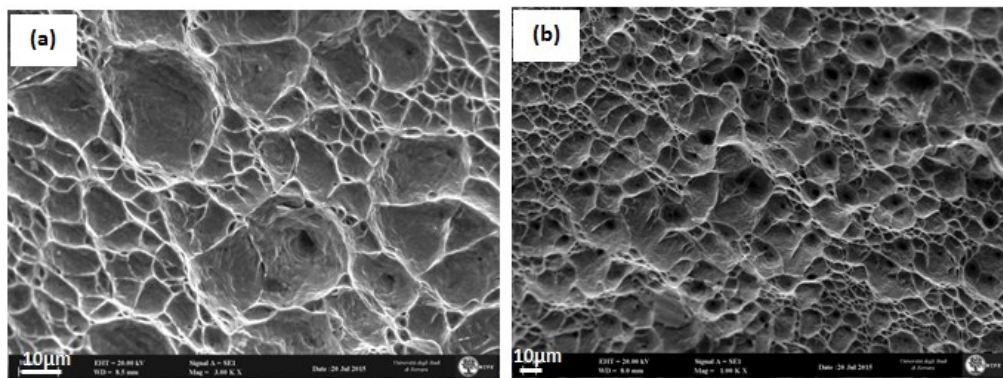


Fig. 2-59. Fracture surface of sample SFN2P

2.4. Conclusions

In this study, the effect of addition of nickel powder, nitrogen gas and applying post weld heat treatment (PWHT) on the microstructure and mechanical properties of the UNS S32304 lean duplex stainless steel and super duplex UNS S32570 welded by manual GTAW process was investigated. From the experimental results, the following conclusions for microstructure and mechanical properties of the duplex and super duplex welded joints can be drawn.

- Acceptable and sound weld can be achieved by using filler metal ER2209 to weld duplex stainless steel UNS S32304 with GTAW process. However, due to reduced quantities of nickel in this filler metal compared to super duplex stainless steel this is not highly recommended.
- Microstructure of welded joints in all conditions are grain boundary, intergranular and widmanstatten austenite with different percentages. In addition, formation of secondary austenite was observed.
- After welding, the percentages of ferrite and austenite in fusion zone are drastically changed. By applying short time PWHT at 1100 °C for 10 min, the amount of phases are restored to equal percentages of ferrite and austenite close to the base metal.
- In all the samples, no evidence of precipitation of intermetallic phase was observed and XRD results simply depict the presence of ferrite and austenite phases.
- Hardness profile of all welded samples using only filler metal before and after PWHT ,welded with addition of nitrogen is roughly the same. However the hardness value of the sample with added nickel powder after PWHT showed a slight decrease due to stress relieving and homogeneous distribution of the nickel element.
- The poorest behavior during tensile tests were obtained for the sample welded using only filler metal. This could be due to the presence of more austenite with Widmanstatten morphology and presence of secondary austenite. The low value of tensile test for the sample with addition of nitrogen before PWHT could be due to precipitation of nitride phase especially in heat affected zone; in all cases however , the tensile strength exceeds the required minimum value of the base metal.
- For the welding of superduplex stainless steels it is highly recommended to use filler metal with higher amount of alloying elements.
- Regarding all welding conditions, the sample with a combination of adding nickel powder followed by PWHT showed the optimum result for microstructure and restored the phases close to the base metal.

Chapter 3: Pitting corrosion resistance of welded duplex stainless steels after addition of alloying elements and PWHT

Abstract

In this chapter of the thesis, effect of addition of alloying elements such as nickel as a powder, nitrogen as a shielding gas and post weld heat treatment on pitting corrosion resistance of lean duplex stainless steel UNS S32304 welded by manual gas tungsten arc welding (GTAW) process in 3.5% NaCl solution was investigated. Post weld heat treatment (PWHT) in 1100 °C for 10 min was applied to all the as welded, welded by nickel powder and nitrogen gas. The microstructure evolution and mechanical properties of the samples was discussed in previous chapter. Here the pitting corrosion resistance of all the samples were evaluated by electrochemical measurement based on ASTM G48 standard. The pitting resistance equivalent number (PREN) was calculated for each ferrite and austenite phase separately in both HAZ and fusion zone. It was found that HAZ is more susceptible to pitting corrosion than the fusion zone. In fact all the pits were formed in HAZ. Also, all the pits initiated and propagated in ferrite phase. This fact is justified by lower PREN value of the ferrite phase. From the obtained results it can be concluded that the effect of PWHT is more than addition of alloying elements to improve the pitting corrosion resistance of the samples. For all conditions, the maximum pitting corrosion resistance was obtained for the sample after PWHT.

Keywords: Duplex stainless steel UNS S32304, GTAW, Pitting corrosion, Electrochemical test, PREN, Nickel, Nitrogen, PWHT.

3.1. Experimental procedure

3.1.1. Material and heat treatment

Duplex stainless steel UNS S32304 with dimension of 50mm× 50mm× 3mm was welded by gas tungsten arc welding (GTAW) process and using ER2209 filler metal (AWS A5.9). Table. 3-1. indicates the chemical compositions of the base (by means of quantometry) and filler materials (certificate of the producer). The value of pitting resistance equivalent number ($PREN = \%Cr + 3.3\%Mo + 16 \cdot 30\%N$) is also specified.

Table. 3-1. Chemical composition(wt%) of base and filler metal

Element wt%	C	Cr	Ni	Mo	Mn	Si	Cu	N	Fe	PREN
UNS S32304	0.02	23.47	5.05	0.36	1.37	0.48	0.31		Bal.	24.65
ER2209	0.01	22.8	8.5	3.1	1.6	0.4	0.16	0.16	Bal.	35.6

Three different welding conditions including welding, just by filler metal, addition of nickel powder and nitrogen gas were tested. To investigate the effect of heat treatment in each condition, the same PWHT procedure at 1100 °C for 10 min and followed by water quenching was applied. Moreover, as received base material and heat treated material were considered as a reference. In Table. 3-2, all the different conditions and name of the samples are summarized. General welding process specifications are shown in Table. 3-3.

Table. 3-2. Nomenclature of the samples

sample	Welding condition
BM	Base metal
BMP	Base metal after heat treatment
F	Filler metal, Argon gas
FP	PWHT on sample F
FNi	Filler metal, Argon gas, adding Nickel powder
FNiP	PWHT on sample FNi
FN2	Filler, using mix Argon and Nitrogen gas
FN2P	PWHT on sample FN2P

Table. 3-3. Welding procedure for all samples

Current (A)	Voltage (V)	Travel speed (mm/min)	Filler material	Heat input (kJ/mm)	Shielding gas	Gas flow (L/min)
80	12-15	50-70 (2-3 in/min)	ER 2209 Φ2.4 mm	1,14	Ar 99,99%	10-12

3.1.2. Microstructure analysis

The samples were characterized with both optical microscope (OM) and scanning electron microscopy (SEM). For the optical microscopy after conventional metallography preparation of the samples based on ASTM E 923A by grinding from 400 to 1200 grit followed by 6 to 3 micron polishing. reagent 50 ml H₂O, 50 ml HCl, 1 g K₂S₂O₅, 10 g NH₄F.HF was used. Due to unsuccessful investigation of etched sample with SEM, because of formation of oxide layer which cause to error especially for EDS analysis, and dissolving and losing some phases in grain boundaries and interphases due to etching. Consequently just the samples after polishing was used for SEM images and EDS analysis. In SEM-backscatter there is ability to differentiate between phases according to their mean atomic number without need of chemical etching. Also, due to high amount of heavy elements such as molybdenum the grey scale contrast can be observed between phases [38,44,52,79].

3.1.3. Sample preparation for the electrochemical test

The electrochemical tests were performed on specimens obtained from sheets of UNS S32304 in the correspondence of the welde zone (HAZ and fusion zone) and base metal. To prevent susceptibility to crevice corrosion, before the preparation of the electrodes, the coupons (10mm × 5mm × 3mm) were submerged into HNO₃ solution for 30 min at room temperature rinsed with deionized water, degreased with acetone and dried with hot air [116,222]. In order to make the electrical connection one side of the samples was connected to a covered copper wire [116,134].

Then the coupons were embedded in an epoxy resin (Epofix Struers) leaving a portion (0.3 mm²) of the transversal section of the welded area exposed to the test solution. The surface of the electrodes was ground down to 2500 grit emery papers, polished with diamond paste (from 6 to 1 μm), rinsed with deionized water and finally degreased with acetone. Pitting potential is determined as the potential at which the current density increases dramatically. The solution temperature could be varied between 30-50 °C. Fig. 3-1 indicate the procedure of cold mounting of the electrodes. To make cold mount combination of Epofix resin and hardener was poured into the die. For metallography and microstructural analysis Leica MEF4M optical microscope and Zeis EVO EMA 15 scanning electron microscope were used.

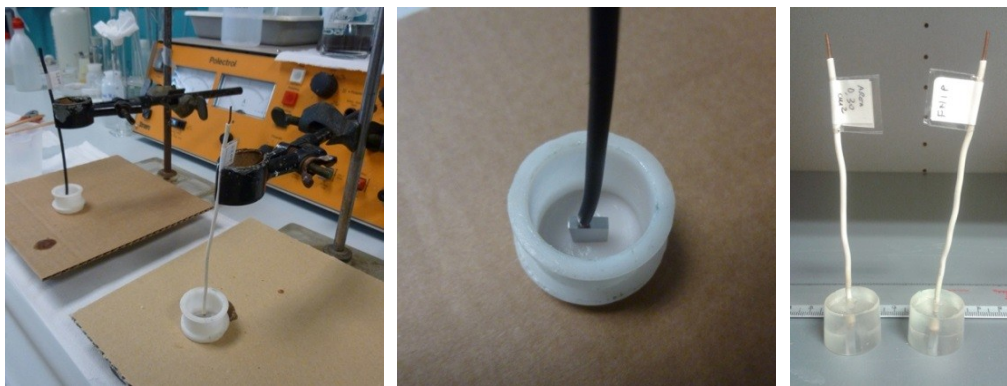


Fig. 3-1. Position of samples for cold mounting and final samples for the electrochemical test

3.1.4. Electrochemical test

The pitting potentials (E_{pit}) were determined by anodic polarization tests after 1 h immersion in 1 M NaCl solution at 20 °C, starting from a potential of -0.1 V vs. the open circuit potential (OCP) with a scan rate of 0.1 mV/s. The results were the average of triplicate tests. Fig. 3-2 indicates the schematic figure for the electrochemical test. Also, experimental set up of the test is shown in Fig.3-3. The electrochemical cell was made of a thermostatted glass vessel. A three electrode configuration was employed with the embedded specimen as working electrode and a saturated calomel electrode (SCE) used as the reference electrode.

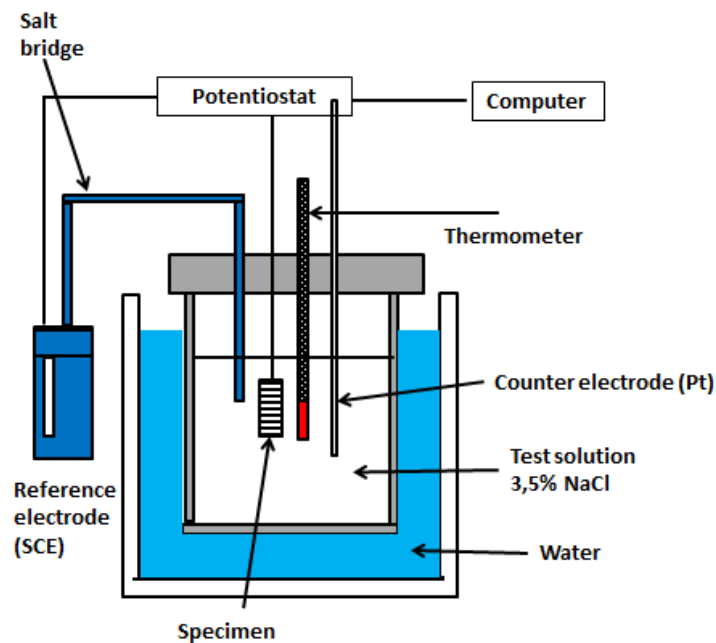


Fig. 3-2. Schematic experimental set up for electrochemical test

The pitting potentials (E_{pitt}) were determined by anodic polarization tests after 1h immersion in 0.6M(3.5%) NaCl solution at 30 °C, starting from a potential of -0.1 V vs. the open circuit potential (OCP) with a scan rate of 0.1 mV/s. The results were the average of triplicate tests. The pitting potential was determined as a potential where the current density continuously exceeded the $10 \mu\text{A}/\text{cm}^2$. After the tests, the electrodes surface was etched with Beraha's reagent and observed by optical microscope (OM).

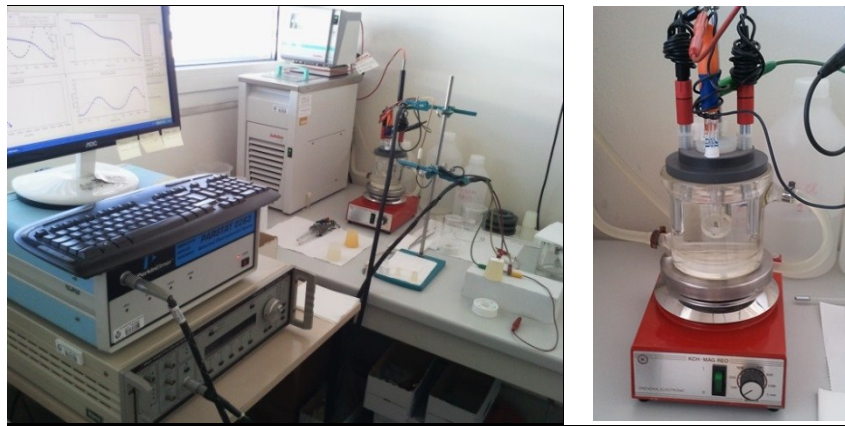


Fig.3-3. Experimental set up of electrochemical polarization cell

3.2. Results and discussions

3.2.1. Microstructure evolution

In the following micrographs (Fig. 3-4 to Fig. 3-9), the microstructure of fusion zone and heat affected zone of all the samples obtained from optical microscope (OM) and scanning electrode microscope (SEM) are shown. In sample F (Fig. 3-4 and Fig. 3-5) before PWHT, the microstructure of the HAZ for all the samples include grain boundary (GB) austenite, widmanstatten (WS) austenite which form on the grain boundary austenite and intergranular (IG) austenite. In addition, precipitation of secondary austenite in the matrix is visible. As specified in the following metallography images, mainly after PWHT, the value of austenite in HAZ increase and the morphology of the austenite become mainly intergranular in circular and smooth shape. HAZ of the sample FNi (Fig. 3-6 and Fig. 3-7) mainly consists of separated grain boundary and widmanstatten austenite which distributed in the ferrite matrix. After PWHT (Fig. 3-6 and Fig. 3-7) the amount of austenite increases and becomes more uniform distributed with curve shape boundaries. Fusion zone of the sample FNi (Fig. 3-6) consists of higher amount of coarse widmānstatten austenite and intergranular austenite, after PWHT microstructure mainly consists of intergranular austenite with smoother grains which distributed in the ferrite matrix.

The microstructure of HAZ in sample FN2 (Fig. 3-8 and Fig. 3-9) is close to the sample F and includes all grain boundary, intergranular and Widmanstätten austenite but the amount of intergranular and Widmanstätten austenite is more than sample F. After PWHT (Fig. 3-8 and Fig. 3-9), many intergranular austenite especially in fusion zone grows significantly, to reach roughly spheroidal shape which uniformly distributed in the matrix, this microstructure is agreed with the results of Zhang et al. [86].

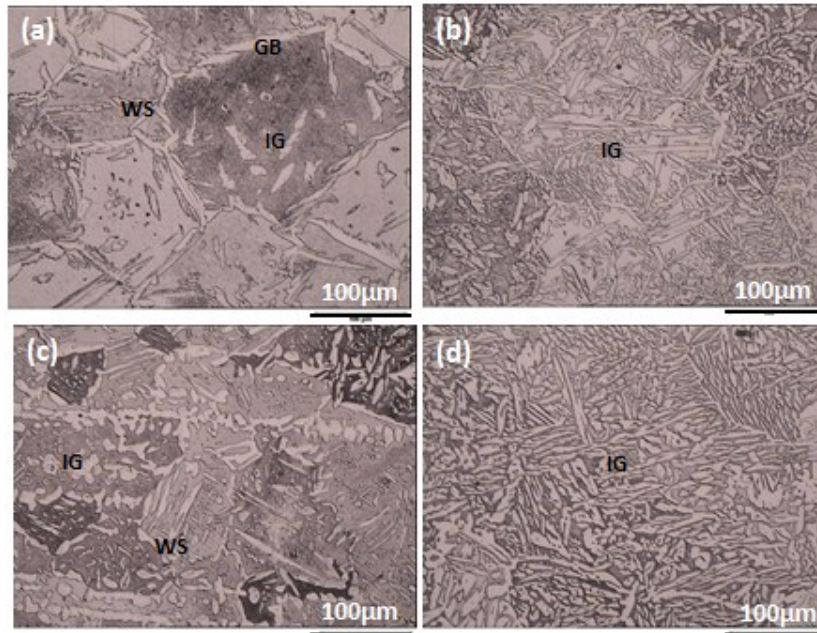


Fig. 3-4. Microstructure of sample F (a) HAZ (b) F.Z and FP (c) HAZ (d) F.Z

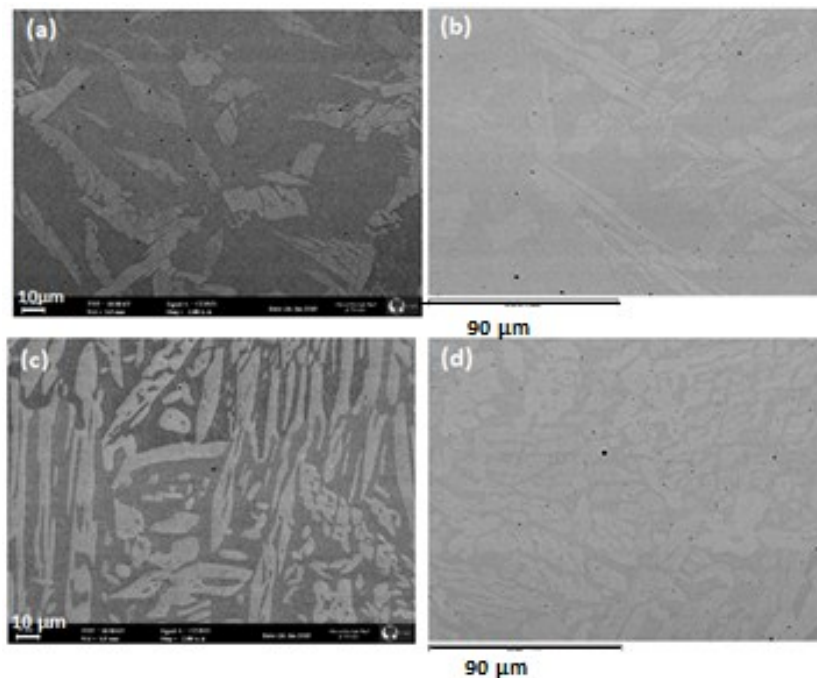


Fig. 3-5. SEM image of sample F (a) HAZ (b) F.Z and FP (c) HAZ (d) F.Z

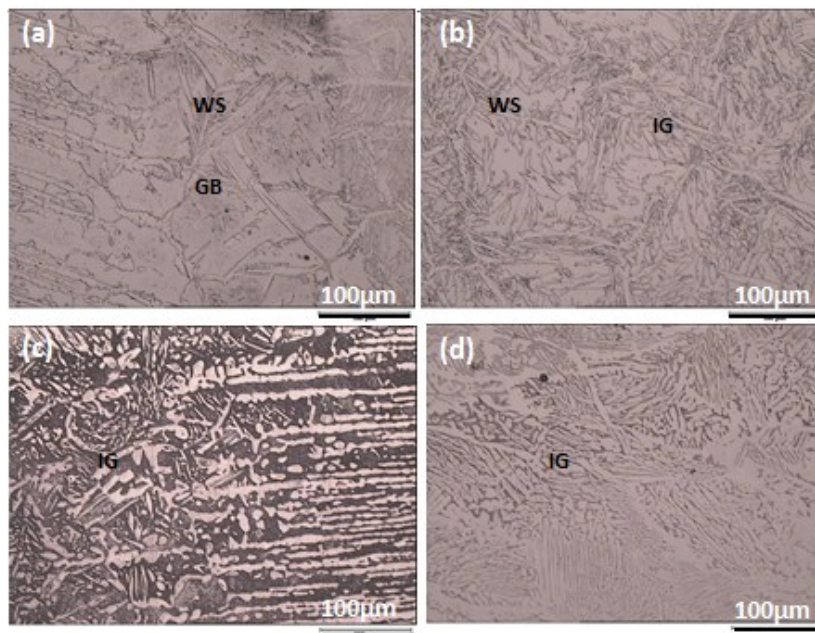


Fig. 3-6. Microstructure of sample FNi (a) HAZ (b) F.Z and FNiP (c) HAZ (d) F.Z

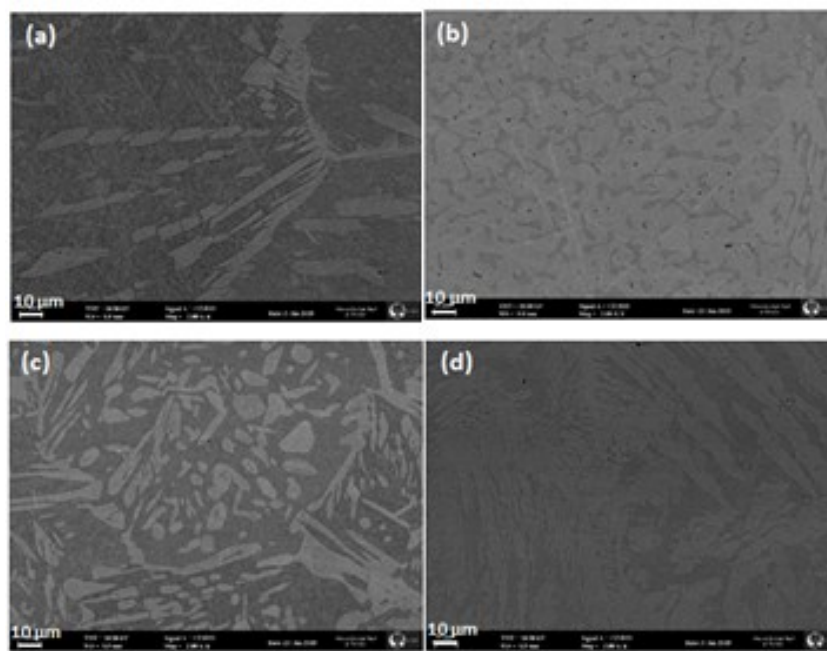


Fig. 3-7. SEM image of sample FNi (a) HAZ (b) F.Z and FNiP (c) HAZ (d) F.Z

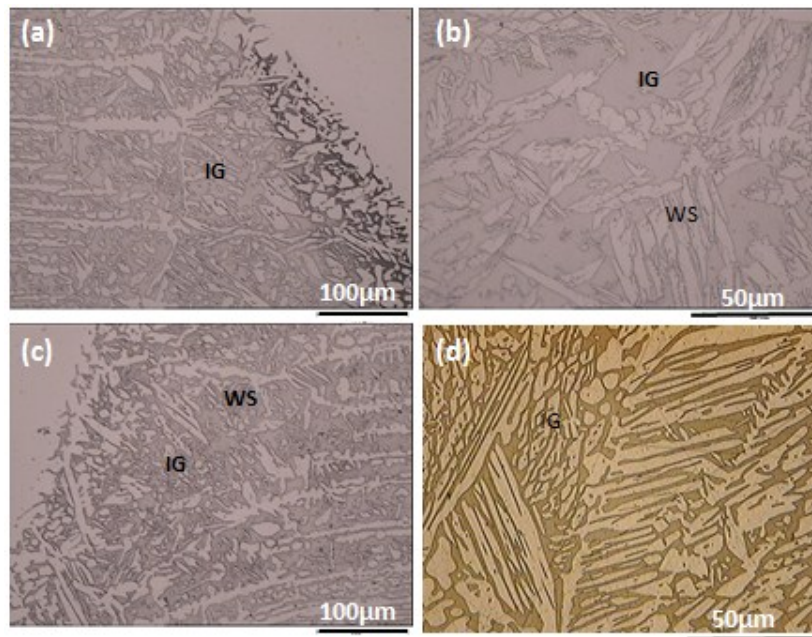


Fig. 3-8. Microstructure of sample FN2 (a) HAZ (b) F.Z and FN2P (c) HAZ (d) F.Z

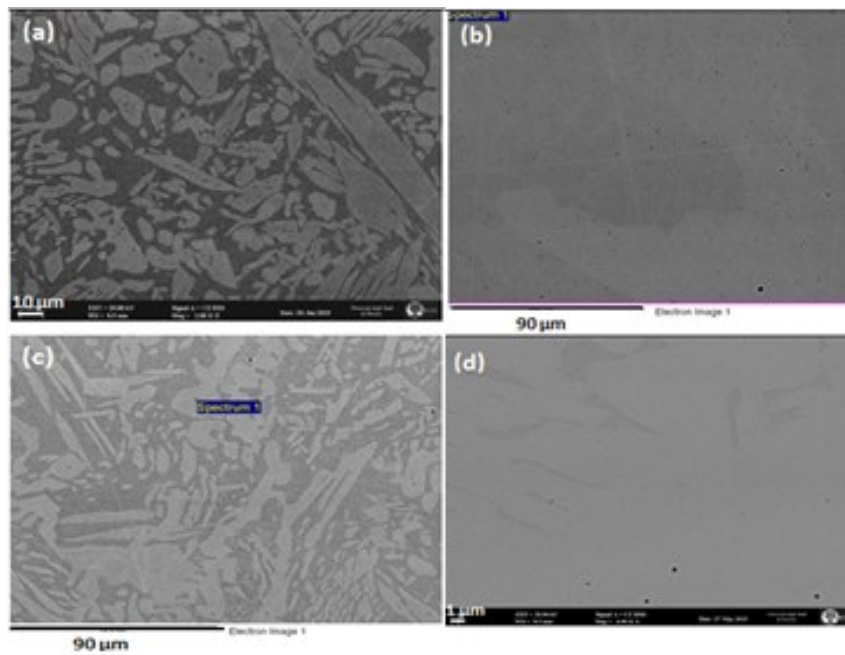


Fig. 3-9. SEM image of sample FN2 (a) HAZ (b) F.Z and FN2P (c) HAZ (d) FZ

Due to existing different types of austenite in various temperatures, intergranular austenite forms at lower temperatures and may have slightly lower nitrogen content when compared to the allotriomorph and widmanstatten which are form at higher temperatures. Consequently, weld metal with addition of nitrogen show higher corrosion resistance which could be due to promotion of higher amount of allotriomorph and widmanstatten austenite with higher nitrogen content [109].

For comparing the microstructure of the HAZ close to the fusion line, the image of whole area was taken by optical microscopy and the images attached to each other with commercial image software. The result for all the samples are shown in Fig. 3-10 to Fig. 3-12. For all the samples, microstructure of HAZ before PWHT consist of grain boundary and widmanstatten austenite, which are distributed in ferrite matrix. After PWHT, mainly microstructure become intergranular austenite and the relevant amount increase compare with the condition of before heat treatment.

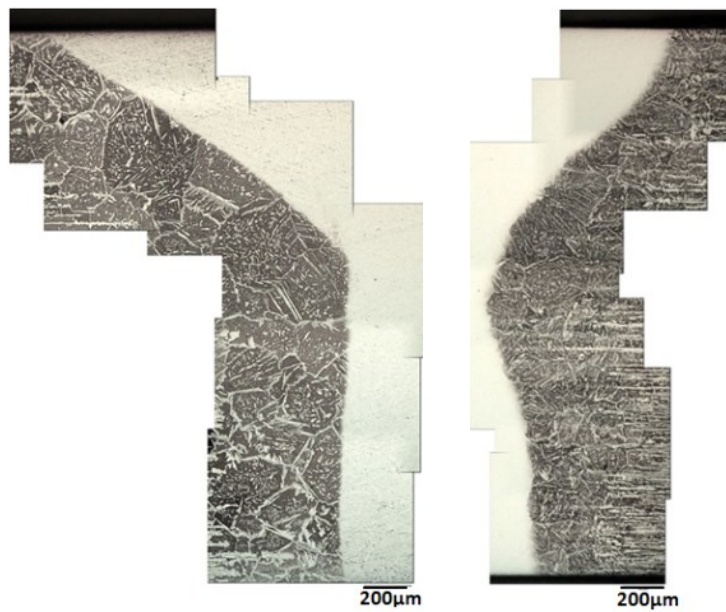


Fig. 3-10. Microstructure of HAZ close to the fusion zone (sample F and FP)

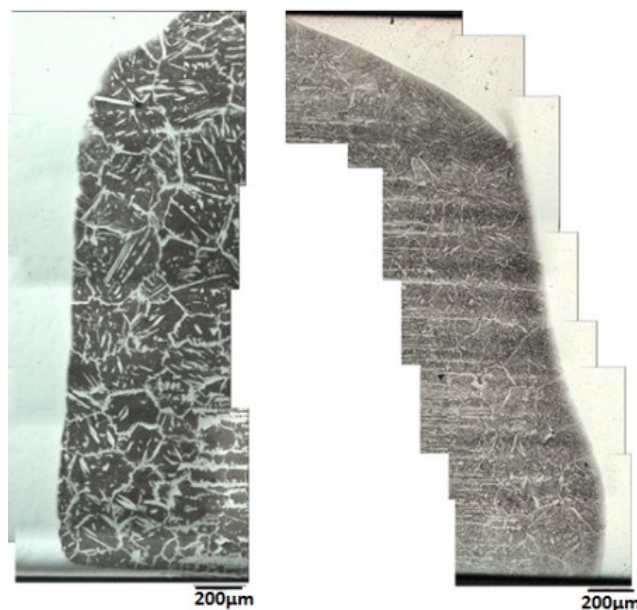


Fig. 3-11. Microstructure of HAZ close to fusion zone (sample FNi, FNiP)

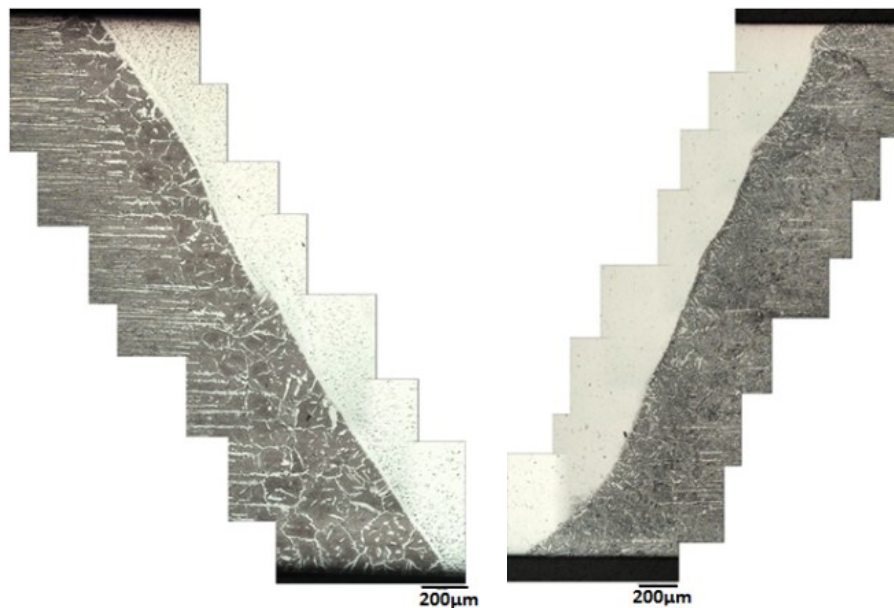


Fig. 3-12. Microstructure of HAZ close to the fusion zone (sample FN2, FN2P)

By comparing the micrographs, it can be concluded that, after PWHT, the amount of austenite in microstructure increase and the morphology of that become from grain boundary and widmanstatten to smoother and more spheroidal intergranular austenite. Generally, it could be said that austenite is formed at temperature lower than 1380 °C, from completely ferrite range. It nucleates first in ferrite grain boundaries and grows as widmanstatten austenite during cooling [12,133]. In addition, as it is clear, after etching the HAZ and base metal were attacked but fusion zone remains unattcked, it means due to existing high amount of alloying elements in that zone it remains more noble than adjuscent area.

3.2.2. EDS analysis and distribution of alloying elements

To observe the distribution of different alloying elements in the microstructure and different phases, EDS analysis was performed and the medium value was reported. The average chemical composition of all welded samples are listed in Table. 3-4 which contains of main alloying elements calculated by EDS analysis accompanied with phase percentages in each phase. It can be observed that, the elements such as Cr, Ni and Mo are homogeneously distributed in different phases due to high temperature. As it is clear, ferrite phase contains more amount of Cr and Mo in addition, also Ni is enrich in austenite phase. In this part elements mainly transformed to ferrite and significant grain growth occurred. After that austenite mainly formed at grain boundaries of ferrite or inside of the ferrite phase. As it is clear in most of the samples, before PWHT, the concentration of Cr and Mo are higher in ferrite phase and concentration of Ni and N are higher in austenite phase. After PWHT, due to higher rate of diffusion and transferring elements between phases, the percentages of elements become close to each other.

It should be added that, after PWHT amount of Cr and Mo in ferrite decrease, while their amount in austenite increase. This could be due to diffusion of this element to large volume of ferrite, while the reverse result occurred in austenite phase. Generally it could be specified that, each element tend to diffuse into the phase which is its stabilizer in fusion zone faster than HAZ due to higher thermodynamic potential.

Also, chromium, nickel and manganese are substitutional elements and diffuse so slow between phases specially in solid state and they cannot partitioned significantly between phases. Fig. 3-13 indicates one example of SEM micrograph for detail analysis of ferrite and austenite phases. Fig. 3-14 to Fig. 3-19 depict the EDS chemical analysis of different points in ferrite and austenite phases. These micrographs and analysis are just for showing the procedure of how completed

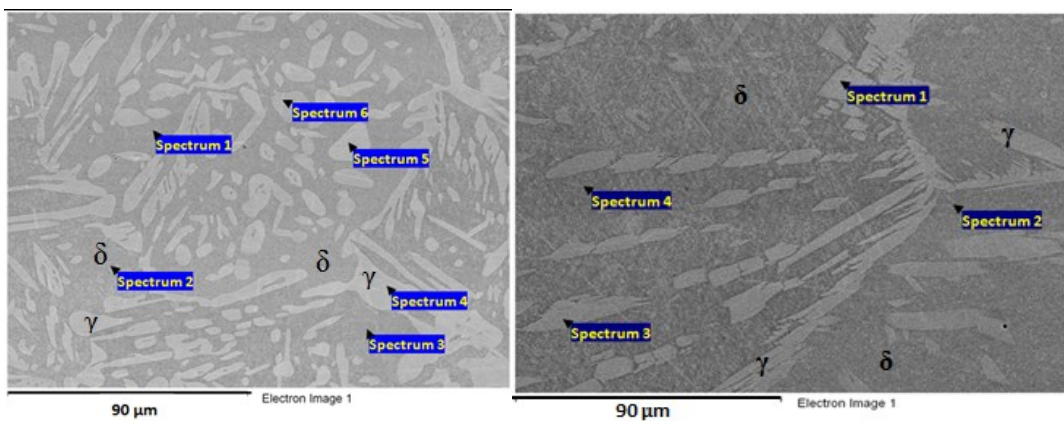
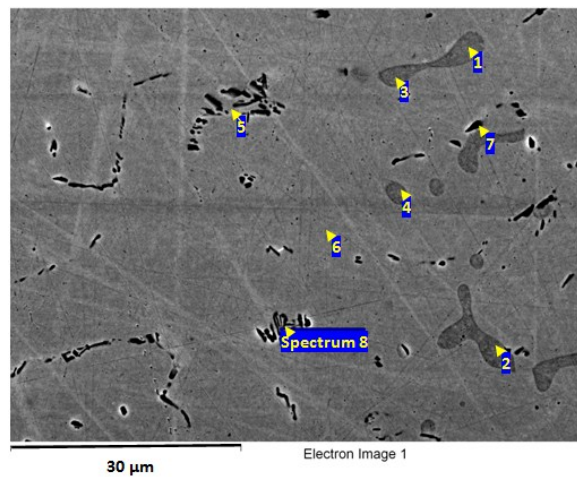
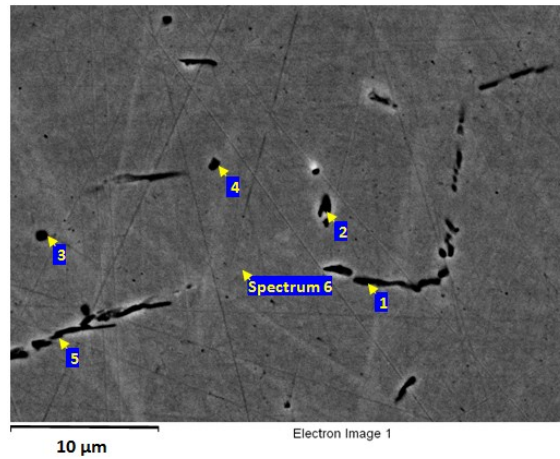


Fig. 3-13. SEM image for specifying the position of ferrite and austenite (FNi and FNiP)



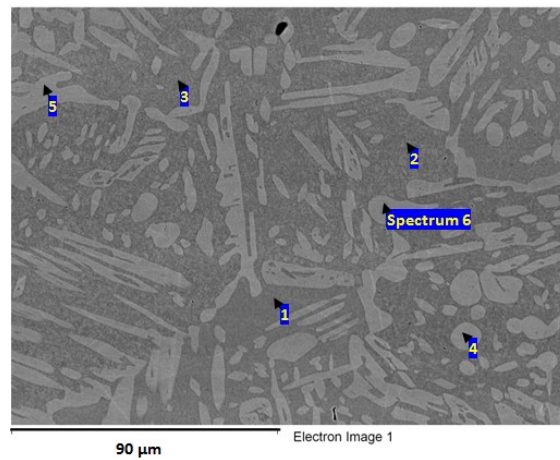
FNi weld	Si	Cr	Mn	Ni	Mo	Fe
1	0.82	26.99	1.28	6.45	3.91	Bal.
2	0.84	27.08	1.23	6.23	4.1	Bal.
3	0.9	27.09	1.33	6.44	4.12	Bal.
4	0.86	27.04	1.18	6.20	4.12	Bal.
5	0.54	37.44	1.56	9.09	5.57	Bal.
6	0.75	25.91	1.44	7.81	3.37	Bal.
7	0.66	29.46	1.37	8.73	3.05	Bal.
8	0.88	28.97	1.47	11.46	4.04	Bal.

Fig. 3-14. SEM image and EDS analysis (wt%) of selected points in fusion (sample FNi)



	FNi fusion zone	Si	Cr	Mn	Ni	Mo	Fe
	1	0.82	30.01	1.48	12.47	3.83	Bal.
	2	0.94	20.95	1.56	13.94	2.19	Bal.
	3	0.95	20.10	2.05	14	2.72	Bal.
	4	0.93	26.42	1.44	13.65	2.83	Bal.
	5	1.03	23.05	1.49	15.82	2.79	Bal.
	6	1.05	21.38	1.55	15.66	2.65	Bal.

• Fig. 3-15. SEM image and EDS analysis (wt%) of selected points in fusion zone (sample FNi)



	FNi HAZ	Si	V	Cr	Mn	Ni	Cu	Mo	Fe
	Spec.1	0.51	0.1	25.09	1.37	3.66	0.21	0.46	Bal.
	Spec.2	0.47	0.09	25.08	1.33	3.68	0.26	0.49	Bal.
	Spec.3	0.5	0.14	24.93	1.38	3.69	0.23	0.5	Bal.
	Spec.4	0.44	0.11	21.82	1.66	5.22	0.25	0.4	Bal.
	Spec.5	0.45	0.12	22.40	1.53	5.64	0.28	0.61	Bal.
	Spec.6	0.42	0.08	22.41	1.47	4.78	0.25	0.35	Bal.

Fig. 3-16. SEM image and EDS analysis (wt%) of selected points in HAZ (sample FNi)

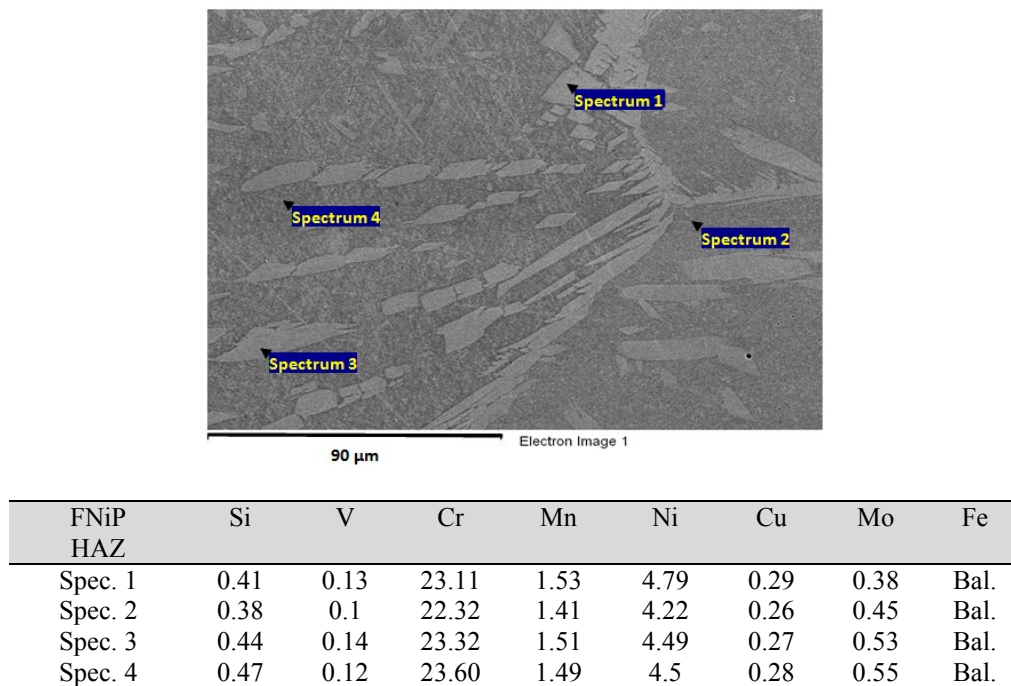


Fig. 3-17. SEM image and EDS analysis (wt%) of selected points in HAZ (sample FNiP)

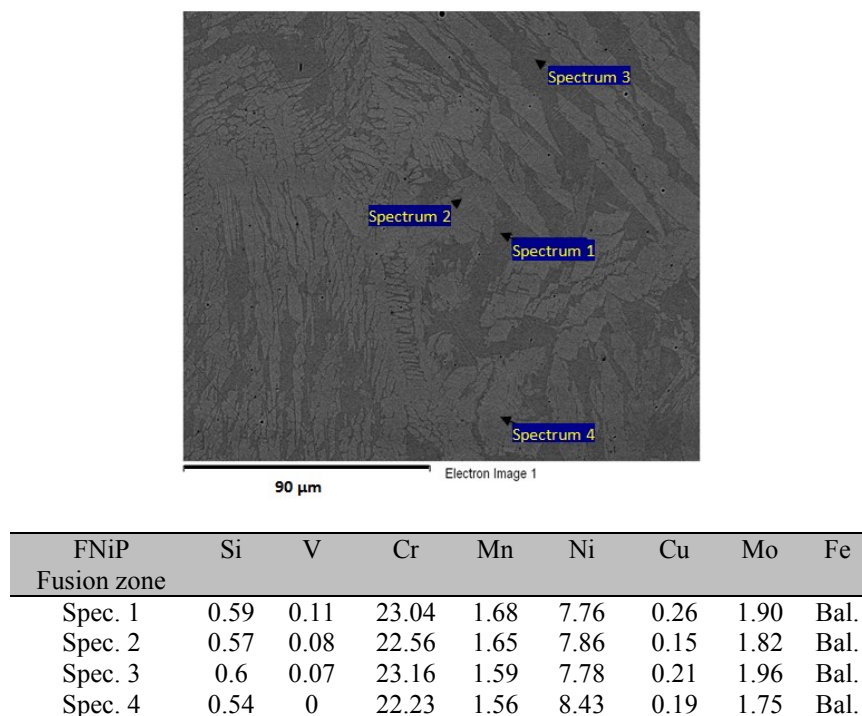
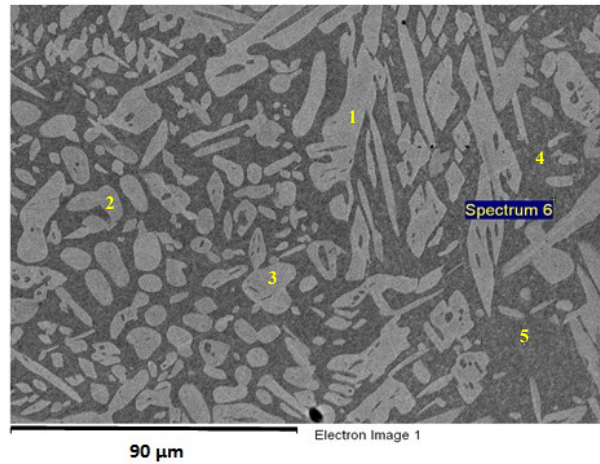


Fig. 3-18. SEM image and EDS analysis (wt%) of selected points in fusion zone (sample FNiP)



FN2 HAZ	Phase	Si	V	Cr	Mn	Ni	Cu	Mo	Fe
Spec.1	Austenite	0.4	0.07	22.46	1.53	4.72	0.3	0.29	Bal.
Spec.2	Austenite	0.47	0.07	22.86	1.52	4.63	0.2	0.4	Bal.
Spec.3	Austenite	0.45	0.09	22.98	1.53	4.8	0.36	0.3	Bal.
Spec.4	Ferrite	0.48	0.13	25.24	1.48	3.65	0.26	0.48	Bal.
Spec.5	Ferrite	0.51	0.13	25.52	1.47	3.73	0.16	0.54	Bal.
Spec.6	Ferrite	0.47	0.13	25.34	1.39	3.66	0.32	0.44	Bal.

Fig. 3-19. SEM image and EDS analysis (wt%) of selected points in HAZ of (sample FN2)

Generally, the content of chromium in GBA is highest and in IGA is the lowest, which is because different diffusion coefficients at different temperatures. Because formation of GBA is so fast and elements do not have time for partitioning but formation of IGA took a little longer. Because of that the PREN IGA is close to ferrite. But this differences between GBA and WA is more. Large heat input cause to higher pitting and corrosion resistance due to variation of chromium percentage [253]. As explained before, Table. 3-4, shows detail medium value chemical composition of main alloying elements. As it is clear ferrite stabilizer elements such as chromium and molybdenum are segregated in ferrite and austenite stabilizers such as nickel and nitrogen are higher in austenite phase.

After PWHT, the volume fraction of ferrite in fusion zone decrease compare to HAZ, also more amount of grain growth in fusion zone occurred. Larger grain size reduce the area of grain boundaries, consequently the number of nucleation site for allotriomorph and widmanstatten austenite decrease. As a result amount of austenite decrease, and thermodynamic potential for precipitation of intergranular austenite in fusion zone is more than HAZ which cause to decrease the volume fraction of ferrite in fusion zone with higher rate compare to HAZ during PWHT.

Table. 3-4. Alloying elements content (Med. wt %) and phase percentages in different samples

Sample	Phase %		EDS chemical analysis (wt%)			
			Cr	Mo	Ni	Mn
BM	δ	57.3	25.18	0.45	3.56	1.35
	γ	42.7	21.59	0.34	5.61	1.61
BMP	δ	51.8	25.03	0.52	3.74	1.41
	γ	48.2	23.54	0.3	4.48	1.48
F (HAZ)	δ	75.8	23.64	0.86	4.99	1.56
	γ	24.2	23.12	0.71	5.29	1.53
F (F.Z)	δ	21.6	23.33	2.89	9.03	1.33
	γ	78.4	22.02	2.47	6.91	1.9
	area		23.04	2.75	7.21	1.63
FP (HAZ)	δ	59.4	25.36	1.1	3.92	1.42
	γ	40.6	22.35	0.81	5.5	1.59
FP (F.Z)	δ	35.3	26.31	3.84	8.46	1.45
	γ	64.7	21.85	2.48	5.67	1.74
	area		23.89	1.56	6.13	1.56
FNi (HAZ)	δ	78.3	25.18	0.48	3.62	1.38
	γ	21.7	22.52	0.4	4.98	1.55
FNi(F.Z)	δ	31.2	26.67	3.39	9.86	1.37
	γ	68.8	22.63	2.27	5.70	1.58
	area		21.99	2.28	12.49	1.46
FNiP(HAZ)	δ	58.1	23.08	0.5	4.3	1.45
	γ	41.9	23.22	0.46	4.64	1.52
FNiP(F.Z)	δ	45.6	23.09	2.10	8.03	1.58
	γ	54.4	22.8	1.93	7.5	1.59
	area		23.07	2.09	7.38	1.57
FN2 (HAZ)	δ	66.5	25.36	0.53	3.62	1.46
	γ	33.5	22.88	0.36	4.8	1.58
FN2 (F.Z)	δ	32.1	-	-	-	-
	γ	67.9				
	area		23	2.95	7.36	1.47
FN2P (HAZ)	δ	59.1	24.96	0.36	3.54	1.37
	γ	40.9	23.05	0.4	4.7	1.49
FN2P (F.Z)	δ	46.3	22.72	2.63	7.20	1.66
	γ	53.7	21.99	2.19	7.09	1.48
	area		22.7	2.8	7.21	1.57

3.2.3. Precipitation of secondary phases

Nitrogen is an critical element in duplex stainless steels which play important roles in properties of stainless steels such as high temperature stability. In addition, nitrogen can improve pitting and crevice corrosion resistance of stainless steels [109]. In case of existing nitrogen, there is a risk of precipitation of undesirable chromium nitride. With considering the low solubility of nitrogen in ferrite phase, chromium nitride generally precipitates at ferrite-austenite grain boundaries and within ferrite grains in both HAZ and fusion zone [12,85,190]. The precipitation of this phase and its negative effect on corrosion resistance and mechanical properties of the welded duplex steels was investigated by many authors [12,86,91]. In this study, based on EDS analysis of the sample with addition of nitrogen (FN2) the precipitation of different types of chromium nitride was observed. Weight fraction of nitrogen and its partitioning between ferrite and austenite are very important for determining the pitting corrosion behavior of duplex stainless steels. Concerning the as welded conditions and higher cooling rate, the interstitial elements such as nitrogen control the reaction and mainly concentrate into the austenite phase [144]. Fig. 3-20 indicates the schematic formation of chromium nitride and susceptible area to corrosion. Chromium depleted zone close to the Cr_2N cause to decrease the corrosion resistance due to lower concentration of chromium in that area than in the matrix. The order of priority for pitting corrosion resistance could be categorized as austenite, ferrite and Cr depleted zone. The reason of low corrosion resistance could be due to decreasing the PREN with increasing the percentage of ferrite.

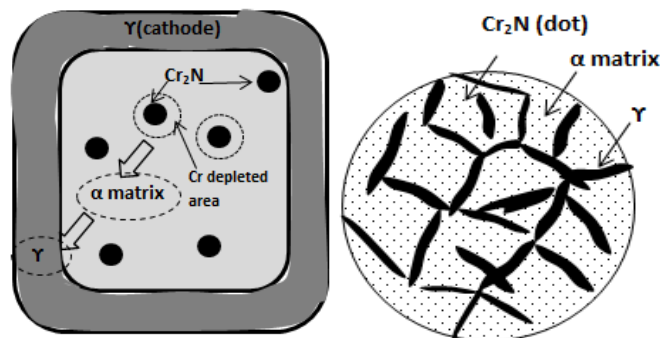


Fig. 3-20. Schematic effect of formation of chromium nitride on microstructure and corrosion resistance

Mechanism of corrosion resistance in case of addition of nitrogen in shielding gas can be categorized first by initiation of pit in the area around chromium nitride which the amount of chromium is less. Then pit grows to ferrite matrix and reach to austenite lathes. Consequently the order of pitting corrosion resistance could be interface of austenite-ferrite and the area close to chromium nitride precipitates. By increasing of chromium nitride, the chromium depleted area around that phase increase and corrosion resistance decrease.

In this study, precipitation of chromium nitride in ferrite phase was observed in samples with addition of nitrogen (FN2 and FN2P) which different types of that are shown in Fig. 3-21 and Fig. 3-22. It is clear that this precipitation can occur in grain boundaries and inside of ferrite phase. It was reported that [70] due to low solubility of nitrogen in ferrite phase, precipitation of chromium nitride increase with increasing the ferrite phase. Consequently ferrite become the first place for pit nucleation.

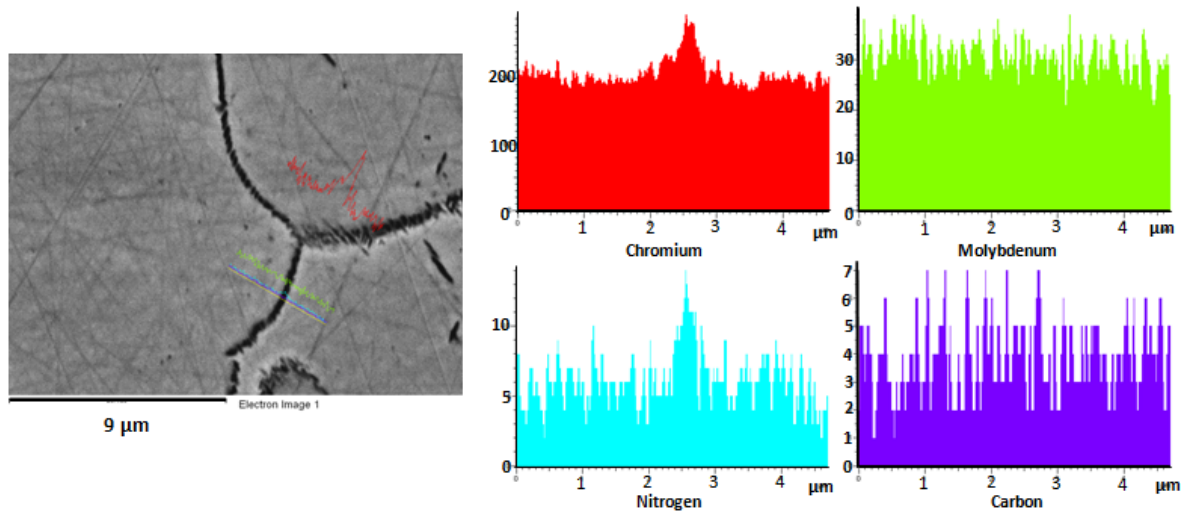


Fig. 3-21. Formation of chromium nitride in sample FN2P in grain boundaries

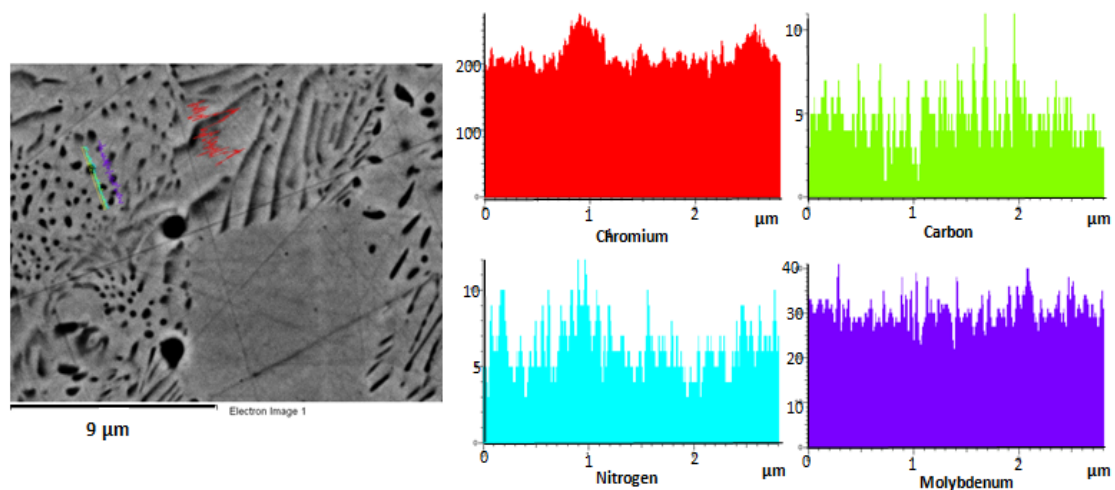


Fig. 3-22. Formation of chromium nitride inside of the grains (sample FN2)

Based on previous studies, the effect of addition of nitrogen in weld metal cause to increase the austenite content, decrease formation of chromium nitride, increase the corrosion resistance properties of the austenite phase, reduce the partitioning of solid solution alloying elements and it changes the solidification mode [109]. Although, the influence of addition of nitrogen in shielding gas have been investigated by many authors and most of them observed the increasing the corrosion properties, but still the exact mechanism for that is not completely clear.

Just some proposed mechanisms can be specified as enrichment of nitrogen signal from a position corresponding to the metal side of metal-film interface observed with X-ray photoelectron analysis[254]. Also it was reported [255] that nitrogen increase dissolution of iron, so that the consequent enrichment in chromium enable the metal to re-passivates. Another mechanism related to the role of nitrogen include prevention of the lowering the PH in solution and arrest the localized corrosion propagation and change the electrochemical properties.

One most reliable mechanism is based on nitrogen enrichment of active surfaces which occurs when the dissolution rate of the material is more than dissolution rate of nitrogen, consequently nitrogen enrich at the surface and block more dissolution of the metal [256]. This phase is not formed during annealing and it mainly precipitated during cooling from annealing temperature. The mass fraction of chromium determined by EDS analysis and it is relatively equivalent to the equilibrium value at the annealing temperature but it was inhomogeneously distributed within the phase after quenching [143].

Hoffmeister et al. [205] found that due to the diffusion controlled transformation and precipitation mechanisms, the amount of chromium nitride phase in case of existing nitrogen mainly are controlled by ferrite-austenite transformation. Also, they reported precipitation of this phase can be decrease by increasing the cooling time, because it has time to be soluble in austenite phase. Liou et al.[230] observed the negative effect of chromium nitride in corrosion resistance properties of the duplex stainless steels, also they found that the amount of chromium nitride increase with increasing the cooling rate. Ramirez et al.[76] observed that, during heat treatment of duplex steel more than 1100 °C, there is possibility of precipitation of Cr₂N within ferrite grains and intergranular nitrides in interface of ferrite and austenite which facilitate the precipitation of secondary austenite in ferrite/nitride interface.

Also, in sample FN2 precipitation of manganese oxide was detected. Manganese showed a different pattern compare to the chromium, with overall increase in ferrite phase and within the oxide formed at phase boundaries. Manganese is not principle element in duplex stainless steel and it mainly exist up to 5wt%, but it can form manganese oxide in the microstructure. In this oxide a little iron and chromium can be observed in the ferrite region. Fig. 3-23 shows the schematic morphology of manganese oxide and Cr oxynitrides on sample in case of addition of nitrogen in the weld pool. EDS analysis, showed that, chemical gradient of the oxide which is manganese and chromium rich oxides with small amount of silicon and iron with general formula of M₂O₃, which was in agreement with the results of Jepson et al.[257].

Henthorne et al.[258] reported that Mn has negative effect on corrosion properties due to formation of (Fe-Mn) Cr₂S₄ at high concentration of Mn, which causes to pit initiation. Also, Westin et al.[259] reported that during welding with pure argon, manganese oxide dominated on duplex steel and addition of nitrogen cause to increase the evaporation of manganese and promote formation of oxynitrides. They observed formation of heat tint and oxide layer during welding in both cases of existing and non-existing nitrogen. In addition they found with increasing the fraction of manganese, oxide become thicker and wider in case of addition of nitrogen, which could be due to absorption-evaporation and deposition process.

Also addition of nitrogen to the gas cause to alter the chemical composition of the heat tint by decreasing iron and chromium oxidation and increasing the evaporation of manganese and formation of oxynitrides a few millimeter far from the fusion line. It mainly contains manganese and chromium. Generally they observed the oxides which form after addition of nitrogen are thicker and sometimes even after polishing remains on the surface. This cause to change the color in that area from rest of the surface. This suggests importance of cleaning after welding by polishing and pickling to increase the corrosion resistance [259,260].

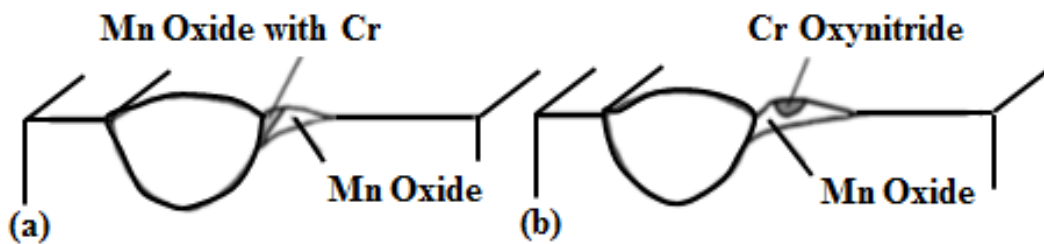


Fig. 3-23. Weld oxide deposition in case of (a) without nitrogen (b) with nitrogen [259,261]

In summary to reach less differences between PREN of both phases and increasing the pitting corrosion resistance of the bulk, addition of nitrogen gas as a strong austenite stabilizer play an important role. With addition of nitrogen, austenite phase increase and solubility of chromium nitride in that phase increase, consequently this phase become less in the matrix and pitting corrosion resistance increase [162]. Fig. 3-24 depicts the EDS map analysis of the manganese oxides which form in the as welded sample with addition of nitrogen gas.

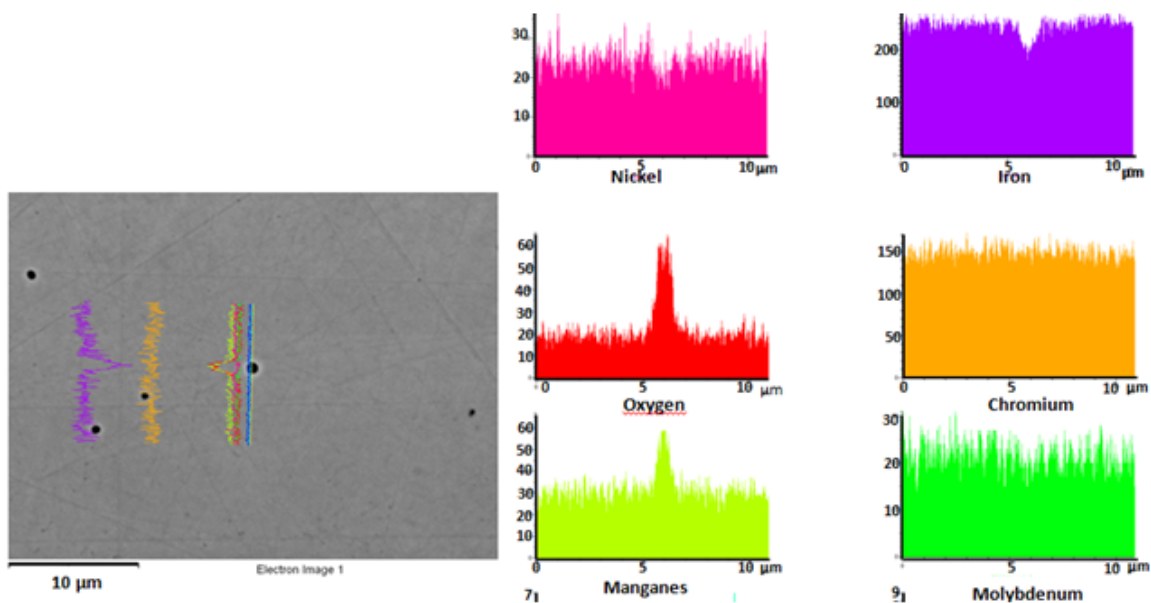


Fig. 3-24 . Formation of Manganese oxide in the sample FN2

In sample with addition of nickel powder precipitation of chromium and manganese oxide was detected which is shown in Fig. 3-25, based on investigation of Jepson et al.[257], this precipitate could be chromium manganese oxide (CrMn_2O_3), which has detrimental effect on corrosion properties. Also, it should be added, mostly the oxides and inclusions are distributed in both ferrite and austenite phases, but mainly pits initiated in ferrite phase, it means corrosion resistance of the ferrite phase is the key points compare to existing the inclusions in the microstructure.

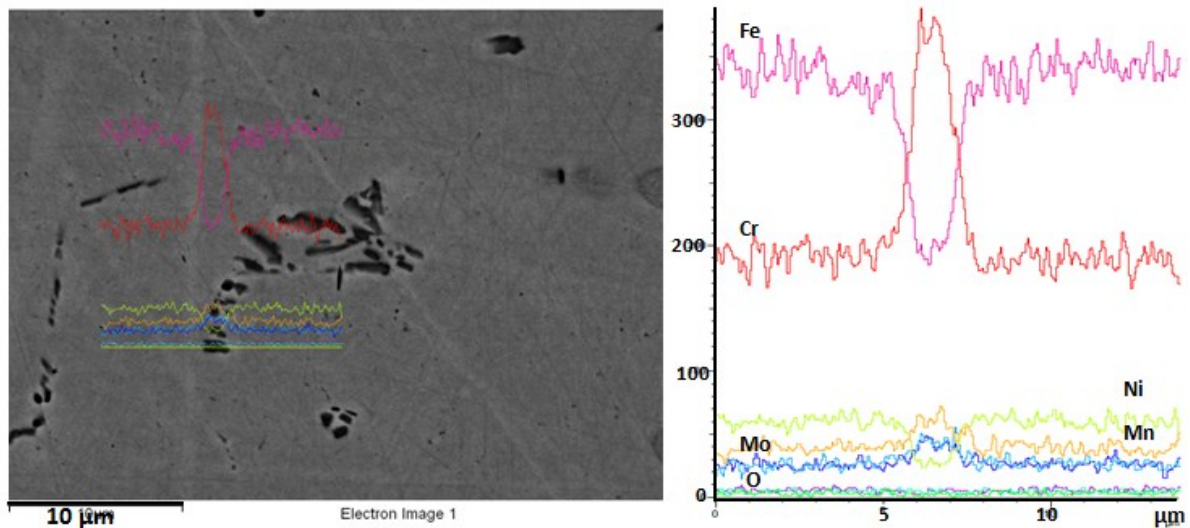


Fig. 3-25. Formation of chromium manganese oxide in sample FNI

3.2.4. Partitioning of elements after welding and heat treatment

Normally partitioning behavior of alloying elements and the microstructure play an important role in determining the pitting resistance of duplex stainless steels. Table. 3-5 indicates the experimentally calculated partitioning ratio for different alloying elements in fusion zone and HAZ of different samples. The data obtained by calculating the ratio between ferrite and austenite. Partitioning of elements, indicates that, the values are relatively close to each other, it means cooling rate was high enough to inhibit the partitioning of elements between phases.

As it is clear the partitioning ratio of chromium in all samples are marginally more than one, it means cooling rate is too high and partitioning is not occur completely, also it confirm the more amount of Cr in ferrite phase compare to austenite.

This trend exist for molybdenum, but the partition ratio is more than chromium, it means the effect of molybdenum in stabilizing the ferrite is more than chromium. Also, as it is clear for the samples after solution treatment, the partitioning ratio of molybdenum decrease, it means more chromium diffuse into the austenite phase due to existing austenite stabilizer elements. But solution treatment of the sample F cause to increase the partitioning ratio, it could be due to not existing austenite former alloying elements and it mainly concentrated in ferrite phase.

Partitioning of nickel is always less than one, which means austenite phase in all situations is rich in this element. Normally after solution treatment, partitioning of elements more occur, ferrite become rich in Cr and Mo and austenite become rich in Nickel. Liljas et al. [144], reported that in high cooling rate interstitial elements such as carbon and nitrogen mainly are concentrated in austenite. For one estimation the partitioning of nitrogen in ferrite and austenite is considered as 0.1.

Table. 3-5. Partitioning ratio of the elements in different conditions

Sample	Cr	Mo	Ni	Mn
BM	1,17	1,32	0,98	0,83
BMP	1,06	1,73	0,83	0,95
F	1,02	1,21	0,94	1,01
FP	1,13	1,35	0,71	0,9
FNi	1,19	1,2	0,72	0,9
FNiP	0,99	1,08	0,92	0,95
FN2	1,1	1,47	0,75	0,92
FN2P	1,08	0,9	0,75	1,14

Nitrogen is mainly concentrated in austenite and enhance the corrosion resistance by increasing the value of PREN. Also nitrogen decrease the formation of sigma phase by reducing the chromium enrich in ferrite. As a result, a high nitrogen content would allow increase of chromium and molybdenum. Apart from partitioning of chromium and molybdenum, nitrogen leads to a higher volume fraction of austenite. To reach equal percentage of phases, the content of other austenite stabilizer elements such as nickel should be considered at the same time with nitrogen [143]. Normally the solubility of nitrogen in steels enhance with addition of manganese. Also the quenching temperature has strong effect on partitioning of elements. At lower temperature the partitioning effect is more. This could be due to thermodynamically concept of entropy and changing the phase equilibrium between ferrite and austenite. The volume fraction of ferrite decrease with decreasing the temperature. Small volume fraction of ferrite cause to high concentration of chromium and molybdenum in ferrite.

Large volume fraction of austenite cause to lower concentration of nickel and nitrogen and lower value of PREN. Fig. 3-26 and Fig. 3-27 indicate the histogram of partitioning ratio for main elements in all samples in HAZ and fusion zone respectively. The EPMA analysis of the welded sample with and without nitrogen which was performed by Muthupandi et al.[109] indicates that the partitioning effect in the sample with addition of nitrogen is not recognizable and relatively uniform composition through the weld can be observed. The microstructure of the weld was mainly austenite with small amount of ferrite and due to that showed excellent pitting resistance.

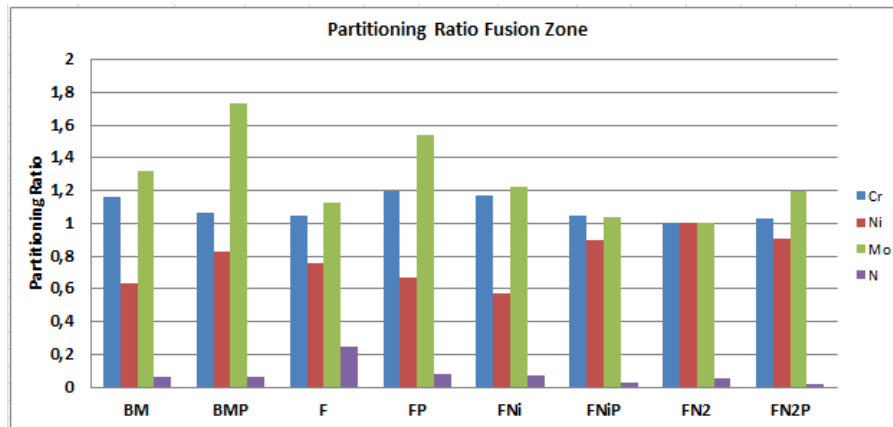


Fig. 3-26. Partitioning ratio of the elements in the fusion zone

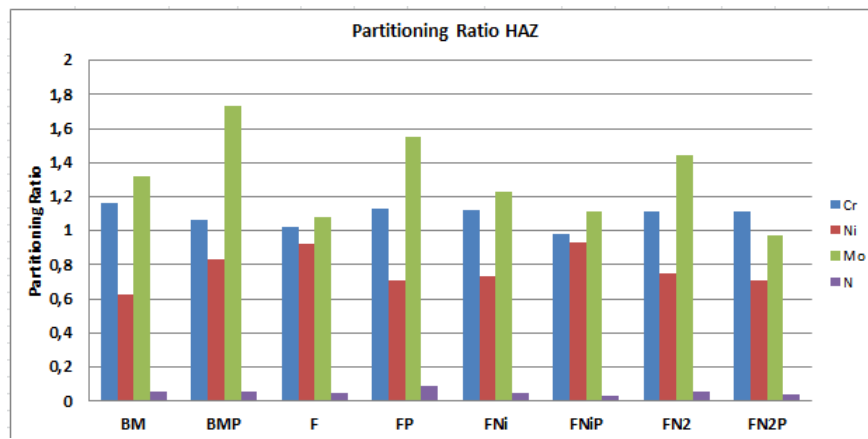


Fig. 3-27. Partitioning ratio of the elements in the heat affected zone

As it is clear from the above table and diagrams, the partitioning ratio of chromium and molybdenum in all the samples are more than one, it is due to their role as ferrite stabilizer elements. nickel and manganese as austenite stabilizer elements showed less than one partitioning ratio, except for sample FN2P which indicated manganese value more than one. Due to difficulty of nitrogen measurement by EDS analysis and roughly estimation of 0.05% solubility in ferrite, partitioning ratio for nitrogen is neglectable. Fig. 3-28 and Fig. 3-29 indicate the histogram for partitioning of the main alloying elements in HAZ and fusion zone respectively. As it is obvious, in both HAZ and FZ the amount of nickel and nitrogen is higher in austenite but chromium and nitrogen are rich in ferrite phase.

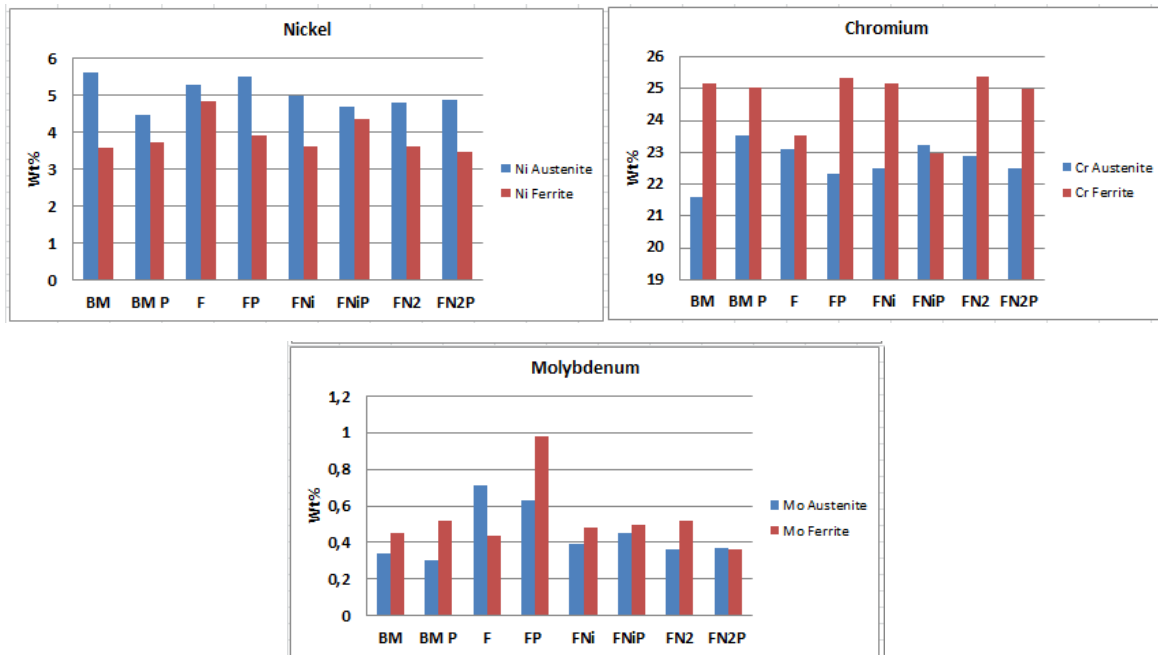


Fig. 3-28. Distribution of main alloying elements in ferrite and austenite phases in HAZ

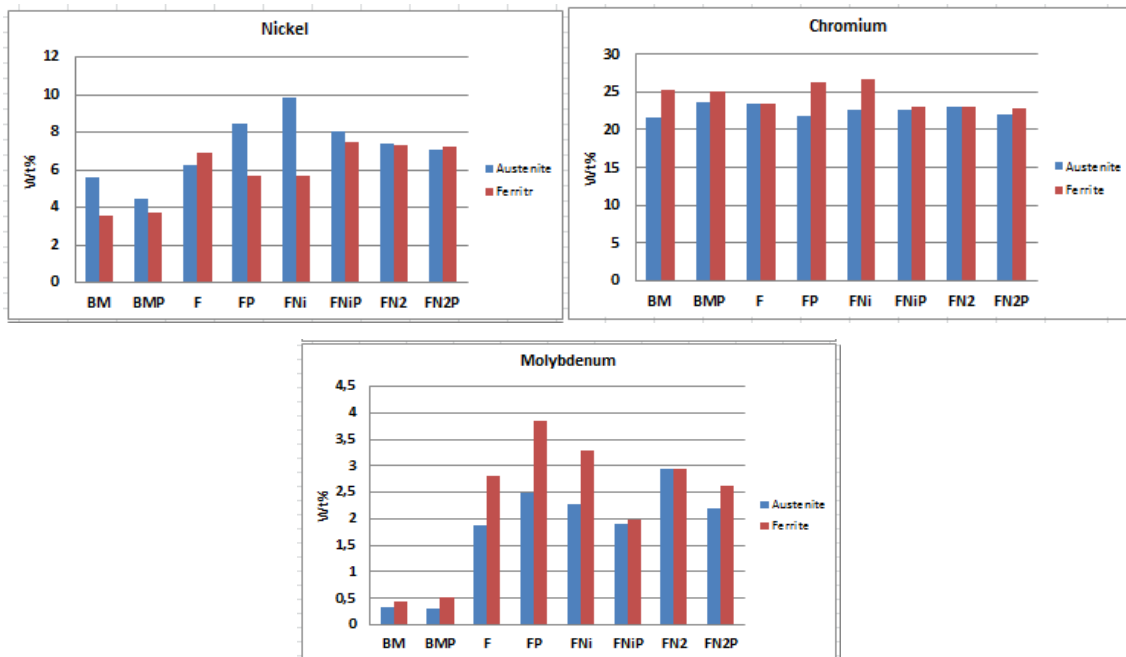


Fig. 3-29. Distribution of main alloying elements in each ferrite and austenite phase in FZ

3.2.5. Pitting potential and its relation to PREN value

The medium value of pitting potential diagram was drawn for all the samples. Fig. 3-30 reports the anodic polarization curves recorded on the base metal and all samples which welded in different conditions after 1 h immersion in 3.5% NaCl solution at 30 °C. Post weld heat treatment induce a remarkable increase in pitting potential compare to untreated samples. Table. 3-6 shows the value of pitting potential for all the samples with relevant standard deviations. After PWHT, the value of pitting potential for sample F, FNi and FN2 increased 13.5, 32.1 and 44.9% respectively.

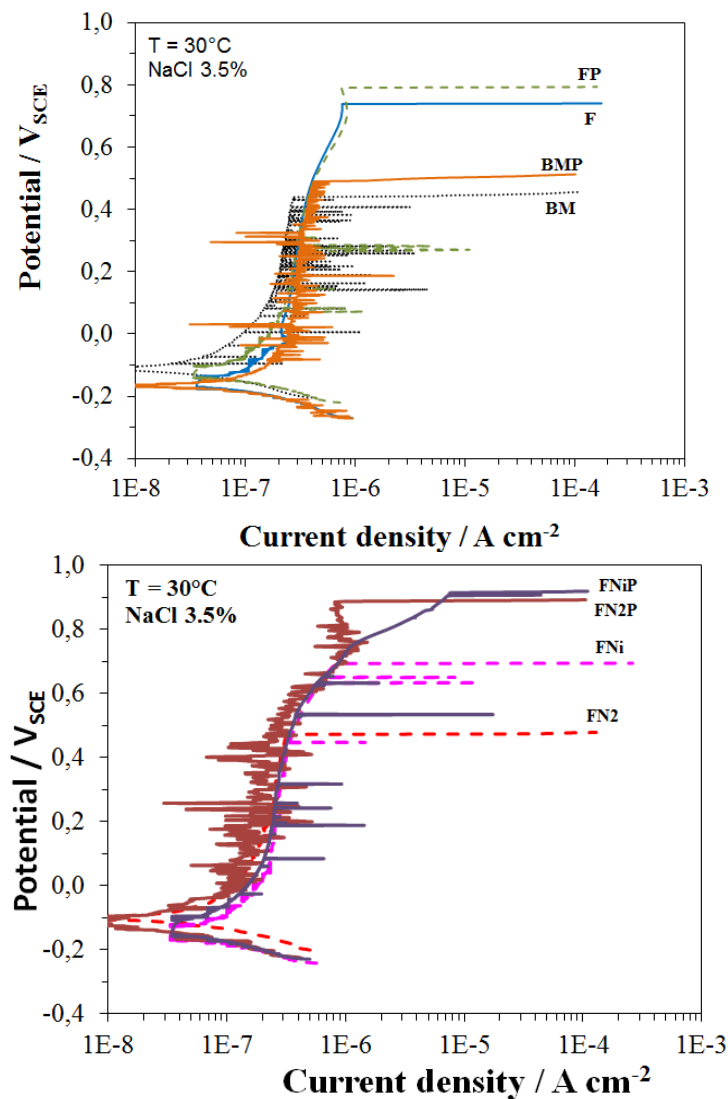
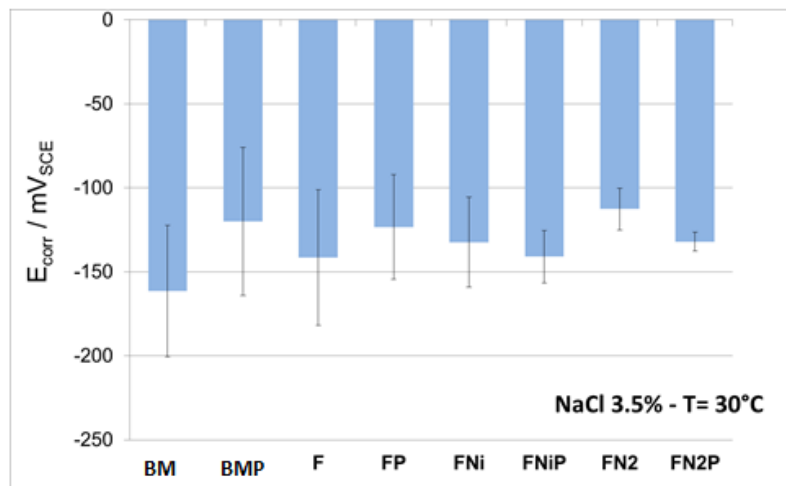


Fig. 3-30. Anodic polarization curves recorded in NaCl 3.5% at 30 °C

Table. 3-6. Actual values of pitting potential and E_{corr}

Sample	Pitting potential (mV _{SCE})	St dev.	E_{corr} (mV _{SCE})	St dev.
BM	512	135	-162	39
BMP	441	158	-120	44
F	763	32	-142	40
FP	883	127	-123	31
FNi	507	174	-132	27
FNiP	921	4	-141	16
FN2	548	166	-113	13
FN2P	808	117	-132	6

From Fig. 3-31 and Fig. 3-32, it can be concluded that the pitting potential for the base metal before and after PWHT roughly remain constant. But for sample F and FP the pitting potential increase, this could be due to the effect of addition of filler metal which contains more amount of the alloying elements such as nickel and nitrogen. For sample with addition of nickel powder and nitrogen gas the pitting potential become lower. This for sample with addition of nickel could be due to variation of percentage of ferrite and austenite and for the sample with addition of nitrogen is due to formation of chromium nitride phase. In both conditions after applying the heat treatment percentage of phases became roughl the same and for sample with addition of nitrogen chromium nitride dissolve in the matrix consequently pitting potential increase.

**Fig. 3-31.** Corrosion potential for all the samples

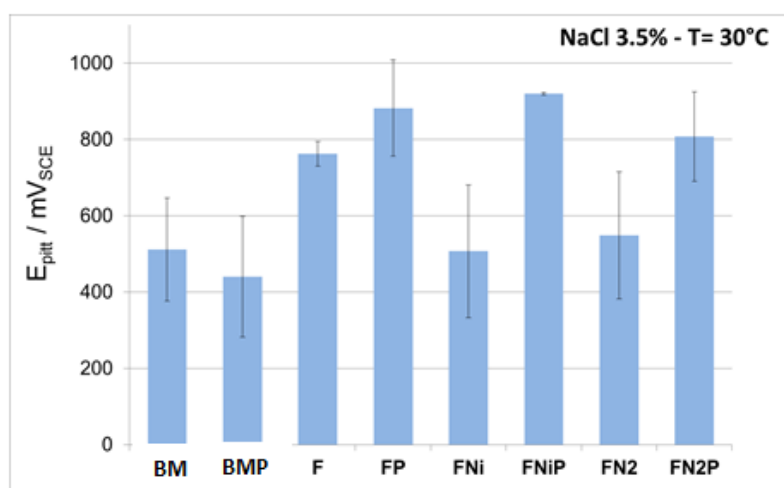


Fig. 3-32. Pitting potential for all the samples

It is accepted that, pitting resistance equivalent number (PREN) could be used as a reliable value for prediction of the pitting corrosion behavior of duplex stainless steels and it mainly depends on chemical composition of the ferrite and austenite phases [86]. The concentration of alloying elements in ferrite and austenite phase were detected by EDS analysis. Generally, the percentage of Cr and Mo are rich in ferrite phase and Ni is rich in austenite phase. Based on previous studies [86,207]. Amount of saturated nitrogen content in ferrite is considered 0.05%, the rest is in austenite. The results of obtained nitrogen from EDS is not reliable. Due to that, Atamert et al.[128] reported that, amount of nitrogen in austenite is seven to eight times more than ferrite when the welded sample annealed between 1050 to 1250 °C. Also because of fast diffusion of the nitrogen into the austenite, the role of temperature is more than time.

The concentration of alloying elements in each phase is controlled by diffusion. Generally, the diffusion rate of nitrogen, as an interstitial element is higher than the diffusion rate of substitutional elements. Consequently nitrogen can easily diffuse and concentrate in austenite phase due to its intrinsic properties for stabilizing this phase, but chromium and molybdenum which are ferrite stabilizers mainly remain in ferrite phase [12]. Nitrogen postpone precipitation of intermetallic phases such as sigma, laves, chi and carbides. It has low solubility because of retarding effect on diffusion of Cr and Mo due to increase concentration of vacancy. Generally, yield and tensile strength of the austenitic stainless steel alloys with nitrogen increase because of solid solution hardening.

To find a relation between chemical composition of phases and pitting potential, the value of PREN for each phase was calculated by the following formula:

$$PREN = \%Cr + 3.3\%Mo + (16 \text{ or } 30)\%N$$

In addition to PREN of the $\Delta PREN$ parameter was calculated as the difference between PREN of austenite and ferrite.

$$\Delta PREN = PREN_{Austenite} - PREN_{Ferrite}$$

To reach higher pitting corrosion resistance the value of PREN should be maximum, and minimum value of $\Delta PREN$ is desirable. Minimum value of $\Delta PREN$ means the differences between PREN value of both phases and pitting corrosion resistance of phases are minimum. Consequently the risk of pitting initiation in weaker phase with lower PREN value decrease. Table. 3-7 reports the PREN and $\Delta PREN$ values for ferrite and austenite in as received base metal and after heat treatment. As it is clear, the value of PREN is not so much different, but the $\Delta PREN$ in sample BMP is more than BM. Due to that the lower pitting potential of the sample can be justified.

Table. 3-7. PREN and $\Delta PREN$ value of as received base metal and after heat treatment

Sample	Phase	PREN		$\Delta PREN$	
		16	30	$\Delta 16$	$\Delta 30$
BM	δ	27.47	28.16	1.65	6.54
	γ	29.11	34.71		
BMP	δ	27.54	28.24	3.38	8.28
	γ	30.93	36.53		

Table. 3-8 depicts the PREN and $\Delta PREN$ value and phase percentage in the HAZ and fusion zone of the all welded samples before and after PWHT which the value of PREN and $\Delta PREN$ was calculated. In all situations after PWHT, the value of PREN increase. In addition due to occurring all the pits in the HAZ, we should consider the obtained value of pitting potential just for HAZ. It is clear that after PWHT, the partitioning of the alloys become lower and volume percentages of the elements became close to each other. It could be due to increasing the diffusion rate at high temperature.

Table. 3-8. PREN and $\Delta PREN$ value of all samples in HAZ and fusion zone

Sample	Phase	PREN (HAZ)		$\Delta PREN$ (HAZ)		PREN (FZ)		$\Delta PREN$ (FZ)	
		16	30	16	30	16	30	$\Delta 16$	$\Delta 30$
								-	-
F	δ	27.28	27.97	4.58	9.48	33.37	34.07	3.20	8.1
	γ	31.86	37.46			36.57	47.27		
FP	δ	29.79	30.49	1.63	6.53	39.78	40.48	0.33	1.55
	γ	31.42	37.02			40.11	42.03		
FNi	δ	27.56	28.26	2.68	7.58	38.36	39.06	2.96	3.06
	γ	30.24	35.84			41.32	42.12		
FNiP	δ	25.53	26.23	5.60	10.51	30.3	31	5.56	10.46
	γ	31.14	36.73			35.85	41.45		
FN2	δ	27.91	28.60	2.56	7.45	39.14	43.85	-	-
	γ	30.47	36.06						
FN2P	δ	26.95	27.65	3.82	8.72	32.2	32.9	3.4	7.66
	γ	30.77	36.37			35.61	40.56		

For the sample F and FP, differences between the PREN values are not too much, but the Δ PREN are more close to each other. But this value for the sample FNi and FN2 after PWHT are less. One effect of PWHT on welded duplex can be specified to dissolve detrimental precipitates. It mainly performed at high temperature which diffusion rate is high and it causes to change the microstructure [111]. From the Table. 3-8, it can be concluded that, for all the samples, value of PREN 30 in austenite is more than ferrite. As a result, most of stable pits occur in ferrite phase of the HAZ. This is in agreement with the results of Tan et al.[92].

Fig. 3-33 indicates the relation between PREN 30 and pitting potential for the ferrite phase. For all the samples the value of PREN for austenite are more than ferrite, consequently ferrite as a weaker phase play an important role to determine the pitting corrosion resistance of the alloy. Sample FP with PREN of 30.49 for ferrite phase indicates high value of pitting resistance. Samples FNiP and FN2P with PREN of 26.23 and 27.65 depict maximum pitting potential. Sample BMP with PREN of 28.24 shows low pitting potential resistance. Based on obtained results it is really difficult to find direct relation between PREN value and pitting potential for all the samples. Generally, it could be said that

By comparing the results of PREN before and after PWHT, it can be found that there is not so much differences between PREN values but in all cases after PWHT, the pitting potential increase. The rate of increasing the PREN value after PWHT for samples FNi and FN2 are more than as welded sample F.

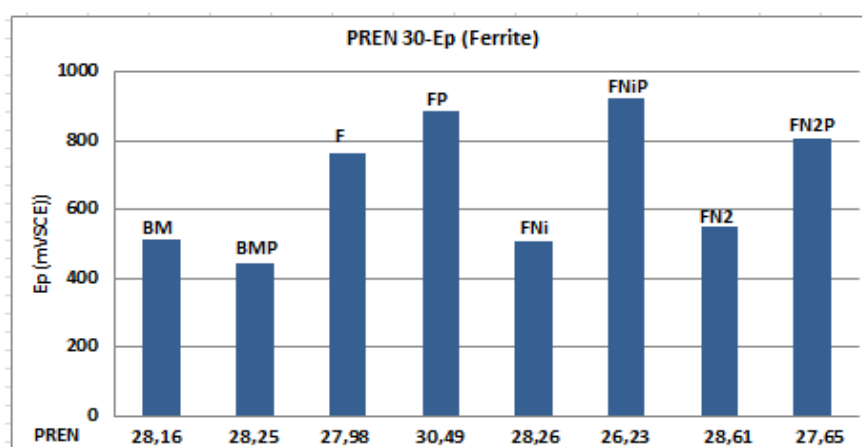


Fig. 3-33. Relation between PREN30 and pitting potential in ferrite phase of HAZ

Fig. 3-34 indicates the relation between pitting potential and Δ PREN 30. Due to significant effect of nitrogen in PREN value and its concentration in austenite phase, the value of Δ PREN30 and 16 are different, but the trend is roughly the same. The minimum value of Δ PREN was obtained for the sample FP, which showed appropriate pitting corrosion resistance. Also, as shown before for this sample, despite of low value of Δ PREN, the pitting first occur in the ferrite phase. Samples FNiP and FN2P with relatively high value of Δ PREN indicate high pitting potential.

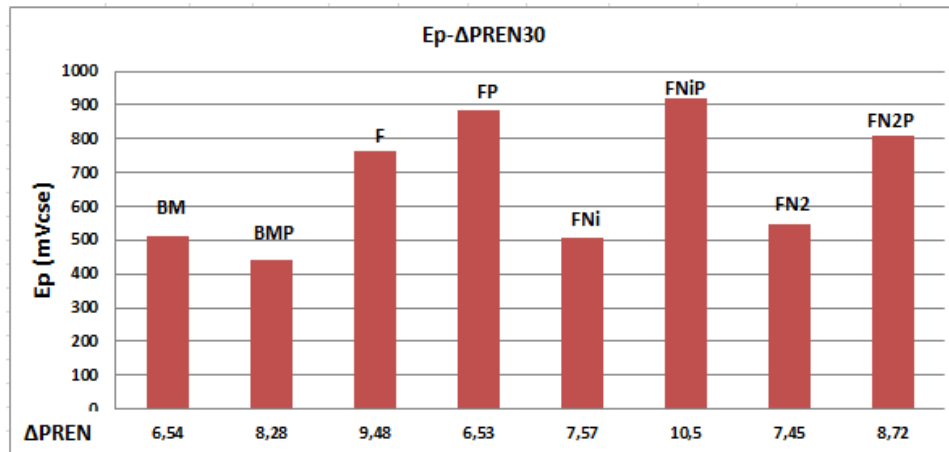


Fig. 3-34. Relation between Δ PREN30 and pitting potential

The maximum value of Δ PREN was obtained for the sample with addition of nickel and nitrogen followed by PWHT. It means the PREN value of austenite is more than ferrite, consequently it remains safe during the test. It is suggested that ferrite percentage have an effect on the pitting resistance. It was recommended that [262] duplex steel should have an optimum amount of ferrite between 40 and 50% to reach higher pitting corrosion resistance. Tan et al.[89] showed that with increasing the PWHT temperature the amount of ferrite increase. The reason for not direct relation between PREN value and pitting potential could be due to the effect of other elements such as phosphorus, sulphur and copper in addition to synergies effect of binary or ternary alloys which is not defined in PREN formula and it could be one weak point of conventional PREN value. As an example one research showed strong synergic effect of molybdenum and nitrogen [263]. Another important issue which should be discussed is the effect of ferrite content on pitting corrosion resistance of duplex stainless steels. Fig. 3-35 indicates, relation between ferrite percentage in the HAZ and value of PREN, Δ PREN30. It was found that, there is not specific relation between value of PREN, Δ PREN and ferrite content. In addition, it shows that, after PWHT and decreasing the ferrite content, the value of PREN and Δ PREN roughly remain constant. Maximum PREN value and minimum Δ PREN value was obtained for the samples after heat treatment.

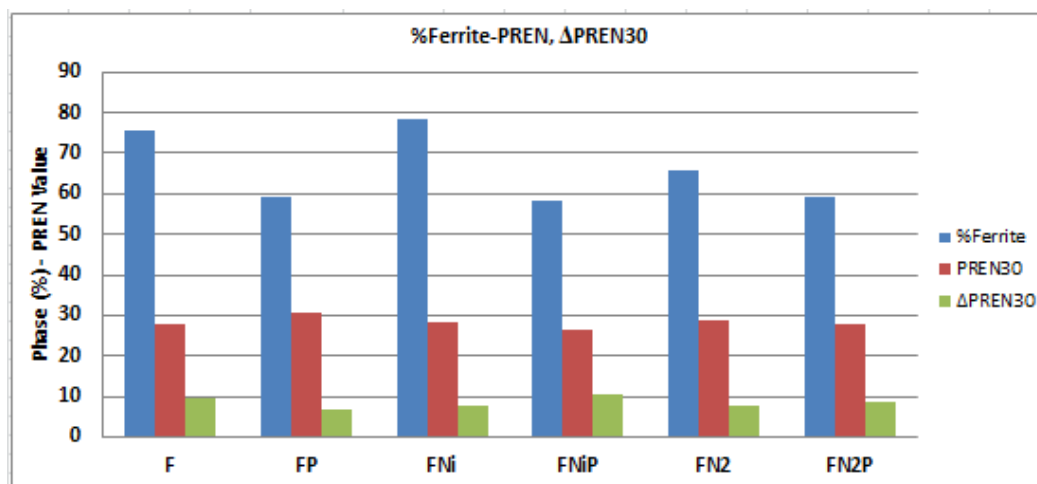


Fig. 3-35. Comparison of percentage of ferrite phase with PREN and Δ PREN

3.2.6. Formation and morphology of the Pits

To observe the position of pits in the microstructure, metallography investigation was performed. It shows that all the pits initiate and propagate in ferrite phase and grain boundary of ferrite and austenite, which is agree with results of Siow et al.[153]. Fig. 3-36 to Fig. 3-39, indicates the morphology and position of the pits in some selected samples before and after etching. It is clear that, after the test austenite lathes remain in microstructure, while ferrite was dissolved, which could be due to higher pitting corrosion resistance of austenite compare to ferrite. Also, all the pits initiate and propagate in the heat affected zone close to the base metal. It means HAZ is more susceptible to corrosion resistance and fusion zone remain unaffected.

For the sample with addition of nitrogen, due to existing high amount of austenite phase, mainly fusion zone and HAZ remain safe and just base metal was affected by pitting. Considering the nitrogen enriched in austenite, it can be concluded that austenite grains in HAZ and FZ were more resistant to the pitting compare with ferritic matrix. Nitrogen has high diffusivity but low solubility in ferrite phase, In case of increasing the amount of ferrite phase, during cooling super saturation of nitrogen occur and it can be precipitated as chromium nitride [264]. The presence of precipitation of Cr_2N causes to decrease the corrosion resistance. The amount of this phase should be minimum by addition of austenite former elements. By adding nitrogen to the shielding gas during GTAW process, mainly the corrosion resistance of the area increase [126,131]. The low pitting corrosion resistance of the heat affected zone, is mainly due to decrease in corrosion resistance of ferrite grains after welding which showed lower chromium content and depletion of chromium compare to ferrite grains in base material [265].

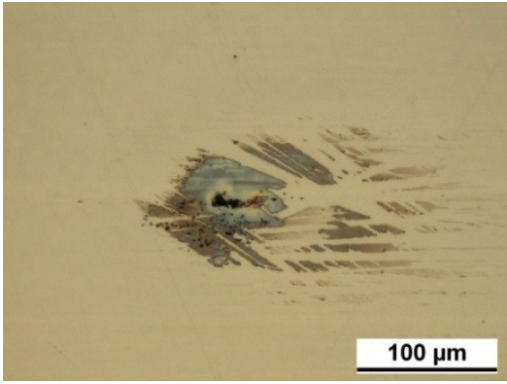
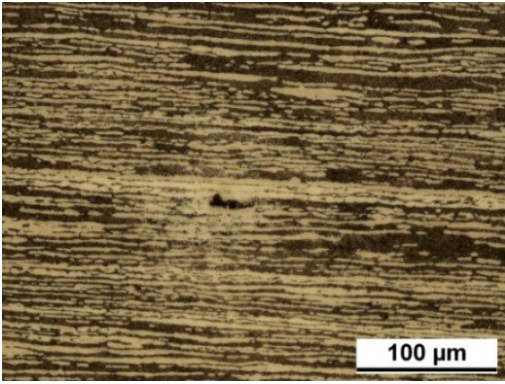
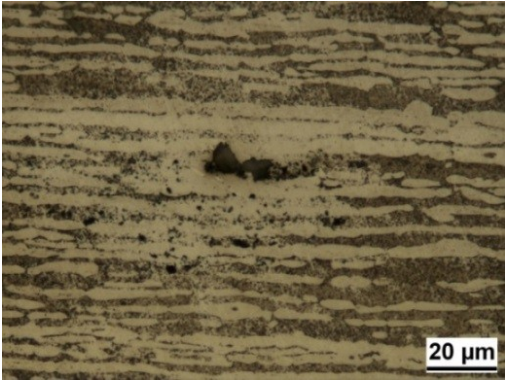
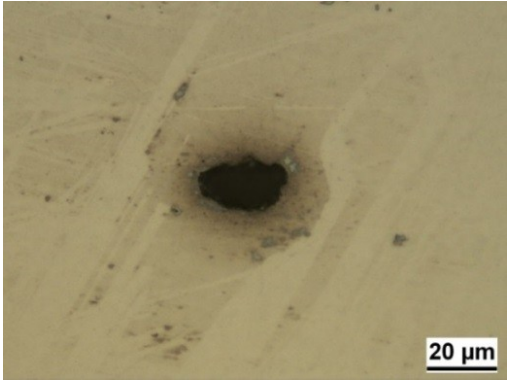
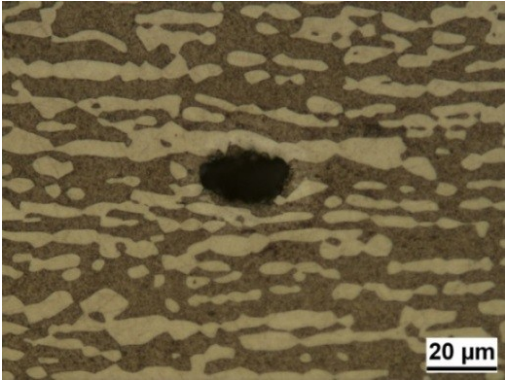
Sample	Pitting position	Morphology of pitting after the test	Microstructure and morphology of pitting after etching
BM	Ferrite phase		 
BMP	Ferrite phase		

Fig. 3-36. Morphology and position of pits in the samples BM and BMP

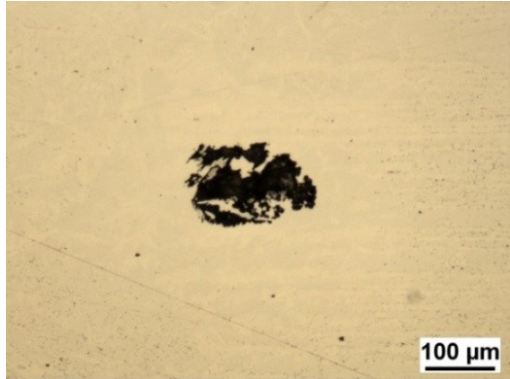
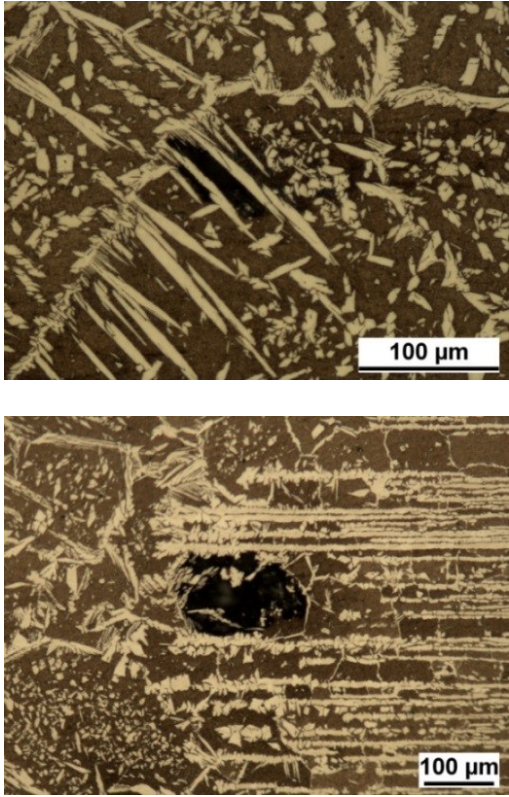
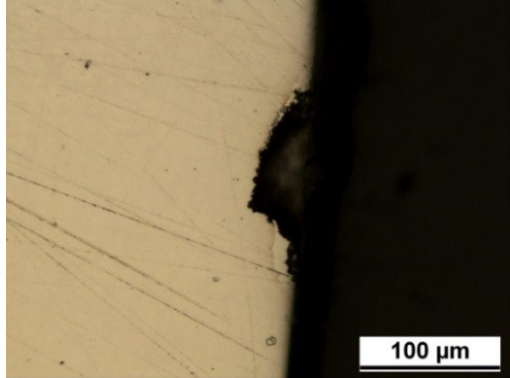
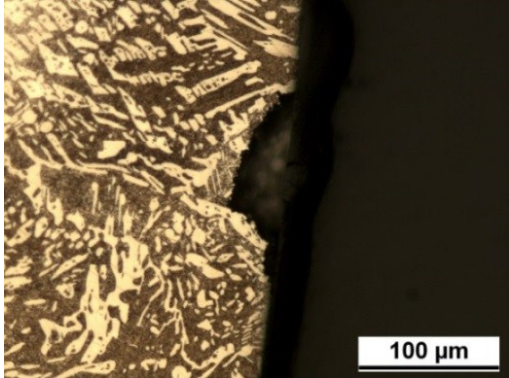
Sample	Pitting Position	Morphology of pitting after the test	Microstructure and morphology of pitting after etching
F	HAZ Ferrite		
FP	HAZ Ferrite		

Fig. 3-37. Morphology and position of pits in the samples F and FP

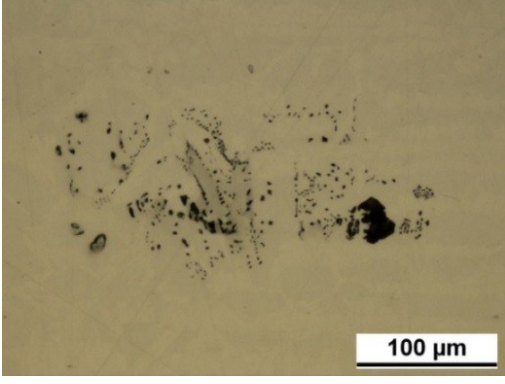
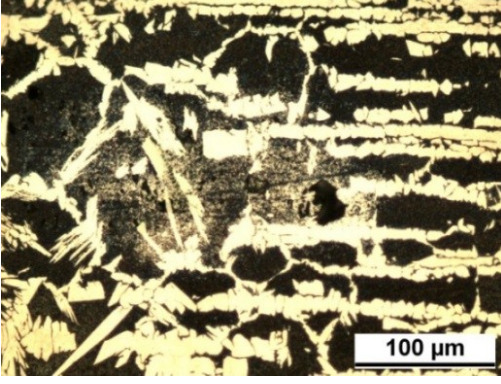
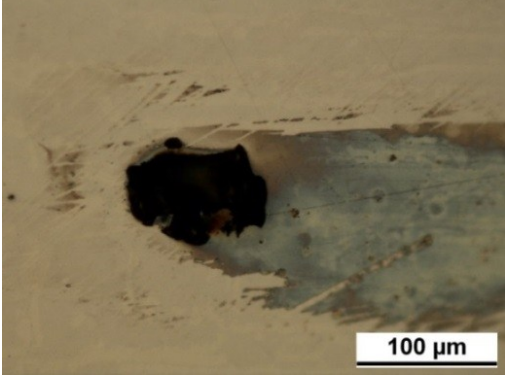
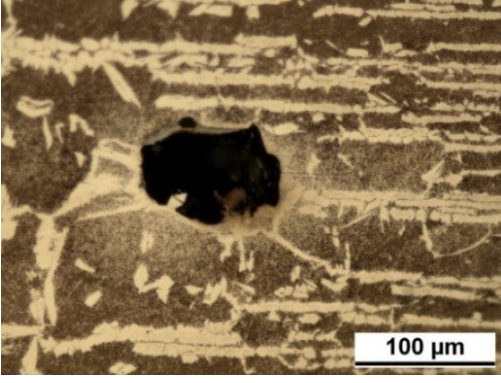
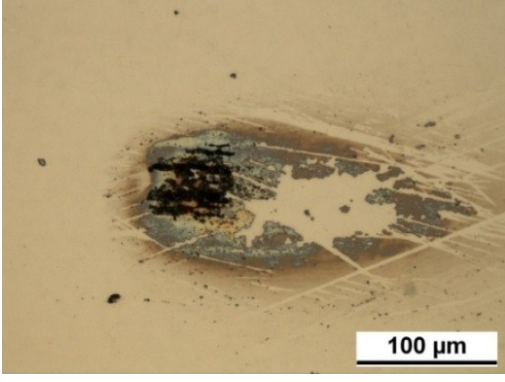
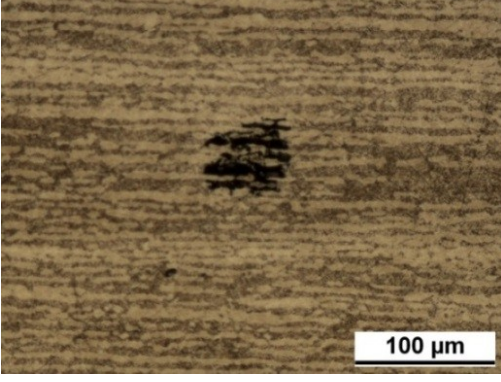

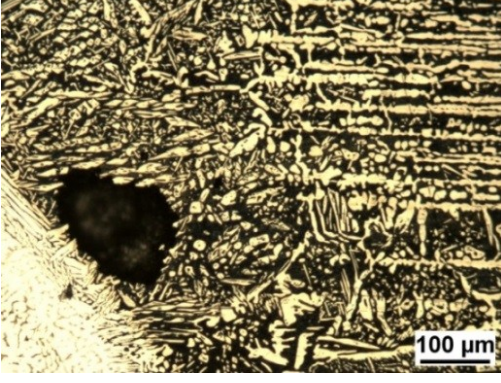
Sample	Pitting position	Morphology of pitting after the test	Microstructure and morphology of pitting after etching
FNi	HAZ/BM Ferrite		
			
FNiP	HAZ/BM Ferrite		
			

Fig. 3-38. Morphology and position of pits in the samples FNi and FNiP

As it is obvious, pit initiation and growth were mainly occurred in ferrite phase. Also, pits formed in the weld metal tend to grow wider and deeper, also existing the austenite phase is important to arrest the pit propagation. In the weld containing high level of nitrogen and consequently austenite phase, mainly pits were not appear. Due to partitioning effect diffusion and dissolution is higher in austenite and it could be the reason for higher pitting corrosion resistance of the weld metal with higher amount of austenite [205].

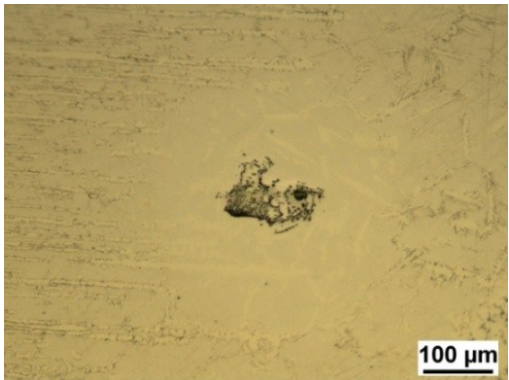
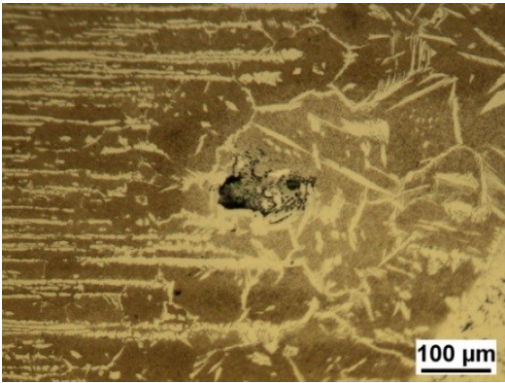
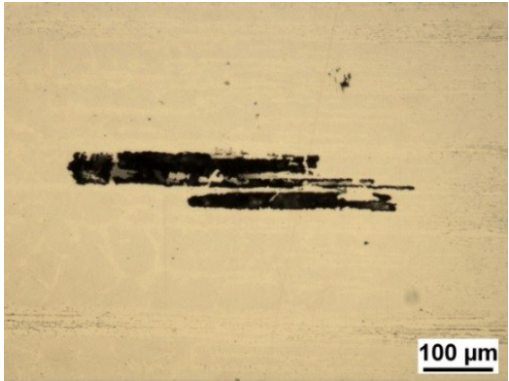
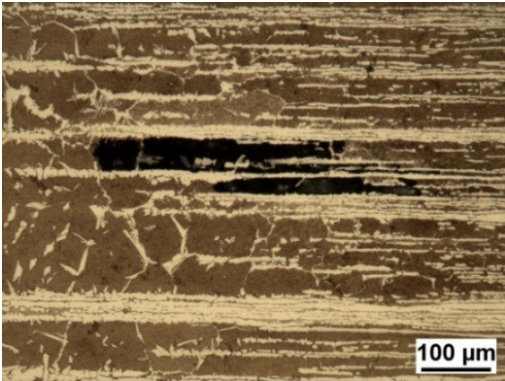
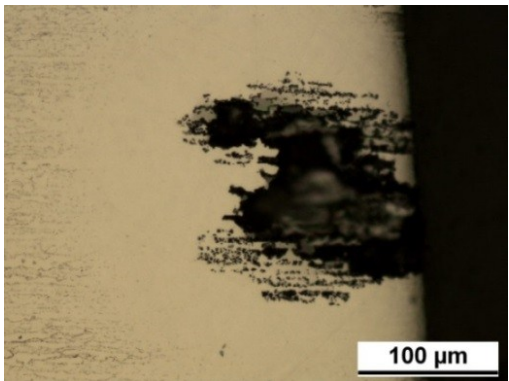
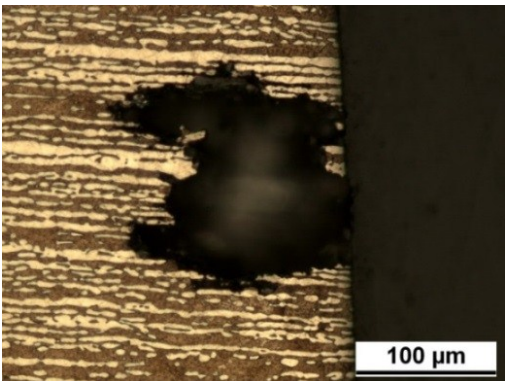
Sample	Pitting position	Morphology of pitting after the test	Microstructure and morphology of pitting after etching
FN2	HAZ/ BM Ferrite		
			
FN2P	BM Ferrite		

Fig. 3-39. Morphology and position of pits in the samples FN2 and FN2P

3.3. Conclusions

In this chapter, pitting corrosion behavior of lean duplex stainless steel UNS S32304 which was welded by addition of nickel powder, nitrogen gas and applying PWHT with considering the PREN value of both ferrite and austenite phases, was investigated. After, characterization of the samples, the following conclusions can be obtained:

- In all samples, pitting occurs in HAZ, which means fusion zone is not susceptible to pitting compare to HAZ. This could be due to different chemical composition of the filler and base metal.
- Ferrite phase due to lower amount of PREN value is much more susceptible to local pitting corrosion compare to austenite.
- Pits mainly initiate and propagate in the ferrite phase and ferrite austenite grain boundaries and grow inside of the austenite phase which cause to arrest the pit, which could be due to partitioning effect of nitrogen during welding.
- In all samples, after PWHT, the pitting corrosion resistance increase, which could be due to uniform distribution of alloying elements in both phases.
- The corrosion resistance of duplex stainless steels is mainly determined by corrosion resistance of weaker phase rather than bulk material.
- In duplex stainless steels, molybdenum and chromium are rich in ferrite while nitrogen and nickel are more in austenite.
- In the sample with addition of nitrogen, detrimental chromium nitride (Cr_2N) was formed in both grain boundaries and inside of the ferrite phase both in fusion zone and HAZ.
- Generally, it was found that effect of PWHT on pitting corrosion is much more than addition of alloying elements.
- To find exact relation between PREN value and pitting corrosion resistance, in addition to the effect of main alloying elements such as nickel, chromium, molybdenum and nitrogen, effect of trace elements such as phosphorous, sulphur, copper and binary or ternary synergy effects of the elements should be considered. Our results showed that there is not specific relation between PREN value and pitting potentials such as results of other researchers.
- The localized pitting occurred preferentially in ferrite phase, and it could be explained by redistribution different alloying elements in both ferrite and austenite phase.

Chapter 4: Literature review of hardfacing by PTA process and methods for surface evaluations

Abstract

This chapter of the thesis contains literature review and equipment descriptions of the two chapters which follow. It considers PTA hardfacing optimization and effect of addition of WC nanoparticles on the mechanical properties of the hardfaced layer. A brief description of hardfacing methods especially plasma transferred arc (PTA) is given and the process explained. Then some characteristics of the plasma transferred arc process are discussed followed by comparison with other welding methods such as GTAW and PAW. Then characteristics of tool steels specially cold work D2 steel are explained. The use of different types of powder in plasma transferred arc process, characterization of nickel-chromium-boron-silicon powder followed by tungsten carbide particles is discussed. The design of experiment for optimization of the process is important and a brief description of the DoE method is discussed. The aim of the following two chapters is to discuss a literature review to investigate what other researchers have done to optimize the PTA process for hardfacing of the steels and the effect of addition of tungsten carbide in both micro size and nano size on the mechanical properties of the layer. Also the effect of dissolution of WC particles in nickel base matrix is discussed. Because of high applications of weld overlays to increase wear resistance of the steels, definition of the wear, relevant wear mechanisms and wear testing (pin-on-disk) are explained. At the end of this chapter, I considered the implications of using different types of equipments for characterization of the weld overlay such as scanning electron microscopy (SEM), energy dispersive spectroscopy (EDS), X-ray diffraction (XRD), tribometer for wear test and 3D non-contact profilometer, small description about each equipment is discussed.

Keywords: Hardfacing, PTA process, Nickel base powder, tool steel, design of experiment (DOE), response surface method.

4.1. Hardfacing

Hardfacing is used to apply thick hard, protective and wear resistance layer specially by welding methods to enhance surface properties of the metallic component. Hardfacing alloys with weld deposition, is commonly used to increase tribological behavior, wear and corrosion resistance of industrial components which are working in harsh situations with high contact stress, abrasion, erosion or pitting and corrosion [266,267].

Thermal spraying is preferable hardfacing method to reach hardfacing with minimum distortion and accurate process control. General materials which applied with this method consists of cermet and other ceramic base coatings such as alumina, tungsten carbide and NiCrBSiC based coatings. In these methods the thickness is limited to 0.3mm. In comparison, weld hardfacing can be used for applying thick coating between 1 to 10mm. different welding methods such as GMAW, GTAW, SAW and PTA can be applied. Also in this method different types of coatings such as cobalt base alloy, martensitic and WC-Co cementite carbides can be used. But in this case mainly after applying the layer, it is necessary to perform surface finish treatment.

Nickel based alloys have gained much attention in recent years owing to their excellent performance under conditions of wear, abrasion and corrosion [268], especially at elevated temperatures with relatively low cost [269]. Conventional weld hardfacing is done by oxyfuel welding, gas tungsten arc welding, GMAW. Different hardfacing processes cause to reach different solidification and solid state phase transformation behavior [270]. By development of new methods such as electric arc, plasma and laser more development was achieved. Fig. 4-1, indicates different types of hardfacing methods which can be used for different application.

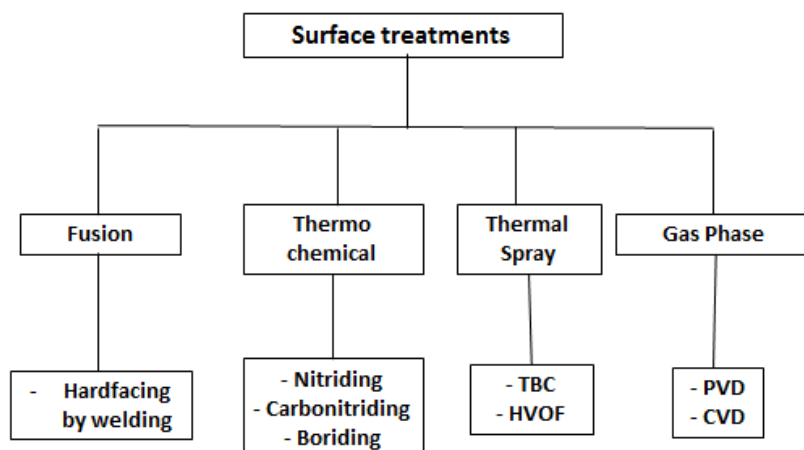


Fig. 4-1. Different types of hardfacing methods

4.2. Plasma transferred arc (PTA) process

Plasma consists neutral particles, ion and electrons in high temperature. The formation of plasma is due to ionization of portion of the plasma gas. In plasma, atoms ionized. Plasma arc welding is kind of gas shielded arc welding process, which fusion of metal is achieved by heat transfer between electron tungsten and base material, because of that there is similarities between Plasma can be considered as advanced Gas Tungsten Arc welding (GTAW) process. The concentration of the arc achieved by copper alloy nozzle and the arc column become collimated. This process can be done with or without using the filler metal based on using melt in and key hole mode. In key hole process, the base metal, arc penetrate to all thickness and form the keyhole through the thickness. In this process the molten weld metal circulate the arc and solidifies behind the key hole[192]. Plasma Transferred Arc (PTA) welding has been used since 1962 for surfacing part, the main application is for hardfacing against extreme harsh conditions such as heat, wear, abrasion and corrosion. Transformation of gas into plasma needs energy and ionization level increases according to temperature range from 6000 to 20000 °C. Plasma is mainly result of gas ionization, it is mainly composed of positive ions and free negative electrons.

Ionized condition enable to conduct current and it focused through the torch nozzle. It works as a source of energy for welding and cutting. Torch of plasma welding works with two different pilot and main arc which each one of them powered from a dedicated power source. The pilot arc is between the cathodic tungsten electrode and anodic copper nozzle. It is ignited with the high frequency voltage and its purpose is to ionize the plasma gas and promote the ignition of the main arc. The main arc is formed between the tungsten electrode and the anodic work piece. In this process, filler material is supplied to the process in form of powder, rod, wire by means of powder feeder and is transported internally through the torch via a carrier gas by specially designed powder feeder, also there is possibility of adding powder externally and manually. This allows using wide range selection of coatings [271,272]. The main parameters can be specified as arte of added powder material, shielding, plasma and carrier gas flow rate, current, travel speed and nozzle to workpiece distance. The weld pool protected by a shielding gas from oxidation. PTA can produce a layer which has strong metallurgical bond with substrate and can work at high temperature with saving the oxidation, corrosion and wear properties. In PTA method, the arc and the weld pool are protected from the oxidizing agents of the atmosphere by an inert or active gas which fed into the shielding gas nozzle at the end of the torch. The cable assembly is fit with all necessary hose and cables connecting elements. Fig. 4-2 indicates schematic figure of the PTA torch.

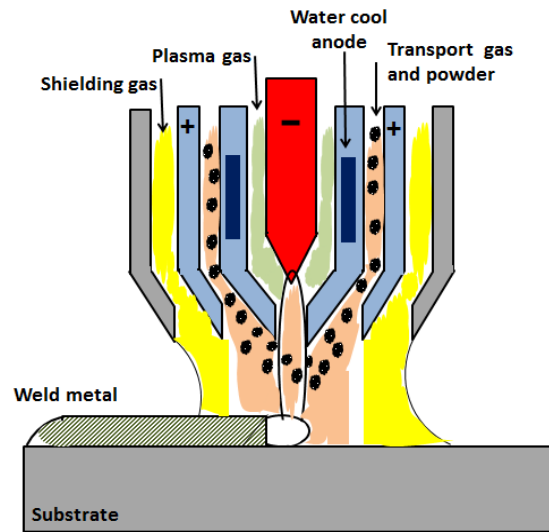


Fig. 4-2. Schematic figure of the PTA process used for deposition of wear resistant overlays

According to the technical data sheet of Ni-WC hardfacing powder, several experiments were previously performed with the aim to optimize the dilution, formability, surface hardness and deposition thickness, as well as to obtain sound and crack free layers. Such conditions are presented in Fig. 4-3 indicates the schematic position of torch on the block for applying the hardfaced layer.

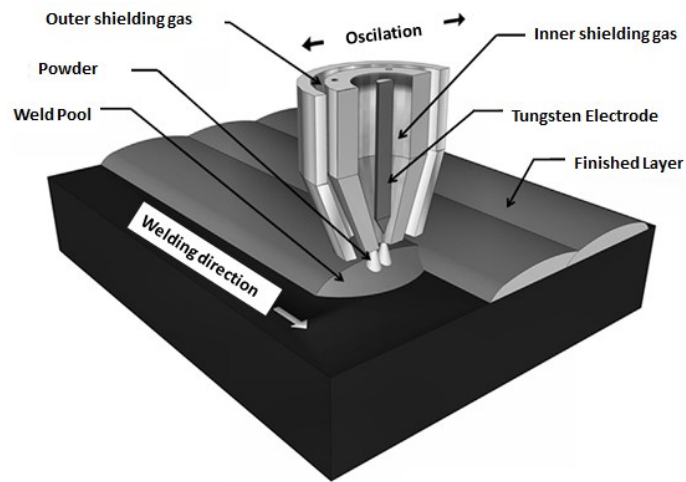


Fig. 4-3. Schematic figure of the PTAW process for deposition of multilayer overlays [273].

4.2.1. Gases for PTA

In PTA process, there are two or three gases which work to carry on operations. The plasma gas is mainly pure argon which is ionized by HF electrical energy and generates the welding plasma. The gas is highly conductive and close the electrical circuit between tungsten electrode and the work piece. The shielding gas enclose the plasma arc and protects the weld pool from the atmosphere. Depends on the base material, weld characterization Ar, He or mixture of these two gases can be used. The carrier gas is mainly used to transfer the powder into the weld pool. For carrier gas, Ar and Ar+H₂ can be used. Also, argon mainly used as inert gas. Helium is an inert shielding gas which can generates hotter weld pool, it has more application for materials with high thermal conductivity. Also, mixture of gases Ar+H₂ is very useful for preventing from oxidation.

4.2.2. Characteristics of PTA process

Some important advantages of PTA process compare to other conventional hardfacing methods can be categorized as following:[271,272]

- Using two independent arc (non-transferred arc as pilot and transferred arc as main)
- Needs less quantity of materials
- Good metallurgical properties
- Accurate metering of metallic powder feedback
- High degree of reproducibility
- Producing smooth deposit which reduce the amount of post weld machining
- High deposition rate
- Low dilution and distortion
- Possibility of wide range of deposits, it can be varied between 0.5mm to 50-60mm
- It can be applied on wide range of materials (steels and super alloys, ceramics, tungsten carbide)
- Limited parameters should be control such as current, voltage, gas flow and welding speed
- It is adaptable for semi or fully automatic manipulation
- Precise method, current can be adjusted even in one Amper DC
- Heavy deposition: possibility to deposit till 10kg powder per hour.
- Possibility of precise controlling the process with numerical control and robotics
- Dilution about one fourth of GTAW, but deposited material is less
- High density bead without porosity, oxidation and inclusions
- Controlled weld bead with relatively low cost, mainly no need to post weld machining
- Possibility of using wider selection of coating compositions
- lower heat input (low distortions), high quality of deposited metal with low dilution
- The divergence of the arc is 20% less than TIG welding.
- The weld depth is two times more than TIG welding.
- Thicker material can be welded in but joint without needing preparation
- The arc of plasma is not sensitive to the edge and weld pool

4.2.3. Comparison between PTAW and PAW and GTAW process

In both processes an inert gas which mainly is argon is uses as plasma gas, which is forced to pass through the orifice of the constrictor nozzle, where the electrode is in fixed position. The shield gas passes through an external opening, concentric to the nozzle which cause to protect the weld from contaminations. Also, in PTA process a carrier gas is used to transport the filler materials through flexible tube to the nozzle which allows to enter into the plasma arc. An electronic igniter provides voltage peak between the tungsten electrode and nozzle, which called pilot arc which forms a pathway of low electrical resistance between the tungsten electrode and the workpiece to be welded. Fig. 4-4 and Fig. 4-5 indicate the comparison between torch of PTAW with PAW and GTAW respectively. As it is clear the arc width in PTA process is much less than TIG welding.

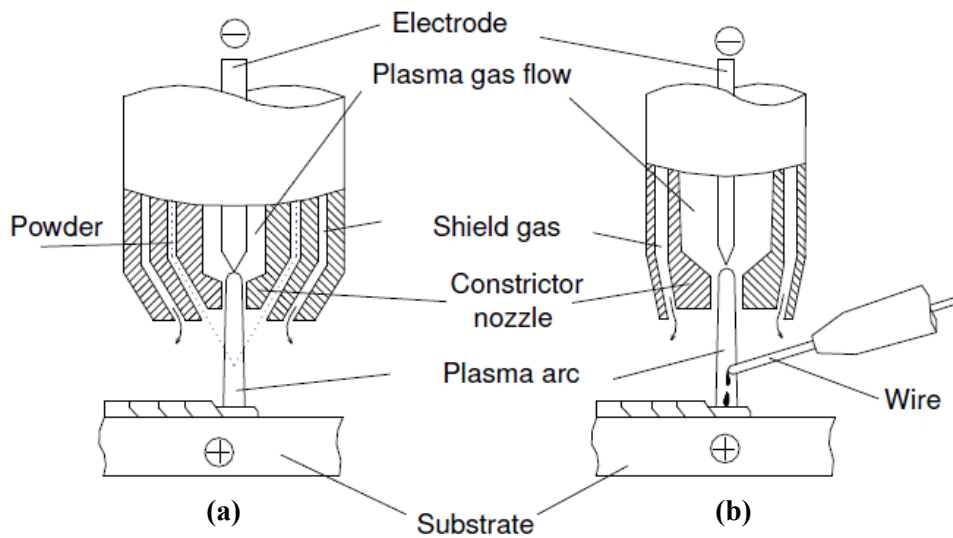


Fig. 4-4. Comparison between torch of (a) PTAW and (b) PAW [274]

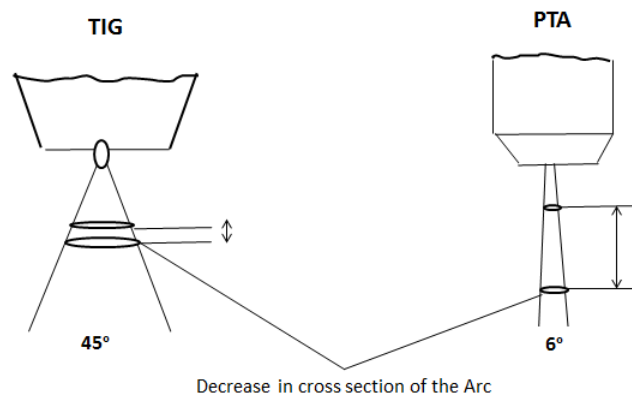


Fig. 4-5. Schematic differences between torch of GTAW and PTAW

Applying powder in plasma transferred arc (PTA) allows to reach homogeneous refined microstructure, low distortion and dilution, which cause to enhanced surface properties when compared to hardfaced deposits processed with other welding techniques [274]. PTA process is preferred on many occasions due to its better process control, ease of use, high deposition rate and lower heat input. In this method, thin deposition of different powder by controlling the feeding rate is possible. Also, this method has more advantageous such as high productivity and ability to automation for weld overlay applications [275]. In addition in PTA process, welding efficiency and dilution can keep in minimum level [276], consequently the chemical composition of the layer can be more close to the deposited powder [277]. Some researches had been directed towards the study of the impact of process parameters on microstructure [278] and mechanical properties of the weld bead [279], and the effect of PTA surface treatment on tool steel before and after heat treatment [280]. Other studies have been conducted on the effect of modification of chemical composition on the hardfacing microstructure. For example the addition of nickel [281] improves the corrosion resistance of steels. Other authors, added tungsten carbide (WC) to the nickel matrix to improve the wear properties [282] and they reached appropriate results.

4.3. Materials

4.3.1. Tools steel

This type of steel mainly refer to the specific types of steel alloys which are particularly suitable to be made into tools. Their appropriate behavior come from their high hardness, resistance to abrasion and deformation. Tool steels are mainly alloyed with different types of carbide forming elements including vanadium, tungsten, molybdenum and chromium. The addition of alloying elements cause to improve hardenability and provide harder and thermally stable carbides. This kind of steels can be categorized in six main groups, which called water hardening, cold work, shock resistance, high speed, hot work and special purpose. Based on the application requirements such as abrasion resistance, high temperature, shock resistance, high corrosion resistance and excessive load appropriate type can be selected. Table. 4-1 indicates different classes of the tools steels with relevant abbreviations.

Table. 4-1. Different types of tool steels

Tool steel code	Class	Attributes
W	Water hardening	-
O, A	Cold work	Oil, Air hardening
D	Cold work	High C high Cr
S	Shock resistance	Shock resistance
H	Hot worked	Cr, W and Mo based
M, T	High speed	Mo- W based
P	Plastic mold	-
L, F	Special purpose	Low alloy, C-W based

4.3.2. Cold work tool steel (D-type)

This type consists of three main groups of oil hardening, air hardening and high carbon-chromium. They have high hardenability and wear resistance. Both types of oil and air hardening reduce the distortion and higher stress and they are less susceptible to crack.

D2 is categorized in the group of cold work tools steel which mainly consists of high carbon, high chromium that has high wear and abrasion resistance in addition to dimension stability in heat treatment. In this steel group, there are other steels such as D3, D4, D5 and D7, but D2 steel has more applications in different industries. Also, in this group, mainly 1.5 to 2.35% carbon with about 10-13% chromium can be detected. D2 steel is an air hardening, high carbon and chrome steel which consists molybdenum and vanadium. These elements allow the steel to have high wear resistance and compressive strength accompanied with good shock resistance. Also, this steel is deep hardened which heat treatment does not have any effect on microstructure changes. A duplex microstructure with relatively coarse complex carbides provide a steel with high wear resistance and good toughness. D2 tool steels are used for long run tooling applications, where wear resistance is important, such as forming dies and thread rolling dies.

Other typical applications of this type of tool steel consist of shear blades, slitting cutters, cold extrusion dies, blanking, forming and forging dies, master tools, die casting and die blocks. Also this type can retain its hardness at high temperatures (425 °C). Nominal chemical composition and physical and mechanical properties of D2 steel is shown in Table. 4-2 and Table. 4-3 respectively. Fig. 4-6, indicates the binary phase diagram of D2 steel, which shows formation of different types of phases with addition of carbon percentage.

Table. 4-2. Nominal chemical composition (wt%) of D2 steel

Element	C	Si	Mn	Cr	Mo	V	Co	Ni	Ni+Cu	Fe
Percentage	1.4-1.6	≤0.6	≤0.6	11.0-13.0	0.7-1.2	≤1.1	≤1.0	≤0.3	≤0.75	Bal.

Table. 4-3. Physical and Mechanical properties of D2 steel

Hardness Vickers (HRC)	Density(Kg/m ³)	Coefficient of thermal expansion	Thermal conductivity (W/m°C)	Module of elasticity (GPa)	Specific heat (J/kg °C)	Melting Point (°C)
748 (60)	7700	(10 -12)*10 ⁻⁶	20	190-210	460	1421
Forging Temp. (°C)	Annealing Temp. (°C)	Hardness after annealing (B)	Hardening		Tempering (°C)	
1010-1093	871-899	217-255	Preheat: 815 °C Hardening Temp: 980-1025°C 15-45 min., Air cool		205-540	

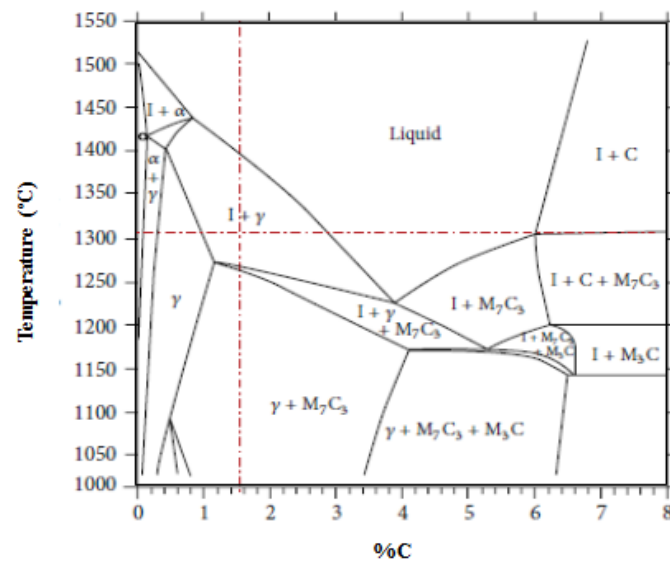


Fig. 4-6. Binary phase diagram of D2 tools steel with increasing the carbon content [283]

Generally, for welding of high carbon and alloy steels, wear resistance and tools steel preheating is suggested. Preheating cause to minimize the distortion and shrinkage of the weld deposit. Also, it causes to reduce the thermal shock of the part. Mainly based on higher amount of carbon and alloying elements, higher preheat temperature is required. Also, preheating cause to retard the cooling rate of the base metal which is helpful to reduce the crack susceptibility.

4.3.3. Powder NiCrBSi-WC

Nickel base matrix powder including chromium, boron and silicon with tungsten carbide overlay are mainly used for wear and corrosion resistance applications such as digging wheel and shovel teeth. This overlay consists of nickel matrix with combination of chromium, boron, and silicon addition and reinforced by monocrystalline WC or eutectoid W_2C/WC carbides. The addition of silicon and boron to the nickel matrix cause to formation of silicide and borides with hardness of 500-860 HV. The feeder powder is a mixture of spherical phase of nickel-chromium-silicon alloy with agglomerated tungsten carbide particles, containing 40% vol. of Ni-Cr-Si alloy matrix and 60% vol of mono tungsten carbide.

In addition, existing chromium in matrix cause to formation of hard chromium carbides. It causes to increase dissolution of tungsten during welding. It is due to higher affinity of chromium for carbon than tungsten at high temperatures [284] NiCrBSi, powder mainly used for fabrication of the wear and corrosion resistance. Gruzdy et al. [266] investigated the effect of adding WC-Co to the NiCrBSi powder and they found the hardness of the coating two times more than base metal. Ni-WC hardfacing alloy was used as feeder powder in a PTA process.

4.3.4. Tungsten carbide particles

Tungsten metal belongs to Group VIB of the periodic table of elements. Tungsten is a refractory metal which characterized by its high melting point (3420 °C), high density (19.3 g/cm³), low coefficient of thermal expansion and high mechanical properties at elevated temperatures, these appropriate behaviors cause to makes it suitable for engineering applications such as lighting filaments, heating source, electronic devices, sport and military facilities.

Tungsten carbide is strong acid resistance, it has high hardness and elastic modulus. Also it can be used for production of nanocrystalline and superfine alloys. In addition, it has many applications for hardface abrasion resistant spraying and petrochemical catalyst, cutting and mining tools, nanocomposites, wear, corrosion and abrasion parts. This kind of powders should be sealed in vacuum and stored in cool and dry conditions, also it should not be under stress [285]. Fig. 4-7, depicts binary phase diagram of tungsten and carbon which consists of different phases.

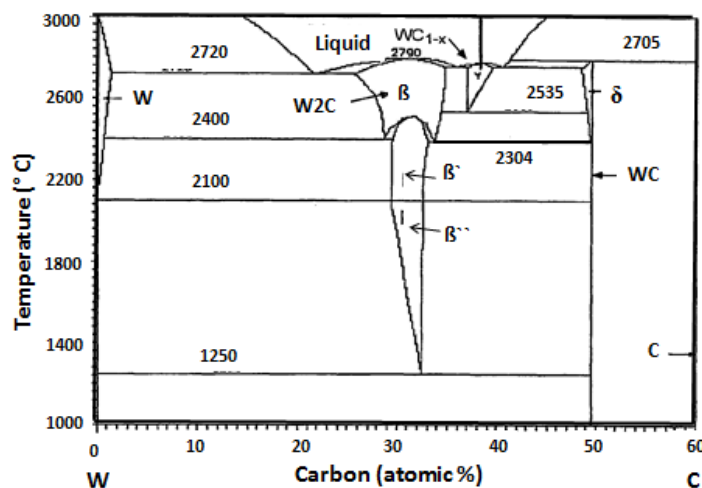


Fig. 4-7. WC binary phase diagram [286]

In many references, different types of carbides added to the nickel matrix. Table. 4-4 shows selected properties of different types of carbides.

Table. 4-4. Comparison of different types of carbides [273]

Carbide type	Hardness (HV)	Density (Kg/m ³)	Melting point (°C)
B ₄ C	3670	2500	2450
TiC	3000	4900	3100
W ₂ C	3100	17200	2785
VC	2900	5700	2700
NbC	2000	7800	3600
WC	2200	15700	2870
Cr ₇ C ₃	1630	6900	1755
Cr ₃ C ₂	1400	6700	1800
Fe ₃ C	1020	7500	1252

Tungsten carbide nanoparticles is combination of carbon with tungsten which can be produced with different methods and it can make two different types of tungsten carbides (WC with 24GPa microhardness and W_2C with microhardness of 30 GPa) [287]. Pure WC does not melt under standard atmospheric conditions, but decomposes into a liquid phase and graphite above a temperature of approximately 2780 °C. The main part of WC which is in hardfacing process consists of cast and crushed eutectoid WC/ W_2C particles with 3.7 to 4.1% carbon. The process of casting and crushing produce angular particles with hardness between 2200 to 2600 HV. Eutectoid carbides are mainly recognizable from other types by W_2C and WC with lamellae microstructure. Macro crystalline WC, is manufactured by carburizing both type carbides at elevated temperature to increase the amount of carbon till 6.1%. It would be suggested that carburizing process perform over casting at higher carbon content due to avoid segregation of carbon and formation of graphite in the carbide microstructure.

It is accepted that the monocrystalline tungsten carbide is more resistant to high temperature dissolution than the eutectoid one, and it has lower hardness (1200-2100 HV). Eutectoid W_2C /WC and mono crystalline WC mainly are in angular form compare to spheroidal shape. Another new type of carbides consists of eutectic W_2C /WC core surrounded with thin layer of monocrystalline tungsten carbide which can be achieved by partial carburizing at high temperature, this outer layer cause to decrease the effect of dissolution of carbides [288].

Table. 4-5 and Table. 4-6 indicate detail typical chemical composition and some physical properties of the nanocrystalline WC respectively. Combination of tungsten and carbon cause to formation of different phases at different temperatures. Table. 4-7 and Fig. 4-8 indicates specification of commercial tungsten carbide produced by Durum and relevant images respectively. In that figure, FTC means fused tungsten carbide and SFTC means spheroidized tungsten carbide.

Table. 4-5. Analysis (wt%) of tungsten carbide nanoparticles (WC)

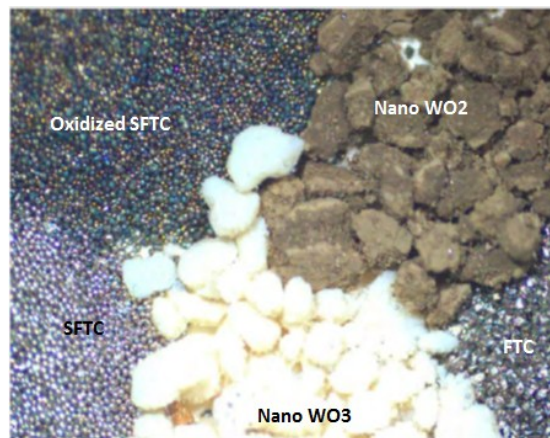
WC	Molecular Weight	Total Carbon	Free Carbon	O	As	Bi	Ca	Cd
99.95	195.86	6.13-6.18	0.05	0.05	0.001	0.0003	0.0015	0.0005
Cr	Cu	Fe	K	Mn	Na	Mo	P	Pb
0.005	0.0003	0.015	0.002	0.001	0.002	0.003	0.001	0.0003
Sb	Si	Sn	Ti	V	Ni	Co	S	Al
0.0005	0.0015	0.0003	0.001	0.001	0.005	0.01	0.001	0.001

Table. 4-6. Physical properties of the WC nanoparticles

Crystal	Density	Melting	Boiling	Color	Size (nm)	Purity (%)
Hexagonal	15.63 g/cm ³	2870 °C	6000 °C	Grey black	30-100	99.95

Table. 4-7. characterization of commercial WC [289]

Carbide type	% C	Composition	Hardness (HV _{0.1})
WC	6.1	-	2000-2400
W ₂ C	3.2	-	Very brittle
FTC (fused tungsten carbide)	3.8-4.1	20-22%WC 78-80%W ₂ C	2200-2500
SFTC (spherical FTC)			3000

**Fig. 4-8.** Different types of tungsten carbides [289]

4.4. Design of Experiment- Response surface methodology (RSM)

Design of experiment is concerned with the planning and conduct of experiments to analyze the resulting data, due to that valid conclusion can be obtained. It is often replicated to obtain accurate estimates of the effects of the input variables on the response variables. With considering various parameters in plasma transferred arc welding, finding the optimum values are not easy. Consequently, in this research, response surface methodology (RSM) which is combination of statistics and mathematical method and can be employed to determine a relationship between input process parameters and output response. The main use of this method is to analysis and modeling of the problems to find optimum combination of process parameters. In this study, a standard RSM design which called central composite design (CCD) has been created which consists of factorial points (cube points), axial points (star points) and central points [290]. In PTA process, there are many variable parameters which have an effect on surface layer quality. Generally, current (A), travel speed (S) and preheat (T), each with five levels, were considered in this work based on the technical specification of the commercial powder. The reason for choosing pre heat as variable, was because the high carbon and high chromium percentage in D2 steel is very sensitive to crack during welding.

The upper limit of the factor was considered as +1.682 (X_{max}) and its lower limit -1.682 (X_{min}), the intermediate levels can be found as $X_i = 1.682[(2X - (X_{max} + X_{min})) / (X_{max} - X_{min})]$. The design matrix chosen to perform the experiment was a central composite rotatable design. This method is useful in response surface methodology, which is a collection of statistical and mathematical methods for analyzing and modeling of engineering issues, for building a quadratic model for response variables without needing to run complete factorial level. For three factors and five levels, the required numbers of experimental runs are equal to $N = 2^3 = 8$ factorials with added six center points and six star points at distance of 1.682 units from the center points, consequently twenty runs ($8 + 6 + 6 = 20$) are required [290]. Based on design of experiment method, the first eight runs related to the factorial portion, runs nine to fourteen correspond to axial portion final six runs related to the center point portion. The experimental runs were conducted randomly to avoid any systematic error into the system.

4.4.1. Mathematical modeling and effect of process parameters

The objective of this research is to find relationships between process parameters and obtained responses in PTA welding process by using the statistical regression analysis carried out on the responses obtained from design of experiment (DOE). The most important parameters for PTA are current and welding speed also due to characteristic of the base metal, also preheat was considered as a variable. As explained in previous part and using response surface methodology, with combination of parameters twenty runs was performed.

Different regression functions are fitted to obtained data. This model can present accurate model for PTA process. As a result in this research, sufficient various of functions have been evaluated by using Analysis of variance (ANOVA) technique. The model checks the test for importance of regression model and test for obtaining the appropriate coefficients [291,292]. The responses function (dilution, penetration and reinforcement) representing weld bead dimensions of one layer which is affected by value of current (I), travel speed (S) and pre heat (T), can be written as followed [290]

Y is the response or Yield which is shown in equation (1)

$$Y = f(I, S, T) \quad (1)$$

the second order polynomial (regression) equation used to represent the response surface for K factors is given by equation (2)

$$Y = b_0 + \sum_{i=1}^k b_i X_i + \sum_{\substack{i=1 \\ i \neq j}}^k b_{ii} x_i^2 + \sum_{i,j=1}^k b_{ij} X_i X_j \quad (2)$$

For three factors, the selected polynomial could be specified as equation (3) and (4)

$$Y = \beta_0 + \beta_1 x_1 + \beta_2 x_2 \quad (3)$$

$$Y = (b_0 + b_i X_i + b_{ii} X_i^2 + b_{ij} X_i X_j) \quad (4)$$

Where b_0 is the free term of the regression equation. The coefficient b_1, b_2, \dots, b_k , are linear terms. $b_{11}, b_{22}, \dots, b_{kk}$ are Quadratic term interaction terms. The coefficient $b_{12}, b_{13}, \dots, b_{k-1,k}$ are interaction terms. For three factors the selected polynomial could be expressed as equation (5)

$$(5)$$

$$Y = b_0 + b_1 * (I) + b_2 * (S) + b_3 * (T) + b_{11} * (I)^2 + b_{22} (S)^2 + b_{33} (T)^2 + b_{12} (I * S) + b_{13} (I * T) + b_{23} (S * T)$$

The value of coefficient this polynomial were calculated by regression analysis with Minitab software. Also, the less important coefficient did not consider.

The second order polynomial (regression equation) used to represent the response surface for K factors which is given by Minitab to determine important coefficients. The final mathematical modeling for each response was determined by regression analysis as following. The adequacies of the models were tested using the analysis of variance technique (*ANOVA*) to study the effect of input parameters on weld bead geometry and properties.

According to this technique, if the calculated value of the F-ratio of the model exceeds the standard tabulated value of F-ratio for desired level of confidence (P-value α is less than 0.05 or 95% confidence level), then the model may be considered appropriate within the confidence limit. It showed that the quadratic model is the best suggested model. The final models were developed using only these significant coefficients.

The squared multiple R value and standard error of estimate of the full models and the reduced models are better than the full models. The adjusted square multiple R-value are improved for reduced the models.

The final mathematical models determined by the above analysis are represented in coded and natural form. To find the bead geometry, the input parameters are to be substituted in coded value for the mathematical equation in coded form. Also actual values are to be substituted in natural form. Both coded and natural form can be used to find the bead geometry. Calculations are simplified by coding.

The range of parameters in actual units are simplified between the limits of -1.682 and +1.682 which are dimensionless [293].

4.5. Wear of the materials

Different industries always deals with the problem of wear on parts in service. Generally each parts of the components that is moving in service will be subjected to wear at the contact point with other parts. The repeated action cause to failure of the sample surface which should be replaced after specific time of working. There are different definitions for wear, one is the result of material removal by physical separation due to microfracture by chemical dissolution or by melting at the interface [294] or it can be defined as progressive damage, involving material loss, which occurs on the surface of a component as result of its motion relative to the adjacent working parts. Bayer et al.[295] specified that, wear is not a material properties and it is system response. Generally, wear changes so much even with a relatively small changes in a tribosystems, which is composed of dynamic and environmental parameters in addition to properties of the material. Due to that, so much cost should be spent in this regard. The important issue for researchers is to find the method to increase the surface quality of the materials in order to extend the life of the parts and decrease the frequency of the replacement of different parts of the components.

4.5.1. Wear mechanisms

The wear mechanism can be categorized as adhesive, abrasive, fatigue, and tribochemical or corrosive wear. Adhesive and abrasive wear are the wear modes which generated under plastic contact. If the plastic contact occur between surface of the materials occurs the contact interface has adhesive bonding strength. Also in this mode, there is possibility of diffusion between contact surfaces. In case of contact between sharp materials with the surfaces and creating micro cutting by indent material the wear mechanism is called abrasive. It can be recognized by interlocking contact configuration necessary for cutting. If repeated friction cycle occur during the contact there is possibility of fatigue wear. In case of contact in corrosive media the possibility of tribochemical reaction increase and the wear mechanism become corrosion wear. With comparing to abrasive and adhesive wear, corrosive and fatigue wear can be generated in elastic and plastic contacts. Also, in adhesive, abrasive and fatigue mechanism of removing the material is based on deformation and fracture in the contact regions. Consequently the type of fracture could be ductile or brittle, due to that these types are called mechanical wear. But in corrosive wear, the mechanism is specified by chemical reactions which accompanied with frictional deformation and heating, microfracture and removal of the corrosive products. In some cases, if the material removal is governed by surface melting due to frictional heating or thermal stress, the wear mechanism can call thermal wear [294]. Fig. 4-9 indicates the schematic figure for basic wear mechanisms.

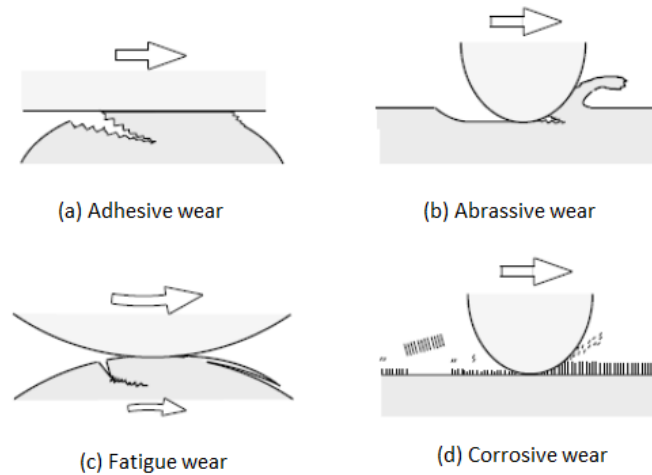


Fig. 4-9. Schematic images of the different wear mechanism [294]

4.5.2. Wear test (Pin on disk) by tribometer

To investigate the wear of the materials, the process should be simply modified in controlled manner. One accepted method in pin on disk test. In this test the sample fixed on a rotating stage and a hard pin come in contact with the sample surface with a known force to create the wear.

Studying about sliding and wear resistance is a field of study for many research groups all over the world. Also there are many parameters which have effect on the sliding wear behavior of materials and coatings.

Fig. 4-10 indicates some important parameters which have effects on the sliding wear behavior. To study wear of the materials, the wear process should be simulated and effect of different samples with the same test condition should be considered. One effective method is pin-on-disk wear test. In this test, the sample is mounted on a rotating stage and a pin come in contact with the sample surface with specific load to perform the wear test. Pin on disk test based on ASTM G99 [296] consists of a rotating disk in contact with a fixed pin with a spherical tip or other shapes, it was originally invented by NASA Lewis research center.

The unit consists of gimbaled arm which pin is attached, a fixture which accommodate disk, there is electronic force gauge for measuring the friction force. A computer should exist for acquiring and saving the data. The machine which used in this test mainly called Tribometer. It is special instrument which designed for precise measurement of the loads. It can be performed in linear and rotating modes. One important feature of this equipment is when the coefficient of friction and distance reach to predefined threshold, the experiment stops automatically. There are some parameters which can be changed during the test such as applied load, unidirectional speed, oscillation frequency, type of gas (vacuum, nitrogen and argon), in addition to temperature in case of existing furnace can be changed. Normal and frictional forces can be measured with transducers. The pin holder is allowed to deflect slightly, the transducer measure the deflection and convert it to a force.

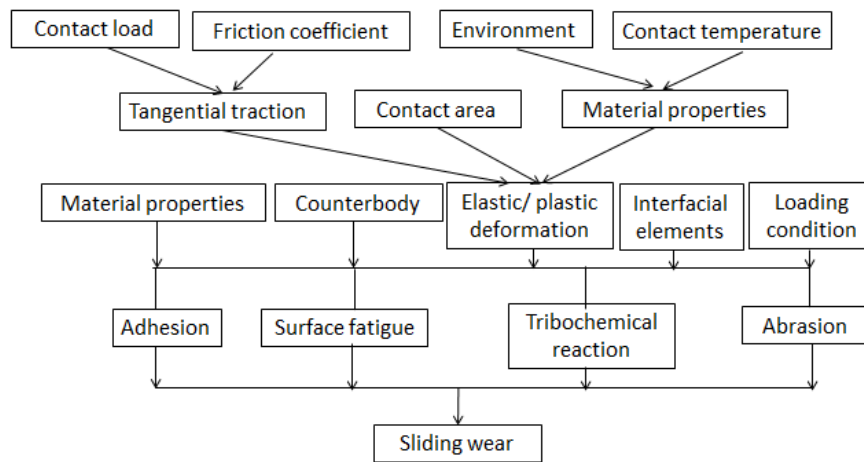


Fig. 4-10. Factors influencing wear during sliding wear [297]

Obtain result of the test is friction coefficient and wear rate which have to be measured. Generally, wear per unit time determine by mass or volume loss. In addition, the debris of the wear can be accumulated for more detailed analysis. Based on the standard, different types of pins with diverse geometries can be used. Also, with using a resistance heating element, the temperature of the test can be reach to 1000 °C. the actual contact of the pin and disk can takes place inside of specific chamber, to keep better the temperature. With this method, coefficient of friction, wear behavior between different materials, wear behavior versus stress and integrity of thin films and coatings can be measured. Also, in pin on disk test, sliding speed, applied pressure, disk and pin material can be changed. In addition, during the test based on requirements different temperatures, atmospheres and lubrication conditions can be applied. Fig. 4-11 shows schematic feature of the pin on disk test. Fig. 4-12 depicts the wear test equipment (CSM instrument) in Cimav which was used in this investigation.

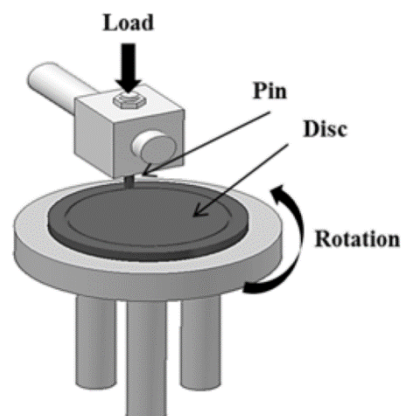


Fig. 4-11. Schematic feature of pin-on-disk test [298]

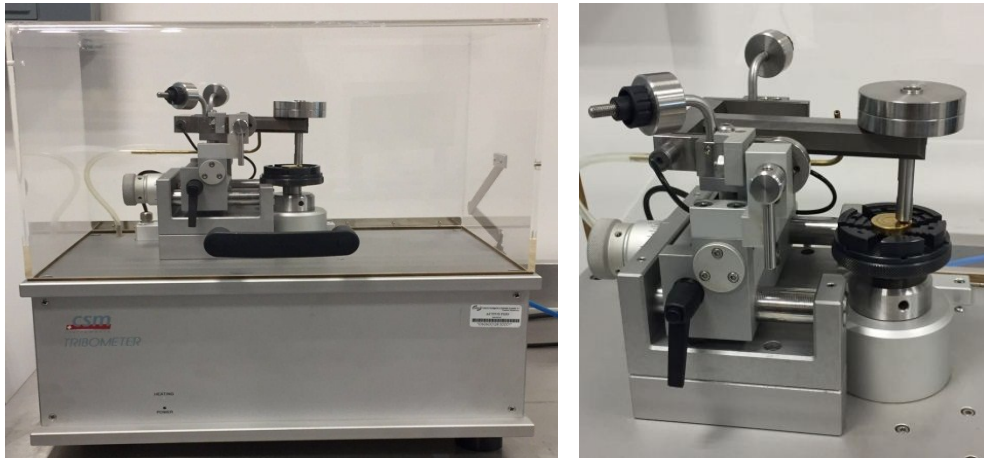


Fig. 4-12. Tribometer in Cimav (CSM instrument)

The temperature during the test was maintained at 26 ± 1 °C with a relative humidity of 30–40 %. Since the wear mass loss values of the samples were inconsistent and the difference between the weight loss was negligible, just the value of volume loss (V) was determined and considered by using a standard test method (ASTM G99-05) [296].

Generally, the volume loss of the pin can be obtained by following formula

$$\text{Pin volume loss} = \frac{\pi(\text{wear scan diameter})^4}{64 (\text{sphere radius})}$$

Assuming that higher hardness of the pin compare to the sample as disk, there was no significant wear on the pin, consequently the volume loss of disk (sample) was determined by using the following equation

$$\text{Disk volume loss } (V) = (\pi R D^3) / 6r \quad (1)$$

Where V is the wear volume (mm^3), R is the rotating radius (mm), D is the wear trace width (mm), and r is the ball radius (mm). Then, the wear rate k is calculated by using the equation given in reference [296,299]:

$$k = V / Lx, \quad (2)$$

Where V is the wear volume (mm^3), L is the applied load (N), x is the sliding distance (m), and k is the wear rate (mm^3/Nm).

4.6. Equipment for surface evaluation

4.6.1. Optical and Scanning Electron Microscopy

Metallography is the investigation of material microstructure by light which reflected from the surface. By adjusting the contrast and brightness on the surface different microstructures can be observed. Series of lenses exist in the microscope which causes reflection of light from the objective to the eye. The strength of this method is easy to use and no need to any special devices. The limitation of optical microscopy is difficulty to have images of small specimens, because microscope resolution is restricted by light wavelength (λ) and angular aperture of objective lens (α). In some references the maximum resolution for optical microscopy specified about 200nm [300].

Electron microscope was invented in 1930s, and development of electron microscope was related to the limitations of optical microscope because of limitation of physics of light, in SEM electron beam is used instead of ray of light. In scanning electron microscope, beam of electrons with high energy produce a different range of signals and focused on the sample surface. Beams usually focus on specific area (5 μm to 1cm) and obtained signal from interaction of electrons with surface consist of many useful information like characterizing of the topography, shape and size of particles (morphology), chemical composition and crystallography information). The magnification of SEM usually is in range of X10 to approximately X500K and 50 to 100nm spatial resolution. Depth of field for optical microscopy and SEM are 0.5mm to 30mm respectively.

High amount of energy exist in SEM accelerated electrons, this energy disintegrate in a range of signals from interaction of incident electron and specimen surface. These signals can produce SEM images from secondary electron, back scatter electron and electron back scatter diffraction. Secondary electron usually used for depicting surface morphology and back scatter electron used for showing contrast in composition of multiphase samples. Also the SEM has ability of finding chemical composition of specific area by EDS system [301].

The secondary electron form from inelastic contact between incident beam and diffracted beam and detected from near surface region. Secondary electrons are relatively low energy electrons, and it can be collected by positioning a positive voltage on the front of detector.

Back scatter electron form from elastic contact between incident and the nuclei of the target atom. Back scatter electron have high energies and cannot be collected like secondary electrons. One suitable detector is surface barrier (semiconducting material) which is located below the objective lens and above the specimen. Main applications of SEM are acquiring chemical analysis and elemental maps, specifying different phases based on atomic number and compositional map based on differences in trace elements. SEM has the ability of accurate measurement of really small objects (50 nm).

The high application of SEM in industry and academic institutions is due to combination of large depth of field, high resolution and magnification, accurate determination of composition and crystallographic information. Fig. 4-13, indicates the image of SEM in Engineering department of the university of Ferrara which was used in this investigation.



Fig. 4-13. Image of the SEM- Zeiss Evo model in ENDIF

4.6.1.1. Advantages and disadvantage of Scanning electron microscope

Scanning electron microscopy (SEM) is one of the best and accurate equipment for high resolution investigation of solid materials. SEM is relatively easy to operate and most of materials need minimum sample surface preparation. Data acquisition in SEM is usually less than 5 minutes for SE, BSE and EDS analysis. Also there is a limitation in size of sample, because sample must be fit into the chamber. Sample should be stable in 10^{-5} - 10^{-6} torr vacuum. EDS system cannot detect very light elements such carbon, nitrogen, hydrogen and helium. EDS system in scanning electron microscope is based on solid state X-ray detector which is really quick and simple to use. The EDS has low sensitivity to low amount of elements and has poor energy resolution in comparison with wavelength dispersive detector [300].

The scanning electron microscopy working procedure is as follows: Filament which is in the top of the electron column heated up to roughly 2400°C , then thermionic emission of electron occurs and streams of electrons produce. This stream is divergent and should be condensed by lens system. There are two condense lenses which first one cause to limit the current of beam and decrease size of high angle electron beams. Second one forms small and fine diameter beams. Between these two lenses there is condenser aperture for eliminating some high angle electrons. After second lens there is another objective aperture which omits some other high angle electrons.

A set of scan coils exist which control the energy of beam and create a magnetic field for beam in the range of microsecond. The final objective lens focuses the beam on to the sample surface. The electron beam strike the sample and diffracted electrons absorbed by detectors, then this information converted to voltage. Before moving the beam to the next stop point, the instrument counts the number of electrons and indicates a point on cathode-ray tube (CRT) and the intensity is specified by this number. Many spots with different intensities cause to formation of sample topography and image on the CRT. Fig. 4-14 shows a schematic interaction of penetrated electron beam in the sample surface and the depth of penetration.

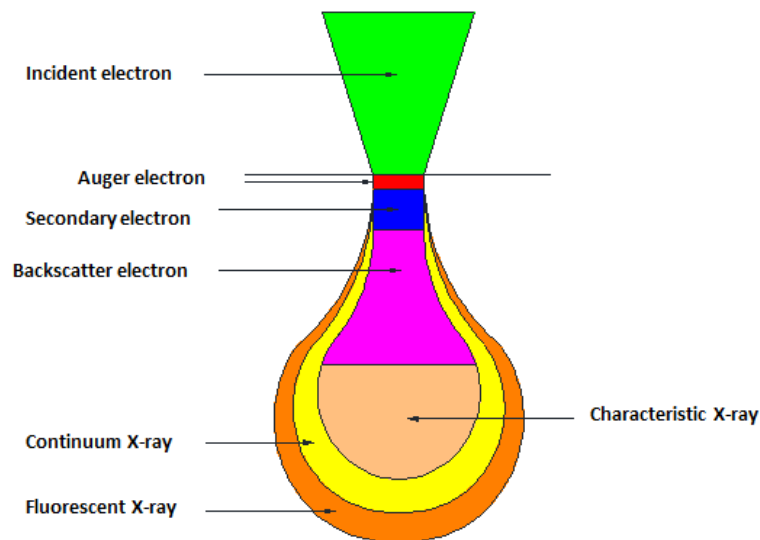


Fig. 4-14. Schematic interaction of penetrated electron beam in the sample surface

The secondary electron form from inelastic contact between incident beam and diffracted beam and detected from inelastic contact between incident and diffracted beam and detected from near surface region. Secondary electrons are relatively low energy electrons, and it can be collected by positioning a positive voltage on the front of detector.

Back scatter electron form from elastic contact between incident and the nuclei of the target atom. Back scatter electron have high energies and cannot be collected like secondary electrons. The position of back scatter detector is perpendicular to the specimen and will detect range of BS electrons in a material proportion of atomic number of elements. One suitable detector is surface barrier (semiconducting material) which is located below the objective lens and above the specimen.

4.6.1.2. EDS in Scanning Electron Microscopy

As mentioned above, scanning electron microscope is used for obtaining very high magnification imaging from the surfaces of different materials. Usually SEM is combining with energy dispersive X-ray spectroscopy (EDS) which is mainly used to find out the material chemical composition. EDS system is appropriate for wide range of materials like paper, metal, plastic and etc. In this research EDS system was used to recognize metal chemical composition of the overlay sample. EDS analysis of metals is easier compare to other materials because of intrinsic conductive behaviour, for other materials specific sample preparation is required. After contacting high energy electron beam to the surface of material, it causes moving out electron from orbits which close to the centre. Then instead of that electron a hole remain in the orbit, some electrons from outer orbits tend to move and fill that vacancy. This action accompanied with energy losses and X-ray photon emission, because of transferring electrons from outer layer to inner layers (N shell to M shell, L shell to K shell,). Elements can be recognized by emitted energy of photons. [302,303]. Fig. 4-15 displays schematically how incident beam act in EDS analysis.

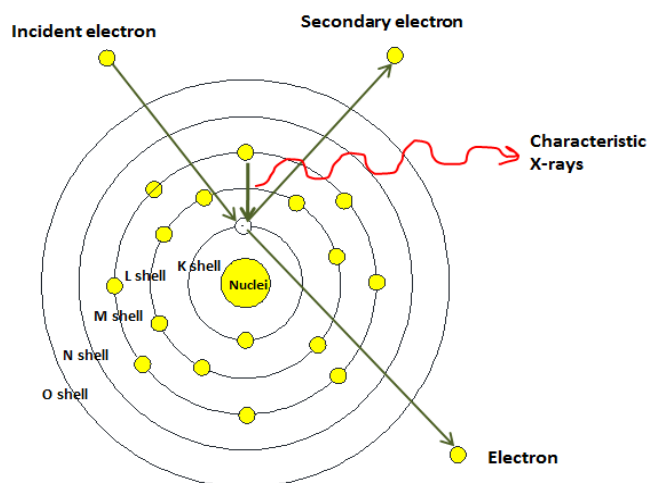


Fig. 4-15. Different layers of electrons and the how incident beam working in EDS analysis

4.6.2. X-ray diffraction analysis

X-ray diffraction is a technique which is used with the aim of determining the crystallographic structure and phase identification of solid crystalline. An ordinary XRD instrument consists of different components such as X-ray source, stage for specimen, receiving optics and detectors. The source and detector with its associated optics lie on the circumference of focusing circle and the sample stage at the center of the circle. The angle between the specimen and source of X-ray is called as Bragg's angle and the angle between the projection of angle and detector is known as 2θ . When a beam of X-ray is incident on the sample, X-rays are scattered by each separated atom [304].

The Bragg's law shows the relationship between the wavelength of the X-ray, the spacing between the atomic planes and the diffraction angle. This can be specified as following:

$$n\lambda = 2d \sin \theta$$

For the first order diffraction $n = 1$, θ and λ can be calculated the inter planar d spacing for specific plane. After recording the X-ray diffraction pattern, the peaks should be recognized which means the correct miller index should be allocated to each peak. In case of dealing with the fine particles, with reduction in the size of particles, the peaks get broader which means the particle size decreases.

The data related to particle size can be obtained from full width at half maximum (FWHM) of the diffraction peaks and can be calculated as following:

$$D = k\lambda / (B \cos \theta)$$

Where D is particle size, λ is X-ray wavelength and B is FWHM of the peak [305].

In this investigation, Bruker AXS D-8 XRD equipment using $\text{CuK}\alpha$ radiation ($\lambda=0.154$ nm) at 40 kV and 20 mA. The XRD spectrum of the specimen was recorded in 2θ range between 10 - 140° with angular step of 0.01° . The analysis of the peaks was performed by Diffrac Plus evaluation software. From the obtained peaks the following information can be drawn:

Peak position identifies the structure and lattice parameter, peak width means size of crystalline, strain and defects, area of each peak or height ratio specifies the preferred orientation and finally peak tails detect diffuse scattering and point defects [304]. Fig. 4-16 indicates the XRD equipment in the chemical engineering department of the University of Ferrara, which was used in this investigation.

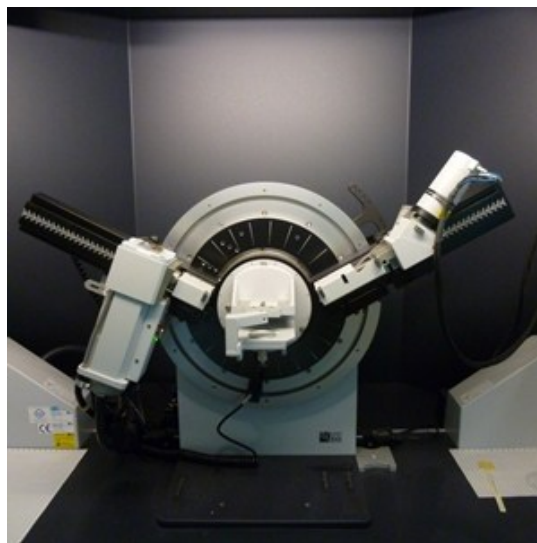


Fig. 4-16. Image of XRD equipment Brucker AXS D-8

4.6.3. Nanoindentation and microhardness

Nanoindentation can be defined as a specific hardness test which can be applied on very small area. It was invented in 1970s and it is the most commonly applied means of testing the mechanical properties of the material. The main aim of nanoindentation testing is to find the elastic modulus and hardness by specifying the indenter load and penetration. The Berkovich indenter normally is used for nanoindentation testing due to its sharper point than the four-sided Vickers hardness which allows more accurate control of the process. The mean contact pressure is usually determined from a measure of the contact depth of penetration. The original Berkovich indenter was designed to have the same ratio of actual surface area to indentation depth as a Vickers indenter [306].

Normally, force and depth of penetration recorded as load and it is applied from zero to maximum level, then from maximum to zero. In case of plastic deformation, there is a residual impression in the surface. The obtained size of indentation in this method is much lower than conventional hardness techniques. The depth of penetration, indicates an indirect measurement of area of contact at maximum load, as a result contact pressure and hardness can be achieved. By removing the load material tends to go back to its original shape just it occurs in limited elastic strain relaxation. Analysis of elastic unloading cause to find the elastic modulus of the material. The typical load-penetration depth curve which mainly obtained in a nanoindentation test is shown in Fig. 4-17.

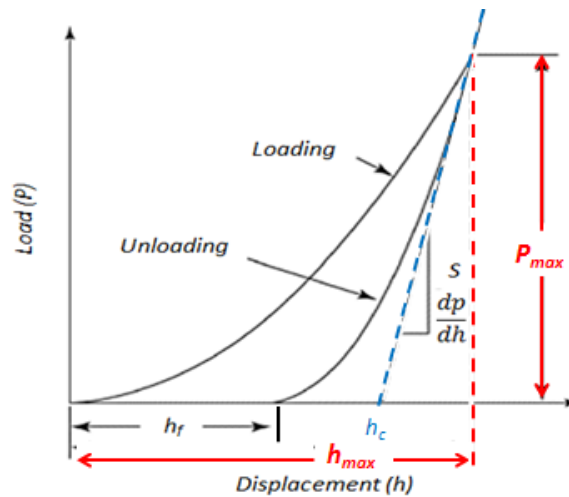


Fig. 4-17. Schematic load-displacement diagram for nanoindentation experiment

In this figure, maximum applied load is P_{max} , and peak indentation depth is denoted by h_{max} and includes elastic and plastic deformation. The depth at which the applied loads become zero on unloading is the final indentation depth is h_f , which represents depth of residual impression this represents the plastic deformation. The slope of the tangent of the load-penetration depth curve during unloading cycle is $S = \left(\frac{dp}{dh}\right)$ which allows measurement of the modulus, the depth h_c , is the contact depth at which the cross section area is taken to calculate the hardness and $h_{max} - h_f$ is the displacement associated with the elastic recovery during unloading [306]. By considering different shapes of the curves, non-linear events such as phase transformations, cracking and film delamination can be identified. In many cases the permanent deformation or residual impression is not the result of plastic flow but may involve phase changes or cracking. Fig. 4-18 indicates the nanoindenter equipment which was used in this study.



Fig. 4-18. Nanoindenter which was used in this study

4.6.4. Surface topography analysis by optical profilometer

The measurement of surface topography become more widespread in different applications. In old systems it is made by means of a mechanical profilometer and the measurement system is based on the vertical displacement of diamond tip in contact with the surface, this method had some disadvantages which come from contact system. But in recent decade optical non-contact system developed to measure the surface topography. In optical profilometry, which is based on a triangulation method, which contain three reference points (A laser diode which is fixed, the point of surface to be analysed and the image of the point which form on the detector plane [307]. In this system white light illuminate the sample and special objective with built in reference mirror used to create interference fringes which appear when the distance between the surface and the reference mirror is matched. The lateral resolution depends on the magnification chosen. Three dimensional surface measurement is used by different industries, in addition to research issues, it cause to improve the fundamental productions. This method was defined in 1991 and developed based on ISO standard to complete existing two dimensional surface measurement [308].

For evaluation of wear tests, standard methods are needed to report volume loss and evaluate the worn surface. Optical profilometer is an appropriate method to measure the volume loss and wear rate of the surfaces which harshly damaged. Also with this method it is possible to identify the surface defects understand the depredation mechanism of the coating. In addition with this method, it is possible to measure small volume loss after sliding wear and increase in volume due to material transfer or accumulation of the coating [309]. It should be mentioned that, in case of identical 2D surface roughness, the 3D topography characteristic of the surface could be more different. 3D non-contact profilometer uses axial chromatic confocal white light source, where light passes through an objective lens.

The refractive index of the objective lens will vary in relation to the wavelength of the light. Every separate wavelength of incident white light will refocus at different height from the surface. When the measurement is in the range of height, monochromatic point focused to wavelength to take an image. Just the focused wavelength will pass through the spatial filter with high efficiency. Diffraction grating can be used for analysis of spectras. This technique deviate each wavelength at a different position, intercepting a line of CCD which in turn shows the position of the maximum intensity and lets direct correspondence to the Z height position [310].

It can measure any type of samples with different size, also due to open staging there is no need for specific sample preparation. This method capable to measure all types of surfaces from high angles and rough surfaces to transparent surface. The non-contact profilometer provides wide range of user friendly abilities to improve understanding of the surface properties specially when wear loss measurement is required. Fig. 4-19 indicates the image of Taylor–Hobson non-contact profilometer which was used in this investigation.

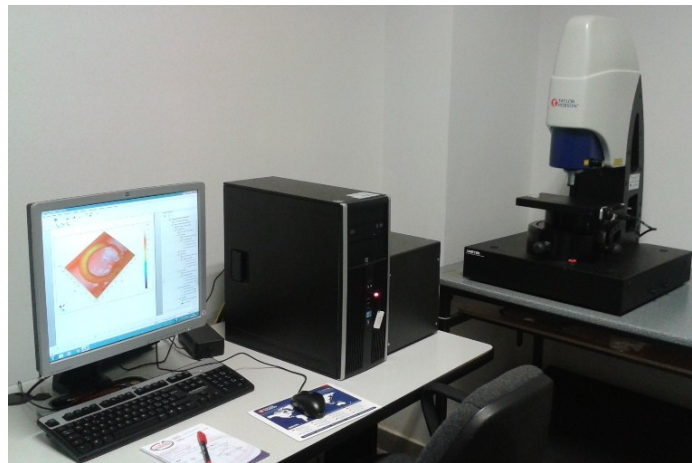


Fig. 4-19. Optical profilometer Taylor- Hobson

Another important information which can be obtained from surface profilometer is calculating the weight loss after wear test. Loss of material due to abrasion, erosion or other types of wear is an important phenomenon in different industries. Wear mainly specified by volume loss measurement after the wear test. Profilometer based on low coherence interferometry can measure the weight loss for different type and size of materials. For measurement of the volume loss, data is collected from the worn surface and the region around it. A reference plane is defined for the intact surface. Volume loss is calculated from the differences between the reference plane and worn surface.

4.6.5. Wear surface analysis by 3D optical profilometer

To observe the surface topography mapping of the worn surfaces, 3D non-contact optical profilometer analysis was performed on all the samples. Profilometer is a strong tool which can quantify the wear depth and volume in addition to evaluate the shape of wear track. The obtained colors specified the depth of surface damage based on the scales.

The 3D topography, average width and depth of wear scars were measured by a 3D surface profilometer. To evaluate the wear resistance of the samples the wear volume V_w and wear rate K can be calculated as following [311].

$$V_w = 2\pi hr (3h^2 + 4b^2)/6b$$

$$K = V_w/PS$$

where h was the wear average depth (μm), b was the wear average width (mm), r was the wear orbital radius (mm), P was the normal load (N) and S was the sliding distance (m).

4.7. Literature review of the previous works

Tungsten carbide is typically used as part of composite overlay mixed with nickel matrix. The wear properties of Ni-WC are based on existing WC. Tungsten carbide have high hardness value and toughness compared to other types of carbides such as titanium carbide, niobium carbide and boron carbide. Dissolution of the WC particles in the matrix cause a decrease in the wear resistance of the layer. It requires deposition of the metal to be performed with the minimum melting temperature. This powder is mainly deposited by PTA or laser beam process due to exceptional heat input control. Ni-WC are consumables which typically exist in NiCrB or NiBSi matrix alloy. The matrix microstructure mainly consists of soft primary nickel microstructure accompanied with interdendritic regions which are comprised of hard boride carbide and silicides in which the hardness and wear resistance of the matrix improved due to presence of interdendritic phases. Fig. 4-20 shows the morphology of the clad layer which consists of eutectoid W_2C/WC and mono-crystalline WC angular cast and crushed particles after deposition.

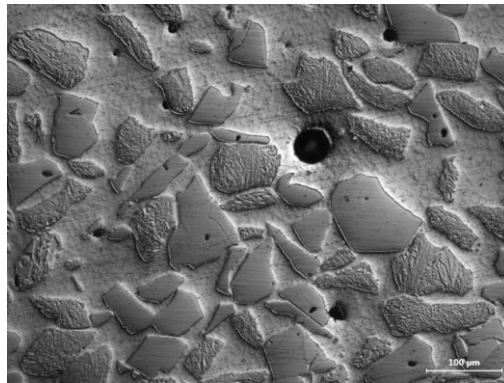


Fig. 4-20. Morphology of WC in the soft matrix after deposition[312]
(Courtesy of Apollo Machine and Welding Ltd)

Addition of boron cause to decrease the melting temperature of the alloy system and increase the temperature range of solidification. Also it causes to form of Ni_3B and decrease the minimum required heat input for fusion of the base metal. The matrix chemistry and temperature cycles have a large effect on the dissolution of carbide [313]. Fig. 4-21 and Fig. 4-22 indicate the SEM cross section of WC distributed in nickel matrix obtained from different references.

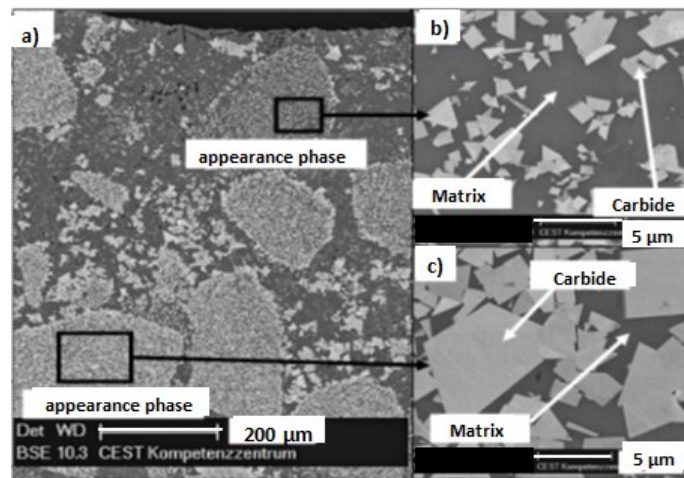


Fig. 4-21. SEM cross section of hardfaced layer reinforced with WC [314]

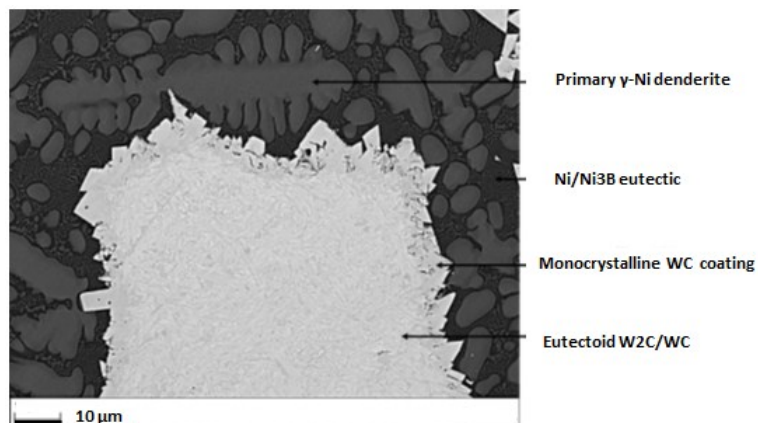


Fig. 4-22. SEM micrograph of the typical microstructures of WC in nickel base matrix [273]

Jones et al.[288] performed comprehensive study on carbon dissolution of WC in nickel base matrix after erosion and corrosion test. They observed the WC shell mainly form around cast tungsten carbide, and indicate the formation of outer layer WC shell and dissolution of that after corrosion test. Fig. 4-23 indicates the result of their works to investigate interface between WC and matrix. Fig. 4-24 depicts the SEM micrograph of the matrix and WC before and after corrosion test. As it is clear outer layer of the WC particles was more corroded.

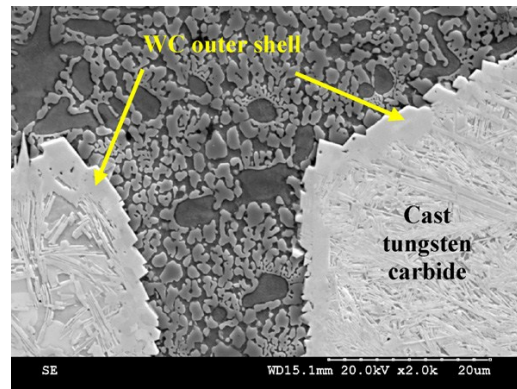


Fig. 4-23. Interface of WC and matrix [288]

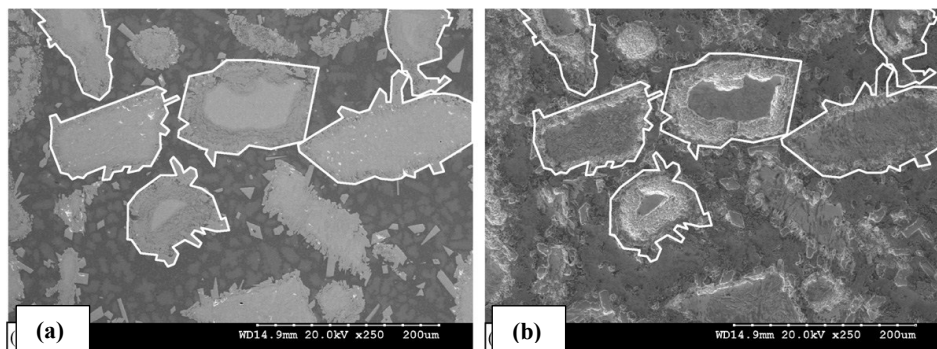


Fig. 4-24. Dissolution of WC layer (a) before and (b) after erosion corrosion test[288]

In addition different types of carbides can be added and applied on the base metal to improve surface properties [315]. Balamurugan et al.[316], investigated on optimization process of PTA for weld overlay of titanium carbide. In their work the effect of parameters such as current, travel speed and preheat on surface quality was discussed. In the same context, weld bead geometry play an important role in properties of the hardfaced metal and its good quality is reached with the selection of appropriate welding parameters. On the other hand, Design of Experiment (DoE) method, is useful to reach appropriate number of trials and conditions with minimum runs of experiments [316]. The development of mathematical models is a useful method to reach suitable process variables and bead geometry without defects for hardfacing applications.

Garcia Vazquez et al. [317], applied design of experiment for applying the nickel base powder on the tools steel and they reached appropriate result in both case of metallurgical aspect and weld bead geometry. Fig. 4-25 indicates the cross section of their optimum weld bead geometry. Another investigation, shows that by using design of experiment it is possible to reach an appropriate model for prediction of desirable weld layer [318].

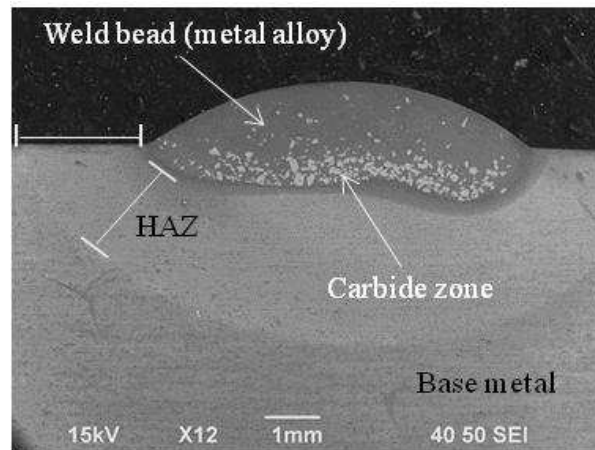


Fig. 4-25. Cross section of weld bead after deposition [319]

The effect of feeding rate and travel speed of Nickel base powder which was applied on low carbon steel was reported by Ming et al. [320]. Palani et al.[321,322], investigated the optimization of parameters for weld overlay of stainless steel on structural steel, also they found appropriate mathematical modeling and good simulated model for prediction of weld bead geometry. Davis et al.(1983), used the result of design of experiment to find appropriate dilution and weld bead geometry after developing the mathematical model. Also, their result was appropriate to obtain optimum parameter for automation of the hardfacing process. In another work, Siva et al.[323], used the DOE method using five level central composite rotatable design for optimization of the PTA process using nickel base powder on stainless steel. In addition to many works, still there is lack of information to find an appropriate model to predict weld bead geometry with considering the metallurgical behavior of the layer.

After reaching appropriate beads on the surface it is necessary to increase metallurgical and wear properties, due to that many investigations were performed. One important method is addition of different types of carbides to the existing commercial powders. In the following a brief literature review was performed about addition of different kinds of elements and specifically tungsten carbide nanoparticles in powder forms in micron and nano size to improve the mechanical properties of the weld overlay.

Flores et al.[324] have shown that if PTAW is used to deposit two NiCrBSi alloys with WC hard particles dissolution of primary carbides occurs which is due to the presence of elongated tungsten-rich precipitates together and small concentration of tungsten in solid solution. As explained before, plasma transferred arc (PTA) overlay welding has attracted more attention for improving the wear resistance of the surface of materials because of its ability to produce the layer with high deposition rate, lower porosity, and a good metallurgical bonding [325]. PTAW process has far less dilution into the substrate than other arc based processes and produces overlays with extremely strong metallurgical bonds to the substrate. Also, the produced overlays are also relatively free of defects [312]. In addition wear related failure of mechanical components is considerable as one of the major reasons for inefficiency of different industrial applications. To decrease the wear value in industrial applications consists of abrasion, material with high hardness such as carbides are appropriate to apply over metals. It should be mentioned that just by using pure carbides, the obtained results are not satisfactory due to low fracture properties especially under impact loading. One useful method is combining hard particles of carbides embedded into tough metallic matrix to improve both formability and abrasion resistance. Hardfacing by welding is accepted as useful technique to improve the surface properties of the components against wear and corrosion. There are several types of metal matrix composites (MMCs) that are used to PTAW depending on the application, those used for hard oxidation and corrosion resistance as NiCrBSi matrix reinforced with Cr_3C_2 or those that have wear resistant hard phases such as Ni-WC, among others. Now several key challenges that are faced when depositing hardfacing overlays with the PTAW process still remain. The two main challenges are the control of the dilution/dissolution and settling of carbides to the bottom of the weld with the Ni-WC family of overlays. The distribution of carbides is being enhanced through the development of experimental designs [316,326]. The importance of carbides dilution is paramount, as it can significantly alter the substrate properties and remove much of the wear resistance of the overlay. The amount of dilution present in welds is directly related to the heat input used during the welding process. The heat input itself is a function of the arc current and travel speed in PTAW [312]. When depositing Ni-WC overlays, the settling of carbides produces a denuded zone of low wear resistance at the top of the deposited layer [327]. The settling of tungsten carbide is attributed to two main factors: density and solidification time. However today there is a lack of information concerning the effect of adding elements to limit the problem of the carbides dissolution or its effect on the solidification microstructure of this kind of alloys. (Qing Yu Hou, 2011), has been investigated on nickel-based alloy coating with addition of nano- Al_2O_3 particles by using PTA overlay welding technique [325]. Adding Al_2O_3 particles could not only refine its microstructure but also change its phase characteristics, leading to increase its wear resistance. The reasons of adding nano particles in the nickel-based alloy coating which could refine its microstructure had been intensively studied [328–330].

Nevertheless, the reasons of adding different nano particles affecting the phase compositions and their mass fractions in the nickel-based alloy coating had not been fully clarified. It was found that adding 0.8 wt.% nano- Al_2O_3 particles does not change the hypoeutectic microstructure of the nickel-based alloy coating, though refines its microstructure and decreases the degree of the component segregation [325].

Farahmand et al.[331] investigated on the effect of addition of WC nanoparticle, molybdenum and lanthanum oxide on the wear and corrosion properties of the Ni-WC powder applied by laser cladding. They observed increase in mechanical properties and microstructure refinement after addition of nanoparticles.

Adding low quantity of nano-particles, increases the mass fraction of the $(\text{Fe}, \text{Cr})_2\text{B}$ phase and decreases that of the $(\text{Fe}, \text{Cr})_7\text{C}_3$ phase, though such adding has little effect on the relative mass fractions of the $\gamma(\text{Ni}, \text{Fe})$ and the (Fe, Cr) -rich phases and also increases the sliding wear resistance of the nickel-based alloy coating. On the other hand, several ways were used to refine the microstructure or change its phase compositions to meet higher wear resistance requirements, for example adding molybdenum [275].

By increasing Mo addition in 4 wt.% and 6 wt.%, a hypereutectic structure can be obtained. Addition of Mo element cause to distributes mainly in the (Fe, Cr) -rich compounds and formation of molybdenum carbides and increase the hardness but a limited increase in the Young's modulus of the deposited coatings. Also the addition of Mo can enhance the abrasive wear resistance and thermal shock resistance of the FeCrBSi alloy coating. The addition of nanoparticles itself in PTA process is very complicated because the process is not designed for that purpose. Generally, addition of different alloying elements on the powders cause to change the layer properties.

Bourithis et al. [332] applied hard titanium carbides, iron boride and iron chromium boride on AISI D2 steel by PTA process and compared their wear rate results. Heng et al.[311] investigated on wear behavior of Ni/WC coating applied by laser on the steel.

Sun et al.[333], added Ti, Mo and Nb elements to the Fe-C-Cr powder to observe their effects on erosion properties of the coating. Gallo et al.[334] investigated the effect of precipitation of TiC applied on mild steel by PTA, their results showed that after adding the titanium, hardness and wear resistance increase. Hou et al.[275], investigated the effect of adding molybdenum in the nickel base powder and they observed changes in form of carbides and better wear resistance. Shipway et al.[335], compared the wear properties of conventional and nanostructure WC in thermal spray coating, they found high surface to volume ratio of nanostructure powders cause to high dissolution of carbides. Yang et al.[336] applied WC nano WC-Co powder by cold spray method and they observed very good wear resistance, the reason was strengthening and toughening effect at the same time which results from the appropriate distribution of particle size. Osman Nuri et al.[337] investigated on effect of WC particles on wear behavior deposited layer by PTA process, they found with increasing the heat input, decomposition of WC to W_2C increase and wear rate decrease. Fig. 4-26 indicates the macro image of distribution of WC in weld overlay.

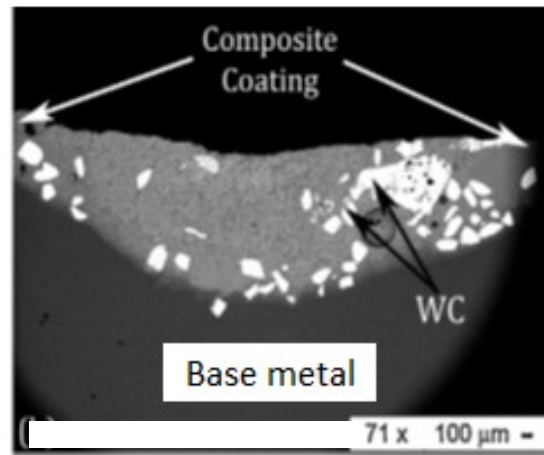


Fig. 4-26. Distribution of WC in weld overlay [337]

Despite these important findings about the effect of addition of some elements on the mechanical and wear properties of PTAW coatings, still there is lack of information to determine the effect of the addition of WC nanoparticles on the dissolution of carbides and final mechanical properties of deposited layer which already mixed with tungsten carbide in micron size to solve the problem of cracking and heterogeneity after deposition.

Chapter 5: Process optimization, weld bead geometry and microstructural evolution of nickel base powder (Ni-WC) deposited by PTA process on tool steel

Abstract

This chapter of the thesis consists of the experimental part, in which Plasma transferred arc (PTA) process was used to apply nickel base powder mixed with tungsten carbide particles on the surface of cold work tool steel. This practice in industry is difficult and involves various problems, because of the crack formation susceptibility of D2 steel during deposition process. Hardfacing is used to enhance surface properties of the metallic component, as a specially designed alloy is surface welded to achieve specific wear properties. To obtain appropriate combination of hardfacing parameters, overlays were deposited based on design of experiment (DoE) method by using response surface methodology (RSM). We started by applying a derive mathematical model to predict and control the parameters of current, travel speed and preheat as main factors, each one with five variables. These parameters are important for reaching final layer with acceptable metallurgical properties in addition to appropriate bead geometry. In total twenty experiments with different parameters were performed. For each run experiment, weld bead geometry parameters, including dilution, penetration and reinforcement were measured.

Characterization of the welding beads were performed by using scanning electron microscopy (SEM) accompanied with EDS, XRD analysis, microhardness and nano-indentation techniques on the samples. It was obtained that the presence of the secondary carbide phase which grows in dendritic shape, is considerably contributes to increase mechanical properties of the beads. Optical profilometry analysis was performed on the surface to evaluate the surface characterization of the samples. Finally based on obtained experimental data and using Minitab software mathematical modeling formula was calculated for prediction of the optimum weld bead geometry. It should be added that, the substrate pre-heat has a defining role for establishment of melt circulation patterns and solidification time. It responsible for final distribution of carbide grains within the bead. It was found that the homogeneous configuration of hard primary carbides can be obtained with the moderate substrate pre-heat temperatures.

Keywords: Hardfacing, PTA process, Nickel base powder, tool steel, design of experiment (DOE), tungsten carbide.

5.1. Materials and Experimental procedure

5.1.1. Base metal

In this part, the experimental procedure for optimization of the PTA process is explained. Table. 5-1, presents the nominal chemical composition (wt%) of D2 steel used as substrate. It was used with plate geometry with dimensions of 130 mm× 50 mm× 12.5 mm. With the aim to achieve an appropriate hardness and toughness, the overall D2 steel samples were subjected to a recommended heat treatment [338] consisted in a preheating stage at 790 °C during 1 hour, next at 1100°C during 35 minutes and then quenching in oil, and finally two step tempering treatments were performed at 315 °C for 2 hours each. Before applying the overlay, the surface of each steel substrate was grinded with SiC paper and sand blasting to remove oxides and contaminates. Fig. 5-1 indicates one sample block after heat treatment, cleaning and sandblasting.

Table. 5-1. Chemical composition of D2 steel in this investigation

Material	Nominal Chemical Composition (wt%)								
	C	Si	Mn	Cr	Mo	V	P	S	Fe
D2 Steel Substrate	1.58	0.37	0.48	11.52	0.89	0.56	0.017	0.029	Bal.



Fig. 5-1. Sample block of D2 as a substrate

Generally, for welding of high carbon and alloy steels, wear resistance and tools steel preheating is suggested. Preheating cause to minimize the distortion and shrinkage of the weld deposit. Also, it causes to reduce the thermal shock during welding. Mainly based on higher amount of carbon and alloying elements, higher preheat temperature is required. Also, preheating causes to retard the cooling rate of the base metal which is helpful to reduce the crack susceptibility.

5.1.2. Powder NiCrBSi-WC

Based on what explained about the powders in previous chapter, in this part the composition and morphology of powder is described. In this study, Ni-WC hardfacing alloy was used as feeder powder in a PTA process with the chemical compositions which is shown. in Table. 5-2. Also Fig. 5-2 indicates the morphology and EDS analysis of the mixed particles in the powder.

Table. 5-2. Chemical composition of the powder

Material		Nominal Chemical Composition (wt%)						
		C	Si	Mn	Cr	B	W	Ni
Hardfacing powder alloy	Matrix	0.6-0.8	3.9-4.9	-	14.0-16.0	3.0-3.4	-	Bal.
	Reinforcement	6.0-6.2	-	-	-	-	Bal.	-

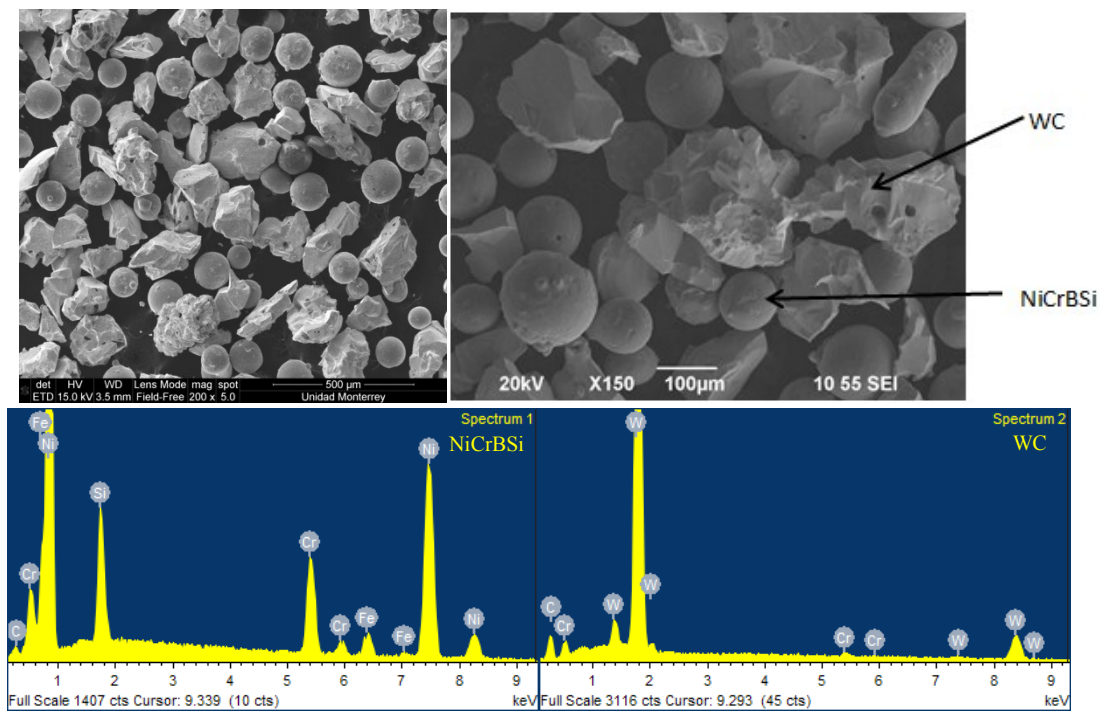


Fig. 5-2. Morphology, and EDS analysis of the nickel base powder

5.1.3. PTA Welding for this experiment

In this investigation, plasma transferred arc equipment, with trade mark of Castolin Eutectic Eutronic Gap 3001DC (Fig. 5-3), was used for applying the hardfaced layer on the D2 tool steel. Due to considering the design of experiment for optimization of the process, just travel speed and current were considered as variables (the relevant theory was explained in previous chapter). Other PTA processing parameters were fixed for all the runs of experiments mainly based on suggestions of the producer. The constant parameters is presented in Table. 5-3. Also, Fig. 5-4 and Fig. 5-5 indicate the position of the block before and during the hardfacing process, respectively.

Table. 5-3. Constant parameters used in the PTA process

Parameter	Value
Voltage (V)	20
Nozzle diameter(mm)	3.2
Torch to work piece distance (mm)	10
Plasma gas Ar (l/min)	12
Shielding gas Ar+10%H ₂ (l/min)	3.5
Carrier gas (l/min)	3.5
Feeding rate (g/min)	29

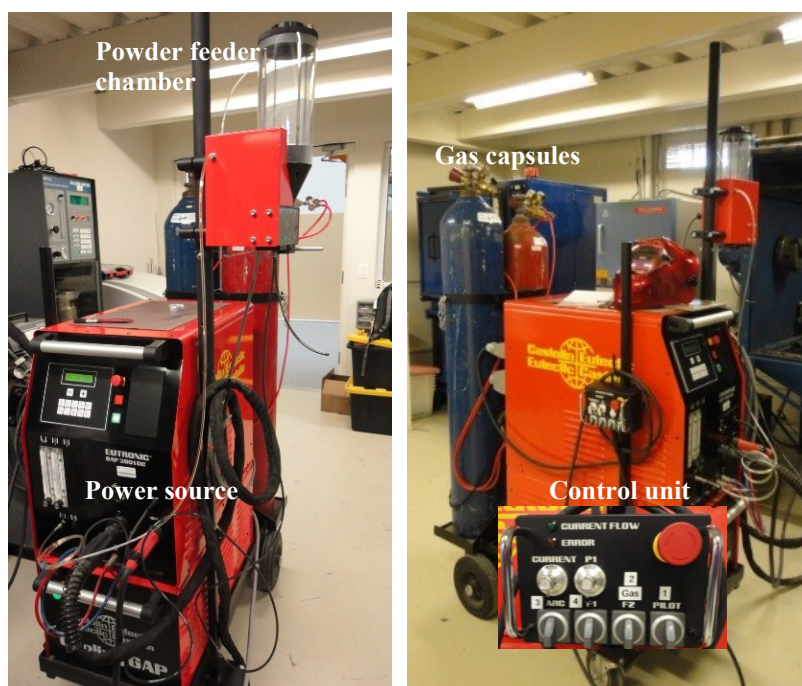


Fig. 5-3. PTA equipment which was used in this study



Fig. 5-4. Adjusting position of the torch on sample surface

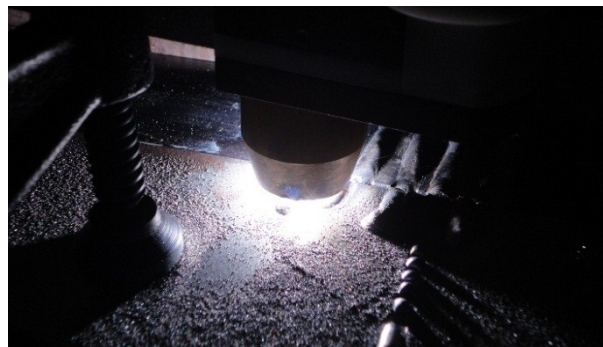


Fig. 5-5. Applying the powder on the surface

5.2. Design of Experiment- Response surface methodology

With considering various parameters in plasma transferred arc welding, finding the optimum values is not easy process. Consequently, in this research, response surface methodology (RSM) which is combination of statistics and mathematical methods can be employed to determine a relationship between input process parameters and output responses. The main use of this method is to analysis and modeling of the problems to find optimum combination of the process parameters. In this study, a standard RSM design (central composite design (CCD)) has been created which consists of factorial points (cube points), axial points (star points) and central points [290]. As discussed earlier, in PTA process, there are many variable parameters. With considering constant parameters in Table. 5-3, Table. 5-4 indicates selected variable parameters for current (A), travel speed (S) and preheat (T), with five levels each, which were considered in this work. The range of parameters were selected based on the technical specification of the powder producer. The reason for choosing pre-heat as variable, was due to the high carbon and high chromium percentage in D2 steel which make it really sensitive to crack initiation during welding. The upper limit of the factor was considered as $+1.682$ (X_{max}) and its lower limit -1.682 (X_{min}), the intermediate levels can be found as $X_i = 1.682[(2X - (X_{max} + X_{min}))]/(X_{max} - X_{min})$.

Table. 5-4. Variable parameters in this investigation

Parameter	Notation	Factor levels				
		-1.682	-1	0	+1	+1.682
Current (A)	I	86.36	100	120	140	153.63
Preheat (°C)	T	181.82	250	350	450	518.18
Travel speed (cm/min)	S	59.7	70	85	100	110.2

Based on design of experiment method, Table. 5-5 shows the detail parameters of each run of experiment. The first eight runs related to the factorial portion, runs nine to fourteen correspond to axial portion and final six runs related to the center point portion. The experimental runs were conducted randomly to avoid any systematic error into the system.

Table. 5-5. Welding parameters for each test based on experimental design

Sample Order No.	X1	X2	X3	Current (A)	Travel speed (cm/min)	Pre heat (°C)
	Data in coded variable			Data in Natural variables		
W1	-1	-1	-1	100	70	250
W2	1	-1	-1	140	70	250
W3	-1	1	-1	100	100	250
W4	1	1	-1	140	100	250
W5	-1	-1	1	100	70	450
W6	1	-1	1	140	70	450
W7	-1	1	1	100	100	450
W8	1	1	1	140	100	450
W9	-1.682	0	1	86	85	350
W10	1.682	0	0	154	85	350
W11	0	-1.682	0	120	60	350
W12	0	1.682	0	120	110	350
W13	0	0	-1.682	120	85	182
W14	0	0	1.682	120	85	518
W15	0	0	0	120	85	350
W16	0	0	0	120	85	350
W17	0	0	0	120	85	350
W18	0	0	0	120	85	350
W19	0	0	0	120	85	350
W20	0	0	0	120	85	350

5.3. Characterization of the samples

After deposition of 20 layers on the samples, liquid penetration test was performed to observe existing surface defects. The overlay samples were cut perpendicular to the welding direction and the relevant cross section was prepared for experimental analysis. After conventional surface preparation of the samples with consecutive emery papers and diamond polishing till 1 μm , Nital 2% and solution of 30% HF and 70% HNO_3 chemical reagent was used for etching of the base metal and weld overlay, respectively. The Olympus SZX A0 stereomicroscope equipped with *Infinity Analyze* software was used for measurement and characterization of each layer (dilution, penetration and reinforcement) according to the methodology explained elsewhere [269]. Fig. 5-6 indicates the schematic figure of one deposited layer, which on that the relevant parameters are specified.

It is an important factor which has to be considered for assessing the quality of weld overlay hardfacing. It can be named as dilution and it can be defined as area percentage of the base metal which has affected by fusion zone divided by whole welded area.

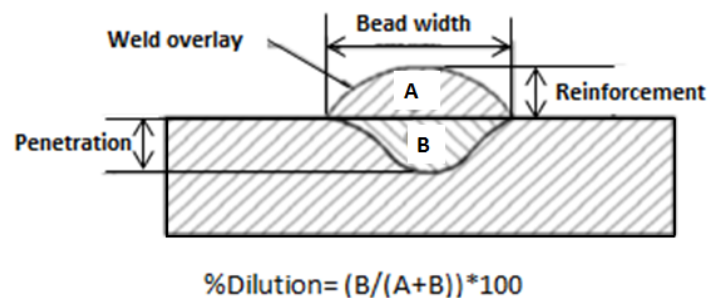


Fig. 5-6. Parameters which measured for each layer

The Vickers microhardness (HV) of the samples was measured through the base metal, heat affected zone and deposited layer using a Micro-Hardness Tester (*Clemex MMT-X7*), with an indentation time of 10 s and a maximum load of 300 gf. The overall indentations were made in profile form, each indentation of 100 μm starting from the surface, in samples that were prepared by conventional metallographic techniques. For microstructural analysis the samples were compared and characterized by using *FEI Nova Nano SEM 200* system equipped with energy dispersive X-ray spectroscopy (EDS) and *INCA* software. In the optimized sample the microstructural and mechanical properties were characterized. The elastic modulus and hardness of the sample were determined by nanoindentation test.

A Berkovich diamond tip was used in a *TI 950 Triboindenter, Hysitron, Minneapolis, USA*. A maximum applied load of 1mN was used for the soft phases, and 1.5 mN for WC phase, all indentations were made with a loading-unloading rate of 150 $\mu\text{N}/\text{sec}$. In order to avoid topographic effects during the nanoindentation process, the top surface of the samples were polished with silicon carbide sandpaper having different particle sizes. Finally to reach mirror surface appearance a commercial diamond polishing paste (500 nm particle sizes) was used.

The structures of the samples were classified according to their variety of phases. Around fifteen indentations were carried out on each structure type of the sample; elastic modulus and hardness were computed from the load-penetration depth ($P-h$) curves, using the Oliver-Pharr method [339]. In the optimized sample X-ray diffraction with aim of determining the crystallographic structure of phases in the surface overlay was performed. The *Brucker AXS D-8 XRD* equipment with using CuK_α radiation ($\lambda=0.154\text{nm}$) at 40Kv and 20mA was hired to do this experiment. The XRD spectrum of the specimen was recorded in 2θ range between $10\text{-}140^\circ$ with angular step of 0.01° . The analysis of the peaks was performed by *Diffrac Plus evaluation* software. Finally, surface profile analysis was performed by optical profilometer (Taylor-Hobson) in 3D form, to observe maximum differences between height of matrix and tungsten carbides in the deposited layer.

5.4. Results and discussions

5.4.1. Characterization of deposited layers

As explained in previous part all twenty layers which were deposited by random run numbers on the surface of the blocks. Roughly 1 to 2 cm distance was considered between each two layers. Fig. 5-7 indicates some deposited layers on the surface. After deposition of all layers, to observe the soundness of the depositions, liquid penetration test was applied on the block surfaces. Fig. 5-8 depicts image of dye penetrant test for some layers.

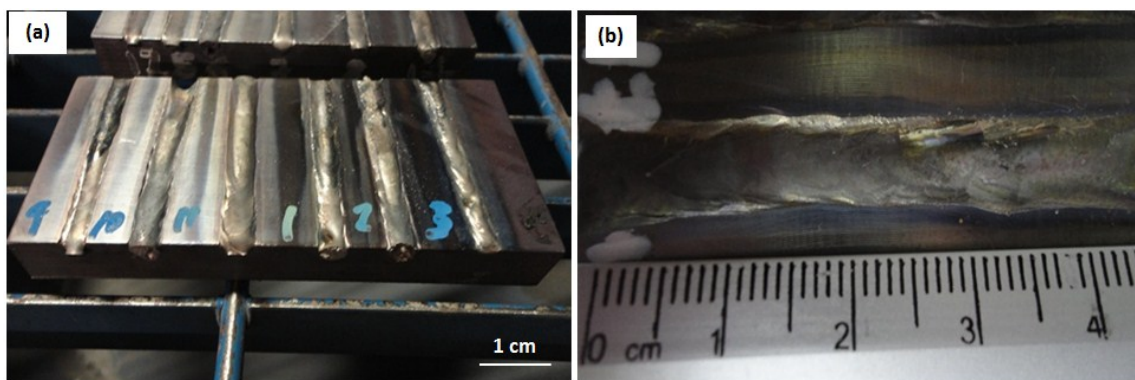


Fig. 5-7. (a) Weldoverlays applied on the block of base metal (b)one sample layer in higher magnification

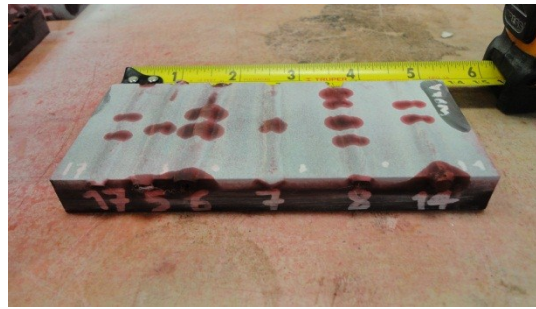


Fig. 5-8. Applying the dye penetration test on the layers

5.4.2. Microstructure evolutions

The cross section of one sample layer after preparation is reported in Fig. 5-9(a). The cross section of each layer can be divided into three distinct parts: the deposited layer, the heat affected zone and the base metal. The presence of carbides in the base metal and the dendritic structure in the deposited layer and in the heat affected zone are specified in Fig. 5-9(b).

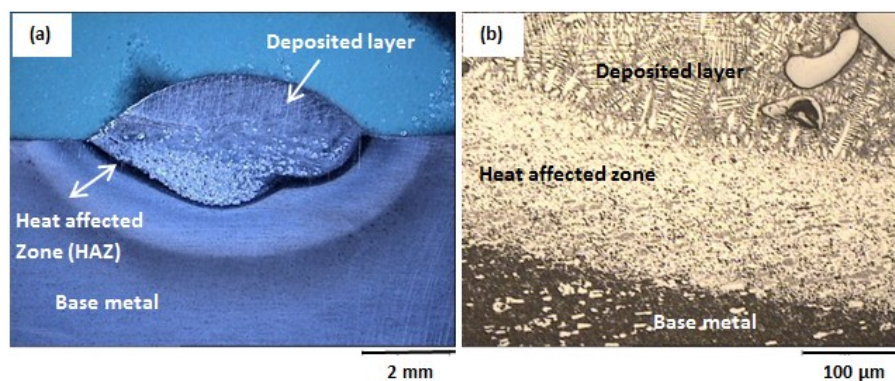


Fig. 5-9. (a) Macrostructure of one weld overlay and (b) Microstructure of the different zones

Fig. 5-10 shows some selected weld profiles. As can be seen, the weld bead shape and the distribution of tungsten carbides in sample W9 is more homogenous than the other samples. For most of the samples, tungsten carbide particles are mainly distributed at the bottom of the weld pool. Also based on different welding parameters, the value of penetration and reinforcement are different.

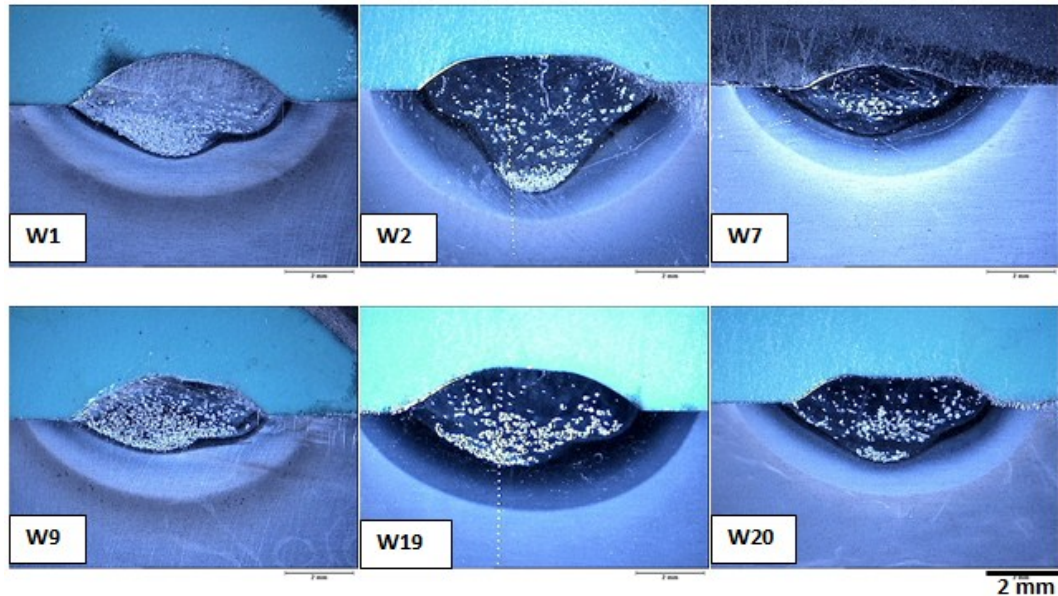


Fig. 5-10. Weld bead shape of some selected samples

The microstructure of base metal D2 steel is shown in Fig. 5-11. The optical microscopy of D2 steel showed martensitic microstructure which contain distributed carbide with different sizes. Large carbides are mainly M_7C_3 , which mainly form during solidification because of existing higher amount of alloying elements. This carbide which mainly are Cr_7C_3 , dispersed in the microstructure during hot working. Finer carbides are secondary one, which precipitated from the austenite phase during cooling [340–342]. EDS analysis of the carbides indicated that, in addition to Chromium carbide, there is Vanadium carbide which distributed in the matrix. Vanadium form very hard and thermally stable VC or V_2C carbides as isolated particles, which cause to improve wear and abrasive resistance. It has limited solubility in matrix, consequently addition of vanadium will not delay the rate of diffusional decomposition of austenite. Chromium carbide, depends on chromium content, mainly form in type of $Cr_{23}C_6$ and Cr_7C_3 . These carbides dissolve during austenization at more than 900 °C.

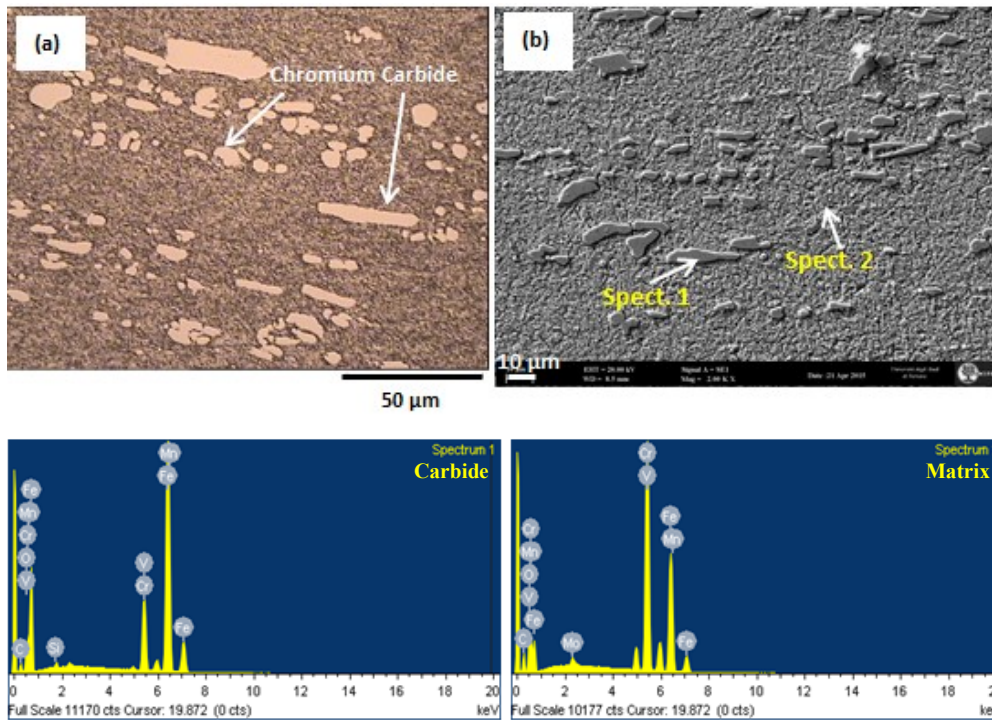


Fig. 5-11. Microstructure of the D2 steel base metal (a) optical microscopy and (b) SEM accompanied with EDS analysis

Heat affected zone (HAZ) is characterized by two different microstructures close to the fusion zone (Fig. 5-12a) and close to the base metal (Fig. 5-12b), respectively. The reason of formation of these zones is probably due to the different heating and cooling therycles during the hardfacing process.

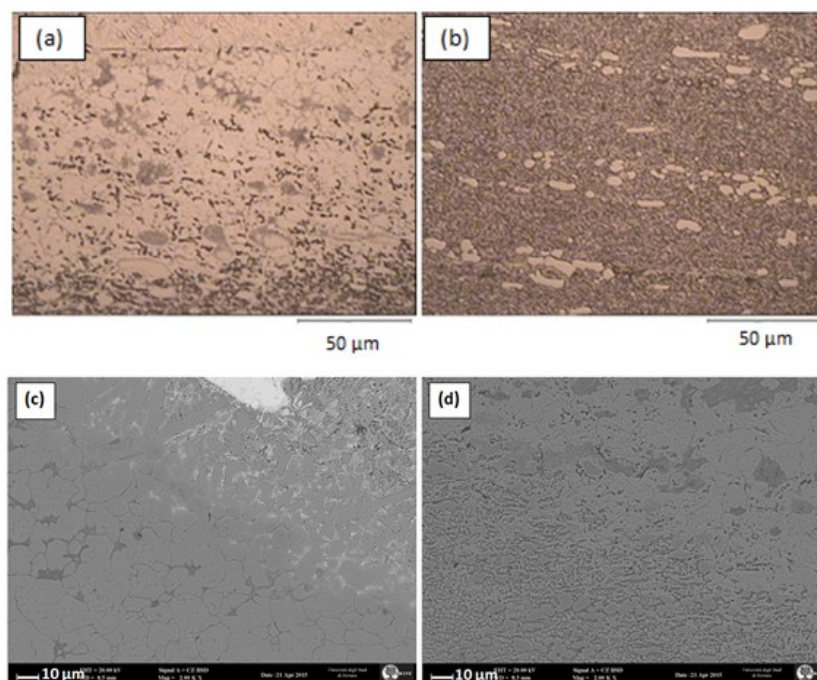
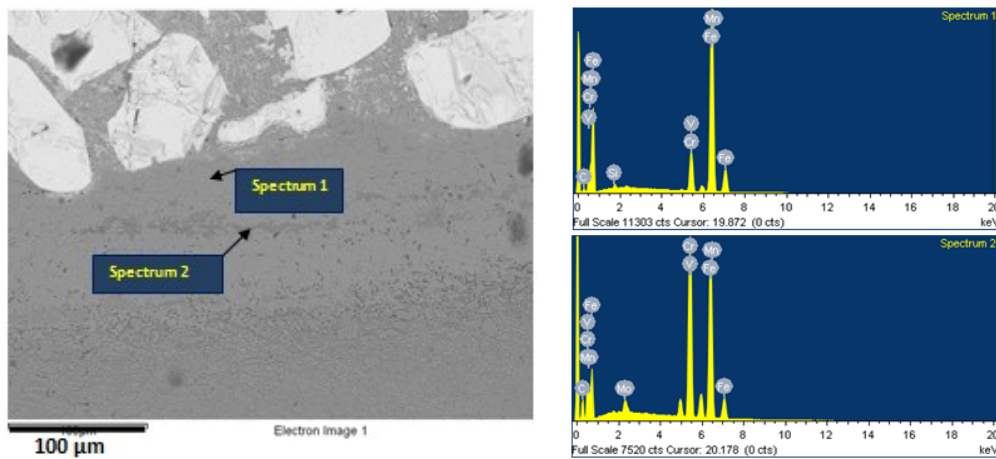


Fig. 5-12. Microstructure of heat affected zone with optical microscope and SEM

(a,c) close to fusion zone (b,d) far from fusion zone

Fig. 5-13 indicates the SEM microstructure of HAZ with EDS analysis of different phases. As it is obvious the dark phase is chromium and vanadium carbide. Fig. 5-14 shows the transition zone between weld overlay and HAZ obtained by optical microscope.



HAZ	C	Si	V	Cr	Mn	Mo	Fe
Spectrum 1	4.08	0.66	0.47	10.45	0.34	-	Bal.
Spectrum 2	12.46	-	2.91	33.72	-	2.62	Bal.

Fig. 5-13. SEM image and EDS analysis (wt%) of heat affected zone

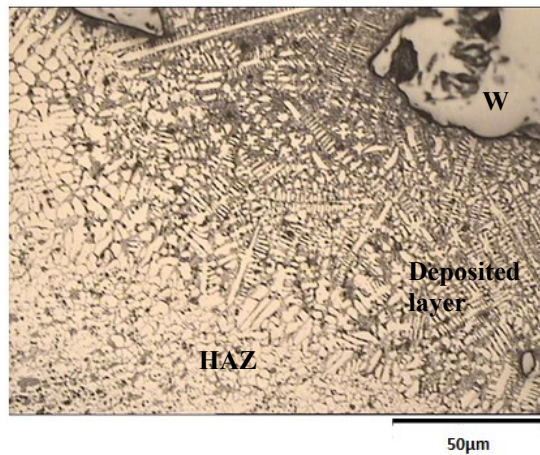


Fig. 5-14. Interface between deposited layer and HAZ

The microstructure of nickel base coating are shown in Fig. 5-15 which is characterized by a hypereutectic dendritic structure and lamellar eutectic in interdendritic region. It consists of primary γ -Ni dendrites and an interdendritic region which concentrates carbide former elements. Tungsten carbide particles, mainly in form of blocky WC/W₂C, are distributed in the layer. Near the substrate, the microstructure consists of very fine interdendritic carbides precipitated during the rapid solidification. Because of their high density, the volume fraction of tungsten carbides close to the top surface is less than in the area close to the base metal. Fig. 5-16

shows the morphology of tungsten carbide particles in nickel matrix by optical microscope, which are accumulated at the bottom of the weld pool.

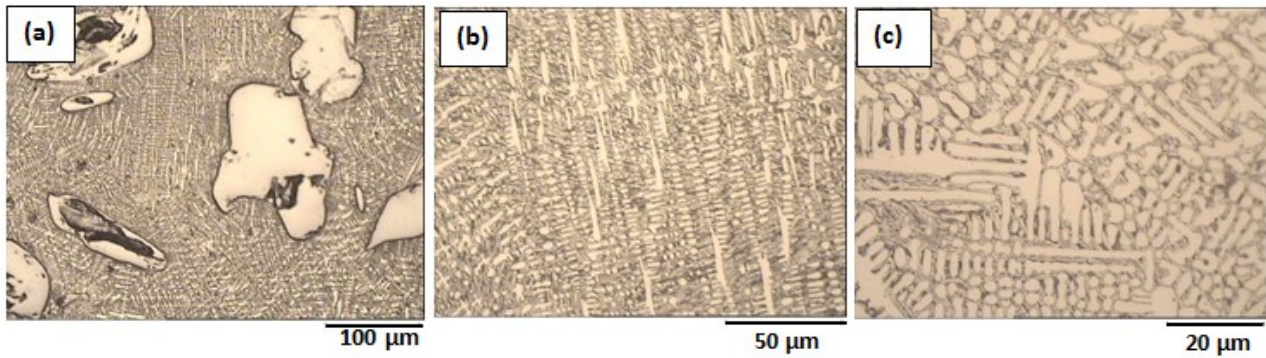


Fig. 5-15. Microstructure of weld overlay: (a) tungsten carbides in the matrix, (b) and (c) dendritic matrix at different magnification

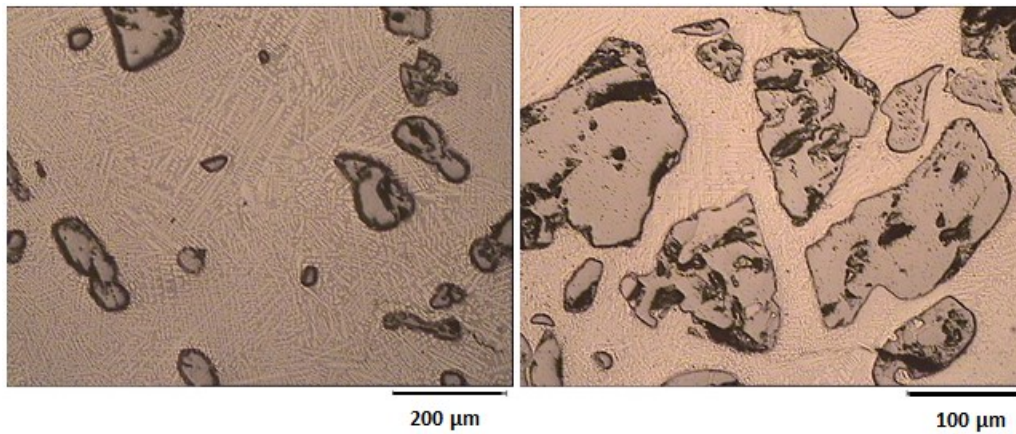


Fig. 5-16. Distribution and morphology of tungsten carbide in deposited layer by OM

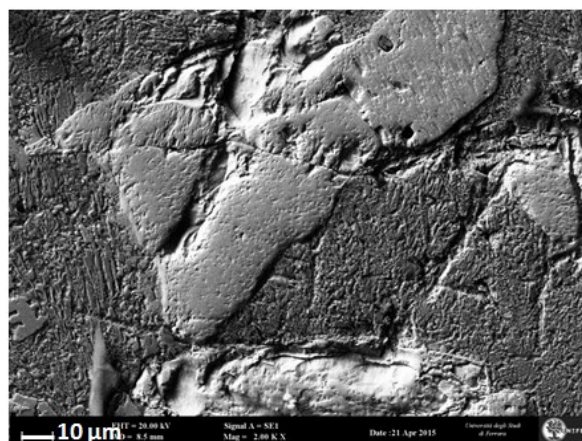


Fig. 5-17. SEM micrograph of on tungsten carbide particle in the matrix

5.4.3. Distribution of Tungsten carbide

The distribution of tungsten carbide in the layer was not completely uniform and homogenous as it shown in Fig. 5-18. They mainly were accumulated near the interface of base material. Just sample W9 which showed good weld bead geometry, indicated more appropriate distribution of tungsten carbide. The interface between WC and Ni matrix was fine but in some cases pores were form inside of the WC particles. Generally, the hardness of WC is very high and it is difficult to grind it with emery papers. During sample preparation by emery papers, some part of carbides were worn and stick to the emery papers, in this case the papers acts as abrasive material, consequently pits and ducts are form on the carbide particles. Based on previous research in case of increasing the heat input, there is possibility of the changing WC phase to W_2C phase which is more brittle than WC [343,344].

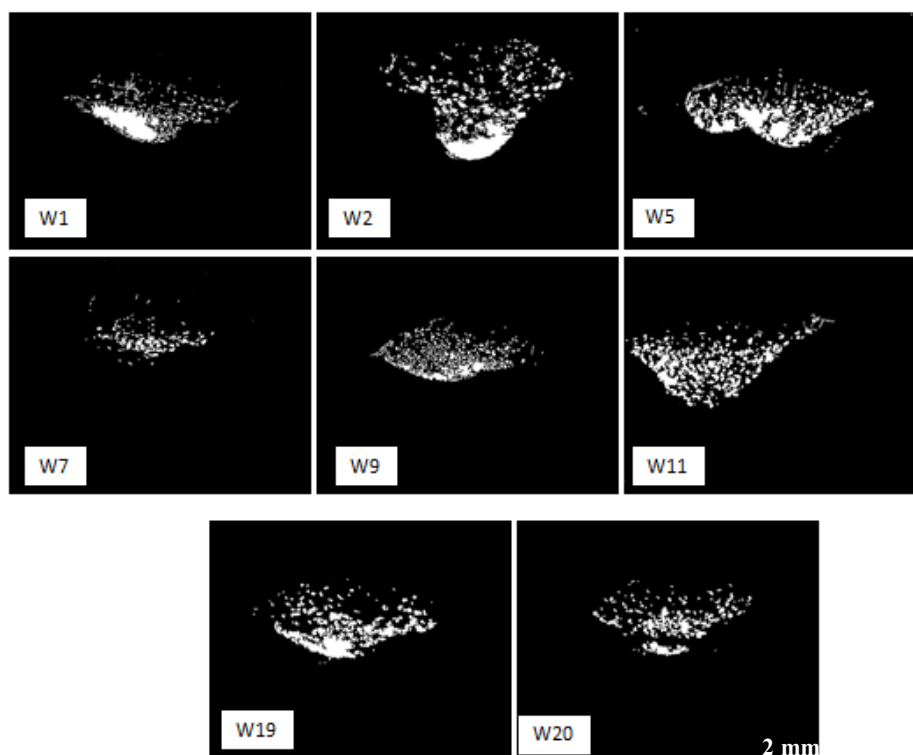
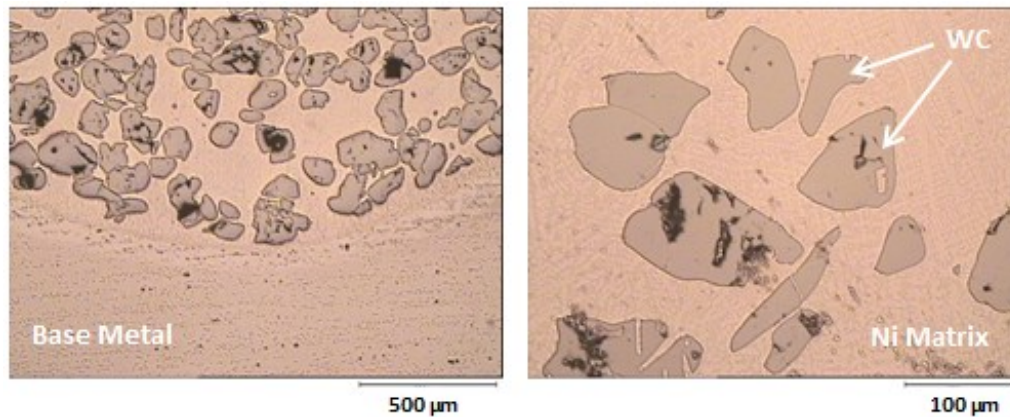
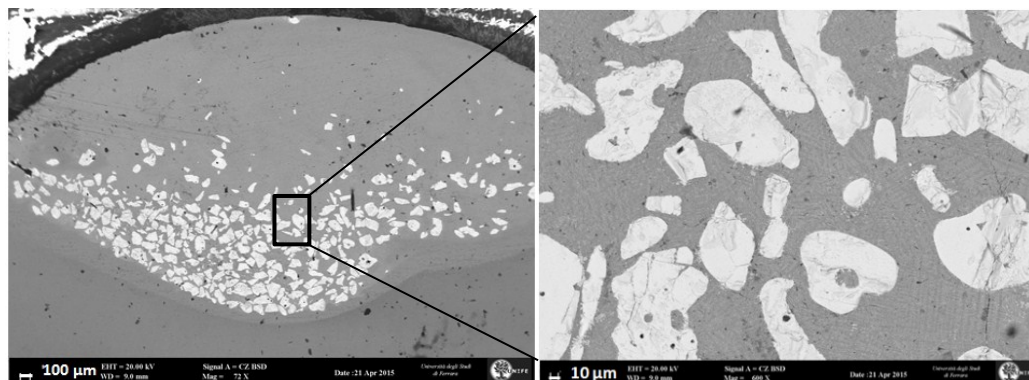


Fig. 5-18. Distribution of tungsten carbide particles in weld pool

Fig. 5-19 and Fig. 5-20 show the distribution of tungsten carbides in nickel matrix obtained by optical microscope. In addition based on calculation of image analyzer, the percentage of tungsten carbide in the weld pool was measured and it showed in Table. 5-6. As it is clear, mainly the percentage is between 30 to 45%, which is appropriate amount. As it is clear, tungsten carbide particles tended to sink to the bottom of the coating due to a stirring motion in the melting pool, during coating process [345].

Table. 5-6. Percentage of WC in the matrix of some selected samples

Sample	W1	W2	W5	W11	W19	W20
WC in matrix (%)	33.65	30.36	43.02	45.04	38.62	34.28

**Fig. 5-19.** Morphology and distribution of tungsten carbide close to the base metal by means of optical microscope with different magnifications**Fig. 5-20.** Morphology and distribution of tungsten carbide close to the base metal by means of SEM (BSE) with different magnifications

5.4.4. Weld bead geometry

In this study as explained before, three responses were considered for each run of experiment which were dilution, penetration and reinforcement. These features were measured in the cross sections of the samples according to what showed schematically in Fig. 5-6. The results for all the samples are listed in Table. 5-7. By just comparing the shape of beads, samples W1, W5, W6, W9, W19 and W20 show better appearance.

Table. 5-7. Measured data for different hardfaced samples.

Sample name.	Order of run	Dilution (%)	Penetration (mm)	Reinforcement (mm)
W1	8	42.03	1.30	1.83
W2	7	72.27	3.06	0.98
W3	4	57.86	0.92	0.74
W4	17	86.50	2.57	0.54
W5	14	51.90	1.63	1.54
W6	11	71.38	4.08	1.32
W7	18	59.97	1.33	0.98
W8	9	73.76	1.51	0.90
W9	2	30.52	0.69	1.43
W10	20	79.91	3.49	0.92
W11	6	55.24	2.66	1.67
W12	12	67.63	1.82	0.66
W13	3	74.39	1.67	0.60
W14	19	45.65	2.38	1.24
W15	5	79.52	2.54	0.60
W16	15	70.70	1.92	0.69
W17	13	74.55	1.75	0.57
W18	10	73.85	2.49	0.67
W19	16	50.10	1.22	1.15
W20	1	59.17	1.60	0.79

5.4.5. Microhardness profiles

Microhardness profile was performed on all samples. Fig. 5-21 presents the cross-section of W1, W6 and W7 samples illustrating the macrostructure of three different overlays geometry. As shown in Fig. 5-21 three typical characteristics (the deposited layer, the heat affected zone and the base metal) of each cross section is visible. For all cases the interface between layer and base metal was crack free. In the deposited layer, heterogeneous distribution of WC carbides in the Ni matrix, can be observed which in the practice is very difficult to control. Based on calculation of image analyzer, the percentage of tungsten carbide in the weld pool is between 30 to 45%. Additionally, to the distribution of the hard phase, the size of heat affected zone is very sensitive to the variation of the process parameters. As first approximation, the main variable parameter that affects the dilution is the current, for example the sample shown in Fig. 5-21(b) was deposited with a current of 140 A and the samples shown in Fig. 5-21(a) and Fig. 5-21(c) with a current of 100 A, but with different travel speed, using 70 cm/min for the sample of Fig. 5-21(a), and 100 cm/min for the sample in Fig. 5-21(c).

This variation on the travel speed causes the formation of bead geometry with more reinforcement. Additionally, the size of the heat affected zone is related with the variation in the preheat treatment used. For example the sample of Fig. 5-21(a) was preheat to a 250 °C before the deposition showing less heat affected zone, regards to the sample from Fig. 5-21(c), which was subjected to a 450 °C before the deposition. Additionally in the Fig. 5-21. the hardness profile is also shown. As it can be seen, the hardness of the matrix is very compatible with the hardness of the substrate. The microhardness of the substrate is affected directly with preheat, it means that the hardness is lower in the samples that were preheated at higher temperatures (Fig. 5-21(b) and Fig. 5-21(c)). The hardness of the hardfaced layer depends again on the process variables, but with major effect from the current used. When high current (140 A) is used, the average microhardness of the Ni matrix is 566 ± 78 HV and the WC phase has 1560 ± 201 HV. On the other hand, when 100 A is used, the average microhardness of the Ni matrix is 667 ± 123 HV and the WC phase is 1591 ± 106 HV.

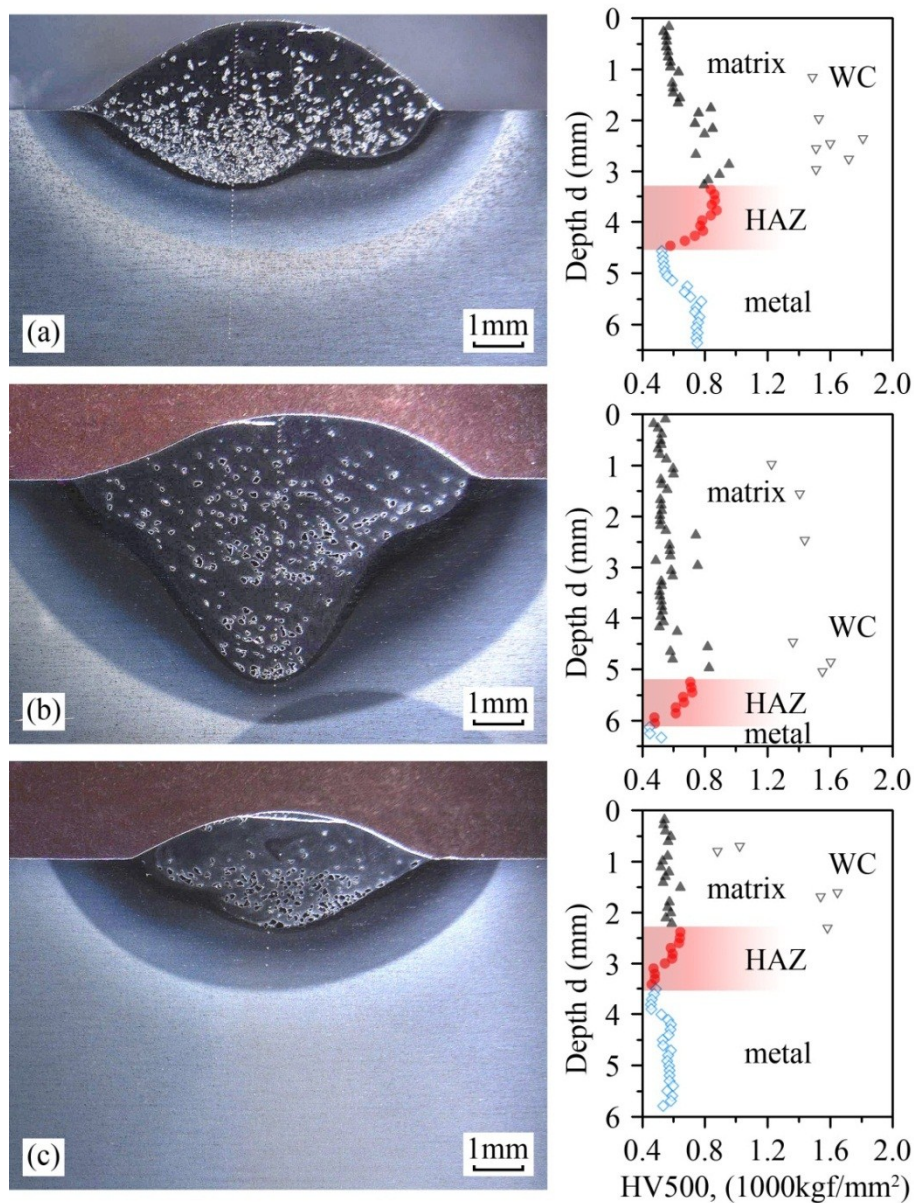


Fig. 5-21. Macrostructure and hardness profile of samples (a) W1, (b) W6 and (c) W7.

The hardness value of the base metal was measured around 48 HRC. For studying the evolution of hardness through the cross section of the layers, Vickers microhardness tests were performed; the results show that the microhardness values vary from the top of the hardfaced layer to the base metal according to the different distribution of tungsten carbides in the weld pool.

Fig. 5-22 indicates the microhardness profiles of some selected samples. The hardness at the top of the layer is not the maximum because, as explained before, tungsten carbides are mainly present at the bottom of the layer due to their higher density compared to the matrix. Based on the measured data, for all the samples in the heat affected zone hardness decreases from fusion zone to the base metal, which is in agreement with the temperature evolution during the hardfacing process. In sample W9 maximum equal hardness value of 800 HV₁ was observed compared to other samples, whose hardness was around 600 HV₁.

The increase of the hardness of sample W9 could be due to equal distribution of tungsten carbides and to a partial decomposition of tungsten carbides causing a solid solution reinforcement of the matrix.

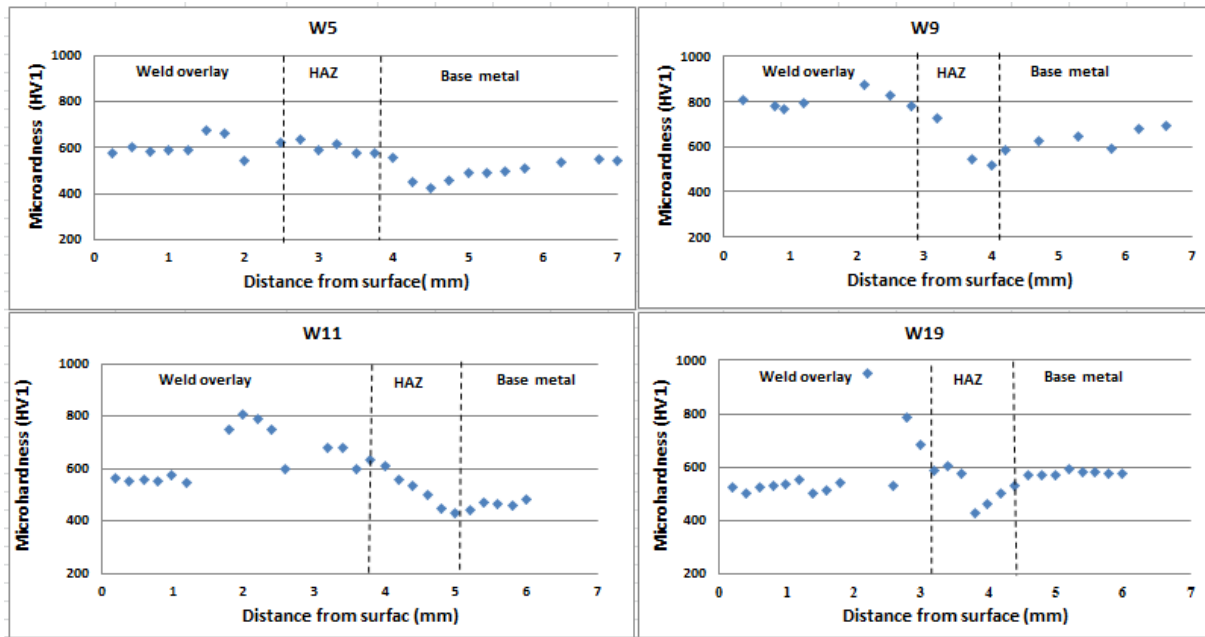


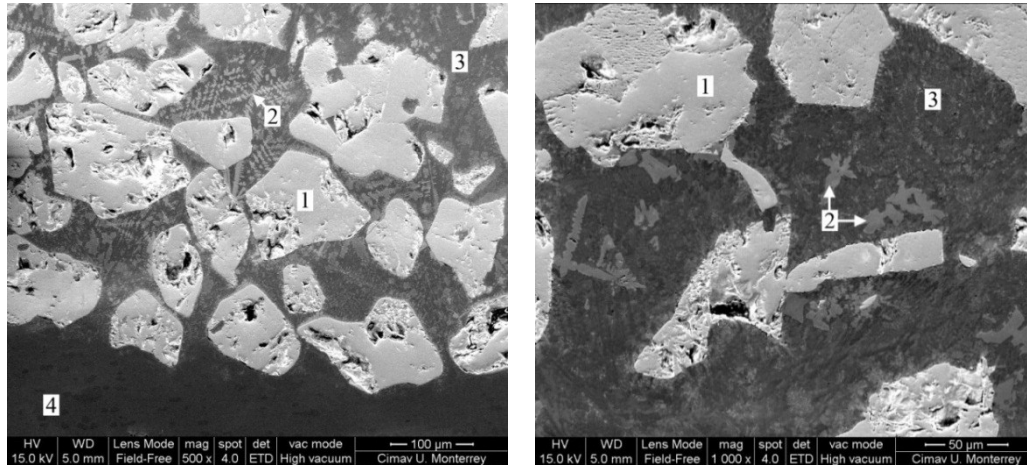
Fig. 5-22. Hardness profiles of some selected samples

The microstructure of nickel base coating is a hypereutectic dendritic structure. It exists primary face center cubic Ni-FCC dendrites which are NiCrFe, and the interdendritic region which has concentrated carbide former elements. Partition of iron-carbon result on the participation in austenite solid solution and interdendritic region [346], specially most of iron is found very close with the interface between the heat affected zone and the reinforcement. Near of the substrate, microstructure consists of very fine dendritic carbides indicative of rapid solidification. For all cases the interface between layer and base metal was sound and crack free. The matrix microstructure is typically comprised of soft primary nickel dendrite (~ 350 HV) while the inter-dendritic regions are comprised of hard borides and carbides (~ 500 to 800 HV) [347].

5.4.6. SEM and EDS analysis of WC and matrix

Different phases involve FeNi+Ni₂B eutectic and Cr₇C₃ can be found in the matrix. Also the tungsten carbide particles are distributed in the layer, mainly in form of blocky W₂C particles. The tungsten carbides are not formed in situ during solidification, but rather must survive the welding thermal cycle. Boron addition decreases the melting temperature of the alloy system and produces a wide solidification temperature range, forming hard Ni₃B phases and decreasing the minimum heat input required for fusion of the substrate [280]. The chemistry of the matrix and temperature cycle has a large effect on the level of carbide dissolution.

The dissolution of primary tungsten carbides occurs and leads to the formation of secondary carbides surrounding the WC particles. A feathery CrWC phase formed at the periphery surrounding the WC particles. No direct correlation could be determined between dissolution and specific alloying additions, since both the Cr and carbon content of each alloy increased in a roughly equal proportion. As shown in Fig. 5-23, EDS analysis and element quantification of this phase suggested that the stoichiometry corresponds to $\text{Cr}_7\text{W}_3\text{C}_6$, which was also reported previously by Liyanage et al.[327]. This phase only was found in regions where WC phase is present in high quantity, i.e. on the bottom of the reinforcement. As it can be seen in Fig. 5-23, when the space between mono tungsten carbide is smaller, the CrWC phase is higher because there is more dissolution from WC phase. On the other hand, the microstructure of HAZ was also characterized but it was not shown here. This region can be divided in two parts, close to weld zone which has larger grain size and close to the base metal with smaller grain size. The first area, chromium and vanadium carbide was detected. In addition, near to the interface, a lamellar eutectic phase is present. This area is transition zone between substrate and deposited layer. During solidification, silicon easily dissolved into nickel solution in the deposited layer. In this area eutectic reaction occurs and lamellar eutectic is formed. Tungsten dissolved into the nickel rich phases by wetting of the matrix during the process. The value of the dissolved tungsten depends on the amount of chromium in the nickel matrix. By increasing the chromium, lower amount of tungsten can dissolve into the solid solution with Ni-Cr. This can be justify by considering the Cr-Ni-W phase diagram [348].



Elements	Phase 1	Phase 2	Phase 3	Phase 4
C	6.72	4.11	4.64	2.70
V	-	0.63	-	0.75
Cr	-	13.97	17.44	12.65
Fe	-	8.09	46.72	82.75
Ni	-	20.14	14.42	-
Mo	-	1.18	0.45	0.58
W	93.28	48.41	16.18	-
Si	-	3.47	0.16	0.56
Total	100.00	100.00	100.00	100.00

Fig. 5-23. Microstructure and EDS chemical composition of W1 sample: (1) Mono tungsten carbide phase, (2) Phases from eutectic reactions in interdendritic regions, (3) nickel base matrix overlay, and (4) Steel substrate.

Back scattered images of the deposited layer, obtained by means of SEM from the sample W1, are reported in Fig. 5-24. To understand the distribution of alloying elements in the matrix several EDS analysis were performed on different positions and the results are collected in Table. 5-8. In addition to large tungsten carbides, there are other different types of particles containing nickel, chromium and silicon; moreover, other complex phases are distributed between WC particles and the matrix. The diffusion of carbon to the matrix, due to its interstitial character, is faster than other carbide former elements; with presence of WC as a reinforced material, formation of complex and brittle carbides was reported in the literatures [349]. EDS analysis of the carbides indicates that, in addition to existing chromium which can precipitate as a chromium carbide, there is vanadium which is distributed in the matrix.

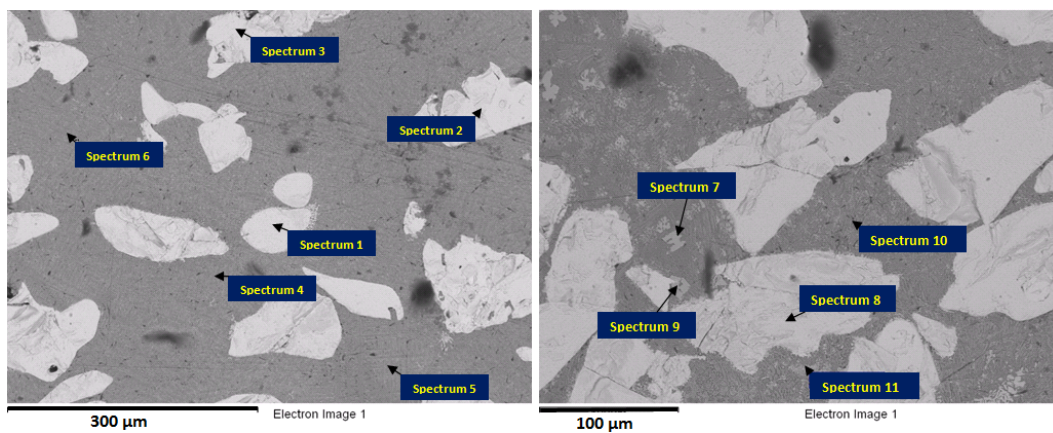


Fig. 5-24. Position of the EDS analysis in the microstructure (SEM back scatter image)

Table. 5-8. Qualitative chemical analysis (wt%) of main elements for each spectrum

Spec No.	Position	C	W	Si	V	Cr	Fe	Ni
Spec. 1	Carbide	7.26	92.74	-	-	-	-	-
Spec. 2	Carbide	7.08	92.92	-	-	-	-	-
Spec. 3	Carbide	7.24	92.76	-	-	-	-	-
Spec. 4	Matrix	5.04	20.71	0.23	0.39	12.71	45.72	13.15
Spec. 5	Matrix	9.49	22.89	-	0.65	17.57	38.60	9.76
Spec. 6	Matrix	5	16.31	0.77	0.35	10.70	44.34	20.38
Spec. 7	Carbide/Matrix	5.01	50.86	3.15	0.37	13.7	9.21	17.7
Spec. 8	Carbide	5.81	81.56	-	0.36	5.50	3.96	2.82
Spec. 9	Carbide/Matrix	8.90	15.05	1.55	0.31	18.90	31.30	24
Spec. 10	Matrix	2.78	15.24	2.56	-	5.61	37.33	36.48
Spec. 11	Carbide	7.82	90.83	-	-	-	-	-

From individual element traces in tungsten carbide particles and matrix, it can be observed that both outer side and center of the WC particles are tungsten rich without evidence of nickel. Also, there is clear boundary between the carbide and matrix due to steep decline in W content and incline in nickel content at the interface between carbide and matrix.

From the obtained results which are reported in Table. 5-8, it can be observed that tungsten is also distributed in the matrix in the range between 15 to 22; spectrum 7 reveals a tungsten content more than 50%. This could be due to decarburization of WC/W₂C during the welding process; moreover, tungsten and carbon could be dissolved into the nickel and nickel-chromium phases. Dissolution of tungsten carbide particles in the matrix causes the precipitation of secondary carbides around the primary carbides. Fig. 5-25 indicates the EDS map analysis of the elements in cross section of the layer. It is clear that tungsten and silicon are the main elements in large particles, also distribution of nickel, chromium and iron elements in matrix are uniform and homogeneously distributed inside of the matrix.

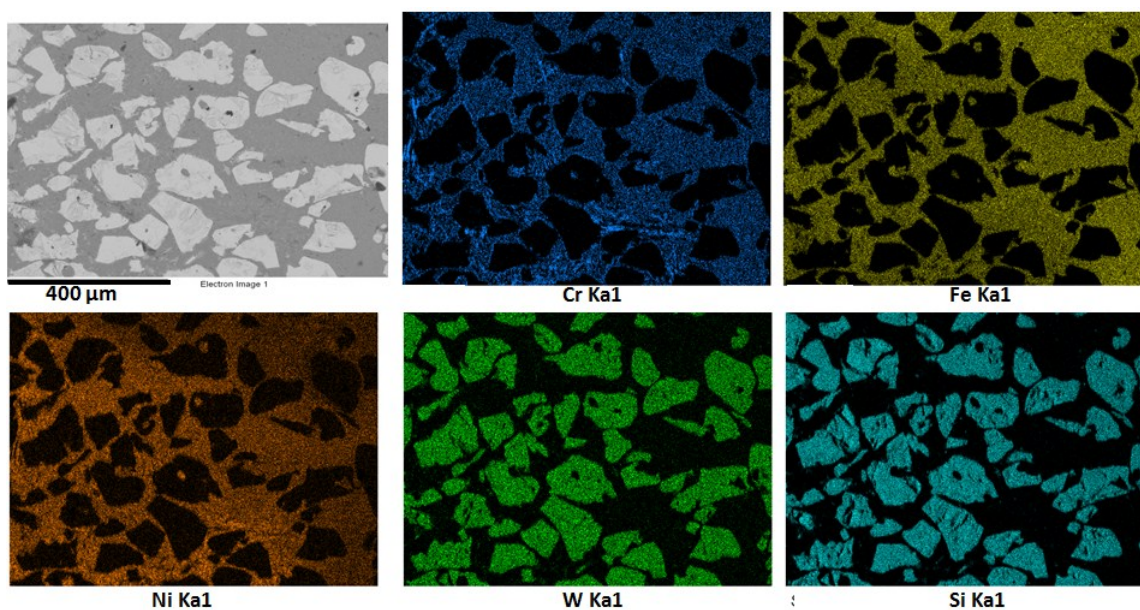


Fig. 5-25. Distribution of elements (EDS map analysis) of weld layer

5.5. Effect of process parameters on bead geometry (Simple prediction)

Based on the obtained data, for detail analysis of all twenty samples in simple model, following results can be obtained. Fig. 5-26 describes the effect of travel speed on penetration and dilution; in particular, with increasing the travel speed, the penetration decreases and, mainly with travel speed between 80 to 100 cm/min, minimum penetration is reached. The increasing of travel speed does not have specific effects on dilution. Because with increasing the travel speed, heat input decreases, consequently rate of diffusion in the surface decrease, as a result penetration decrease, but in some cases the reinforcement increases which causes to keep the dilution relatively constant with smooth upward trend. Fig. 5-27 depicts the effect of current on dilution and penetration. As it is clear, with increasing the current, the value of penetration and dilution steeply increase; this could be due to the increasing of the heat input in unit cell. As a result, selecting the appropriate parameters to reach optimum weld bead geometry is an important issue which should be considered.

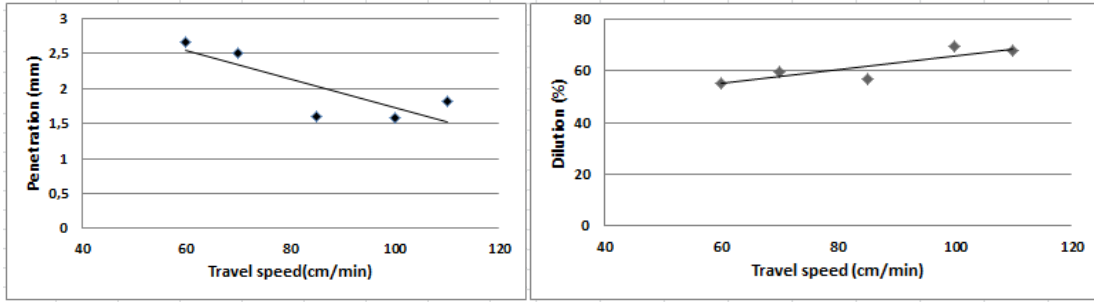


Fig. 5-26. Effect of travel speed on penetration and dilution

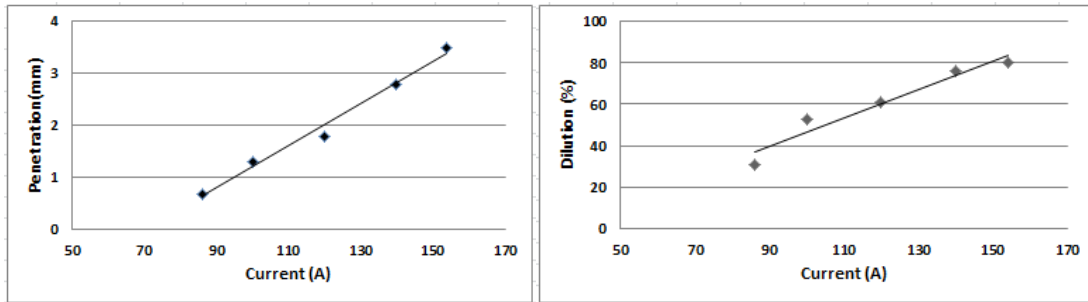


Fig. 5-27. Effect of current on penetration and dilution

5.5.1. Mathematical modeling and effect of process parameters

The range of parameters in actual units are simplified between the limits of -1.682 and +1.682 which are dimensionless [293]. Equations (6), (7) and (8) indicate the obtained model for prediction of dilution, penetration and reinforcement respectively. (Current : I , Travel speed: S , Preheat: T)

(6)

$$Dilution(\%) = -82 + 0.81(I) + 0.46(S) + 0.207(T) + 1.4 \times 10^{-3}(I * I) + 4 \times 10^{-3}(S * S) + 3.7 \times 10^{-3}(T * T) - 2.4 \times 10^{-3} * (I * S) - 1.05 \times 10^{-3}(I * T) - 1.71 \times 10^{-3}(S * T)$$

(7)

$$Penetration (mm) = -4.48 + 3.6 \times 10^{-2}(I) + 9 \times 10^{-3}(S) + 1.35 \times 10^{-2}(T) + 3.83 \times 10^{-4}(I * I) + 7.02 \times 10^{-4}(S * S) + 8 \times 10^{-6}(T * T) - 8.71 \times 10^{-4}(I * S) - 5.1 \times 10^{-5}(I * T) - 1.39 \times 10^{-4}(S * T)$$

(8)

$$Reinforcement = 13.99 - 9.12 \times 10^{-2} (I) - 0.1283(S) - 5.9 \times 10^{-3}(T) + 1.79 \times 10^{-4}(I * I) + 3.38 \times 10^{-4}(S * S) - 10^{-6}(T * T) + 3.12 \times 10^{-4}(I * S) + 4.1 \times 10^{-5}(I * T) + 3.8 \times 10^{-5}(S * T)$$

The comparison between predicted and desired values of process responses showed that there is limited differences between actual values and from the model. These results proved that the proposed procedure can be efficiently used to determine optimal process parameters for any desired weld bead geometry output values in PTA process.

Based on analyzing the data with *Minitab* software, the following data and model was found for prediction of the reinforcement. According to the obtained data, It is clear that, decreasing the current cause to increase the value of reinforcement. Also, with increasing the travel speed the reinforcement decrease. It could be due to fusion rate of the powder which keep constant for all value of travel speed. The 2D sections of the 3D distributions given by the equations 6 to 8 are shown in Fig. 5-28.

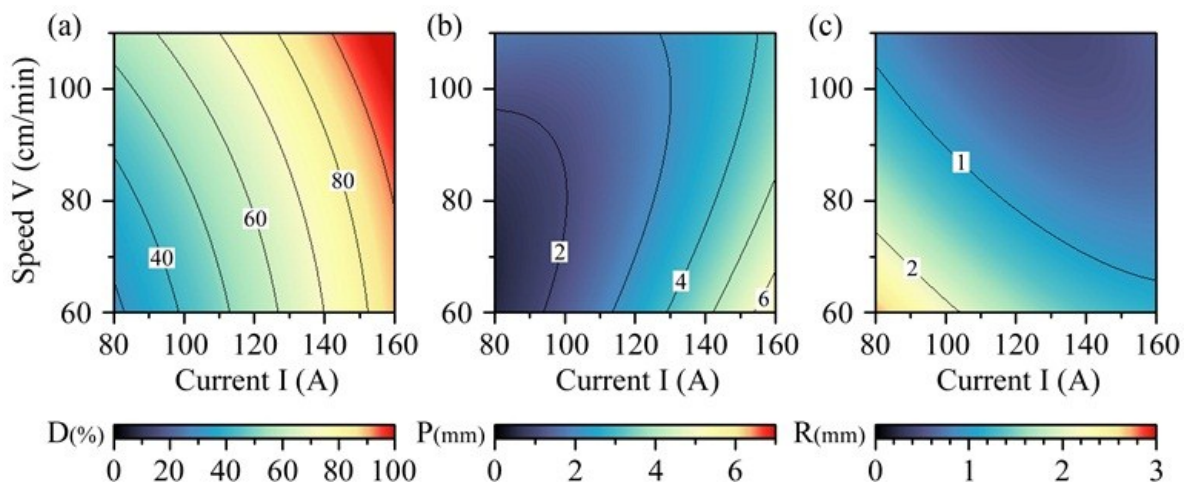


Fig. 5-28. Dependence of a) dilution D , b) penetration P and c) reinforcement R on current I and travel speed V for the constant substrate pre-heat temperature $T = 250\text{ }^{\circ}\text{C}$

For hardfacing applications, it is desirable to achieve high reinforcement by keeping weld penetration and dilution low. The condition of low dilutions met for the bottom left part of the plot, corresponding to low welding current (100 A) and travel speed (90 cm/min). This results can be explained by reduced heat input under smaller currents, which causes lower degree of substrate melting and as consequence lower dilution. The penetration value below 2mm are predicted for an elliptically-shaped area are limited with welding current $I=100\text{ A}$ and travel speed equal to 95 cm/min (b).

For the same parameter ranges, the reinforcement features inverse dependence on both current and travel speed, predicting the highest value for $I= 80\text{ A}$ and $S= 60\text{ cm/min}$ (c). Indeed, if the heat input from a low current plasma is insufficient for producing deep melting pool, the weld material will be rather deposited on top of the substrate, resulting in higher reinforcement. However, while all the observed individual parameter range seemingly define the optimal deposition conditions a low-current welding with slow nozzle movement, the combined response of D , P and R functions may compose more complicated picture.

To address this issue, the 2D plots of a cumulative parameter defined as $C = 35R - D - 15P + 10$. The positive sign of R means that larger values of reinforcement are desirable; the negative signs by D and P reflect the preference for low dilution and penetration. The coefficients by R, P and free term were chosen to balance the contributions of individual parameters basing on their maximum values.

This choice of coefficient is considered acceptable due to dependence on $C(I, V)$ which shows positive value in the major part of the plot (Fig. 5-29). The saturated red area in the bottom left corner of each panel corresponds to the maximum value $C > 90$, clearly showing the ranges of control parameters for which the model predicts the best welding bead geometry.

In all cases the low welding currents and slow travel speed are preferable. Remarkably, preheating limit the current values required to achieve $C > 90$; at $S = 60$ cm/min and $T = 250$ °C welding current should be less than 110 A, while at the same travel speed less than $T = 450$ °C the maximum welding current is about 95 A (a, c). This effect occurs because for higher substrate pre-heat the required thermal regime within the bead can be established with a lower heat input.

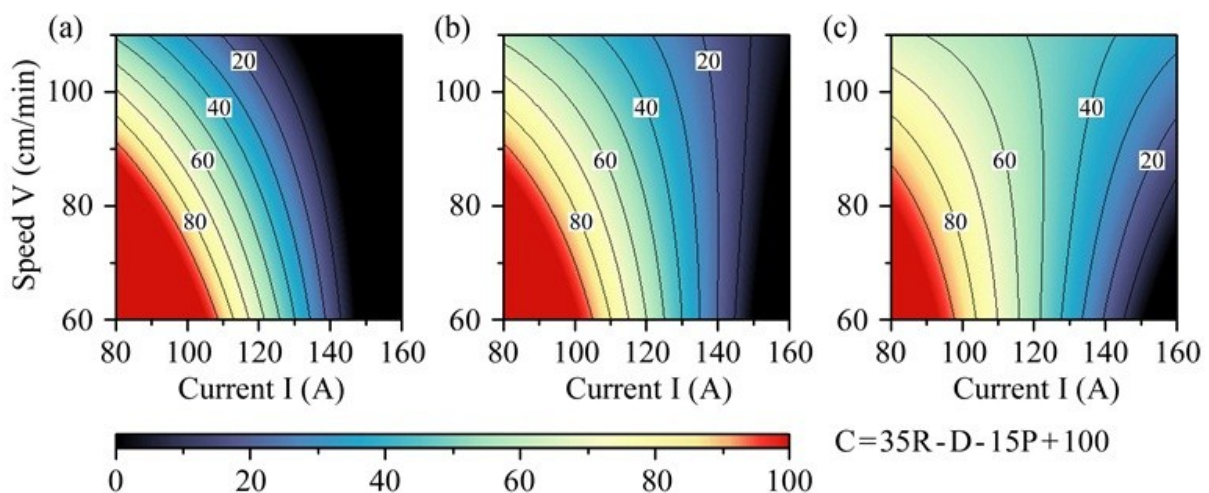


Fig. 5-29. Dependence of a combined parameter $C = 35R - D - 15P + 100$ on current I and nozzle travel speed S for different substrate pre-heat temperatures: a) $T = 250$ °C, b) $T = 350$ °C, and c) $T = 450$ °C.

It is important to specify that the increase of preheat changes considerably the behavior of the $C(I, V)$ dependence. A narrow arched band corresponding to C between 20 to 80 observed for low T changes into a fan shaped area embracing almost the entire area of the plot under elevated T . This means that, as long as moderate value of C are acceptable, the welding with fast travel speed (more than 100 cm/min) can be carried out for the currents varying in wide ranges. For a slow travel speed, a precise control of welding current is required. This result is of importance for fast welding applications.

5.6. Optimization of the obtained data

Based on experimental data, sample W9 with the following parameters and responses which specified in Table. 5-9 indicated the best results amongst all twenty samples. Based on these measurements, distribution of tungsten carbides and the hardness profile, sample W9 can be considered as optimum condition.

Table. 5-9. Parameters and results of optimum experimental sample

Sample name.	Current (A)	Travel speed (cm/min)	Preheat (°C)	Dilution (%)	Penetration (mm)	Reinforcement (mm)	Bead width (mm)
W9	86.36	85	350	30.52	0.69	1.43	6.53

But, it is relatively difficult to perform the welding process to reach suitable bead geometry with using different sets of process variable. Based on what suggested in literatures [269,322], to reach appropriate weld layer geometry, the reinforcement should be maximum, in addition penetration and dilution should be in minimum value.

It is very important to select appropriate process parameter to obtain optimal weld bead geometry [350,351]. To find the optimum parameters, there are many optimization methods [352], which needs more in depth mathematical investigation, but according to optimization of the parameters with using the multiple objectives, it is possible to obtain optimum parameters. Table. 5-10 indicates the optimum process parameters and estimation of weld bead geometry parameters based on the mathematical modelling. But this value should be validated by another experimental process to be sure about obtained data.

Table. 5-10. Optimize variable parameters and estimation of optimum responses based on the model

Sample	Current (A)	Travel speed (cm/min)	Preheat (°C)	Dilution (%)	Penetration (mm)	Reinforcement (mm)
optimum	86	60	225	36.84	1.38	1.80

Nevertheless, considering the several possible sets of process variables, it is relatively difficult to find the best welding parameters to predict and reach appropriate weld bead characteristics. Based on what suggested in literatures [319,353], to reach appropriate weld layer geometry, the reinforcement should be maximum, while penetration and dilution should be the minimum. In order to obtain optimum weld bead geometries, it is very important to select appropriate process parameters [279,354].

5.7. Characterization of optimized sample

5.7.1. Hardness profile

In the same context, the optimized sample was characterized. Fig. 5-30, shows the macrostructure of cross section hardfaced and its hardness profile. In this sample the matrix and the hard phase have an homogeneous distribution and the heat affected zone is smaller than the previous samples. As it can be seen in Fig. 5-30, the microhardness value of the base metal was measured around 790 HV. The hardness value of hardfaced layer through the cross section for different samples are varied, because of different size and distribution of tungsten carbides in the weld pool. However in this optimized sample there are more WC particles distributed in all the reinforcement. This phase reaches a hardness of 1850 HV, and the matrix has a similar hardness of substrate around 780 HV.

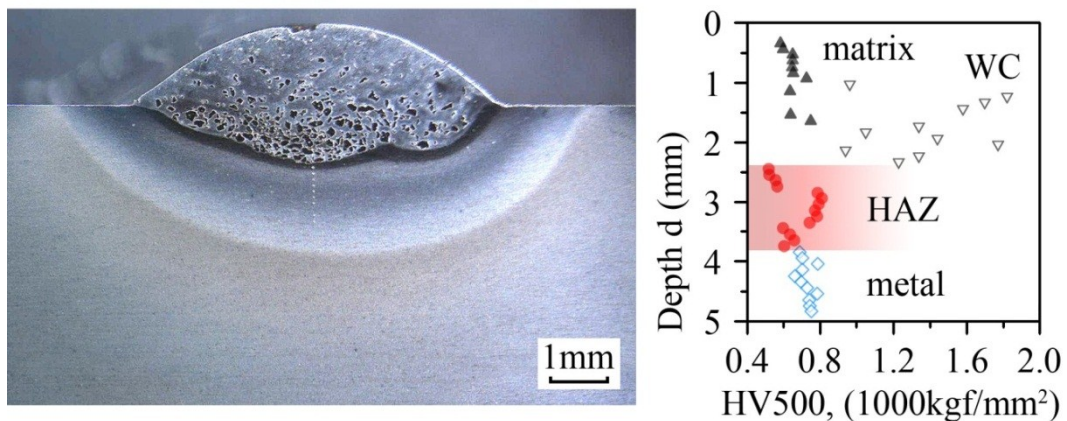


Fig. 5-30. Macrostructure of the cross section hardfaced optimized sample and its hardness profile

5.7.2. Microstructure evolution and EDS analysis

The SEM micrograph of the optimized sample is shown in Fig. 5-31. In general, the phases are the same as what we found in previous samples. The main difference is in the distribution and size of the phases. For example, the WCrC phase is smaller and the WC phase has more homogeneous distribution. From EDS chemical composition analysis, it is clear that tungsten in addition to existing in WC particle, is distributed in all part of the matrix in the range between 15 to 50 %. It was reported that WC/W₂C decarburized during thermal process and W and C dissolved into Ni and NiCr matrix [355]. There is generally less W dissolved in NiCr than there is in Ni, this could be due to presence of Cr which stop diffusion of W into Ni and it is in agreement to the phase diagram of the alloys. As it is clear from Fig. 5-31 spectrum 1 is the mono tungsten carbide phase which is not melted. Point 2 indicates the eutectic phase which is form due to the partial dissolution of tungsten carbide in the matrix. Phase 3 depicts the microstructure of nickel base matrix.

Normally, the dissolution of WC in the matrix is not more than 5%. The matrix is composed of nickel dendrite and lamellar eutectic in interdendritic region which was showed previously. In this sample, secondary phases like β -W₂C, or quadrilateral precipitates such as η 1-M₆C were not observed. However, the Ni–WC overlay produced in alloys which contained the highest fractions of Cr, C, and Si contained blocky Cr–Ni–Si–W–C phases located around the WC particles. The chemistry of these carbides is suggested as (NiSi)_X(CW)_Y which X and Y taking value in the range of (2.2-2.9) and (2.5-3.6) respectively [356,357]. In addition it has been suggested that, secondary phases which form due to dissolution around the reinforcing WC phase is useful to increase the wear resistance because it works as binder of WC particles to the matrix [358]. By comparing the corresponding images of Fig. 5-23 and Fig. 5-31, it can be seen that the optimized sample benefit from uniform distribution of carbide grains positively influencing the growth of (Cr, Ni)₃W₃C dendrites. Shorter dendrite branches point to faster solidification of the optimized sample. This mechanism leads to formation of isolated dendrite nucleation sites which homogeneously distributed in the bead matrix, forming a mixture of the different phases that improves wear resistance and strength of the material. The improvement of PTAW process efficiency can be illustrated by noting more pronounced primary carbide melting in the optimized sample under lower heat input (I = 86 A and V = 85 cm/min) in comparison with that of non-optimized sample (I = 100 A and V = 70 cm/min). Also, Table. 5-11 indicates the EDS chemical composition of different phases in optimum sample which specified in Fig. 5-31.

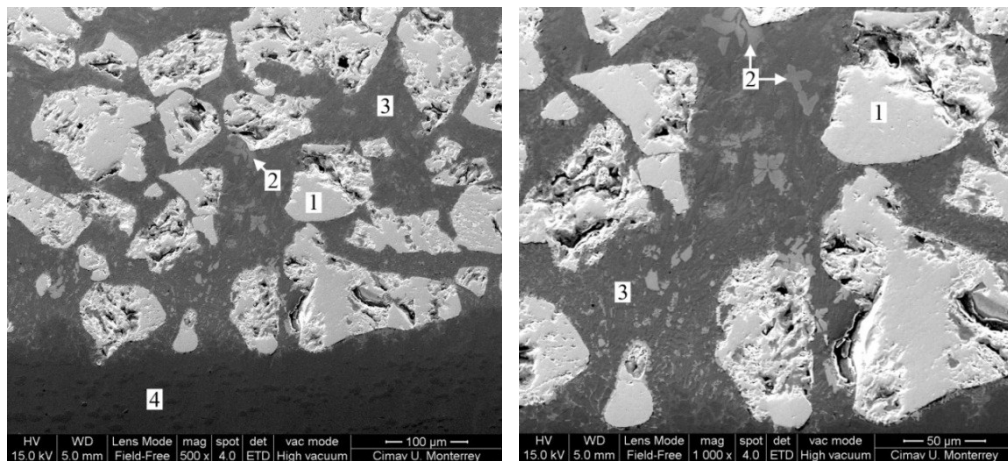


Fig. 5-31. Microstructure and EDS analysis of optimized sample: (1) Mono tungsten carbide phase, (2) Phases from eutectic reactions in interdendritic regions, (3) nickel base matrix overlay, and (4) Steel substrate.

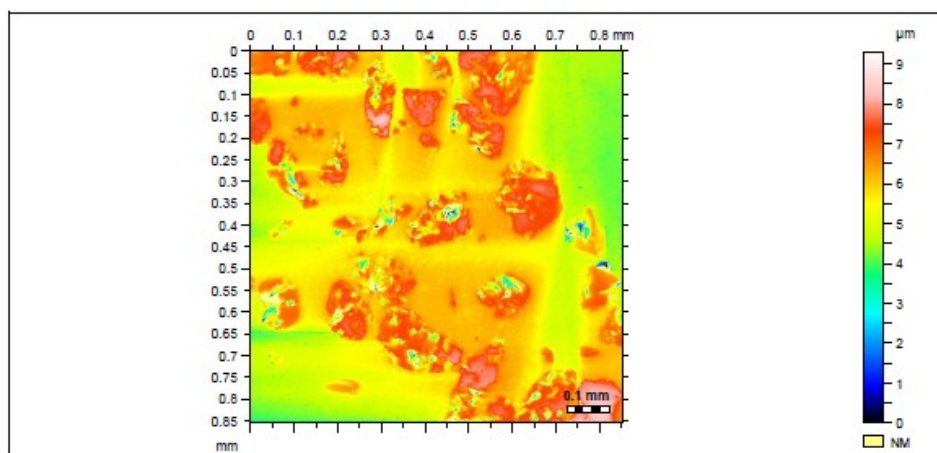
Table. 5-11. Chemical Composition (Wt %) of the different phases specified in Fig. 5-24

Elements	Phase 1	Phase 2	Phase 3	Phase 4
C	5.96	3.99	1.07	2.53
V	-	-	-	0.50
Cr	-	15.15	4.24	11.28
Fe	-	9.61	36.20	83.91
Ni	-	21.08	51.80	-
Mo	-	1.00	-	1.18
W	94.04	45.30	3.93	-
Si	-	3.87	2.77	0.6
Total	100.00	100.00	100.00	100.00

5.7.3. Surface profilometry

Also, Surface topography analysis was performed by light non-contact profilometer (Taylor Hobson) in 2D and 3D modes. Fig. 5-32 depicts the 2D top view of the surface. Tungsten carbide particles can be recognized by red color with higher height. Based on obtained data maximum differences between matrix and tungsten carbides are around 9 μm . Fig. 5-33 indicates 3D surface profile of distribution of tungsten carbides on the sample. Fig. 5-34 depicts one single tungsten carbide in the matrix accompanied with one line scan profile between two points. As it is visible, there is differences between height of tungsten carbide and matrix even if after metallographic preparation.

Two dimensional profile line scan specified that for one single tungsten carbide particle is about one micron higher than matrix close to interface, but the maximum height differences reach to 3.5 μm . Also, 3D profile of the sample in that figure indicates the distribution and height of the tungsten carbide on matrix. Also based on intrinsic irregular morphology of tungsten carbide, some holes and voids on the particles and interface of particles and matrix are visible.

**Fig. 5-32.** 2D Top surface profile of tungsten carbide in the matrix

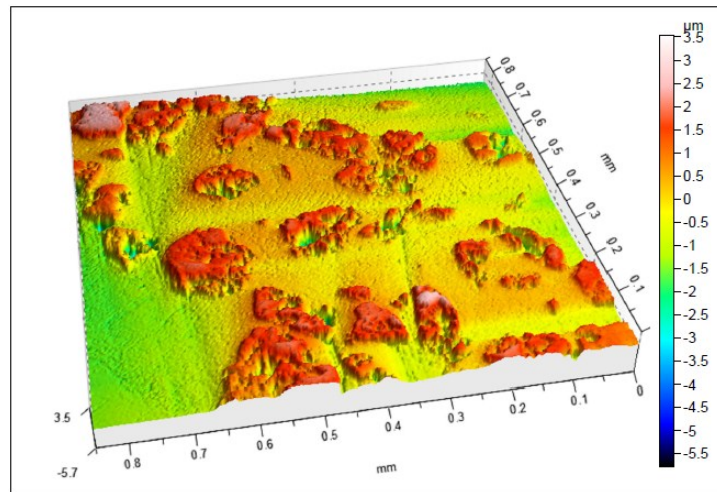


Fig. 5-33. 3D surface profile of distribution of tungsten carbide of optimized sample

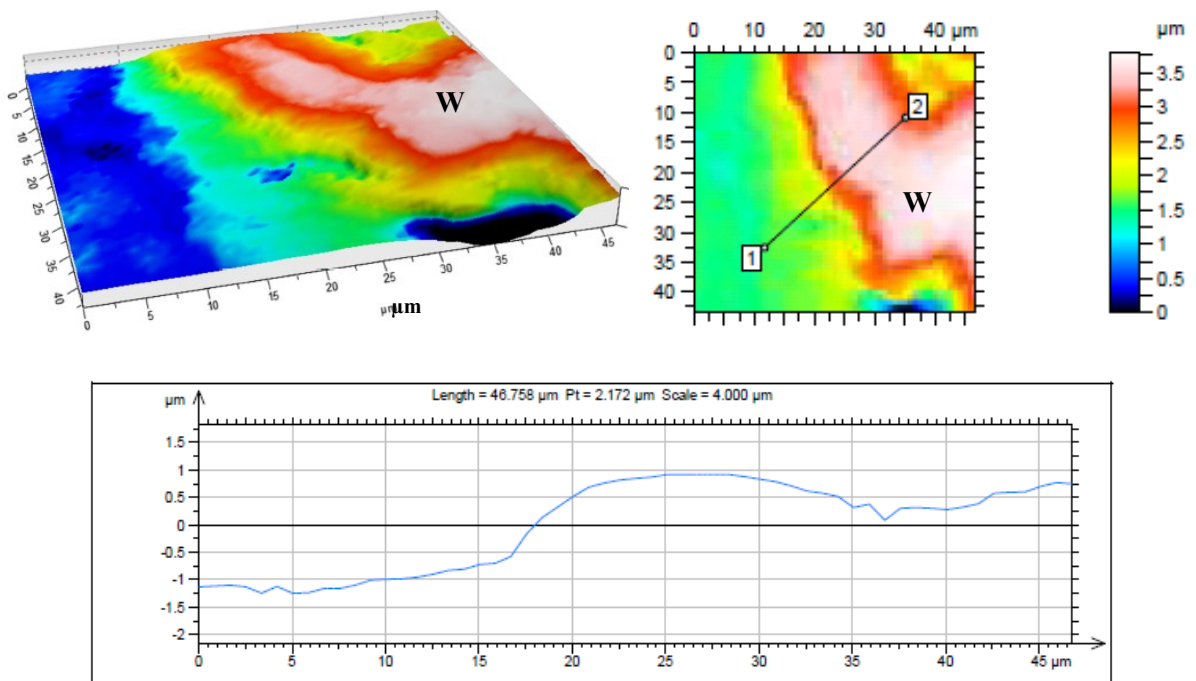


Fig. 5-34. Profile of a single tungsten carbide in matrix (a) 3D (b) 2D (c) surface profile between line 1 and 2

5.7.4. X-ray diffraction analysis

To identify the main crystalline phases composing the reinforcement layer, we conducted XRD analysis in addition to the EDS studies which was reported above. The resulting spectra (Fig. 5-35) reveals a number of phases that were not observed in EDS measurements. As it can be seen from the figure, the welding bead contains W_2C , WC, Cr_3Si , Ni_2B and FeNiCr. Though tungsten enters into the both semi-carbide W_2C and mono carbide WC, the concentration of the former is considerably lower than that of the latter, judging from the XRD peak intensities. The main phase representing the bead matrix is the solid solution FeNiCr. The dendrites of $(Cr, Ni)_3W_3C$ which was observed in the SEM did not appear in the XRD data because they predominantly form at the bottom of the weld pool, which for prepared sample geometry was outside of the XRD detector range.

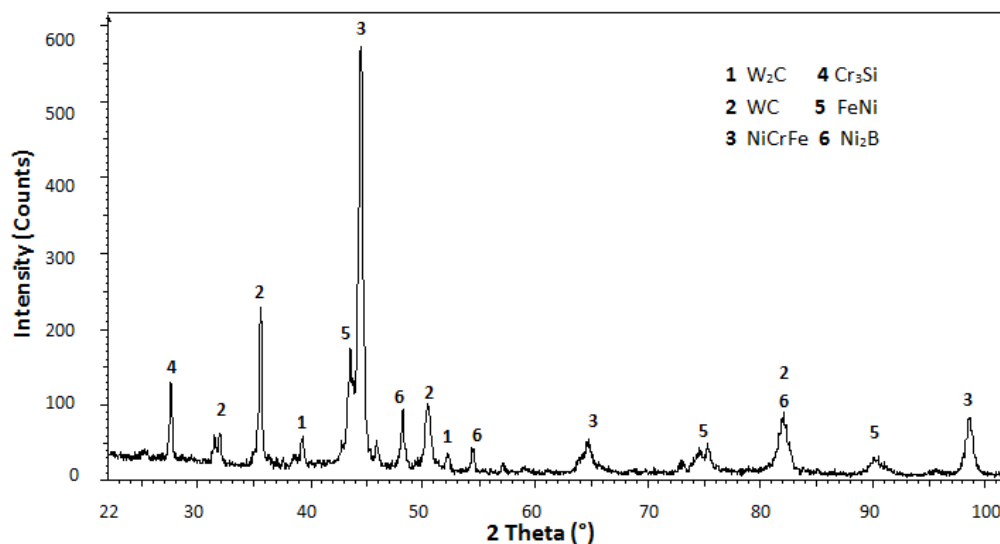


Fig. 5-35. XRD spectrum of the optimized sample

5.7.5. Element distribution and effect of pre heat temperature

To observe the effect of pre heat on the bead quality, at first a set of samples were hardfaced with optimal parameters ($I=80A$, $S=60$ cm/min). Three different temperatures of 250, 350 and 450°C were considered as a reference, all samples were cross sectioned and observed by microscope. indicates the cross section of the samples. It should be mentioned that for several cross sections prepared from the weld sample with preheat 450°C, the one with clearest flow pattern was selected. The cross section of the sample without pre heat was investigated by SEM followed by line scan EDS analysis (Fig. 5-36). As it is clear, the distribution of the elements inside of the bead is markedly inhomogeneous. There is a developed lamellar structure at the bottom of the welding pool. To clarify the nature of this phase, chemical profiling along several straight segments inside the bead. The area A is HAZ of the substrate featuring refined martensitic structure.

The general trend in this region is incrementing iron content towards the welding pool. The maximum concentration of Cr are aligned with the minimum concentration of the iron.

The B area is characterized with high iron concentration, the formation of this area can be attributed to a lower melting temperature of iron in comparison with the other elements in the substrate. So that the pool of iron can endure in the molten state the entire welding and most of solidification process.

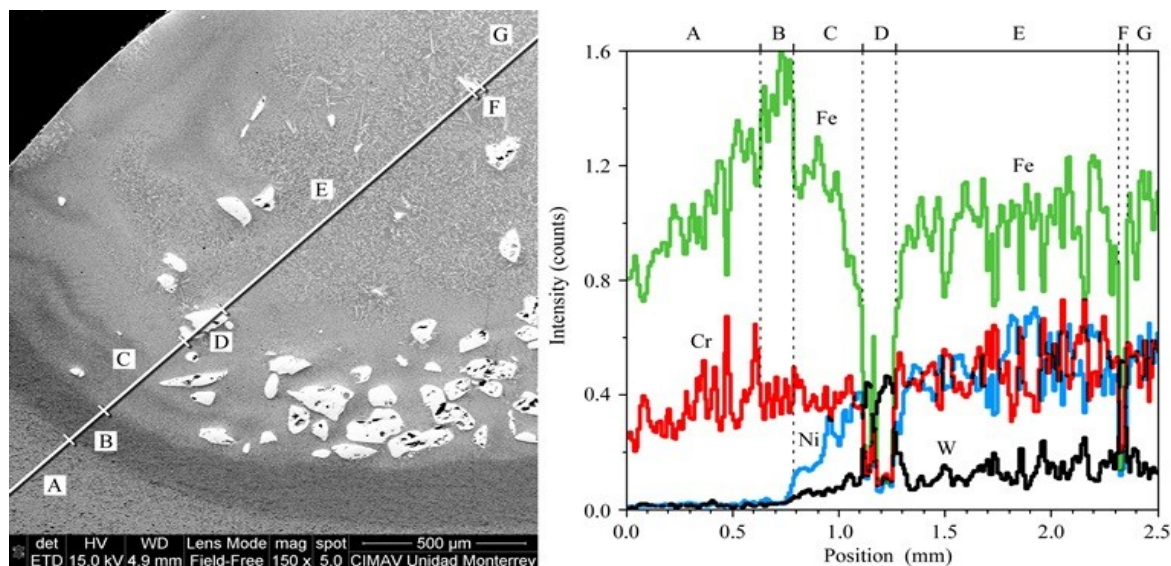


Fig. 5-36. Weld bead section and composition profile along the line with the letters denoting the characteristic phases:
 A) heat-affected zone of the substrate; B) solidified pool of iron;
 C) solidified traces of weld flows; D, F) WC carbide grains; E, G) FeNiCr dendrites

Inside of the bead, one observed quick increase of Ni concentration starting from the metallurgical boundaries, matched by increasing concentration outside of the carbide particles, points towards partial melting of carbide grains followed by subsequent mixture of tungsten with other elements of the bead. The smoother outline of the WC particles compare to the original rough surface, confirm this. The most important observation, to our opinion is the formation of a lamellar structure at the boundary that is directly associated with carbide particles. Area C which mainly is matrix consists flow patterns of iron concentration. Thus the sequence of darker and brighter strips in SEM micrographs represents flow lines with predominant content of the substrate material and nickel powder material. Fig. 5-37 indicates close-up images of transversal bead sections showing the solidified flow patterns of tungsten carbides in the weld pool (marked in part with white arrows) that influenced the final distribution of the carbide particles. The images correspond to different substrate pre-heat temperatures: a) $T = 250^{\circ}\text{C}$, b) $T = 350^{\circ}\text{C}$, and c) $T = 450^{\circ}\text{C}$. The images are aligned at the substrate level that is marked with a white dashed line. Also, it can be seen that with 250°C preheat the tungsten carbide flow patterns are linear, at 350°C the flow pattern are barely distinguishable and at high pre heat (450°C) the flow pattern is roughly curling. This changes in bead profiles could be justified by variation of fluid dynamics and temperature range of solidification. At low temperature preheat the plasma heats the substrate, melting out more material from the center of the welding pool so that the bead profile acquires a U-shape.

The carbide articles of different sizes are carried upwards by the flow of molten metal and gradually settle down. The forward motion of the welding torch causes the longitudinal component of liquid metal flow, so that the carbides mainly shift to the center of the bead (Fig. 5-37 a). Increasing the pre heat temperature cause to formation of deeper welding pool and keep the bead in a molten state for a long time, disrupting linear flow pattern. Thus for pre heat at 350°C the flow pattern are so weak that they are barely discernable (Fig. 5-37 b). Finally at 450°C both the depth of the melting pool and the solidification time increase to a degree that WC particles have sufficient time to move to the bottom of the melting pool due to their higher density. Only a few small carbide particles remain in the upper part of the bead, dragged by circulating metal flow (Fig. 5-37 c).

Consequently, the substrate pre heat temperature considered as a single parameter, but it has significant effects on the weld bead geometry. It influences on the depth of welding pool, the profile of the bead bottom and also changes the time of solidification. All these parameters are important to solidification dynamics, establishing different types of melt flow and defining the time at which the melt becomes too viscous to allow motion of the carbide grains. As one can be seen from Fig. 5-37 despite the original hypothesis considering that highest pre heat temperatures would be better for reduction of thermal stress of the substrate, but lower pre heat is actually more beneficial by ensuring linear metal flow mode and creating homogeneous distribution of carbide particles in beads. This cause to improve the quality of hardfacing. In case of no pre heat the traces of the metal flow are seen only at the bottom of the weld pool, without homogeneous distribution of carbide particles within the beads, so that carbide particles are mostly clustered at the bottom of the bead. Comparing different pre heat temperature, it can be said that under moderate pre heat ($T=250^{\circ}\text{C}$) most uniform distribution of carbide can be observed. This result also confirm.

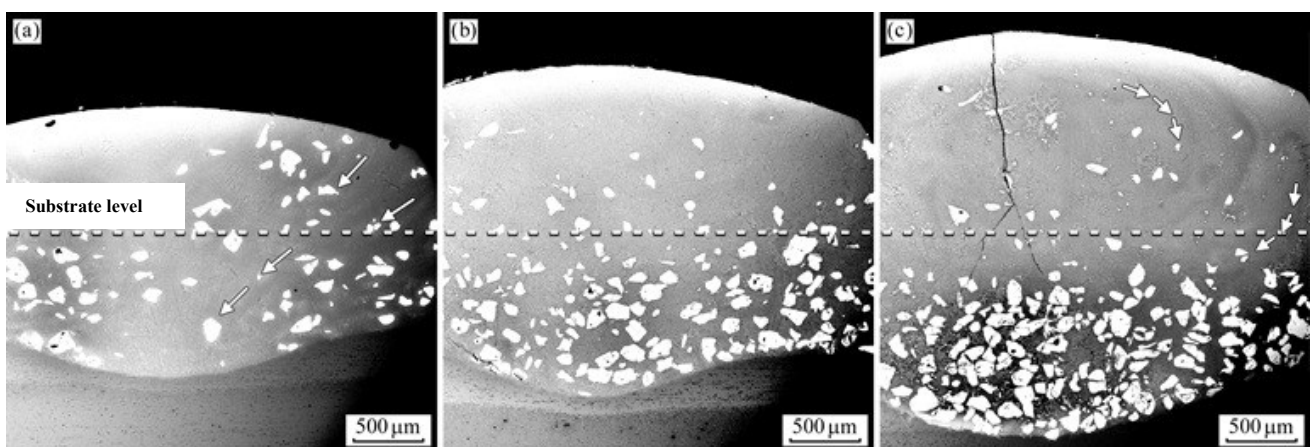


Fig. 5-37. Micro section of transversal bead sections showing the solidified flow patterns in the welding material (marked in part with white arrows) that influenced the final distribution of the carbide particles in different pre-heat temperature a) $T = 250^{\circ}\text{C}$, b) $T = 350^{\circ}\text{C}$, and c) $T = 450^{\circ}\text{C}$.

5.7.6. Nanoindentation

For a more detail study, the nano-indentation analysis of the optimized sample focusing on individual phases observed in scanning probe microscopy. The most representative structure formations in the bead matrix are larger dendrites. To diminish point to point variation of the measured data, at least ten nano-indentation tests for different spots within the same phases were performed according to Oliver and Pharr method. Fig. 5-38, presents the mechanical properties of the optimized sample which obtained from nanoindentation test.

In the nanoindentation three prominent phases were detected in scanning electron microscopy which are clear in the Fig. 5-38, FeNiCr dendritic matrix phase, large WCrC (carbide) phase and mono tungsten carbide WC phase. The representative structures of interest (WCrC phase, and NiCrFe matrix) are shown in the scanning probe microscopy of Fig. 5-38a and Fig. 5-38b.

As it can be seen in Fig. 5-38a, the WCrC phase is present in the sample with a homogeneous distribution, having branches forms with length and thickness around 3 μm and 1 μm , respectively. Nanoindentation tests were carried out in a representative WCrC phase, where the $P-h$ curves (light gray line in Fig. 5-38d) shows high scattering due to the low homogeneity in material, letting calculate a reduce elastic modulus of $E_r = 217 \pm 64$ GPa, and hardness of $H = 13 \pm 7$ GPa.

In the other hand, for the case of matrix phase, also an increased scattering was present in nanoindentation tests (Fig. 5-38d). Fig. 5-38a shows how the bulk sample surface consist of several reliefs, which it is associated with the highest disparities of the $E_r = 196 \pm 25$ GPa, and hardness $H = 6 \pm 3$ GPa values. The differences of the penetration resistance between both structures can be seen in Fig. 5-38b, were the indentation at the matrix phase shows the biggest deformation, with an indentation imprint of about 1 μm , while the indentation imprint at the WCrC structure shows a very small deformation of about 200nm of length. In the same way, for the case of the tungsten carbide WC particles, similar results were calculated in both samples, with an increase elastic modulus of $E_r = 384.29 \pm 41.69$ GPa, and hardness of $H = 26.07 \pm 3.55$ GPa.

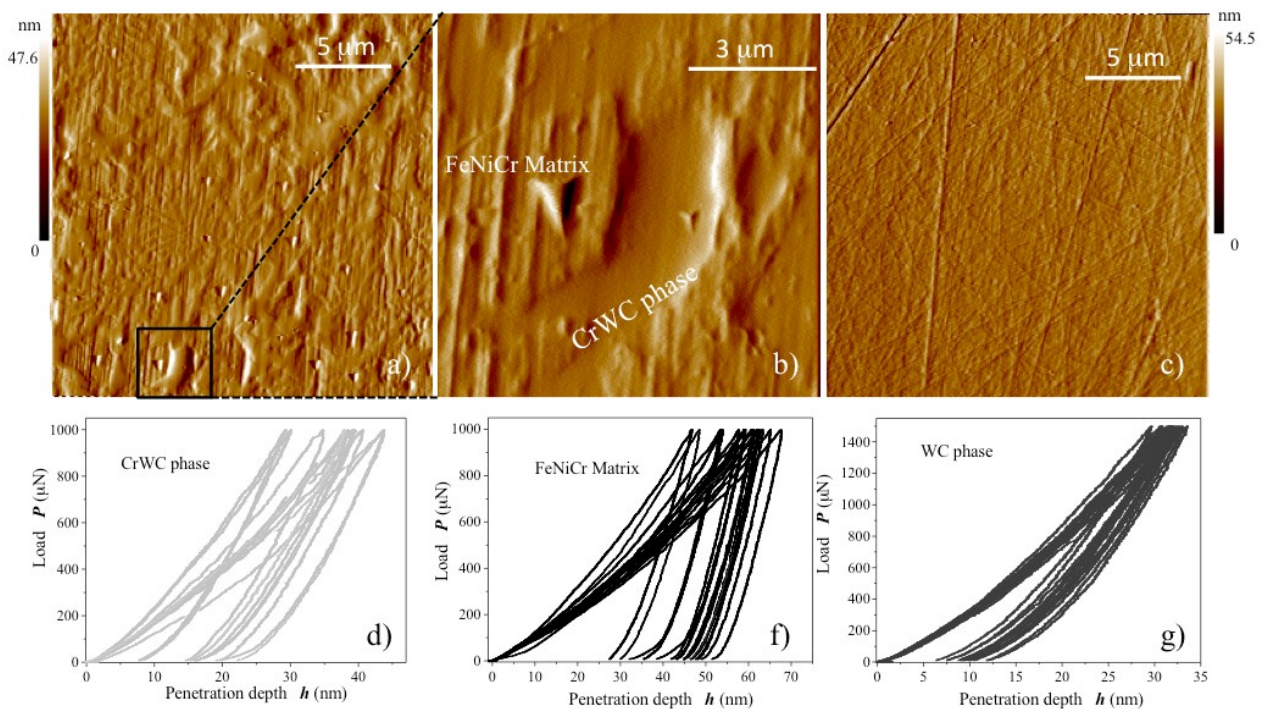


Fig. 5-38. Nanoindentation profiles and location in the main phases measured in the optimized sample

5.8. Conclusions

The PTA process hardfacing technique with using Ni-based powder reinforced by tungsten carbide composite was optimized by using design of experiments (response surface methodology) for hardfacing of the D2 tool steel. It was shown that the best bead properties in terms of reinforcement and dilution can be achieved under low welding current ($I \leq 100\text{A}$) and travel speed ($S \leq 90\text{ cm/min}$). Based on experimental investigation and mathematical modelling for prediction of the weld bead geometry and metallurgical characterization, the following results can be obtained:

- Design of experiments is an effective method to study the effect of process parameters on the weld bead geometry in PTA process.
- The mechanical properties of the welding bead benefit much from the presence of the secondary dendrites that on one hand, has the intermediate hardness values between those of the bead matrix and hard carbide phase; on the other hand due to their shape, provide enhanced interlocking between the phases.
- Current is the main parameter which has direct effect on weld bead geometry, and distribution of tungsten carbides, after that travel speed is important. Mainly with increasing the current, penetration and dilution increase, but reinforcement decrease. Based on the mathematical modeling and using software optimum parameters was found as current = 86 A, travel speed=60 cm/min and 225 °C preheat.

- The numerical predictions suggested that lower substrate preheat can further improve the bead parameters. The detailed characterization of the optimized samples shown that the welding leads to partial melting of tungsten from carbide particles, with the formation of secondary carbides (Cr, N)₃W₃C with dendritic structure.
- The distribution of WC particles in the weld pool was not completely homogeneous and it was accumulated in lower part of the weld pool, close to the base metal, which could be due to higher density of these particles.
- The mechanical properties with micro and nano hardness of the sample were characterized. The identification of the phases was corroborated by the reproducibility of their mechanical responses. Significant differences were observed for the young module or hardness values between structures, tungsten carbides (WC), WCrC and matrix. Such behavior should be related to the improvement of their mechanical properties at macro scale performances, since the dendrite structures would provide stiffness to the sample, while the bulk offers formability.
- The distribution of WC particles in the weld pool was not homogenous. Carbides mainly accumulated in lower part of the layer, close to the base metal. According to only one set of parameters their distribution was quite uniform in the layer.
- SEM and EDS analysis of the samples showed that, in addition to blocky WC particles, tungsten was dissolved in the matrix. Complex phases containing tungsten and other carbides former elements were detected in the layers.
- From the microstructural and geometrical data obtained from the analyzed samples, the optimum parameters for hardfacing were actually found as: current=86.36 A, travel speed=85 cm/min and preheat=350 °C. With this parameters, the values of dilution, penetration, reinforcement and bead width were 30.52%, 0.69mm, 1.43mm and 6.53mm, respectively. It is very difficult to find the optimum parameters to obtain high quality weld bead geometries, but by developing the mathematical modelling as a guide to select the best process parameters, appropriate results can be achieved.

Chapter 6: Influence of addition of WC nano-particles on the hardfacing properties of the nickel-based coating deposited by PTA process

Abstract

In this chapter based on obtained data parameters from chapter five for optimization of hardfacing process, the effect of addition of tungsten carbide (WC) nanocrystalline on the microstructure and wear performance of the Ni–WC (nickel–tungsten carbide) composite overlays is studied. In commercial powders, the dimension of Tungsten carbide particles are in micron size and after precipitation and distribution in the matrix, there is risk of crack formation and propagation. To concur this problem, in addition to increase fraction of retained WC phase, and reduced fraction of brittle secondary carbide phases I considered the effect of addition of tungsten carbide in nano size, in microstructure and mechanical properties of the deposited layer. First of all, some tests were performed to find the optimum welding parameters. Another controversial issue was to find how much percentage addition of nanoparticle cause to reach optimum properties. To do this, tungsten carbide nano particle 1 to 7 % was added to existing commercial powder and mechanically mixed to homogenize the powder. After mechanically mixing the powders, all powders were deposited on the surface with the same parameters. After deposition, first of all weld bead characteristic for each sample was performed. Microstructure evolution by means of optical and scanning electron microscopy was carried out. EDS analysis was performed to find distribution of different alloying elements in the microstructure. To find possibility of formation of different phases, XRD analysis was performed on all samples. To evaluate the mechanical properties of the layers, macro and nano hardness test accompanied with wear test was performed. The Ni–WC overlays had microstructures consist of γ -Ni dendrites, with interdendritic Ni-Fe based eutectics, borides $(\text{Fe-Cr})_2\text{B}$ and carbides $(\text{Fe,Cr})_7\text{C}_3$. Overlays with addition of WC-nanocrystalline produces important changes in refining the microstructure, which produces an interesting effect on the mechanical and wear properties, this effect is mainly related to the dissolution of the tungsten carbide nanoparticles from the starting powder. The dissolution of WC particles promoted the formation and growth of secondary carbide phases. Ni-alloys with low amount of carbon and chromium content exhibited the least dissolution of WC. The Ni–WC overlays produced using these dilute alloys generally performed better in wear tests.

Keywords: Plasma Transferred Arc welding (PTA), nano-crystals tungsten carbide, hardfacing coatings, nickel alloy.

6.1. Materials and experimental procedure

6.1.1. Base Material

In this investigation block of D2 tool steel was used as substrate with dimensions of 130 mm× 50 mm× 12.5 mm. With the aim to reach an appropriate hardness and toughness, the D2 steel sample blocks were subjected to a recommended heat treatment [338] consisting in a preheating at 790 °C during 1 hour, next stage was heating at 1100 °C for 35 minutes and then samples were quenched in oil. Finally, two steps tempering treatments were performed at 315 °C for 2 hours each. The nominal chemical compositions of the D2 steel and relevant heat treatments are given in Table. 6-1 and Table. 6-2 respectively.

Table. 6-1. Chemical composition (wt%) of D2 base metal

Elements	C	Si	Mn	Cr	Mo	V	P	S	Fe
wt%	1.58	0.37	0.48	11.52	0.89	0.56	0.017	0.029	Bal.

Table. 6-2. Heat treatment cycle for D2 steel blocks

Heat Treating	Preheating	Main treatment	Quenching	Tempering 1	Tempering 2
Temperature	790°C	1100°C	Oil	315°C	315°C
Time	1hr	35 min		2hr	2h

Based on DoE method which was explained in previous chapter, before PTA welding process, each plate was preheated at 300 °C for 30 minutes in a muffle furnace in order to avoid thermal shock that might cause to crack formation on the substrate. Fig. 6-1 indicates the image of furnace which was used for pre heating the samples.



Fig. 6-1. Furnace for preheating the samples before PTA process

6.1.2. Powder filler materials

6.1.2.1. Nickel base powder reinforced with WC

Nickel-based powder mixed with tungsten carbide was used as a main powder material. It consists of 60 % mono tungsten carbide and 40 % matrix with hardness of 60 HRC and particle size of $180 \pm 63 \mu\text{m}$ in diameter. This powder was commercially supplied by Oerlikon-Metco company. Table. 6-3 indicates the chemical composition of the powder. Morphology of the powder is shown in Fig. 6-2.

Table. 6-3. Nominal chemical composition (wt.%) of nickel base powder and reinforce WC

Material		Chemical composition						
		C	Si	Mn	Cr	B	W	Ni
Hardfacing powder alloy	Ni Matrix	0.6-0.8	3.9-4.9	-	14.0-16.0	3.0-3.4	-	Bal.
	WC Reinforce	6.0-6.2	-	-	-	-	Bal.	-

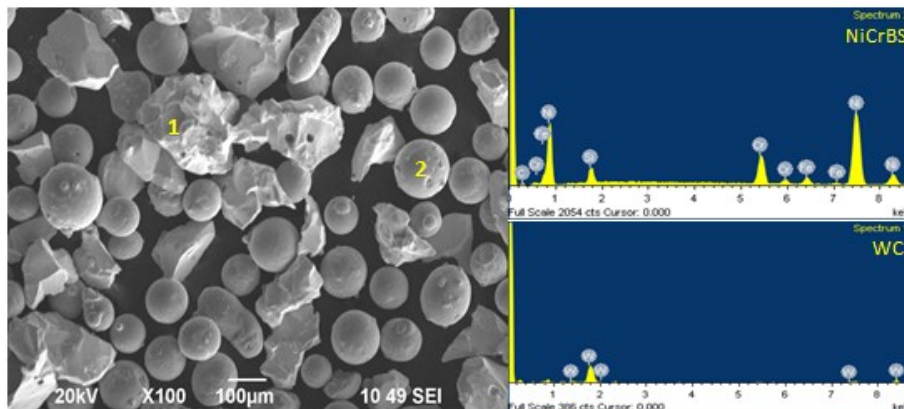


Fig. 6-2. Morphology and EDS analysis of the Nickel base powder

6.1.2.2. Nanocrystalline tungsten carbide particles

Tungsten carbide nanoparticles which was used in this study, supplied from Inframat® Advanced Materials™, it is a nano-crystalline tungsten carbide with a purity of 99.95 %, average particle size $\sim 200 \text{ nm}$ and crystal size 40–100 nm. Fig. 6-3 shows the SEM micrographs of agglomerated nanoparticles tungsten carbide in different magnifications which is used in this investigation. For detail analysis and observation of single particles, TEM analysis is required.

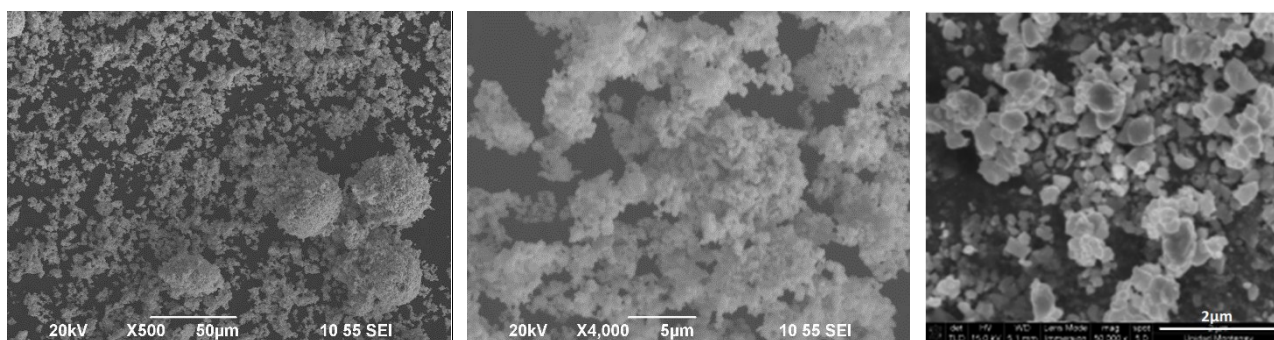


Fig. 6-3. Morphology of agglomerated WC nanoparticle in different magnifications obtained by SEM

6.1.2.3. Mixing the powders and homogenizing

A mixer is high energy ball mill which accommodates sample in different sizes. It is appropriate for grinding dry and brittle samples. The mixing balls can be in form of hardened stainless steel, tungsten carbide and alumina. To mix homogeneously the Ni-WC powder with WC nanocrystalline particles in different percentages (1, 3, 5 and 7 wt.%) a SPEX Mixer/Mill model 8000M during 15 min with the aim of preserving the original particles morphology was used. In this case we will be sure about the homogeneity of the mixed powders. Fig. 6-4 indicates the out frame and inter of the mixer mill machine which was used in this study.



Fig. 6-4. The mechanical mixer for mixing and homogenizing the powders

Fig. 6-5 shows the morphology of the Ni-WC with addition of nanoparticles to use as extra reinforced material for PTA process obtained by scanning electron microscopy. It is obvious that, the distribution of nanocrystalline WC are homogeneous and mainly stick on the outer surfaces of both nickel base and tungsten carbide particles in micron size.

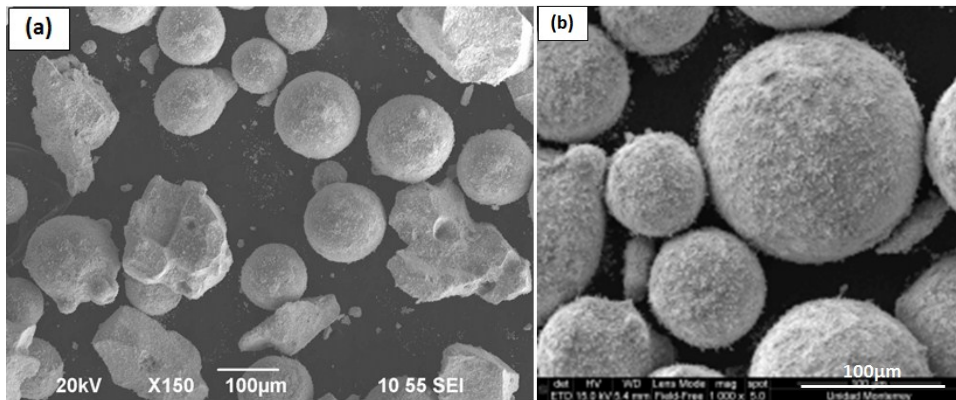


Fig. 6-5. Morphology of the Ni-WC powder after mixing with nanocrystalline WC in different magnifications

6.1.3. Plasma Transferred Arc (PTA) process

The PTA process was performed by a Castolin Eutectic Eutronic Gap 3001 DC equipment. The details of the PTA process and equipment was described in previous chapter. According to the technical data sheet of Ni-WC hardfacing powder, several experiments were previously performed with the aim to optimize the dilution, formability, surface hardness and deposition thickness, as well as to obtain sound and crack free layers. Such conditions are presented in Table. 6-4. Fig. 6-6, indicates the schematic and real position of torch on the block for applying the hardfaced layer respectively.

Table. 6-4. Experimental conditions for PTA overlay welding

Parameter (Units)	Value
Transferred arc current (A)	80
Transferred arc voltage (V)	20
Feeding rate (%) (50 gr/min)	50
Preheating (°C)	300
Nozzle diameter(mm)	3.2
Torch to work piece distance (mm)	10
Ion gas: Ar (l/min)	12
Shielding gas: Ar+10 % H ₂ (l/min)	3.5
Carrier gas: Ar (l/min)	3.5
Travel speed (m/min)	0.3
Torch gap (mm)	10

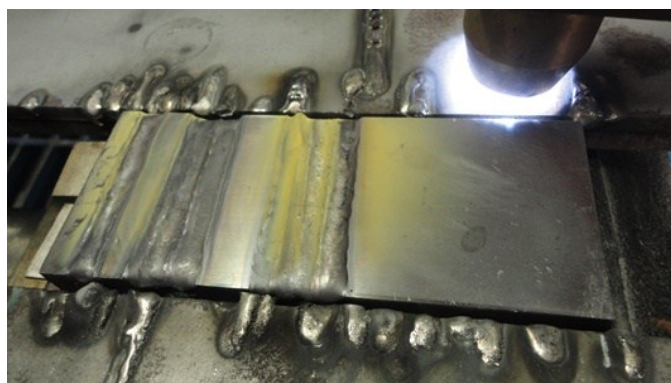


Fig. 6-6. Position of the torch for the process

6.1.4. Microstructural characterization

The overlaid samples were cut perpendicular to the welding direction. The obtained cross sections were prepared by conventional metallographic techniques. The polished samples were etched with the Marbles and mixture of HF+HNO₃ reagent. For microstructural characterization a FEI Nova Nano SEM 200 system equipped with energy dispersive X-ray spectroscopy (EDS) and INCA software with resolution of 1.5 nm at 20 kV was used.

6.1.5. Microhardness and nanoindentation

Room temperature hardness on the cross-section of the hardfacing coatings was acquired by means of a Micro-Hardness Tester (Clemex MMT-X7) at a load of 300 g and a loading time of 10 s. The overall indentations were made in profile form, each indentation of 100 μ m starting from the surface, in samples that were previously prepared by metallographic techniques. Hardness for the whole hardfacing coating was then averaged by all tested values. The hardness and elastic modulus of the samples were characterized by nanoindentation technique using a Berkovich diamond tip in a TI 950 Triboindenter, Hysitron, Minneapolis, USA. A maximum applied load of 1.5 mN was used, with a loading-unloading rate of 150 μ N/sec.

In order to avoid topographic effects during the nanoindentation tests, the top surface of the samples were polished with silicon carbide sandpaper having different particle sizes, and in the final step, using a commercial diamond polishing paste (500 nm particle size), thus obtaining a mirror surface appearance.

The diverse structures of the samples were classified according to the characterization of their variety of phases. Around twenty indentations were performed on each structure type of the samples; hardness and elastic modulus were calculated from the load-displacement ($P - h$) curves, using the Oliver-Pharr method [339].

6.2. Results and discussions

6.2.1. Weld bead geometry measurement

After visual and liquid penetration test of the layers, the samples were cut through cross section the samples, the surface preparation was performed on all the samples. According to schematic Fig. 6-7, the weld bead geometry was calculated. Table. 6-5 indicates the results of weld bead geometry for all samples. Dilution with the base material was around 50 % and was measured geometrically by the formula $\frac{A}{A+B}$.

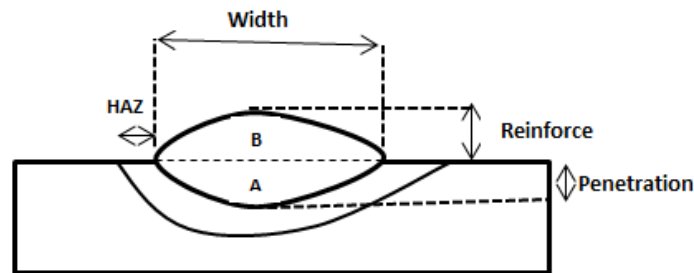


Fig. 6-7. Schematic form for characteristic parameters measurement of the layer

Table. 6-5. Results of the weld bead geometry measurement

Sample	Dilution%	Width (mm)	Penetration (mm)	Reinforce (mm)	HAZ (mm)
Woka	52	6.83	1.34	1.02	2.06
W1NP	52.76	6.28	0.73	0.74	1.73
W3NP	46.14	6.69	0.85	1.21	1.54
W5NP	46.62	6.05	0.88	1.08	1.86
W7NP	51.96	6.6	1.09	1.11	0.58

As it is clear the percentage of dilution for all samples were relatively high, which could be due to high current which used in this work. Normally, penetration increase with increasing the welding current. Fig. 6-8 indicates macrograph cross section of one random sample after metallography preparation.

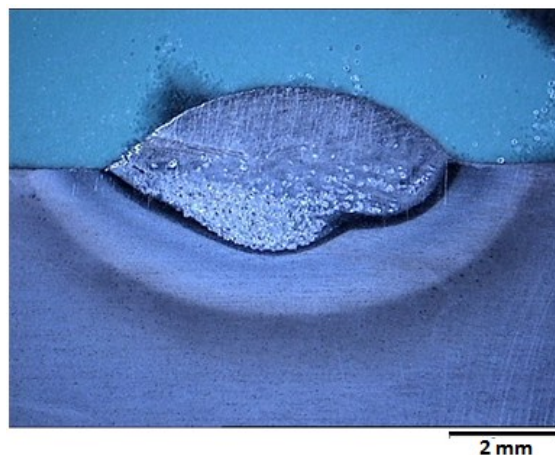


Fig. 6-8. Micro-image of one deposited layer after preparation

6.2.2. Microstructure evolution by optical microscopy

After cutting the samples and metallography preparation, first of all the macro section of the samples was evaluated by means of stereomicroscope. The distribution of tungsten carbides are like what discussed in previous chapter. Also as we expected, due to small dimension of the nanoparticles, no evidence of that were observed in macrosections. Fig. 6-9 indicates the distribution of tungsten carbide for sample W5NP and W7NP.

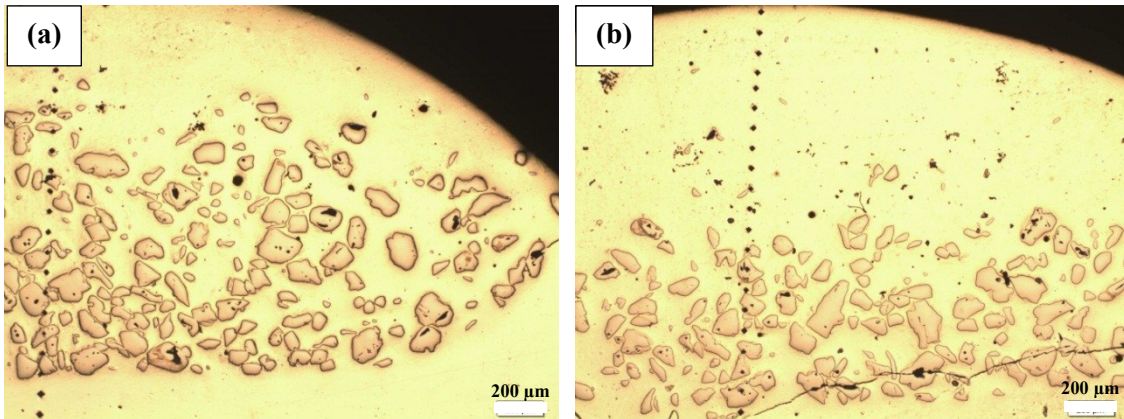


Fig. 6-9. Distribution of WC in sample (a) W5NP and (b) W7NP

Then, the microstructure evolution of all the samples with different percentages of WC nanoparticles was evaluated by means of optical microscopy. Fig. 6-10 indicates the microstructure of weld overlay in which the distributions of micron size tungsten carbides are visible. In addition Fig. 6-11 shows the microstructure of dendrites with higher magnifications in which the distribution of agglomerated nanocrystalline tungsten carbides between dendrites are visible. Fig. 6-12 indicates the dimension of agglomerated WC nanoparticles in the microstructure. The sizes of agglomerated WC nanoparticles which mainly agglomerated and located inside of interdendritic positions are between 3 and 7 μm . Also, with addition of different weight percentage of nanocrystalline WC, the distributions of agglomerated particles increase. Fig. 6-13 depicts the size of large WC inside of the matrix for comparison with dimension of agglomerated nanoparticle tungsten carbides, the dimension of WC are between 30 to 70 μm .

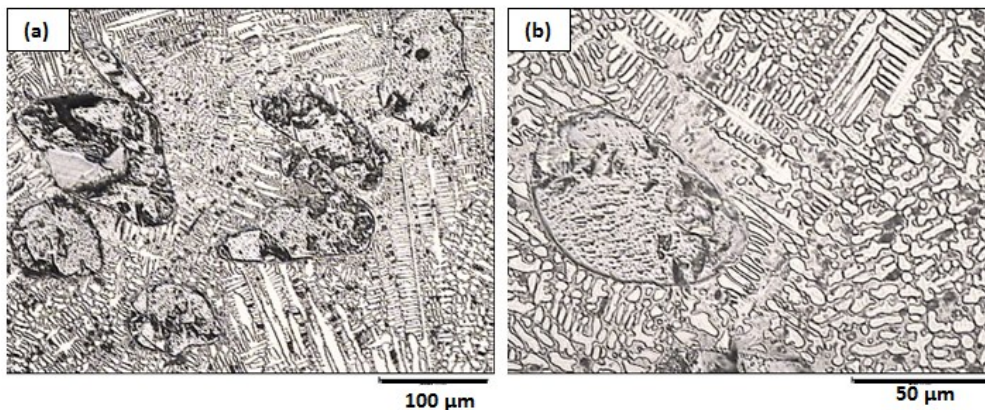


Fig. 6-10. Distribution of WC in micron size and nano size in weld overly

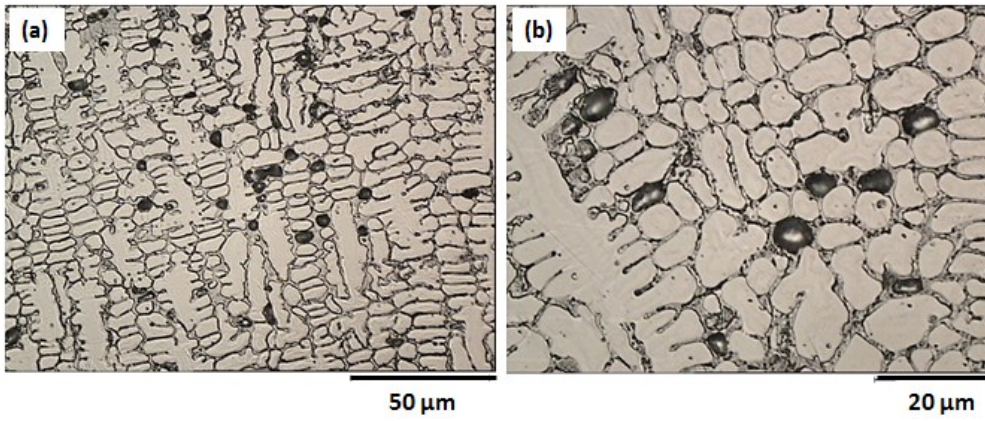


Fig. 6-11. Distribution of agglomerated nanocrystalline WC in weld overlay

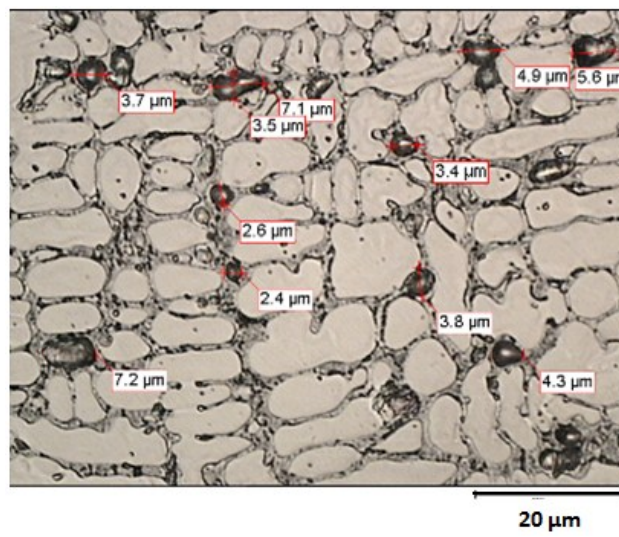


Fig. 6-12. Dimension of agglomerated WC nanoparticles in the microstructure

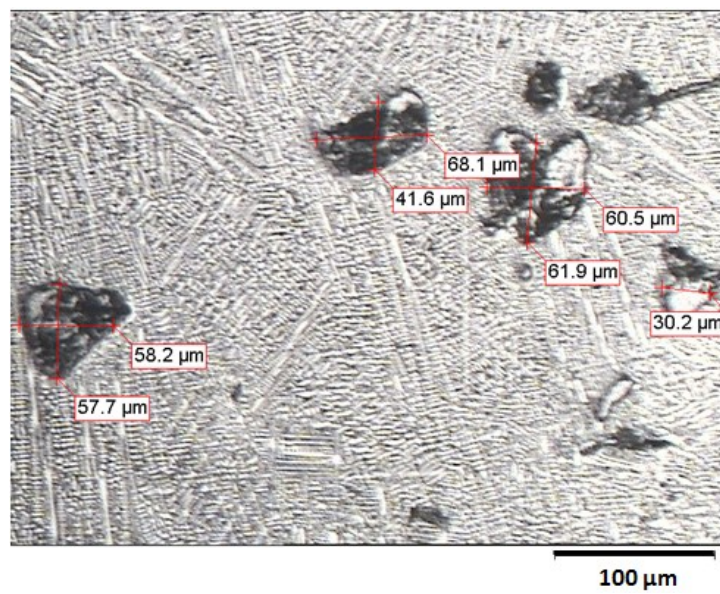


Fig. 6-13. Dimension of large WC particles in the microstructure

In addition, the microstructure evolution was performed to observe changing the microstructure from the top layer to the base metal. Fig. 6-14 depicts detail microstructural evolution of different zones by optical microscopy. In this figure microstructure of nickel base matrix, distribution of tungsten carbides in the nickel matrix, interface of layer-base metal, heat affected zone and base metal is recognizable.

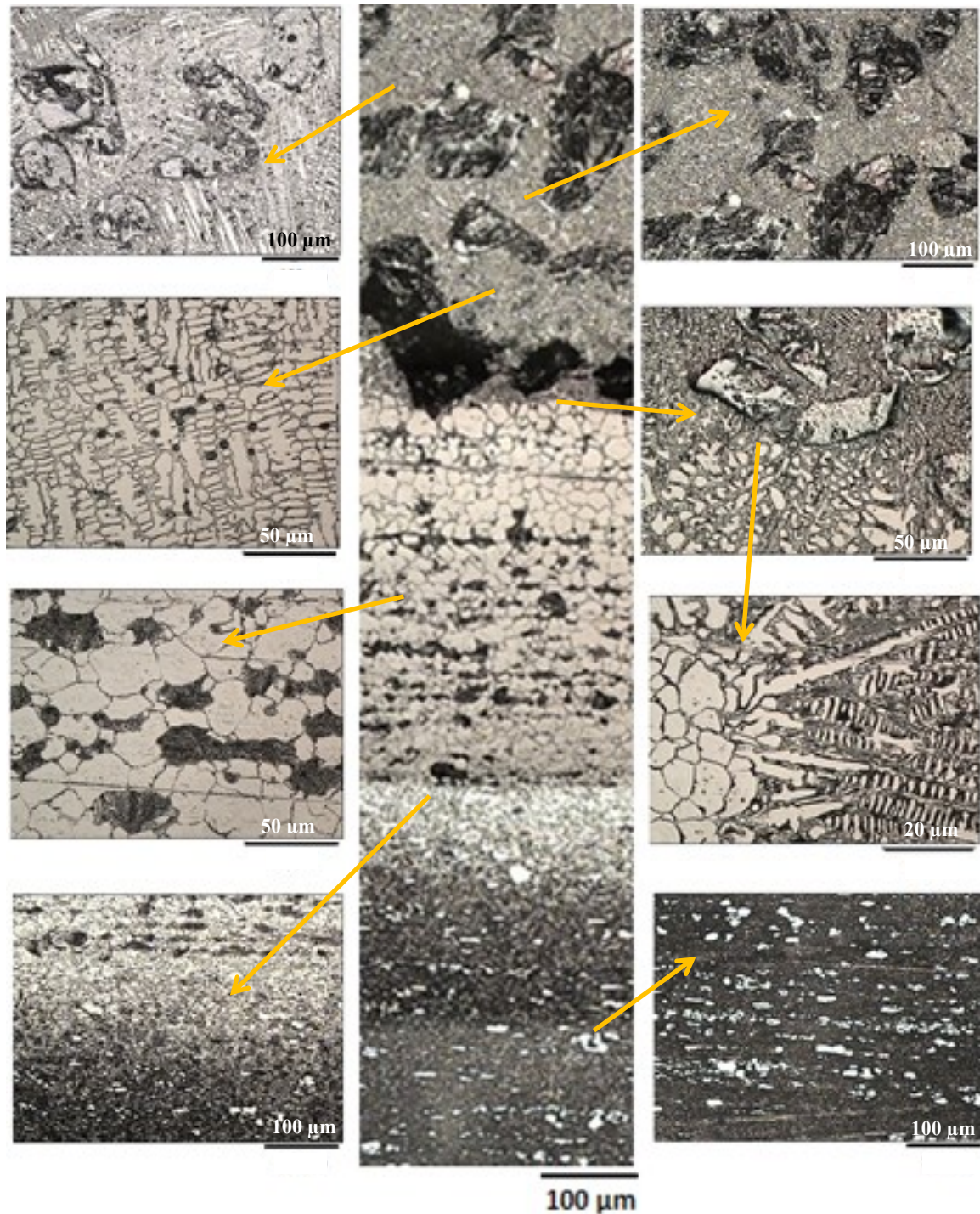


Fig. 6-14. Microstructure evolution of one layer from top to the base metal

6.2.3. Microstructure evolution by SEM and EDS analysis

In all samples, microstructure and distribution of WC were investigated. The obtained results with different magnifications are shown in Fig. 6-15. Microstructure of sample without addition of nanoparticles mainly consists of typical hypereutectic microstructure, the first phase precipitating from the liquid is solid solution of nickel, rest of that solidified as Fe-Cr rich phase by eutectic reaction inside of the nickel matrix. In addition, segregation exists in the microstructure due to high cooling rate in PTA process. With addition of nanoparticles, the degree of segregation becomes lower due to presence of particles in the microstructure. This cause to more heterogeneous nucleation and refining the microstructure. As a result, the volume fraction of the grain boundaries and rate of diffusion of alloying elements increase and segregation decrease which cause to reach homogeneous microstructure. The microstructure mainly consists of solid solution, continues plate like, discontinuous short bar and the morphology of islands. Also, different kinds of tungsten carbides in forms of globular, block and nanocrystalline are visible. Generally, the hypoeutectic microstructure can be obtained. Addition of nanoparticles do not change the mass fraction of Ni-Fe solid solution and total Fe-Cr compounds and mainly the hypoeutectic remain constant and just cause to refine the microstructure and decrease the element segregation.

Also, existing the nanoparticles cause to decrease the amount of M_7C_3 carbide type and increase the $M_{23}C_6$ and $(Fe-Cr)_2B$ phase [359]. In addition, there is the possibility of decomposition of WC nanoparticle and formation of single atoms in the matrix, which could decrease the diffusion rate of carbon. As a result, during solidification rate of precipitation of M_7C_3 type carbide decrease and more amount of Fe and Cr can be mixed with B atom to precipitate as $(Fe-Cr)_2B$ phase [360]. The nanoparticles mainly distributed over the grain boundaries of the solid solution and cause to dragging effect on the movement of grain boundaries, as a result grain growth decrease and microstructure would be refined [361]. It should be mention that, mainly the dimension of decomposed nanoparticles are higher than as received nanoparticles, this is due to existing large specific surface area and high surface energy. Therefore, the nanoparticles could be easily agglomerated under high temperature of PTA process [362].

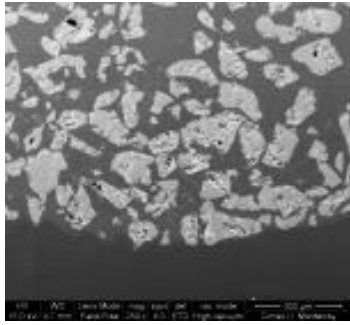
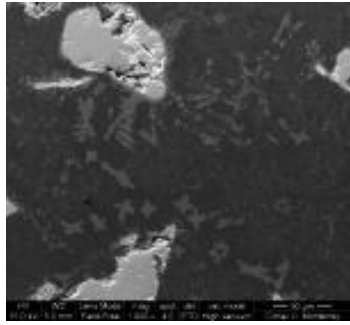


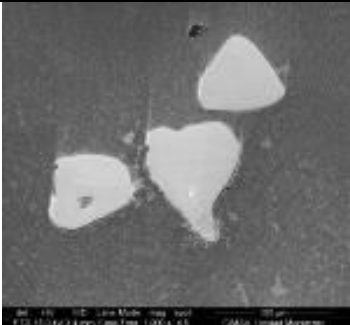
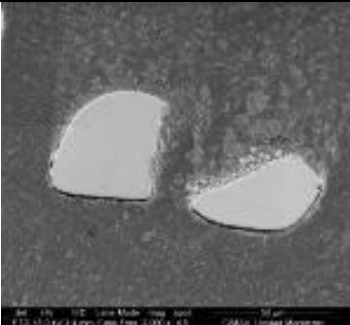
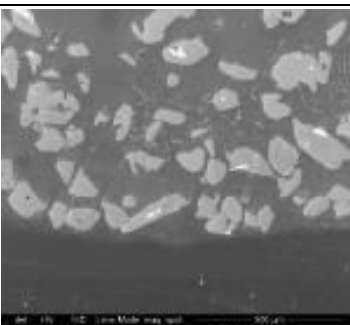
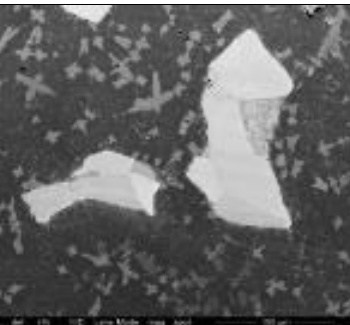
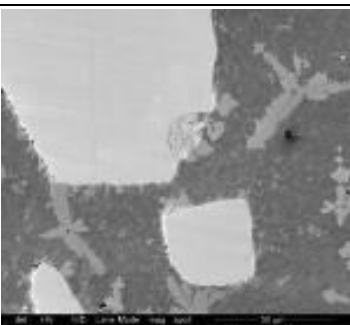
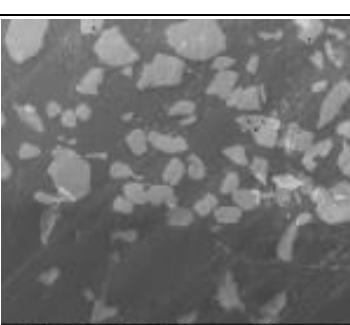
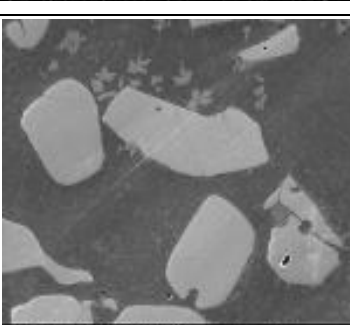

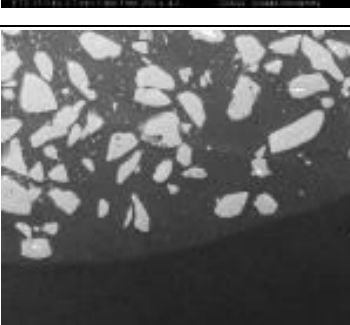
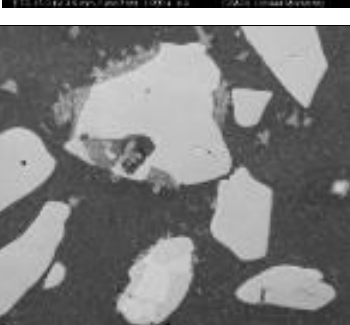

Sample	Magnification		
	250X	1000X	2000X
W0NP			
W1NP			
W3NP			
W5NP			
W7NP			

Fig. 6-15. Effect of WC nanoparticles addition on the microstructure of Ni-Cr-Fe hardfacing alloy.

Table. 6-6 indicates the EDS analysis of existing phases and compounds in the microstructure of all samples with addition of different percentages of WC nanoparticles. In sample W3NP, amount of W in WC₃ phase is more than 70% which is higher than other values. Also in blocky WC the percentage of tungsten in sample W3NP is more than 90% which is much higher than other samples. Existing high amount of hard tungsten in this sample could be reason of high hardness and wear resistance compare to other samples. Also, it can be say that, tungsten element exists in both Ni matrix solid solution and carbide. Generally, WC nanoparticles would be decomposed in tungsten atom and some particles would be preserved in WC coating. Those atoms cause to decrease the diffusion rate of C atom. As a result, precipitation of carbides would be difficult, also it causes to change the morphology of the eutectic carbide from continuous plate like into short bar shape [363,364]. Also, it can be found that the percentages of tungsten in CrC are much more than solid solution; it means tungsten is more distributed in the matrix. In addition, by comparing the EDS results, it is obvious that there is element segregation in the solid solution matrix and iron chromium carbide. This segregation is mainly visible for the nickel and iron elements.

Table. 6-6. EDS chemical composition (wt %) of microstructural phases.

Phase	WC nano-crystalline added (Wt %)	Chemical composition (wt%)							
		C	V	Cr	Fe	Ni	Mo	W	Si
WC	0	5.96	-	-	-	-	-	94.04	-
	1	7.95	-	-	-	-	-	92.05	-
	3	5.46	-	-	-	-	-	94.54	-
	5	3.68	-	-	-	-	-	96.32	-
	7	0.77	-	-	-	-	-	99.23	-
Matrix Fe-Ni-Cr	0	1.07	-	4.24	36.20	51.80	-	3.93	2.77
	1	3.13	-	10.69	58.76	9.05	-	17.89	0.03
	3	0.85	-	5.17	44.02	40.39	-	9.57	-
	5	-	0.70	6.95	42.91	37.99	-	11.46	-
	7	-	-	6.41	52.14	33.89	-	4.71	2.85
WC ₃ C	0	3.77	-	15.02	9.51	20.79	0.95	49.96	-
	1	3.24	1.13	13.26	30.70	6.58	1.65	43.43	-
	3	5.11	1.16	15.51	4.61	1.43	0.95	71.24	-
	5	-	-	19.09	32.61	12.45	-	35.85	-
	7	-	-	10.64	16.78	13.79	-	57.01	1.79
WC Globular	0	2.35	-	4.73	18.14	8.13	1.54	65.11	-
	1	2.97	-	5.91	23.93	4.31	-	62.88	-
	3	-	-	-	-	-	-	-	-
	5	-	-	23.22	5.90	-	-	70.88	-
	7	-	-	-	-	-	-	-	-
WC Bloque	0	6.08	0.49	23.51	26.43	13.31	0.77	29.41	-
	1	-	-	-	-	-	-	-	-
	3	5.84	-	-	1.55	1.53	-	91.07	-
	5	-	-	-	-	-	-	-	-
	7	-	-	7.42	13.96	11.91	-	66.71	-
WC Nano-Crystalline	0	-	-	-	-	-	-	-	-
	1	1.06	-	8.42	42.67	12.23	-	35.62	-
	3	4.76	-	2.02	10.44	9.69	-	73.09	-
	5	3.14	-	1.51	8.82	7.88	-	78.65	-
	7	-	-	5.77	22.94	14.43	-	56.86	-

6.2.4. X-Ray diffraction analysis

To observe formation of different phases in the microstructure, X-ray diffraction analysis was performed on separate and mixed powders in addition to all the deposited layers. Generally, the following phases are detected: FeNi, NiCrFe, WC, W_2C , CrC and NiB. Fig. 6-16 indicates the XRD spectrums of the WC nanoparticle powders which just consists of tungsten carbide phase with sharp peaks and high crystallinity. Fig. 6-17 depicts XRD analysis of deposited WOKA powder which includes mixture of many different phases with much lower intensity compare to nanocrystalline WC. To observe the effect of peaks from D2 base metal on the final deposited layer, XRD analysis is performed just on the base metal which the relevant result is presented in Fig. 6-18.

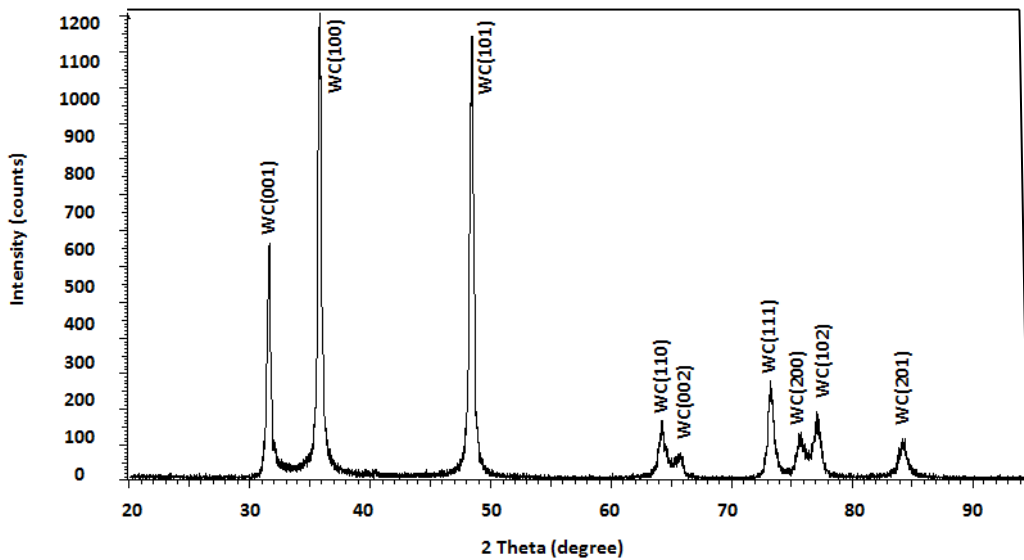


Fig. 6-16. XRD analysis of WC powder

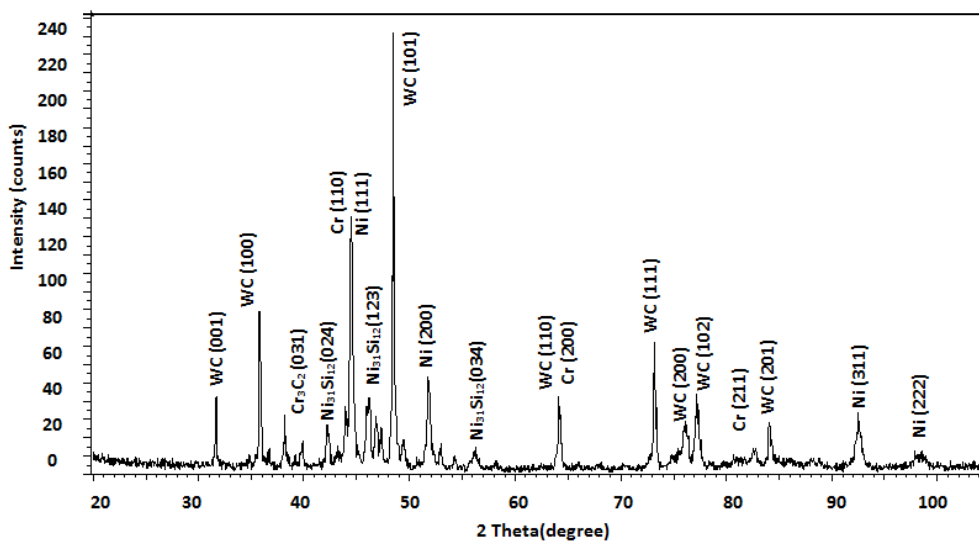


Fig. 6-17. XRD analysis of WOKA powder

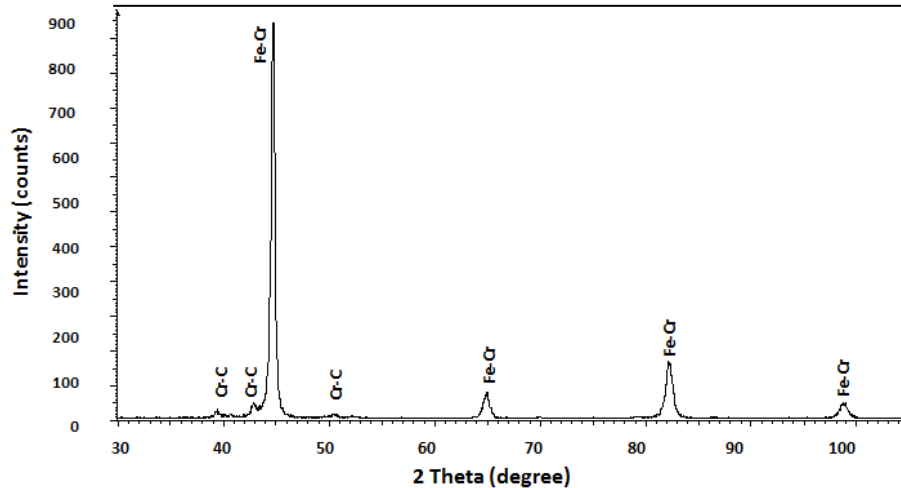


Fig. 6-18. XRD analysis of the D2 base metal

Also XRD analysis of the all mixed powders (WOKA + 1-7 %WC) are shown in Fig. 6-19, due to low intensity of the phases in WOKA powder, mainly WC peaks which belong to the nanoparticles are visible.

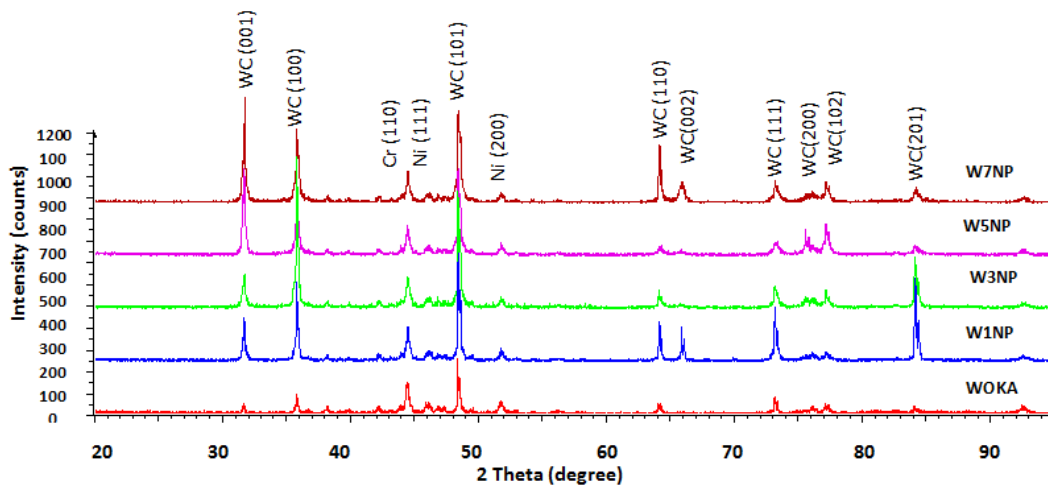


Fig. 6-19. XRD Analysis of mixture of WOKA powder with nano particles WC

After deposition of mixed powders on the substrate, other phases are formed which are specified in Fig. 6-20. Due to reaction of carbon mainly with chromium and other existing elements, different chromium carbides can be formed. The γ (Fe-Ni) solid solution with FCC crystal structure, Cr_7C_3 with hexagonal crystal structure and lath morphology, Cr_2C_3 with FCC crystal structure and Ni_2B phase with tetragonal crystal structure with blocky morphology is present. It can be found that, the matrix consists of Ni-Fe solid solution phase, because the mass fraction is more than Fe-Cr rich compounds.

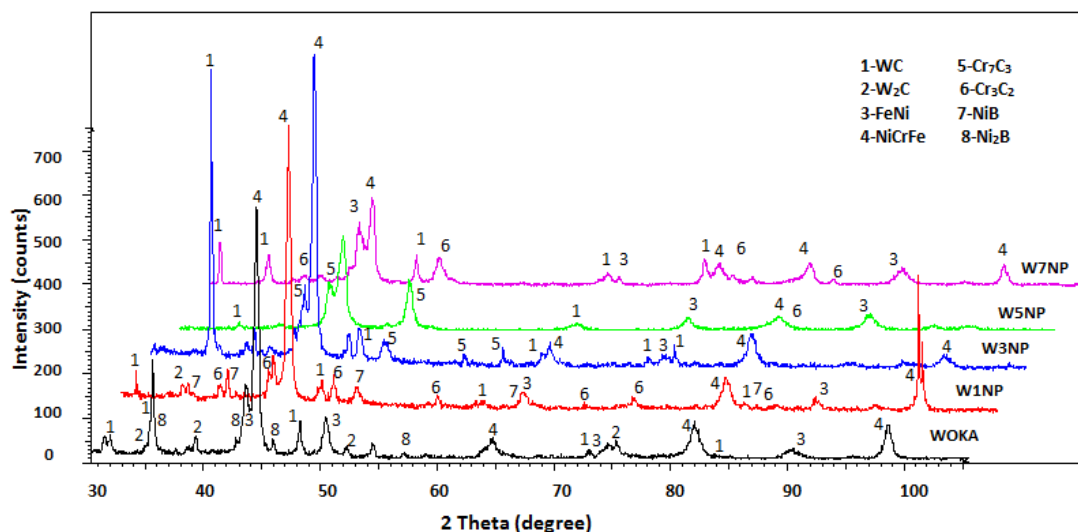


Fig. 6-20. XRD analysis of deposited layer with addition of 0 to 7 % WC nanoparticles

With comparing the peaks of different percentage of the WC nanoparticles, it can be found that, in just WOKA sample and addition of 1% nanoparticles there are NiB and Ni₂B phases also, due to the decomposition of WC, W₂C phase is form which is more brittle in comparison with WC, also the type of carbide in this sample is Cr₃C₂ with orthorhombic crystal structure and 9-11 %C, but with addition of 3 and 5% nanoparticles no evidence of W₂C was observed, and instead of Cr₃C₂ phase, chromium carbide in form of Cr₇C₃ with hexagonal crystal structure and 12-13% carbon was detected. The microhardness value for both carbides were reported between 2000-2300 VHN kg/mm² [365]. With addition of 7% nanoparticles, again the type of carbide changes to Cr₃C₂ but no formation of tungsten carbide in form of W₂C was detected.

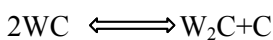
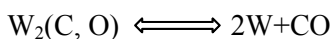
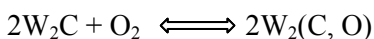
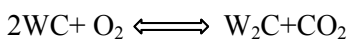
After deposition, WC decomposes to W₂C and W phases which is due to the high input energy and high temperature (10,000–25,000 °C) of the PTA process, this is confirmed by the results of many authors [337,366,367]. The hardness of W₂C and WC was reported 1400 HV and 1730 HV respectively [337]. The homogeneity and volume fractions of the carbide phases in the composite layers were responsible for the improvement in the wear resistance of the alloy.

6.2.5. Decomposition of tungsten carbide in the matrix

During applying the Ni–WC powder on the surface by PTA process, there is risk of decomposition and decarburization of WC particles into the nickel base matrix, it is mainly due to increasing the heat input which provides sufficient heat for dissolving part of tungsten carbide into the matrix. Decarburization of WC causes to specific change in the microstructure. The carbides usually turned to round morphology with WC in center and W_2C as a surrounding [368–370]. The color of W_2C as a shell is a little lighter than WC. The primary carbon loss of WC in formation of W_2C cause to grow and formation of columnar W_2C grains along the direction perpendicular to the WC grains.

Decomposition process can occur as following: first surface of WC melted partially, then tungsten and carbon diffuse from WC to the matrix, during solidification, both W and C exist and precipitate in the matrix as a W_2C and W. Also some of the constituent remains as solid solution.

Decarburization process can be specified as following:[371,372]



The WC phase after degradation process cause to produce W_2C which due to high temperature and oxidation [371] All these equations occurs at the surface of WC particles. Just the oxidation cannot be the reason for carbon loss of WC to form W_2C . Particles of WC mainly embedded in the matrix, consequently W and C can diffuse into the matrix especially at high temperature. Because of higher atomic weight of the tungsten compare to carbon, it shows lower diffusion rate. As a result, the concentration of tungsten becomes higher than carbon at boundaries between WC grains and liquid phase. When the atomic ratio of tungsten and carbon reaches to 2:1, and primary carbon loss occur, columnar form W_2C is form irregularly and grows epitaxially and perpendicularly on the surface of the WC particles and make a chemical bond with that. The color of W_2C as a shell is a little lighter than WC. This phase due to lower thermal stability compare to WC tend to more dissolution in the matrix which is not useful, because it causes to reduce the toughness and increase the risk of crack initiation [373]. Also, for improving the wear behavior it is better WC particles keep their forms with sharp edges [374,375]. Irregular shape of the particles causes to increase the rate of dissolution due to sharp edges which in some parts could be useful, because sharp edges are preferential position for more dissolution, and it causes to improve the bonding strength between carbide and matrix.

This can decrease the tendency of particles pull out during wear test. Dissolution cause to decrease the wear resistance as there is less amount and smaller size of WC particles remain in the matrix to keep wear resistance high [376]. Generally decomposition reaction in case of existing nanoparticles more occurs due to smaller size and its porous morphology [377]. For both W and C elements, decomposition from WC particle to the matrix occurs due to diffusion process which this value for carbon is higher than other carbide-forming elements. In addition, it causes to formation of brittle compound carbides such as M_3W_3C due to lower amount of carbon concentration and rapid cooling after welding which has detrimental effect on wear resistance [316,372,378,379].

For the particles with lower size the rate of solubility increase. In this case the particles can be dissolved and cause to form atoms of carbon and tungsten, one part of atom interacted with solvent to form carbide during solidification. Another reason for decomposition of WC nanoparticles could be due to its large surface area compare to volume of the particle [370].

6.2.6. Microhardness and nanoindentation

The microhardness values measured for the Ni–WC composite overlays and the effect of WC-nanocrystalline addition in different zones are shown and compared in Fig. 6-21. The strengthening contribution of the WC particles is clear in overall alloys, but in alloy with 3 wt% of WC-nanocrystalline addition the microhardness of this phase reach to 1927.1 ± 102 HV. In addition, Vickers microhardness testing was also performed on the heat affected zone and the substrate, in these locations the addition of nanoparticles has an effect. As it is clear, addition of WC nanoparticles in 1 and 3 % has positive effect on increasing the hardness of the matrix. Also, maximum hardness value of WC phase was observed for the sample with addition of 3 % nanoparticles.

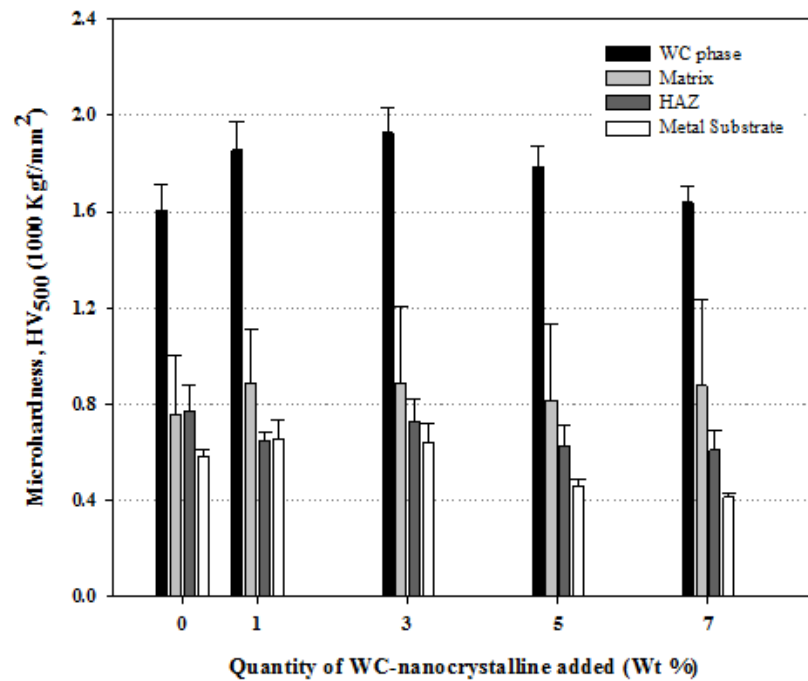


Fig. 6-21. Average microhardness of different phases of hardfacing alloys

Fig. 6-22 depicts the nanoindentation profiles in the main phases of Ni-WC overlay. For the case of the W0 sample, four different structures were classified, WCrC dendritic phase, NiCrFe dendritic phase, tungsten carbide (WC) particles and NiFe bulk. The representative structures of both samples, with and without addition of WC nanocrystalline particles, are shown in this figure, which are taken by optical microscopy. The results of the mechanical properties and relevant curves for nanoindentation measurement is shown in Fig. 6-23.

As it can be seen in Fig. 6-22b, the WCrC dendritic phase is present in the W0 sample with a homogeneous distribution, having shaped cross dendrites with length and thickness around $30\mu\text{m}$ and $5\mu\text{m}$, respectively. Nanoindentations test were carried out in a representative WCrC dendrite, where the P-h curves (dark gray line in Fig. 6-23) show low scattering due to the material homogeneity, allowing calculate an effective elastic modulus of $E_{eff} = 258 \pm 49 \text{ GPa}$, and hardness of $H = 17 \pm 2 \text{ GPa}$. In the same way, a representative NiCrFe dendrite, with branches forms of length and thickness around $32\mu\text{m}$ and $3\mu\text{m}$, respectively, show P-h curves (light gray line in Fig. 6-22b) with low scattering. In this case an effective elastic modulus of $E_{eff} = 184 \pm 51 \text{ GPa}$, and hardness of $H = 5 \pm 1 \text{ GPa}$ were calculate.

In the other hand, for the case of the NiFe bulk, an increased scattering was present in nanoindentation tests (black line in Fig. 6-22b). Fig. 6-22d shows how the NiFe bulk sample surface consist of several reliefs, which it is associated with the highest disparities of the $E_{eff} = 214 \pm 90 \text{ GPa}$, and hardness $H = 8 + 8 \text{ GPa}$ values. For the case of the tungsten carbide WC particles, an effective elastic modulus of $E_{eff} = 447 \pm 60 \text{ GPa}$, and hardness of $H = 29 \pm 6 \text{ GPa}$ were calculated.

As it can be seen in Fig. 6-22b the WCrC dendritic phase is present in the W0 sample with a homogeneous distribution, having shaped cross dendrites with length and thickness around 30 μm and 5 μm , respectively. Nanoindentations test were carried out in a representative CrC dendrite, where the P - h curves (dark gray line in Fig. 6-22b) show low scattering due to the material homogeneity, allowing calculate a reduce elastic modulus of $E_r = 258 \pm 49 \text{ GPa}$, and hardness of $H = 17 \pm 2 \text{ GPa}$. In the same way, a representative FeNiCr dendrite, with branches forms of length and thickness around 32 μm and 3 μm , respectively (see Fig. 6-22c), show P - h curves with low scattering. In this case a reduce elastic modulus of $E_r = 184.39 \pm 50.96 \text{ GPa}$, and hardness of $H = 4.65 \pm 0.69 \text{ GPa}$ were calculate. In the other hand, for the case of the FeNi bulk, an increased scattering was present in nanoindentation tests (black line in Fig. 6-23). Fig. 6-22d shows how the FeNi bulk sample surface consist of several reliefs, which it is associated with the highest disparities of the $E_r = 214 \pm 90 \text{ GPa}$, and hardness $H = 8 \pm 8 \text{ GPa}$ values. In the other hand, the W3NP sample shows similar structures as the W0 sample. The representative phases of the W3NP sample are shown in the optical microscopy of Fig. 6-22. However, some effects due to the addition of nanoparticles can be observed, as their accumulation at the boundaries of several tungsten carbides WC particles (see Fig. 6-22e), as well as the decreased generation of the NiCrFe dendrites. In the other hand, the W3NP sample shows edge geometries with rounded finishes mainly characteristic in WC particles.

Again, the WCrC dendritic phase shows a homogeneous distribution, with shaped cross dendrites of length and thickness around 25 μm and 5 μm , respectively. Nanoindentations test carried out in a representative WCrC dendrite, shows low scattering. Then, an effective elastic modulus of $E_{eff} = 249 \pm 21 \text{ GPa}$, and hardness $H = 17 \pm 2 \text{ GPa}$, were calculated.

Also, for the case of the NiFe bulk, an increased scattering was present in nanoindentation tests. Fig. 6-22h shows how the FeNi bulk sample surface consist of several reliefs, which promote the highest disparities of the $E_{eff} = 201 \pm 28 \text{ GPa}$, and hardness $H = 9 \pm 5 \text{ GPa}$, values. Nonetheless, the representative NiCrFe phase of this sample shows geometries as dendrites partially formed, with segments of length and thickness around 10 μm and 3 μm (see Fig. 6-22g).

Such structures shows nanoindentation test with low scattering. In this case, an effective elastic modulus of $E_{eff} = 192 \pm 21 \text{ GPa}$, and hardness $H = 4 \pm 1 \text{ GPa}$ were calculated. Also, nanoindentation test were carried out at the grain boundaries with nanoparticles, however, the P - h curves obtained had inconsistent behavior, and such results may it produced by the movement of nanoparticles during material deformation.

Finally, for the case of the tungsten carbide WC particles, a decrease in the mechanical responses against the W0 sample were determined; with an effective elastic modulus of $E_{eff} = 393 \pm 12 \text{ GPa}$, and hardness of $H = 23 \pm 2 \text{ GPa}$.

A general comparison of the nanoindentation behaviors of each phase in both samples is shown in Fig. 6-23, also Table. 6-7 indicates the obtained value young modulus and nano hardness for the sample without and with 3 % nanoparticles. A slight differences in the mechanical performances can be seen between both samples, for the cases of the NiFe, NiCrFe and the WCrC phases, where a better mechanical response were determined for the W3NP sample, since their residual penetrations depths shows the minor values, resulting in improved elastic recovery. However, for the case of the WC particles, the W3NP sample shows a decreased mechanical response, since such phase shows maximal as well as residual penetrations depths with the higher values. Also Farahmand et al.[331] observed the same results, they found that with addition of nanoparticles, the agglomerated nanoparticle act as an inhibitor of grain growth. Also, it is clear that with decreasing the grain size, the amount of grain boundaries increase. It was reported that the hardness of eutectic at grain boundaries is higher than in nickel matrix solid solution [380]. As a result, grain size of the matrix decrease and hardness increase. Also, they found that with addition of more percentage of the nanoparticles, risk of formation of porosity and inhomogeneity increase and the hardness value decrease.

Table. 6-7. Young modulus and nanohardness test result of sample without and 3 % nanoparticle

Phase	W0NP				W3NP			
	WCrC dendrite	NiCrFe dendrite	NiFe bulk	WC	WCrC dendrite	NiCrFe dendrite	NiFe bulk	WC
E_{eff} (GPa)	258 ± 49	184 ± 51	214 ± 90	393 ± 12	249 ± 21	192 ± 21	201 ± 28	447 ± 60
H (GPa)	17 ± 2	5 ± 1	8 ± 8	23 ± 2	17 ± 2	4 ± 1	9 ± 5	29 ± 6

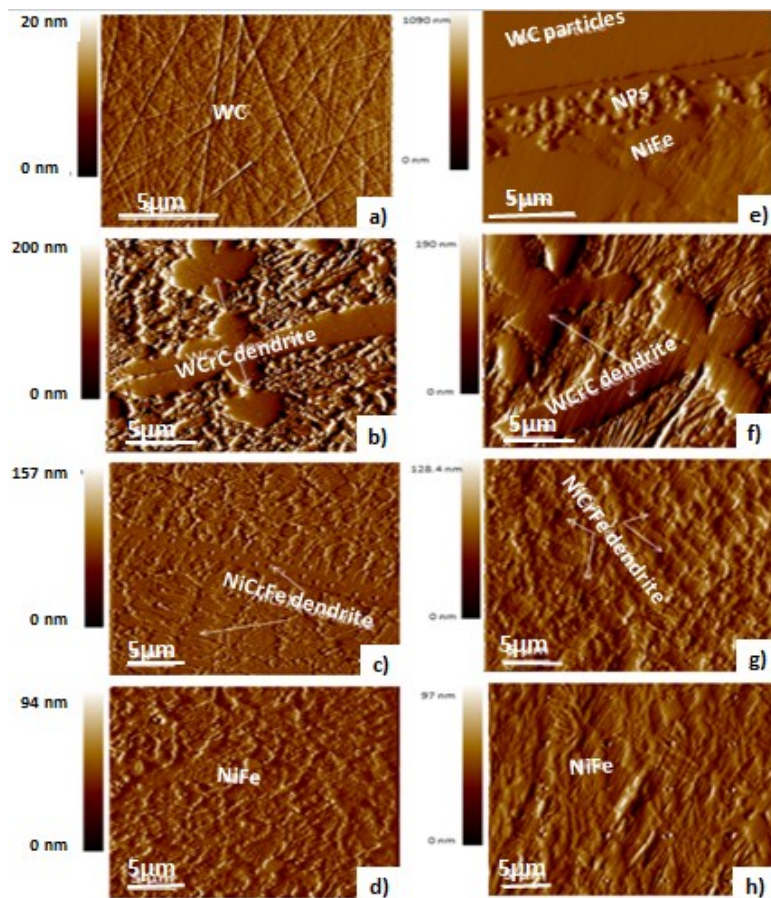


Fig. 6-22. Nanoindentation profiles in the main phases of Ni-WC overlay: (a) to (d) Sample Ni-WC from commercial powder, (e) to (h) Sample Ni-WC with addition of 3 Wt% of WC-nanocrystalline particles.

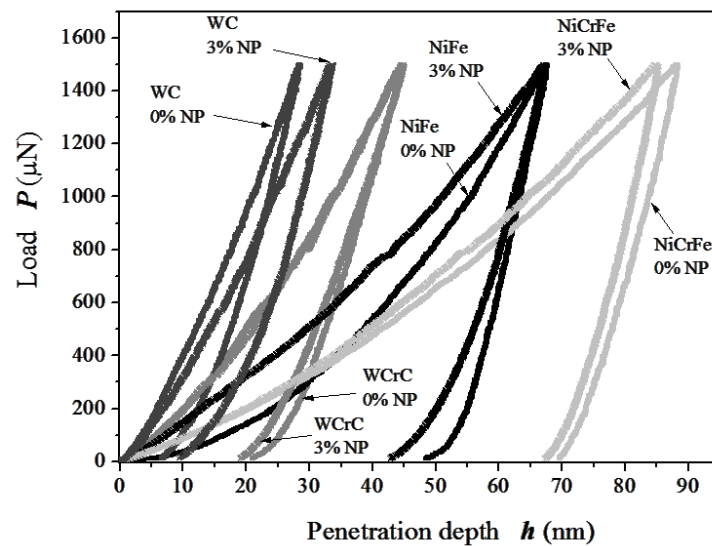


Fig. 6-23. Comparison of nanoindentation profiles in the main phases of Ni-WC overlay with and without addition of WC-nanocrystalline particles

6.2.7. Wear test results

It is important to consider the formation of secondary particles resulting after WC dissolution occurs in the matrix, since during abrasive wear the surface of a soft material is gouged out by the abrasive particles/phases of the harder material and produces wear chips when the abraded material is elastoplastic or viscoelastic-plastic. Abrasive wear involves subsurface plastic deformation (increases as wear particles themselves develop flat surfaces) in addition to cutting of the surface and generation of wear chips [332].

Pin-on-disc wear testing showed that smaller carbides were more effective for dry sliding wear resistance since coatings with large carbides revealed evidence of cracks at the interface between carbides and matrix [275]. Fig. 6-24 depicts a graph for comparison of wear rate and coefficient of friction for all the samples, without and with addition of tungsten carbide nanoparticles in range of 1 to 7%. It is obvious that, generally with addition of even 1% nanoparticles, the wear rate decrease significantly. Also for all the samples, with increasing the load wear rate and coefficient of friction decrease, which could be due to occurrence of plastic flow on the surface, changing the wear mechanism from abrasive to adhesive and formation of compact layer on the surface to prevent direct contact between metals [374]. Also it was reported that [375] in case of existing carbide in both form of WC and W_2C with addition of normal load the stability of friction coefficient increase and its value decrease, also the sustainability under plastic deformation increase.

In this case nickel matrix which is soft and ductile, can control the wear rate. It can form a thin layer at sliding interface which cause to decrease the wear rate by acting as lubricant [345,381]. Among all samples with addition of nanoparticles, sample with 3% nanoparticle shows minimum wear rate under both low and high loads.

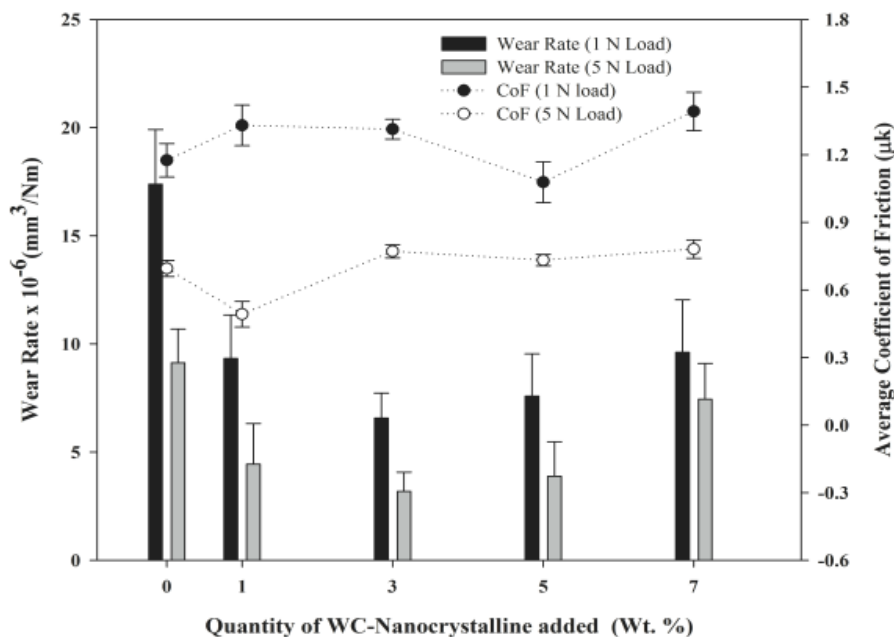


Fig. 6-24. Effect of WC-nanocrystalline addition on the wear rate and coefficient of friction of Ni-WC overlays

Fig. 6-25 to Fig. 6-29 to show the relevant coefficient of friction(CoF) graphs for the samples with different percentage of nanoparticle tungsten carbide.

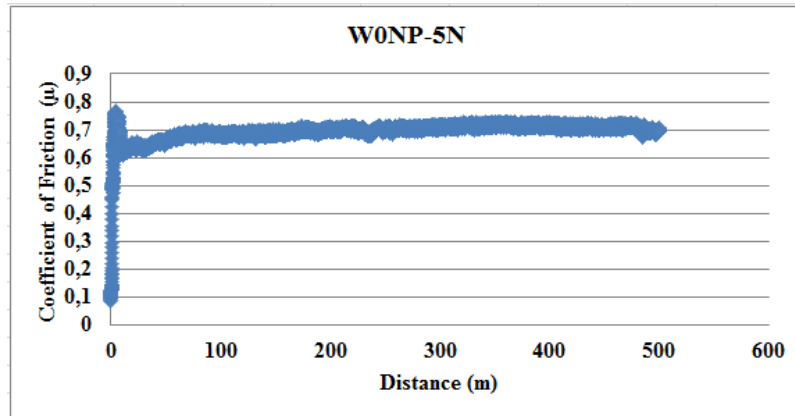


Fig. 6-25. Friction coefficient graph for the sample W0NP

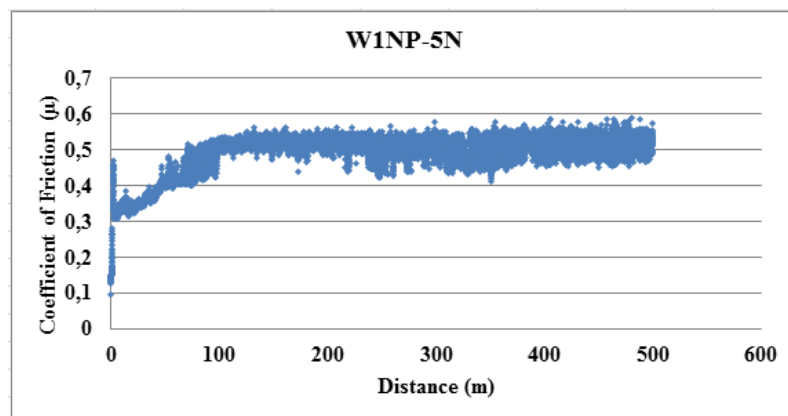


Fig. 6-26. Friction coefficient graph for the sample W1NP

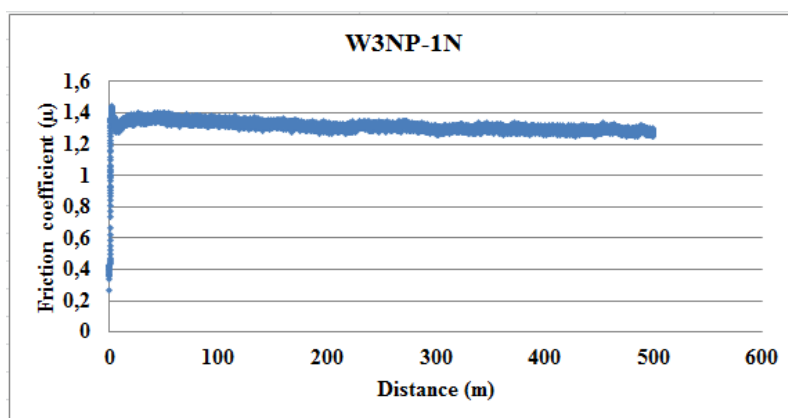


Fig. 6-27. Friction coefficient graph for the sample W3NP

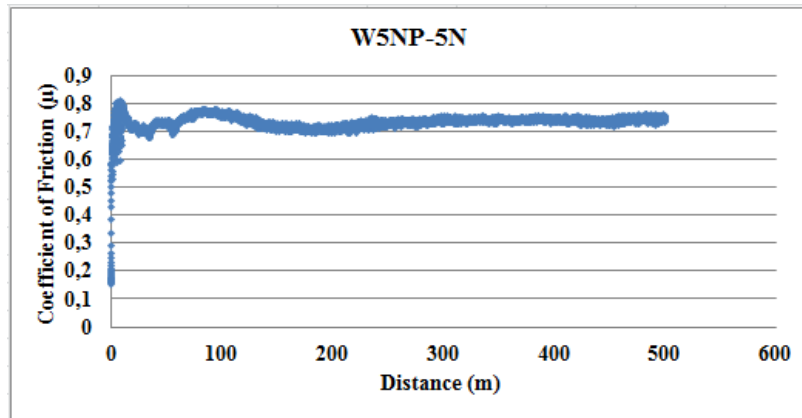


Fig. 6-28. Friction coefficient graph for the sample W5NP

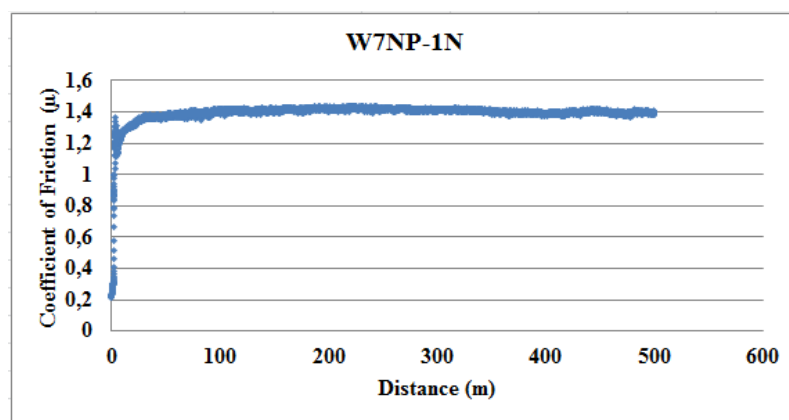


Fig. 6-29. Friction coefficient graph for the sample W7NP

Generally, with increasing the load the wear rate increase, which could be due to run-in wear phase during which the rough surface asperities get removed. Also, during sliding distance the wear rate decrease because of smoothing of the wear track, this zone can be named as steady wear zone. With increasing the load, the pressure between the surfaces increase consequently binder removal and fragmentation of carbide grains occur. Presence of nanoparticles cause to increase the reinforcement and hardness of the layer [370]. Fig. 6-30 and Fig. 6-31 show the stereomicroscope images of worn surfaces after pin-on-disk test after applying 1 and 5N loads respectively. As it is clear with increasing the load the wear track width become larger and in case of contacting the pin with tungsten carbides, the digging close to WC particles occurs and wear track become inhomogeneous.


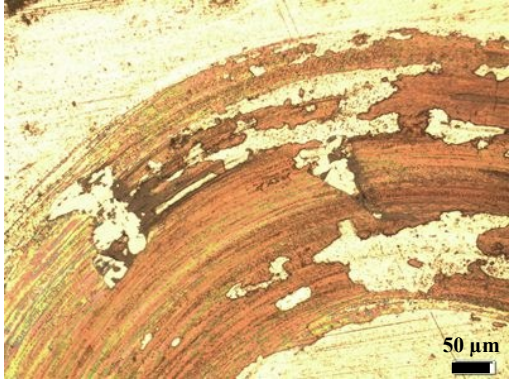

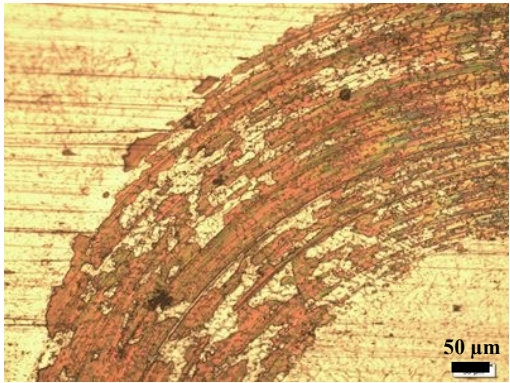

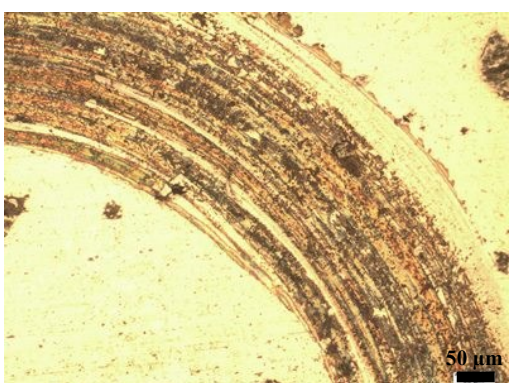

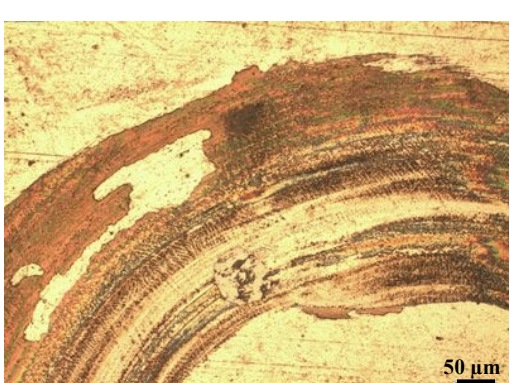
The reasons for increasing the wear resistance of the sample with addition of nanoparticles can be specified as following:

One important reason could be due to refining the microstructure of nickel base coating matrix which lead to grain refinement strengthening. Also it was reported that, nanoparticles cause to increase $(\text{Fe-Cr})_2\text{B}$ phase and decrease the M_7C_3 type carbide, which generally accepted that borides show higher wear resistance and hardness compare to the carbide (2575 HVN for boride and 1670 HVN for carbide [279]). It was reported that nanoparticles cause to increase the volume fraction of carbides [382]. In addition, nanopowder distributed on the matrix solid solution which cause to dispersion strengthening. Also, existing hard nanoparticles cause to decrease the friction between soft Ni base matrix and the pin [360].

Finally, during the wear test under normal load, nanoparticles have an effect on reducing the movement of dislocations on grain boundaries, which cause to reduce the deformation and failing of the coating and increase the ability of composite coating to resist under the high plastic deformation, as a result the wear resistance increase [325,360]. It was reported that, in sample with addition of nano particles, there is stacking fault energy, which has softening effect and mainly cause to decrease the deformation difficulties. Detailed TEM investigations of previous researches [325,383] showed that, with addition of nanoparticles, stacking fault energy (SFE) decrease compare to nickel base matrix and it can be formed easily in the microstructure. This cause to formation of strain free dislocations walls. Also, decreasing the SFE of the overlay enhance formation of dislocation cell walls which act as barrier and increase the wear resistance. At the same time there is strain hardening effect which has more effect compare to the effect of existing stacking fault energy, as a result wear resistance increase [384].

Also, generally distribution of nanoparticles in the solid solution matrix cause to pin the dislocations and increase the overlay properties. In addition the nanoparticles could become source of heterogeneous nucleation in the matrix which cause to refine the microstructure, consequently it causes to increase obstruction of crack propagation [382].

Increasing the load cause to more removal of the matrix, microcracking and detachment of carbide particles accompanied with deformation of matrix and fragmentation and pull out of the carbide particles [345,385]. The material removal from the surface during the wear test is due to extrusion of ductile Ni-Cr matrix followed by the crack and the removal of the tungsten carbide particles. Generally, increasing the hardness of the material cause to decrease the penetration of the abrasive particles which cause to reduce the wear rate.

Sample	Complete worn surface	1 N	Partial worn surface
W0NP			
W1NP			
W3NP			
W5NP			

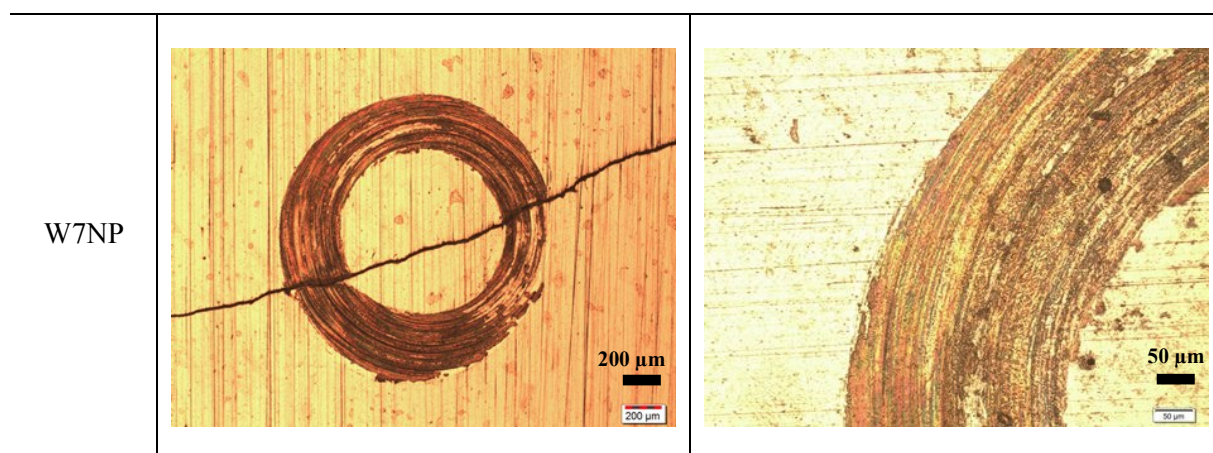



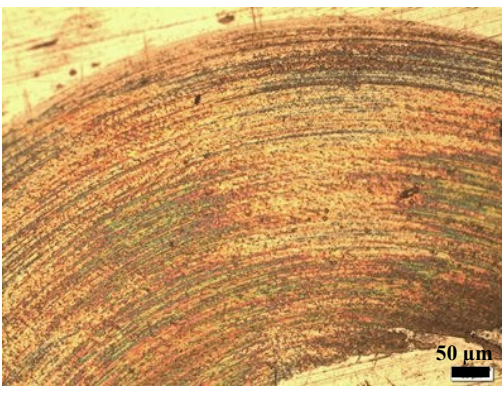
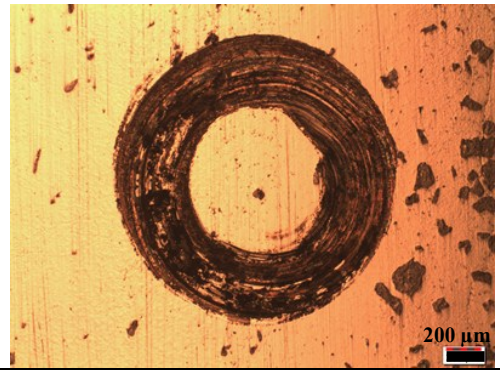
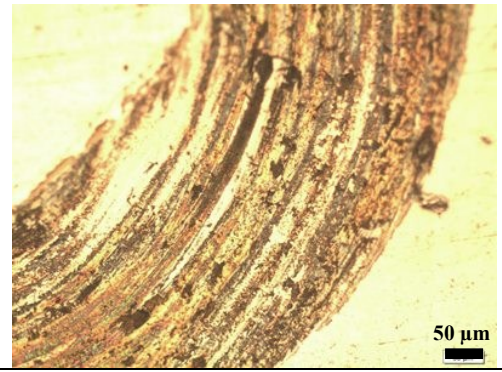


Fig. 6-30. Stereomicroscope images of complete and part of worn surfaces (1 N load)

Sample	Complete surface	5 N Partial surface
W0NP		
W1NP		
W3NP		

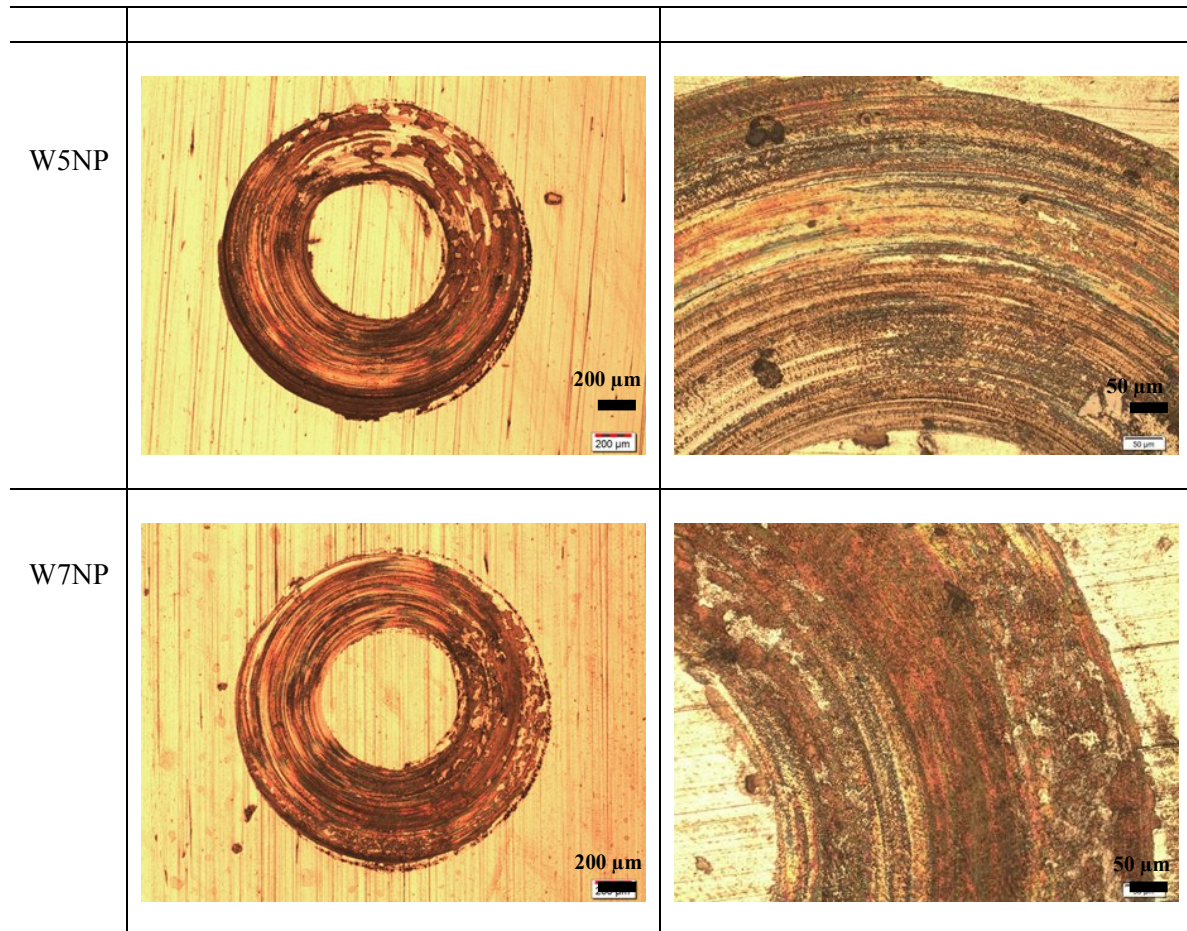


Fig. 6-31. Stereomicroscope images of worn surfaces (5 N load)

6.2.8. SEM analysis of the surface after wear test

To observe detail surface condition of the worn sample, the surfaces was evaluated by scanning electron microscope. Fig. 6-32 to Fig. 6-34 indicates the SEM micrographs of the worn samples without and with 3 and 7% nanoparticles respectively after pin on disk test in different magnifications. As it is clear sample with 3 % nanoparticles indicates nearly smooth surface with small wear track which are sign of higher wear resistance. Also with increasing the loads no evidence of changing the wear mechanism was observed. Consequently just image of one sample for each condition brought and discussed. As it is clear mainly wide wear scar, severe plastic deformation and delamination can be observed. Also cutting was observed as the material removal mechanism in coating. In addition as can be seen with the sample without addition of nanoparticles wide wear scar, severe plastic deformation and delamination is detectable.

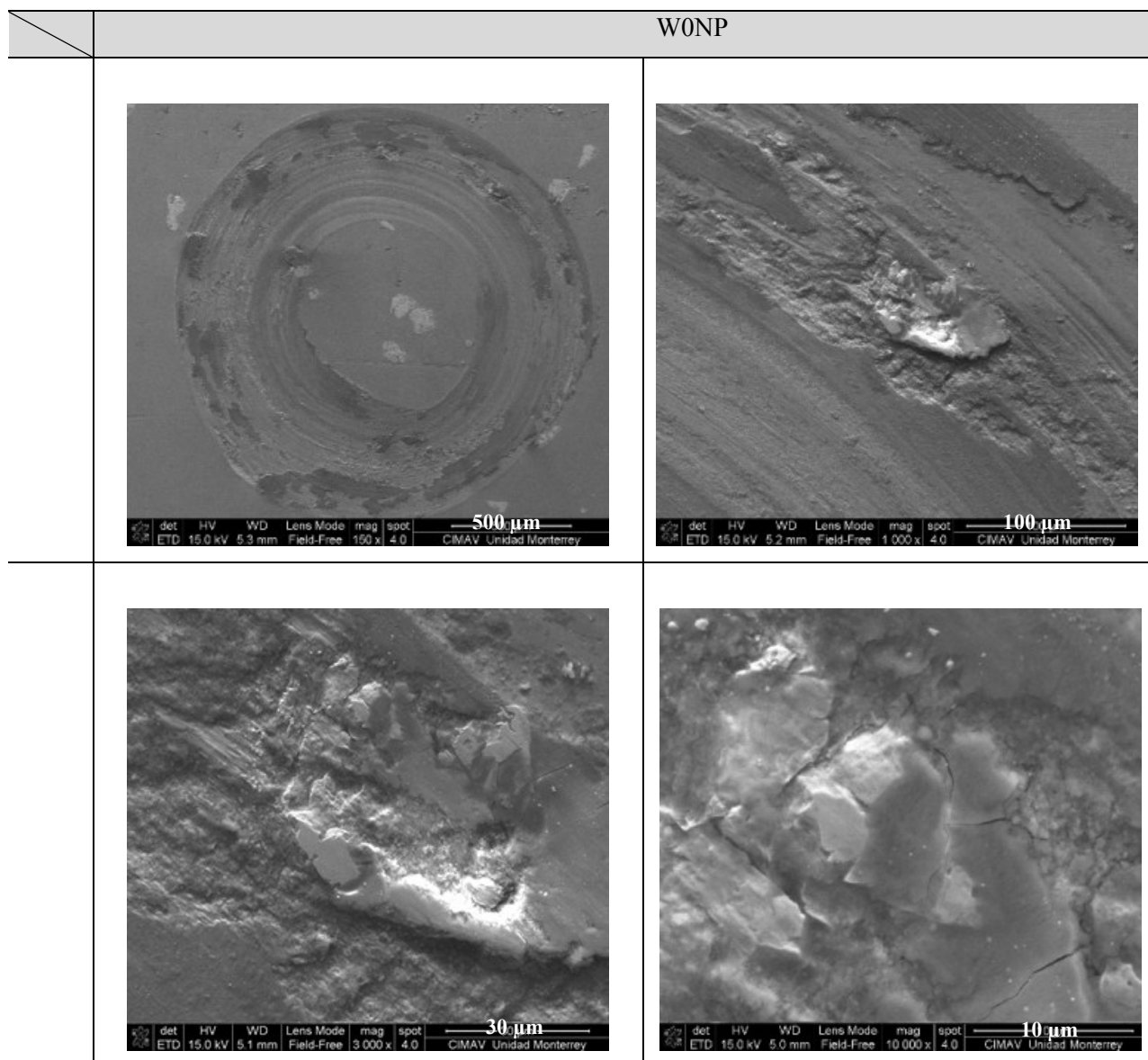


Fig. 6-32. SEM images of worn surfaces sample W0NP

As it is clear from Fig. 6-33 in sample with addition of 3% nanoparticles, due to contact of the pin during the test with WC, the wear surface become more rough and digging occurs. Also cracks on the tungsten carbide is visible which is due to applying more loads. For this sample the wear mechanism is abrasive.

Fig. 6-34 shows the worn surface of the sample with addition of 7% nanoparticles, compare with sample W3NP the surface are more smooth and less digging occurred. With addition of more amount of nanoparticles, the wear mechanism has been changed to adhesive wear. In addition, oxidational wear with the production of oxide layers, patches and particles could have a dominant effect on the wear behavior. Based on investigation of Holmberg et al.[386] it is more probable to specify that mechanical wear is concur compare with chemical wear. Formation of oxide and tribo-patches on the mating surfaces showed adhesion between pin and disk in case of addition of nanoparticles.

Also SEM micrograph of the worn surface after the test showed that existing of blocky spalling, grooves and debris which agglomerated in the matrix. Also, there is possibility of oxides on the surface. The debris which are produced during the test has effect on the wear process by getting lock between the surfaces and promoting the three body abrasive wear test which leads to increase the wear rate. Also, the oxide particle can be compacted between surfaces and form a protective layer [387]. Also compared with un modified sample, the sample with addition of nanoparticles showed narrower and shallower wear scar. In addition small amount of transferred solid film can be formed. For the sample W3NP due to the contact of the pin with tungsten carbide, the effect of abrasion and digging is more obvious.

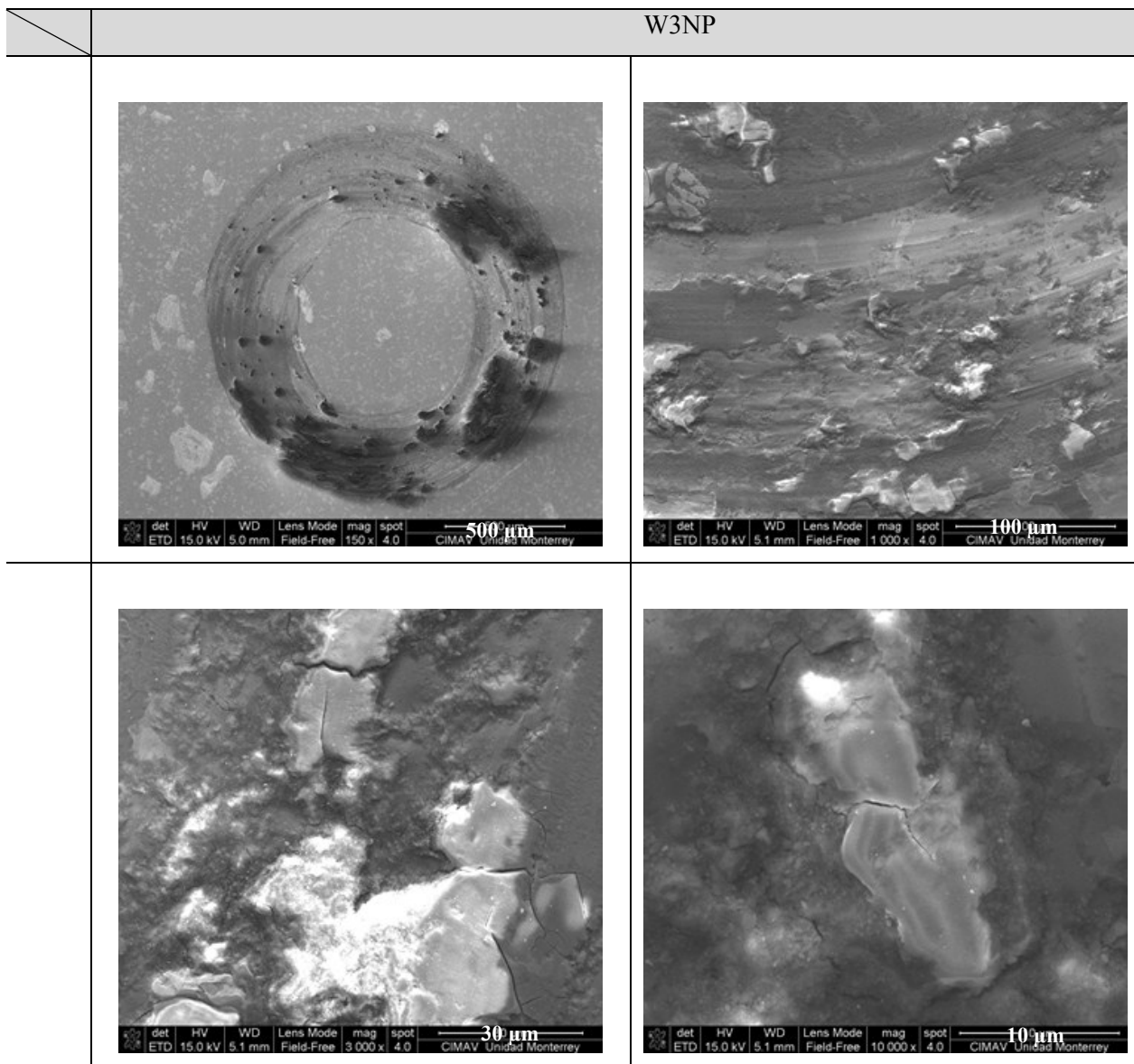


Fig. 6-33. SEM images of worn surfaces sample W3NP

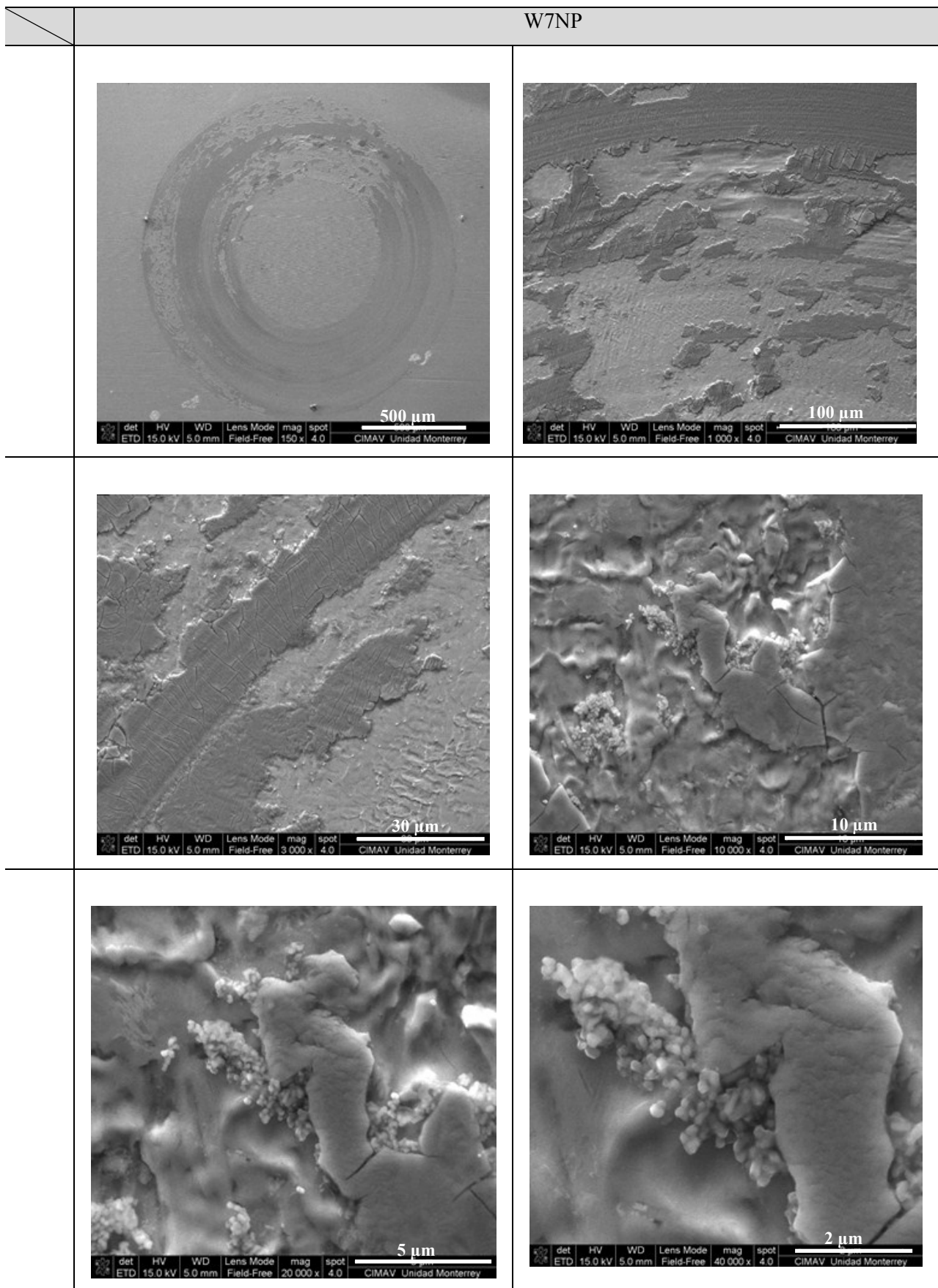


Fig. 6-34. SEM images of worn surfaces sample W7NP

6.2.9. Wear surface analysis by 3D optical profilometer

To observe the surface topography mapping of the worn surfaces, 3D non-contact optical profilometer analysis was performed on all the samples. Profilometer is a strong tool which can quantify the wear depth and volume in addition to evaluate the shape of wear track. The obtained colors specified the depth of surface damage based on the scales. Fig. 6-35 and Fig. 6-36 indicate one 3D images of the complete worn surface for sample W0 and W1. In the wear track, different pits which belongs to removal of the material can be observe. It can be concluded that in modified coatings, the wear tracks are narrower and shallower which means increasing the wear resistance of the coating. The wear track of coating indicates deep grooves parallel to the direction of sliding, it means major wear mechanism is abrasion. The wear tracks consists shallow grooves and cleavage from the combination of plastic deformation and brittle fracture. Also, the shallower wear track in case of addition of nanoparticle means increasing the strength of nickel matrix by embedded nanoparticles. The plastic deformation in the coating for sample with addition of nanoparticles decrease.

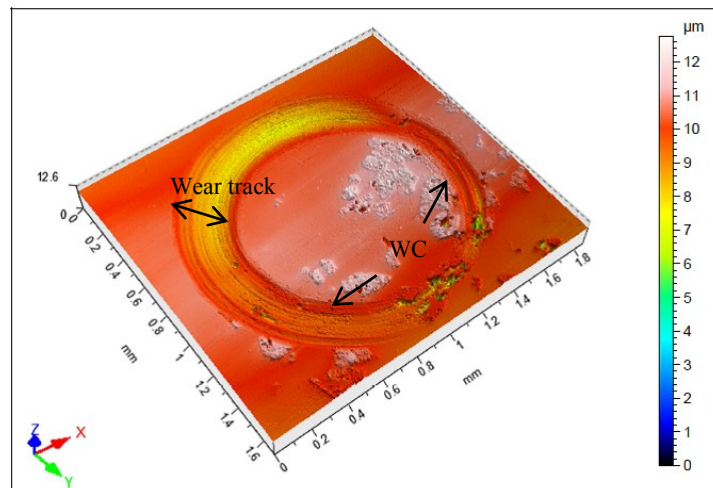


Fig. 6-35. 3D worn surface of the sample W0NP

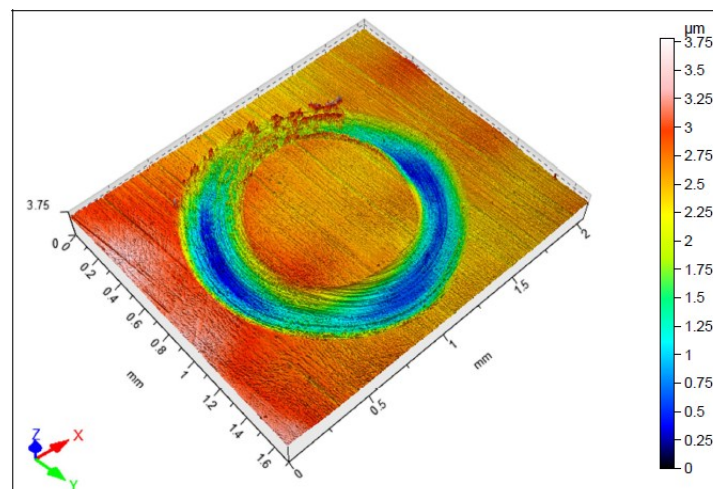


Fig. 6-36. 3D worn surface of the sample W1NP

Fig. 6-37 and Fig. 6-38 show the complete worn surface of the sample surfaces after applying 1 and 5 N load respectively. It is clear that with contact of pin with WCs the wear resistance of that part increase.

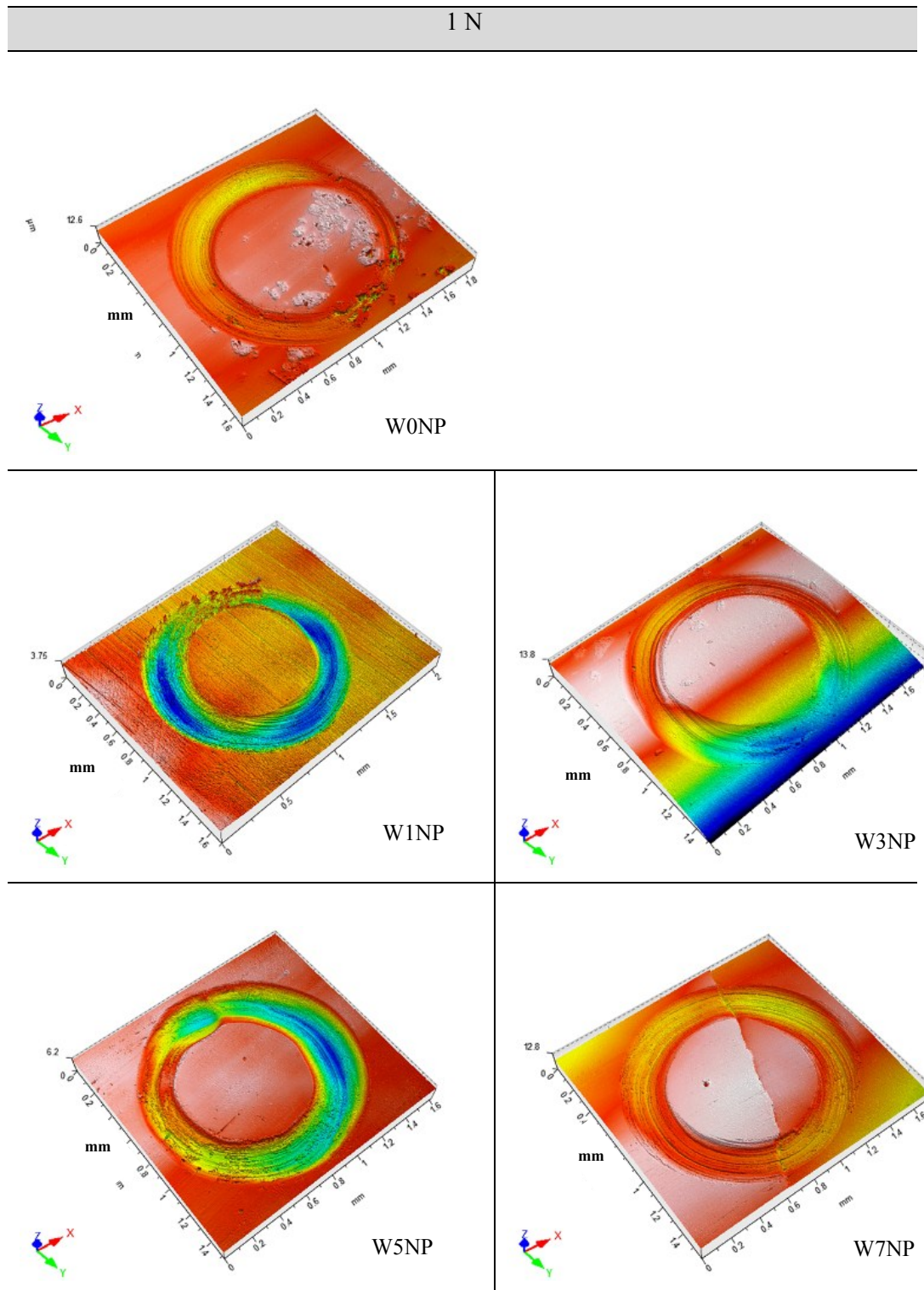


Fig. 6-37. Results of 3D complete worn surface (1 N load) topography by means of profilometer

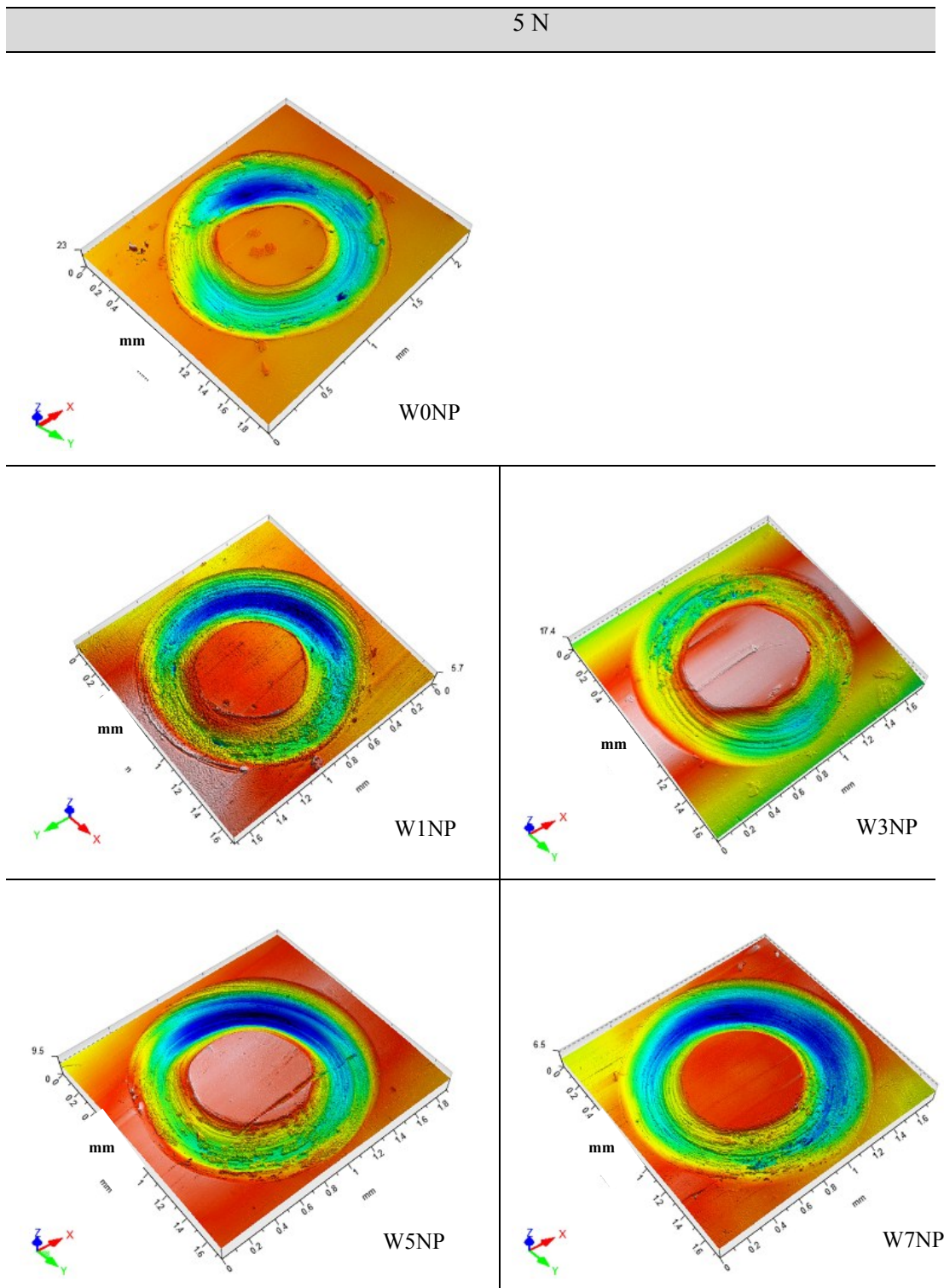


Fig. 6-38. Results of 3D complete worn surface (5 N load) topography by means of profilometer

Fig. 6-39 and Fig. 6-40 depict the part of worn surface for all the samples based on applying different loads.

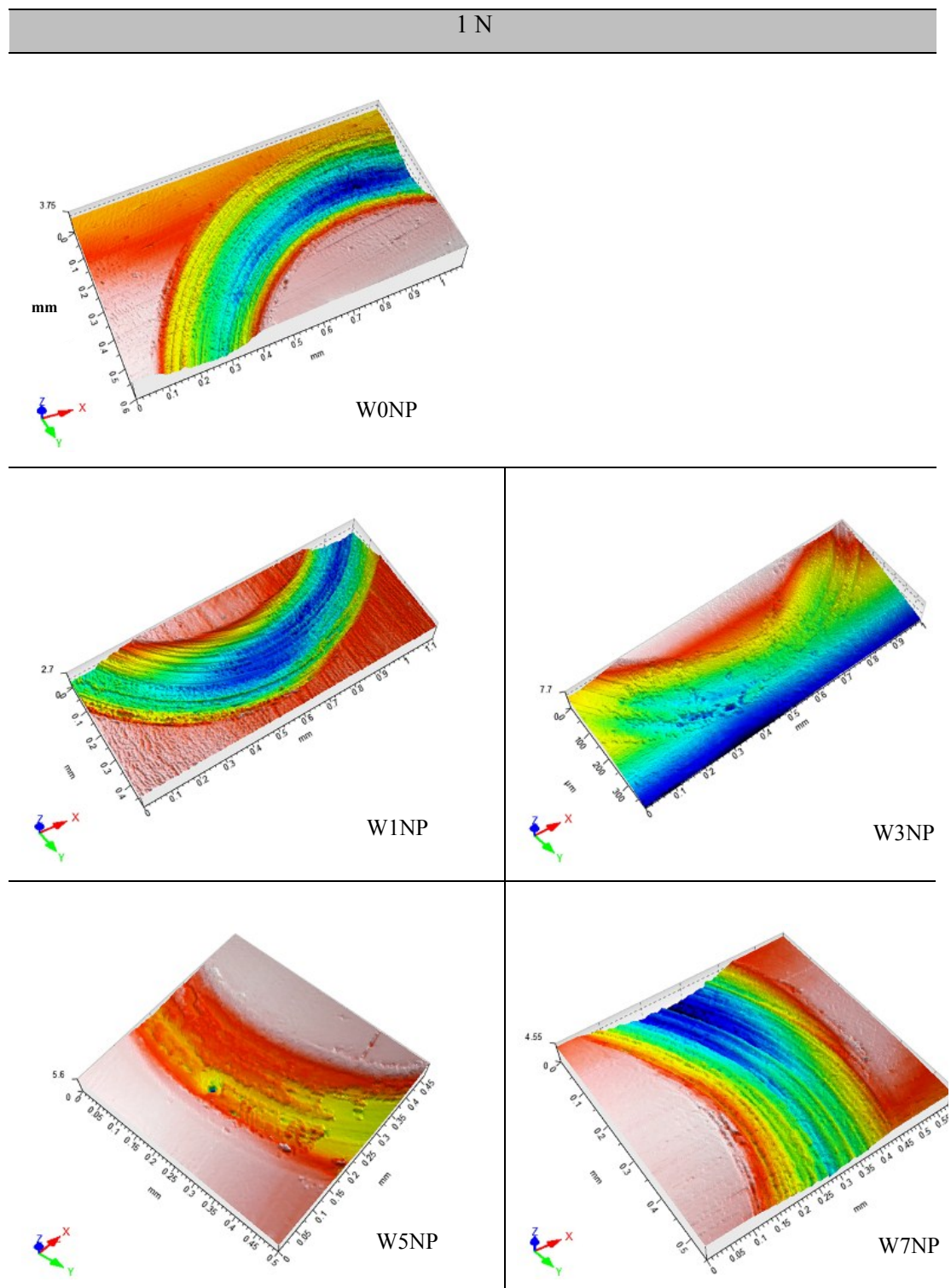


Fig. 6-39. Results of 3D part of worn surface (5N load) topography by means of profilometer

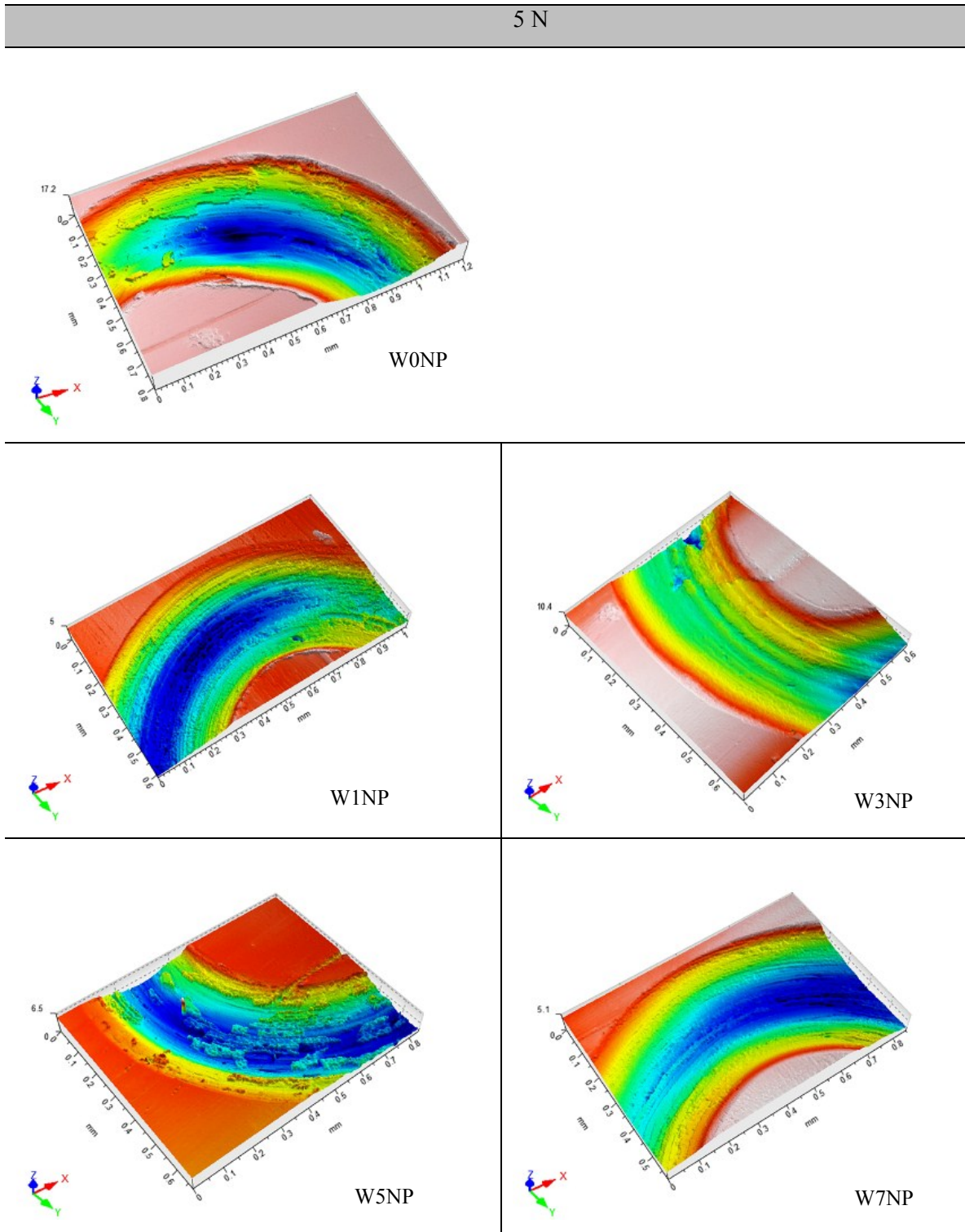


Fig. 6-40. Results of 3D part of worn surface (5N load) topography by means of profilometer

6.2.10. Wear rate measurement by profilometer

As explained before, one important application of profilometer in addition to surface topography, is measurement of the wear rate of the surfaces. Volume loss describes the amount of material lost from the surface due to erosion, abrasion and wear.

In this investigation volume loss directly with micron size precision was calculated and the worn region of the sample and intact region around it was scanned. A reference plain was considered for the intact surfaces. Also, there is possibility of calculating volume loss from the differences between the interpolated reference plane and the actual worn surface. Due to not equivalent wear track width, four lines around circumstances of the worn surfaces were considered. To reach rough value of wear volume and compare the results with tribometer, medium area of four cross sections were calculated. Based on obtained data from the profilometer surface of each cross section was calculated abd it was multiplied by the distance which is equal to circumference of the wear circle. The 3D topography, average width and depth of wear scars in addition to wear area cross section were calculated by a 3D optical profilometer. To evaluate the wear resistance of the samples the wear volume V_w and wear rate K (mm^3/Nm) can be calculated as following [311] :

$$V_w = 2\pi r (\text{Average area of surface})$$
$$K = V_w/PS$$

Where

r is the wear orbital radius (mm), P was the normal load (N) and S is the sliding distance (m).

To find the relevant wear volume loss, this value multiplied by the length (circumferential of the wear track circle). For each condition medium value of four measurement was reported for wear rate of each condition. The rough calculated results and relevant medium value are shown in Table. 6-8 and Table. 6-9.

To observe the detail micrographs and finding how data was obtained,

Fig. 6-41 to Fig. 6-44 show the examples of some 2D line profile which applied on different part of wear tracks in different situations. The obtained 2D graphs consists of maximum depth of the samples accompanied with area cross section.

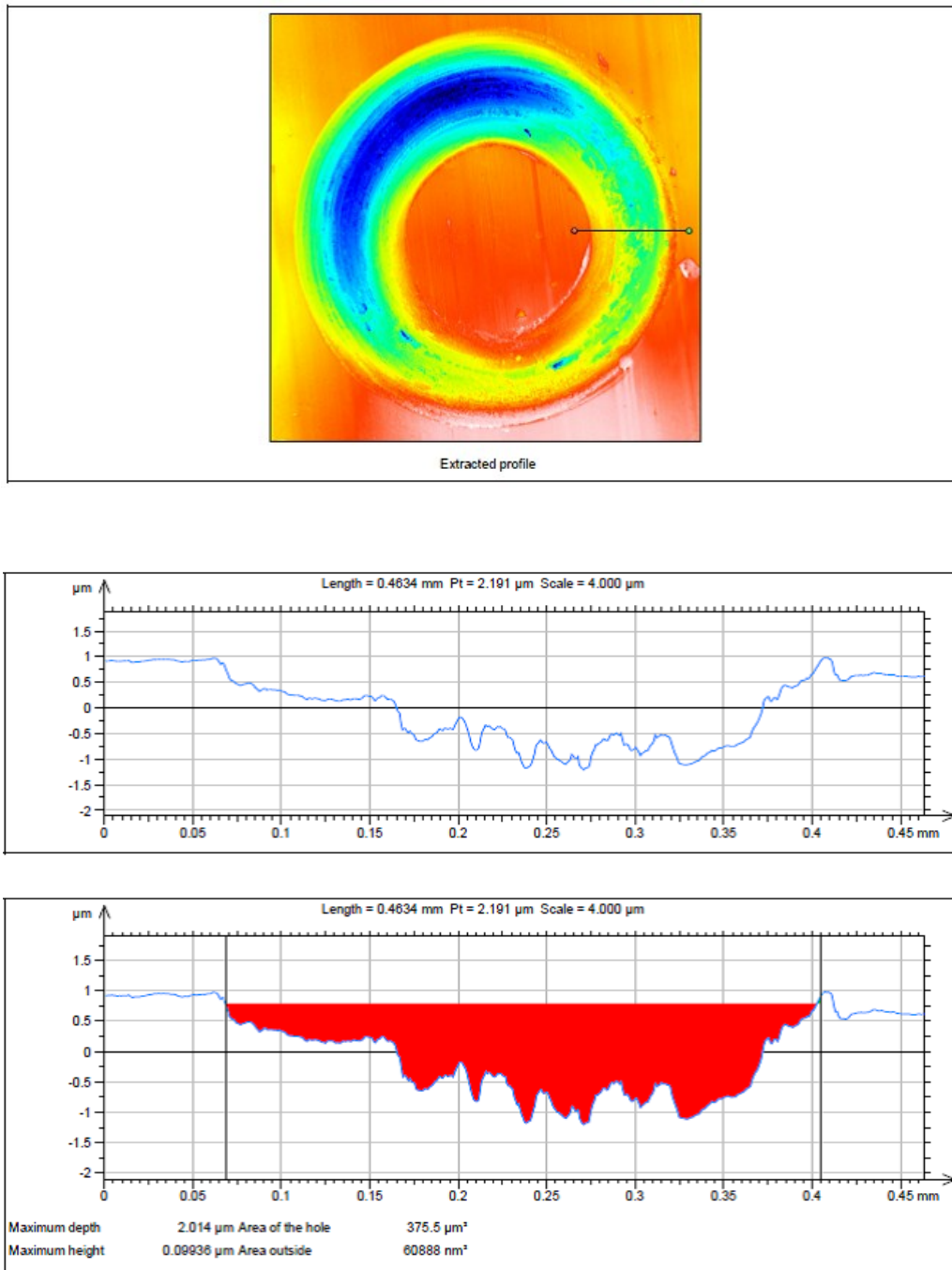


Fig. 6-41. 2D Top image of worn surface and linear profile of the specified line (W1NP)

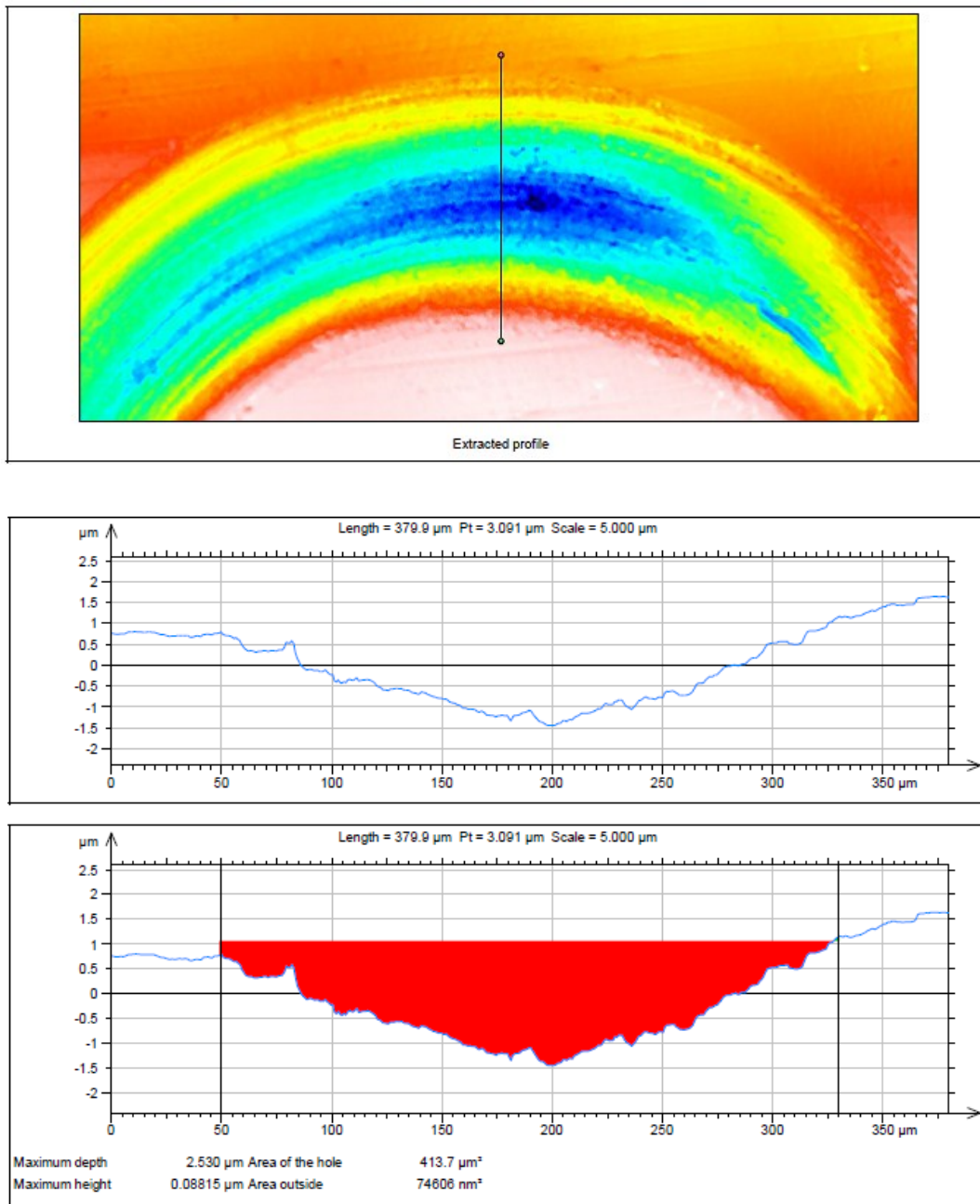


Fig. 6-42. One example of line surface profile to measure area of cross section (sample W0NP)

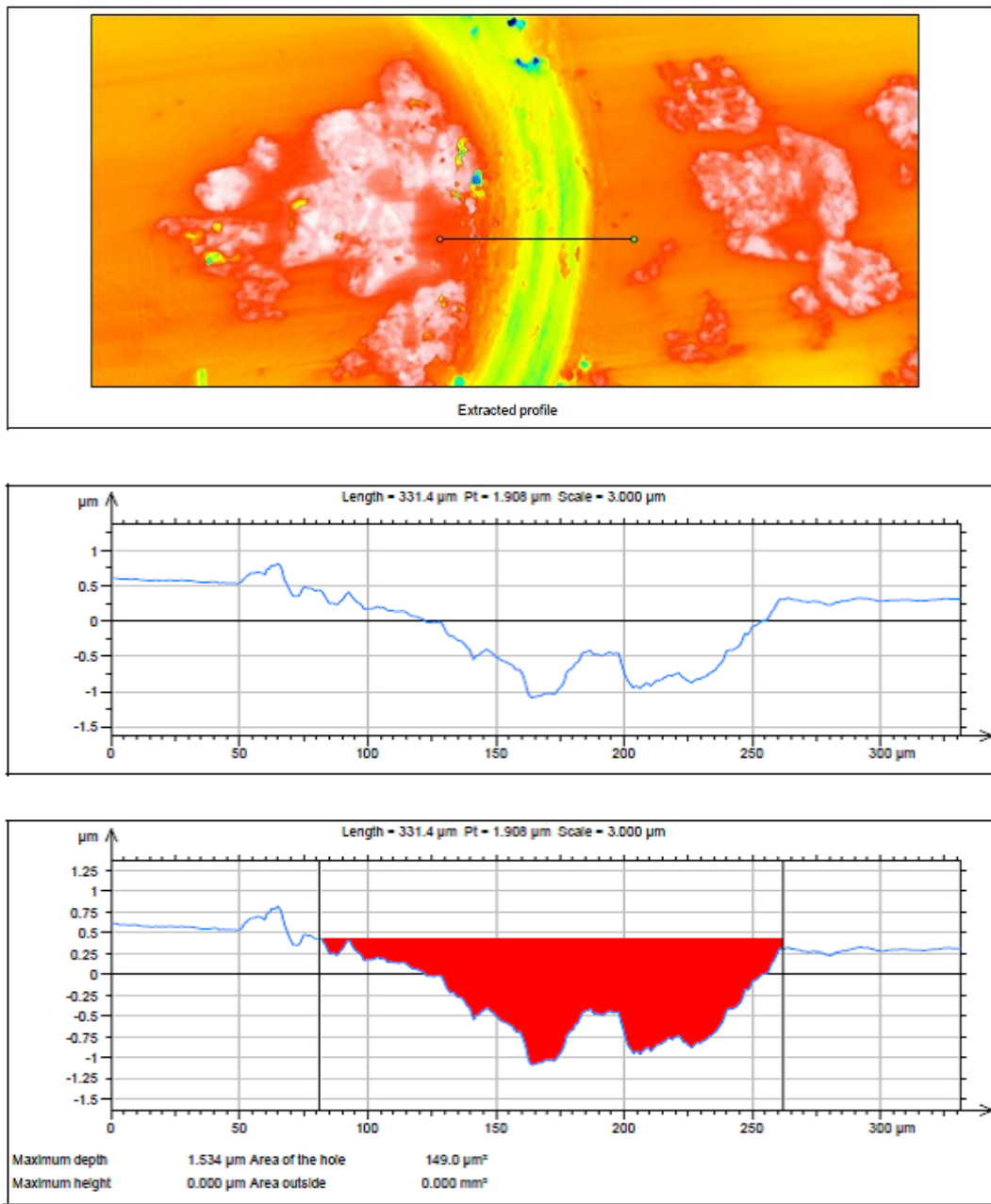


Fig. 6-43. line surface profile to measure area of cross section (sample W0NP)

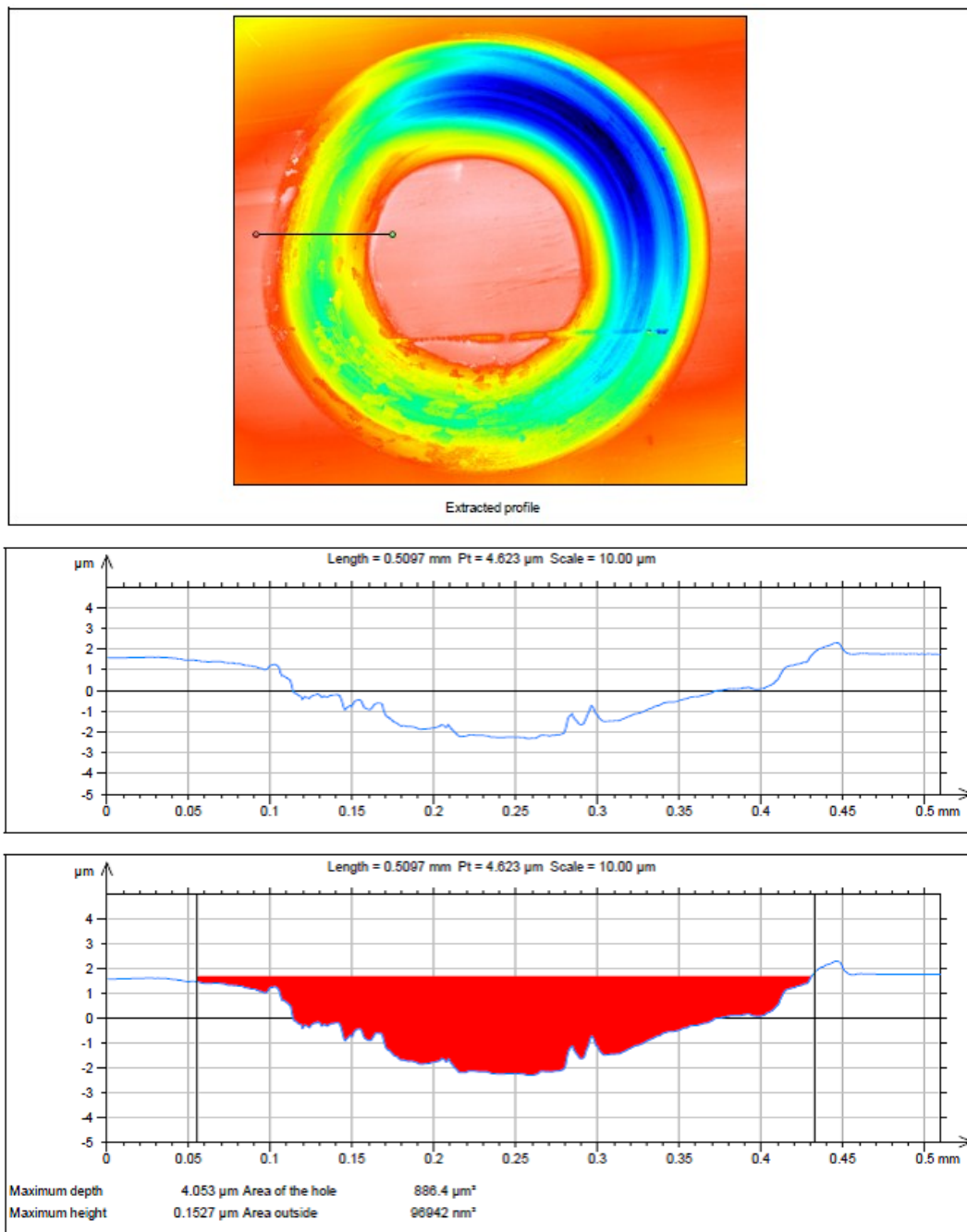


Fig. 6-44. line surface profile to measure area of cross section (sample W5NP)

Table. 6-8. Results of wear rate measurement (1N load) obtained from profilometer

Sample	Max. depth (μm)	Area (μm^2)	Width (μm)	Length (μm)	Volume (mm^3)	Wear rate (mm^3/Nm)
W0NP						
1	2,17	405,7	315	10932	0,0044	2,956E-06
2	2,53	413,7	280	10932	0,0045	3,015E-06
3	1,09	190,1	285	10932	0,0020	1,385E-06
4	1,54	149	183	10932	0,0016	1,085E-06
Med.	1,83	289,62	265,8	10932	0,0031	2,110E-06
W1NP						
1	2,5	525,7	335	10932	0,0057	3,831E-06
2	1,98	34,1	275	10932	0,0003	2,485E-07
3	1,88	418,8	310	10932	0,0045	3,052E-06
4	0,94	130,3	290	10932	0,0014	9,496E-07
Med.	1,83	277,23	302,5	10932	0,0030	2,020E-06
W3NP						
1	3,35	558,5	280	10932	0,0061	4,070E-06
2	2,41	353,6	280	10932	0,0038	2,577E-06
3	3,02	545,8	295	10932	0,0059	3,977E-06
4	2,6	329,3	255	10932	0,0035	2,399E-06
Med.	2,84	446,8	277,5	10932	0,0048	3,256E-06
W5NP						
1	4,28	1005	375	10932	0,0109	7,324E-06
2	1,64	249,8	290	10932	0,0027	1,820E-06
3	3,61	757,5	340	10932	0,0082	5,520E-06
4	3,27	615,9	300	10932	0,0067	4,488E-06
Med.	3,2	657,05	326,25	10932	0,0071	4,788E-06
W7NP						
1	2,68	425,9	296	10932	0,0046	3,103E-06
2	3,24	683	357	10932	0,0074	4,970E-06
3	2,55	545,3	325	10932	0,0059	3,974E-06
4	1,75	286,5	280	10932	0,0031	2,088E-06
Med.	2,55	485,18	314,5	10932	0,0053	3,535E-06

Table. 6-9. Results of wear rate measurement (5 N load) obtained from profilometer

Sample	Max. depth(μm)	Area (μm^2)	Width (μm)	Length (μm)	Volume (mm^3)	Wear rate ($\text{mm}^3/\text{N.m}$)
W0NP						
1	10,72	3577	510	10932	0,0391	1,303E-05
2	9,78	3015	470	10932	0,0329	1,098E-05
3	9,36	2640	450	10932	0,0288	9,620E-06
4	10,94	3374	520	10932	0,0368	1,229E-05
Med.	10,2	3151,5	487,5	10932	0,0344	1,148E-05
W1NP						
1	4,03	1088	460	10932	0,0118	3,964E-06
2	2,19	361,3	310	10932	0,0039	1,316E-06
3	3,17	836,5	445	10932	0,0091	3,048E-06
4	2,014	375,5	340	10932	0,0041	1,368E-06
Med.	2,85	665,3	388	10932	0,0072	2,424E-06
W3NP						
1	6,92	1562	350	10932	0,0170	5,691E-06
2	6,2	1603	385	10932	0,0175	5,841E-06
3	6,19	1382	365	10932	0,0151	5,036E-06
4	6,06	1189	335	10932	0,0129	4,332E-06
Med.	6,34	1434	358,75	10932	0,0156	5,225E-06
W5NP						
1	7,79	2759	551	10932	0,0301	1,005E-05
2	4,29	1148	465	10932	0,0125	4,183E-06
3	7,28	2468	530	10932	0,0269	8,993E-06
4	4,05	886,4	383	10932	0,0096	3,230E-06
Med.	5,85	1815,3	482,25	10932	0,0198	6,614E-06
W7NP						
1	3,93	1162	460	10932	0,0127	4,234E-06
2	2,84	693,9	480	10932	0,0075	2,528E-06
3	2,98	633,8	405	10932	0,0069	2,309E-06
4	4,58	1577	518	10932	0,0172	5,746E-06
Med.	3,58	1016,7	465,75	10932	0,0111	3,704E-06

Based on obtained results from optical profilometer, Fig. 6-45 shows the histogram for wear rate of different samples with relevant standard deviation. It can be said that for the sample without nanoparticles with addition of load increase significantly but for the sample with addition of nanoparticles the differences between wear rate decrease. By comparing the the obtained samples with 1 Wt% addition is good to wear, because a small amount of NP helps lower the coefficient of friction, but 3 Wt% addition is good to improve mechanical properties in general form.

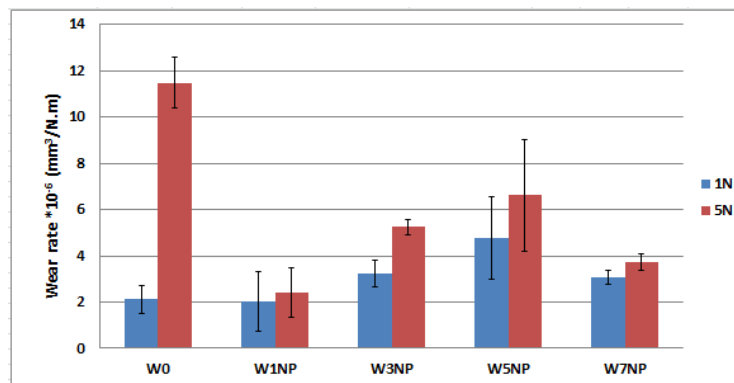


Fig. 6-45. Wear rate results obtained from optical profilometry

6.3. Conclusions

The present research was focused on the nano-scale composite system created by WC powder (with characteristic grain size of 40-100 nm), added in quantity of 1 to 7 Wt% to nickel base powder already reinforced by WC particles in micron size. The resulting multi-phase powder was used for plasma transferred arc welding (PTA) hardfacing of D2 tool steel. The mechanical behaviour of the samples at micro- and nano-scale was characterized with nano-indentation and sliding wear test. The microstructure and phases of the sample were determined with SEM/XRD analysis. The control sample without nanoparticle features hypoeutectic microstructure.

The addition of nano-particles in concentrations below 3 Wt% does not lead to drastic changes in microstructure, yet it is detectable by variation of the mass fraction of Ni-Fe solid solution and the balance of the total Fe-Cr compounds, leading to general refinement of the microstructure. For the sample with 3 Wt% of nano-particles, the most notable observations were the pronounced accumulation of the NPs at the boundaries of primary tungsten carbides, as well as decreased nucleation of the FeNiCr dendrites. As the grain boundaries act as barriers for propagating dislocations, it is preferable to produce the samples with tight-packed smaller grains, which will contribute to improvement of overlay's mechanical properties.

Another relatively new strengthening technology consists in agglomeration of nanoparticles agglomeration at the dendritic nickel base matrix which may favor stress relaxation due to enhanced material mobility under deformation. Such behavior should be related with improvement of material's mechanical properties at macro scale performance. The observed increase of wear resistance in the sample with nanoparticles is attributed to a uniform distribution and high volume fraction of the nanocarbides in the matrix. The results of XRD analysis showed that addition of different Wt% of WC nanoparticle dispersed in the matrix produces different types of chromium carbide and borides compounds.

The high surface area to volume ratio in the WC nanostructure achieved under nano-particle content of 3 Wt% and above, one can observe decomposition of carbide grains during the overlay process. The precipitation of nanocarbides in the matrix is due to the decrease of tungsten solubility and diffusion coefficient at lower temperature. It was observed that the structure-debilitating effect proceeds from the clusters of nano-scale secondary carbide grains that grow inside the primary carbide matrix and in the areas directly adjacent to deplete carbide phase. This occurs due to partial melting and diffusion of the primary WC phase into the carbide network.

References

- [1] J.C. Lippold, D.J. Kotecki, *Welding Metallurgy and Weldability of Stainless Steels*, John Wiley and Sons, 2005.
- [2] J. Gagnepain, Duplex Stainless Steels : Success Story and Growth Perspectives, *Stainl. Steel World*. Dezembro (2008) 31–36.
- [3] Knudtzon, Metallographic preparation of stainless steel, *Struers Appl. Notes*. (n.d.) 32–37.
- [4] G. Krauses, *Steels Processing, Structure and performance* (Second Ed.), ASM International, 2015.
- [5] A.J. Sedricks, *Corrosion of Stainless Steels*, John Wiley and Sons, 1979.
- [6] J. Chater, The European market for duplex stainless steels: rapid growth expected, *Duplex Steel Word*. March (2010) 1–4.
- [7] International Molybdenum, Association, *Practical Guidelines for the Fabrication of Duplex Stainless Steels*, (2014) 1–68.
- [8] M.F. McGuire, *Stainless steels for design engineers*, ASM International, 2008.
- [9] H.R. Copson, F.S. Lang, Some Experiments on Internal Oxidation Of Nickel Chromium Alloys. *Corrosion: Corrosion*. 15 (1959) 44–58.
- [10] H. Tan, Y. Jiang, B. Deng, T. Sun, J. Xu, J. Li, Effect of annealing temperature on the pitting corrosion resistance of super duplex stainless steel UNS S32750, *Mater. Charact.* 60 (2009) 1049–1054.
- [11] H. Hänninen, J. Romu, R. Ilola, J. Tervo, A. Laitinen, Effects of processing and manufacturing of high nitrogen-containing stainless steels on their mechanical, corrosion and wear properties, *J. Mater. Process. Technol.* 117 (2001) 424–430.
- [12] T. Ogawa, T. Koseki, Effect of composition profiles on metallurgy and corrosion behavior of duplex stainless steel weld metals, *Weld. Res. Suppl.* (1989) 182–191.
- [13] D.J. Kotecki, J.C. Lippold, *Welding metallurgy and weldability of stainless steels.*, Hoboken, New Jersey: John Wiley, 2005.
- [14] A. Hermas, K. Ogura, S. Takagi, T. Adachi, A. A. Hermas, K. Ogura, S. Takagi and T. Adachi, *Corrosion* 51, 3 (1995)., *Corrosion*. 51 (1995) 3.
- [15] J. Banas, A. Mazurkiewicz, The effect of copper on passivity and corrosion behaviour of ferritic and ferritic – austenitic stainless steels., *Mater. Sci. Eng. A*. 277 (2000) 183–191.
- [16] P. Paulraj, R. Garg, Effect of Intermetallic Phases on Corrosion Behavior and Mechanical Properties of Duplex Stainless Steel and Super-Duplex Stainless Steel, *Adv. Sci. Technol. Res. J.* 9 (2015) 87–105.
- [17] R. Gunn, *Duplex stainless steels: microstructure, properties and applications*, 1997.
- [18] S. Bernhardsson, The corrosion resistance of duplex stainless steels, in: *Int. Conf. Duplex Stainl. Steel*, Beaune Bourgogne Fr., 1991: p. 185.
- [19] H. Krawiec, V. Vignal, O. Heintz, R. Oltra, Influence of the dissolution of MnS inclusions under free corrosion and potentiostatic conditions on the composition of passive films and the electrochemical behaviour of stainless steels., *Electrochim. Acta*. 51 (2006) 3235–3243.
- [20] K.H. Lo, C.H. Shek, J.K.L. Lai, Recent developments in stainless steels, *Mater. Sci. Eng. R Reports*. 65 (2009) 39–104.
- [21] W. Luu, P. Liu, J. Wu, Hydrogen transport and degradation of a commercial duplex stainless steel, *Corros. Sci.* 44 (2002) 1783.
- [22] T. Zakroczymski, A. Glowacka, W. Swiatnicki, Effect of hydrogen concentration on the embrittlement of a duplex stainless steel, *Corros. Sci.* 47 (2005) 1403.
- [23] P. Zahumensky, S. Tuleja, J. Orszagova, V. Janovec, Corrosion resistance of 18Cr-12Ni-2.5Mo steel annealed at 500–1050°C, *Corros. Sci.* 41 (1999) 1305.
- [24] A. Barbucci, G. Cerisola, P. Cabot, Effect of Cold-Working in the Passive Behavior of 304 Stainless Steel in Sulfate Media, *J. Electrochem. Soc.* 149 (2002) B534.
- [25] U.K. Mudali, P. Shankar, S. Ningshen, R.K. Dayal, H.S. Khatak, B. Raj, On the pitting corrosion resistance of nitrogen alloyed cold worked austenitic stainless steels, *Corros. Sci. Sci.* 44 (2002) 2183.
- [26] K.. Sreekumari, K. Nandakumar, K. Yakao, Y. Kikuchi, *ISIJ International* 43 (2003) 1799., *ISIJ Int.* 43 (2003) 1799.
- [27] M.F. McGuire, *Stainless steels for design engineers*, ASM International, Materials Park, Ohio, 2008.
- [28] A.J. Ramirez, The Relationship between Chromium Nitride and Secondary Austenite Precipitation in Duplex Stainless Steels, *Metall. Mater. Trans. A*. 34A (2003) 1575–1597.
- [29] M. Pohl, O. Storz, T. Glogowski, Effect of intermetallic precipitations on the properties of duplex stainless steel, *Mater. Charact.* 58 (2007) 65–71.

- [30] D. Dyja, Z. Stradomski, A. Pirek, Microstructural and fracture analysis of aged cast GX2CrNiMoCu25-6-3-3 duplex stainless steel, *Met.* 2006. 23 (2006) 6.
- [31] C.R. Xavier, H.G.D. Junior, J.A. de Castro, An Experimental and Numerical Approach for the Welding Effects on the Duplex Stainless Steel Microstructure, *Mater. Res.* 18 (2015) 489–502.
- [32] I.V. Aguiar, P.J. Pérez Escobar, Diana Brandão Santos, Dagoberto Modenesi, Microstructure characterization of a duplex stainless steel weld by electron backscattering diffraction and orientation imaging microscopy techniques, *Riv. Mater.* 20 (2015) 212–226.
- [33] M. Vasudevan, M. Muruganath, A. Bhaduri, R. Baldev, K. Prasad Rao, Prediction of Ferrite Number in Stainless Steel Welds, *Sci. Technol. Weld. Join.* 9 (2004) 109.
- [34] C. Lundin, W. Ruprecht, G. Zhou, Ferrite Measurement in Austenitic and Duplex Stainless Steel Castings, (1999) 87.
- [35] D. Kotecki, T. Siewert, WRC-1992 Constitution diagram for stainless steel weld metals: a modification of the WRC-1988 DIAGRAM, *Weld. J.* 71 (1992) 171.
- [36] I. Calliari, K. Brunelli, M. Dabalà, E. Ramous, Measuring Secondary Phases in Duplex Stainless Steels, *J. Miner. Met. Mater. Soc. (TMS), JOM.* 61 (2009) 80–83.
- [37] L. Karlsson, Intermetallic phase precipitation in duplex stainless steels and weld metals, *Metall. Influ. Prop. Weld. Test. Asp.* (1999).
- [38] Y.-L. He, N.-Q. Zhu, X.-G. Lu, L. Li, Experimental and computational study on microstructural evolution in 2205 duplex stainless steel during high temperature aging, *Mater. Sci. Eng. A.* 528 (2010) 721–729.
- [39] AWS Welding Handbook 9.4, United States of America, Am. Weld. Soc. Stand. (2011).
- [40] J.F. Almagro, Microstructure and phase analysis of duplex stainless steel after heat treatment, *HKL Technol. Oxford Instrum. App.* 7 (2005) 34–37.
- [41] S.M. Dubiel, C. Jakub, Sigma-phase in Fe-Cr and Fe-V alloy systems and its physical properties, AGH University of Science and Technology, (2011) 1–27.
- [42] J.A. Platt, A. Guzman, A. Zuccari, D.W. Thornburg, B.F. Rhodes, Y. Oshida, et al., Corrosion behavior of 2205 duplex stainless steel, *Am. J. Orthod. Dentofac. Orthop.* 112 (1997) 69–79.
- [43] M.V. Biezma, C. Berlanga, G. Argandon, Relationship between Microstructure and Fracture Types in a UNS S32205 Duplex Stainless Steel, *Mater. Res.* 16 (2013) 965–969.
- [44] N. Llorca Isern, H. Lopez Luque, I. Lopez Jimenez, M.V. Biezma, Identification of sigma and chi phases in duplex stainless steels, *Mater. Charact.* (2015) In press.
- [45] Y.S. Sato, H. Kokawa, Preferential precipitation site of sigma phase in duplex stainless steel weld metal, *Scr. Mater.* 40 (1999) 659–663.
- [46] H. Matsunaga, Y.S. Sato, H. Kokawa, T. Kuwana, Effect of nitrogen on corrosion of duplex stainless steel weld metal, *Sci. Technol. Weld. Join.* 3 (1998) 225–232.
- [47] S.S.M. Tavares, J.M. Pardal, L.D. Lima, I.N. Bastos, A.M. Nascimento, J.A. de Souza, Characterization of microstructure, chemical composition, corrosion resistance and toughness of a multipass weld joint of superduplex stainless steel UNS S32750, *Mater. Charact.* 58 (2007) 610–616.
- [48] D.D. Z. Stradomski, Sigma phase precipitation in duplex phase stainless steels 1), (n.d.) 4–5.
- [49] C.-C. Hsieh, W. Wu, Overview of Intermetallic Sigma (σ) Phase Precipitation in Stainless Steels, *Int. Sch. Res. Netw. ISRN Metall.* 12 (2012) 16.
- [50] H.D. Solomon, T.M. Devine, Duplex stainless steels - a tale of two phases, *ASM Int. Met. Park. Ohio.* (1982) 693–756.
- [51] H. Solomon, T. Devine, R. Lula, Duplex stainless steels - a tale of two phases, *Met. Park. Ohio ASM.* (1982) 693–756.
- [52] J. Michalska, M. Sozańska, Qualitative and quantitative analysis of σ and χ phases in 2205 duplex stainless steel, *Mater. Charact.* 56 (2006) 355–362.
- [53] T.H. Chen, J.R. Yang, Effects of solution treatment and continuous cooling on σ -phase precipitation in a 2205 duplex stainless steel, *Mater. Sci. Eng. A.* 311 (2001) 28–41.
- [54] J. Michalska, B. Chmiela, Phase analysis in duplex stainless steel: comparison of EBSD and quantitative metallography methods, *IOP Conf. Ser. Mater. Sci. Eng.* 55 (2014).
- [55] H. Sieurin, R. Sandström, Sigma phase precipitation in duplex stainless steel 2205, *Mater. Sci. Eng. A.* 444 (2007) 271–276.
- [56] Y. Yang, B. Yan, J. Li, J. Wang, The effect of large heat input on the microstructure and corrosion behaviour of simulated heat affected zone in 2205 duplex stainless steel, *Corros. Sci.* 53 (2011) 3756–3763.
- [57] B. Deng, Z. Wang, Y. Jiang, H. Wang, J. Gao, J. Li, Evaluation of localized corrosion in duplex stainless steel aged at 850 °C with critical pitting temperature measurement, *Electrochim. Acta.* 54 (2009) 2790–2794.
- [58] S.S.M. Tavares, M.R. da Silva, J.M. Pardal, H.F.G. Abreu, A.M. Gomes, Microstructural changes produced by plastic deformation in the UNS S31803 duplex stainless steel, *J. Mater. Process. Technol.* 180 (2006) 318–322.

-
- [59] M. Young, L. Tsay, C. Shin, S. Chan, The effect of short time post-weld heat treatment on the fatigue crack growth of 2205 duplex stainless steel welds, *Int. J. Fatigue*. 29 (2007) 2155–2162.
- [60] H. Ghazanfari, M. Naderi, M. Iranmanesh, M. Seydi, A. Poshteban, A comparative study of the microstructure and mechanical properties of HTLA steel welds obtained by the tungsten arc welding and resistance spot welding, *Mater. Sci. Eng. A*. 534 (2012) 90–100.
- [61] I. Calliari, M. Zanesco, Analysis of secondary phases precipitation in duplex stainless steels, *J. Innov.* (2009) 1–6.
- [62] I. Calliari, M. Zanesco, M. Ramous, Influence of isothermal aging on secondary phases precipitation and toughness of a duplex steel SAF 2205, *J. Mater. Sci.* 41 (2006) 7643–7649.
- [63] M. Martins, L.C. Casteletti, Sigma phase morphologies in cast and aged super duplex stainless steel, *Mater. Charact.* 60 (2009) 792–795.
- [64] J.-O. Nilsson, Super duplex stainless steels, *Mater. Sci. Technol.* 8 (1992) 685–700.
- [65] M. Rosso, I. Peter, D. Suani, About heat treatment and properties of Duplex Stainless Steels, *J. Achiev. Mater. Manuf. Eng.* 59 (2013) 26–36.
- [66] J. Nowacki, A. Łukojc, Microstructural transformations of heat affected zones in duplex steel welded joints, *Mater. Charact.* 56 (2006) 436–441.
- [67] J. Luo, Y. Yuan, X. Wang, Z. Yao, Double-Sided Single-Pass Submerged Arc Welding for 2205 Duplex Stainless Steel, *J. Mater. Eng. Perform.* 22 (2013) 2477–2486.
- [68] H.-S. Wang, Effect of Welding Variables on Cooling Rate and Pitting Corrosion Resistance in Super Duplex Stainless Weldments, *Mater. Trans.* 46 (2005) 593–601.
- [69] S.K. Ghosh, S. Mondal, High temperature ageing behaviour of a duplex stainless steel, *Mater. Charact.* 59 (2008) 1776–1783.
- [70] D.H. Kang, H.W. Lee, Study of the correlation between pitting corrosion and the component ratio of the dual phase in duplex stainless steel welds, *Corros. Sci.* 74 (2013) 396–407.
- [71] J. Nilsson, L. Karlsson, J. Andersson, Secondary austenite formation and its relation to pitting corrosion in duplex stainless steel weld metal., *Mater. Sci. Technol.* 11 (1995) 276–283.
- [72] R. Badji, B. Bacroix, M. Bouabdallah, Texture, microstructure and anisotropic properties in annealed 2205 duplex stainless steel welds, *Mater. Charact.* 62 (2011) 833–843.
- [73] M.C. Young, S.L.I. Chan, L.W. Tsay, C.S. Shin, Hydrogen-enhanced cracking of 2205 duplex stainless steel welds, *Mater. Chem. Phys.* 91 (2005) 21–27.
- [74] M. Rahmani, A. Eghlimi, M. Shamanian, Evaluation of Microstructure and Mechanical Properties in Dissimilar Austenitic/Super Duplex Stainless Steel Joint, *J. Mater. Eng. Perform.* 23 (2014) 3745–3753.
- [75] R. a. Perren, T. Suter, C. Solenthaler, G. Gullo, P.J. Uggowitzer, H. Böhm, et al., Corrosion resistance of super duplex stainless steels in chloride ion containing environments: Investigations by means of a new microelectrochemical method. II. Influence of precipitates, *Corros. Sci.* 43 (2001) 727–745.
- [76] C.M. Garzon, C.A. Serna, S.D. Brandi, A.J. Ramirez, The relationship between atomic partitioning and corrosion resistance in the weld-heat affected zone microstructures of UNS S32304 duplex stainless steel, *J. Mater. Sci.* 42 (2007) 9021–9029.
- [77] K.. Andrews, A new intermetallic phase in alloy steels, *Nature*. 164 (1949) 1015.
- [78] J.. Kasper, The ordering of atoms in the chi-phase of the iron–chromium–molybdenum system, *Acta Metall. Mater.* 2 (1954) 456–461.
- [79] D.M. Escriba, E. Materna-Morris, R.L. Plaut, A.F. Padilha, Chi-phase precipitation in a duplex stainless steel, *Mater. Charact.* 60 (2009) 1214–1219.
- [80] R. Kaçar, M. Acarer, Microstructure–property relationship in explosively welded duplex stainless steel–steel, *Mater. Sci. Eng. A*. 363 (2003) 290–296.
- [81] J. Dobranszky, P.J. Szabo, T. Berecz, V. Hrotko, M. Portko, Energy-dispersive spectroscopy and electron backscatter diffraction analysis of isothermally aged SAF 2507 type superduplex stainless steel, *Spectrochim. Acta - Part B At. Spectrosc.* 59 (2004) 1781–1788.
- [82] M. Esmailzadeh, M. Shamanian, A. Kermanpur, T. Saeid, Microstructure and mechanical properties of friction stir welded lean duplex stainless steel, *Mater. Sci. Eng. A*. 561 (2013) 486–491.
- [83] H. Sieurin, R. Sandström, Austenite reformation in the heat-affected zone of duplex stainless steel 2205, *Mater. Sci. Eng. A*. 418 (2006) 250–256.
- [84] K. Chan, S. Tjong, Effect of Secondary Phase Precipitation on the Corrosion Behavior of Duplex Stainless Steels, *Materials (Basel)*. 7 (2014) 5268–5304.
- [85] R. Cervo, P. Ferro, A. Tiziani, Annealing temperature effects on super duplex stainless steel UNS s32750 welded joints. I: Microstructure and partitioning of elements, *J. Mater. Sci.* 45 (2010) 4369–4377.
- [86] Z. Zhang, Z. Wang, Y. Jiang, H. Tan, D. Han, Y. Guo, et al., Effect of post-weld heat treatment on microstructure evolution and pitting corrosion behavior of UNS S31803 duplex stainless steel welds, *Corros. Sci.* 62 (2012) 42–50.

- [87] T.-H. Lee, S.-J. Kim, S. Takaki, Time-temperature-precipitation characteristics of high-nitrogen austenitic Fe-18Cr-18Mn-2Mo-0.9N steel, *Metall. Mater. Trans. A*. 37 (2006) 3445–3454.
- [88] V.S. Moura, L.D. Lima, J.M. Pardal, a. Y. Kina, R.R. a Corte, S.S.M. Tavares, Influence of microstructure on the corrosion resistance of the duplex stainless steel UNS S31803, *Mater. Charact.* 59 (2008) 1127–1132.
- [89] H. Tan, Z. Wang, Y. Jiang, D. Han, J. Hong, L. Chen, et al., Annealing temperature effect on the pitting corrosion resistance of plasma arc welded joints of duplex stainless steel UNS S32304 in 1.0M NaCl, *Corros. Sci.* 53 (2011) 2191–2200.
- [90] B. Deng, Y. Jiang, J. Liao, Y. Hao, C. Zhong, J. Li, Dependence of critical pitting temperature on the concentration of sulphate ion in chloride-containing solutions, *Appl. Surf. Sci.* 253 (2007) 7369–7375.
- [91] K. Migiakis, G.D. Papadimitriou, Effect of nitrogen and nickel on the microstructure and mechanical properties of plasma welded UNS S32760 super-duplex stainless steels, *J. Mater. Sci.* 44 (2009) 6372–6383.
- [92] H. Tan, Z. Wang, Y. Jiang, Y. Yang, B. Deng, H. Song, et al., Influence of welding thermal cycles on microstructure and pitting corrosion resistance of 2304 duplex stainless steels, *Corros. Sci.* 55 (2012) 368–377.
- [93] T.. Palmer, J.. Elmer, S.. Babu, Observations of ferrite/austenite transformations in the heat affected zone of 2205 duplex stainless steel spot welds using time resolved X-ray diffraction, *Mater. Sci. Eng. A*. 374 (2004) 307–321.
- [94] K.M. Lee, H. Cho, D.C. Choi, Effect of isothermal treatment of SAF 2205 duplex stainless steel on migration of δ/γ interface boundary and growth of austenite, *J. Alloys Compd.* 285 (1999) 156–161.
- [95] R.T. Loto, Pitting corrosion evaluation of austenitic stainless steel type 304 in acid chloride media, *J. Mater. Eng. Environ. Sci.* 4 (2013) 448–459.
- [96] J.. Lippold, I. Varol, W.. Baeslack III, The Influence of composition and microstructure on the HAZ toughness of duplex stainless steels at -20 °C, *Weld. J.* 73 (1994) 75–79.
- [97] J.. Sahu, U. Krupp, R.. Ghosh, H.. Christ, Effect of 475 °C embrittlement on the mechanical properties of duplex stainless steel, *Mater. Sci. Eng. A*. 508 (2009) 1–14.
- [98] S.S.. Tavares, R.. De Noronha, M.. Da Silva, J.. Neto, S. Pairis, 475 °C Embrittlement in a Duplex Stainless Steel UNS S31803, *Mater. Res.* 4 (2001) 237–240.
- [99] T. Saeid, A. Abdollah-zadeh, H. Assadi, F. Malek Ghaini, Effect of friction stir welding speed on the microstructure and mechanical properties of a duplex stainless steel, *Mater. Sci. Eng. A*. 496 (2008) 262–268.
- [100] L.J. Nelson DE, Baeslack IIIWA, Characterization of the weld structure in a duplex stainless steel using color metallography, *Mater. Charact.* 39 (1997) 467–477.
- [101] G.F. Vander Voort, Applied metallography: The metallography of stainless steels, *J. Mater.* 41 (1989) 6–11.
- [102] Michalska J, S. M, Selective etching of phases and structural constituents in duplex stainless steel., in: *Proc Mass Charg. Transp. Mater. Krakov, Pol.*, 2004: pp. 3–34.
- [103] G. Vander Voort, *Metallography: Principles and Practice*, ASM International., 2nd edition, ASM International, Materials Park, Ohio, 2000.
- [104] G.F. Vander Voort, Color Metallography, *Micros. Today*. 13 (2005) 22–27.
- [105] M. Mohammed Asif, K. Anup Shrikrishna, P. Sathiya, Effects of post weld heat treatment on friction welded duplex stainless steel joints, *J. Manuf. Process.* In press (2015).
- [106] A.-H.I.. c Mourad, A.. Khourshid, T.. Sharef, Gas tungsten arc and laser beam welding processes effects on duplex stainless steel 2205 properties, *Mater. Sci. Eng. A*. 549 (2012) 105–113.
- [107] G. Vander Voort, *Introduction to Quantitative Metallography*, Image (Rochester, N.Y.). 1 (n.d.).
- [108] M. Gholami, M. Hoseinpoor, M.H. Moayed, A statistical study on the effect of annealing temperature on pitting corrosion resistance of 2205 duplex stainless steel, *Corros. Sci.* 94 (2015) 156–164.
- [109] V. Muthupandi, P.B. Srinivasan, S.K. Seshadri, S. Sundaresan, Corrosion behaviour of duplex stainless steel weld metals with nitrogen additions, *Corros. Eng. Sci. Technol.* 38 (2003) 303–308.
- [110] J. Pekkarinen, V. Kujanpää, The effects of laser welding parameters on the microstructure of ferritic and duplex stainless steels welds, *Phys. Procedia*. 5 (2010) 517–523.
- [111] J. Pilhagen, H. Sieurin, R. Sandström, Fracture toughness of a welded super duplex stainless steel, *Mater. Sci. Eng. A*. 606 (2014) 40–45.
- [112] M.V. Biezma, C. Berlanga, G. Argandona, Relationship between microstructure and fracture types in a UNS S32205 duplex stainless steel, *Mater. Res.* 16 (2013) 965–969.
- [113] K. Yurtisik, S. Tirkes, I. Dykhno, C. Hakan Gur, R. Gurbuz, Characterization of Duplex Stainless Steel Weld Metals Obtained by Hybrid Plasma-Gas Metal Arc Welding, *Soldag. Inspeção*. 18 (2013) 207–216.
- [114] Z. Zhang, D. Han, Y. Jiang, C. Shi, J. Li, Microstructural evolution and pitting resistance of annealed lean duplex stainless steel UNS S32304, *Nucl. Eng. Des.* 243 (2012) 56–62.
- [115] H. Hwang, Y. Park, Effects of Heat Treatment on the Phase Ratio and Corrosion Resistance of Duplex Stainless Steel, *Mater. Trans.* 50 (2009) 1548–1552.
- [116] M. Naghizadeh, M.H. Moayed, Investigation of the effect of solution annealing temperature on critical pitting temperature of 2205 duplex stainless steel by measuring pit solution chemistry d, *Corros. Sci.* 94 (2015) 35–39.

-
- [117] L.F. Garfias-Mesias, J.M. Sykes, C.D.S. Tuck, The effect of phase compositions on the pitting corrosion of 25 Cr duplex stainless steel in chloride solutions, *Corros. Sci.* 38 (1996) 1319–1330.
- [118] L. Schwarz, T. Vrtochová, K. Ulrich, Laser Beam Welding of Superduplex Stainless Steel With Post-Heat Treatment, (n.d.) 20–26.
- [119] ASTM E562-05, Standard Test Method for Determining Volume Fraction by Systematic Manual Point Count, ASTM International, West Conshohocken, PA, 2005, (n.d.).
- [120] ASTM E1245-03, Standard Practice for Determining the Inclusion or Second-Phase Constituent Content of Metals by Automatic Image Analysis, ASTM International, West Conshohocken, PA, 2003., (n.d.).
- [121] A.-H. Mourad, A. Khouirshid, T. Sharef, Gas tungsten arc and laser beam welding processes effects on duplex stainless steel 2205 properties, *Mater. Sci. Eng. A.* 549 (2012) 105–113.
- [122] a. Vinoth Jebaraj, L. Ajaykumar, Influence of Microstructural Changes on Impact Toughness of Weldment and Base Metal of Duplex Stainless Steel AISI 2205 for Low Temperature Applications, *Procedia Eng.* 64 (2013) 456–466.
- [123] S.N.-11 007 Nickel Development Institute Reference Book, Guidelines for the welded fabrication of nickel containing stainless steels for corrosion resistant services, (n.d.) 44.
- [124] Outokumpo stainless steel & high performance alloys, Duplex Stainless Steel, (2014) 12.
- [125] C.W. Patrick, M.A. Cox, Challenges welding duplex and superduplex stainless steel, in: *Am. Fuels Petrochemical Manuf. 2014 Reliab. Maint. Conf.*, 2014: p. 13.
- [126] E.M. Westin, M.M. Johansson, R.F.A. Pettersson, Effect of nitrogen-containing shielding and backing gas on the pitting corrosion resistance of welded lean duplex stainless steel LDX 2101® (EN 1.4162, UNS S32101), *Weld. World.* 57 (2013) 467–476.
- [127] P. Sathiya, S. Aravindan, R. Soundararajan, a. Noorul Haq, Effect of shielding gases on mechanical and metallurgical properties of duplex stainless-steel welds, *J. Mater. Sci.* 44 (2009) 114–121.
- [128] S. Atamert, J.E. King, Elemental partitioning and microstructural development in duplex stainless steel weld metal, *Acta Metall. Mater.* 39 (1990) 273–285.
- [129] J.S. Ku, N.J. Ho, S.C. Tjong, Properties of Electron Beam Welded SAF 2205 Duplex Stainless Steel, *Mater. Process. Technol.* 63 (1997) 770–775.
- [130] H. Matsunaga, Y.S. Sato, H. Kokawa, T. Kuwana, Effect of nitrogen on corrosion of duplex stainless steel weld metal, *Sci. Technol. Weld. Join.* 3 (1998) 225–232.
- [131] O. Jonsson, M. Liljas, P. Stenvall, The role of nitrogen in longitudinal welding of tubing in duplex stainless steels, in: *Duplex Stainl. steels'91*, 1991: pp. 461–468.
- [132] C.M. Garzón, A.J. Ramirez, Growth kinetics of secondary austenite in the welding microstructure of a UNS S32304 duplex stainless steel, *Acta Mater.* 54 (2006) 3321–3331.
- [133] E.M. Westin, S. Hertzman, Element distribution in Lean duplex stainless steel welds, *Weld. World.* 58 (2014) 143–160.
- [134] S.T. Kim, S.H. Jang, I.S. Lee, Y.S. Park, Effects of solution heat-treatment and nitrogen in shielding gas on the resistance to pitting corrosion of hyper duplex stainless steel welds, *Corros. Sci.* 53 (2011) 1939–1947.
- [135] R. Badji, M. Bouabdallah, B. Bacroix, C. Kahloun, B. Belkessa, H. Maza, Phase transformation and mechanical behavior in annealed 2205 duplex stainless steel welds, *Mater. Charact.* 59 (2008) 447–453.
- [136] P. Ferro, A. Tiziani, F. Bonollo, Influence of Induction and Furnace Postweld Heat Treatment on Corrosion Properties of SAF 2205 (UNS 31803), *Weld. J.* 87, no. 12 (2008) 298S–306S.
- [137] J. Luo, Y. Dong, L. Li, X. Wang, Microstructure of 2205 duplex stainless steel joint in submerged arc welding by post weld heat treatment, *J. Manuf. Process.* 16 (2014) 144–148.
- [138] M. Kikuchi, Y. Mishima, Proceeding of the conference on High Nitrogen steels (HNS95), *ISISJ Intenational.* 36 (1996).
- [139] V. Gavriljuk, H. Berns, High nitrogen steels, Springer, Berlin, 1999.
- [140] V. Gavriljuk, H. Berns, High Nitrogen Steels: Structure, Properties, Manufacture, Applications, Springer, 1999.
- [141] H.-Y. Liou, R.-I. Hsieh, W.-T. Tsai, Microstructure and stress corrosion cracking in simulated heat-affected zones of duplex stainless steels, *Corros. Sci.* 55 (2002) 2841–2856.
- [142] M. Cortie, J. Potgieter, The Effect of Temperature and Nitrogen Content on the Partitioning of Alloy Elements in Duplex Stainless Steels, *Metall. Trans. A.* 22A (1991) 2173–2179.
- [143] L. Weber, P.J. Uggowitzer, Partitioning of chromium and molybdenum in super duplex stainless steels with respect to nitrogen and nickel content, *Mater. Sci. Eng. A.* 242 (1998) 222–229.
- [144] M. Liljas, The welding metallurgy of duplex stainless steels, in: *Proceeding Duplex Stainl. Steels*, Glasgow, Scotland, 1994.
- [145] G. Gooch, Corrosion Behavior of Welded Stainless Steel, *Weld. J.* (1995) 135s–154s.
- [146] G.S. Frankel, Pitting Corrosion of Metals A Review of the Critical Factors, *J. Electrochem. Soc.* 145 (1998) 2186–2198.
- [147] M. Fontana, Corrosion Engineering 3rd Ed., Mc-Grow-Hill, 2005.
- [148] Arcelor Mittal, Stainless Steel and Corrosion, *Stainl. Eur.* (2010) 6.

- [149] P.K. Pohjanne, L. Carpén, T. Hakkarainen, A method to predict pitting corrosion of stainless steels in evaporative conditions, *J. Constr. Steel Res.* 64 (2008) 1325–1331.
- [150] R. Francis, Environmental cracking and embrittlement of duplex stainless steels, in: 4th Int. Conf. "Duplex Stainl. Steels, Woodhead Publishing, Abington, England, Glasgow, Scotland, 1994: p. Paper IV.
- [151] K. Sugimoto, Y. Sawada, Role of alloyed molybdenum in austenitic stainless steels in the inhibition of pitting in neutral halide solutions, *Corrosion.* 32 (1976) 347–352.
- [152] N. Boucherit, A. Hugot-Le Goff, S. Joiret, Influence of Ni, Mo, and Cr on Pitting Corrosion of Steels Studied by Raman Spectroscopy, *Corrosion.* 48 (1992) 569–579.
- [153] K.S. Siow, T.Y. Song, J.H. Qiu, Pitting corrosion of duplex stainless steels, *Anti-Corrosion Methods Mater.* 48 (2001) 31–37.
- [154] A. Moskowitz, R. Gunia, Effects of Residual Elements on Properties of Austenitic Stainless Steels, *ASTM STP418.* (1967).
- [155] K.S. Siow, T.Y.S. And, J.H. Qiu, Pitting corrosion of duplex stainless steels, *Anti-Corrosion Methods Mater.* 48 (2001) 31–37.
- [156] E. Symiotis, Dissolution Mechanism of Duplex Stainless Steels in the Active-to-Passive Transition Range and the Role of Microstructure, *Corrosion.* 51 (1995) 571–580.
- [157] L. Ödegård, L. Ödegård, Contributed papers Welding of stainless steels corrosion in welds : effect of oxides , slag and weld defects on the pitting resistance, (1996).
- [158] G.. Coates, Effect of some surface treatments on corrosion of stainless steel, *Mater. Perform.* 29 (1991) 61–67.
- [159] L. Odegard, Contributed papers Welding of stainless steels corrosion in welds : effect of oxides, slag and weld defects on the pitting resistance, *Anti-Corrosion Methods Mater.* 43 (1996) 11–17.
- [160] J. Vagn Hansen, T. Nielsen, P. Aastrup, No Title, in: *Proc. Duplex Stainl. Steels '94*, TWI, Glasgow, Scotland, 1994: p. 13.
- [161] E.M. Westin, D. Serrander, No Title, *Weld. World.* 56 (2012) 13.
- [162] S.-H. Jang, S.-T. Kim, I.-S. Lee, Y.-S. Park, Effect of Shielding Gas Composition on Phase Transformation and Mechanism of Pitting Corrosion of Hyper Duplex Stainless Steel Welds, *Mater. Trans.* 52 (2011) 1228–1236.
- [163] B. Deng, Y. Jiang, J. Gong, C. Zhong, J. Gao, J. Li, Critical pitting and repassivation temperatures for duplex stainless steel in chloride solutions, *Electrochim. Acta.* 53 (2008) 5220–5225.
- [164] S.-T. Kim, S.-Y. Kim, I.-S. Lee, Y.-S. Park, M.-C. Shin, Y.-S. Kim, Effects of shielding gases on the microstructure and localized corrosion of tube-to-tube sheet welds of super austenitic stainless steel for seawater cooled condenser, *Corros. Sci.* 53 (2011) 2611–2618.
- [165] J.Y. Jonsson, A. Thulin, S. Hägg, R. Pettersson, *Jernkontoret*, The two phased optimization of duplex stainless steel, (2013).
- [166] S. Wang, Q. Ma, Y. Li, Characterization of microstructure, mechanical properties and corrosion resistance of dissimilar welded joint between 2205 duplex stainless steel and 16MnR, *Mater. Des.* 32 (2011) 831–837.
- [167] H. Liu, X. Lu, X. Jin, Phase transformation and mechanical properties in laser continuous heat treatment welds, *Mater. Des.* 32 (2011) 2269–2276.
- [168] A. Bhattacharya, P. Singh, Stress Corrosion Cracking of Welded 2205 Duplex Stainless Steel in Sulfide-containing Caustic Solution, *J. Fail. Anal. Prev.* 7 (2007) 371–377.
- [169] D.W. Kang, H.W. Lee, Study of Pitting Resistance of Duplex Stainless Steel Weldment Depending on the Si Content, 9 (2014) 5864–5876.
- [170] V. Muthupandi, P. Bala Srinivasan, V. Shankar, S.K. Seshadri, S. Sundaresan, Effect of nickel and nitrogen addition on the microstructure and mechanical properties of power beam processed duplex stainless steel (UNS 31803) weld metals, *Mater. Lett.* 59 (2005) 2305–2309.
- [171] E. Capello, P. Chiarello, B. Previtali, M. Vedani, Laser welding and surface treatment of a 22Cr–5Ni–3Mo duplex stainless steel, *Mater. Sci. Eng. A.* 351 (2003) 334–343.
- [172] Y. Yang, Z. Wang, H. Tan, J. Hong, Y. Jiang, L. Jiang, et al., Effect of a brief post-weld heat treatment on the microstructure evolution and pitting corrosion of laser beam welded UNS S31803 duplex stainless steel, *Corros. Sci.* 65 (2012) 472–480.
- [173] G. Magudeeswaran, S.R. Nair, L. Sundar, N. Harikannan, Optimization of process parameters of the activated tungsten inert gas welding for aspect ratio of UNS S32205 duplex stainless steel welds, *Def. Technol.* 10 (2014) 251–260.
- [174] M. Yousefieh, M. Shamanian, A. Saatchi, Influence of Heat Input in Pulsed Current GTAW Process on Microstructure and Corrosion Resistance of Duplex Stainless Steel Welds, *Int. J. Iron Steel Res.* 18 (2011) 65–69.
- [175] K. Devendranath Ramkumar, A. Singh, S. Raghuvanshi, A. Bajpai, T. Solanki, M. Arivarasu, et al., Metallurgical and mechanical characterization of dissimilar welds of austenitic stainless steel and super-duplex stainless steel – A comparative study, *J. Manuf. Process.* 19 (2015) 212–232.
- [176] P.K. Giridharan, N. Murugan, Optimization of pulsed GTA welding process parameters for the welding of AISI 304L stainless steel sheets, *Int. J. Adv. Manuf. Technol.* 40 (2009) 478–489.

- [177] J. Pilhagen, R. Sandström, Influence of nickel on the toughness of lean duplex stainless steel welds, *Mater. Sci. Eng. A.* 602 (2014) 49–57.
- [178] S. Azuma, T. Kudo, H. Miyuki, M. Yamashita, H. Uchida, Effect of nickel alloying on crevice corrosion resistance of stainless steels, *Corros. Sci.* 46 (2004) 2265–2280.
- [179] H. Miyaji, A. Hoshino, H. Nakajima, Effect of nickel addition on the toughness of 18Cr-1 Mo stainless steels, *J. Mater. Sci.* 25 (1990) 673676.
- [180] S. a. Távara, M.D. Chapetti, J.L. Otegui, C. Manfredi, Influence of nickel on the susceptibility to corrosion fatigue of duplex stainless steel welds, *Int. J. Fatigue.* 23 (2001) 619–626.
- [181] J. Wang, P.J. Uggowitzer, R. Magdowski, M.O. Speidel, Nickel-free duplex stainless steels, *Scr. Mater.* 40 (1999) 123–128.
- [182] J.W. Simmons, Overview: high-nitrogen alloying of stainless steels, *Mater. Sci. Eng. A.* 207 (1996) 159–169.
- [183] C.C. Tseng, H.H. Liou, W.W. Tsai, The influence of nitrogen content on corrosion fatigue crack growth behavior of duplex stainless steel, *Mater. Sci. Eng. A.* 344 (2003) 190–200.
- [184] R.B. Bhatt, H.S. Kamat, S.K. Ghosal, P.K. De, Influence of Nitrogen in the Shielding Gas on Corrosion Resistance of Duplex Stainless Steel Welds, *J. Mater. Eng. Perform.* 8 (1999) 591–597.
- [185] S. Kou, *Welding Metallurgy*, Wiley, New York, 1987.
- [186] B. Bauer, A. Topi, S. Kralj, Z. Kozuh, Influence of the gas composition on the geometry of laser-welded joints in duplex stainless steel, *Mater. Technol.* 45 (2011) 413–419.
- [187] R. Lai, Y. Cai, Y. Wua, F. Li, X. Hua, Influence of absorbed nitrogen on microstructure and corrosion resistance of 2205 duplex stainless steel joint processed by fiber laser welding, *J. Mater. Process. Technol.* 231 (2016) 397–405.
- [188] S. Kim, Z. Zhang, Y. Furuya, C. Kang, J. Sung, Q. Ni, et al., Effect of Precipitation of Sigma-Phase and N Addition on the Mechanical Properties in 25Cr–7Ni–4Mo–2W Super Duplex Stainless Steel, *Mater. Trans.* 46 (2005) 1656–1662.
- [189] V.A. Hosseini, S. Wessman, K. Hurtig, L. Karlsson, Nitrogen loss and effects on microstructure in multipass TIG welding of a super duplex stainless steel, *Mater. Des.* 98 (2016) 88–97.
- [190] V. Muthupandi, P. Bala Srinivasan, S.K. Seshadri, S. Sundaresan, Effect of weld metal chemistry and heat input on the structure and properties of duplex stainless steel welds, *Mater. Sci. Eng. A.* 358 (2003) 9–16.
- [191] B. Deng, Y.M. Jiang, J. Gao, J. Li, Effect of annealing treatment on microstructure evolution and the associated corrosion behavior of a super-duplex stainless steel, *J. Alloys Compd.* 493 (2010) 461–464.
- [192] D. Olson, T. Siewert, S. Liu, G. Edward, eds., *ASM Handbook Volume 6: Welding, Brazing and Soldering*, ASM International, 1993.
- [193] D. Du, J. Liu, G. Li, J. Liu, Effect of N₂ addition on microstructure and properties of SAF 2507 duplex stainless steels GTAW welded joint, *Mater. Sci. Forum.* 724 (2012) 127–130.
- [194] K. Devendranath Ramkumar, D. Mishra, B. Ganesh Raj, M.K. Vignesh, G. Thiruvengatam, S.P. Sudharshan, et al., Effect of optimal weld parameters in the microstructure and mechanical properties of autogeneous gas tungsten arc weldments of super-duplex stainless steel UNS S32750, *Mater. Des.* 66 (2015) 356–365.
- [195] M. Sadeghian, M. Shamanian, a. Shafyei, Effect of heat input on microstructure and mechanical properties of dissimilar joints between super duplex stainless steel and high strength low alloy steel, *Mater. Des.* 60 (2014) 678–684.
- [196] F. Tehovnik, B. Arzenšek, B. Arh, D. Skobir, B. Pirnar, B. Žužek, Microstructure evolution in SAF 2507 super duplex stainless steel, *Mater. Tehnol.* 45 (2011) 339–345.
- [197] Z. Wei, J. Laizhu, H. Jincheng, S. Hongmei, Study of mechanical and corrosion properties of a Fe–21.4Cr–6Mn–1.5Ni–0.24N–0.6Mo duplex stainless steel, *Mater. Sci. Eng. A.* 497 (2008) 501–504.
- [198] G. Rondelli, B. Vicentini, A. Cigada, Influence of nitrogen and manganese on localized corrosion behaviour of stainless steels in chloride environments, *Werkstoffe Und Korrosion.* 46 (1995) 628632.
- [199] S. Bernhardsson, No Title, in: *Int. Conf. Duplex Stainl. Steel*, Corros. Resist. Duplex Stainl. Steels, Beaune Bourgogne France, 1991: p. 185.
- [200] A.M. do Nascimento, M.C.F. Jerardi, A.Y. Kina, S.S.M. Tavares, Pitting corrosion resistance of cast duplex stainless steels in 3.5%NaCl solution, *Mater. Charact.* 59 (2008) 1736–1740.
- [201] E.A.M. Hussain, M.J. Robinson, Erosion–corrosion of 2205 duplex stainless steel in flowing seawater containing sand particles, *Corros. Sci.* 49 (2007) 1737–1754.
- [202] S.-H. Jeon, S.-T. Kim, I.-S. Lee, J.-H. Park, K.-T. Kim, J.-S. Kim, et al., Effects of copper addition on the formation of inclusions and the resistance to pitting corrosion of high performance duplex stainless steels, *Corros. Sci.* 53 (2011) 1408–1416.
- [203] R. Merello, F.J. Botana, J. Botella, M.V. Matres, M. Marcos, Influence of chemical composition on the pitting corrosion resistance of non-standard low-Ni high-Mn–N duplex stainless steels, *Corros. Sci.* 45 (2003) 909–921.
- [204] H. Luo, X.G. Li, C.F. Dong, K. Xiao, Effect of solution treatment on pitting behavior of 2205 duplex stainless steel, *Arab. J. Chem.* (2012).

- [205] H. Hoffmeister, G. Lothongkum, Effect of chemical composition of duplex stainless steels on microstructure and pitting corrosion after solution heat treatment and various weld simulation cooling cycle, *Weld. World*. 33 (1994) 91–96.
- [206] Y. Guo, T. Sun, J. Hu, Y. Jiang, L. Jiang, J. Li, Microstructure evolution and pitting corrosion resistance of the Gleeble-simulated heat-affected zone of a newly developed lean duplex stainless steel 2002, *J. Alloys Compd.* 628 (2016) 1031–1040.
- [207] R. Cervo, P. Ferro, A. Tiziani, F. Zucchi, Annealing temperature effects on superduplex stainless steel UNS S32750 welded joints. II: pitting corrosion resistance evaluation, *J. Mater. Sci.* 45 (2010) 4378–4389.
- [208] Y.J. Lindou Chen, Hua Tan, Zhiyu Wang, Jin Li, Influence of cooling rate on microstructure evolution and pitting corrosion resistance in the simulated heat-affected zone of 2304 duplex stainless steelso Title, *Corros. Sci.* 58 (2012) 168–174.
- [209] A. Bhattacharya, P.M. Singh, Electrochemical behaviour of duplex stainless steels in caustic environment, *Corros. Sci.* 53 (2011) 71–81.
- [210] H. Miyuki, T. Kudo, M. Koso, M. Miura, T. Moroishi, 25% Chromium Containing Duplex Phase Stainless Steel for Hot Sea Water Application, *Duplex Stainl. Steels*, R.A. Lula, Ed., (1983) 95–112.
- [211] N. Ebrahimi, M. Momeni, M.H. Moayed, a. Davoodi, Correlation between critical pitting temperature and degree of sensitisation on alloy 2205 duplex stainless steel, *Corros. Sci.* 53 (2011) 637–644.
- [212] J.H. Potgieter, P.A. Olubambi, L. Cornish, C.N. Machio, E.-S.M. Sherif, Influence of nickel additions on the corrosion behaviour of low nitrogen 22% Cr series duplex stainless steels, *Corros. Sci.* 50 (2008) 2572–2579.
- [213] G. Lothongkum, P. Wongpanya, S. Morito, T. Furuhashi, T. Maki, Effect of nitrogen on corrosion behavior of 28Cr-7Ni duplex and microduplex stainless steels in air-saturated 3.5 wt% NaCl solution, *Corros. Sci.* 48 (2006) 137–153.
- [214] G.R.M. Arturo, L.M.V. Hugo, G.H. Rafael, B.B. Egberto, G.S.J. Antonio, Electrochemical Characterization of AISI 2205 Duplex Stainless Steel Welded Joints with Electromagnetic Interaction, *Procedia Mater. Sci.* 8 (2015) 950–958.
- [215] R. Pettersson, O.S. Ab, Corrosion performance of welds in duplex, superduplex and lean duplex stainless steels Corrosion performance of welds in duplex, superduplex and lean duplex stainless steels, (2014) 1–8.
- [216] H. Ha, M. Jang, T. Lee, J. Moon, Interpretation of the relation between ferrite fraction and pitting corrosion resistance of commercial 2205 duplex stainless steel, *Corros. Sci.* 89 (2014) 154–162.
- [217] Z. Sun, M. Kuo, I. Annergren, D. Pan, Effect of dual torch technique on duplex stainless steel welds, *Mater. Sci. Eng. A*. 356 (2003) 274–282.
- [218] O.A. Olaseinde, J. Van Der Merwe, L. Cornish, E.T. Al, Characterization and Corrosion Behaviour of Selected Duplex Stainless Steels in Acidic and Acidic-Chloride Solution, 2014 (2014) 89–93.
- [219] Y. Jiang, H. Tan, Z. Wang, J. Hong, L. Jiang, J. Li, Influence of Creq/Nieq on pitting corrosion resistance and mechanical properties of UNS S32304 duplex stainless steel welded joints, *Corros. Sci.* 70 (2013) 252–259.
- [220] B. Deng, Z. Wang, Y. Jiang, T. Sun, J. Xu, J. Li, Effect of thermal cycles on the corrosion and mechanical properties of UNS S31803 duplex stainless steel, *Corros. Sci.* 51 (2009) 2969–2975.
- [221] A. Pardo, M.C. Merino, A.E. Coy, F. Viejo, R. Arrabal, E. Matykina, Pitting corrosion behaviour of austenitic stainless steels – combining effects of Mn and Mo additions, *Corros. Sci.* 50 (2008) 1796–1806.
- [222] F. Eghbali, M.H. Moayed, a. Davoodi, N. Ebrahimi, Critical pitting temperature (CPT) assessment of 2205 duplex stainless steel in 0.1 M NaCl at various molybdate concentrations, *Corros. Sci.* 53 (2011) 513–522.
- [223] R.F.A. Jargelius-Pettersson, Application of the Pitting Resistance Equivalent Concept to Some Highly Alloyed Austenitic Stainless Steels., *Corrosion*. 54 (1998) 162–168.
- [224] R. Merello, F.J. Botana, J. Botella, M. Marcos, Determination of the weaker phase in the pitting corrosion of non-standard low-Ni high-Mn-N duplex stainless steels, *Mater. Corros.* 55 (2004) 95–101.
- [225] ASTM E3-11, Standard Guide for Preparation of Metallographic Specimens, ASTM International, West Conshohocken, PA, 2011., (n.d.).
- [226] J.C. Lippold, W.A. Baeslack III, I. Varol, Heat-affected zone liquation cracking in austenitic and duplex stainless steels, *Weld. Res. Suppl.* (1992) 1–14.
- [227] J.F. Lancaster, *Metallurgy of Welding*, 6th ed., Woodhead Publishing, 1999.
- [228] J.M. Gómez De Salazar, A. Soria, M.I. Barrera, The effect of N₂ addition upon the MIG welding process of duplex steels, *J. Mater. Sci.* 42 (2007) 4892–4898.
- [229] L.W. Tsay, M.C. Young, C.S. Shin, S.L.I. Chan, Hydrogen-enhanced cracking of 2205 duplex stainless steel, *Fatigue Fract. Eng. Mater. Struct.* 30 (2007) 1228–1236.
- [230] H.Y. Liou, R.I. Hsieh, W.T. Tsai, Microstructure and pitting corrosion in simulated heat-affected zones of duplex stainless steels, *Mater. Chem. Phys.* 74 (2002) 33–42.
- [231] X. Yuan, C. Yun Kang, M.B. Kim, Microstructure and XRD analysis of brazing joint for duplex stainless steel using a Ni-Si-B filler metal, *Mater. Charact.* 60 (2009) 923–931.
- [232] M. Keskitalo, K. Mäntyjärvi, J. Sundqvist, J. Powell, A.F.H. Kaplan, Laser welding of duplex stainless steel with nitrogen as shielding gas, *J. Mater. Process. Tech.* 216 (2015) 381–384.

- [233] B.I. Mendoza, Dissimilar Welding of Superduplex Stainless Steel/HSLA Steel for Offshore Applications Joined by GTAW, *Engineering*. 02 (2010) 520–528.
- [234] J.K. Du, C.H. Wang, K.C. Wang, K.K. Chen, TEM analysis of 2205 duplex stainless steel to determine orientation relationship between M₂₃C₆ carbide and austenite matrix at 950 C, *Intermetallics*. 45 (2014) 80–83.
- [235] R.-I. Hsieh, H.-Y. Liou, Y.-T. Pan, Effects of Cooling Time and Alloying Elements on the Microstructure of the Gleeble-Simulated Heat-Affected Zone of 22% Cr Duplex Stainless Steels, *J. Mater. Eng. Perform.* 10 (2001) 526–536.
- [236] I. V Hagen, M. Keller, Interrelation Between Fabrication Processes and Mechanical Properties of AF 22 Duplex Tubes, in: *Duplex Stainl. Steels Conf. Proc.* (St. Louis, Missouri), 1983: pp. 325–353.
- [237] B.D. Cullity, *Elements of X-ray Diffraction*, second ed., Addison-Wesley Publishing Company, 1978.
- [238] J.W. Elmer, T. a. Palmer, E.D. Specht, Direct Observations of Sigma Phase Formation in Duplex Stainless Steels Using In-Situ Synchrotron X-Ray Diffraction, *Metall. Mater. Trans. A*. 38 (2007) 464–475.
- [239] T. Udayakumar, K. Raja, a. Tanksale Abhijit, P. Sathiyaa, Experimental investigation on mechanical and metallurgical properties of super duplex stainless steel joints using friction welding process, *J. Manuf. Process.* 15 (2013) 558–571.
- [240] DNV Rules, *Submarine Pipelines Systems, Offshore Standard DNV-OSF101*, 2007, (n.d.).
- [241] ASTM E 8-04, *Standard Test Methods for Tension Testing of Metallic Materials*, (2004) 24.
- [242] J. Rawers, M. Grujcic, Effects of metal composition and temperature on the yield strength of nitrogen strengthened stainless steels, *Mater. Sci. Eng. A*. 207 (1996) 188–194.
- [243] F.. Pickering, *Proceeding stainless steels 84*, in: *Proceeding Stainl. Steels 84*, The Institute of Metals, London UK, Goteborg, 1985: p. 12.
- [244] ASM Specialty handbook on stainless steels, 1994. Ohio: American Society for Metals., (n.d.).
- [245] F. Abbassi, S. Mistou, A. Zghal, Failure analysis based on microvoid growth for sheet metal during uniaxial and biaxial tensile tests, *Mater. Des.* 49 (2013) 638–646.
- [246] J.R. Tarpani, M.H.P. Braz, W.W.B. Filho, D. Spinelli, Microstructural and Fractographic Characterization of a Thermally Embrittled Nuclear Grade Steel : Part II - Quenching and Tempering, *Mater. Res.* 5 (2002) 365–371.
- [247] M.C. Young, L.W. Tsay, S.I.I. Chen, M.C. Young, L.W. Tsay, S.I.I. Chen, *Int. J. Fatigue*. 29 (2007) 2115–2112.
- [248] K.N. Krishnan, Mechanism of corrosion fatigue in super duplex stainless steel in 3.5 percent NaCl solution, *Int. J. Fract.* 88 (1998) 205–213.
- [249] T.J. Marrow, J.E. King, Fatigue crack growth mechanisms in a thermally aged duplex stainless steel, *Fatigue Fract. Eng. Mater. Struct.* 17 (1994) 761–771.
- [250] U. Graziano, D. Firrao, G. Taveri, Characterization of Welded Joints (MIG and SAW) on LDX 2101 Duplex SS, *Procedia Eng.* 109 (2015) 484–491.
- [251] Y. Jiang, H. Tan, Z. Wang, J. Hong, L. Jiang, J. Li, Influence of Creq/Nieq on pitting corrosion resistance and mechanical properties of UNS S32304 duplex stainless steel welded joints, *Corros. Sci.* 70 (2013) 252–259.
- [252] Y. Zou, R. Ueji, H. Fujii, Mechanical properties of advanced active-TIG welded duplex stainless steel and ferrite steel, *Mater. Sci. Eng. A*. 620 (2015) 140–148.
- [253] L. Karlsson, S. Pak, L. Ryen, Precipitation of intermetallic phases in 22% Cr duplex stainless weld metals, *Weld. J.* 74 (1995) 28–39.
- [254] A.J. Sedricks, a, *Corrosion*. 42 (1986) 376–389.
- [255] G.. Palit, No Title, *Corrosion*. 49 (1993) 979–991.
- [256] J. Foct, T. Magnin, P. Perrot, J.. Vogt, No Title, *Duplex Stainl. Steels Conf. Proceedings*, Hague, Netherlands. (1986) 59–63.
- [257] M. a E. Jepson, R.L. Higginson, In situ observation of the oxidation of S32101 duplex stainless steel at 900 degrees C, *Corros. Sci.* 59 (2012) 263–269.
- [258] M. Henthorne, (197, *Corrosion*. 26 (1970) 511.
- [259] E.M. Westin, C.-O.A. Olsson, S. Hertzman, Weld oxide formation on lean duplex stainless steel, *Corros. Sci.* 50 (2008) 2620–2634.
- [260] E.M. Westin, Pitting corrosion resistsnce of GTA welded lean duplex stainless steel, *Weld. World*. 64 (2010) 308–321.
- [261] E.M. Westin, PhD Thesis, *Welds in the Lean Duplex Stainless Steel LDX 2101 Effect of Microstructure and Weld Oxides on Corrosion Properties*, 2009.
- [262] T. Ogawa, T. Koseki, Fusion welding of stainless steel, *IIW Doc. IX-1416-86*],. 27 (1988) 65–77.
- [263] R.F. a Jargelius-Pettersson, Electrochemical investigation of the influence of nitrogen alloying on pitting corrosion of austenitic stainless steels, *Corros. Sci.* 41 (1999) 1639–1664.
- [264] T. Omura, T. Kushida, Y. Komizo, Microstructural features and corrosion properties in laser welded duplex stainless steels, *Weld. Int.* 14 (2000) 257–260.

- [265] C.M. Garzón, C.A. Serna, S.D. Brandi, A.J. Ramirez, The relationship between atomic partitioning and corrosion resistance in the weld-heat affected zone microstructures of UNS S32304 duplex stainless steel, *J. Mater. Sci.* 42 (2007) 9021–9029.
- [266] E. Gruzdys, S. Meskinis, Influence of Plasma Transferred Arc Process Parameters on Structure and Mechanical Properties of Wear Resistive NiCrBSi-WC/Co Coatings, *Mater. Sci.* 17 (2011) 140–144.
- [267] B. Venkatesh, K. Sriker, V.S.V. Prabhakar, Wear Characteristics of Hardfacing Alloys: State-of-the-art, *Procedia Mater. Sci.* 10 (2015) 527–532.
- [268] T. Liyanage, G. Fisher, A.P. Gerlich, Influence of alloy chemistry on microstructure and properties in NiCrBSi overlay coatings deposited by plasma transferred arc welding (PTAW), *Surf. Coatings Technol.* 205 (2010) 759–765.
- [269] S. Balasubramanian, R. Lakshminarayanan, A.K. Varahamoorthy, S. Babu, Application of Response Surface Methodology to Prediction of Dilution in Plasma Transferred Arc Hardfacing of Stainless Steel on Carbon Steel, *J. Iron Steel Res. Int.* 16 (2009) 44–53.
- [270] C.S. Ramachandran, V. Balasubramanian, R. Varahamoorthy, Evaluation of Dry Sliding Wear Behaviour of Plasma Transferred Arc Hardfaced Stainless Steel, *J. Iron Steel Res. Int.* 16 (2009) 49–54.
- [271] K. Graf, E.Y. Kuwabara, A.S.C.M.D. Oliveira, Plasma Transferred Arc Hardfacing with a Ni-based Alloy, (n.d.).
- [272] W. Xibao, L. Hua, Metal powder thermal behaviour during the plasma transferred-arc surfacing process, 106 (1998) 156–161.
- [273] P.F. Mendez, N. Barnes, K. Bell, S.D. Borle, S.S. Gajapathi, S.D. Guest, et al., Welding processes for wear resistant overlays, *J. Manuf. Process.* 16 (2014) 4–25.
- [274] V.V. Díaz, J.C. Dutra, A. Sofia, C.D. Oliveira, Hardfacing by Plasma Transferred Arc Process, (2008) 3–21.
- [275] Q.Y. Hou, Y.Z. He, Q.A. Zhang, J.S. Gao, Influence of molybdenum on the microstructure and wear resistance of nickel-based alloy coating obtained by plasma transferred arc process, *Mater. Des.* 28 (2007) 1982–1987.
- [276] R.L. Deuis, J.M. Yellupb, C. Subramanian, Metal-matrix composite coatings by PTA surfacing, 3538 (1998) 299–309.
- [277] K. Siva, N. Murugan, A Study on the Influence of PTAW Process Parameters on Pitting Corrosion Resistance of Nickel Based Overlays, 64 (2013) 1147–1156.
- [278] E. Bourithis, A. Tazedakis, G. Papadimitriou, A study on the surface treatment of “Calmax” tool steel by a plasma transferred arc (PTA) process, *J. Mater. Process. Technol.* 128 (2002) 169–177.
- [279] C. Sudha, P. Shankar, R.V.S. Rao, R. Thirumurugesan, M. Vijayalakshmi, B. Raj, Microchemical and microstructural studies in a PTA weld overlay of Ni – Cr – Si – B alloy on AISI 304L stainless steel, 202 (2008) 2103–2112.
- [280] H. Kim, B. Yoon, C. Lee, Wear performance of the Fe-based alloy coatings produced by plasma transferred arc weld-surfacing process, 249 (2002) 846–852.
- [281] D. Kesavan, M. Kamaraj, Surface & Coatings Technology The microstructure and high temperature wear performance of a nickel base hardfaced coating, 204 (2010) 4034–4043.
- [282] A. Zikin, I. Hussainova, C. Katsich, E. Badisch, C. Tomastik, Surface & Coatings Technology Advanced chromium carbide-based hardfacings, *Surf. Coat. Technol.* 206 (2012) 4270–4278.
- [283] D.I. Uhlenhaut, J.F. Lo, Structure and properties of a hypoeutectic chromium steel processed in the semi-solid state, 54 (2006) 2727–2734.
- [284] S.D. Guest, A.P. Gerlich, P.F. Mendez, Depositing Ni-WC wear resistant coatings with hot-wire assisted Oil Sands and Wear, (n.d.) 1–15.
- [285] P. Wu, H.M. Du, X.L. Chen, Z.Q. Li, H.L. Bai, E.Y. Jiang, Influence of WC particle behavior on the wear resistance properties of Ni – WC composite coatings, 257 (2004) 142–147.
- [286] A.S. Kurlov, A.I. Gusev, Tungsten Carbides and W–C Phase Diagram, *Inorg. Mater.* 42 (2006) 121–127.
- [287] D.N. French, D.A. Thomas, Hardness anisotropy and slip in WC crystals, *Trans. AIME.* 233 (1965) 950–952.
- [288] M. Jonesa, U. Waag, The influence of carbide dissolution on the erosion–corrosion properties of cast tungsten carbide/Ni-based PTAW overlays, *Wear.* 27 (2011) 1314–1324.
- [289] Durum Catalogue, Quality Makes the Difference, (n.d.) 12.
- [290] D.C. Montgomery, Design and analysis of experiment, 5th ed., John Wiley and Sons, 2001.
- [291] A. Sen, S. Mukherjee, An Experimental Study to Predict Optimum Weld Bead Geometry through Effect of Control Parameters for Gas Metal Arc Welding Process in Low Carbon Mild Steel, *Int. J. Mod. Eng. Res.* 3 (2013) 2572–2576.
- [292] D.C. Montgomery, E.A. Peck, G. Vining, Introduction to Linear Regression Analysis, 3rd ed., John Wiley and Sons, New York, 2003.
- [293] K.M.N.M.G. Buvanasekaran, Effects of process parameters on the bead geometry of laser beam butt welded stainless steel sheets, (2007) 1125–1133.
- [294] K. Kato, K. Adachi, Wear Mechanism, Tohoku University, 2001.
- [295] R. Bayer, Mechanical Wear Prediction and Prevention, Marcel Dekker, New York, 1994.

- [296] ASTM Standard G99-05:2005, Standard Test Method for Wear Testing with a Pin-on-Disk Apparatus. ASTM, West Conshohocken, 2005, (n.d.).
- [297] D.M. Kennedy, M.S.J. Hashmi, Methods of wear testing for advanced surface coatings and bulk materials, *J. Mater. Process. Technol.* 77 (1998) 246–253.
- [298] S.Y. Hwang, N.R. Lee, N. Kim, Experiment and Numerical Study of Wear in Cross Roller Thrust Bearings, *Lubricants*. 3 (2015) 447–458.
- [299] X.-M. He, X.-B. Liu, M.-D. Wang, M.-S. Yang, S.-H. Shi, G.-Y. Fu, et al., Elevated temperature dry sliding wear behavior of nickel-based composite coating on austenitic stainless steel deposited by a novel central hollow laser cladding, *Appl. Surf. Sci.* 258 (2011) 535–541.
- [300] M. Dunlap, J.E. Adaskaveg, Introduction to the Scanning Electron Microscope Theory, Practice, & Procedures, in: *Facil. Adv. Instrumentation*, U. C. Davis, 1997: p. 52.
- [301] W. Zhou, R. Apkarian, Z. Lin, Fundamentals of Scanning Electron Microscopy (SEM), in: *Scanning Microsc. Nanotechnology*, Tech. Appl., 2007: pp. 1–40.
- [302] Douglas Vaughan, *ENERGY-DISPERSIVE X-RAY MICROANALYSIS An Introduction*, 1999.
- [303] J. Heath, *Energy Dispersive Spectroscopy* 2nd Ed., 2015.
- [304] Z. Jian, W. Heijing, The physical meanings of 5 basic parameters for an X-Ray diffraction peak and their application, *Chinese J. Geochemistry*. 22 (2003) 38–44.
- [305] S. Kumar, XRD Investigation of Tungsten Carbide Nanoparticles Prepared by Displacement Reaction Technique, *Int. J. Eng. Manag. Res.* 4 (2014) 28–30.
- [306] A.R. Franco Jr, G. Pintaude, A. Sinatora, C.E. Pinedoc, A.P. Tschiptschin, The Use of a Vickers Indenter in Depth Sensing Indentation for Measuring Elastic Modulus and Vickers Hardness, *Mater. Res.* 7 (2004) 483–491.
- [307] M. Zahidi, M. Assoul, J. Mignot, B. Bellaton, A fast 2D/3D optical profilometer for wide range topographical measurement, *Wear*. 165 (1993) 197–203.
- [308] D.-H. Lee, N.-G. Cho, Assessment of surface profile data acquired by a stylus profilometer, *Meas. Sci. Technol.* 23 (2012) 12.
- [309] S. Dallaire, M. Dufour, B. Gauthier, Characterization of Wear Damage in Coatings by Optical Profilometry, *J. Therm. Spray Technol.* 2 (1993) 363–368.
- [310] A.T. Pérez, A.H. Battez, G. García-Atance, J.L. Viesca, R. González, M. Hadfield, Use of optical profilometry in the ASTM D4172 standard, *Wear*. 271 (2011) 2963–2967.
- [311] H. Cheng, J. Yi, Z. Fang, S. Dai, X. Zhao, Tribology Property of Laser Cladding Crack Free Ni/WC Composite Coating, *Mater. Trans.* 54 (2013) 50–55.
- [312] P.F. Mendez, N. Barnes, K. Bell, S.D. Borle, S.S. Gajapathi, S.D. Guest, et al., Welding processes for wear resistant overlays, 16 (2014) 4–25.
- [313] P. Balu, S. Hamid, R. Kovacevi, Finite element modeling of heat transfer in single and multilayered deposits of Ni-WC produced by the laser-based powder deposition process, *Int. J. Adv. Manuf. Technol.* 68 (2013) 85–98.
- [314] A. Zikin, S. Ilo, P. Kulu, I. Hussainova, C. Katsich, E. Badisch, Plasma Transferred ARC (PTA) Hardfacing of Recycled Hardmetal Reinforced Nickel-matrix Surface Composites, *Mater. Sci.* 18 (2012) 12–17.
- [315] A.E. Yaedu, A.S.C.M.D. Oliveira, Cobalt based alloy PTA hardfacing on different substrate steels, *Mater. Sci. Technol.* 21 (2005) 459–466.
- [316] S. Balamurugan, N. Murugan, Deign of Experiment and Optimization of Plasma Transferred Arc Hardfacing on Structural Steel with Titanium Carbide, *Res. J. Appl. Sci. Eng. Technol.* 7 (2014) 2362–2370.
- [317] M. a. García-Rentería, V.H. López-Morelos, R. García-Hernández, L. Dzib-Pérez, E.M. García-Ochoa, J. González-Sánchez, Improvement of localised corrosion resistance of AISI 2205 Duplex Stainless Steel joints made by gas metal arc welding under electromagnetic interaction of low intensity, *Appl. Surf. Sci.* 321 (2014) 252–260.
- [318] T. Juang SC, Process parameter selection for optimizing the weld pool geometry in the tungsten inert gas welding of stainless steel, *J. Mater. Process. Technol.* 122 (2002) 33–37.
- [319] A. Aguirre, A. Arizmendi, C. De Investigación, A.S.C. Unidad, A. Norte, Analysis of weld bead parameters of overlay deposited on D2 steel components by plasma transferred arc (PTA) process ., 755 (2013) 39–45.
- [320] Q. Ming, L.C. Lim, Z.D. Chen, Laser cladding of nickel-based hardfacing alloys, 106 (1998) 174–182.
- [321] P.K. Palani, N. Murugan, Optimization of weld bead geometry for stainless steel claddings deposited by FCAW, 190 (2007) 291–299.
- [322] P.K.P.N. Murugan, Development of mathematical models for prediction of weld bead geometry in cladding by flux cored arc welding, (2006) 669–676.
- [323] K. Siva, N. Murugan, V.P. Raghupathy, Modelling , analysis and optimisation of weld bead parameters of nickel based overlay deposited by plasma transferred arc surfacing, 3 (n.d.) 174–182.
- [324] J.F. Flores, A. Neville, N. Kapur, A. Gnanavelu, An experimental study of the erosion – corrosion behavior of plasma transferred arc MMCs, 267 (2009) 213–222.

- [325] Q.Y. Hou, Z. Huang, J. Tao, Influence of nano-Al₂O₃ particles on the microstructure and wear resistance of the nickel-based alloy coating deposited by plasma transferred arc overlay welding, *Surf. Coat. Technol.* 205 (2011) 2806–2812.
- [326] F. García-Vázquez, A. Aguirre, A. Arizmendi, H.M. Hernández-García, L. Santiago-Bautista, J. Acevedo, et al., Analysis of weld bead parameters of overlay deposited on D2 steel components by plasma transferred arc (PTA) process., *Mater. Sci. Forume.* 755 (2013) 39–45.
- [327] T. Liyanage, G. Fisher, A.P. Gerlich, Microstructures and abrasive wear performance of PTAW deposited Ni–WC overlays using different Ni-alloy chemistries, *Wear.* 275 (2012) 345–354.
- [328] Q.Y. Hou, Influence of molybdenum on the microstructure and properties of a FeCrBSi alloy coating deposited by plasma transferred arc hardfacing, *Surf. Coat. Technol.* 225 (2013) 11–20.
- [329] F. Fernandes, A. Ramalho, A. Loureiro, J.M. Guilemany, M. Torrell, A. Cavaleiro, Influence of nanostructured ZrO₂ additions on the wear resistance of Ni-based alloy coatings deposited by APS process, *Wear.* 303 (2013) 591–601.
- [330] K. Borodianskiy, M. Zinigrad, Mechanical Properties and Microstructure Characterization of Al-Si Cast Alloys Formation Using Carbide Nanoparticles, *J. Mater. Sci. Appl.* 1 (2015) 85–90.
- [331] P. Farahmand, R. Kovacevic, Surface & Coatings Technology Corrosion and wear behavior of laser clad Ni – WC coatings, 276 (2015) 121–135.
- [332] L. Bourithis, G.D. Papadimitriou, The effect of microstructure and wear conditions on the wear resistance of steel metal matrix composites fabricated with PTA alloying technique, *Wear.* 266 (2009) 1155–1164.
- [333] D. Sun, W. Wang, Z. Xuan, Y. Xu, Z. Zhou, Effect of alloying elements on microstructure and erosion resistance of Fe-C-Cr weld surfacing layer, *J. Mater. Sci. Technol.* 19 (2003) 351–354.
- [334] S.C. Gallo, N. Alam, R.O. Donnell, In-situ precipitation of TiC upon PTA hardfacing with grey cast iron and titanium for enhanced wear resistance, *Surf. Coat. Technol.* 214 (2013) 63–68.
- [335] Z. Kamdi, P.H. Shipway, K.T. Voisey, A.J. Sturgeon, Abrasive wear behaviour of conventional and large-particle tungsten carbide-based cermet coatings as a function of abrasive size and type, 271 (2011) 1264–1272.
- [336] G. Yang, P. Gao, C. Li, C. Li, Simultaneous strengthening and toughening effects in WC–(nanoWC–Co), *Scr. Mater.* 66 (2012) 777–780.
- [337] C. Osman Nuri, Microstructure and wear properties of WC particle reinforced composite coating on Ti6Al4V alloy produced by the plasma transferred arc method, *Appl. Surf. Sci.* 274 (2013) 334–340.
- [338] H. Chandler, Heat Treaters Guide Practices and Procedures for Iron and Steels, ASM International, Materials Park, Ohio, 1994.
- [339] W.C. Oliver, G.M. Pharr, Improved technique for determining hardness and elastic modulus using load and displacement sensing indentation experiments, *J. Mater. Res.* 7 (1992) 1564–1580.
- [340] M. Ulutan, C. Osman Nuri, H. Gasan, E. Umit, Effect of Different Surface Treatment Methods on the Friction and Wear Behavior of AISI 4140 Steel, *J. Mater. Sci. Technol.* 26 (2010) 251–257.
- [341] R. Sekharbabu, H.K. Rafi, K.P. Rao, Characterization of D2 tool steel friction surfaced coatings over low carbon steel, 50 (2013) 543–550.
- [342] G. Robert, Tool steels. 5th ed. ASM, International, ASM International, 1998.
- [343] V. Stoica, R. Ahmed, T. Itsukaichi, Influence of heat-treatment on the sliding wear of thermal spray cermet coatings, 199 (2005) 7–21.
- [344] M.F. Morks, Y. Gao, N.F. Fahim, F.U. Yingqing, Microstructure and hardness properties of cermet coating sprayed by low power plasma, *Mater. Lett.* 60 (2006) 1049–1053.
- [345] V.K. Balla, S. Bose, A. Bandyopadhyay, Microstructure and wear properties of laser deposited WC–12 % Co composites, *Mater. Sci. Eng. A.* 527 (2010) 6677–6682.
- [346] R. Liu, S.Q. Xi, S. Kapoor, X.J. Wu, Effect of chemical composition on solidification, microstructure and hardness of Co-Cr-Mo-Ni alloy systems, *IJRRAS.* 5 (2010) 110–122.
- [347] N. Yasavol, A. Abdollah-zadeh, M.T. Vieira, H.R. Jafarian, Microstructure evolution and texture development in a friction stir-processed AISI D2 tool steel, *Appl. Surf. Sci.* 293 (2014) 151–159.
- [348] P. Sheppard, H. Koiprasert, Effect of W dissolution in NiCrBSi – WC and NiBSi – WC arc sprayed coatings on wear behaviors, 317 (2014) 194–200.
- [349] W. Song, G. Yang, J. Lu, Y. Hao, Microstructure of Ni / WC surface composite on a copper substrate, 446 (2007) 537–542.
- [350] M. Nouri, F. Malek, Effect of Welding Parameters on Dilution and Weld Bead Geometry in Cladding, 23 (2007) 817–822.
- [351] E.B. Dasgupta, S. Mukherjee, Optimisation of Weld Bead Parameters of Nickel Based Overlay Deposited By Plasma Transferred Arc Surfacing, 3 (2013) 1330–1335.
- [352] D.S. Nagesh, G.L. Datta, Prediction of weld bead geometry and penetration in shielded metal-arc welding using artificial neural networks, 123 (2002) 303–312.
- [353] M. Kirchgäßner, E. Badisch, F. Franek, Behaviour of iron-based hardfacing alloys under abrasion and impact, 265 (2008) 772–779.

- [354] L. Bourithis, S. Papaefthymiou, G. Papadimitriou, Plasma transferred arc boriding of a low carbon steel : microstructure and wear properties, *Appl. Surf. Sci.* 200 (2002) 203–218.
- [355] S.W. Huang, M. Samandi, M. Brandt, Abrasive wear performance and microstructure of laser clad WC / Ni layers, 256 (2004) 1095–1105.
- [356] Q. Li, T.C. Lei, W.Z. Chen, Microstructural characterization of WCp reinforced Ni – Cr – B – Si – C composite coatings, 114 (1999) 285–291.
- [357] I.C. Grigorescu, C. Di Rauso, R. Drira-halouani, B. Lavelle, R. Di Giampaolo, J. Lira, Phase characterization in Ni alloy-hard carbide composites for fused coatings, 77 (1995) 494–498.
- [358] M.J. Tobar, C. Álvarez, J.M. Amado, G. Rodríguez, A. Yáñez, Morphology and characterization of laser clad composite NiCrBSi – WC coatings on stainless steel, 200 (2006) 6313–6317.
- [359] Q.Y. Hou, Z.Y. Huang, N. Shi, J.S. Gao, Effects of molybdenum on the microstructure and wear resistance of nickel-based hardfacing alloys investigated using Rietveld method, 9 (2008) 2767–2772.
- [360] L.M. Chang, M.Z. An, H.F. Guo, S.Y. Shi, Microstructure and properties of Ni–Co/nano-Al₂O₃ composite coatings by pulse reversal current electrodeposition, *Appl. Surf. Sci.* 253 (2006) 2132–2137.
- [361] K.L. Wang, Q.B. Zhang, M.L. Sun, X.G. Wei, Microstructural characteristics of laser clad coatings with rare earth metal elements, 139 (2003) 448–452.
- [362] Q.Y. Hou, J.T. Wang, Influence of CeO₂ on the microstructure and wear resistance of iron-based alloy coating studied by Rietveld refinement method, *Surf. Coat. Technol.* 204 (2010) 2677–2682.
- [363] M. Li, Y. He, X. Yuan, S. Zhang, Microstructure of Al₂O₃ nanocrystalline cobalt-based alloy composite coatings by laser deposition, *Mater. Des.* 27 (2006) 1114–1119.
- [364] P.Q. La, S.G. Liu, Effect of aluminum on microstructure and mechanical properties of 310S steel, *J. Mater. Eng.* (2009) 36–40.
- [365] R. Chattopadhyay, *Surface Wear: Analysis, Treatment, and Prevention*, ASM International, Technology & Engineering, 2001.
- [366] P. Suresh Babu, B. Basu, G. Sundararajan, Processing – structure – property correlation and decarburization phenomenon in detonation sprayed WC – 12Co coatings, *Acta Mater.* 56 (2008) 5012–5026.
- [367] H. Kim, B. Yoon, C. Lee, Sliding wear performance in molten Zn–Al bath of cobalt-based overlayers produced by plasma-transferred arc weld-surfacing, *Wear.* 254 (2003) 408–414.
- [368] J.M. Guilemany, J.M. De Paco, J. Nutting, J.R. Miguel, Characterization of the W₂C Phase Formed during the High Velocity Oxygen Fuel Spraying of a W₂C-12 pct Co Powder, *Metall. Mater. Trans. A.* 30 (1999) 1913–1921.
- [369] J. Gong, T. Tang, Y. Xiao, Effect of WC/W₂C on the microstructure and abrasion resistance of high-boron hardfacing alloys, *Acta Met. Sin(Engl. Lett.)*. 23 (2010) 439–445.
- [370] N.S. Lim, S. Das, S.Y. Park, M.C. Kim, C.G. Park, Fabrication and microstructural characterization of nano-structured WC/Co coatings, *Surf. Coat. Technol.* 205 (2010) 430–435.
- [371] Q. Zhan, L. Yu, F. Ye, Q. Xue, H. Li, Quantitative evaluation of the decarburization and microstructure evolution of WC–Co during plasma spraying, *Surf. Coat. Technol.* 206 (2012) 4068–4074.
- [372] J. Yuan, Q. Zhan, J. Huang, S. Ding, H. Li, Decarburization mechanisms of WCeCo during thermal spraying : Insights from controlled carbon loss and microstructure characterization, *Mater. Chem. Phys.* 142 (2013) 165–171.
- [373] M. Rombouts, R. Persoons, E. Geerinckx, R. Kemps, M. Mertens, W. Hendrix, et al., Development and characterization of nickel based tungsten carbide laser clad coatings, 5 (2010) 333–339.
- [374] C. Guoqing, F. Xuesong, W. Yanhui, L. Shan, Z. Wenlong, Microstructure and wear properties of nickel-based surfacing deposited by plasma transferred arc welding, *Surf. Coat. Technol.* 228 (2013) 276–282.
- [375] Y. Yuan, Z. Li, Effects of rod carbide size, content, loading and sliding distance on the friction and wear behaviors of (Cr ,Fe)₇C₃ -reinforced α -Fe based composite coating produced via PTA welding process, *Surf. Coat. Technol.* 248 (2014) 9–22.
- [376] E. Badisch, M. Kirchgaßner, Influence of welding parameters on microstructure and wear behaviour of a typical NiCrBSi hardfacing alloy reinforced with tungsten carbide, *Surf. Coatings Technol.* 202 (2008) 6016–6022.
- [377] P.H. Shipway, D.G. McCartney, T. Sudaprasert, Sliding wear behaviour of conventional and nanostructured HVOF sprayed WC–Co coatings, *Wear.* 259 (2005) 820–827.
- [378] S. Zhou, X. Dai, H. Zheng, Microstructure and wear resistance of Fe-based WC coating by multi-track overlapping laser induction hybrid rapid cladding, *Opt. Laser Technol.* 44 (2012) 190–197.
- [379] M.A. Hamidzadeh, M. Meratian, M.M. Zahrani, A study on the microstructure and mechanical properties of AISI D2 tool steel modified by niobium, *Mater. Sci. Eng. A.* 556 (2012) 758–766.
- [380] S. Sharma, Wear study of Ni–WC composite coating modified with CeO₂, *Int J Adv Manuf Technol.* 61 (2012) 889–900.
- [381] J. Larsen-Basse, E.T. Koyanagi, Abrasion of WC-Co alloy by quartz, *J. Lubr. Technol. ASME.* 101 (1979) 208–211.

- [382] S. Zafar, A. Kumar, Dry sliding wear performance of nanostructured WC–12Co deposited through microwave cladding, *Tribol. Int.* 91 (2015) 14–22.
- [383] J.D.M. Van Otterloo, J.T. De Hosson, Microstructural features and mechanical properties of a cobalt-based laser coating, *Acta Mater.* 45 (1997) 1225–1236.
- [384] D.K. Chaudhun, D. Xie, A.N. Lakshmanan, The influence of stacking fault energy on the wear resistance of nickel base alloys, *Wear.* 9 (1997) 140–152.
- [385] J.M.U. Guilemany, J.M. Miguel, S. Vizcaino, F. Climent, Role of three-body abrasion wear in the sliding wear behaviour of WC . Co coatings obtained by thermal spraying, *Surf. Coat. Technol.* 140 (2001) 141–146.
- [386] K. Holmberg, A. Matthews, Coatings tribology-properties, mechanisms, techniques and applications in surface engineering, *Tribol. Interface Eng. Ser.* 28 (2009).
- [387] R. Tyagi, D. Xiong, J. Li, Effect of load and sliding speed on friction and wear behavior of silver/h-BN containing Ni-base P/M composites, *Wear.* 270 (2011) 423–430.